THE UNIVERSITY of ADELAIDE

New geochronological tool for Cu-Au mineralisation in the Arabian Shield, Saudi Arabia: Testing in-situ Rb-Sr dating via LA-ICP-MS/MS

Ahmad A. Redaa

Department of Earth Sciences
School of Physical Sciences
The University of Adelaide

This thesis is submitted in fulfilment of the requirements
for the degree of Doctor of Philosophy

January 2022

Contents

ABSTRACT

In-situ Rb-Sr dating by a laser ablation inductively-coupled plasma mass spectrometry (LA-ICP-MS/MS) has been recently developed for geoscience applications, taking advantage of a reaction cell capability of new generation ICP MS/MS instruments to resolve isobaric interferences specifically for beta-decay geochronometers. This development allows a rapid and interference free analysis of ^{87}Rb and ^{87}Sr isotopes via the reaction/collision cell filled with a reactive gas such as N_2O and or SF_6 to separate more reactive Sr ions from inert Rb species. The other advantage of the collision cell ICP-MS/MS instruments is their compatibility with a LA system which in tandem open up *in-situ* Rb-Sr dating applications of various geological materials at micro-scale level and directly from 'solid' samples or minerals of interest. Yet, the main drawback or limitation of a successful application of the LA-ICP-MS/MS systems for Rb-Sr dating are currently poorly quantified and unconstrained 'elemental fractionation phenomena' and 'matrix effects', as well as the general lack of suitable chemically/mineralogically well characterised reference materials (i.e., mineral-specific standards) that are homogeneous at micro-scale level. Thus, this PhD thesis aims to fill some of these knowledge gaps by investigating and quantifying the impact of the elemental fractionation and matrix effects on the accuracy and precision of *in-situ* Rb-Sr dating of selected K-rich silicate minerals (micas, feldspar and clays), including phlogopite, biotite, K-feldspar and glauconite (Mica-Mg, Mica-Fe, FK-N and GL-O). These minerals were formed as nano-powders and fused glasses and analysed by the LA-ICP-MS/MS approach. Results are assessed and discussed in terms of suitability of the above materials/mineral standards for the *in-situ* Rb-Sr dating applications. Overall, results suggest that nano-powder mineral standards represent suitable reference materials for reliable *in-situ* Rb-Sr dating applications, but 'chemical matching' between unknown sample/mineral and nano-powder standard is important to minimize the above-mentioned 'matrix effects' and their impact on the precision and accuracy of acquired Rb-Sr data. Finally, our validated *in-situ* Rb-Sr dating approach (using Mica-Mg-NP as a standard) was also used on a case study to constrain the timing and origin of a Cu-Au mineralisation in the Mount Ablah region in Saudi Arabia (Arabian Shield), based on the analysis and *in-situ* dating of selected micas and feldspars associated with the above mineralised system linked to a regional shear zone. The results and acquired *in-situ* Rb-Sr ages indicate that the development of the Umm Farwah shear zone occurred at 651 $\pm$ 20 Ma, followed by the emplacement of Mount Ablah pegmatite dated at 625 $\pm$ 19 Ma. Subsequent greisenisation of local

igneous rocks took place between 613 Ma and 589 Ma, followed by a younger reactivation event(s) - dated between 580 Ma and 530 Ma - that are believed to form the Cu-Au mineralisation in the Mount Ablah region.

DECLARATION

I certify that this work contains no material which has been accepted for the award of any other degree or diploma in my name, in any university or other tertiary institution and, to the best of my knowledge and belief, contains no material previously published or written by another person, except where due reference has been made in the text. In addition, I certify that no part of this work will, in the future, be used in a submission in my name, for any other degree or diploma in any university or other tertiary institution without the prior approval of the University of Adelaide and where applicable, any partner institution responsible for the joint-award of this degree.

I acknowledge that copyright of published works contained within the thesis resides with the copyright holder(s) of those works.

I also give permission for the digital version of my thesis to be made available on the web, via the University's digital research repository, the Library Search and also through web search engines, unless permission has been granted by the University to restrict access for a period of time.

I acknowledge the support I have received for my research through the provision of King Abdulaziz University and Saudi Arabian Cultural Mission in Australia.

Ahmad A. Redaa

21st January, 2022

ACKNOWLEDGEMENTS

To my wife Afnan and to my fabulous little boys Battal and Saif, I am so grateful for having you with me during my PhD journey, away from our home country. Thank you for your patient, understanding and your endless support and love. I know that this was not an easy journey on all of us, but I strongly believe that, by passing these times, we can go together, far beyond, and I look forward to our next adventures.

To my dad, sorry for that you are not with us today, but this thesis is for your memory. Thank you for you love and support, and I am always including you in my prayer.

To my mum, thank you so much for your never-ending love and support, and I will forever appreciate the sacrifices that you have made for me.

To my brothers and sister, I can't wait to back home and unite with you again. During my studying abroad, annoying you over our daily video calls is my favorite time during the day. Thank you for your love and support.

To my supervisors Juraj Farkaš and Alan Collins, this work would not be done without your guidance and support. Juraj, you have played a significant role in me which is shaping me into what I am today, and I am so grateful having you as a supervisor. Alan, I always benefit from our discussions, and I am grateful for you pushing me to learn how to code in R at early stage in my PhD. Also, I always appreciate your end-of-the year messages and invitations to celebrate different occasions during the last few years. You have been always supportive in different ways.

To Sarah Gilbert, Ben Wade, Ken Neubauer, Stefan Loehr and David Bruce, I learnt a lot from you about the analytical equipment and data processing. Thank you so much for your time and patient. Without your assistance, I would not be able to complete my project.

To my mentors Prof. Hesham Harbi and Prof. Ahmed Hassan, thank you for your guidance and support during my PhD work.

Publications arising from this PhD research

Journal articles

Redaa, A, Farkaš, J, Gilbert, S, Collins, AS, Wade, B, Löhr, s, Zack, T & Garbe-Schönberg, D 2021, 'Assessment of elemental fractionation and matrix effects during in-situ Rb–Sr dating of phlogopite by LA-ICP-MS/MS: Implications for the accuracy and precision of mineral ages', *Journal of Analytical Atomic Spectrometry*, no. 36, pp. 322-344.

Redaa, A, Farkaš, J, Hassan, A, Collins, AS, Gilbert, S, & Löhr, S 2022, 'Constraints from *in-situ* Rb-Sr dating on the timing of tectono-thermal events in the Umm Farwah shear zone and associated Cu-Au mineralisation in the Southern Arabian Shield, Saudi Arabia', Journal of Asian Earth Science, vol. 224, p. 105037.

Other journal articles produced during PhD

Subarkah, D, Blades, ML, Collins, AS, Farkaš, J, Gilbert, S, Löhr, SC, Redaa, A, Cassidy, E & Zack, T 2021, 'Unraveling the histories of Proterozoic shales through in situ Rb-Sr dating and trace element laser ablation analysis', *Geology*, vol. In press.

Shanshan, L, Santosh, M, Farkas, J, Redaa, A, Ganguly, S, Kim, SW, Zhang, C, Gilbert, S & Zack, T 2020, 'Coupled U-Pb and Rb-Sr laser ablation geochronology trace Archean to Proterozoic crustal evolution in the Dharwar Craton, India', *Precambrian Research*, vol. 343, p. 105709.

Armistead, SE, Collins, AS, Redaa, A, Jepson, G, Gillespie, J, Gilbert, S, Blades, ML, Foden, JD & Razakamanana, T 2020, 'Structural evolution and medium-temperature thermochronology of central Madagascar: implications for Gondwana amalgamation', *Journal of the Geological Society*, vol. 177, pp. 784-798.

Conference abstracts

Redaa, A, Ahmed, AH, Farkas, J, Gilbert, SE, Zack, T & Collins, AS 2018, 'A New Technique in Dating Proterozoic Shear Zones: In-situ Rb-Sr dating of Umm Farwah Shear zone, Arabian Shield using LA-QQQ', presented at Australian Geoscience Council

Convention, Adelaide, Australia.

Redaa, A, Farkas, J, Gilbert, SE, Zack, T, Fryer, F, Wade, B & Collins, AS 2018, 'Testing the limits of in-situ Rb-Sr dating of igneous minerals by LA-ICP-QQQ', presented at Geoanalysis 2018, Sydney, Australia.

Redaa, A, Jensen, L, Farkas, J, Zack, T, Collins, AS & Foden, J 2018, 'The first in-situ Rb/Sr dating of biotite in the Arabian Shield', presented at 12th International Geological Conference, Jeddah, Saudi Arabia.

CHAPTER 1

Introduction and background

1.1 Motivation

In-situ Rb-Sr dating has been recently developed to exploit the analytical capabilities of a reaction cell coupled with an inductively coupled plasma mass-spectrometry (ICP-MS/MS) and a laser-ablation (LA) and/or solution based sample introduction systems (Bolea-Fernandez et al., 2016; Hogmalm et al., 2017; Zack and Hogmalm, 2016). Attaching the LA system to the ICP-MS/MS offers a direct *in-situ* Rb-Sr dating of K- and Rb-rich geological materials (micas, feldspars, clay minerals) to rapidly and cost-efficiently constrain the 'age' or the timing of geological events. These include phenomena such as the crystallisation of igneous rocks, metamorphism, hydrothermal alterations, formation of ore deposits, and the timing of deposition of sedimentary sequences (Armistead et al., 2020; Bevan et al., 2021; Laureijs, Coogan, and Spence, 2021b; Olierook et al., 2020; Şengün et al., 2019; Li et al., 2020; Subarkah et al., 2021; Tillberg et al., 2020). Briefly, the Rb-Sr dating of minerals and rocks requires precise measurements of $^{87}Rb/^{86}Sr$ and $^{87}Sr/^{86}Sr$ from the phases of interest, and from these data the Rb-Sr age can be calculated based on the slope of a line of best fit (i.e., isochron) fitted through the Rb-Sr data plotted in a cross-plot (i.e., Nicolaysen diagram) where $^{87}Rb/^{86}Sr$ and $^{87}Sr/^{86}Sr$ data are plotted on a horizontal and vertical axes, respectively. Traditionally, the $^{87}Rb/^{86}Sr$ and $^{87}Sr/^{86}Sr$ ratios have been analysed by a multi-collector (MC) mass spectrometer instruments (MS) such as TIMS (Thermal Ionisation MS) and/or MC-ICP-MS (Inductively Coupled Plasma MS) which can distinguish atoms/ions and their isotopes based on their mass-to-charge ratio (m/z). However, the above mass spectrometers (TIMS and MC-ICP MS) cannot separate or resolve isobaric ^{87}Rb and ^{87}Sr ions, which are thus detected simultaneously at the same mass of 87 amu (atomic mass units), which is a phenomenon known as isobaric interference. This interference can be resolved by chemically separating Rb from Sr via an eluent chromatography (using cation-exchange or Sr-specific resins), which however is a time consuming process that needs to be done prior to TIMS and MC-ICP-MS analyses. Importantly, the recent development of ICP-MS/MS systems allow for a direct or 'online' separation of isobaric Rb from Sr interferences during the analysis within an instrument, using a reaction/collision cell. The latter can be filled with a specific reaction gas, such as N_2O and FS_6, which can convert $^{87}Sr^+$ to a reaction product (i.e., $^{87}Sr^{16}O^+$ or $^{87}Sr^{19}F^+$, respectively) that in turn can be measured as 'mass-shifted' Sr species (Hogmalm et al., 2017), while $^{87}Rb^+$ is inert to the above gases.

Another key advantage of the ICP-MS/MS is its capability to be connected with a

laser ablation system thus allowing for a direct or *in-situ* Rb-Sr dating which was not feasible with the currently available or commercial MC ICP-MS and/or TIMS instruments. This novel LA-ICP-MS/MS approach thus allows a rapid and *in-situ* dating at micro-scale level. However, using the LA system for *in-situ* Rb-Sr dating can introduce various undesirable analytical effects and artifacts, such as elemental or down-hole fractionation effects as well as matrix effects (discussed in detail in Chapter 2), thus impacting and biasing the accuracy and precision of obtained Rb and Sr relative to the true values. The impact of these LA and ICP related analytical effects on the accuracy of data has been investigated extensively for other isotope systems or geochronometers such as the *in-situ* U-Pb dating (e.g., Jackson et al., 2004; Marillo-Sialer et al., 2016; Marillo-Sialer et al., 2014), and several 'calibration' strategies have been developed and validated to improve the accuracy of the obtained data and U-Pb ages using various certified reference materials (Agatemor and Beauchemin, 2011; Lin et al., 2016; Marillo-Sialer et al., 2014). In contrast, the impact of the above effects on the accuracy of *in-situ* Rb-Sr dating has not been yet investigated systematically for Rb-Sr isotope system/geochronometer, but it is anticipated that these effects can be minimised in a similar way as done for U-Pb application, by calibrating or normalising the acquired Rb-Sr data to certified reference materials with known $^{87}Rb/^{86}Sr$ and $^{87}Sr/^{86}Sr$ ratios and 'ages'. Thus, such reference material should be well characterised with respect to Rb-Sr isotopic composition, and ideally a sample of interest (i.e., a specific mineral) should be also chemically matched (i.e., matrix-matched) with such reference material (i.e., both having identical or similar chemical composition and physical properties) to obtain robust and accurate Rb-Sr ages. Currently, only a limited number of verified and well-characterised reference materials (RM) are available for *in-situ* Rb-Sr analysis and dating, and such lack of suitable matrix-matched RMs is the main challenge that has limited this novel dating technique to be used more widely for various applications by a geoscience community. Thus, this thesis aims to fill such knowledge gaps by investigating (i) the impact of the elemental fraction and matrix effects on the accuracy of the Rb-Sr ages acquired via the LA-ICP-MS/MS, and also via (ii) testing and calibration of various RMs such as nano-powders and fused mineral glasses for the *in-situ* Rb-Sr dating. Finally, the third aim of the thesis is to (iii) apply this novel *in-situ* Rb-Sr dating approach as a tool to further constrain the timing of Cu-Au mineralisation and associated geological (igneous, metamorphic and alteration) events using a case study in Saudi Arabia, specifically a copper-gold mineralisation in the Mount Ablah area in the Southern Arabian Shield.

1.2 Background

1.2.1 Rb-Sr dating

The Rb-Sr dating system is one of the negative beta-decay radiometric geochronological tools that relies on the constant and natural decay of a radioactive isotope ^{87}Rb (parent) to produce a radiogenic ^{87}Sr isotope (daughter). Natural Rb has two isotopes ^{85}Rb and ^{87}Rb, and their relative abundances are 72.17% and 27.83%, respectively (Rosman and Taylor, 1998). The radionuclide ^{87}Rb emits negative beta particles to generate ^{87}Sr at a decay rate (i.e., decay constant λ) of $1.3972 \pm 0.0045 \times 10^{-11}$ yr^{-1}, with a corresponding half-life of 49.61 $\pm$ 0.16 Ga (Villa et al., 2015). Thus, the Rb-Sr dating system can be used to constrain the timing or 'absolute ages' of geological and planetary events that occurred since the formation of the Solar System and/or early Earth evolution, assuming a 'closed system' behaviour for the Rb and Sr isotopes.

Overall, a mineral system can be a closed system for a certain isotopic pair (i.e., Rb and Sr) at certain temperature known as the closure temperature. When this temperature is reached, the mineral becomes closed to diffusional loss of atoms, and the radiogenic atoms that are produced via decay process, such as Sr, will start accumulation and recording the age information. Some common Rb bearing minerals such as muscovite have relatively higher closure temperature constrained at ca. 500 °C compared to other Rb bearing minerals such as biotite which has closure temperature of ca. 300 °C (Dodson, 1973; Eberlei et al., 2015). At rapid cooling conditions, these minerals will yield similar ages that can be considered as a crystallisation age, and these ages generally will agree with other isotopic systems that have higher closure temperature such as U-Pb in zircon. At slow cooling conditions, minerals with high closure temperature will crystallise and become a closed system before minerals with lower closure temperature that remain open to the diffusional exchange of elements until their closure temperature is achieved. Then, the Rb-Sr system in the above minerals can be used to constrain the cooling history. However, thermal events with relatively low temperature such as metamorphism and metasomatism can disturb the isotopic system and cause diffusion and mobility of Rb and Sr. Such thermal events can erase the crystallisation age and reset the system, and in this case, the Rb-Sr system can be used to constrain the timing of these thermal events.

If the Rb-Sr isotope system remains 'closed' since the last event, the timing of that event can be calculated using the following geochronology equation:

$$^{87}Sr_p = ^{87}Sr_i + ^{87}Rb_p \times (e^{\lambda t} - 1) \quad (1.1)$$

where, $^{87}Sr_p$ is the amount of radiogenic Sr in the system at 'present' or specific time = t, $^{87}Sr_i$ is the initial amount of ^{87}Sr at the time of mineral/rock formation (t = 0), and $^{87}Rb_p$ is the amount of the radioactive Rb at 'present' or specific time = t, and e is Euler's number (which approximately equals 2.71828) and λ is the above-mentioned decay constant for Rb-Sr system. As it is challenging to measure precisely the abundance of ^{87}Rb and ^{87}Sr isotopes in the sample, the above are rather expressed relative to the abundance of stable ^{86}Sr isotope, providing more precise data (i.e., isotope ratios) and thus Rb-Sr ages. Consequently, the above geochronology equation (Eq. 1.1) can be modified using ^{87}Rb/^{86}Sr and ^{87}Sr/^{86}Sr ratios (rather than ^{87}Rb and ^{87}Sr abundances) into the following formula or equation:

$$(\frac{^{87}Sr}{^{86}Sr})_p = (\frac{^{87}Sr}{^{86}Sr})_i + (\frac{^{87}Rb}{^{86}Sr})_p \times (e^{\lambda t} - 1) \quad (1.2)$$

where the age (t) can be calculated by rearranging the Eq 1.2 and expressing 't':

$$t = \frac{1}{\lambda} \ln \left\{ 1 + \frac{(\frac{^{87}Sr}{^{86}Sr})_p - (\frac{^{87}Sr}{^{86}Sr})_i}{(\frac{^{87}Rb}{^{86}Sr})_p} \right\} \quad (1.3)$$

However, apart from 't' the other unknown parameter in Eqs 1.2 and 1.3 is the initial Sr isotope ratio of a sample or mineral (^{87}Sr/^{86}Sr)i, thus preventing direct calculation of the 'age' without assuming an initial Sr isotope ratio. To circumvent this complication the acquired ^{87}Rb/^{86}Sr and ^{87}Sr/^{86}Sr data from multiple minerals (or different parts of a single mineral) can be plotted in a Nicolaysen diagram (i.e., ^{87}Rb/^{86}Sr vs ^{87}Sr/^{86}Sr) or an isochron cross-plot (Nicolaysen, 1961), and the best-fit line (i.e., isochron) through the data can be determined using a weighted maximum likelihood linear regression (York, 1968; York et al., 2004), the latter described by the equation of the straight line:

$$y = a + xb \quad (1.4)$$

where, y = y-variable (i.e., ^{87}Sr/^{86}Sr data), a= y-intercept (i.e., Sr isotope initial), x = x-variable (^{87}Rb/^{86}Sr data) and b = the slope of an isochron. By combining the Equation 1.2 with the Eq. 1.4 of the straight line, the age (t) of the mineral can be calculated from the slope (b= $e^{\lambda t}$ -1) of the isochron and the Rb-Sr decay constant (λ), using the equation below:

$$t = \frac{\ln\left(slope + 1\right)}{\lambda} \tag{1.5}$$

A mixture of two minerals with different ages or geological histories can also yield a straight line in the Rb-Sr isochron diagram (Figure 1.1), producing an apparent 'isochron' whose slope will however not reflect the true 'age' of this mineral assemblage but rather a mixing proportion of these two distinct mineral phases with variable $^{87}Sr/^{86}Sr$ and $^{87}Rb/^{86}Sr$ ratios. Mixing of two components can also increase the Sr concentration of the final product but the isotopic composition will not be changed. Thus, the two lines (the mixing line and the isochron line) can be distinguished using a ratio-element plot (i.e., $^{87}Sr/^{86}Sr$ vs Sr ppm) as the mixing line will appear as a hyperbola curve whereas materials that originated from one source, and thus having the same or identical age, will yield a straight line or true isochron (White, 2015 and references therein). In addition, plotting the $^{87}Sr/^{86}Sr$ vs 1/Sr of the mixture will yield a straight line where the lower and higher y-values ($^{87}Sr/^{86}Sr$) indicate the initial $^{87}Sr/^{86}Sr$ ratios of the two components, as shown in Figure 1.1

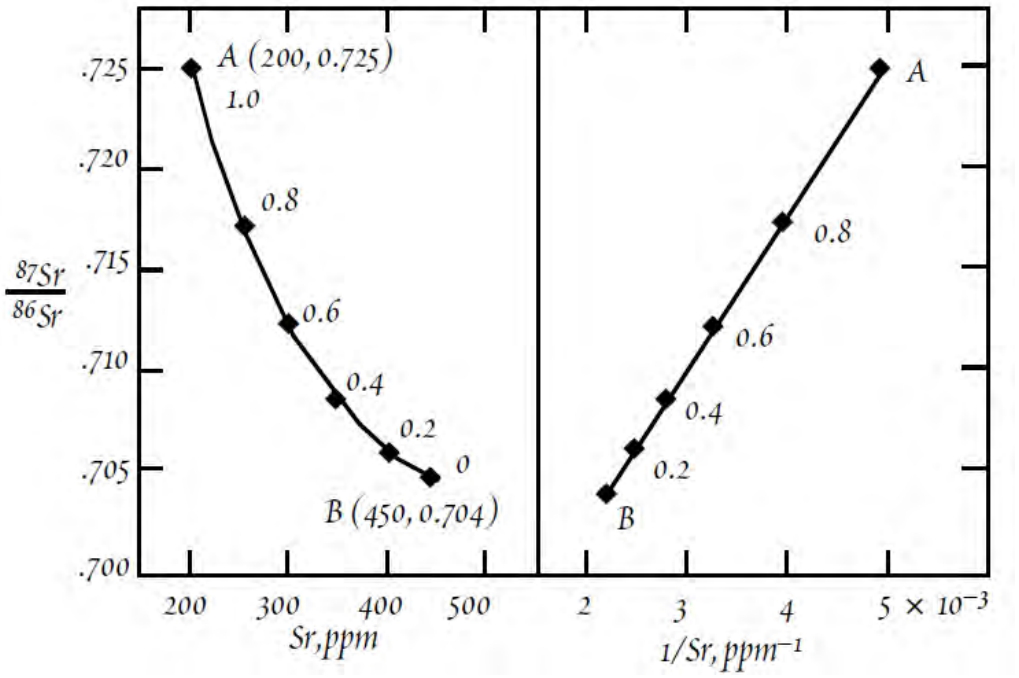

Figure 1.1: Mixing lines formed by two components A and B plotted in Sr isotope versus concentration diagrams (adopted from White, 2015).

1.2.2 Analytical techniques for the Rb-Sr geochronology: Review of traditional and new approaches

Sample preparation

Geological materials can be analysed by a number of different mass spectrometry systems such as TIMS, MC-ICP-MS and/or ICP-MS/MS for their $^{87}Rb/^{86}Sr$ and $^{87}Sr/^{86}Sr$ (e.g., Charlier et al., 2006; Laureijs, Coogan, and Spence, 2021a; Waight, Baker, and Willigers, 2002; Waight, Baker, and Peate, 2002), but the above approaches also require specific treatment of a sample prior to isotope analysis and introduction of Rb or Sr into the MS instrument (Birck, 1986). Such step is necessary to overcome the isobaric interference between ^{87}Rb and ^{87}Sr and to remove other major elements from a sample matrix prior to isotope analysis. Hence, traditionally this sample preparation step involved the dissolution (acid digestion) of mineral/rock and its subsequent chemical purification (i.e., separation of Rb and Sr fractions from each other and from the matrix) using eluent chromatography. The sample for the isotope analysis can be either in the form of mixed phases (i.e., whole rock) or as a single mineral phase, which are either mechanically separated or micro-drilled to produce a representative sample/powder. Such powdered sample (i.e., silicate mineral) can be dissolved using concentrated hydrofluoric acid (HF) and nitric acid (HNO_3) at higher temperatures (>120 °C) over several days to yield a clean 'sample solution' (Dickin, 2005; Philip Horwitz, Chiarizia, and Dietz, 1992). After complete evaporation, HNO_2 is typically added to the sample (i.e., evaporated residue) to diminish the chance of fluoride formation and/or to dissolve any CaF_2 phase. Hydrochloric acid HCl can be also added to the mixture to ensure complete dissolution of the sample, which is then ready for the eluent chromatography and chemical separation of Rb and Sr. The elemental separation of Rb and Sr is normally conducted by ion exchange columns (filled with a cation exchange resin or Sr-specific resin) (Charlier et al., 2006; Philip Horwitz, Chiarizia, and Dietz, 1992; Yang et al., 2010). The acid-digested sample (mineral, bulk rock) can be loaded onto the column as a solution and Rb and Sr fractions can be separated using different normality or type of 'working' acids (i.e., HNO_3 or HCl acids). Finally, the elute (i.e., pure Sr and Rb fractions) containing the desired elements can be collected from the columns and be used for isotope analysis using MS techniques.

However, the above and time-consuming chemical separation of Rb and Sr can be avoided when the isotope analysis is conducted via the reaction-cell LA-ICP-MS/MS. In this case, the sample can be introduced directly as a solution (containing both Rb and

Sr) or prepared as a polished mount or polished-thin section (for *in-situ* analysis via LA), and the necessary chemical separation of Rb and Sr can be performed online within the ICP-MS/MS instrument in the reaction-cell (Bolea-Fernandez et al., 2016; Hogmalm et al., 2017; Zack and Hogmalm, 2016).

Thermal Ionisation Mass Spectrometry (TIMS)

$^{87}Rb/^{86}Sr$ and $^{87}Sr/^{86}Sr$ can be determined by the TIMS which distinguishes between atoms or ions based on their mass-to-charge (m/z) ratio using heat (i.e., high temperature, typically in excess of 1000 °C) to ionise a sample and separate isotopes via a magnetic sector. After the Rb-Sr chemical separation on chromatography columns, as described above, the collected Sr or Rb fraction can be loaded on a metal filament (typically made of highly refractory materials such as Re, Ta, W) using phosphoric or nitric acid that helps to destroy organic residues and to 'glue' the sample onto the filament (Dickin, 2005). The filament is then loaded into the TIMS instrument and heated up under high vacuum to ionise the sample for isotope analysis. The produced ions or ion beams (made of positively charged Sr and Rb species) are then focused and accelerated toward the analyser made of array of Faraday collectors and/or ion counting detectors. Within the magnetic field, and under high acceleration voltages (∼10,000 Volts), the lighter ions (^{85}Rb, and ^{86}Sr isotopes) are deflected more than the heavier ions (^{87}Rb and ^{87}Sr isotopes) based on their mass-to-charge (m/z) ratios. Such separated ions beams are then detected in the Faraday collectors as Voltages (i.e., signals in mV to Volts) from which the corresponding isotope ratios of interest (i.e., $^{87}Sr/^{86}Sr$ or $^{87}Rb/^{86}Sr$) are calculated.

Multi-collector Inductively Coupled Plasma Mass Spectrometry (MC-ICP-MS)

Alternatively, $^{87}Rb/^{86}Sr$ and $^{87}Sr/^{86}Sr$ can be also determined by the MC-ICP-MS in either a solution or LA mode, the latter however applicable only for Sr isotopes (Charlier et al., 2006; Waight, Baker, and Willigers, 2002; Waight, Baker, and Peate, 2002; Yang et al., 2010) . The difference between the TIMS and the MC-ICP-MS is the source of heat or energy to ionise samples, and for MC-ICP-MS it is plasma that is being used, which can produce extremely high temperature (∼5000 °C) to ionise most of elements in the sample of interest. The plasma torch used in ICP-MS systems was originally invented in 1961 by Thomas Reed, and it generally produces a stream of ionised gas (i.e., using Ar as carrying gas) that is inductively heated (to temperatures about 5000

°C) by a radiofrequency generator under an atmospheric pressure (Dickin, 2005; Mueck, 2015). The advantage of the multi-collector ICP-MS, over the conventional single-collector ICP-MS instrument, is that the former is equipped with a magnetic sector and multiple collectors (i.e., Faraday or a multi-dynode electron multiplier) whereas the ICP-MS typically contains a quadruple mass separator and only a single pulse-analogue detector. Briefly, the quadruple mass separator is composed of rods that are electrically charged and arranged parallel to the ion flight path. The function of the quadruple is to allow a selected m/z travelling in a helical path to pass through to the detector whereas the ions with other mass are de-focused. This process can be controlled by rapid changes of voltages in the quadruple's rods which allows scanning a wide range of spectrum and detect their counts at precision typically of about 1% or better (∼0.2%) (Dickin, 2005). In contrast, the simultaneous collection of different ion beams (isotopes), which is possible by MC-ICP-MS and TIMS systems with sector magnets, can produce isotopic ratios at precision of 0.01 and 0.001 % (Mueck, 2015). Similar to TIMS, when the mass-resolved ion beams reach the detectors in MC-ICP-MS, they are converted into voltage, and the isotopic ratios can be calculated by comparing voltages from the different detectors (Dickin, 2005).

Inductively coupled plasma tandem mass spectrometry (ICP-MS/MS) with a collision cell

As described in the section above, the Rb-Sr isotopic ratios can be now also measured directly by the ICP-MS/MS equipped with a collision cell, and the analysis and Rb-Sr dating can be thus also done *in-situ* using a laser ablation (LA) system (Hogmalm et al., 2017; Zack and Hogmalm, 2016). As the acronym indicates, this instrument has two mass spectrometers or two quadrupoles (Q) used for mass discrimination. The critical and necessary advantage of the ICP-MS/MS over the conventional single-collector ICP-MS instruments is the capacity of a reaction or collision cell that allows an on-line (within the instrument) separation of isobaric elemental or polyatomic interferences (Eiden, Barinaga, and Koppenaal, 1997; Fernández et al., 2012). Therefore, unlike for traditional TIMS or MC-ICP-MS approaches, no prior chemical separation of Rb-Sr in a sample is required for ICP-MS/MS systems.The geometry of the single-collector ICP-MS/MS comprises two quadrupoles (Q) or mass separators which are: Q1 that is located between the plasma torch and the reaction cell, and Q2 which is located between the reaction cell and the detector. To remove the spectral interference, the reaction cell is filled with a reactive gas (N_2O or FS_6 for removal of ^{87}Rb and ^{87}Sr interference), and

the separation process for spectral or isobaric interference is conducted in the following way. The reaction cell is filled with a gas that is inert to one analyte ion (i.e., Rb) but reactive with the other (i.e., Sr), which allows to measure the new product as different and mass-shifted species that are interference free. Because ionization in an Ar plasma leads to the production of Rb^+, which has a noble gas configuration, it is innately stable and does not react post-plasma with other products, whereas Sr^+ is not in its desired state of 2^+ and will react with negative ions such as O and F. The necessary assumption is that the mass distribution of the Sr isotopes is maintained after mass shifting so that the ratios among the isotopes is maintained. For the Rb-Sr analysis, Rb ions or isotopes can be measured on-mass (i.e., $^{85}Rb^+$) whereas Sr can be measured in the mass-shift mode as either SrO^+ or SrF^+ species, based on the selection of reaction gas (N_2O or FS_6).

The ion detector in the ICP-MS/MS can measure the count per second (cps) of the ions at either pulse (P) or analog (A) mode. Lower count rate is measured at pulse mode whereas the higher count rate is measured at analog mode. The current version of the MassHunter software that controls the ICP-MS/MS used in this project (Agilent 8900QQQ) is uncapable to determine precise and accurate P/A factors. Thus, Rb and Sr in samples and standards must be analysed at the same P/A settings (Zack and Hogmalm, 2016). This condition was maintained in this project by correcting Rb and Sr data of a sample against a standard that have Rb and Sr detected in the same mode (i.e., Rb at analog mode and Sr at pulse mode), and this has been done in all experiments listed in chapter 2 and the experiment noted as session 4 in chapter 3. Alternatively, the crossover limit between the two modes was adjusted to be at ca. 4×10^6 cps and detect both Rb and Sr in samples and standards at pulse mode as it has been done in experiments listed in chapter 4 and experiments noted as session 1, 2 and 3 in chapter 3.

The other complexity that associate detecting Rb on-mass and Sr in the mass shifted mode is the presence of other elements that could cause spectrum interference with the above Rb and Sr products such as Cr, Si and Ti (Hogmalm et al., 2017). Thus, the first quadruple (Q1) needs to be adjusted in MS/MS mode to remove these elements as when N_2O is used as a reaction gas Cr is converted to $^{53}Cr^{16}O_2^+$ (mass 85) which overlaps directly with $^{85}Rb^+$ (Hogmalm et al., 2017). Similarly, if FS_6 is used as a reaction gas, ^{28}Si and ^{48}Ti are forming $^{28}Si^{19}F_3^+$ and $^{48}Ti^{19}F_3^+$ species which overlap with the spectrum of $^{85}Rb^+$ and $^{86}Sr^{19}F^+$, respectively (Hogmalm et al., 2017). The above analytical challenges can be however resolved with the novel ICP-MS/MS approach and suitable strategies for monitoring of isobaric interferences and/or removing them via the above-

mentioned 'mass shifting' approaches. Finally, the future application of ICP-MS/MS approaches for *in-situ* dating will benefit from the introduction of new generation of MC-ICP-MS/MS instruments, equipped with a collision cell and two mass filters, and these advanced geochronological approaches have been recently demonstrated on prototype instruments such as Proteus or Vienna (Thermo Scientific) used for a high-precision *in-situ* Rb-Sr dating (Bevan et al., 2021).

1.3 Thesis outline

One of the aims of this thesis is to assess the fidelity and robustness of *in-situ* Rb-Sr dating of silicate minerals (micas, feldspars, glauconite) analysed by a single collector ICP-MS/MS coupled with LA system, and to assess the effects of down-hole fractionation and matrix-matching on the accuracy and precision of Rb-Sr ages for the above minerals. The second goal is to develop and validate suitable mineral reference materials (nano-powders and fused glasses) for *in-situ* Rb-Sr dating phlogopite, biotite, K-feldspar and glauconite via the LA-ICP-MS/MS. Finally, the third and overarching aim of this thesis is to apply this novel *in-situ* Rb-Sr dating approach to investigate and better constrain the timing of regional Cu-Au mineralisation along a major shear zone in the Arabian Shield, in Saudi Arabia, with implications for the underlying geological, metamorphic and fluid-related alteration events linked to this mineralisation. In summary, this thesis includes either published chapters (Chapter 2) or manuscripts that are submitted or formatted for publication (Chapters 3 and 4); and thus there are also unavoidable repetitions in the Introduction, background, and methodological sections of some of these chapters.

Chapter 2 is published in Journal of Analytical Atomic Spectrometry (JAAS), 2021, and titled: *'Assessment of elemental fractionation and matrix effects during in-situ Rb–Sr dating of phlogopite by LA-ICP-MS/MS: Implications for the accuracy and precision of mineral ages'*, (Authors: Redaa, A, Farkaš, J, Gilbert, S, Collins, AS, Wade, B, Löhr, S, Zack, T & Garbe-Schönberg, D; JAAS, no. 36, pp. 322-344). In this chapter, a relatively homogeneous phlogopite sample (MDC) or natural mineral, collected from Bekily area in Madagascar, was dated using two different laser systems to evaluate the elemental and down-hole fractionation of Rb and Sr during the *in-situ* Rb-Sr analysis. In addition, this chapter describes the calibration process or normalisation of Rb-Sr isotopic data, investigating also the impact of chemically-matched reference material (phlogopite

pressed nano-powder pellet: Mica-Mg-NP), with different ablation properties to MDC, to assess the accuracy and precision of the acquired *in-situ* Rb-Sr age of phlogopite.

Chapter 3 is formatted for a submission to Geostandards and Geoanalytical Research, and titled *'Testing nano-powder and fused-glass mineral reference materials for in-situ Rb-Sr dating of glauconite, phlogopite, biotite and feldspar via LA ICP-MS/MS'*, (Authors: Redaa, A, Farkaš, J, Gilbert, S, Collins, AS, Löhr, S, Vasegh, D, Forster, M, Blades, M, Zack, T, Baldermann, A, Dietzel, M & Garbe-Schönberg, D). The aim of this chapter is to develop and validate a set of mineral reference materials (RMs) for *in-situ* Rb-Sr dating by the LA-ICP-MS/MS. Four well-characterised reference materials of phlogopite, biotite, K-feldspar and glauconite were prepared either as flux-free fused glasses or acquired as pressed nano-powder pellets for *in-situ* Rb-Sr dating. The investigated materials were studied through multiple analytical sessions, and the pressed nano-powder pellets were tested to calibrate and normalise Rb-Sr data and 'ages' of three corresponding natural minerals which are: GL-O glauconite, MDC phlogopite, and FK-N K-feldspar.

Chapter 4 is published in Journal of Asian Earth Sciences (JAES), and titled: *'Constraints from in-situ Rb-Sr dating on the timing of the Umm Farwah shear zone and associated copper-gold mineralisation in the Mount Ablah area in the Southern Arabian Shield, Saudi Arabia'*, (Authors: Redaa, A, Farkaš, J, Hassan, A, Collins, AS, Gilbert, S & Löhr, S; JAES, vol. 224, p. 105037). This chapter is a case study that shows the novelty of *in-situ* Rb-Sr dating to constrain timing of major geological, metamorphic and alteration events associated with the regional Cu-Au mineralisation in Saudi Arabia. This study investigates the timing of development a major shear zone, located in the southern part of the Arabian Shield, known as Umm Farwah shear zone. In addition, this work also determined Rb-Sr age of two types of mineralisation located within the Umm Farwah shear zone which are (i) greisenisation and (ii) Cu-Au mineralisation in quartz veins, both exposed and investigated in the Mount Ablah region.

Finally, there are a number of published papers and conference abstracts that utilised the *in-situ* Rb-Sr dating technique, where Ahmad Redaa is listed as a co-author, and these published studies are also included and presented in the appendix.

References

Agatemor, C and D Beauchemin (2011). "Matrix effects in inductively coupled plasma mass spectrometry: a review". In: *Anal Chim Acta* 706.1, pp. 66–83.

Armistead, Sheree E, Alan S Collins, Ahmad Redaa, Gilby Jepson, Jack Gillespie, Sarah Gilbert, Morgan L Blades, John D Foden, and Théodore Razakamanana (2020). "Structural evolution and medium-temperature thermochronology of central Madagascar: implications for Gondwana amalgamation". In: *Journal of the Geological Society* 177, pp. 784–798.

Bevan, Dan, Christopher D Coath, Jamie Lewis, Johannes Schwieters, Nicholas Lloyd, Grant Craig, Henning Wehrs, and Tim Elliott (2021). "In situ Rb–Sr dating by collision cell, multicollection inductively-coupled plasma mass-spectrometry with pre-cell mass-filter,(CC-MC-ICPMS/MS)". In: *Journal of Analytical Atomic Spectrometry* 36.5, pp. 917–931.

Birck, Jean Louis (1986). "Precision K-Rb-Sr isotopic analysis: Application to Rb-Sr chronology". In: *Chemical Geology* 56.1, pp. 73–83.

Bolea-Fernandez, Eduardo, Stijn J M Van Malderen, Lieve Balcaen, Martin Resano, and Frank Vanhaecke (2016). "Laser ablation-tandem ICP-mass spectrometry (LA-ICP-MS/MS) for direct Sr isotopic analysis of solid samples with high Rb/Sr ratios". In: *Journal of Analytical Atomic Spectrometry* 31.2, pp. 464–472.

Charlier, B. L. A., C. Ginibre, D. Morgan, G. M. Nowell, D. G. Pearson, J. P. Davidson, and C. J. Ottley (2006). "Methods for the microsampling and high-precision analysis of strontium and rubidium isotopes at single crystal scale for petrological and geochronological applications". In: *Chemical Geology* 232.3, pp. 114–133.

Dickin, A P (2005). *Radiogenic Isotope Geology*. Second. New York, USA: Cambridge University Press.

Dodson, Martin H (1973). "Closure Temperature in Cooling Geochronological and Petrological Systems". In: *Contributions to Mineralogy and Petrology* 40.3, pp. 259–274.

Eberlei, T, G Habler, W Wegner, R Schuster, W Körner, M Thöni, and R Abart (2015). "Rb/Sr isotopic and compositional retentivity of muscovite during deformation". In: *Lithos* 227, pp. 161–178.

Eiden, Gregory C., Charles J. Barinaga, and David W. Koppenaal (1997). "Beneficial Ion/Molecule Reactions in Elemental Mass Spectrometry". In: *Rapid Communications in Mass Spectrometry* 11.1, pp. 37–42.

Fern$\acute{a}$ndez, Silvia Diez, Naoki Sugishama, Jorge Ruiz Encinar, and Alfredo Sanz-Medel (2012). "Triple quad ICPMS (ICPQQQ) as a new tool for absolute quantitative proteomics and phosphoproteomics". In: *Analytical chemistry* 84.14, pp. 5851–5857.

Hogmalm, K. Johan, Thomas Zack, Andreas K. O. Karlsson, Axel S. L. Sjöqvist, and Dieter Garbe-Schönberg (2017). "In situ Rb-Sr and K-Ca dating by LA-ICP-MS/MS: an evaluation of N^2O and SF^6 as reaction gases". In: *Journal of Analytical Atomic Spectrometry* 32.2, pp. 305–313.

Jackson, Simon E., Norman J. Pearson, William L. Griffin, and Elena A. Belousova (2004). "The application of laser ablation-inductively coupled plasma-mass spectrometry to in situ U–Pb zircon geochronology". In: *Chemical Geology* 211.1–2, pp. 47–69.

Laureijs, Christiaan T., Laurence A. Coogan, and Jody Spence (2021a). "A high throughput Rb-Sr dating method using solution tandem ICP-MS/MS ($^{87}Sr/^{86}Sr$) and standard addition calibration ICP-MS (Rb/Sr)". In: *MethodsX* 8, p. 101309.

Laureijs, Christiaan T, Laurence A Coogan, and Jody Spence (2021b). "In-situ Rb-Sr dating of celadonite from altered upper oceanic crust using laser ablation ICP-MS/MS". In: *Chemical Geology* 579, p. 120339.

Li, Shan-Shan, M Santosh, Juraj Farkaš, Ahmad Redaa, Sohini Ganguly, Sung Won Kim, Cun Zhang, Sarah Gilbert, and Thomas Zack (2020). "Coupled U-Pb and Rb-Sr laser ablation geochronology trace Archean to Proterozoic crustal evolution in the Dharwar Craton, India". In: *Precambrian Research* 343, p. 105709.

Lin, Jie, Yongsheng Liu, Yueheng Yang, and Zhaochu Hu (2016). "Calibration and correction of LA-ICP-MS and LA-MC-ICP-MS analyses for element contents and isotopic ratios". In: *Solid Earth Sciences* 1.1, pp. 5–27.

Marillo-Sialer, E., J. Woodhead, J. M. Hanchar, S. M. Reddy, A. Greig, J. Hergt, and B. Kohn (2016). "An investigation of the laser-induced zircon 'matrix effect'". In: *Chemical Geology* 438, pp. 11–24.

Marillo-Sialer, Estephany, J Woodhead, Janet Hergt, Alan Greig, Marcel Guillong, Andrew Gleadow, Noreen Evans, and Chad Paton (2014). "The zircon 'matrix effect':

evidence for an ablation rate control on the accuracy of U–Pb age determinations by LA-ICP-MS". In: *Journal of Analytical Atomic Spectrometry* 29.6, pp. 981–989.

Mueck, Leonie (2015). "A technique to carry a torch for". In: *Nature Methods* 12.1, pp. 12–12.

Nicolaysen, L. O. (1961). "Graphic interpretation of discordant age measurements on metamorphic rocks". In: *Annals of the New York Academy of Sciences* 91.2, pp. 198–206.

Olierook, Hugo K H, Kai Rankenburg, Stanislav Ulrich, Christopher L Kirkland, Noreen J Evans, Stephen Brown, Brent I A McInnes, Alexander Prent, Jack Gillespie, and Bradley McDonald (2020). "Resolving multiple geological events using in situ Rb–Sr geochronology: implications for metallogenesis at Tropicana, Western Australia". In: *Geochronology* 2.2, pp. 283–303.

Philip Horwitz, E., Renato Chiarizia, and Mark L. Dietz (1992). "A novel strontium-selective extraction chromatographic resin". In: *Solvent Extraction and Ion Exchange* 10.2, pp. 313–336.

Rosman, K. J. R. and P. D. P. Taylor (1998). "Isotopic compositions of the elements 1997 (Technical Report)". In: *Pure and Applied Chemistry* 70.1, pp. 217–235.

Subarkah, Darwinaji, Morgan L Blades, Alan S Collins, Juraj Farkaš, Sarah Gilbert, Stefan C Löhr, Ahmad Redaa, Eilidh Cassidy, and Thomas Zack (2021). "Unraveling the histories of Proterozoic shales through in situ Rb-Sr dating and trace element laser ablation analysis". In: *Geology*.

Tillberg, Mikael, Henrik Drake, Thomas Zack, Ellen Kooijman, Martin J Whitehouse, and Mats E Åström (2020). "In situ Rb-Sr dating of slickenfibres in deep crystalline basement faults". In: *Scientific Reports* 10.1, pp. 1–13.

Villa, I M, P De Bièvre, N E Holden, and P R Renne (2015). "IUPAC-IUGS recommendation on the half life of ^{87}Rb". In: *Geochimica et Cosmochimica Acta* 164, pp. 382–385.

Waight, Tod, Joel Baker, and David Peate (2002). "Sr isotope ratio measurements by double-focusing MC-ICPMS: techniques, observations and pitfalls". In: *International Journal of Mass Spectrometry* 221.3, pp. 229–244.

Waight, Tod, Joel Baker, and Bart Willigers (2002). "Rb isotope dilution analyses by MC-ICPMS using Zr to correct for mass fractionation: towards improved Rb–Sr geochronology?" In: *Chemical Geology* 186.1, pp. 99–116.

White, William M (2015). *Isotope geochemistry*. John Wiley & Sons.

Yang, Yue-heng, Hong-fu Zhang, Zhu-yin Chu, Lie-wen Xie, and Fu-yuan Wu (2010). "Combined chemical separation of Lu, Hf, Rb, Sr, Sm and Nd from a single rock digest and precise and accurate isotope determinations of Lu–Hf, Rb–Sr and Sm–Nd isotope systems using Multi-Collector ICP-MS and TIMS". In: *International Journal of Mass Spectrometry* 290.2, pp. 120–126.

York, Derek (1968). "Least squares fitting of a straight line with correlated errors". In: *Earth and planetary science letters* 5, pp. 320–324.

York, Derek, Norman M Evensen, Margarita López Martınez, and Jonás De Basabe Delgado (2004). "Unified equations for the slope, intercept, and standard errors of the best straight line". In: *American Journal of Physics* 72.3, pp. 367–375.

Zack, Thomas and K Johan Hogmalm (2016). "Laser ablation Rb/Sr dating by online chemical separation of Rb and Sr in an oxygen- fi lled reaction cell". In: *Chemical Geology* 437, pp. 120–133.

Şengün, Fırat, Viktor Bertrandsson Erlandsson, Johan Hogmalm, and Thomas Zack (2019). "In situ Rb-Sr dating of K-bearing minerals from the orogenic Akçaabat gold deposit in the Menderes Massif, Western Anatolia, Turkey". In: *Journal of Asian Earth Sciences* 185, p. 104048.

CHAPTER 2

Assessment of elemental fractionation and matrix effects during *in-situ* Rb–Sr dating of phlogopite by LA-ICP-MS/MS: Implications for the accuracy and precision of mineral ages

This chapter has been published in *Journal of Analytical Atomic Spectrometry* as:
Redaa, A, Farkaš, J, Gilbert, S, Collins, AS, Wade, B, Löhr, s, Zack, T & Garbe-Schönberg, D 2021, 'Assessment of elemental fractionation and matrix effects during *in-situ* Rb–Sr dating of phlogopite by LA-ICP-MS/MS: Implications for the accuracy and precision of mineral ages', *Journal of Analytical Atomic Spectrometry*, no. 36, pp. 322-344.

Statement of Authorship

Title of Paper	Assessment of elemental fractionation and matrix effects during in situ Rb–Sr dating of phlogopite by LA-ICP-MS/MS: implications for the accuracy and precision of mineral ages
Publication Status	☑ Published ☐ Accepted for Publication ☐ Submitted for Publication ☐ Unpublished and Unsubmitted w ork w ritten in manuscript style
Publication Details	Redaa, A, Farkaš, J, Gilbert, S, Collins, AS, Wade, B, Löhr, s, Zack, T & Garbe-Schönberg, D 2021, 'Assessment of elemental fractionation and matrix effects during in-situ Rb–Sr dating of phlogopite by LA-ICP-MS/MS: Implications for the accuracy and precision of mineral ages', *Journal of Analytical Atomic Spectrometry*, no. 36, pp. 322-344.

Principal Author

Name of Principal Author (Candidate)	Ahmad Redaa		
Contribution to the Paper	Work planning, sample preparation, carried out analytical work, data collection, processing, and interpretation, designing and writing the manuscript.		
Overall percentage (%)	80%		
Certification:	This paper reports on original research I conducted during the period of my Higher Degree by Research candidature, and it is not subject to any obligations or contractual agreements with a third party that would constrain its inclusion in this thesis. I am the primary author of this paper.		
Signature		Date	20/6/2020

Co-Author Contributions

By signing the Statement of Authorship, each author certifies that:

i. the candidate's stated contribution to the publication is accurate (as detailed above);
ii. permission is granted for the candidate in include the publication in the thesis; and
iii. the sum of all co-author contributions is equal to 100% less the candidate's stated contribution.

Name of Co-Author	Juraj Farkaš		
Contribution to the Paper	Supervised work, helped with data interpretation and manuscript revision		
Signature		Date	20/6/2020

Name of Co-Author	Sarah Gilbert		
Contribution to the Paper	Assisted with the analytical work on the ICP-MS/MS, data process and interpretation and manuscript revision.		
Signature		Date	20/6/2020

Name of Co-Author	Alan S. Collins		
Contribution to the Paper	Supplied the main mineral sample used in the study, assist with data interpretation and manuscript revision.		
Signature		Date	20-06-2020

Name of Co-Author	Ben Wade		
Contribution to the Paper	Assisted with Rb-Sr raw data processing, imaging the samples and manuscript revision.		
Signature		Date	22-6-2020

Name of Co-Author	Stefan Löhr		
Contribution to the Paper	Curried out the analytical work on the FE-SEM and assisted with data processing and interpretation.		
Signature		Date	20/6/2020

Name of Co-Author	Thomas Zack		
Contribution to the Paper	Assisted with providing samples for analysis, initial setup of the in-situ Rb-Sr analysis and manuscript revisions		
Signature		Date	22/11/2021

Name of Co-Author	Dieter Garbe-Schönberg		
Contribution to the Paper	Assisted with providing samples for analysis and manuscript revisions		
Signature		Date	20/6/2020

Abstract

Laser-ablation inductively coupled plasma tandem mass-spectrometry (LA-ICP-MS/MS) allows for rapid and interference free analyses of Rb and Sr isotopes, permitting *in-situ* Rb–Sr dating of minerals. However, the general lack of matrix-matched reference materials remains one of its main obstacles, affecting both precision and accuracy. This study systematically investigates the impact of matrix effects and down-hole fractionation (DHF) on the *in-situ* Rb–Sr ages of an igneous phlogopite mineral (MDC) analysed by an ICP-MS/MS using two different LA systems: (i) a RESOlution ArF (193nm) excimer and (ii) a NWR (213nm) Nd-YAG laser system. A phlogopite reference material (Mica-Mg), originating from the same location as the MDC, was prepared as a pressed nano-powder pellet (NP) and used in this study as a primary reference material. The results revealed that the accuracy of the Rb–Sr ages is typically within about 3% (for 70% of analysed samples), but occasionally higher errors ranging between 4 to 8% were observed (ca. 30% of cases). We hypothesize that the above bias and uncertainty in the Rb–Sr ages are related to matrix effects between Mica-Mg-NP and MDC, due to their specific ablation characteristics and different physical properties. In addition, the elemental fractionation effects observed in this study for $^{87}Rb/^{86}Sr$ are also dependent on laser wavelength (i.e., 193nm vs. 213nm). Hence, developing an improved nano-powder reference material, or a mineral or glass with better matrix matching to natural phlogopite minerals would be desirable to further improve the accuracy of *in-situ* Rb–Sr dating. Currently, regular monitoring of secondary and matrix-matched reference minerals such as the MDC phlogopite can be used to assess and evaluate the accuracy of *in-situ* Rb–Sr dating of phlogopite, yielding ages within accuracy of ca. 3% or better.

2.1 Introduction

The Rb–Sr geochronological technique is a well-established dating tool used to constrain the crystallisation and/or cooling ages of igneous minerals and rocks, and the timing of alteration events or processes such as metamorphism, metasomatism and diagenesis (Page, 1978; Terakado and Nohda, 1993; Nyquist et al., 2016). Rubidium has two naturally occurring isotopes, ^{85}Rb and ^{87}Rb. The latter undergoes beta decay to form radiogenic ^{87}Sr with a decay constant of $1.3972 \pm 0.0045 \times 10^{-11}$ per year (Villa et al., 2015). To establish the age of geological materials via the Rb–Sr dating method, the measured $^{87}Rb/^{86}Sr$ and $^{87}Sr/^{86}Sr$ ratios (i.e., from co-genetic minerals or whole

rock samples) are cross-plotted to define an isochron; the slope of which is a function of age. Historically, $^{87}Rb/^{86}Sr$ and $^{87}Sr/^{86}Sr$ isotopic ratios were measured by thermal ionisation mass spectrometry (TIMS) or more recently via multi collector inductively coupled plasma mass spectrometry (MC-ICP-MS) (Yang et al., 2010; Beranoaguirre et al., 2019; Nakai et al., 1993). These approaches, however, require isotopic spiking and time-consuming chemical separation of Rb and Sr from the sample matrix for precise ratio determination via eluent chromatography (Ward and Bell, 1990). Uncertainties associated with the gravimetric calibration of isotope spikes remain the dominant source of error on the accuracy of ages calculated via TIMS and MC-ICP-MS, with typical errors on Rb–Sr ages determined by the above techniques below 1%, and for more recent studies as low as 0.1–0.2% (Nebel, 2015).

The chemical separation of Rb from Sr for conventional TIMS and MC-ICP-MS approaches is required to resolve isobaric interference between ^{87}Rb and ^{87}Sr. Importantly, the recent development of tandem ICP mass spectrometers (ICP-MS/MS), equipped with a reaction/collision cell located between two quadrupoles (Q1 and Q2) and coupled with a laser-ablation (LA) system, allows for in situ Rb–Sr dating of geological materials at the micro-scale level (Hogmalm et al., 2017; Zack and Hogmalm, 2016; Bolea-Fernandez et al., 2016). Using such a setup, the first quadrupole (Q1) can be set independently to allow only isotopes with a mass-to-charge ratio of 87 ($^{87}Rb^+$ and $^{87}Sr^+$ in this case) to enter the reaction cell of the ICP-MS/MS system. The cell can be filled with reaction gases such as O_2 or N_2O gas (Bohme, 2019; Bolea-Fernandez et al., 2015; Bolea-Fernandez et al., 2016; Eiden, Barinaga, and Koppenaal, 1999; Hogmalm et al., 2017; Tanner, Baranov, and Bandura, 2001; Zack and Hogmalm, 2016), as both react with $^{87}Sr^+$ ions to form $^{87}Sr^{16}O^+$ with typical efficiencies and yields around 85-99% (Gorojovsky and Alard, 2020; Hogmalm et al., 2017; Zack and Hogmalm, 2016). In contrast, $^{87}Rb^+$ is unreactive with the above reaction gases, and, thus, such distinct behaviour of Rb and Sr ions with O_2 and N_2O gases allow for interference-free measurements of ^{87}Sr abundances as a 'mass-shifted' $^{87}Sr^{16}O^+$ reaction product with a mass of 103 amu.

Hence, coupling the ICP-MS/MS with a laser ablation (LA) system and using a suitable reaction gas allows for targeted analysis of samples at the 50-100 μm scale, making *in-situ* Rb–Sr dating of minerals possible (Zack and Hogmalm, 2016; Hogmalm et al., 2017; Tillberg et al., 2017; Tillberg et al., 2020; Armistead et al., 2020; Li et al., 2020; Gorojovsky and Alard, 2020). An additional advantage of LA-ICP-MS/MS over conventional TIMS or MC-ICP-MS based Rb–Sr dating techniques is that *in-situ* dating can be done rapidly and with minimal sample preparation, as mounted minerals and/or

polished rock chips can be used. However, the accuracy and precision of this technique can be affected by several factors including the laser wavelength and frequency, and the external reference materials used for calibration (matrix effect) (Gorojovsky and Alard, 2020). Elemental fractionation effects, and the current lack of matrix-matched reference materials, coupled with using a single-collector design of ICP-MS/MS, remain the main limitations in terms of accuracy and precision for *in-situ* dating purposes (Agatemor and Beauchemin, 2011; Claverie et al., 2009; Fryer, Jackson, and Longerich, 1995; Jackson and Günther, 2003; Outridge, Doherty, and Gregoire, 1997; Rodushkin et al., 2002; Sylvester, 2008; Zhang et al., 2016).

The mechanism and impact of elemental fractionation during LA-ICP-MS analysis have been studied in detail for other element/isotope systems (Agatemor and Beauchemin, 2011; Claverie et al., 2009; Fryer, Jackson, and Longerich, 1995; Jackson and Günther, 2003; Outridge, Doherty, and Gregoire, 1997; Rodushkin et al., 2002; Sylvester, 2008; Zhang et al., 2016), and these effects are related to phenomena such as (i) the laser-sample interaction, (ii) aerosol formation and transportation, and (iii) ionisation of aerosols in the ICP. Also, elemental fractionation effects are most pronounced for element pairs where one element volatilises more readily than the other (more refractory) element under certain conditions (Claverie et al., 2009; Jackson and Sylvester, 2008), which is a common feature for pairs such as U/Pb, Rb/Sr and K/Ca (Jackson and Günther, 2003; Zack and Hogmalm, 2016).

These effects can be further magnified if a sample and reference material have different physical and chemical properties that translate into different ablation rates and elemental fractionation patterns (Agatemor and Beauchemin, 2011; Sylvester, 2008). Nevertheless, the influence of elemental fractionation on the accuracy and precision of the LA-ICP-MS/MS analysis can be controlled by (i) filtering the produced aerosol, (ii) calibration against matrix-matched reference materials, and (iii) strictly controlled and monitored analytical conditions (Agatemor and Beauchemin, 2011; Claverie et al., 2009; Guillong and Günther, 2002; Jackson and Günther, 2003; Jackson and Sylvester, 2008; Mank and Mason, 1999; Miliszkiewicz, Walas, and Tobiasz, 2015; Rodushkin et al., 2002; Sylvester, 2008).

To date, only a limited number of well-characterised reference materials are available for *in-situ* Rb–Sr dating and $^{87}Sr/^{86}Sr$ isotopic analysis by LA-ICP-MS/MS. These include phlogopite Mica-Mg (Centre de Recherches Pétrographiques et Géochimiques (CRPG)) (Govindaraju, 1979; Govindaraju, 1994), and synthetic glasses NIST SRM 610 (Hogmalm et al., 2017; Woodhead and Hergt, 2001), which have been used in several previous studies (Hogmalm et al., 2017; Armistead et al., 2020; Li et al., 2020; Tillberg

et al., 2020). The original CRPG Mica-Mg has been processed into nano-particulate pressed powder pellets (Garbe-Schönberg and Müller, 2014) (Mica-Mg-NP) and was validated by measuring its $^{87}Sr/^{86}Sr$ ratios via LA-ICP-MS/MS and calibrating it against NIST 610. The $^{87}Rb/^{86}Sr$ ratio was then calculated based on the mean of reported crystallisation ages (i.e. using Rb–Sr phlogopite and U–Pb zircon) in the Bekily area (from which this phlogopite sample/standard originated), which is constrained at 519.4 $\pm$ 6.5 Ma with an initial $^{87}Sr/^{86}Sr$ ratio of 0.72607 $\pm$ 0.0007 (see Hogmalm et al., 2017).

In this study, we investigate the fractionation of Rb from Sr in natural and nano-powder phlogopite (MDC and Mica-Mg-NP) and synthetic glass NIST 610 during LA-ICP-MS/MS analysis and its overall effect on the accuracy and precision of *in-situ* Rb–Sr isochron ages. Specifically, this study compares ablation properties, down-hole fractionation (DHF) patterns and matrix effects between MDC, Mica-Mg-NP phlogopites (both sourced from the Ampandrandava mine, Bekily area, Madagascar) and the synthetic glass NIST 610 and their effects on the precision and accuracy of acquired *in-situ* Rb–Sr ages of phlogopite. In addition, two different LA systems were used in this study, specifically: (i) a RESOlution ArF (193nm) excimer laser and (ii) a NWR (213nm) Nd-YAG laser. A better understanding of the above processes and associated effects is critical to further improve the precision and accuracy of this novel geochronological tool, and results of this study provide new insights into these complex phenomena and how to monitor and tackle these analytical challenges for *in-situ* Rb–Sr dating applications.

2.2 Materials and Methods

2.2.1 Investigated materials

This study investigates and compares DHF, ablation properties and matrix effects between three types of materials, including: (i) a natural igneous phlogopite mineral (MDC), (ii) the Mica-Mg-NP phlogopite reference material (supplied by J. Hogmalm and T. Zack), and (iii) the synthetic glass NIST 610. The natural MDC phlogopite, with flakes large enough to be mounted and analysed by the LA-ICP-MS/MS, was sourced from the same area (Bekily, Madagascar) as the Mica-Mg reference material. In our experiment, four large flakes of MDC were mounted into resin, with cleavage planes perpendicular to the polished sample-mount surface (see the image inset in Figure 2.1), and these flakes were treated in this study as unknown samples. For *in-situ* Rb–Sr dating, both Mica-Mg-NP and NIST 610 were used as the primary reference materials and MDC was used as secondary reference material. Based on published data, the expected

$^{87}Rb/^{86}Sr$ and $^{87}Sr/^{86}Sr$ ratios and corresponding Rb–Sr ages of the above investigated reference materials are summarised in Table 2.1.

Table 2.1: The expected values of $^{87}Rb/^{86}Sr$ and $^{87}Sr/^{86}Sr$ ratios for investigated materials. Elburg et al., 2005; Hogmalm et al., 2017; Woodhead and Hergt, 2001 Note that the reported errors represent 2σ uncertainties (i.e., 95% confidence intervals).

Material	$^{87}Rb/^{86}Sr$	$^{87}Sr/^{86}Sr$	Age (Ma)
Mica-Mg (nano-powder)	154.6 ± 1.93	1.8525 ± 0.0024	519.4 ± 6.5 Ma
NIST 610 (Glass)	2.3300	0.709699 ± 0.000018	N/A
MDC (Phlogopite mineral)	N/A	N/A	519.4 ± 6.5 Ma

2.2.2 TIMS analysis - Sr isotopic composition of MDC

High-precision measurements of $^{87}Sr/^{86}Sr$ ratios of the MDC phlogopite were obtained via thermal ionisation mass spectrometry (TIMS) using a Phoenix IsotopX TIMS instrument and clean-laboratory procedures established at the Metal Isotope Group (MIG) facilities in the Department of Earth Sciences at the University of Adelaide (for details see Shao et al., 2018). In brief, four aliquots of MDC phlogopite flakes were digested in a mixture of HF-HNO_3 acid, and then evaporated and re-dissolved in 4 mL 8M nitric acid. Following this step, two 1 ml aliquots from each sample were passed through cation-exchange columns and subsequently analysed for $^{87}Sr/^{86}Sr$ ratios. Strontium extraction and purification was carried out using Bio-Spin columns filled with 200 μL of Eichrom Sr resin. Measured $^{87}Sr/^{86}Sr$ ratios were internally normalised to a $^{86}Sr/^{88}Sr$ ratio of 0.1194 using an exponential mass fractionation correction (Nier, 1938). The NIST SRM 987 reference material was used as the primary standard to monitor and assess data quality and reproducibility. The above analytical procedure yielded a typical $^{87}Sr/^{86}Sr$ external reproducibility of $\pm$0.000015 (2σ), and a total procedural Sr blank was on the order of ca. 100 pg. The latter is negligible as it represents $<$0.1% of the total amount of Sr processed through the columns for each sample, as a typical sample size was about 500 ng of Sr. Only the Sr isotope ratios (i.e., $^{87}Sr/^{86}Sr$) of MDC flakes were analysed in this study by TIMS, and the other desirable elemental ratio ($^{87}Rb/^{86}Sr$) was not measured via TIMS due to the lack of gravimetrically calibrated Sr and Rb single spikes in the MIG laboratories.

2.2.3 LA-ICP-MS/MS instrumentation and analytical set-up

All *in-situ* Rb–Sr analyses were conducted at Adelaide Microscopy, University of Adelaide, Australia. An Agilent 8900 ICP-MS/MS instrument, coupled with a laser ablation (LA)

system, was used to determine simultaneously both $^{87}Rb/^{86}Sr$ and $^{87}Sr/^{86}Sr$ ratios of the studied samples and reference materials. Two different laser systems were used, specifically (i) a RESOlution ArF excimer (193nm) and (ii) a NWR213 Nd-YAG (213nm) system. Each laser was coupled to the ICP-MS/MS with the same length of interface tubing, and included a Squid mixing device (Laurin Technic). The instrumental setup and tuning parameters of the ICP-MS/MS are summarised in Table 2.2. All samples were ablated in a He atmosphere and mixed with Ar as the carrier gas to the ICP, with 3.5 mL/min of N_2 added before the ICP torch to enhance the signal sensitivity (Hu et al., 2008), and using N_2O reaction gas to separate ^{87}Sr from ^{87}Rb.

2.2.4 Optimising analytical conditions for LA-ICP MS/MS

The carrier gas flow rates (He, Ar $\&$ N_2) and plasma conditions were tuned daily in normal 'no-gas' mode (i.e. no gas in the reaction cell), using the NIST 612 glass, and parameters optimized (i) to minimise oxide production ($<$0.2% ThO/Th), (ii) ensure efficient ionisation of the aerosol in the plasma (U/Th ratio $<$ 1.05) (Guillong and Günther, 2002) , and (iii) high element sensitivity. The reaction gas (N_2O) flow rate was optimised at 0.37 mL/min to achieve the highest sensitivity for both on-mass Rb (85 and 87 m/z), as well as mass shifted Sr reaction product ions (e.g. $^{88}Sr^{16}O^+$ at 104 m/z). A preliminary test showed almost complete conversion of ^{88}Sr ions (close to $\sim$99% yield) with N_2O to form $^{88}Sr^{16}O^+$, with no detectable reaction of ^{85}Rb occurring ($<$0.00001% reaction). In addition, the efficiency of the reaction did not change with different matrices (i.e. glass reference material vs nano-powder vs natural phlogopite mineral) and thus our analytical setup was able to effectively separate ^{87}Sr (via $^{87}Sr^{16}O^+$) from ^{87}Rb for the purposes of *in-situ* Rb–Sr dating.

2.2.5 Sampling strategy and data processing

In this study, we analysed Mica-Mg-NP as a primary reference material/standard to correct for drift and instrument mass-bias, and the above standard was measured after every 20 unknown samples. Data measured with the 193 nm LA system, were collected over eight individual analytical sessions, which were spread over a 10 month period to evaluate the long-term stability and reproducibility of *in-situ* Rb–Sr ages. In addition to 'spots' analyses (see parameters in Table 2.2), line scans or 'raster' analyses were also performed using the following LA settings: 74 µm beam diameter, fluence of 3.5 J/cm^2, repetition rate of 10Hz and scan speed of 7.4 µm/s. Analyses conducted on the 213 nm

Table 2.2: Instrumental parameters for two laser ablation systems (193nm and 213nm) and the ICP-MS/MS (Agilent 8900), used in this study.

	Units	193nm	213nm
Laser parameters			
He carrier gas	ml/min	350	700
Ar carrier gas	ml/min	1050	880
N_2 addition	ml/min	3.5	3.5
Spot size	μm	74	75
Repetition Rate	Hz	5	5
Fluence	J/cm^2	3.5	10
Sample Chamber		S155 large format	TV2
ICP-MS/MS			
Plasma Parameters			
RF Power	W	1350	1350
Sample Dept	mm	4	4
Lens Parameters			
Extract 1	V	-2.0	-1.0
Extract 2	V	-150	-140
Omega Bias	V	75	50
Omega Lens	V	7.0	7.0
Q1 entrance	V	2.0	1.0
Q1 exit	V	-1.0	-1.0
Cell focus	V	-2.0	4.0
Cell entrance	V	-100	-80
Cell exit	V	-150	-150
Deflect	V	-10	-10
Plate bias	V	-80	-90
Q1 Parameters			
Q1 bias	V	-2.0	-1.0
Q1 prefilter bias	V	-9.0	-9.0
Q1 postfilter bias	V	-10	-10
Cell Parameters			
N_2O flow rate	mL/min	0.37	0.37
OctP Bias	V	-23	-23
Axial acceleration	V	2.0	2.0
OctP RF	V	180	180
Energy discrimination	V	-10	-10
Q2 Parameters			
Q2 Bias	V	-33	-33

LA system were carried out over two separate analytical sessions using a spot size of 75 μm (laser parameters are available in Table 2.2).

All data collected in this study via LA-ICP MS/MS were processed using the Iolite 3 software (Paton et al., 2011). A customised data reduction algorithm was programmed for the purpose of *in-situ* Rb–Sr dating, which includes the following steps: 1) calculation

of the average background-subtracted ^{85}Rb, ^{86}Sr and ^{87}Sr count per second (cps) from signals collected on masses 85, 102, and 103 amu, respectively; 2) a conversion of ^{85}Rb cps signal to ^{87}Rb cps based on the natural abundance of Rb isotopes where ^{87}Rb = ^{85}Rb $\times$ 0.38562 (Nebel, 2015; Rosman and Taylor, 1999); 3) calculation of the raw and interference-free ^{87}Sr/^{86}Sr and ^{87}Rb/^{86}Sr ratios; and 4) drift corrected normalisation of the ratios using correction factors obtained by dividing the measured ^{87}Sr/^{86}Sr and ^{87}Rb/^{86}Sr ratios of reference materials, by their expected ratios (see data in Table 2.1). Since Rb was measured in analog mode and Sr was measured at pulse mode during all sessions for all samples (MDC, NIST 610 and Mica-Mg-NP) with count rate for Rb ranged between 3.5×10^6 to 5×10^6 and ranged between 2.5×10^5 to 4.5×10^5 for Sr, no additional correction for the Pulse–Analog (P/A) factor was required. Finally, the plotting of processed and normalised data (^{87}Sr/^{86}Sr and ^{87}Rb/^{86}Sr ratios) in conventional isochron plots, and the calculation of corresponding Rb–Sr ages and the Sr isotope initial ratios, were performed using IsoplotR (Vermeesch, 2018).

2.2.6 Three-dimensional (3D) imaging and analysis of laser ablation craters

The shape and morphology of laser craters can provide valuable information about laser-sample interactions and specific ablation rates of the studied materials. A laser scanning confocal microscope (LSCM) was used to characterise the morphology of the produced LA craters in the investigated samples. The laser craters were imaged using an Olympus LEXT OLS5000-SAF 3D LSCM at Adelaide Microscopy, University of Adelaide. The images were acquired with a x50/0.60NA lens, and the measurements of crater depths and geometry were performed using the Olympus Data Analysis Application software.

2.2.7 BSE Imaging

High-resolution backscatter electron (BSE) images covering the entire mineral mount or pressed powder pellet were collected to characterise 1) morphology of laser craters, 2) distribution of ejecta material, 3) impact of laser damage on subsequent analyses, and also 4) to investigate possible grain-size heterogeneity in the Mica-Mg-NP. Samples were carbon coated after completion of the laser experiments and imaged using a FEI Teneo LoVac Field Emission Scanning Electron Microscope (FE-SEM) at Macquarie University (13 mm working distance, 15 kV accelerating voltage). BSE image tile sets covering the entire sample ($\sim$450 nm pixel resolution) and smaller higher resolution regions of

interest (∼45 nm pixel resolution) were collected and stitched together using FEI Maps Mineralogy software.

2.3 Results

2.3.1 TIMS analysis of MDC

To indirectly constrain the expected ^{87}Rb/^{86}Sr ratios of the MDC phlogopite (assuming its crystallisation age of 519.4 ± 6.5 Ma, Hogmalm et al., 2017), subsamples of the mounted MDC flakes were analysed via TIMS for high-precision ^{87}Sr/^{86}Sr ratios. The measured ^{87}Sr/^{86}Sr ratio can be substituted into the conventional Rb–Sr geochronology equation (Eq. 2.1) to calculate the expected ^{87}Rb/^{86}Sr ratio:

$$(\frac{^{87}Sr}{^{86}Sr})_p = (\frac{^{87}Sr}{^{86}Sr})_i + (\frac{^{87}Rb}{^{86}Sr})_p \times (e^{\lambda t} - 1) \tag{2.1}$$

Where $(\frac{^{87}Sr}{^{86}Sr})_p$ and $(\frac{^{87}Rb}{^{86}Sr})_p$ are the 'present-day' measured isotope compositions, $(\frac{^{87}Sr}{^{86}Sr})_i$ is the 'initial' ^{87}Sr/^{86}Sr ratio in a sample which has been estimated for Mica-Mg-NP phlogopite by previous studies at 0.72607 ± 0.0007 (Hogmalm et al., 2017), λ is the ^{87}Rb decay constant of 1.3972 ± 0.0045 × 10^{-11}yr^{-1} (Villa et al., 2015), and *t* is the crystallisation age (in years) of MDC and/or Mica-Mg-NP constrained at 519.4 ± 6.5 Ma (Hogmalm et al., 2017). The above equation (Eq. 2.1) can then re-arranged to solve for the expected ^{87}Rb/^{86}Sr ratio:

$$(\frac{^{87}Rb}{^{86}Sr})_p = \frac{(\frac{^{87}Sr}{^{86}Sr})_p - (\frac{^{87}Sr}{^{86}Sr})_i}{(e^{\lambda t} - 1)} \tag{2.2}$$

Using the TIMS measured $(^{87}Sr/^{86}Sr)_p$ ratios (see data in Table 2.3), the calculated ^{87}Rb/^{86}Sr ratios for MDC sample yield a range from 42.51 to 44.20 (Table 2.3). Note that the stated uncertainties for these ^{87}Rb/^{86}Sr ratios were calculated using the following equation for a combined uncertainty:

$$(\frac{^{87}Rb}{^{86}Sr})_{\,error\%} = \frac{(\sqrt{(a\%)^2 + (b\%)^2 + (c\%)^2 + (d\%)^2} \times (\frac{^{87}Rb}{^{86}Sr}))}{100} \tag{2.3}$$

Where *a* is the analytical uncertainty (2σ) of $(^{87}Sr/^{86}Sr)_p$ acquired by TIMS, *b* is the uncertainty of $(^{87}Sr/^{86}Sr)_I$ as stated in Hogmalm et al., 2017, *c* is the uncertainty in the Rb–Sr decay constant (Villa et al., 2015), and *d* is the uncertainty in the expected age of MDC 519.4 ± 6.5 Ma (Hogmalm et al., 2017).

The TIMS data show variations in measured present-day $^{87}Sr/^{86}Sr$ ratios, and thus a corresponding spread is also observed for the calculated $^{87}Rb/^{86}Sr$ ratios of MDC (see Eq. 2.2 and Figure 2.1). This spread of data along the theoretical Rb–Sr isochron, defined by a crystallisation age of 519.4 Ma and an initial $^{87}Sr/^{86}Sr$ of 0.72607 (see also Table 2.1), is thus due to the natural variation of Rb and Sr concentrations in the MDC flakes.

Table 2.3: Measured $^{87}Sr/^{86}Sr$ ratios of MDC flakes analysed by TIMS and calculated (theoretical) $^{87}Rb/^{86}Sr$ ratios based on an assumed age of 519.4 Ma for MDC, using an initial $^{87}Sr/^{86}Sr$ ratio of 0.72607. The reported errors represent 2σ uncertainties (i.e., 95% confidence intervals).

Sample ID	$^{87}Sr/^{86}Sr$	2σ	$^{87}Rb/^{86}Sr$	2σ
MDC - 1a	1.041116	0.000003	43.26	0.56
MDC - 1b	1.041399	0.000004	43.29	0.56
MDC - 2a	1.039637	0.000004	43.05	0.56
MDC - 2b	1.039656	0.000004	43.05	0.56
MDC - 3a	1.035708	0.000004	42.51	0.55
MDC - 3b	1.035696	0.000004	42.51	0.55
MDC - 4a	1.047962	0.000014	44.20	0.57
MDC - 4b	1.047992	0.000004	44.20	0.57
Average	1.041145	0.009477	43.26	1.30

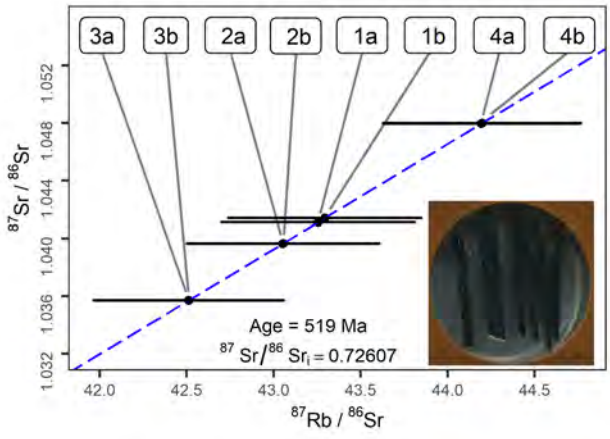

Figure 2.1: A theoretical Rb–Sr isochron of MDC based on $^{87}Sr/^{86}Sr$ data acquired by TIMS and the calculated $^{87}Rb/^{86}Sr$ ratios (see Eq. 2.2), corresponding to an age of 519 Ma. The results show the spread of the data along the theoretical isochron, reflecting the natural variation in $^{87}Rb/^{86}Sr$ and $^{87}Sr/^{86}Sr$ ratios of the MDC sample, most likely linked to minor inhomogeneity in elemental Rb/Sr ratios within the studied phlogopite crystal flakes.

2.3.2 Reproducibility of $^{87}Rb/^{86}Sr$ and $^{87}Sr/^{86}Sr$ ratios in the igneous phlogopite

LA spot analyses

In order to examine the reproducibility and robustness of Rb–Sr isochron ages, the Mica-Mg-NP, MDC and NIST 610 data were compared from 10 individual sessions (eight analysed via 193nm laser and two via 213nm laser), each consisting of approx. 20-40 individual LA spot analyses. The raw $^{87}Rb/^{86}Sr$ and $^{87}Sr/^{86}Sr$ ratios for Mica-Mg-NP obtained by the 193nm and 213nm laser systems are presented in Figure 2.2, and Table 2.A in the Supplementary material. The raw $^{87}Sr/^{86}Sr$ ratios were consistent within their respective analytical errors (i.e., internal reproducibility), and the measured Sr isotope data did not show significant variations from session to session, and/or drift during an individual analytical session (Figure 2.2A). In contrast, the raw $^{87}Rb/^{86}Sr$ ratio varied significantly during a single session, and also from session to session (see Figure 2.2B).

The $^{87}Rb/^{86}Sr$ and $^{87}Sr/^{86}Sr$ ratios of MDC, normalised to Mica-Mg-NP, also vary from session to session (see Figure 2.3, and data in Table. 2.B in the Supplementary material). The $^{87}Sr/^{86}Sr$ ratios of MDC are more robust and less variable from session to session (or within the session) compared to the $^{87}Rb/^{86}Sr$ ratios (see Figure 2.3). However, some of the $^{87}Sr/^{86}Sr$ data from MDC yielded more radiogenic values (e.g. data collected during sessions 4 and 6, Figure 2.3A). Overall, the normalised $^{87}Rb/^{86}Sr$ ratios of MDC displayed more variation than the $^{87}Sr/^{86}Sr$ ratios, often exhibiting a detectable increasing trend in $^{87}Rb/^{86}Sr$ over the course of an individual analytical session (see Figure 2.3B). Accordingly, when plotted as an isochron, these variations translate to an excessive spread in $^{87}Rb/^{86}Sr$ ratios along the x-axis (Figure 2.4A).

The calculated ages for MDC analysed via 193nm laser during the eight sessions tend to give systematically older Rb–Sr ages than the expected age of 519.4 $\pm$ 6.5 Ma. About 70% of the calculated ages are falling within 3.2% accuracy (Figure 2.4A), whereas the remaining data (ca. 30% of runs from the sessions 2, 6 and 7) showed less accurate results, with ages that are 4 to 7.7% older than the expected age (see Figure 2.4B). However, the internal precision of all calculated Rb–Sr ages for MDC is less than 1.4% (see Figure 2.A in the Supplementary material).

Two analytical sessions were also conducted with the 213nm laser to assess the laser wavelength-dependent effects on Rb/Sr elemental fractionation during LA-ICP-MS/MS. The analyses yielded ages of 503 $\pm$ 7 Ma and 509 $\pm$ 7 Ma (Figure 2.4B), which are thus 1.9 and 3.1% younger than the expected age of 519.4 $\pm$ 6.5 Ma (Hogmalm et al.,

2017), respectively.

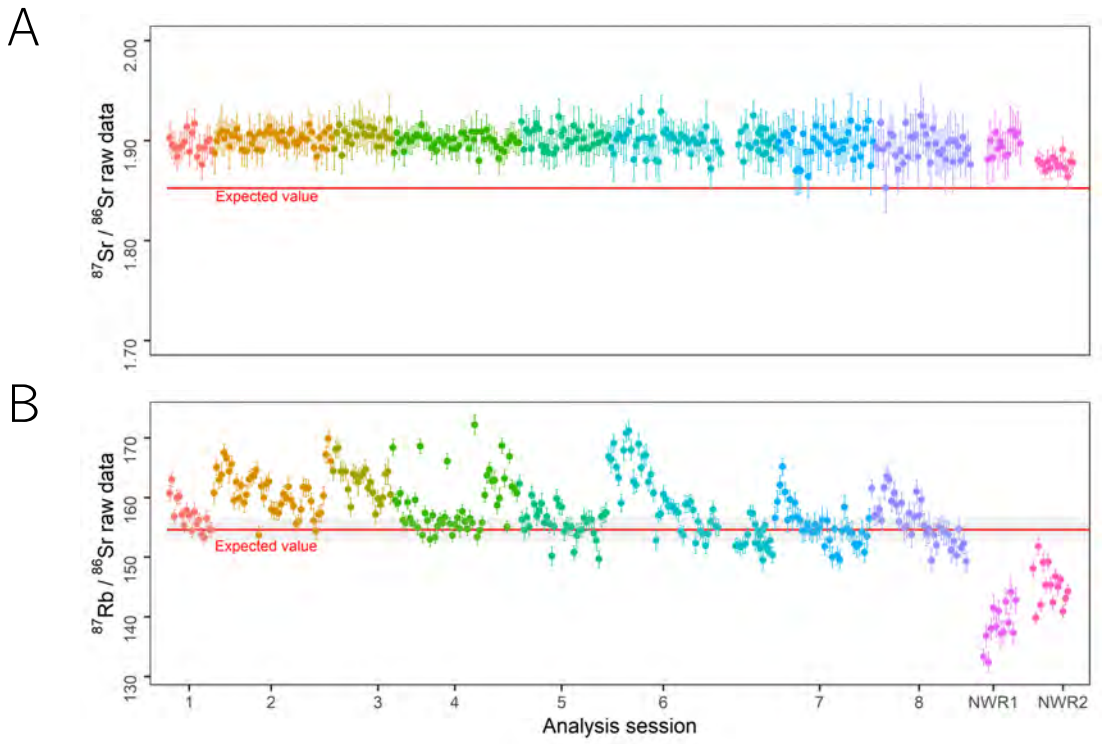

Figure 2.2: Long-term and within-session reproducibility of raw (A) $^{87}Sr/^{86}Sr$ and (B) $^{87}Rb/^{86}Sr$ ratios of Mica-Mg-NP over multiple analytical sessions using two laser systems. Data labelled 1 to 8 were obtained with the 193nm laser whereas NWR refers to 213nm laser and the numbers refer to analytical session. Note that there is more variation in the $^{87}Rb/^{86}Sr$ ratios within the analytical session compared to the $^{87}Sr/^{86}Sr$ ratios.

MDC was also normalised using NIST 610 glass as a reference material for data collected with the 193nm and 213mn laser systems to further investigate the effects of non-matrix-matched reference materials on *in-situ* Rb–Sr dating. The results are listed in Table. 2.C in the Supplementary material. The data acquired via the 193nm and 213nm laser resulted in a calculated age of 455 $\pm$ 6 Ma and 456 $\pm$ 6 Ma for MDC, respectively, which are thus significantly (up to 12%) younger than the expected age of 519.4 $\pm$ 6.5 Ma (Figure 2.5), and hence considerably less accurate than when normalised to the chemically-matched phlogopite Mica-Mg-NP standard (see data in Figure 2.4B). Such inconsistency in ages is due to a larger offset in $^{87}Rb/^{86}Sr$ ratios (measured vs expected) rather than uncertainty in $^{87}Sr/^{86}Sr$, as the latter is less effected by matrix match effect.

Line rasters analysis

A line raster analytical approach was also adopted to investigate its impacts on elemental fractionation and measured $^{87}Rb/^{86}Sr$ ratios. Ten raster lines were ablated in each ma-

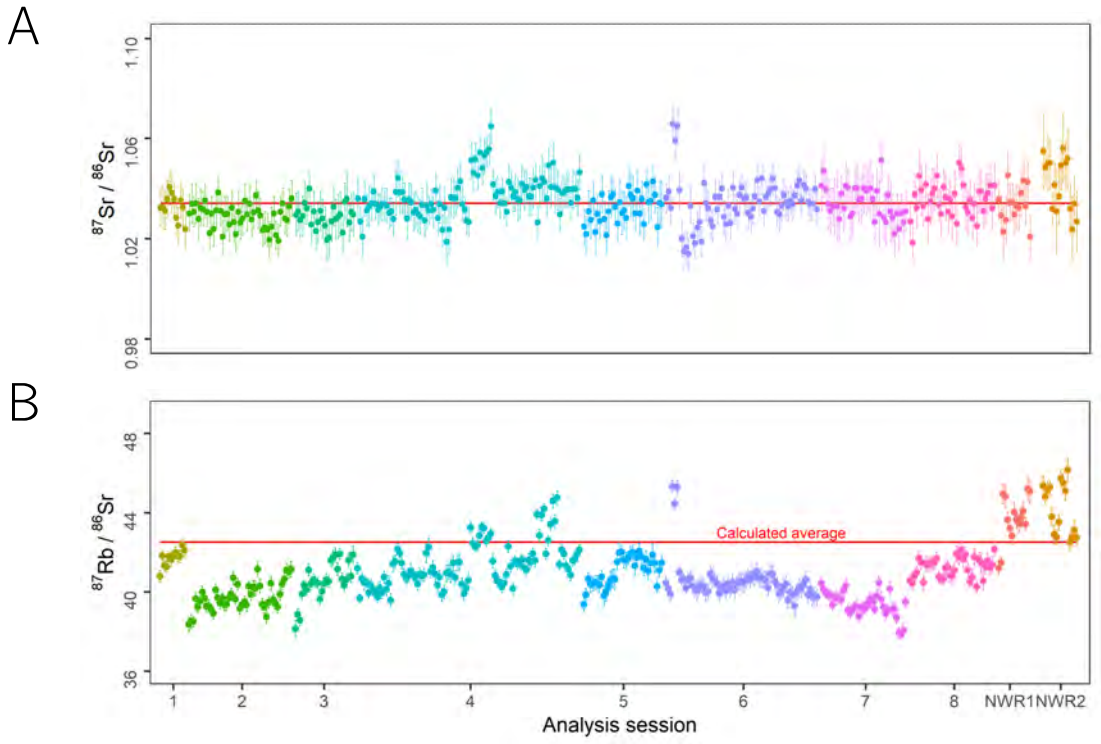

Figure 2.3: (A) $^{87}Sr/^{86}Sr$ and (B) $^{87}Rb/^{86}Sr$ isotopic ratios of MDC analysed over ten sessions, normalised to Mica-Mg-NP. The first eight sessions of data were collected using the 193nm laser whereas NWR1 and 2 refers to data obtained with the 213nm laser. The red line in (A) shows the $^{87}Sr/^{86}Sr$ average of all acquired data, and in (B) shows) the expected $^{87}Rb/^{86}Sr$ calculated from the $^{87}Sr/^{86}Sr$ average in A, with most of the measured $^{87}Rb/^{86}Sr$ data lower than that this expected value, which corresponds to older calculated ages.

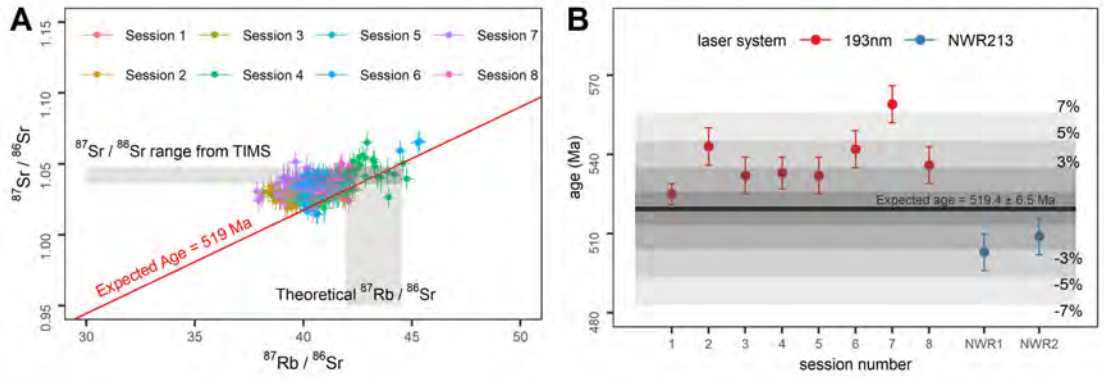

Figure 2.4: (A) A Rb–Sr isochron diagram for MDC obtained over eight sessions using the 193nm laser, producing generally higher variation of $^{87}Rb/^{86}Sr$ ratios along the x-axis, compared to $^{87}Sr/^{86}Sr$ data. The grey rectangles represent the range of $^{87}Sr/^{86}Sr$ acquired by TIMS and the calculated $^{87}Rb/^{86}Sr$ ratios of MDC (see section 2.3.1). The red line represents the isochron line of the expected age for MDC of 519 Ma. For more detailed data from each analytical session, see Figure 2.A in the Supplementary material. (B) Variation in the calculated average age of MDC from session to session obtained using the 193nm and 213nm laser systems. The black rectangle represents the expected age of MDC of 519.4 ± 6.5 Ma (Hogmalm et al., 2017), and the lighter grey areas show the error range in percentage.

terial (using the 193nm laser system), including Mica-Mg-NP, MDC and NIST610, and the data were normalised to Mica-Mg-NP (see Figure 2.6, and data in Supplementary

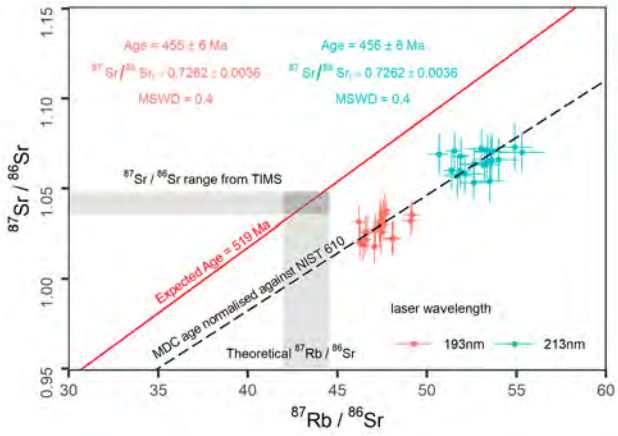

Figure 2.5: A Rb–Sr isochron age for MDC, where $^{87}Rb/^{86}Sr$ and $^{87}Sr/^{86}Sr$ ratios were normalised to a non-matrix matched NIST 610 glass. The red and blue points represent the 193 nm and 213 nm laser wavelengths respectively, and the red line illustrates the expected isochron and/or age for MDC phlogopite (519 Ma, Hogmalm et al., 2017), and the gray rectangles illustrate the range of $^{87}Rb/^{86}Sr$ and $^{87}Sr/^{86}Sr$ ratios constrained via TIMS data (see section 2.3.1).

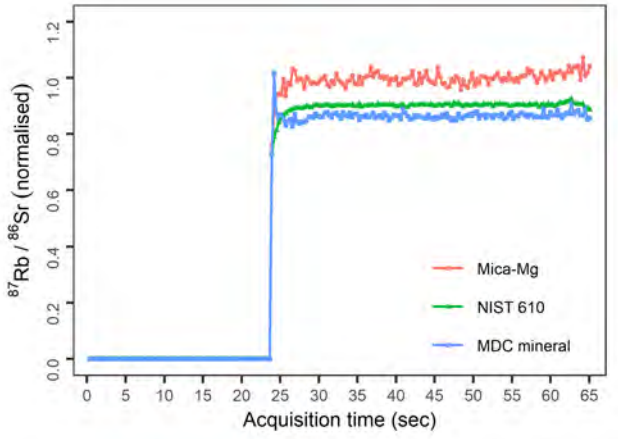

Figure 2.6: Average of $^{87}Rb/^{86}Sr$ ratios of Mica-Mg-NP, MDC and NIST610 (normalised to Mica-Mg-NP and its expected values (Table 2.1)), acquired from 10 line rasters using the 193nm laser with a 74 μm beam diameter and scan speed of 7.4 $\mu m/s$.

material Table 2.D) and also to NIST 610 (see Table 2.E in the Supplementary material). The time-resolved $^{87}Rb/^{86}Sr$ ratios of MDC and NIST 610 were relatively stable. However, Mica-Mg-NP signals were generally noisier with larger variability in $^{87}Rb/^{86}Sr$ ratios (Figure 2.6).

The Rb–Sr age of MDC phlogopite acquired via the line raster approach yielded an age of 601 $\pm$ 8 Ma when normalised to Mica-Mg-NP and an age of 545 $\pm$ 8 Ma when normalised to NIST 610 (Figure 2.7), which are about 15% and 5% older than the expected age of this phlogopite (519.4 $\pm$ 6.5 Ma, Hogmalm et al., 2017), respectively. This inconsistency in the Rb–Sr age is primary controlled by the offset between the expected and measured $^{87}Rb/^{86}Sr$ ratios, depending on which reference material was

used for the normalisation. The $^{87}Rb/^{86}Sr$ ratios of MDC were about 13% lower relative to the expected ratio when data were normalised to Mica-Mg nano-powder (Table. 2.D in the Supplementary material), and they were 6% lower when data were normalised to NIST 610 (Table. 2.E in the Supplementary material). In contrast the $^{87}Sr/^{86}Sr$ ratios varied by less than 0.7%, which is within the internal error for this data set.

2.3.3 Reproducibility of NIST 610 using the 193nm laser system

The NIST 610 glass reference material was analysed over eight sessions as discussed previously. The average ratios are displayed in Figure 2.8, with source data listed in Table 2.F in the Supplementary material. The $^{87}Rb/^{86}Sr$ and $^{87}Sr/^{86}Sr$ raw ratios showed limited variation within the sessions (after correction of instrumental drift) with an internal precision ranging between 0.33% and 0.69% (1σ), and between 0.09% and 0.18% (1σ), respectively. The data were normalised to Mica-Mg-NP, but the raw $^{87}Rb/^{86}Sr$ ratios were more consistent from session to session ($1\sigma = 0.66\%$) compared to the normalised ratios ($1\sigma = 1.84\%$). The normalised $^{87}Rb/^{86}Sr$ ratios show a significant offset being 13% to 18% lower than the expected ratio of 2.33 (see Hogmalm et al., 2017). In contrast, the variation of raw $^{87}Sr/^{86}Sr$ ratios for NIST 610 between the sessions was 0.36% (1σ) but improved to 0.12% after normalisation, with normalised values falling within the expected range 0.709699 $\pm$ 0.000018 (see Woodhead and Hergt, 2001 and Figure 2.8).

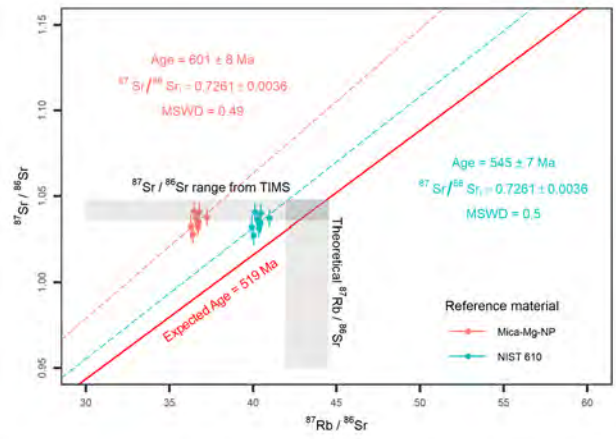

Figure 2.7: Rb–Sr age of MDC acquired from line rasters using the 193nm laser. The red line illustrates the expected isochron age of MDC (519.4 $\pm$ 6.5 Ma, Hogmalm et al., 2017) and the gray rectangles shows the range of $^{87}Rb/^{86}Sr$ and $^{87}Sr/^{86}Sr$ ratios constrained via TIMS data (see also section 2.3.1). The colour of points shows the reference material that was used for normalisation.

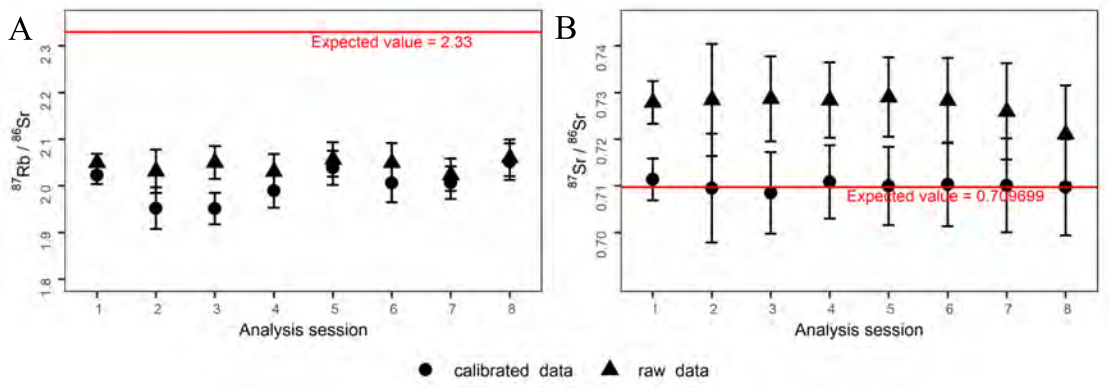

Figure 2.8: The average raw and calibrated ratios of NIST 610 analysed with the 193nm laser over eight different sessions. (A) diagram shows significant offset in $^{87}Rb/^{86}Sr$ from the expected value, and the calibrated $^{87}Rb/^{86}Sr$ values showed more variation from session to session compared to the raw ratios. (B) $^{87}Sr/^{86}Sr$ of NIST 610 overlap the expected value of 0.709699 $\pm$ 0.000018 after the normalisation or calibration against Mica-Mg-NP.

2.3.4 Down hole fractionation effects on $^{87}Rb/^{86}Sr$ ratios

193nm laser

The $^{87}Rb/^{86}Sr$ ratios of Mica-Mg-NP, MDC, and NIST 610 were collected using the 193nm laser system over a period of ca. 40 seconds (sec) for 30 individual LA spot analyses in each material, and data were then averaged and normalised to Mica-Mg-NP (Figure 2.9A). The results show that the DHF profiles for $^{87}Rb/^{86}Sr$ vary with time during the ablation, and these profiles are also sample-specific.

Both MDC and NIST 610 display a progressively increasing trend in $^{87}Rb/^{86}Sr$ ratios, with MDC being steeper. In contrast, the Mica-Mg-NP has a more complex DHF pattern, where $^{87}Rb/^{86}Sr$ ratios gradually rise over the first ca. 10 sec but then systematically decrease during an interval from ca. 15 to 35 sec, and eventually flatten out over the last ca. 5 sec (Figure 2.9A). In contrast, no detectable DHF effects were observed for the radiogenic $^{87}Sr/^{86}Sr$ ratios in any of the above materials.

213nm laser

The DHF profiles for $^{87}Rb/^{86}Sr$ were also investigated using the 213nm laser with a spot size of 75 μm (Figure 2.9B). These DHF profiles for Mica-Mg-NP, MDC and NIST 610 were different compared to those measured with the 193nm laser (compare Figure 2.9A and B). Specifically, $^{87}Rb/^{86}Sr$ ratios of MDC increased gradually during the first 5 seconds and then flattened out towards the end of the acquisition. For NIST 610, the $^{87}Rb/^{86}Sr$ ratios increased continuously following a linear trend, whereas data from the Mica-Mg-NP gradually decreased (Figure 2.9B).

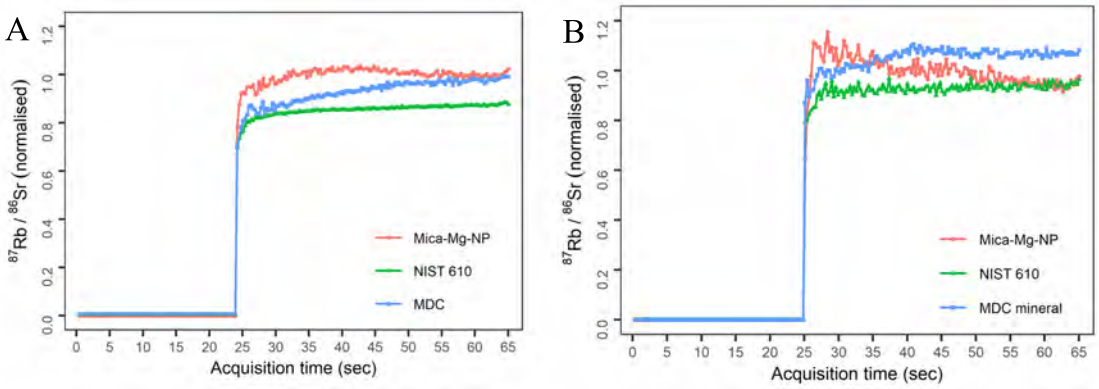

Figure 2.9: The DHF profiles for ^{87}Rb/^{86}Sr ratios of Mica-Mg-NP, MDC and NIST 610 obtained with (A) the 193nm laser and 74 µm laser beam and (B) with the 213nm laser, and 75 µm laser beam; all data are normalised to Mica-Mg-NP and its expected ^{87}Rb/^{86}Sr value (see data in Table 2.1).

2.3.5 Evaluation of ablation characteristics of different materials: MDC, Mica-Mg-NP and NIST 610

Laser profilometry analysis

The ablation craters in MDC phlogopite, Mica-Mg-NP, and NIST 610 glass were imaged via the laser scanning confocal microscope (LSCM) to characterise the different ablation properties of these different materials and to assess and calculate the crater 'depths', which, in turn, can be used to quantify absolute ablation rates (e.g., nanometres per a pulse) of the different materials.

The craters in the Mica-Mg-NP show an elevated crater rim and a very uneven and irregular base (Figure 2.10A and B). Calculated ablation rates for the Mica-Mg-NP varied among individual craters, with the crater depths ranging from ca. 33.5 µm to 39 µm, giving an average ablation rate of ∼181 nm/pulse.

The LA craters in MDC also display high rims, but have very smooth convex bases and tend to be much shallower with an average ablation rate of about 90 nm/pulse (Figure 2.10C and D). This is almost 50% lower than the ablation rate of Mica-Mg-NP.

Finally, the NIST 610 glass exhibits very similar crater morphologies to those observed in the MDC, with a typically smooth and convex base, but with almost flat crater rims (Figure 2.10E and F). The average ablation rate in NIST 610 glass is about 155 nm/pulse, which is closer to that observed in Mica-Mg NP than MDC. Overall, the crater dimensions and morphologies of NIST 610 and MDC materials were relatively constant and reproducible from spot to spot, unlike the craters observed in Mica-Mg-NP, which showed more spatial variation.

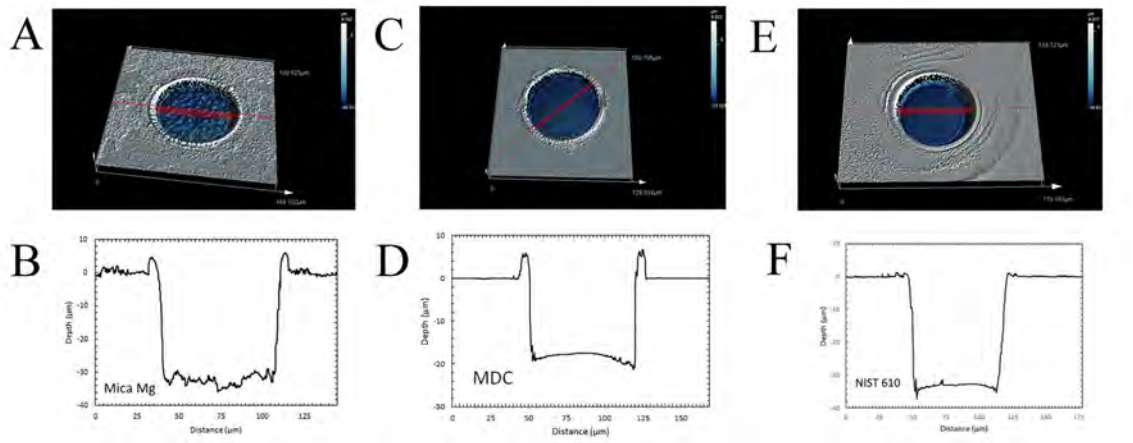

Figure 2.10: Laser profilometry images of the laser ablation crater and the DHF profiles illustrating the differences between (A and B) Mica-Mg.NP, (C and D) MDC and (E and F) NIST 610 in terms of crater morphology.

High-resolution backscatter electron (BSE) imaging

The Mica-Mg-NP was imaged by scanning electron microscopy to investigate the homogeneity of particle sizes within the pellet, and to assess the physical damage of the NP material after the LA analysis. Backscatter electron images show that there is a considerable degree of heterogeneity in the particle sizes within the pellet, and larger µm-scale fragments of phlogopite (up to 15-20 µm in diameter) were occasionally observed at the surface of the pellet but also in the subsurface (Figure 2.11A and B, respectively).

In addition, the craters in Mica-Mg-NP ablated using both 213nm and 193nm lasers were also imaged to inspect the impact of the laser wavelength on the NP pellet. There are noticeable differences in the friability and physical damage of the craters induced by different lasers (Figure 2.11C and D). Specifically, the 213nm laser produced uneven craters with a more friable texture. The uneven energy distribution in the 213nm laser beam is apparent, where one side of the crater tended to be ablated more than the other (Figure 2.11D). The base of the 213nm craters were relatively flat comparing to those produced by the 193nm laser that have a more irregular base with a granular texture (Figure 2.11C) as described in the previous section.

The ejecta blankets around the craters also varied between the different laser systems. The 213nm laser produced a thicker and uneven deposit around the craters, with the ejected material extending further around the craters (Figure 2.11D), compared to the ejecta produced by the 193nm laser (Figure 2.11C).

The trenches produced by the line rasters were also imaged. The 193nm laser produced lines in MDC with a flat base and only a small amount of ejecta around the ablated area (Figure 2.11G). In contrast, the lines produced in Mica-Mg-NP showed an irregular

base with ejecta accumulated at the edges of the trenches (Figure 2.11E). However, the 213nm laser was much more destructive in Mica-Mg-NP, and it produced trenches with uneven texture and crumbled edges, separated by areas exhibiting extensive physical damage (Figure 2.11F).

2.4 Discussion

2.4.1 Ablation characteristics of MDC and Mica-Mg-NP

Considering presumably identical, or very similar, major element compositions of MDC and Mica-Mg-NP phlogopites (both originating from the same Bekily area of Madagascar), it is likely that the observed differences in elemental Rb/Sr fractionation patterns between these two materials (i.e., nano-powder vs. natural mineral flakes) are related to their different ablation properties. The friable and granular nature of the nano-powder material (Mica-Mg-NP) is thus likely responsible for the specific ablation characteristics and texture observed at the base of craters in Mica-Mg-NP, compared to the flat-base craters in the natural mineral MDC (see section 2.3.5). It is therefore not surprising that these two phlogopite materials, MDC and Mica-Mg-NP, have also very different ablation rates and associated DHF patterns for the $^{87}Rb/^{86}Sr$ ratios. The shapes and depths of the ablated craters in Mica-Mg-NP were also different from spot to spot. This is likely related to the fact that Mica-Mg phlogopite is a difficult mineral to pulverize due to its flaky nature and perfect cleavage, hence, it is not an ideal material for the preparation of equi-granular nano-pellets with constant porosity and ablation characteristics. This can thus explain the observed results and internal variability in ablation characteristics across the Mica-Mg-NP pellet (e.g., due to its variable porosity, compaction, and particle size, see Figure 2.11).

In addition, it is also possible that some of the observed variability in measured $^{87}Rb/^{86}Sr$ ratios in analysed phlogopites could also arise from the positioning and spacing of LA spots within the Mica-Mg-NP reference material. When a sequence of LA spots were performed using an evenly spaced array, the previously ablated craters were observed to have an effect on the Rb/Sr ratio, and caused the apparent 'drift' seen in some runs (Figure 2.2B), which then biased the corrected MDC ages. Possible factors to consider are the potential for physical damage to the material from the previous LA spots especially in the nano-powder pellet (Figure 2.11C and 2.11D), re-ablation of the ejecta blanket from previous spots (see Košler et al., 2005) or effects of gas flow turbulence from previously ablated craters. The exact physical processes involved require

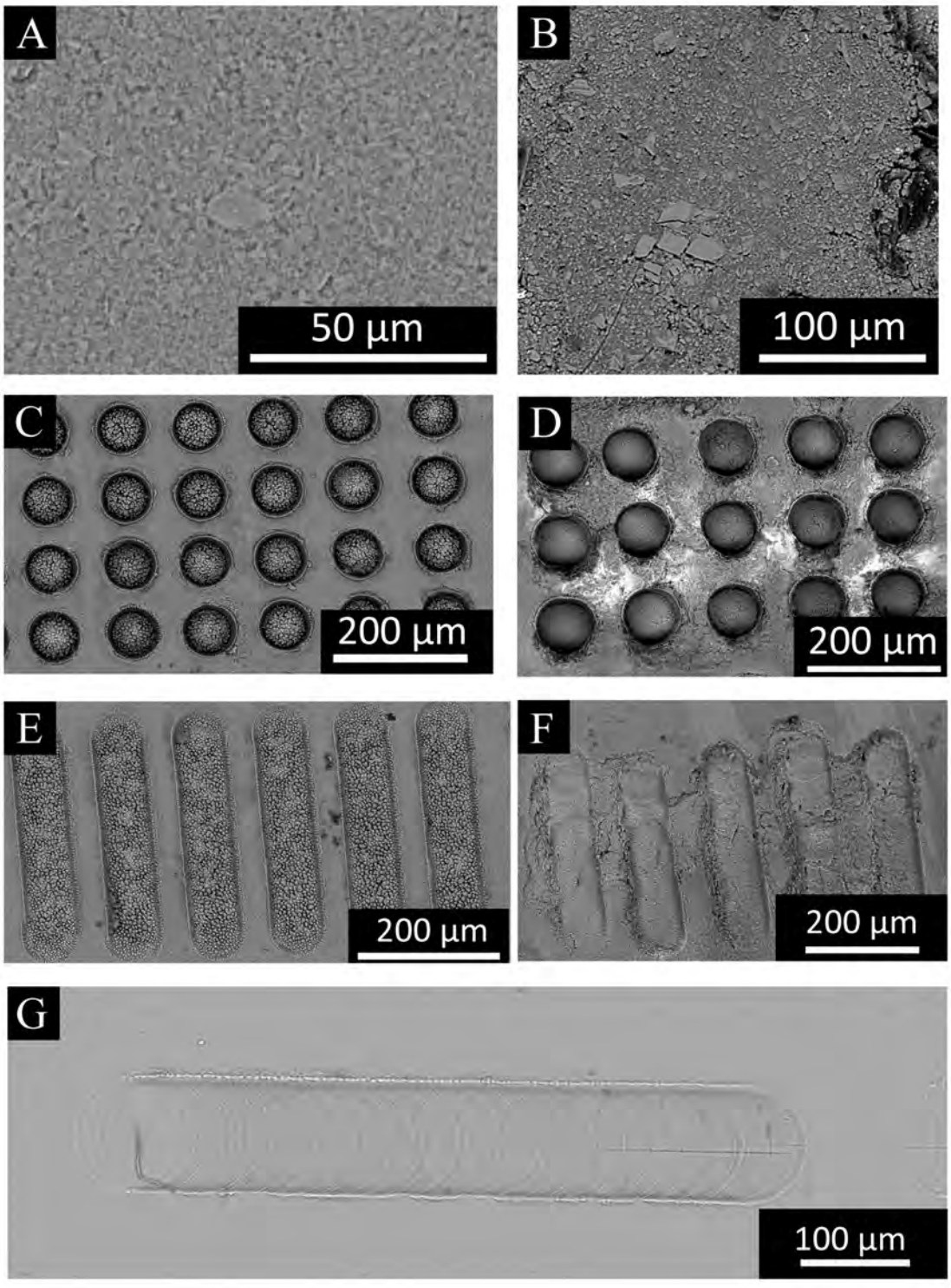

Figure 2.11: The BSE images of (A) the surface and (B) subsurface of Mica-Mg-NP from the chipped edge of the pellet, illustrating the variation in particles sizes, which range from a dominant nano-powder ($<1\mu\mathrm{m}$), to occasionally larger particles (10 $\mu\mathrm{m}$). (C) Laser craters within Mica-Mg-NP produced by 193nm laser and (D) 213nm laser system. (E) Lines raster ablated on Mica-Mg-NP by the 193nm laser system and (F) the 213nm laser system. (G) Lines raster ablated on MDC by the 193nm laser system.

further investigation, but preliminary work indicates that Rb/Sr ratios are more sensitive to these effects than other element pairs (such as U/Pb), and consistency of spot spacing is an important consideration to minimise Rb/Sr fractionation in Mica-Mg-NP.

2.4.2 The Rb/Sr elemental fractionation effects

The apparent session to session variation in *in-situ* Rb–Sr ages of MDC (Figure 2.4B) is most likely related to a higher variability in the $^{87}Rb/^{86}Sr$ ratios within, and between sessions from Mica-Mg-NP. Less variability in the calculated age for MDC is seen when it is normalised to the NIST 610 (Figure 2.5); however, matrix effects (due to chemical differences with respect to MDC) are greater for this glass standard, relative to Mica-Mg-NP.

The higher variability in $^{87}Rb/^{86}Sr$ ratios between materials analysed, compared to $^{87}Sr/^{86}Sr$, indicates that elemental fractionation effects are occurring between Rb and Sr during the LA-ICP-MS/MS analysis. Commonly, during the ablation, element–signal intensities of refractory elements (e.g., Sr, Ca, U) decrease more rapidly compared to more volatile elements (e.g., Rb, K, Pb) (Eggins, Kinsley, and Shelley, 1998). Thus ratios of volatile to refractory elements (e.g. $^{208}Pb/^{238}U$) generally display increasing trends during the analysis, as the aerosol size distribution decreases with time and these smaller particles are more enriched in the volatile elements (Eggins, Kinsley, and Shelley, 1998). Such anticipated increase in $^{87}Rb/^{86}Sr$ ratios during the ablation was indeed observed for MDC when it was ablated by the 193nm laser but when the sample ablated with the 213nm laser, the measured $^{87}Rb/^{86}Sr$ increased during the first 15 seconds and became constant afterward (see section 2.3.4, Figure 2.9B). NIST 610 showed slightly increase in the measured $^{87}Rb/^{86}Sr$ during the first few seconds and stabilised during the rest of ablation time (Figure 2.9). However, data from Mica-Mg-NP (acquired using both the 213 nm and 193 nm lasers (Figure 2.9)) show a more complex DHF pattern that suggests that other processes, apart from volatilisation effects, are also occurring.

We speculate that the observed Rb/Sr fractionation trends for Mica-Mg-NP (see section 2.3.4) are partly related to variable aerosol particle size distribution during the ablation (Kuhn and Günther, 2004). The BSE images show a degree of heterogeneity in the grain sizes within the Mica-Mg-NP pellet (ranging from nm to μm sizes, see section 2.3.5, which may cause the variable ablation observed between craters due to differences in compaction or differential ablation of these larger particles. We speculate that some original mineral particles may also be incorporated in the aerosol stream reaching the ICP due to mechanical disintegration of the pellet (e.g., linked to physical

damage around the lines and craters, see Figure 2.11C, D,E and F). These processes and physical/ablation characteristics of the phlogopite nano-powder pellet could partly explain the observed variation in raw $^{87}Rb/^{86}Sr$ ratios of Mica-Mg-NP within the sessions and from session to session (section 2.3.2). Accordingly, the distribution of aerosol size produced during the ablation might have varied from spot to spot, influencing the Rb/Sr elemental fractionation and the corresponding $^{87}Rb/^{86}Sr$ ratios. Although, DHF has been studied extensively for the U–Pb system in a number of minerals (Jackson and Günther, 2003; Wang, Hattendorf, and Günther, 2006; Weis, Beck, and Günther, 2005), further and more systematic investigations are needed to better understand the impact of DHF effects on the accuracy and precision for *in-situ* Rb–Sr dating.

2.4.3 Laser-wavelength dependent effects on Rb/Sr elemental fractionation

Rb/Sr elemental fractionation occurs in both 213nm and 193nm laser systems, and it seems to be relatively consistent for NIST 610, but more complicated for Mica-Mg-NP and MDC (see section 2.3.4). The DHF pattern for Rb/Sr observed in NIST 610 does not significantly change between the two different laser wavelengths, which explains the consistency of the calculated Rb–Sr ages for MDC when normalised to NIST 610 (for data analysed by both LA systems; see Figure 2.5). In contrast, the increased physical damage around the ablated areas observed in Mica-Mg-NP analysed with the 213nm laser (see also section 2.3.5) is likely partly responsible for the very different DHF pattern for Mica-Mg-NP (see the decreasing of the Rb/Sr ratio with time, Figure 2.9B). Such marked differences in Mica-Mg-NP DHF patterns produced by two LA systems (Figure 2.9) can in part account for the observed systematic offsets in the calculated Rb–Sr ages for MDC (normalised to Mica-Mg-NP). The 193nm laser tends to produce ages that are generally older compared to ages acquired via the 213nm laser system (Figure 2.4B). These laser specific differences are further amplified by the fact that no DHF correction has been applied for $^{87}Rb/^{86}Sr$ data during processing, as the DHF in the Mica-Mg-NP reference material is not transferable to the samples.

This indicates there are laser specific effects on the accuracy of the *in-situ* Rb–Sr ages, especially when the nano-powder is used as a primary reference material for normalisation, which thus needs to be taken into account and carefully evaluated by future studies.

2.4.4 Matrix effects and their impact on *in-situ* Rb–Sr ages

Matrix effects caused by differences in chemical composition between phlogopites (MDC, Mica-Mg-NP) and NIST 610 glass and their ablation characteristic are most apparent for line rasters due to constant ablation over time (i.e., minimum or no DHF present) (Gilbert et al., 2014). The Rb–Sr age of MDC obtained by normalising the line raster data against Mica-Mg-NP was less accurate than the age obtained when normalising to NIST 610 (Figure 2.7)). This suggests that the difference in ablation characteristics between MDC and Mica-Mg-NP has more influence on the accuracy than the difference in chemical composition between MDC and NIST 610. For spot analyses, the DHF increases the $^{87}Rb/^{86}Sr$ ratio with time, which, in this case, offsets some of the observed matrix effects between MDC, NIST 610 and Mica-Mg-NP since the DHF was steepest for MDC. The overall impact of matrix effects is dependent on a combination of the physical properties of ablated materials, laser wavelength, chemical composition of materials, ablation mode and analytical setup, and it may thus vary considerably and should be assessed and monitored closely.

2.4.5 Implications for the accuracy of *in-situ* Rb–Sr ages of phlogopite (MDC)

Assuming that the $^{87}Sr/^{86}Sr$ initial ratio is identical for MDC and Mica-Mg materials, the overall accuracy of our LA-ICP-MS/MS method and acquired Rb-Sr age for MDC were typically within 3% and occasionally up to 8% (see section 2.3.2 and Figure 2.4B). Considering that MDC and Mica-Mg-NP phlogopites were both sourced from the same area (Bekily, Madagascar), we assume that these materials should have also identical Rb–Sr ages. However, they are unlikely to have the same Rb and Sr concentrations and will also have different $^{87}Rb/^{86}Sr$ and $^{87}Sr/^{86}Sr$ ratios. In this study, the ages of MDC were all calculated using an assumed initial $^{87}Sr/^{86}Sr$ ratio of 0.72607 ± 0.0007, as reported for Mica-Mg phlogopite (Hogmalm et al., 2017). One possibility for the age discrepancies (between acquired and expected ages) could be related to potential natural variation in MDC, and differences in the initial $^{87}Sr/^{86}Sr$ of MDC vs. Mica-Mg-NP phlogopites. The initial $^{87}Sr/^{86}Sr$ ratio used in this study for MDC and Mica-Mg-NP was constrained based on published $^{87}Rb/^{86}Sr$ and $^{87}Sr/^{86}Sr$ data of two samples from Bekily area (15527 and 15529) (Morteani et al., 2013), each containing phlogopite and diopside mineral pairs, which were used to construct Rb-Sr isochron and the Sr initial (see Hogmalm et al., 2017 for details). Calculating the initial $^{87}Sr/^{86}Sr$ ratios

separately for these two phlogopite-diopside pairs yielded the Sr initials of 0.72585 and 0.72625, respectively (Morteani et al., 2013), with an average of ∼0.7261. Changing the Sr isotope initial ratio of MDC from 0.72607 (used in this study, and adopted from Hogmalm et al., 2017) to a lower value of 0.72585 (i.e., the minimum estimate) or a higher initial of 0.72625 (the maximum based on the above mineral pair data (Morteani et al., 2013)) would only have a minor impact on the calculated Rb-Sr ages of MDC (for all analysed sessions). Specifically, the recalculated age of MDC would change only by 0.09% (for a minimum value) and 0.04% (for the maximum Sr initial), which thus have a very minor effect on the overall accuracy. The initial $^{87}Sr/^{86}Sr$ of the analysed MDC would have to be significantly more radiogenic (>0.73) than the above reported maximum (0.72625) to reconcile the systematically older Rb–Sr ages for MDC acquired in this study using 193nm laser (see Figure 2.4B). Such more radiogenic initial $^{87}Sr/^{86}Sr$ ratios up to 0.74239 were reported for other pegmatitic rocks (syenite) within the Beraketa shear zone in which the Bekily area is located (Morteani et al., 2013). Using a much more radiogenic initial ratio (0.73311) for our MDC data, measured by 193nm laser, which would be within the range of published Sr initials for syenite (Morteani et al., 2013), would yield an average age of 520 Ma, which would thus be in agreement with the expected age of 519.4 ± 6.5 Ma (Hogmalm et al., 2017); corresponding to about 2.3% improvement in the overall accuracy relative to data acquired with the assumed Sr initial of 0.72607 (Hogmalm et al., 2017). However, using such hypothetical and highly radiogenic Sr initial of ∼0.73311 for MDC is in our view not well justified due to the fact that this high Sr initial is derived based on the analysis of syenite and not phlogopite data (i.e., phlogopite-diopside pairs, Morteani et al., 2013). Regardless of the initial Sr ratio used it would not reconcile the observed session-to-session variability in ages measured for MDC. We conclude that the variation in apparent Rb–Sr ages for MDC (see Figure 2.4B), are related to the variable elemental fractionation and ablation characteristics of Mica-Mg-NP relative to the natural mineral (MDC). At present, Mica-Mg-NP is the most commonly available nano-powder reference material for *in-situ* LA-ICP-MS/MS Rb–Sr dating of phlogopite, but additional secondary mineral standards of known age are required for more accurate Rb–Sr age determination. Such approach using a secondary mineral standard enables proper assessment of data quality and a possible age-offset correction, if required (Armistead et al., 2020; Li et al., 2020 see).

2.5 Conclusions

In-situ Rb–Sr dating via LA-ICP-MS/MS still faces certain analytical challenges which currently limits its wider applications and accuracy for age determination. The main challenges include (i) sample-specific Rb–Sr elemental fractionation effects, (ii) different ablation properties between nano-powder standards and natural minerals, and (iii) a lack of matrix-matched reference materials. All of the above have an impact on the measured $^{87}Rb/^{86}Sr$ ratios but have minimum effects on measured $^{87}Sr/^{86}Sr$ ratios, which were more reproducible for all studied materials (Mica-Mg-NP, MDC phlogopite mineral, and NIST 610 glass) using both 193nm and 213nm laser systems.

For phlogopite dating, the Mica-Mg-NP is currently the best nano-powder reference material that is available, but it is still not ideal due to observed differences in ablation rates, crater shapes, and DHF patterns compared to the natural phlogopite mineral (MDC). Therefore, further investigation is required to constrain the sources and mechanisms of $^{87}Rb/^{86}Sr$ fractionation during *in-situ* Rb–Sr dating. In addition, developing more reliable and matrix-matched reference materials for phlogopite, and other rock-forming K-rich minerals, is needed.

With the current reference materials available for *in-situ* Rb–Sr dating, we recommend regular analysis of a secondary matrix-matched mineral standard (such as MDC-phlogopite, Högsbo-muscovite (Hogmalm et al., 2017) etc.) to assess the accuracy of the calculated *in-situ* Rb–Sr ages. With this method we have shown that ages are achievable within an accuracy of about 3%, which can however be further improved to about 1% (i.e., typical internal precision), if an unknown sample and the mineral standard have identical ablation properties and chemical compositions, thus minimising the impact from DHF and matrix effects.

Alternatively, one can calculate an age-offset correction factor derived from the secondary mineral standard which can be then applied to unknown samples. Such approach has been used recently to successfully date micas via *in-situ* Rb–Sr technique in a range of geological settings to better understand the tectonic and geological history of our planet (see Armistead et al., 2020; Li et al., 2020).

2.6 Conflicts of interest

There are no conflicts of interest to declare.

2.7 Acknowledgment

This research was funded via the Australian Research Council – ARC Linkage grant LP160101353, and the Mineral Exploration Cooperative Research Centre (MinEx CRC Project 8). Additional financial support was received from Agilent Technologies and the technical assistance of Fred Fryer (Agilent) is also gratefully acknowledged. We also thank Carl Spandler for revising the manuscript and for his constructive feedback. Finally, we thank David Bruce for his assistance in analysing the Sr isotope compositions of MDC phlogopite samples by TIMS at the Metal Isotope Group (MIG) facilities at the Department of Earth Sciences, University of Adelaide. This is a MinEx CRC contribution No. 2020/6.

References

Agatemor, C and D Beauchemin (2011). "Matrix effects in inductively coupled plasma mass spectrometry: a review". In: *Anal Chim Acta* 706.1, pp. 66–83.

Armistead, Sheree E, Alan S Collins, Ahmad Redaa, Gilby Jepson, Jack Gillespie, Sarah Gilbert, Morgan L Blades, John D Foden, and Théodore Razakamanana (2020). "Structural evolution and medium-temperature thermochronology of central Madagascar: implications for Gondwana amalgamation". In: *Journal of the Geological Society* 177, pp. 784–798.

Beranoaguirre, Aratz, Christian Pin, Maria Eugenia Sanchez-Lorda, Sonia de Madinabeitia, and Jose Ignacio Gil Ibarguchi (2019). "An evaluation of Rb-Sr isotope dilution analyses with a ^{86}Sr-enriched tracer and Multiple Collection-ICP-MS". In: *International Journal of Mass Spectrometry* 435, pp. 234–240.

Bohme, Diethard (2019). *M^+ Chemistry*. URL: `http://www.yorku.ca/dkbohme/research/selection_table.html`.

Bolea-Fernandez, Eduardo, Lieve Balcaen, Martín Resano, and Frank Vanhaecke (2015). "Tandem ICP-mass spectrometry for Sr isotopic analysis without prior Rb/Sr separation". In: *Journal of Analytical Atomic Spectrometry* 31.1, pp. 303–310.

Bolea-Fernandez, Eduardo, Stijn J M Van Malderen, Lieve Balcaen, Martin Resano, and Frank Vanhaecke (2016). "Laser ablation-tandem ICP-mass spectrometry (LA-ICP-MS/MS) for direct Sr isotopic analysis of solid samples with high Rb/Sr ratios". In: *Journal of Analytical Atomic Spectrometry* 31.2, pp. 464–472.

Claverie, Fanny, Beatriz Fernndez, Christophe Pcheyran, Joël Alexis, and Olivier F X Donard (2009). "Elemental fractionation effects in high repetition rate IR femtosecond laser ablation ICP-MS analysis of glasses". In: *Journal of Analytical Atomic Spectrometry* 24.7, pp. 891–902.

Eggins, S M, L P J Kinsley, and J M G Shelley (1998). "Deposition and element fractionation processes during atmospheric pressure laser sampling for analysis by ICP-MS". In: *Applied Surface Science* 127-129, pp. 278–286.

Eiden, C G, J C Barinaga, and W D Koppenaal (1999). "Analytical performance of the plasma source RF quadrupole ion trap in elemental and isotopic MS". In: *Journal of Analytical Atomic Spectrometry* 14.8, pp. 1129–1132.

Elburg, Marlina, Pieter Vroon, Bas van der Wagt, and Arnaud Tchalikian (2005). "Sr and Pb isotopic composition of five USGS glasses (BHVO-2G, BIR-1G, BCR-2G, TB-1G, NKT-1G)". In: *Chemical Geology* 223.4, pp. 196–207.

Fryer, Brian J, Simon E Jackson, and Henry P Longerich (1995). "The design, operation and role of the laser-ablation microprobe coupled with an inductively coupled plasma; mass spectrometer (LAM-ICP-MS) in the earth sciences". In: *The Canadian Mineralogist* 33.2, pp. 303–312.

Garbe-Schönberg, Dieter and Samuel Müller (2014). "Nano-particulate pressed powder tablets for LA-ICP-MS". In: *Journal of Analytical Atomic Spectrometry* 29.6, pp. 990–1000.

Gilbert, S E, L V Danyushevsky, K Goemann, and D Death (2014). "Fractionation of sulphur relative to iron during laser ablation-ICP-MS analyses of sulphide minerals: implications for quantification". In: *Journal of Analytical Atomic Spectrometry* 29.6, pp. 1024–1033.

Gorojovsky, Lauren and Olivier Alard (2020). "Optimisation of laser and mass spectrometer parameters for the in situ analysis of Rb/Sr ratios by LA-ICP-MS/MS". In: *Journal of Analytical Atomic Spectrometry* 35.10, pp. 2322–2336.

Govindaraju, K (1979). "Report (1968–1978) on Two Mica Reference Samples: Biotite Mica-Fe and Phlogopite Mica-Mg". In: *Geostandards and Geoanalytical Research* 3.1, pp. 3–24.

— (1994). "1994 compilation of working values and sample description for 383 geostandards". In: *Geostandards Newsletter* 18, pp. 1–158.

Guillong, Marcel and Detlef Günther (2002). "Effect of particle size distribution on ICP-induced elemental fractionation in laser ablation-inductively coupled plasma-mass spectrometry". In: *Journal of Analytical Atomic Spectrometry* 17.8, pp. 831–837.

Hogmalm, K. Johan, Thomas Zack, Andreas K. O. Karlsson, Axel S. L. Sjöqvist, and Dieter Garbe-Schönberg (2017). "In situ Rb-Sr and K-Ca dating by LA-ICP-MS/MS: an evaluation of N^2O and SF^6 as reaction gases". In: *Journal of Analytical Atomic Spectrometry* 32.2, pp. 305–313.

Hu, Zhaochu, Shan Gao, Yongsheng Liu, Shenghong Hu, Haihong Chen, and Honglin Yuan (2008). "Signal enhancement in laser ablation ICP-MS by addition of nitrogen

in the central channel gas". In: *Journal of Analytical Atomic Spectrometry* 23.8, pp. 1093–1101.

Jackson, Simon E and Detlef Günther (2003). "The nature and sources of laser induced isotopic fractionation in laser ablation-multicollector-inductively coupled plasma-mass spectrometry". In: *Journal of Analytical Atomic Spectrometry* 18.3, pp. 205–212.

Jackson, Simon E and P Sylvester (2008). "Calibration strategies for elemental analysis by LA–ICP–MS". In: *SIGNAL* 10.1,000, p. 100.

Košler, Jan, Michael Wiedenbeck, Richard Wirth, Jan Hovorka, Paul Sylvester, and Jitka Míková (2005). "Chemical and phase composition of particles produced by laser ablation of silicate glass and zircon—implications for elemental fractionation during ICP-MS analysis". In: *Journal of Analytical Atomic Spectrometry* 20.5, pp. 402–409.

Kuhn, Hans-Rudolf and Detlef Günther (2004). "Laser ablation-ICP-MS: particle size dependent elemental composition studies on filter-collected and online measured aerosols from glass". In: *Journal of Analytical Atomic Spectrometry* 19.9, pp. 1158–1164.

Li, Shan-Shan, M Santosh, Juraj Farkaš, Ahmad Redaa, Sohini Ganguly, Sung Won Kim, Cun Zhang, Sarah Gilbert, and Thomas Zack (2020). "Coupled U-Pb and Rb-Sr laser ablation geochronology trace Archean to Proterozoic crustal evolution in the Dharwar Craton, India". In: *Precambrian Research* 343, p. 105709.

Mank, Arjan. J G and Paul R D Mason (1999). "A critical assessment of laser ablation ICP-MS as an analytical tool for depth analysis in silica-based glass samples". In: *Journal of Analytical Atomic Spectrometry* 14.8, pp. 1143–1153.

Miliszkiewicz, Natalia, Stanisław Walas, and Anna Tobiasz (2015). "Current approaches to calibration of LA-ICP-MS analysis". In: *Journal of Analytical Atomic Spectrometry* 30.2, pp. 327–338.

Morteani, G, Y A Kostitsyn, H A Gilg, C Preinfalk, and T Razakamanana (2013). "Geochemistry of phlogopite, diopside, calcite, anhydrite and apatite pegmatites and syenites of southern Madagascar: evidence for crustal silicocarbonatitic (CSC) melt formation in a Panafrican collisional tectonic setting". In: *International Journal of Earth Sciences* 102.3, pp. 627–645.

Nakai, Shun'ichi, Alex N Halliday, Stephen E Kesler, Henry D Jones, J Richard Kyle, and Thomas E Lane (1993). "Rb-Sr dating of sphalerites from Mississippi Valley-type (MVT) ore deposits". In: *Geochimica et Cosmochimica Acta* 57.2, pp. 417–427.

Nebel, Oliver (2015). "Rb–Sr Dating". In: *Encyclopedia of Scientific Dating Methods*. Ed. by W Jack Rink and Jeroen W Thompson. Dordrecht: Springer Netherlands, pp. 686–698.

Nier, Alfred O (1938). "The isotopic constitution of strontium, barium, bismuth, thallium and mercury". In: *Physical Review* 54.4, p. 275.

Nyquist, Laurence E, Chi-Yu Shih, Francis M McCubbin, Alison R Santos, Charles K Shearer, Zhan X Peng, Paul V Burger, and Carl B Agee (2016). "Rb-Sr and Sm-Nd isotopic and REE studies of igneous components in the bulk matrix domain of Martian breccia Northwest Africa 7034". In: *Meteoritics & Planetary Science* 51.3, pp. 483–498.

Outridge, P M, W Doherty, and D C Gregoire (1997). "Ablative and transport fractionation of trace elements during laser sampling of glass and copper". In: *Spectrochimica Acta Part B: Atomic Spectroscopy* 52.14, pp. 2093–2102.

Page, R W (1978). "Response of U-Pb zircon and Rb-Sr total-rock and mineral systems to low-grade regional metamorphism in Proterozoic igneous rocks, Mount Isa, Australia". In: *Journal of the Geological Society of Australia* 25.3-4, pp. 141–164.

Paton, Chad, John Hellstrom, Bence Paul, Jon Woodhead, and Janet Hergt (2011). "Iolite: Freeware for the visualisation and processing of mass spectrometric data". In: *Journal of Analytical Atomic Spectrometry* 26.12, pp. 2508–2518.

Rodushkin, Ilia, Mikael D Axelsson, Dmitry Malinovsky, and Douglas C Baxter (2002). "Analyte-and matrix-dependent elemental response variations in laser ablation inductively coupled plasma mass spectrometry part 2. Implications for multi-element analyses". In: *Journal of Analytical Atomic Spectrometry* 17.10, pp. 1231–1239.

Rosman, K J R and P D P Taylor (1999). "Table of isotopic masses and natural abundances". In: *Pure and Applied Chemistry* 71, pp. 1593–1607.

Shao, Yuexiao, Juraj Farkaš, Chris Holmden, Luke Mosley, Isaac Kell-Duivestein, Christopher Izzo, Patrick Reis-Santos, Jonathan Tyler, Philip Törber, and Jiří Frýda (2018). "Calcium and strontium isotope systematics in the lagoon-estuarine environments

of South Australia: Implications for water source mixing, carbonate fluxes and fish migration". In: *Geochimica et Cosmochimica Acta* 239, pp. 90–108.

Sylvester, PaulJ (2008). "Matrix effects in laser ablation ICP-MS". In: *Laser ablation ICP-MS in the earth sciences: Current practices and outstanding issues*. Vol. 40. Mineralogical Association of Canada, pp. 67–78.

Tanner, Scott D, Vladimir I Baranov, and Dmitry R Bandura (2001). "Reaction cells for ICP-MS". In: *Plasma Source Mass Spectrometry: The New Millennium*. Ed. by Scott D Tanner and Grenville Holland. The Royal Society of Chemistry, pp. 97–98.

Terakado, Y and S Nohda (1993). "RbSr dating of acidic rocks from the middle part of the Inner Zone of southwest Japan: tectonic implications for the migration of the Cretaceous to Paleogene igneous activity". In: *Chemical Geology* 109.1, pp. 69–87.

Tillberg, Mikael, Henrik Drake, Thomas Zack, Johan Hogmalm, and Mats Åström (2017). "In Situ Rb-Sr Dating of Fine-grained Vein Mineralizations Using LA-ICP-MS". In: *Procedia Earth and Planetary Science* 17, pp. 464–467.

Tillberg, Mikael, Henrik Drake, Thomas Zack, Ellen Kooijman, Martin J Whitehouse, and Mats E Åström (2020). "In situ Rb-Sr dating of slickenfibres in deep crystalline basement faults". In: *Scientific Reports* 10.1, pp. 1–13.

Vermeesch, Pieter (2018). "IsoplotR: A free and open toolbox for geochronology". In: *Geoscience Frontiers* 9, pp. 1479–1493.

Villa, I M, P De Bièvre, N E Holden, and P R Renne (2015). "IUPAC-IUGS recommendation on the half life of ^{87}Rb". In: *Geochimica et Cosmochimica Acta* 164, pp. 382–385.

Wang, Zhongke, Bodo Hattendorf, and Detlef Günther (2006). "Analyte Response in Laser Ablation Inductively Coupled Plasma Mass Spectrometry". In: *Journal of the American Society for Mass Spectrometry* 17.5, pp. 641–651.

Ward, David B and Mike Bell (1990). "Determination of rubidium by isotope dilution—inductively-coupled plasma mass spectrometry as an alternative to thermal ionization mass spectrometry". In: *Analytica Chimica Acta* 229, pp. 157–162.

Weis, Peter, Horst P Beck, and Detlef Günther (2005). "Characterizing ablation and aerosol generation during elemental fractionation on absorption modified lithium

tetraborate glasses using LA-ICP-MS". In: *Analytical and Bioanalytical Chemistry* 381.1, pp. 212–224.

Woodhead, Jon D and Janet M Hergt (2001). "Strontium, neodymium and lead isotope analyses of NIST glass certified reference materials: SRM 610, 612, 614". In: *Geostandards Newsletter* 25.2-3, pp. 261–266.

Yang, Yue-heng, Hong-fu Zhang, Zhu-yin Chu, Lie-wen Xie, and Fu-yuan Wu (2010). "Combined chemical separation of Lu, Hf, Rb, Sr, Sm and Nd from a single rock digest and precise and accurate isotope determinations of Lu–Hf, Rb–Sr and Sm–Nd isotope systems using Multi-Collector ICP-MS and TIMS". In: *International Journal of Mass Spectrometry* 290.2, pp. 120–126.

Zack, Thomas and K Johan Hogmalm (2016). "Laser ablation Rb/Sr dating by online chemical separation of Rb and Sr in an oxygen- fi lled reaction cell". In: *Chemical Geology* 437, pp. 120–133.

Zhang, Shudi, Miaohong He, Zhibin Yin, Eryi Zhu, Wei Hang, and Benli Huang (2016). "Elemental fractionation and matrix effects in laser sampling based spectrometry". In: *Journal of Analytical Atomic Spectrometry* 31.2, pp. 358–382.

CHAPTER 3

Testing nano-powder and fused-glass mineral reference materials for in-situ Rb-Sr dating of glauconite, phlogopite, biotite and feldspar via LA ICP-MS/MS

This chapter is written for submission to *Geostandards and Geoanalytical Research* as: Redaa, A, Farkaš, J, Gilbert, S, Collins, AS, Löhr, s, Vasegh, D, Forster, M, Blades, ML, Zack, T, Baldermann, A, Dietzel, M & Garbe-Schönberg, D 'Testing nano-powder and fused-glass mineral reference materials for in-situ Rb-Sr dating of glauconite, phlogopite, biotite and feldspar via LA ICP-MS/MS'

Statement of Authorship

Title of Paper	Testing nano-powder and fused-glass mineral reference materials for *in-situ* Rb-Sr dating of glauconite, phlogopite, biotite and feldspar via LA ICP-MS/MS
Publication Status	☐ Published ☐ Accepted for Publication ☐ Submitted for Publication ☑ Unpublished and Unsubmitted w ork w ritten in manuscript style
Publication Details	Redaa, A, Farkaš, J, Gilbert, S, Collins, AS, Löhr, S, Vasegh, D, Forster, M, Blades, ML, Zack, T, Baldermann, A, Dietzel, M & Garbe-Schönberg, D 'Testing nano-powder and fused-glass mineral reference materials for in-situ Rb-Sr dating of glauconite, phlogopite, biotite and feldspar via LA ICP-MS/MS'.

Principal Author

Name of Principal Author (Candidate)	Ahmad Redaa		
Contribution to the Paper	Plan for experiments, sample preparation, data collection, data processing, interpretation, visualisation, writing the initial draft and editing.		
Overall percentage (%)	80%		
Certification:	This paper reports on original research I conducted during the period of my Higher Degree by Research candidature and is not subject to any obligations or contractual agreements with a third party that would constrain its inclusion in this thesis. I am the primary author of this paper.		
Signature		Date	11/11/2021

Co-Author Contributions

By signing the Statement of Authorship, each author certifies that:

i. the candidate's stated contribution to the publication is accurate (as detailed above);

ii. permission is granted for the candidate in include the publication in the thesis; and

iii. the sum of all co-author contributions is equal to 100% less the candidate's stated contribution.

Name of Co-Author	Juraj Farkaš		
Contribution to the Paper	Supervision, interpretation, reviewing and editing		
Signature		Date	11/11/2021

Name of Co-Author	Sarah Gilbert		
Contribution to the Paper	Set-up the LA-ICP-MS/MS for the in-situ Rb-Sr analysis, reviewing and editing.		
Signature		Date	22/11/2021

Name of Co-Author	Alan S. Collins		
Contribution to the Paper	Discussion of ideas, supervision and editing		
Signature		Date	27/10/21

Name of Co-Author	Stefan Löhr		
Contribution to the Paper	Imaging the samples by the SEM, reviewing, and editing the manuscript.		
Signature		Date	28/10/21

Name of Co-Author	Davood Vasegh		
Contribution to the Paper	Sample preparation and fusing them inside an Ultra-High vacuum set up		
Signature		Date	28/10/21

Name of Co-Author	Marnie Forster		
Contribution to the Paper	Discussion on preparation of grains for their analysis. Setting up mass spectrometer and laser for preparing of samples in Ultra-high vacuum system.		
Signature		Date	28/10/21

Name of Co-Author	Morgan Blades		
Contribution to the Paper	Assistance in the analysis by LA-ICP-MS/MS, data processing and reviewing the manuscript.		
Signature		Date	27/10/2021

Name of Co-Author	Thomas Zack		
Contribution to the Paper	Discussion of ideas, editing		
Signature		Date	22/11/2021

Name of Co-Author	Andre Baldermann		
Contribution to the Paper	Discussion of ideas, editing		
Signature		Date	27.10.2021

Name of Co-Author	Martin Dietzel		
Contribution to the Paper	Discussion of ideas, editing		
Signature		Date	27.10.2021

Name of Co-Author	Dieter Garbe-Schönberg		
Contribution to the Paper	Preparing the nano-powder pellets refence materials.		
Signature		Date	Oct 29, 2021

Abstract

Reference materials (RMs) with well-characterised composition are necessary for reliable quantification and quality control of geochemical and isotopic analyses of mineral samples. For the in-situ Rb-Sr analysis of silicate minerals via a laser ablation (LA) coupled with an inductively coupled plasma - tandem mass spectrometry (LA-ICP-MS/MS), a general lack of certified mineral-specific and matrix-matched RMs is limiting wider application of this new dating technique to only certain minerals. In this work, we attempted to develop flux-free and well-characterized 'mineral glasses' from certified reference materials (i.e., mineral powders/grains), including GL-O (glauconite), Mica-Mg (phlogopite), Mica-Fe (biotite), and FK-N (K-feldspar). In addition, pressed nano-powder (NP) pellets of the above minerals (Mica-Mg-NP, GL-O-NP, Mica-Fe-NP, and FK-N-NP) were also investigated as alternative and currently more established RMs for the in-situ Rb-Sr dating. The results showed that the produced mineral glasses were heterogeneous with respect to Rb and Sr concentrations and isotope ratios, thus rendering them unsuitable for in-situ dating. In contrast, the nano-powder (NP) pellets produced from the investigated mineral standards were all homogeneous isotopically and chemically at micro-scale level. Consequently, we used these NP materials to constrain representative $^{87}Rb/^{86}Sr$ and $^{87}Sr/^{86}Sr$ ratios for Mica-Mg-NP, GL-O-NP and Mica-Fe-NP mineral standards, and these in turn were used to calculate Rb-Sr ages for two natural minerals including MDC phlogopite and GL-O glauconite. Importantly, GL-O grains analysed via in-situ Rb-Sr dating yielded an age of 100 $\pm$ 2 Ma (normalised to Mica-Mg-NP and/or GL-O-NP), which is in excellent agreement with the expected depositional or stratigraphic age of GL-O glauconite constrained at 99.6 $\pm$ 1 Ma (i.e., the basal Cenomanian). Previous studies and dating of GL-O grains via K-Ar methods, however, yielded problematic and consistently younger ages with a mean of 95 $\pm$ 1 Ma, indicating that K-Ar isotope system was likely partly reset in GL-O, unlike the presumably more robust Rb-Sr system. MDC phlogopite mineral also yielded ages that are in agreement (within 3% uncertainty) with its expected age of 519 Ma, when the sample was normalised to Mica-Mg-NP (phlogopite) and/or GL-O-NP (glauconite) standards. Overall, these results confirmed that both Mica-Mg-NP and GL-O-NP are suitable RMs for in-situ Rb-Sr dating of K-rich mica group minerals such as phlogopite and glauconite. However, Mica-Fe-NP (biotite) and FK-N-NP (K-feldspar) require further testing and validation to better constrain their Rb and Sr elemental/isotope compositions, to allow more robust application of these RMs for in-situ Rb-Sr dating of biotite and K-feldspar.

3.1 Introduction

In-situ Rb-Sr analysis and dating of silicate minerals and rocks, using a laser ablation (LA) coupled with an inductively coupled plasma - tandem mass spectrometer (ICP-MS/MS), is becoming a more popular geochronological technique to constrain the timing of mineral formation, cooling ages and/or duration of geological events (e.g., Armistead et al., 2020; Hogmalm et al., 2017; Olierook et al., 2020; Li et al., 2020; Tillberg et al., 2017; Tillberg et al., 2020). This novel technique allows for interference-free measurement of isobaric ^{87}Rb and ^{87}Sr isotopes in K-bearing and thus Rb-rich minerals (i.e., glauconite, illite, mica and K-feldspars). The in-situ Rb-Sr dating is facilitated via a reaction cell filled with N_2O or SF_6 gases, which allows an on-line chemical separation of Sr from Rb, as the latter does not react with either of these gases (Hogmalm et al., 2017). Thus, Rb can be measured at mass 87 (as ^{87}Rb or ^{85}Rb), while the reactive Sr and its isotopes can be measured as 'mass-shifted' Sr species (e.g., $^{87}Sr^{16}O^+$ or $^{87}Sr^{19}F^+$ at masses 103 or 106 amu, respectively). Apart from the above on-line separation of isobaric ^{87}Rb and ^{87}Sr isotopes, another advantage of the in-situ Rb-Sr dating is that these measurements can be done rapidly, precisely and relatively cheaply with minimal sample preparation steps, as the mineral of interest can be analysed directly 'in-situ' from rock chips as polished-mounts and/or from thin-sections, without the need for time-consuming mineral separation. In addition, contamination by other phases in the mineral of interest (from inclusions or overgrowths) can be avoided on micro-scale level as typical LA spot size for Rb-Sr dating is on the order of ca. 50-75 μm (Hogmalm et al., 2017; Redaa et al., 2021; Zack and Hogmalm, 2016). However, currently the accuracy and precision of in-situ Rb-Sr dating of silicate minerals is restricted by a number of factors including (i) elemental fractionation effects, (ii) non-ideal matrix matching, and also (iii) mineral/material specific ablation properties between reference materials (RMs) and samples of interest (Redaa et al., 2021). These limitations thus call for the development and testing of new mineral-specific standards to further improve the precision, accuracy and robustness of in-situ Rb-Sr dating of silicate minerals with relevance to earth and planetary sciences. This study aims to fill such gap by testing a set of mineral standards (glauconite, phlogopite, biotite and feldspar), prepared in the form of fused glasses and nano-powder pellets, specifically prepared and designed for in-situ Rb-Sr dating applications.

During the LA-ICP-MS/MS analysis, the signal intensity of ion beams of certain elements (e.g., more volatile Rb vs more refractory Sr) tends to change with time and

Table 3.1: The reported $^{87}Rb/^{86}Sr$ and $^{87}Sr/^{86}Sr$ values of reference materials that are commonly used for in-situ Rb-Sr analysis via LA-ICP-MS/MS.

Reference material	Type	$^{87}Rb/^{86}Sr \pm 2SD$	$^{87}Sr/^{86}Sr \pm 2SD$	References
NIST SRM 610	Glass	2.33 ± 0.0049	0.709699 ± 0.000018*	(Hogmalm et al., 2017)
		2.3894 ± 0.8	0.709699 ± 0.000018*	(Bevan et al., 2021)
		2.390 ± 0.005	0.709699 ± 0.000018*	(Olierook et al., 2020)
BCR-2G	Glass	0.3901	0.705003	(Elburg et al., 2005; Hogmalm et al., 2017)
USGS BHVO-2G	Glass	0.06557 ± 0.00066	0.703469 ± 0.000007	(Elburg et al., 2005; Gorojovsky and Alard, 2020)
Mica-Mg-NP	Pressed nano-powder pellet	154.6 ± 1.93	1.8525 ± 0.0024	(Hogmalm et al., 2017)
		156.9 ± 2.3	1.8692 ± 0.0022	(Olierook et al., 2020)

This value is originally reported in Woodhead and Hergt, 2001

increasing laser penetration through a sample/mineral, which in turn causes a phenomenon known as elemental or down-hole fractionation (DHF) effect (Gilbert et al., 2014; Lin et al., 2016; Zhang et al., 2016). Such elemental fractionation can occur at any stage of the analysis, originating at the ablation site (LA crater) during initial material vaporisation, followed by a later transport of ablated aerosols, and ionisation in the ICP source (Claverie et al., 2009; Cromwell and Arrowsmith, 1995; Eggins, Kinsley, and Shelley, 1998; Jackson and Günther, 2003; Longerich, Günther, and Jackson, 1996; Zhang et al., 2016). In addition, the degree of the elemental fractionation during LA-ICP-MS/MS analysis is also influenced by the chemical composition and physical nature (i.e., specific ablation properties) of the analysed material, and these combined phenomena are known as matrix effects (Agatemor and Beauchemin, 2011; Sylvester, 2008). Hence, the accuracy and precision of the Rb-Sr analysis and dating by the LA-ICP-MS/MS can be significantly affected by the above processes, especially for elements such as Rb and Sr (or other volatile vs refractory elemental pairs, e.g., K/Ca), which have large differences in their volatilization temperatures (i.e., boiling points) and sensitivity to different matrices (Jochum et al., 2007).

The accuracy and fidelity of the LA-ICP-MS/MS elemental and isotope analysis can however be improved via application of suitable calibration and data quality monitoring strategies that relay on RMs and correction routines summarised in Miliszkiewicz, Walas, and Tobiasz, 2015. For LA analysis, matrix-matched RMs are recommended to achieve highly accurate analysis (Jackson and Sylvester, 2008; Košler et al., 2005; Miliszkiewicz, Walas, and Tobiasz, 2015). However, lack of matrix-matched reference material for the in-situ Rb-Sr analysis is the main challenge, and thus far only a limited number of suitable and mineral-specific RMs is available to calibrate acquired $^{87}Rb/^{86}Sr$ and

$^{87}Sr/^{86}Sr$ data obtained via LA-ICP-MS/MS. Specifically, most of recent in-situ Rb-Sr dating studies relied on a combination of the following RMs, including glasses NIST SRM 610, BCR-2G and USGS BHVO-2G, and a single available nano-powder phlogopite mineral standard (Mica-Mg-NP), (Table 3.1), (Armistead et al., 2020; Gorojovsky and Alard, 2020; Hogmalm et al., 2017; Laureijs, Coogan, and Spence, 2021; Olierook et al., 2020; Redaa et al., 2021; Şengün et al., 2019; Li et al., 2020; Tillberg et al., 2020; Zack and Hogmalm, 2016). However, thus far, $^{87}Rb/^{86}Sr$ ratios of the above RMs have not been directly measured or reported in published studies, and to the best of our knowledge these ratios have been constrained and derived either from (i) Rb and Sr concentration measurements, and/or (ii) calculated from measured $^{87}Sr/^{86}Sr$ (via LA-ICP-MS/MS, TIMS) and published 'age' data (i.e., expected/reported mineral age and its assumed 'initial Sr' isotope composition); following the approach of Hogmalm et al., 2017. Due to these complications, a range of accepted $^{87}Rb/^{86}Sr$ and $^{87}Sr/^{86}Sr$ ratios have been used to date for these RMs (Table 3.1). In addition, as illustrated by Redaa et al., 2021, using the different RMs listed in Table 3.1 for in-situ Rb-Sr dating of natural minerals (e.g. natural phlogopite crystals) could impact the accuracy and precision of the obtained Rb-Sr ages by up to 7% (i.e. difference between observed and expected ages), which is mostly due to non-matching chemical and physical properties between the RMs and the sample of interest (i.e., natural minerals). The current approach for in-situ Rb-Sr dating, designed to overcome these problems, relies primarily on the analysis of secondary RMs (i.e., well-characterised and homogeneous natural minerals) with known ages and chemical/isotope compositions, which can be used to monitor the quality of acquired Rb-Sr data, including possible elemental fractionation and/or instrument drift effects (Armistead et al., 2020; Bevan et al., 2021; Laureijs, Coogan, and Spence, 2021; Olierook et al., 2020; Redaa et al., 2021; Li et al., 2020). Such careful monitoring of data quality, along with the application of secondary correction, allows in-situ Rb-Sr ages to be determined with an accuracy ranging between 1.5 to 3% (Armistead et al., 2020; Bevan et al., 2021; Olierook et al., 2020; Redaa et al., 2021; Li et al., 2020; Subarkah et al., 2021).

In the light of the above limitations related to a lack of suitable mineral standards for high-precision in-situ Rb-Sr dating, the development of new mineral-specific RMs is of high importance and interest to further improve the accuracy and robustness of this novel laser-based geochronological technique. Such new mineral-specific RMs need to be homogeneous at a micro-scale level, and thus can be produced either in the form of (i) nano-powder mineral pellets with binders (O'Connor, Landon, and Sharp, 2007; Tabersky et al., 2014) or without binders (Garbe-Schönberg and Müller, 2014), or

alternatively as (ii) fused mineral glasses with flux (Awaji et al., 2006; Eggins, 2003; Yu, Norman, and Robinson, 2003) or as flux-free glasses (Fedorowich et al., 1993; He et al., 2016). Specifically, the pressed nano-powder mineral pellet can be produced by grinding the samples to < 1.5 μm, then mixing the powder with binders before compacting the material into a homogenised sample-binder mixture, and eventually into a pressed pellet (O'Connor, Landon, and Sharp, 2007). Alternatively, the pressed nano-powder can be produced without binders by homogenising ground samples/mineral powders with ultrapure water before their mechanical compaction into nano-powder pellet (Garbe-Schönberg and Müller, 2014). Finally, the fused glasses can be produced by melting the mineral powders without flux at high temperature (1700 °C) (He et al., 2016), or this temperature can be reduced to about 1200 °C by adding a flux into the sample before its melting, which will facilitate the formation of glass at lower temperatures via alkali fusion flux (Awaji et al., 2006; Yu, Norman, and Robinson, 2003).

In this study, we used the LA-ICP-MS/MS to measure ^{87}Rb/^{86}Sr and ^{87}Sr/^{86}Sr isotopic compositions of four certified mineral reference materials prepared as pressed nano-powder (NP) pellets including phlogopite (Mica-Mg-NP), glauconite (GL-O-NP), biotite (Mica-Fe-NP), and K-feldspar (FK-N-NP). In addition, we also attempted to develop and produce a set of flux-free mineral glasses for in-situ Rb-Sr dating applications using the above certified mineral reference materials (Mica-Mg, GL-O, Mica-Fe; and FK-N), which were fused into a glass using a large and energetic laser beam produced by a Photon Machine 100 W Fusion CO_2 laser system. Finally, the effects of such high-energy and laser-based melting processes (including Rb loss due to volatilisation) on the Rb-Sr isotopic composition of produced mineral glassess were investigated and quantified by comparing the Rb-Sr isotopic data collected from the glasses against those obtained from the nano-powder mineral pellets. From this comparison and generated datasets, conclusions are drawn on the suitability of studied mineral standards (nano-powders vs laser-fused glasses) for improved in-situ Rb-Sr dating of K-rich silicate minerals via LA-ICP-MS/MS.

3.2 Samples and Analysed Materials

3.2.1 GL-O glauconite

This reference material consists of presumably mineralogically homogenous glauconite grains sampled near the beach of Cauville (Normandy), France (Govindaraju, 1994). However, a recent study shows that the GL-O glauconite grains are rather complex and

inhomogeneous at the micro-scale level, containing also minor phases enriched in phosphorus and calcium (i.e., apatite and calcite inclusions and rims), which were detected in a large number of GL-O grains (Boulesteix et al., 2020). As to Rb-Sr system, the recommended $^{87}Sr/^{86}Sr$ value of the GL-O is 0.7535 ± 0.0010 (Govindaraju, 1995), but no $^{87}Rb/^{87}Sr$ data have been found in the literature. As to GL-O dating, published results from K-Ar geochronology suggest the age of GL-O of 95 ± 1 Ma (Derkowski et al., 2009; Fiet et al., 2006), with slightly younger Ar-Ar age of 93.6 ± 1 Ma reported for GL-O. Importantly, the expected stratigraphic or depositional age for GL-O glauconite is actually close to 100.5 Ma (i.e., the Albian-Cenomanian boundary) or more specifically 99.6 ± 1 Ma, which is the age of the basal Cenomanian deposits from which GL-O was collected (see Gradstein et al., 2012; Selby, 2009).

3.2.2 Mica-Mg phlogopite

Mica-Mg is a phlogopite reference mineral standard/material, which was sampled and separated from a pegmatitic unit from the Ampandrandava quarry in Bekily region, Madagascar (Govindaraju, 1979; Govindaraju, 1994), and distributed by Centre de Recherches Pétrographiques et Géochimiques (CRPG). The age of Mica-Mg was constrained by different geochronological methods, and the average crystallisation age of the Mica-Mg phlogopite is estimated at 519.4 ± 6.5 Ma (Hogmalm et al., 2017 and references therein). The recommended $^{87}Rb/^{87}Sr$ and $^{87}Sr/^{86}Sr$ ratios of Mica-Mg reported in the literature are variable. For example, Hogmalm et al., 2017 reported $^{87}Rb/^{87}Sr$ and $^{87}Sr/^{86}Sr$ ratios for Mica-Mg of 154.6 ± 1.93 and 1.8525 ± 0.0024, respectively; whereas Olierook et al., 2020 reported 156.9 ± 2.3 and 1.8692 ± 0.0022, respectively (Table 3.1).

3.2.3 Mica-Fe biotite

Mica-Fe is a biotite reference material that was sampled from Massif de Saint-Sylvestre, France; and distributed by CRPG (Govindaraju, 1979). This mineral standard contains high Rb concentrations (2200 ± 2 ppm), and low Sr (5 ± 9.3 ppm) (Govindaraju, 1979; Govindaraju, 1994). K-Ar age of Mica-Fe is reported at 316 ± 9 Ma Zimmermann et al., 1985; Govindaraju, 1979 proposed Rb-Sr and K-Ar ages of 316 ± 10 Ma and 310 ± 10 Ma, respectively. However, Zimmermann et al., 1985 indicated that Mica-Fe should not be used as a reference material for K-Ar dating as the sample yielded varied Ar-Ar ages ranged between 290 and 330 Ma, with an average of 313.5 Ma. The initial $^{87}Sr/^{86}Sr$

ratio for Mica-Fe has not been found in the literature, but it might be inferred from the Rb-Sr system of the coeval Saint-Sylvestre granite, which has a reported Sr-isotope initial of 0.709797 ± 0.016 (Turpin et al., 1990). The recommended $^{87}Rb/^{86}Sr$ and $^{87}Sr/^{86}Sr$ values of the Mica-Fe and Rb-Sr isochron diagram have not been found in the literature.

3.2.4 FK-N K-feldspar

FK-N reference material is potassium feldspar (microcline), which was sourced from Madras area in India and distributed by the CRPG. This reference mineral standard contains 860 ± 56 ppm of Rb and 39 ± 8.64 ppm of Sr (Govindaraju, 1984). No geochronological ages and $^{87}Rb/^{87}Sr$ and $^{87}Sr/^{86}Sr$ data on FK-N have been found in the literature.

3.3 Methodology for Mineral Standards

3.3.1 Sample preparation: Nano-powders and fused glasses

The above CRPG mineral standards (GL-O, Mica-Mg, Mica-Fe and FK-N) were prepared in this study as (i) pressed nano-powder pellets (GL-O-NP, Mica-Mg-NP, Mica-Fe-NP and FK-N-NP) and also as (ii) flux-free glasses (Mica-Mg G1, Mica-Fe G1 & G2, FK-N G1 & G2, GL-O G1 & G2) fused via a high-energy laser beam (see below). An additional sample containing GL-O glauconite grains was also prepared as a polished-mount (GL-O) with glauconite grains embedded in a resin. The nano-powder pellets (GL-O-NP, Mica-Mg-NP, Mica-Fe-NP, and FK-N-NP) were prepared following the method described by Garbe-Schönberg and Müller, 2014. The flux-free mineral glasses produced in this study were melted and fused by the energy of laser beam at the RSES Argon Facility in The Australian National University (ANU), using a Photon Machine 100 W Fusions 10.6 CO_2 laser system. This laser system is attached to an ARGUS VI Multi-collector Mass Spectrometer, which is commonly used for Ar-Ar dating (Forster, Lister, and Lennox, 2014). In this study, we used the above laser system independently to melt and fuse the mineral standard materials from CRPG (Mica-Mg, Mica-Fe, FK-N and GL-O). In our melting/fusion experiments, a portion of each mineral standard (i.e., powdered material and/or grains) were loaded into miniature alumina crucibles, and then all crucibles were placed in the laser chamber. Mica-Mg, Mica-Fe and FK-N were loaded as powders whereas GL-O was loaded as grains. Each portion was heated up by focusing the laser

beam on the surface of the powder/grains located inside the crucible for 10-15 minutes. The laser energy was gradually increased during the melting process, and the maximum energy used for each sample is listed in Table 3.3.

3.3.2 Impact of laser-based melting/fusion on produced mineral glasses

The samples of mineral powders and grains (GL-O, Mica-Mg, Mica-Fe and FK-N) interacted differently with the laser beam, generated by the Photon Machine CO2 laser system at ANU, due to their distinct physical properties and variable melting points of the above silicate minerals. When the Mica-Mg and Mica-Fe (phlogopite and biotite) powders were exposed to the laser beam, they produced melts with low viscosity that randomly spread at the bottom of the crucible (Figure 3.1), showing portions of melt and mineral powder dragged away from the area of the laser beam, which translated to incomplete melting and inhomogeneities within the fused glasses. The produced mineral glasses of the above mica minerals (Mica-Mg-G1 and G2, Mica-Fe-G1 and G2) yielded irregular shapes with reticulated patterns (Figure 3.1), with remnants of the mineral powders accumulated and preserved beneath the fussed surface of the glasses, which is not surprising considering a relatively high melting point for mica minerals that is typically in excess of 1100°C (Gardien et al., 1995). In contrast, the powdered sample of K-feldspar (FK-N) melted faster than Mica-Mg and Mica-Fe without any evidence for remnant of the original mineral powder within the fused glass. The sample of FK-N powder was fused immediately when the laser beam was focused on the sample surface, producing a melt with high viscosity, which accumulated at the bottom of the crucible. The produced FK-N glasses (FK-N G1 and G2) were semi-spheroidal with a flat surface, and typical diameter of the fused glass sphere of about one millimetre (Figure 3.1). Finally, GL-O glauconite grains required a slightly longer time (about 2-3 minutes) to melt compared to the time needed for powdered phlogopite and biotite samples (Mica-Mg, Mica-Fe and FK-N). Also, the produced GL-O melt accumulated at centre of the crucible creating a semi-spheroidal glass with a flat surface and typical diameter of about 1 mm (Figure 3.1). All produced mineral glasses (GL-O G1 & G2, Mica-Mg G1, Mica-Fe G1 & G2, FK-N G1 & G2) contained random hollows and vesicles, visible on the surface of fused glasses, which thus significantly limited the area that could be targeted for LA-ICP MS/MS analysis. All fussed mineral glasses were mounted in epoxy resin and polished before SEM/EDS and LA-ICP-MS/MS analytical work (see below).

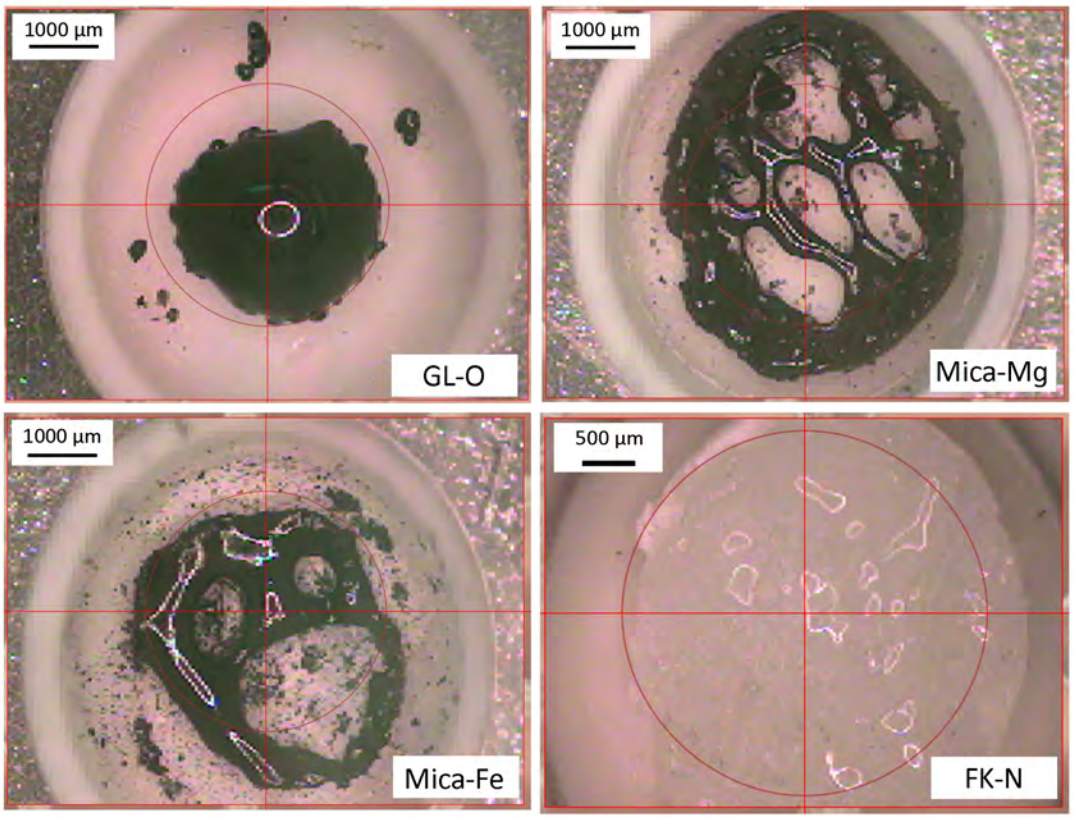

Figure 3.1: Captured images of fused glasses from GL-O, Mica-Mg, Mica-Fe and FK-N minerals inside a laser chamber after experimental melting using a Photon Machine 100 W Fusion CO_2 laser system at Ar-Ar laboratory, ANU.

3.3.3 Analytical setup and data processing

SEM/EDS Instrumentation

The produced mineral glasses (GL-O G1 & G2, Mica-Mg G1, Mica-Fe G1 & G2, FK-N G1 & G2) were mapped via SEM/EDS for their major element compositions and homogeneity using an FEI Quanta 450 high-resolution field emission Scanning Electron Microscope (SEM), equipped with energy dispersive x-ray spectroscopy (EDS) detector at the Adelaide Microscopy (AM) facilities, the University of Adelaide. In addition, further imaging and micro-scale mineral mapping were conducted on the GL-O glauconite grains at Macquarie University, using a FEI Teneo LoVac field emission SEM, equipped with EDS detectors (dual Bruker XFlash, Series 6). The above SEM/EDS setup, coupled with a specialised Nanomin software (Rafiei et al., 2020), was used to investigate and confirm the previously reported micro-scale mineralogical heterogeneities and impurities within the GL-O glauconite grains (Boulesteix et al., 2020).

LA-ICP MS/MS Instrumentation

The Rb and Sr concentrations, as well as $^{87}Rb/^{86}Sr$ and $^{87}Sr/^{86}Sr$ isotopic ratios, were analysed in the investigated mineral materials (i.e., grains, fused glasses, and nano-powder pellets) using an Agilent 8900 ICP-MS/MS coupled with a RESOlution ArF excimer (193nm) laser ablation (LA) system at the University of Adelaide. The first session (Session 1) was conducted using the 74 μm laser spot, and it includes two nano-powder pellets (Mica-Mg-NP and GL-O-NP) and also natural minerals of glauconite grains (GL-O) and phlogopite (MDC). Session 2 and Session 3 were conducted using the 62 μm laser spot, and the samples included in these sessions were mineral nano-powders (Mica-Mg-NP, GL-O-NP, Mica-Fe-NP, FK-N-NP) as well as GL-O grains and MDC. Finally, the glass materials (GL-O G1 & G2, Mica-Mg G1, Mica-Fe G1 & G2, FK-N G1 & G2) were analysed in Session 4, along with nano-powder samples (Mica-Mg-NP, Mica-Fe-NP and FK-N-NP), using a 74 μm laser spot. For all of the above sessions, the LA-ICP-MS/MS setup was tuned using NIST 612 glass, and the tuning parameters and settings are listed in Table 3.2. Briefly, all samples were ablated in a He atmosphere, mixed with Ar as the carrier gas, with 3.5 mL/min flow rate of N_2 added to enhance the signal sensitivity (Hu et al., 2008). In addition, N_2O gas was used as a reaction gas (0.35 mL/min) to resolve the isobaric interference between ^{87}Rb and ^{87}Sr using a collision cell or MS/MS setup (Hogmalm et al., 2017). The efficiency of Sr reaction with the N_2O gas was close to 99%, with no detectable $^{85}Rb^{16}O$ signal (mass 101 $<$ 0.00001%) in 'mass shifted' products; and Mica-Mg-NP and NIST 610 were used as primary RMs to calibrate and normalise $^{87}Rb/^{86}Sr$ and $^{87}Sr/^{86}Sr$ data using a sample-standard-sample bracketing method (see Redaa et al., 2021). Specifically, NIST 610 was used to calibrate Rb and Sr concentrations, and Al was used for the internal calibration during the analysis of silicate minerals (Miliszkiewicz, Walas, and Tobiasz, 2015). The $^{87}Rb/^{86}Sr$ and $^{87}Sr/^{86}Sr$ data were processed using the Iolite v4 software (Paton et al., 2011), coupled with a customised data reduction scheme (Redaa et al., 2021), and Rb-Sr isochrons and ages were calculated using the IsoplotR software (Vermeesch, 2018).

3.4 Results and discussion

3.4.1 Chemical and isotope homogeneity of the produced mineral materials

The homogeneity of the produced mineral glasses was investigated through the elemental and mineral maps generated by SEM/EDS. The results indicate that Mica-Mg-G1, Mica-Fe-G1 & G2, FK-N G1 & G2 glasses were all homogeneous at micro-scale level with respect to the major elements in studied minerals. Overall, the elemental maps confirmed that the major elements, including K, Al, Si, Fe, and Mg, were all distributed equally within the glasses (Figure 3.2-3.6). However, Ca and P concentrations in GL-O glasses revealed spatial heterogeneity and random distribution patterns in glauconite glasses (Figure 3.5 and 3.6), but these two elements (Ca and P) are trace elements and not major components of the glauconite mineral. To further investigate such elemental and mineralogical heterogeneity of GL-O glauconite, the grains were imaged by the SEM-EDS, and mapped at micro-scale level using the Nanomin software, to confirm the source of Ca and P in GL-O grains and glasses. The results indeed corroborated the presence of minor apatite, plagioclase and quartz inclusions in GL-O grains (see Figure 3.7), presumably also complemented by calcite (Boulesteix et al., 2020 see also).

Although the elemental maps showed that all glasses, apart from GL-O G1 & G2, are homogenous with respect to the major oxide concentrations, the follow-up Rb-Sr spot analysis by the LA-ICP-MS/MS, revealed that the glasses are in fact heterogeneous with respect to trace element concentrations of Rb and Sr. In contrast, the nano-pwoder pellets (Mica-Mg-NP, GL-O-NP, Mica-Fe-NP and FK-N-NP) all showed high level of homogeneity at micro-scale level with respect to both major elements as well as trace elements such Rb and Sr.

The measured Rb and Sr concentration data obtained from mineral glasses (Mica-Mg-G1, Mica-Fe-G1 & G2, FK-N G1 & G2) and nano-powder pellets (GL-O-NP, Mica-Mg-NP, Mica-Fe-NP and FK-N-NP) are listed in Table 3.A in the Supplementary Material, and also summarised in Table 3.3. These results indicate that Rb (ppm) concentrations of the above mineral glasses are generally lower than the reported or certified Rb concentrations of the studied mineral standards (powders, grains), whereas Rb concentrations of the NP pellets agree and overlap (within the uncertainty) with the certified and published values (see Table.3 Govindaraju, 1995; Govindaraju and Roelandts, 1988; Odin, 1976). The large variability (between 3% and 28%, 2σ) in measured Rb con-

centrations of fused mineral glasses (Mica-Mg-G1, Mica-Fe-G1 & G2, FK-N G1 & G2; Table. 3.3) indicates that Rb was (i) mobilised and inconsistently distributed within the glasses during the melting process, and/or (ii) preferentially lost from the sample due to Rb volatilisation. Related to the latter, the systematically lower Rb concentrations in the glasses, compared to certified values, indicate that Rb was indeed lost during the melting process at higher laser energy and associated temperatures. Note that such Rb loss is particularly obvious in data from biotite (Mica-Fe-G2) and feldspar (FK-N-G2) fused glasses, and these were also melted at relatively higher energy laser conditions (25-30 %) and elevated temperatures, where the latter had to be higher than the boiling point of Rb at atmospheric pressure which is close to 688 °C (Gray, 2009).

The Sr (ppm) in the fused glasses (Mica-Mg-G1, Mica-Fe-G1 & G2, FK-N-G1 & G2) were generally overlapping with certified and published Sr concentration data for the studied minerals (see Table 3.3). Such overlap and general agreement between Sr concentration data in fused glasses vs. source minerals indicates that Sr has not volatilised significantly, or at all, during the melting process. This observation and conclusion is not surprising considering that the boiling point of Sr of about 1382 °C is significantly higher compared to that for Rb (688 °C) (Gray, 2009), suggesting that the temperature of the laser beam most likely did not exceed the above temperature in excess of 1300 °C. Even though it seems that Sr was not significantly affected by volatilisation during the melting process (as suggested by the agreement with published Sr concentration data), the above mineral glasses yielded spatially heterogeneous Sr concentrations at micro-scale level. This is obvious from the large variability of the acquired Sr concentrations data from individual mineral glasses, which is most likely because the newly produced melt was not mixed and homogenised thoroughly at micro-scale level before the solidification and formation of the fused mineral glass.

The GL-O-G1 and G2 glasses also showed spatial heterogeneity in Rb and Sr concentration data at the micro-scale level, but in contrast the GL-O-NP nano-powder showed high level of homogeneity. The averages of Rb and Sr concentrations in the GL-O glasses are associated with large uncertainty of $> 25\%$ (Table 3.3), confirming the above mentioned inhomogeneity and variability in Rb and Sr data in GL-O glasses G1 and G2. Interestingly, the results also showed that the averages of Rb and Sr concentrations in both GL-O-NP nano-powder and GL-O glasses generally overlap and also agree with the certified values for GL-O reference mineral (Table 3.3). This in turn indicates that neither Rb nor Sr experienced significant loss due to volatilisation during the melting process, even though the high energy of the laser beam used in the experiment most likely exceeded the boiling point of Rb. We speculate that the significant amount of

minerally bound water (H_2O^+, O_2H^-) present in GL-O glauconite grains (5.58 and 2.52 wt%, respectively) might have contributed to lowering the melting point of glauconite and thus preventing significant loss of Rb. In addition, part of the laser energy might have been also consumed to breakdown the glauconite grain structure of GL-O, as the latter was not in the form of powder as other investigated minerals fused in this study.

Noticeably, the average Rb and Sr concentrations obtained from the natural glauconite GL-O grains were different compared to the Rb and Sr concentration data acquired from the GL-O glasses and NP (Table 3.3). Rb concentrations obtained from the studied GL-O grains were higher than those from GL-O glasses and nano-powder (i.e., GL-O G1 & G2 and GL-O-NP) by about 15-25% (see Table 3.3). On the other hand, Sr concentrations were lower in the GL-O grains compared to Sr levels in the fused GL-O glasses and nano-powder by 60-77% (see Table 3.3). These differences seem to suggest that homogenisation of GL-O grains to form (i) fused glasses and/or (ii) pressed nano-powder pellet, led to an apparent increase in the Sr concentrations in the products (GL-O G1 & G2, and GL-O-NP) and/or caused relative loss and decrease in Rb concentrations. We speculate that these observations and differences in Rb and Sr concentration data between GL-O grains versus glasses/nano-powder materials is due to combined effects of micro-scale mineral impurities (e.g., apatite inclusions) and related "sampling bias" during LA-ICP MS/MS analysis. Specifically, during the LA analysis of GL-O grains we primarily targeted the centre of individual glauconite grains, which tend to be more 'pristine' and made of pure glauconite (i.e., devoid of apatite), compared to rims of the grains that show relatively higher abundance and presence of apatite inclusions and/or replacement zones (see Figure 3.7). Such distribution of Rb-poor (and Sr-rich) apatite phases within GL-O grains can explain the observed differences in Rb and Sr concentration data between the nano-powder/glass materials versus pure GL-O grains. As for the latter (GL-O grains) we generally targeted the 'apatite poor' centres of the grains (yielding elevated Rb and lower Sr) while for the glass/nano-powder materials the entire grains had to be sampled and homogenised (including the outer and apatite-rich zones), which thus translated to generally lower Rb and higher Sr contents observed in GL-O glasses and nano-powder GL-O-NP. Also, such additional source of Sr in the GL-O glasses and nano-powder pellet is expected to be non-radiogenic (with lower $^{87}Sr/^{86}Sr$ ratios), because it is expected to be primarily sourced from Rb-poor and Sr-rich phase such as apatite, but possibly also calcite and plagioclase (see Figure 3.7). These mineralogical complexities of GL-O grains at micro-scale level highlight the advantage and importance of the in-situ Rb-Sr analysis and dating approach via LA-ICP-MS/MS. As the latter allows to avoid possible contamination by other and presumably secondary

(i.e., younger) mineral phases present in GL-O glauconite grains, which can also impact the acquired 'age' of the bulk or analysed GL-O material.

3.4.2 $^{87}Rb/^{86}Sr$ and $^{87}Sr/^{86}Sr$ isotopic ratios determined via LA-ICP-MS/MS

GL-O glauconite

The above-discussed elemental concentration data showed that the GL-O glasses are heterogeneous with respect to Rb and Sr concentrations. To further investigate such heterogeneities for $^{87}Rb/^{86}Sr$ and $^{87}Sr/^{86}Sr$ ratios in the GL-O glasses (GL-O-G1 and G2), GL-O nano-powder pellet (GL-O-NP), and GL-O natural grains (GL-O), these were also investigated with the data calibrated and normalised to NIST 610 reference material, to assess the homogeneity of these materials and the impact of LA-analysis and melting process on the Rb-Sr isotopic system. These results are listed in Table 3.B in the Supplementary Materials. GL-O-NP shows high level of homogeneity with respect to both $^{87}Rb/^{86}Sr$ and $^{87}Sr/^{86}Sr$ ratios with variation between sessions of 0.3% and 0.09%, respectively. Noticeably, the obtained $^{87}Sr/^{86}Sr$ of GL-O-NP (0.7548 $\pm$ 0.0007, Table 3.4) overlaps within the uncertainty with the reported $^{87}Sr/^{86}Sr$ for GL-O of 0.7535 $\pm$ 0.001 (Govindaraju, 1995; Odin, 1976). However, the other studied GL-O materials (GL-O-G1 and G2 glasses, and GL-O grains) were significantly more heterogeneous with respect to their Rb-Sr isotopic composition (see Table 3.4).

To compare the level of heterogeneity among the above GL-O materials, their normalised $^{87}Rb/^{86}Sr$ and $^{87}Sr/^{86}Sr$ ratios are plotted in the 'Nicolaysen diagram' or isochron plots with an anchored y-intercept (i.e., $^{87}Sr/^{86}Sri$) of 0.70740 (Figure 3.8D). The latter represents the expected Sr isotope composition of seawater at 95-100 Ma ago (see McArthur, Howarth, and Shields, 2012; Veizer et al., 1999 and references therein) when the GL-O is expected to form in marine settings from palaeo-seawater or coeval seawater-derived fluids. Results confirmed that GL-O-NP shows high level of homogeneity in $^{87}Rb/^{86}Sr$ and $^{87}Sr/^{86}Sr$ ratios at micro-scale level, whereas the fused GL-O glasses (GL-O-G1 and G2) and also natural GL-O grains exhibit spatially variable $^{87}Rb/^{86}Sr$ and $^{87}Sr/^{86}Sr$ data (Figure 3.8D). Interestingly, the majority of GL-O data points (from NP, Glasses and Grains) plot within their uncertainty along a 'common' isochron line (Figure 3.8D) with a slope corresponding to an expected depositional age for GL-O glauconite at around 100 Ma. The SEM/EDS images (Figure 3.7) confirmed that GL-O grains are indeed more complex and composed of glauconite with other minor and Rb-poor and

Sr-rich mineral phases (i.e., apatite, calcite, and plagioclase). Thus, one also needs to keep in mind that the obtained isochron line of the GL-O samples could also represent a 'mixing line' rather than a true 'isochron'. To further investigate such possibility, GL-O data were also plotted in a element-ratio plot (i.e., Sr concentration data vs $^{87}Sr/^{86}Sr$ ratios; (Langmuir et al., 1978) to confirm possible mixing phenomena or trends between (i) Rb-rich and radiogenic glauconite phase and (ii) Rb-poor and less radiogenic apatite and/or calcite phases, which might have been mixed or fused during sample preparation and homogenising process (i.e., during laser beam fusion, or preparation of pressed nano-powder pellet). Results confirmed that GL-O glasses (i.e., GL-O-G1 and G2) indeed yielded such two-component mixing curves in $^{87}Sr/^{86}Sr$ vs Sr concentration (or 1/Sr) plots (see Figure 3.9), illustrating a systematic decrease in $^{87}Sr/^{86}Sr$ ratios with an increasing Sr (ppm) concentrations. However, GL-O-NP nano-powder did not show obvious variability or 'mixing' of such components, which is not surprising considering that above-mentioned high homogeneity of NP material at micro-scale level. Yet the influence of Sr-rich and Rb-poor phase (i.e., apatite) in GL-O nano-powder is obvious from systematically less radiogenic and Sr-rich data collected for GL-O-NP, compared to data from natural GL-O grains (see Figure 3.9), as for the latter more 'pristine' and thus more radiogenic and Sr-poor 'centre areas' of glauconite grains were targeted.

Overall, $^{87}Sr/^{86}Sr$ ratios plotted against an inverse Sr (ppm) concentrations (1/Sr) for GL-O fused glasses (Figure 3.9B) fitted well a 'straight line' trend or 'mixing trend' using the least-squares algorithm of York et al. (2004). The generated and projected y-intercepts (i.e., $^{87}Sr/^{86}Sr$) of the obtained correlation or regression lines were 0.70478 $\pm$ 0.0059 (SE) for GL-O G1 glass, and 0.70613 $\pm$ 0.0032 (SE) for GL-O G2 (Figure 3.9B), which are thus within the uncertainty of the expected Sr isotope composition (0.70740) of palaeo-seawater at 95-100 Ma (McArthur et al. 2012). Finally, the fact that both phases (i) Rb-rich glauconite as well as (ii) Rb-poor and Sr-rich apatite (or calcite), plot together along a common isochron yielding an age of 100 Ma (see Figure 3.8D and Figure 3.11) suggests that both phases are actually coeval and formed early on after sediment deposition via early diagenetic processes. Hence, we argue that Rb-Sr isotope system of GL-O glauconite grains, including minor apatite or calcite inclusions, has not been reset since the deposition and subsequent early diagenetic (authigenic) formation of the studied glauconite-apatite mineral assemblages. Considering these observations and acquired data, we argue that the newly produced GL-O nano-powder (GL-O-NP) is suitable reference materials for future in-situ Rb-Sr dating applications of 'glauconite-celadonite group' minerals.

Mica-Mg phlogopite

Measured $^{87}Rb/^{86}Sr$ and $^{87}Sr/^{86}Sr$ ratios in the Mica-Mg-NP and Mica-Mg glass were normalised to NIST 610 (data in Table 3.B in the Supp. Material) to investigate the consistency and variability in $^{87}Rb/^{86}Sr$ and $^{87}Sr/^{86}Sr$ ratios of these phlogopite sample materials. The normalised data were plotted in the $^{87}Rb/^{86}Sr$ vs $^{87}Sr/^{86}Sr$ isochron diagram (Figure 3.8A), and the results show that $^{87}Rb/^{86}Sr$ ratios of Mica-Mg-NP nano-powder were noticeably variable within the sample, exhibiting up to 5.88% variability from the mean value, which is likely due to particle size differences and related inconsistencies in ablation rates within the pellet (Redaa et al., 2021). Importantly, Mica-Mg-G1 glass material also showed variation and systematic decrease in $^{87}Rb/^{86}Sr$ ratios by up to 40% (Figure 3.8A), which must reflect a progressive loss of Rb during the formation of a fused mineral glass via the laser based melting. Also, the average of normalised $^{87}Sr/^{86}Sr$ in the Mica-Mg-G1 glass (Table 3.4) is slightly lower than the published $^{87}Sr/^{86}Sr$ values of Mica-Mg (listed in Table 3.1), which renders the produced Mica-Mg-G1 fused glass unsuitable as a reference material for in-situ Rb-Sr dating.

Although, we observed session-to-session variability in $^{87}Rb/^{86}Sr$ ratios of Mica-Mg-NP, with largest drifts in data obtained from the Session 4, while data from other sessions (1 to 3) were relatively more consistent and reproducible (see data in Table 3.4 and Figure 3.10). In these three additional sessions (Session 1, 2 and 3), $^{87}Rb/^{86}Sr$ and $^{87}Sr/^{86}Sr$ data of Mica-Mg-NP were calibrated to NIST 610 to investigate the consistency and reproducibility of Rb/Sr isotopic ratios. The detectors settings were adjusted to collect all Rb and Sr (count per seconds, cps) at pulse mode. The results are listed in Table 3.B of the Supplementary Material, and also summarised in Table 3.4 and Figure 3.10. The results indicate that the variation of $^{87}Rb/^{86}Sr$ between all sessions (1, 2 and 3) were 0.29% (SE, n = 187) but their average (173.32 $\pm$ 0.51) is higher than the expected ratios (listed in Table 3.1) by about 12%, which is probably due to the difference in matrix between phlogopite Mica-Mg-NP and NIST 610 reference glass. However, $^{87}Sr/^{86}Sr$ ratios were more consistent between the sessions (SE = 0.065%, n = 187), compared to $^{87}Rb/^{86}Sr$ data, and their average of 1.8583 $\pm$ 0.0012 is only slightly higher (by about 0.3%) than the published values (see in Table 3.1). Nevertheless, we still consider Mica-Mg-NP nano-powder standard as a suitable reference material for in-situ Rb-Sr dating of phlogopite and related mica group minerals, especially if these are analysed together with secondary and in-house 'phlogopite' material such as the MDC or natural phlogopite mineral, which was sourced from the same location as Mica-Mg (see Redaa et al., 2021).

Mica-Fe biotite

Measured $^{87}Rb/^{86}Sr$ and $^{87}Sr/^{86}Sr$ ratios of Mica-Fe-NP and Mica-Fe glasses (Mica-Fe G1 and G2) were normalised to NIST 610 (see Table 3.B in the Supp. Material). The results show that $^{87}Rb/^{86}Sr$ ratios of the Mica-Fe-G1 and G2 (glasses) are generally lower than the $^{87}Rb/^{86}Sr$ of Mica-Fe-NP nano-powder pellet (Figure 3.8B), and also with larger uncertainty of 20% and 34% for G1 and G2 glasses, respectively (Table 3.4). The decrease of $^{87}Rb/^{86}Sr$ ratios in the Mica-Fe glasses, compared to data from Mica-Fe-NP (nano-powder), points to the loss of Rb due to volatilisation during the melting process. The average $^{87}Sr/^{86}Sr$ ratios of Mica-Fe-G1 and G2 overlap with each other, and also with the average $^{87}Sr/^{86}Sr$ of Mica-Fe-NP analysed in the same session (Session 4), within the analytical uncertainty of 12% (see data in Table 3.4). This large uncertainty associated with the averages of $^{87}Rb/^{86}Sr$ and $^{87}Sr/^{86}Sr$ in the Mica-Fe glasses, in turn, indicate that glasses are heterogeneous in Rb/Sr isotopic ratios at the micro-scale level, and they are thus not suitable for calibration Rb-Sr data collected via the LA-ICP-MS/MS. In contrast, Mica-Fe-NP (biotite nano-powder pellet) showed high level of homogeneity with respect to $^{87}Rb/^{86}Sr$ and $^{87}Sr/^{86}Sr$ ratios, specifically when the sample was analysed in the sessions 1, 2, and 3 (see Figure 3.10). Overall, the variability of $^{87}Rb/^{86}Sr$ and $^{87}Sr/^{86}Sr$ ratios measured in Mica-Fe-NP during all analytical sessions was 1.03% and 0.88%, respectively (Figure 3.10), and this biotite nano-powder seems to be promising reference material to calibrate data for in-situ Rb-Sr dating of unknown biotite samples by the LA-ICP-MS/MS.

FK-N K-feldspar

Measured $^{87}Rb/^{86}Sr$ and $^{87}Sr/^{86}Sr$ ratios of the FK-N mineral (K-feldspar: FK-N-G1 and G2 glasses, and FK-N-NP nano-powder) were normalised to NIST 610, and results are reported in Table 3.B of the Supplementary Material. The results show that $^{87}Rb/^{86}Sr$ ratios in the FK-N-G1 and G2 fused glasses generally overlap or are lower than $^{87}Rb/^{86}Sr$ ratios in the FK-N NP nano-powder (Figure 3.8C), which in turn indicates volatilisation and loss of Rb from a feldspar melt/glass produced during the experimental melting process. On the other hand, $^{87}Sr/^{86}Sr$ ratios in the FK-N-G1 and G2 overlapped with the $^{87}Sr/^{86}Sr$ ratio of the FK-N-NP nano-powder (Figure 3.8C), which suggests that Sr has not evaporated or been lost from the glasses during the experimental melting. The in-situ Rb-Sr analysis of FK-N-NP was repeated three times (session 1, 2 and 3) to examine its reproducibility with respect to $^{87}Rb/^{86}Sr$ and $^{87}Sr/^{86}Sr$. The results show that $^{87}Rb/^{86}Sr$ and $^{87}Sr/^{86}Sr$ in FK-N-NP varied between the sessions by 0.58% and

0.12%, respectively (see also data in Figure 3.10).

3.4.3 Additional constraints on $^{87}Rb/^{86}Sr$ and $^{87}Sr/^{86}Sr$ of studied mineral nano-powder standards

All analysed mineral nano-powder materials (Mica-Mg-NP, GL-O-NP, and Mica-Fe-NP and FK-N-NP) showed high level of homogeneity with respect to $^{87}Rb/^{86}Sr$ and $^{87}Sr/^{86}Sr$, indicating that these nano-powder pellets can be used as suitable and mineral-specific reference materials for in-situ Rb-Sr dating. However, $^{87}Rb/^{86}Sr$ and $^{87}Sr/^{86}Sr$ reference values for the above material standards have not yet been reported or certified in published literature, with a few exceptions (see below, and data in Table 3.1). Considering such lack of reliable analytical data in the literature, previous studies (e.g., Hogmalm et al., 2017) tried to constrain $^{87}Rb/^{86}Sr$ values of a reference material (RM) via measured $^{87}Sr/^{86}Sr$ ratios of this RM (normalised to NIST 610), and the revised $^{87}Rb/^{86}Sr$ ratios were then calculated from such normalised $^{87}Sr/^{86}Sr$ data and published or expected 'age' of the mineral RM (plus its assumed initial $^{87}Sr/^{86}Sr$ ratio), using the decay constant of 1.3972 $\pm$ 0.0045 x $10^{-}11$ for Rb-Sr system (Villa et al., 2015). Accordingly, the $^{87}Rb/^{86}Sr$ isotopic ratios of studied mineral nano-powders (Mica-Mg-NP, GL-O-NP, and Mica-Fe-NP) were calculated using the above approach and the average $^{87}Sr/^{86}Sr$ values of specific NP standards obtained from three separate analytical sessions (see Table 3.4). In addition, BCR-2G glass reference material was analysed during these sessions to validate the normalised $^{87}Sr/^{86}Sr$ ratios; and the average $^{87}Sr/^{86}Sr$ obtained from the BCR-2G was 0.70505 $\pm$ 0.00021 which agrees well with the published $^{87}Sr/^{86}Sr$ reference value of 0.705003 (Elburg et al., 2005). Following the above approaches, the mean $^{87}Rb/^{86}Sr$ of phlogopite Mica-Mg-NP was calculated at 155.39 $\pm$ 2.03 (2SD, propagated uncertainty), based on the average $^{87}Sr/^{86}Sr$ of 1.8583 $\pm$ 0.0012 (2SE, n = 187), an expected age of 519.6 $\pm$ 6.5 Ma, and initial Sr ratio of 0.72607 $\pm$ 0.0007 (Hogmalm et al., 2017). For glauconite GL-O-NP, the calculated $^{87}Rb/^{86}Sr$ ratio yielded 34.56 $\pm$ 1.52 (2SD, propagated uncertainty), using the reported $^{87}Sr/^{86}Sr$ of GL-O reference material of 0.7535 $\pm$ 0.001 (Govindaraju, 1995; Odin, 1976), the average of published K-Ar and Ar-Ar ages of GL-O (Derkowski et al., 2009) (95.5 $\pm$ 4.18 Ma, 2σ, n= 4), and the expected initial $^{87}Sr/^{86}Sr$ ratio of GLO glauconite of 0.70740 $\pm$ 0.0001 (McArthur, Howarth, and Shields, 2012; Rousset et al., 2004), the latter reflecting the Sr isotope composition of Albian-Cenomanian palaeo-seawater. Note that, the theoretical $^{87}Rb/^{86}Sr$ for GL-O-NP was calculated here using the published average $^{87}Sr/^{86}Sr$ of 0.7535 $\pm$ 0.001 for GL-O reference mineral (Govindaraju, 1995; Odin, 1976)

rather than the obtained average of $^{87}Sr/^{86}Sr$ for GL-O-NP (0.7548 $\pm$ 0.0007), because the later overlapped within the uncertainty with the above published or certified value. Also, we noticed that by applying the obtained $^{87}Sr/^{86}Sr$ value for GL-O-NP of 0.7548 (along with calculated $^{87}Rb/^{86}Sr$ of 35.50 $\pm$ 1.60) to calibrate the Rb-Sr data would impact on the accuracy of the Rb-Sr ages by about 1%. Thus, for this study we opted to apply the previously reported $^{87}Sr/^{86}Sr$ for GL-O (Govindaraju, 1995; Odin, 1976) of 0.7535 $\pm$ 0.001 as a reference value also for GL-O-NP to calculate its corresponding $^{87}Rb/^{86}Sr$ and to acquire the correction factors used to calibrate Rb-Sr data. For biotite Mica-Fe-NP, the calculated $^{87}Rb/^{86}Sr$ ratio was 1655.22 $\pm$ 65.60 (2SD, propagated uncertainty) based on average $^{87}Sr/^{86}Sr$ of 8.036 $\pm$ 0.057 (2SE, n = 80), the initial Sr ratio of 0.709797 $\pm$ 0.016 (Turpin et al., 1990), and the published Rb-Sr age for Mica-Fe of 360 $\pm$ 10 Ma (Govindaraju, 1979; Zimmermann et al., 1985).

3.4.4 Assessment of nano-powder mineral pellets as reference materials for in-situ Rb-Sr dating

In this section, Mica-Mg-NP, GL-O-NP and Mica-Fe-NP were used as a primary reference material for the in-situ Rb-Sr geochronology and 'age' determination of two natural minerals: glauconite grains (GL-O) and phlogopite (MDC) crystal/flakes, and also one nano-powder K-feldspar sample (FK-N-NP). These analyses and in-situ Rb-Sr dating sessions were repeated three times, and the results including: Ages, $^{87}Rb/^{86}Sr$ and $^{87}Sr/^{86}Sr$ ratios are presented in Table. 3.C of the Supplementary Materials. The calculated Rb-Sr ages of the above mineral standards (GL-O, MDC and FK-N-NP) are also summarized and plotted in Figure 3.11, and the source Rb-Sr isochrons for these age data can be found in the Supplementary Materials (Fig 3.A, 3.B and 3.C).

Briefly, $^{87}Rb/^{86}Sr$ and $^{87}Sr/^{86}Sr$ data of the MDC phlogopite were separately normalised to three NP reference materials: Mica-Mg-NP, GL-O-NP and Mica-Fe-NP, and the ages were calculated by anchoring the data to an initial $^{87}Sr/^{86}Sr$ ratio to 0.72607 $\pm$ 0.0007 (Hogmalm et al., 2017). The obtained ages from MDC, with data calibrated to Mica-Mg-NP, varied in two sessions (Session 1 and 3) yielding 3.5% differences from the expected age of 519.6 $\pm$ 6.5 Ma (Hogmalm et al., 2017), and the most accurate age was obtained from Session 2 at 521 $\pm$ 8 Ma (see Figure 3.11). This variation in the MDC ages between the sessions can be attributed to many factors including the matrix-effect, the heterogeneity of Mica-Mg-NP in the particle size at micro-scale level and the spacing between laser spots during the sampling (for more details see Redaa et al., 2021). When the MDC Rb-Sr data were normalised to GL-O-NP, the sample yielded

an accurate age (within 1% or less) for all three analytical sessions (Figure 3.11), even though the MDC was analysed using different laser spot size (i.e., 74 μm for Session 1 and 62 μm for Session 2 & 3). This consistency in the produced Rb-Sr age for MDC, normalised to GL-O-NP, indicate that the latter nano-powder glauconite standard is also suitable reference material for in-situ Rb-Sr dating of phlogopite, and perhaps also other mica group minerals. Thus, the matrix-effect likely has minimum impact on the accuracy of the obtained Rb-Sr age from the MDC. Finally, using Mica-Fe-NP as a reference material for MDC dating yielded ages of phlogopite that were shifted form the expected age by about 6-7% (Figure 3.11), which in turn indicates that biotite Mica-Fe-NP is either ablated differently compared to MDC phlogopite, or there is stronger impact from matrix-effects when using Mica-Fe-NP. Thus, we conclude that biotite Mica-Fe-NP is not suitable to calibrate $^{87}Rb/^{86}Sr$ and $^{87}Sr/^{86}Sr$ data of phlogopite.

As to GL-O, the age of glauconite grains was calculated by normalising $^{87}Rb/^{86}Sr$ and $^{87}Sr/^{86}Sr$ data from GL-O to three different NP standards (Mica-Mg-NP, GL-O-NP and also Mica-Fe-NP), and by anchoring the Rb-Sr isochron to an initial $^{87}Sr/^{86}Sr$ of 0.70740 $\pm$ 0.0001 (McArthur, Howarth, and Shields, 2012). Importantly, using this approach the GL-O grains yielded accurate ages that ranged between 97 and 102 Ma, when normalised to Mica-Mg-NP or GL-O-NP (Figure 3.11), which are in excellent agreement with an expected stratigraphic age for GL-O (Selby, 2009 see also below). In contrast, the published Ar-Ar ages of GL-O of 93.6 $\pm$ 1 Ma (Charbit, Guillou, and Turpin, 1998) and 95 $\pm$ 1 Ma (Derkowski et al., 2009; Fiet et al., 2006) are thus systematically younger than our Rb-Sr age and also the expected stratigraphic age (i.e., the basal Cenomanian) for GL-O of 99.6 $\pm$ 1 Ma (Gradstein et al., 2012; Selby, 2009). Thus, both Mica-Mg-NP and GL-O-NP nano-powder standards can be used to generate robust and reliable Rb-Sr ages for glauconite dating via LA-ICP-MS/MS. In contrast, the obtained Rb-Sr ages from GL-O grains were inaccurate by 4% when normalised to biotite Mica-Fe-NP (Figure 3.11), but nevertheless these ages still overlap (at lower limit of 4.5% uncertainty) with the expected age for GL-O of 99.6 $\pm$ 1 Ma (Figure 3.11). Thus, overall our data suggest that Mica-Fe-NP is less suitable as a reference material for in-situ Rb-Sr dating of glauconite, compared to Mica-Mg-NP /or GL-O-NP standards.

Finally, as to the FK-N-NP feldspar, the lack of information about this sample, including the expected age and initial $^{87}Sr/^{86}Sr$ ratios, prevented at this stage to constrain its Rb-Sr age accurately. Also, determination of the initial Sr value for the FK-N feldspar by the LA-ICP-MS/MS is difficult because of the relative homogeneity of this sample and general lack of spread in $^{87}Rb/^{86}Sr$ and $^{87}Sr/^{86}Sr$ data. Thus, the 'model age' of FK-N-NP was calculated by assuming an initial $^{87}Sr/^{86}Sr$ for FK-N-NP feldspar of 0.707,

which however needs to be confirmed and validated by future studies. When $^{87}Rb/^{86}Sr$ and $^{87}Sr/^{86}Sr$ data of FK-N-NP was calibrated to Mica-Mg-NP, GL-O-NP or Mica-Fe-NP, the sample yielded an average Rb-Sr age of 496 $\pm$ 4 Ma (SD, n= 3), 482 $\pm$ 11 Ma (SD, n= 2), 536 $\pm$ 22 (SD, n= 3), respectively (Figure 3.11). Setting the Sr initial ratio to higher and more radiogenic value (i.e., 0.72000) would affect the obtained ages for the FK-N-NP by about 2.5%. Thus, further work on the FK-N is needed to constrain its Rb-Sr age and its initial Sr ratio accurately.

3.5 Conclusions

Fused flux-free mineral glasses and nano-powder (NP) pellets of four silicate mineral reference materials were produced to be tested and used for in-situ Rb-Sr dating by the LA-ICP-MS/MS. These reference materials include GL-O glauconite, Mica-Mg phlogopite, Mica-Fe biotite and FK-N feldspar. The produced mineral glasses (melted using a Photon Machine 100 W Fusions 10.6 CO_2 laser system) were heterogeneous at micro-scale levels with respect to Rb and Sr, with evidence also for Rb volatilisation, which thus render these mineral glasses not suitable reference materials for in-situ Rb-Sr dating applications. In contrast, the nano-powder mineral pellets (Mica-Mg-NP, GL-O-NP, Mica-Fe-NP and FK-N-NP) were all homogeneous at micro-scale level, and our testing also confirmed that they be used as reliable standards to normalise $^{87}Rb/^{87}Sr$ and $^{87}Sr/^{86}Sr$ data in micas and feldspars for in-situ and 'mineral-specific' Rb-Sr dating via LA-ICP-MS/MS. In this study, the recommended $^{87}Rb/^{87}Sr$ and $^{87}Sr/^{86}Sr$ values for Mica-Mg-NP, GL-O-NP and Mica-Fe-NP were also calculated based on published information and background data (i.e., expected ages and initial Sr ratios) available for these mineral reference materials. Importantly, our results and testing confirmed that both Mica-Mg-NP and GL-O-NP can produce reliable and robust Rb-Sr ages for phlogopite and glauconite minerals (i.e., MDC and GL-O), which were within 1-3% accuracy of the expected ages for these minerals. However, MDC (phlogopite) and GL-O (glauconite) natural minerals/grains yielded ages that are shifted by 4.5-7% from their expected ages when the data are normalised to Mica-Fe-NP (biotite) standard, suggesting that the latter is less suitable reference material for phlogopite and glauconite dating. Finally, the lack of published data and information on the age of FK-N-NP feldspar, including Sr isotope initial, limits its current application as suitable reference material for the in-situ Rb-Sr dating. Our analysis suggests that the age of FK-N-NP (calculated using an assumed Sr initial of 0.707 and 0.720) ranges between 475 and 550 Ma, which however

needs further validation. Overall, both Mica-Fe-NP (biotite) and FK-N-NP (K-feldspar) could be potentially used as suitable reference materials for the in-situ Rb-Sr dating via LA-ICP-MS/MS, but further work towards constraining the $^{87}Rb/^{87}Sr$ and $^{87}Sr/^{86}Sr$ of these materials is necessary. Future work and detail studies, including high-precision Rb-Sr dating of mineral-specific nano-powders (NP) by ID-TIMS and MC-ICP-MS or MS/MS, is needed to further expand the utility of NP for in-situ Rb-Sr dating via LA-ICP-MS/MS, to allow its wider applicability for earth and planetary sciences as a relatively rapid, cost-effective and non-destructive method for dating of silicate minerals.

3.6 Acknowledgement

This work was supported by ARC Discovery Project (DP210100462) titled "Glauconite: Archive recording timing and triggers of Cambrian radiation", and partly also by MinEx CRC, to develop and validate a new set mineral standards for in-situ Rb-Sr dating applications using LA-ICP MS/MS techniques. Finally, we acknowledge assistance with analytical work on selected standards by Wei Hong from the University of Adelaide.

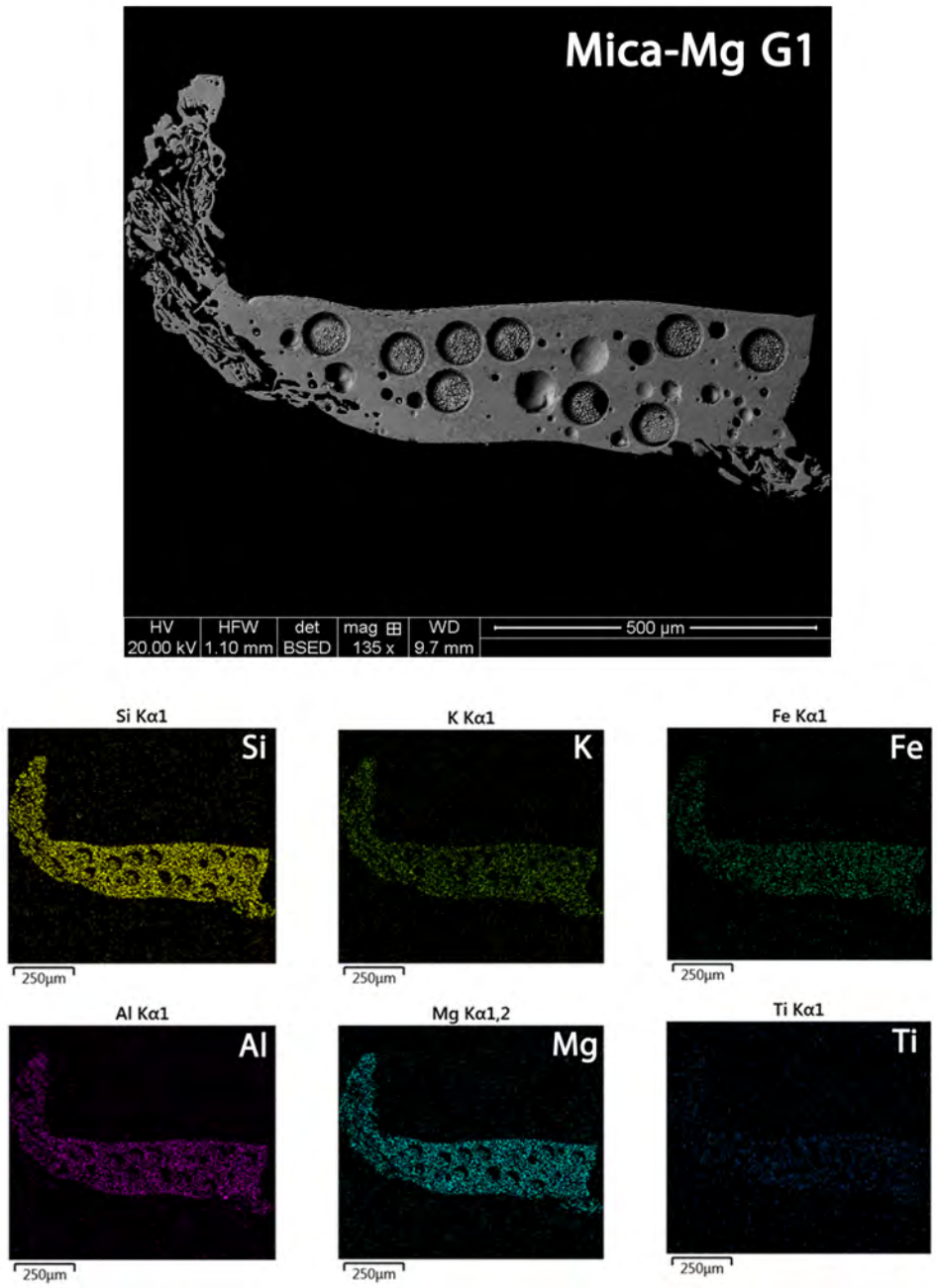

Figure 3.2: SEM image and elemental map of Mica-Mg G1 acquired via Quanta 450. 'Black circles' in a top image (SEM) are vesicles or bubbles in the melt/fused glass, and 'larger grey circles' with granulated texture at the base are laser pits/craters after LA-ICP MS/MS analysis.

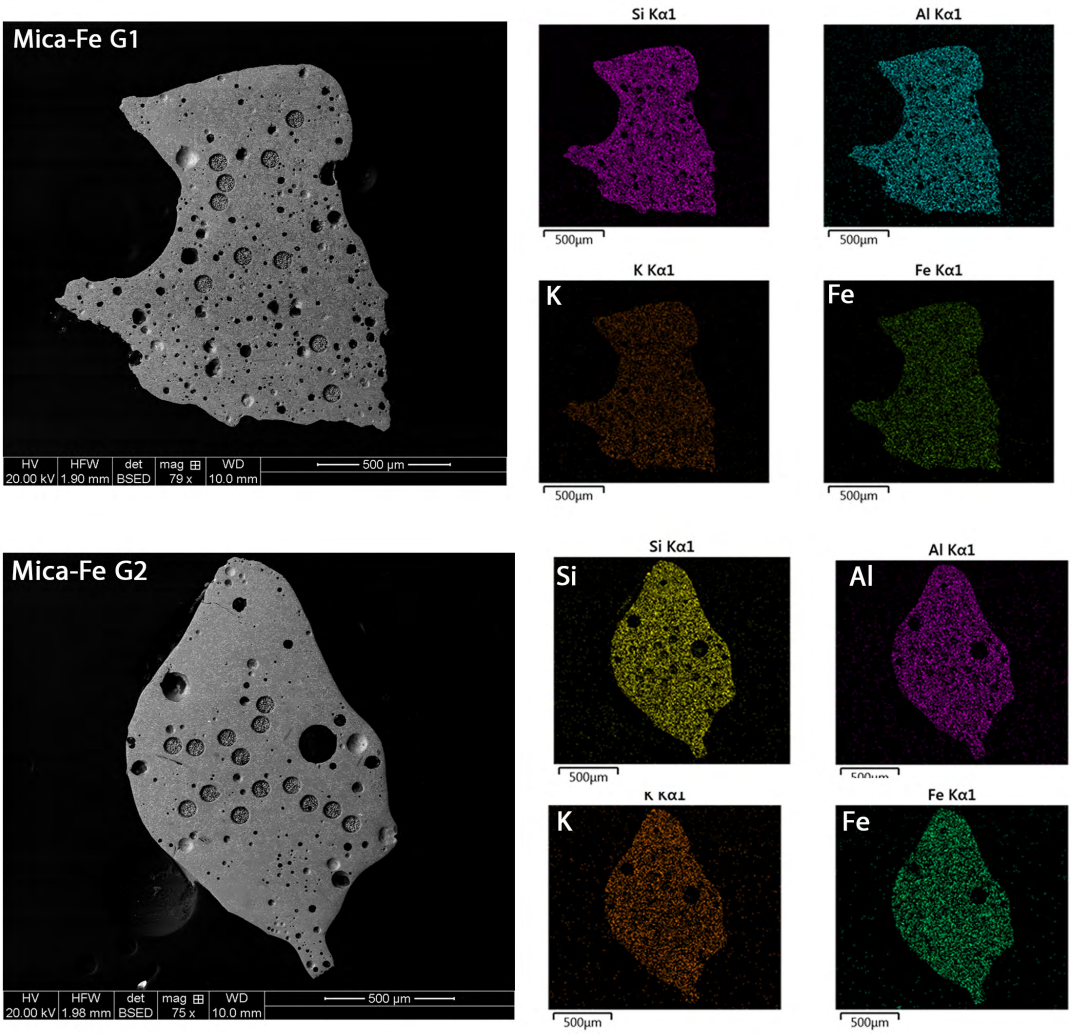

Figure 3.3: SEM image and elemental map acquired via Quanta 450 from Mica-Fe G1 (top) and Mica-Fe G2 (bottom). The dark hollow the left SEM image represents vesicles or bubbles in the melt/fused glass, and 'larger grey circles' with granulated texture at the base represent laser pits/craters after LA-ICP MS/MS analysis.

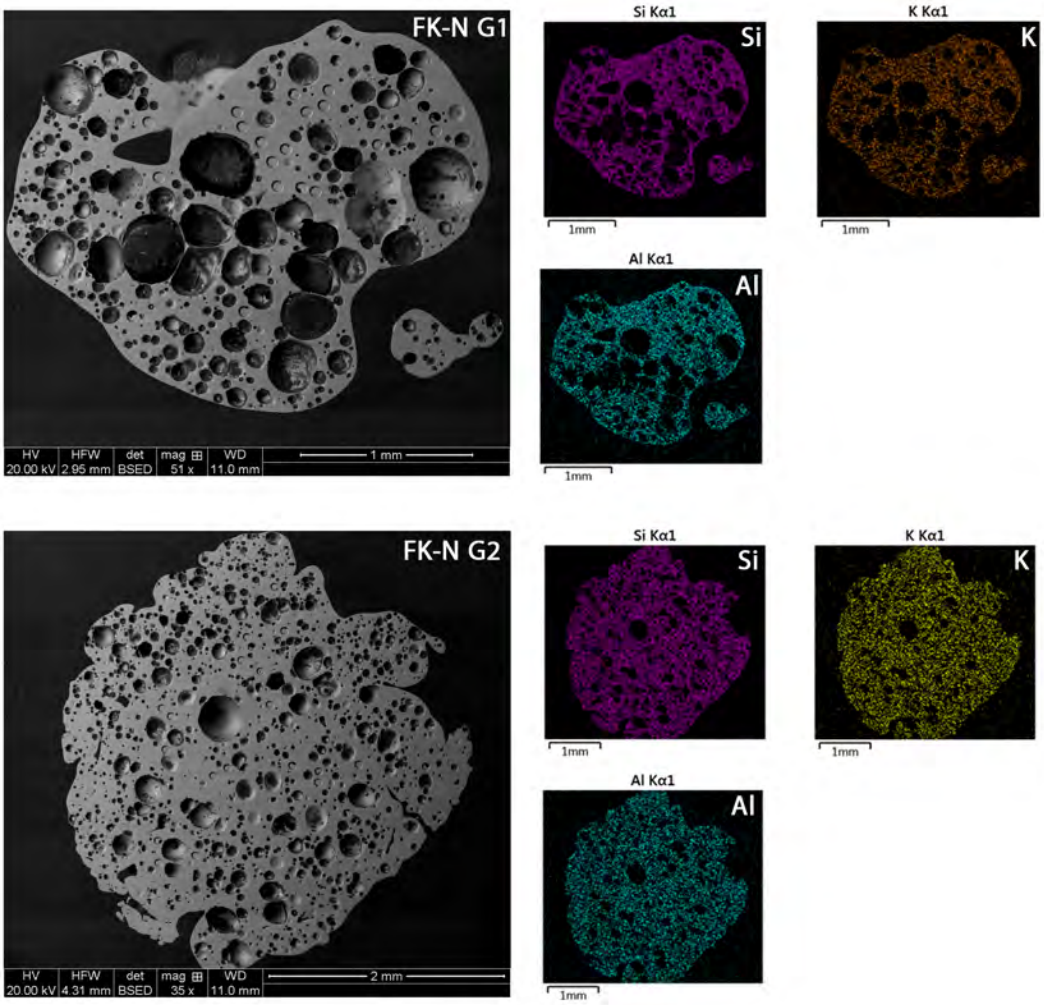

Figure 3.4: SEM image and elemental map of FK-N G1 (top) and FK-N G2 (bottom). Vesicles or bubbles in the melt/fused glass are presented as dark areas. The small circles, in the SEM image, with smooth texture at the base represent laser pits/craters after LA-ICP MS/MS analysis.

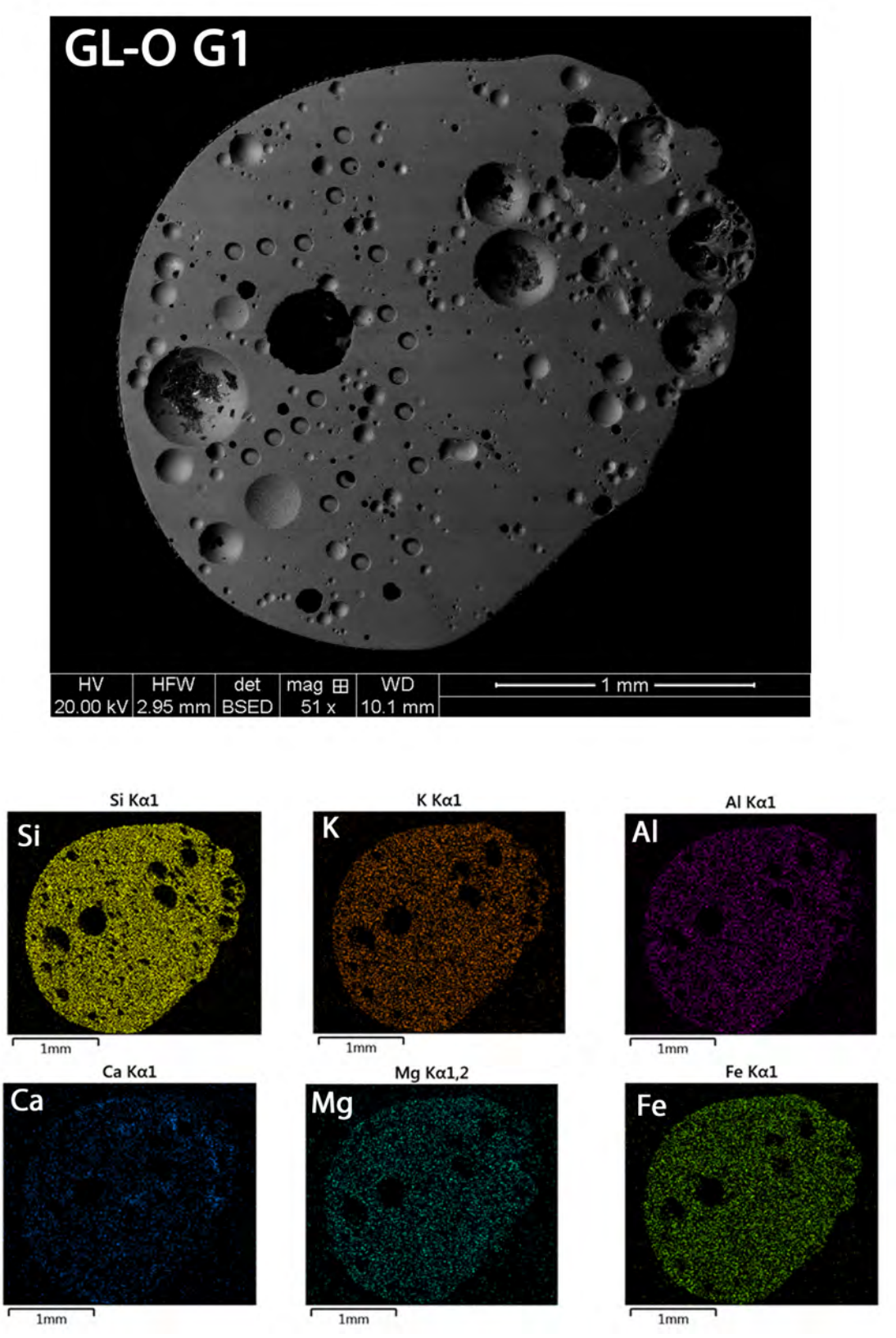

Figure 3.5: SEM image and elemental map of GL-O G1. The large circles in the top SEM image represents vesicles or bubbles in the melt/fused glass, and 'smaller grey circles' with smooth texture at the base represent laser pits/craters after LA-ICP MS/MS analysis.

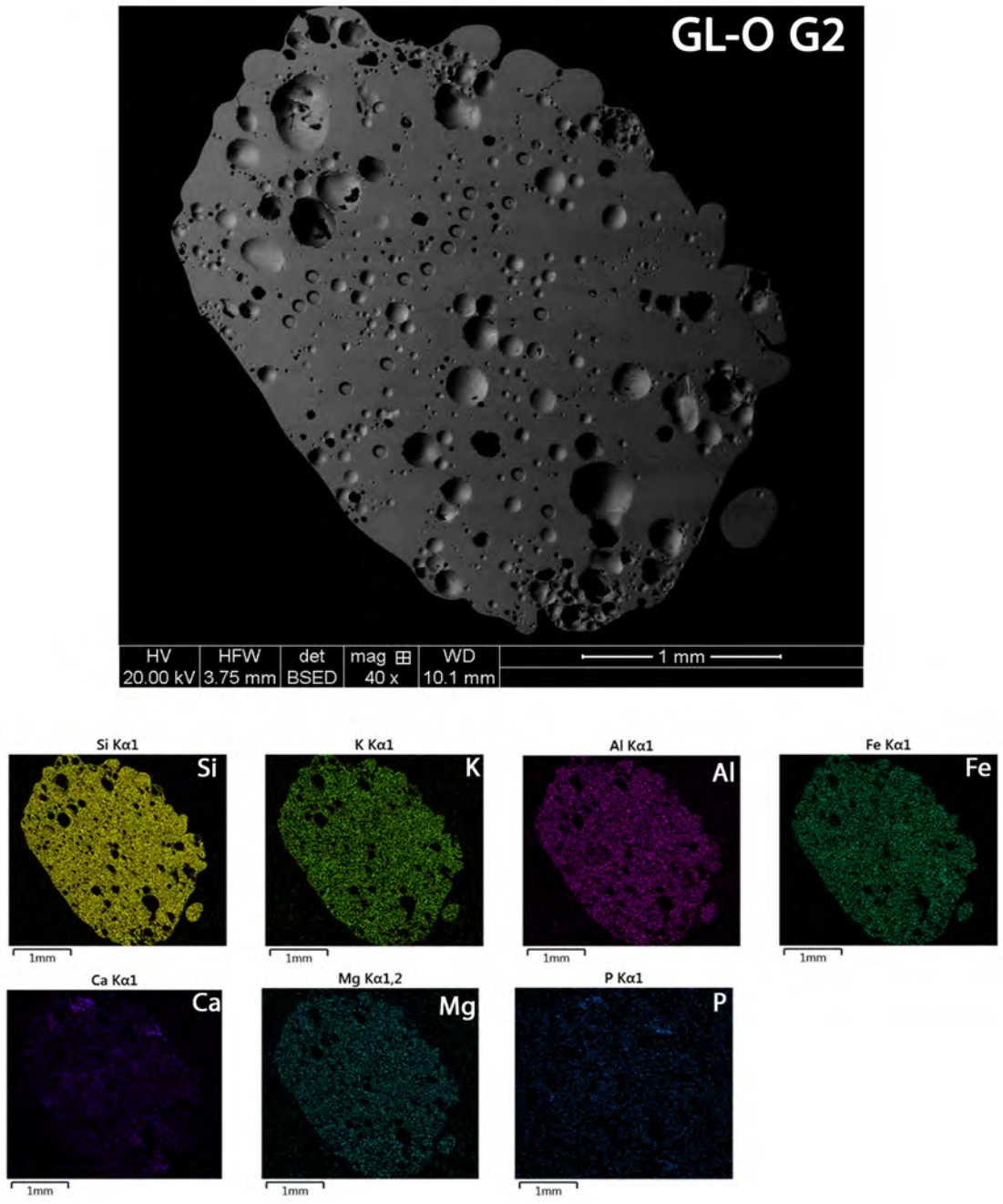

Figure 3.6: SEM image and elemental map of GL-O G2 acquired via Quanta 450.

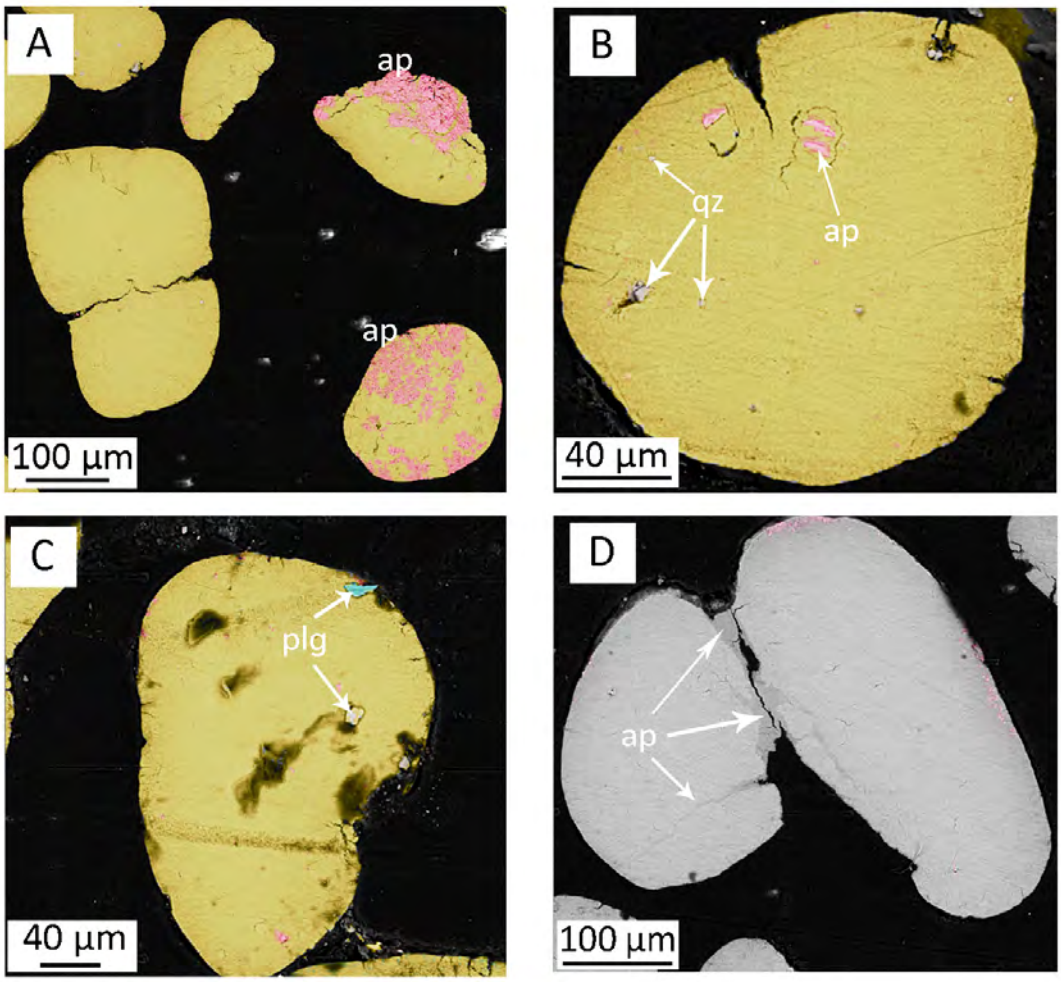

Figure 3.7: SEM/EDS and Nanomin 'micro-scale mineral' images of GL-O glauconite grains showing the presence of minor phases and mineral inclusions (ap = apatite; plg = plagioclase; qz = quartz) within the glauconite grains. (A) apatite-rich zones appear at the rims of glauconite grains. (B) Minor presence of quartz with apatite micro-inclusions within a glauconite grain. (C) Minor plagioclase phase within a glauconite grain. (D) SEM image shows zones of apatite (i.e., darker grey) concentrated at the rim and within fractures of GL-O glauconite grains.

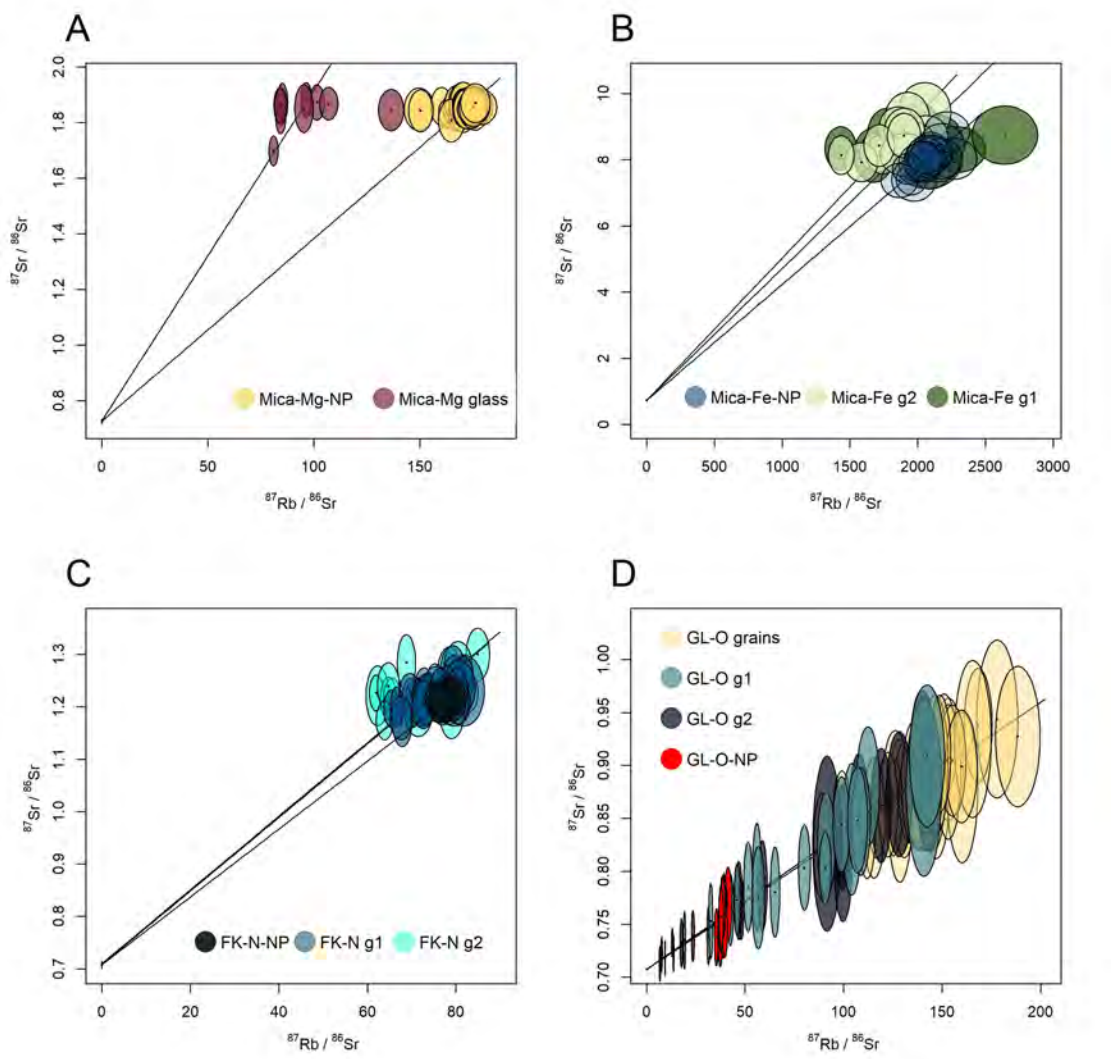

Figure 3.8: The Rb-Sr isochron plots (Nicolaysen diagrams) showing variations in $^{87}Rb/^{86}Sr$ and $^{87}Sr/^{86}Sr$ ratios measured in the produced fused mineral glasses (G1, G2 data), plotted along with data from nano-powder pellets (NP) from the following minerals: (A) Mica-Mg - Phlogopite; (B) Mica-Fe - Biotite, (C) FK-N – K-Feldspar, (D) GL-O - Glauconite.

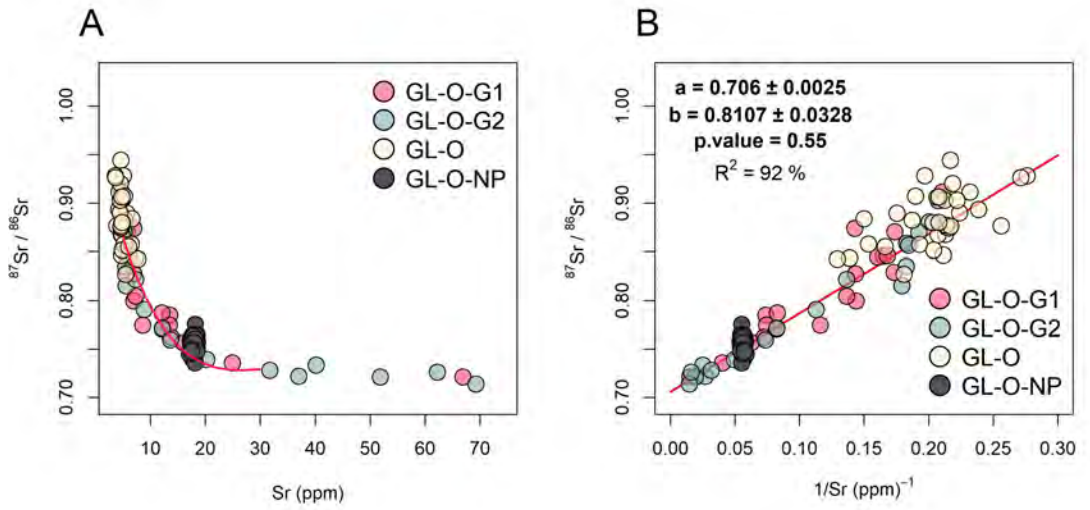

Figure 3.9: (A) A cross-plot of $^{87}Sr/^{86}Sr$ vs Sr concentration data from GL-O glasses (G1: red, and G2: blue), GL-O grains (yellow) and GL-O-NP nano-powder (dark grey), plotted along with two-component theoretical mixing lines (red curve). (B) A cross plot of $^{87}Sr/^{86}Sr$ vs 1/Sr data showing statistically significant correlation which further confirms the presence of two components (Sr-poor and radiogenic 'pure glauconite' versus Sr-rich and less radiogenic apatite/calcite) within GL-O glauconite grains, fused glasses and nano-powder materials. Also the calculated y-intercepts 'a' indicates that the lower limit of $^{87}Sr/^{86}Sr$ values in the GL-O materials (i.e., data dominated by apatite/calcite signal) overlap with the expected $^{87}Sr/^{86}Sr$ of palaeo-seawater (0.70740) during the formation of the GL-O grains at around 100 Ma ago (Albian-Cenomanian boundary).

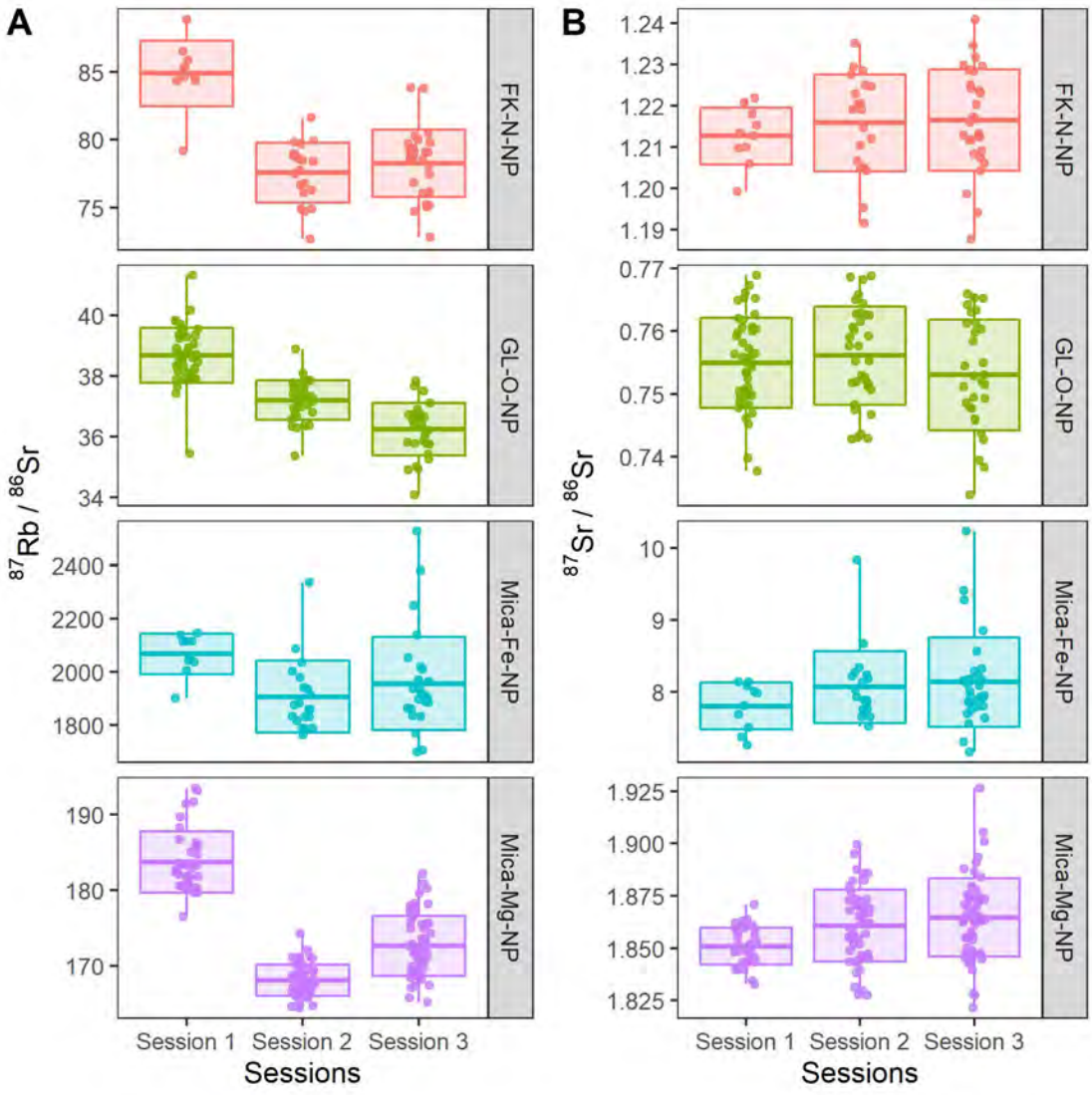

Figure 3.10: Variations in $^{87}Rb/^{86}Sr$ and $^{87}Sr/^{86}Sr$ ratios (A and B columns, respectively), normalised to NIST 610, measured in the nano-powder (NP) mineral reference materials/pellets (FK-N-NP, GL-O-NP, Mica-Fe-NP, Mica-Mg-NP) as analysed within individual sessions and/or between the sessions (Sessions 1 to 3 at the horizontal axis). The boxes illustrate the mean and the standard deviation of $^{87}Rb/^{86}Sr$ and $^{87}Sr/^{86}Sr$ data within the sessions. Session 1 and 2 were conducted using 74 μm laser spot size, whereas the spot size of 62 μm was used for Session 3.

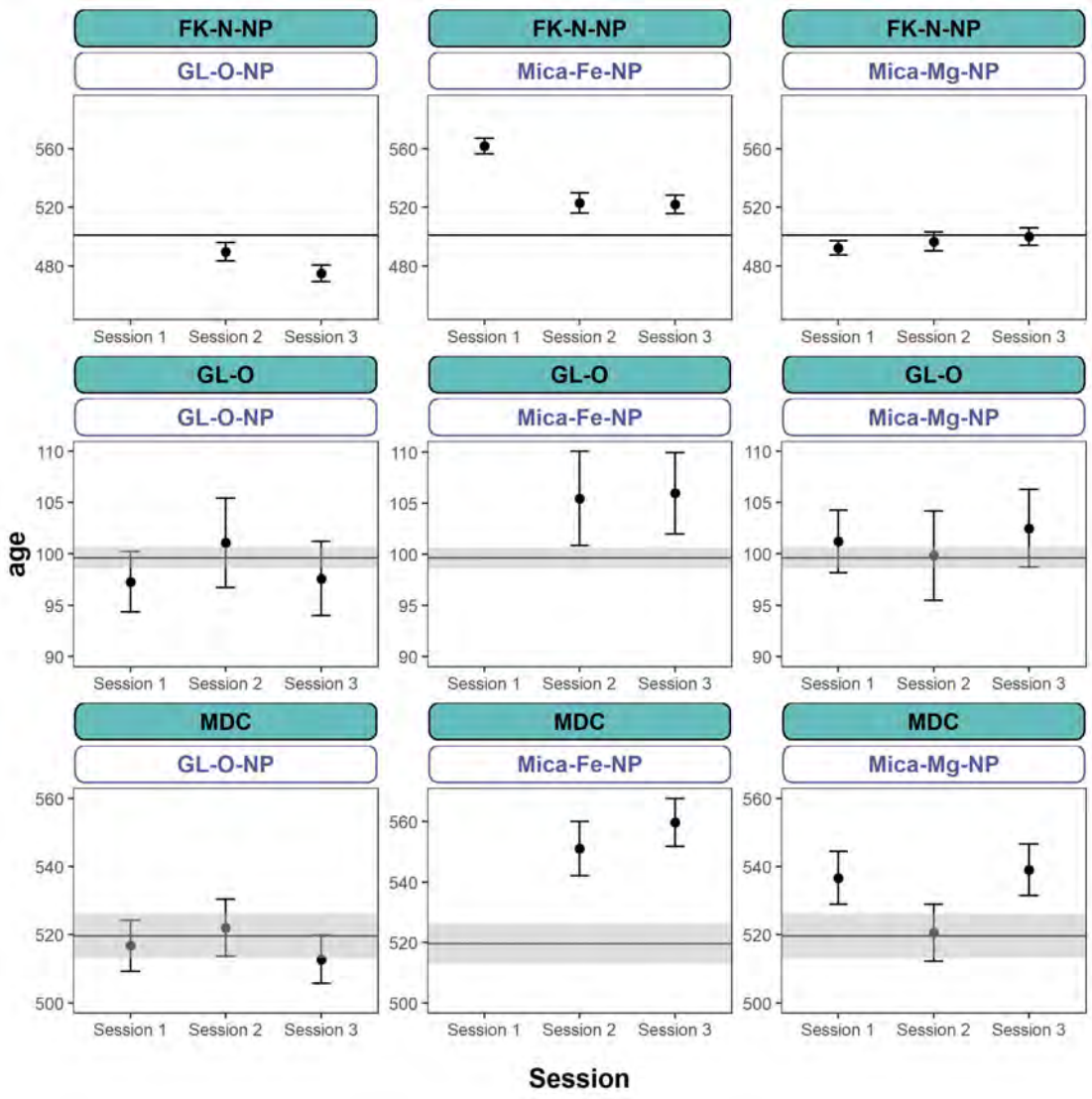

Figure 3.11: A summary plot showing calculated Rb-Sr ages of MDC phlogopite, GL-O glauconite and FK-N-NP feldspar, derived from Rb-Sr isochrons and measured $^{87}Rb/^{86}Sr$ and $^{87}Sr/^{86}Sr$ data, which were calibrated using different nano-powder materials (i) Mica-Mg-NP, (ii) Mica-Fe-NP and (iii) GL-O-NP. Labels in the green rectangle refer to the sample/mineral name (i.e., FK-N, GL-O and MDC) whereas labels in white rectangle refer to the specific nano-powder (NP) reference material used for data normalisation. The black horizontal line with grey shade represents, respectively, the expected/published 'mean age' of the sample (i.e., FK-N, GL-O and MDC) and the associated uncertainty (1SD). The black lines in the FK-N-NP diagram show the average Rb-Sr age of this sample (i.e., n = 8) obtained by this study, as there is no published age on this mineral standard in the available literature.

Table 3.2: Settings of laser ablation and ICP-MS/MS used in this study.

	Units	
Laser parameters		
He carrier gas	ml/min	350
Ar carrier gas	ml/min	1050
N2 addition	ml/min	3.5
Spot size	µm	74 or 62
Repetition Rate	Hz	5
Fluence	J/cm^2	3.5
Sample Chamber		S155 large format
ICP-MS/MS		
Plasma Parameters		
RF Power	W	1350
Sample Depth	mm	5
Lens Parameters		
Extract 1	V	-2
Extract 2	V	-140
Omega Bias	V	-80
Omega Lens	V	7
Q1 entrance	V	1.5
Q1 exit	V	-2
Cell focus	V	-2
Cell entrance	V	-90
Cell exit	V	-120
Deflect	V	-11
Plate bias	V	-80
Q1 Parameters		
Q1 bias	V	-2
Q1 prefilter bias	V	-10
Q1 postfilter bias	V	-7
Cell Parameters		
N_2O flow rate	mL/min	0.35
OctP Bias	V	-23
Axial acceleration	V	2
OctP RF	V	180
Energy discrimination	V	-8
Q2 Parameters		
Q2 Bias	V	-31

Table 3.3: Rb and Sr concentrations of the investigated materials analysed via LA-ICP-MS/MS.

Sample	Laser power	Rb (ppm) $\pm$ 2σ	Reported Rb (ppm) $\pm$ 1σ	Sr (ppm) $\pm$ 2σ	Reported Sr (ppm) $\pm$ 1σ	n
Mica-Mg NP	-	1413.28 $\pm$ 38.93	1300 $\pm$ 114.3$^{\&}$	20.51 $\pm$ 1.03	27 $\pm$ 7.1$^{\&}$	39
Mica-Mg glass	25%	837.09 $\pm$ 245.60	1300 $\pm$ 114.3$^{\&}$	22.72 $\pm$ 5.57	27 $\pm$ 7.1$^{\&}$	11
FK-N NP	-	887.6 $\pm$ 27	860 $\pm$ 56*	28.12 $\pm$ 1.25	39 $\pm$ 8.64*	21
FK-N G1	15%	842.53 $\pm$ 25	860 $\pm$ 56*	29.07 $\pm$ 3.55	39 $\pm$ 8.64*	21
FK-N G2	25%	821.44 $\pm$ 62.80	860 $\pm$ 56*	28.7 $\pm$ 7.32	39 $\pm$ 8.64*	20
Mica-Fe-NP	-	2643 $\pm$ 168.01	2200 $\pm$ 269$^{\&}$	3.2 $\pm$ 0.29	5 $\pm$ 9.3$^{\&}$	20
Mica-Fe glass 1	20%	2413.38 $\pm$ 346.7	2200 $\pm$ 269$^{\&}$	3.16 $\pm$ 0.72	5 $\pm$ 9.3$^{\&}$	10
Mica-Fe glass 2	25%	2131.22 $\pm$ 256.15	2200 $\pm$ 269$^{\&}$	2.98 $\pm$ 0.80	5 $\pm$ 9.3$^{\&}$	14
GL-O mineral	-	279.82 $\pm$60.39	238 $\pm$ 5$^{\#}$	5.03 $\pm$ 1.81	19.3 $\pm$ 0.5$^{\#}$	33
GL-O NP	-	240.39 $\pm$ 4.77	238 $\pm$ 5$^{\#}$	17.99 $\pm$ 0.65	19.3 $\pm$ 0.5$^{\#}$	76
GL-O glass 1	20%	243.57 $\pm$ 58.94	238 $\pm$ 5$^{\#}$	13.1 $\pm$ 26.79	19.3 $\pm$ 0.5$^{\#}$	20
GL-O glass 2	35%	225.2 $\pm$ 61.02	238 $\pm$ 5$^{\#}$	21.74 $\pm$42.26	19.3 $\pm$ 0.5$^{\#}$	18

*Govindaraju and Roelandts, 1988
$^{\&}$Govindaraju, 1995
$^{\#}$Govindaraju, 1995; Odin, 1976

Table 3.4: $^{87}Rb/^{86}Sr$ and $^{87}Sr/^{86}Sr$ averages of the investigated materials analysed via LA-ICP-MS/MS and calibrated to NIST 610.

Sample	Sessions	$^{87}Rb/^{86}Sr$	SD	SE	$^{87}Sr/^{86}Sr$	SD	SE	n
FK-N-NP	Session 1	84.9	2.3	-	1.212	0.007	-	10
	Session 2	77.57	2.14	-	1.215	0.011	-	20
	Session 3	78.27	2.44	-	1.217	0.012	-	29
	Session 4	77.67	1.43	-	1.212	0.008	-	21
	Mean	78.84	-	0.35	1.215	-	0.001	80
FK-N-G1	Session 4	73.8	4.89	-	1.22	0.02	-	21
FK-N-G2	Session 4	73.08	8.52	-	1.23	0.003	-	20
GL-O-NP	Session 1	38.69	0.9	-	0.755	0.007	-	46
	Session 2	37.21	0.64	-	0.756	0.008	-	34
	Session 3	36.25	0.85	-	0.753	0.009	-	30
	Mean	37.56	-	0.13	0.7548	-	0.0007	110
GL-O-G1	Session 4	74.27	38.06	-	0.805	0.051	-	20
GL-O-G2	Session 4	65.25	49.08	-	0.791	0.063	-	18
GL-O	Session 4	140.36	20.38	-	0.884	0.028	-	34
Mica-Fe-NP	Session 1	2066.62	71.75	-	7.8	0.31	-	10
	Session 2	1906.38	131.26	-	8.07	0.49	-	20
	Session 3	1955.82	171.37	-	8.14	0.61	-	30
	Session 4	2071.62	97.41	-	7.97	0.35	-	20
	Mean	1986.26	-	17.03	8.036	-	0.057	80
Mica-Fe-G1	Session 4	2000.78	332.62	-	8.49	0.31	-	9
Mica-Fe-G2	Session 4	1836.9	174.1	-	8.57	0.43	-	14
Mica-Mg-NP	Session 1	183.7636	3.978725	-	1.85	0.009	-	37
	Session 2	168.1207	2.056153	-	1.86	0.017	-	51
	Session 3	172.6673	3.919801	-	1.864	0.018	-	60
	Session 4	171.21	6.29	-	1.852	0.013	-	39
	Mean	173.32	-	0.51	1.8583	-	0.0012	187
Mica-Mg-G1	Session 4	95.58	15.95	-	1.842	0.051	-	10
BCR-2G	Session 1	0.445	0.01	-	0.7048	0.0012		26
	Session 2	0.421	0.006	-	0.7055	0.002		26
	Session 3	0.407	0.004	-	0.7048	0.0027		34
	Session 4	0.419	0.008	-	0.70508	0.0024		26
	Mean	0.4217	-	0.0015	0.70505		0.00021	112

References

Agatemor, C and D Beauchemin (2011). "Matrix effects in inductively coupled plasma mass spectrometry: a review". In: *Anal Chim Acta* 706.1, pp. 66–83.

Armistead, Sheree E, Alan S Collins, Ahmad Redaa, Gilby Jepson, Jack Gillespie, Sarah Gilbert, Morgan L Blades, John D Foden, and Théodore Razakamanana (2020). "Structural evolution and medium-temperature thermochronology of central Madagascar: implications for Gondwana amalgamation". In: *Journal of the Geological Society* 177, pp. 784–798.

Awaji, Shunsaku, Kentaro Nakamura, Tatsuo Nozaki, and Yasuhiro Kato (2006). "A Simple Method for Precise Determination of 23 Trace Elements in Granitic Rocks by ICP-MS after Lithium Tetraborate Fusion". In: *Resource Geology* 56.4, pp. 471–478.

Bevan, Dan, Christopher D Coath, Jamie Lewis, Johannes Schwieters, Nicholas Lloyd, Grant Craig, Henning Wehrs, and Tim Elliott (2021). "In situ Rb–Sr dating by collision cell, multicollection inductively-coupled plasma mass-spectrometry with pre-cell mass-filter,(CC-MC-ICPMS/MS)". In: *Journal of Analytical Atomic Spectrometry* 36.5, pp. 917–931.

Boulesteix, Thomas, Jesús Solé, Teresa Pi, and Michel Cathelineau (2020). "Reappraisal of the GL-O Reference Material for K-Ar Dating: New Insight from Microanalysis, Single-Grain and Milligram Ar Measurements". In: *Geostandards and Geoanalytical Research* 44.2, pp. 287–306.

Charbit, S, H Guillou, and L Turpin (1998). "Cross calibration of K–Ar standard minerals using an unspiked Ar measurement technique". In: *Chemical Geology* 150.1, pp. 147–159.

Claverie, Fanny, Beatriz Fernndez, Christophe Pcheyran, Joël Alexis, and Olivier F X Donard (2009). "Elemental fractionation effects in high repetition rate IR femtosecond laser ablation ICP-MS analysis of glasses". In: *Journal of Analytical Atomic Spectrometry* 24.7, pp. 891–902.

Cromwell, Evan F and Peter Arrowsmith (1995). "Fractionation Effects in Laser Ablation Inductively Coupled Plasma Mass Spectrometry". In: *Applied Spectroscopy* 49.11, pp. 1652–1660.

Derkowski, Arkadiusz, Jan Srodon, Wojciech Franus, Peter Uhlík, Grzegorz Banas Michałand Zielinski, Maria Caplovicova, Małgorzata Franus, Michał Banas, Grzegorz Zielinski, Maria Caplovicova, and Małgorzata Franus (2009). "Partial dissolution of glauconitic samples: implications for the methodology of K-Ar and Rb-Sr dating". In: *Clays and Clay Minerals* 57.5, pp. 531–554.

Eggins, S M, L P J Kinsley, and J M G Shelley (1998). "Deposition and element fractionation processes during atmospheric pressure laser sampling for analysis by ICP-MS". In: *Applied Surface Science* 127-129, pp. 278–286.

Eggins, Stephen M (2003). "Laser Ablation ICP-MS Analysis of Geological Materials Prepared as Lithium Borate Glasses". In: *Geostandards Newsletter* 27.2, pp. 147–162.

Elburg, Marlina, Pieter Vroon, Bas van der Wagt, and Arnaud Tchalikian (2005). "Sr and Pb isotopic composition of five USGS glasses (BHVO-2G, BIR-1G, BCR-2G, TB-1G, NKT-1G)". In: *Chemical Geology* 223.4, pp. 196–207.

Fedorowich, J S, J P Richards, J C Jain, R Kerrich, and J Fan (1993). "A rapid method for REE and trace-element analysis using laser sampling ICP-MS on direct fusion whole-rock glasses". In: *Chemical Geology* 106.3, pp. 229–249.

Fiet, N, X Quidelleur, O Parize, L G Bulot, and P Y Gillot (2006). "Lower Cretaceous stage durations combining radiometric data and orbital chronology: Towards a more stable relative time scale?" In: *Earth and Planetary Science Letters* 246.3, pp. 407–417.

Forster, M A, G S Lister, and P G Lennox (2014). "Dating deformation using crushed alkali feldspar: 40Ar/39Ar geochronology of shear zones in the Wyangala Batholith, NSW, Australia". In: *Australian Journal of Earth Sciences* 61.4, pp. 619–629.

Garbe-Schönberg, Dieter and Samuel Müller (2014). "Nano-particulate pressed powder tablets for LA-ICP-MS". In: *Journal of Analytical Atomic Spectrometry* 29.6, pp. 990–1000.

Gardien, Véronique, Alan Bruce Thompson, Djordje Grujic, and Peter Ulmer (1995). "Experimental melting of biotite+ plagioclase+ quartz±muscovite assemblages and implications for crustal melting". In: *Journal of Geophysical Research: Solid Earth* 100.B8, pp. 15581–15591.

Gilbert, S E, L V Danyushevsky, K Goemann, and D Death (2014). "Fractionation of sulphur relative to iron during laser ablation-ICP-MS analyses of sulphide minerals: implications for quantification". In: *Journal of Analytical Atomic Spectrometry* 29.6, pp. 1024–1033.

Gorojovsky, Lauren and Olivier Alard (2020). "Optimisation of laser and mass spectrometer parameters for the in situ analysis of Rb/Sr ratios by LA-ICP-MS/MS". In: *Journal of Analytical Atomic Spectrometry* 35.10, pp. 2322–2336.

Govindaraju, K (1979). "Report (1968–1978) on Two Mica Reference Samples: Biotite Mica-Fe and Phlogopite Mica-Mg". In: *Geostandards and Geoanalytical Research* 3.1, pp. 3–24.

— (1994). "1994 compilation of working values and sample description for 383 geostandards". In: *Geostandards Newsletter* 18, pp. 1–158.

— (1995). "1995 Working values with confidence limits for twenty-six CRPG, ANRT and IWG-GIT geostandards". In: *Geostandards Newsletter* 19.s1, pp. 1–32.

Govindaraju, K and I Roelandts (1988). "Compilation Report (1966–1987) on Trace Elements in five CRPG Geochemical Reference Samples: Basalt BR; Granites, GA and GH; Micas, Biotite Mica-Fe and Phlogopite Mica-Mg". In: *Geostandards Newsletter* 12.1, pp. 119–201.

Govindaraju, Kuppusami (1984). "Report (1973–1984) on Two ANRT Geochemical Reference Samples: Granite GS-N and Potash Feldspar FK-N". In: *Geostandards Newsletter* 8.2, pp. 173–206.

Gradstein, Felix M, James George Ogg, Mark D Schmitz, and Gabi M Ogg (2012). *The geologic time scale 2012*. elsevier.

Gray, Theodore (2009). *Elements: A visual exploration of every known atom in the universe*. New York: Black Dog & Leventhal Publishers, Inc.

He, Zhiwei, Fang Huang, Huimin Yu, Yilin Xiao, Fangyue Wang, Qiuli Li, Ying Xia, and Xingchao Zhang (2016). "A flux-free fusion technique for rapid determination of major and trace elements in silicate rocks by LA-ICP-MS". In: *Geostandards and Geoanalytical Research* 40.1, pp. 5–21.

Hogmalm, K. Johan, Thomas Zack, Andreas K. O. Karlsson, Axel S. L. Sjöqvist, and Dieter Garbe-Schönberg (2017). "In situ Rb-Sr and K-Ca dating by LA-ICP-MS/MS:

an evaluation of N^2O and SF^6 as reaction gases". In: *Journal of Analytical Atomic Spectrometry* 32.2, pp. 305–313.

Hu, Zhaochu, Shan Gao, Yongsheng Liu, Shenghong Hu, Haihong Chen, and Honglin Yuan (2008). "Signal enhancement in laser ablation ICP-MS by addition of nitrogen in the central channel gas". In: *Journal of Analytical Atomic Spectrometry* 23.8, pp. 1093–1101.

Jackson, Simon E and Detlef Günther (2003). "The nature and sources of laser induced isotopic fractionation in laser ablation-multicollector-inductively coupled plasma-mass spectrometry". In: *Journal of Analytical Atomic Spectrometry* 18.3, pp. 205–212.

Jackson, Simon E and P Sylvester (2008). "Calibration strategies for elemental analysis by LA–ICP–MS". In: *SIGNAL* 10.1,000, p. 100.

Jochum, K P, B Stoll, K Herwig, and M Willbold (2007). "Validation of LA-ICP-MS trace element analysis of geological glasses using a new solid-state 193 nm Nd:YAG laser and matrix-matched calibration". In: *Journal of Analytical Atomic Spectrometry* 22.2, pp. 112–121.

Košler, Jan, Michael Wiedenbeck, Richard Wirth, Jan Hovorka, Paul Sylvester, and Jitka Míková (2005). "Chemical and phase composition of particles produced by laser ablation of silicate glass and zircon—implications for elemental fractionation during ICP-MS analysis". In: *Journal of Analytical Atomic Spectrometry* 20.5, pp. 402–409.

Langmuir, Charles H, Robert D Vocke, Gilbert N Hanson, and Stanley R Hart (1978). "A general mixing equation with applications to Icelandic basalts". In: *Earth and Planetary Science Letters* 37.3, pp. 380–392.

Laureijs, Christiaan T, Laurence A Coogan, and Jody Spence (2021). "In-situ Rb-Sr dating of celadonite from altered upper oceanic crust using laser ablation ICP-MS/MS". In: *Chemical Geology* 579, p. 120339.

Li, Shan-Shan, M Santosh, Juraj Farkaš, Ahmad Redaa, Sohini Ganguly, Sung Won Kim, Cun Zhang, Sarah Gilbert, and Thomas Zack (2020). "Coupled U-Pb and Rb-Sr laser ablation geochronology trace Archean to Proterozoic crustal evolution in the Dharwar Craton, India". In: *Precambrian Research* 343, p. 105709.

Lin, Jie, Yongsheng Liu, Yueheng Yang, and Zhaochu Hu (2016). "Calibration and correction of LA-ICP-MS and LA-MC-ICP-MS analyses for element contents and isotopic ratios". In: *Solid Earth Sciences* 1.1, pp. 5–27.

Longerich, H P, D Günther, and S E Jackson (1996). "Elemental fractionation in laser ablation inductively coupled plasma mass spectrometry". In: *Fresenius' journal of analytical chemistry* 355.5, pp. 538–542.

McArthur, J M, R J Howarth, and G A Shields (2012). "Strontium isotope stratigraphy". In: *The geologic time scale*. Ed. by Felix M Gradstein, James George Ogg, Mark D Schmitz, and Gabi M Ogg. Elsevier, pp. 127–144.

Miliszkiewicz, Natalia, Stanisław Walas, and Anna Tobiasz (2015). "Current approaches to calibration of LA-ICP-MS analysis". In: *Journal of Analytical Atomic Spectrometry* 30.2, pp. 327–338.

O'Connor, Ciaran, Mark R Landon, and Barry L Sharp (2007). "Absorption coefficient modified pressed powders for calibration of laser ablation inductively coupled plasma mass spectrometry". In: *Journal of Analytical Atomic Spectrometry* 22.3, pp. 273–282.

Odin, G S (1976). "Glauconite GL-O, interlaboratory standard for radiochronometric analysis". In: *Analusis* 4.6, pp. 287–291.

Olierook, Hugo K H, Kai Rankenburg, Stanislav Ulrich, Christopher L Kirkland, Noreen J Evans, Stephen Brown, Brent I A McInnes, Alexander Prent, Jack Gillespie, and Bradley McDonald (2020). "Resolving multiple geological events using in situ Rb–Sr geochronology: implications for metallogenesis at Tropicana, Western Australia". In: *Geochronology* 2.2, pp. 283–303.

Paton, Chad, John Hellstrom, Bence Paul, Jon Woodhead, and Janet Hergt (2011). "Iolite: Freeware for the visualisation and processing of mass spectrometric data". In: *Journal of Analytical Atomic Spectrometry* 26.12, pp. 2508–2518.

Rafiei, Mehrnoush, Stefan Lhr, Andre Baldermann, Richard Webster, and Charlie Kong (2020). "Quantitative petrographic differentiation of detrital vs diagenetic clay minerals in marine sedimentary sequences: Implications for the rise of biotic soils". In: *Precambrian Research* 350, p. 105948.

Redaa, Ahmad, Juraj Farkašš, Sarah Gilbert, Alan S. Collins, Benjamin Wade, stefan Löhr, Thomas Zack, and Dieter Garbe-Schönberg (2021). "Assessment of elemental fractionation and matrix effects during in-situ Rb–Sr dating of phlogopite by LA-ICP-MS/MS: Implications for the accuracy and precision of mineral ages". In: *Journal of Analytical Atomic Spectrometry* 36, pp. 322–344.

Rousset, Davy, Sylvie Leclerc, Norbert Clauer, Joel Lancelot, Michel Cathelineau, and Jean-Francois Aranyossy (2004). "Age and origin of Albian glauconites and associated clay minerals inferred from a detailed geochemical analysis". In: *Journal of Sedimentary research* 74.5, pp. 631–642.

Selby, David (2009). "U-Pb zircon geochronology of the Aptian/Albian boundary implies that the GL-O international glauconite standard is anomalously young". In: *Cretaceous Research* 30.5, pp. 1263–1267.

Subarkah, Darwinaji, Morgan L Blades, Alan S Collins, Juraj Farkaš, Sarah Gilbert, Stefan C Löhr, Ahmad Redaa, Eilidh Cassidy, and Thomas Zack (2021). "Unraveling the histories of Proterozoic shales through in situ Rb-Sr dating and trace element laser ablation analysis". In: *Geology*.

Sylvester, PaulJ (2008). "Matrix effects in laser ablation ICP-MS". In: *Laser ablation ICP-MS in the earth sciences: Current practices and outstanding issues*. Vol. 40. Mineralogical Association of Canada, pp. 67–78.

Tabersky, Daniel, Norman A Luechinger, Michael Rossier, Eric Reusser, Kathrin Hametner, Beat Aeschlimann, Daniel A Frick, Samuel C Halim, Jay Thompson, Leonid Danyushevsky, and Detlef Günther (2014). "Development and characterization of custom-engineered and compacted nanoparticles as calibration materials for quantification using LA-ICP-MS". In: *Journal of Analytical Atomic Spectrometry* 29.6, pp. 955–962.

Tillberg, Mikael, Henrik Drake, Thomas Zack, Johan Hogmalm, and Mats Åström (2017). "In Situ Rb-Sr Dating of Fine-grained Vein Mineralizations Using LA-ICP-MS". In: *Procedia Earth and Planetary Science* 17, pp. 464–467.

Tillberg, Mikael, Henrik Drake, Thomas Zack, Ellen Kooijman, Martin J Whitehouse, and Mats E Åström (2020). "In situ Rb-Sr dating of slickenfibres in deep crystalline basement faults". In: *Scientific Reports* 10.1, pp. 1–13.

Turpin, Laurent, Michel Cuney, Marc Friedrich, Jean-Luc Bouchez, and Monique Aubertin (1990). "Meta-igneous origin of Hercynian peraluminous granites in N.W. French Massif Central: implications for crustal history reconstructions". In: *Contributions to Mineralogy and Petrology* 104.2, pp. 163–172.

Veizer, Ján, Davin Ala, Karem Azmy, Peter Bruckschen, Dieter Buhl, Frank Bruhn, Giles A F Carden, Andreas Diener, Stefan Ebneth, Yves Godderis, Torsten Jasper,

Christoph Korte, Frank Pawellek, Olaf G Podlaha, and Harald Strauss (1999). "$^{87}Sr/^{86}Sr$, δ13C and δ18O evolution of Phanerozoic seawater". In: *Chemical Geology* 161.1, pp. 59–88.

Vermeesch, Pieter (2018). "IsoplotR: A free and open toolbox for geochronology". In: *Geoscience Frontiers* 9, pp. 1479–1493.

Villa, I M, P De Bièvre, N E Holden, and P R Renne (2015). "IUPAC-IUGS recommendation on the half life of ^{87}Rb". In: *Geochimica et Cosmochimica Acta* 164, pp. 382–385.

Woodhead, Jon D and Janet M Hergt (2001). "Strontium, neodymium and lead isotope analyses of NIST glass certified reference materials: SRM 610, 612, 614". In: *Geostandards Newsletter* 25.2-3, pp. 261–266.

Yu, Zongshou, Marc D Norman, and Philip Robinson (2003). "Major and Trace Element Analysis of Silicate Rocks by XRF and Laser Ablation ICP-MS Using Lithium Borate Fused Glasses: Matrix Effects, Instrument Response and Results for International Reference Materials". In: *Geostandards Newsletter* 27.1, pp. 67–89.

Zack, Thomas and K Johan Hogmalm (2016). "Laser ablation Rb/Sr dating by online chemical separation of Rb and Sr in an oxygen- fi lled reaction cell". In: *Chemical Geology* 437, pp. 120–133.

Zhang, Shudi, Miaohong He, Zhibin Yin, Eryi Zhu, Wei Hang, and Benli Huang (2016). "Elemental fractionation and matrix effects in laser sampling based spectrometry". In: *Journal of Analytical Atomic Spectrometry* 31.2, pp. 358–382.

Zimmermann, J L, M Vernet, G Guyetand, and D Dautel (1985). "Données sur potassium et argon (de 1976 à 1984) dans quelques échantillons géochimiques de référence". In: *Geostandards Newsletter* 9.2, pp. 205–208.

Şengün, Fırat, Viktor Bertrandsson Erlandsson, Johan Hogmalm, and Thomas Zack (2019). "In situ Rb-Sr dating of K-bearing minerals from the orogenic Akçaabat gold deposit in the Menderes Massif, Western Anatolia, Turkey". In: *Journal of Asian Earth Sciences* 185, p. 104048.

CHAPTER 4

Constraints from *in-situ* Rb-Sr dating on the timing of the Umm Farwah shear zone and associated copper-gold mineralisation in the Mount Ablah area in the Southern Arabian Shield, Saudi Arabia

This chapter has been published in *Journal of Asian Earth Sciences* as: Redaa, A, Farkaš, J, Hassan, A, Collins, AS, Gilbert, S, & Löhr, S 2022, 'Constraints from *in-situ* Rb-Sr dating on the timing of tectono-thermal events in the Umm Farwah shear zone and associated Cu-Au mineralisation in the Southern Arabian Shield, Saudi Arabia', *Journal of Asian Earth Sciences*, vol. 224, p. 105037.

Statement of Authorship

Title of Paper	Constraints from *in-situ* Rb-Sr dating on the timing of the Umm Farwah shear zone and associated copper-gold mineralisation in the Mount Ablah area in the Southern Arabian Shield, Saudi Arabia
Publication Status	☐ Published ☐ Accepted for Publication ☑ Submitted for Publication ☐ Unpublished and Unsubmitted w ork w ritten in manuscript style
Publication Details	Redaa, A,Farkaš, J, Hassan, A, Collins, AS, Gilbert, S & Löhr, s In Review, 'Constraints from in-situ Rb-Sr dating on the timing of the Umm Farwah shear zone and associated copper-gold mineralisation in the Mount Ablah area in the Southern Arabian Shield, Saudi Arabia', Journal of Asian Earth Sciences.

Principal Author

Name of Principal Author (Candidate)	Ahmad Redaa		
Contribution to the Paper	Data collection, data processing, interpretation, visualisation, writing initial draft and editing.		
Overall percentage (%)	80%		
Certification:	This paper reports on original research I conducted during the period of my Higher Degree by Research candidature and is not subject to any obligations or contractual agreements with a third party that would constrain its inclusion in this thesis. I am the primary author of this paper.		
Signature		Date	11/11/2021

Co-Author Contributions

By signing the Statement of Authorship, each author certifies that:

i. the candidate's stated contribution to the publication is accurate (as detailed above);

ii. permission is granted for the candidate in include the publication in the thesis; and

iii. the sum of all co-author contributions is equal to 100% less the candidate's stated contribution.

Name of Co-Author	Juraj Farkaš		
Contribution to the Paper	Supervision, discussion the ideas, reviewing and editing.		
Signature		Date	11/11/2021

Name of Co-Author	Ahmed Hassan		
Contribution to the Paper	Supervision the field work and reviewing and editing the manuscript.		
Signature		Date	31/10/21

Name of Co-Author	Alan S. Collins		
Contribution to the Paper	Supervision, reviewing and editing the manuscript.		
Signature		Date	31/10/2021

Name of Co-Author	Sarah Gilbert		
Contribution to the Paper	Set-up the LA-ICP-MS/MS for the in-situ Rb-Sr analysis and reviewing the draft.		
Signature		Date	31/10/2021

Name of Co-Author	Stefan C. Löhr		
Contribution to the Paper	Analysing the samples by the SEM and reviewing the draft.		
Signature		Date	31/10/2021

Abstract

Constraining the tectonic history and timing of major shear zone structures in the Arabian Shield is critical for better understanding of the origin, tectonic history and distribution of ore deposits within this Precambrian crystalline crustal block. Here, we used a novel *in-situ* Rb-Sr dating of micas and K-feldspar to constrain the age of the Umm Farwah Shear Zone, which represents a regional tectonic feature that extends about 200 km across the southern part of the Arabian Shield. We also constrain the timing of Mount Ablah mineralisations which are exposed within the Umm Farwah Shear Zone and contains two styles of mineralisations including a greisen and Cu-Au mineralisation. These ore deposits are hosted in a pegmatite body that formed during the development of the Umm Farwah Shear Zone. Two main groups of muscovite (i.e., Group I and Group II) and K-feldspar mineral phases were identified based on ages and elemental variations in the mineralised zone and the host rocks. Results of *in-situ* Rb-Sr dating in the above K-rich minerals show that the Umm Farwah Shear Zone was initiated at ca. 651 Ma, and the emplacement of the Mount Ablah pegmatite occurred between 626 and 611 Ma, followed by the formation of greisen at 601 $\pm$ 12 Ma. *In-situ* Rb–Sr data also highlight a younger 'alteration' event occurred at ca. 556 $\pm$ 23 Ma, which partially reset the Rb–Sr system in the pegmatite and may thus reflect hydrothermal circulation event or overprint due to formation of Cu-Au mineralisation.

Highlights

- *In-situ* Rb-Sr dating constrains tectonic and igneous events in mineralised systems.
- Umm Farwah Major Shear Zone was developed between 671 Ma and 631 Ma.
- Ablah pegmatite was emplaced following the shear zone between 626 and 611 Ma.
- Greisen and Cu-Au deposits in the Mount Ablah were formed due to two separate hydrothermal events.

4.1 Introduction

The Mount Ablah area comprises a pegmatite body composed of orthoclase and quartz, with quartz veins and breccia-associated Cu-Au mineralisation, which is located to the north of the Ablah graben on the western part of Asir terrane in the Arabian Shield

(Figure 4.1). The Proterozoic basement of Saudi Arabia forms the eastern part of the, largely juvenile, Arabian-Nubian Shield. It is exposed in the western part of the Arabian Peninsula and has been affected by accretionary and collisional orogenesis associated with subduction of the Neoproterozoic Mozambique Ocean (Collins et al., 2021) and the amalgamation of central Gondwana (Collins, Blades, and Merdith, 2021; Collins and Pisarevsky, 2005; Stern, 2002; Stoeser and Frost, 2006).

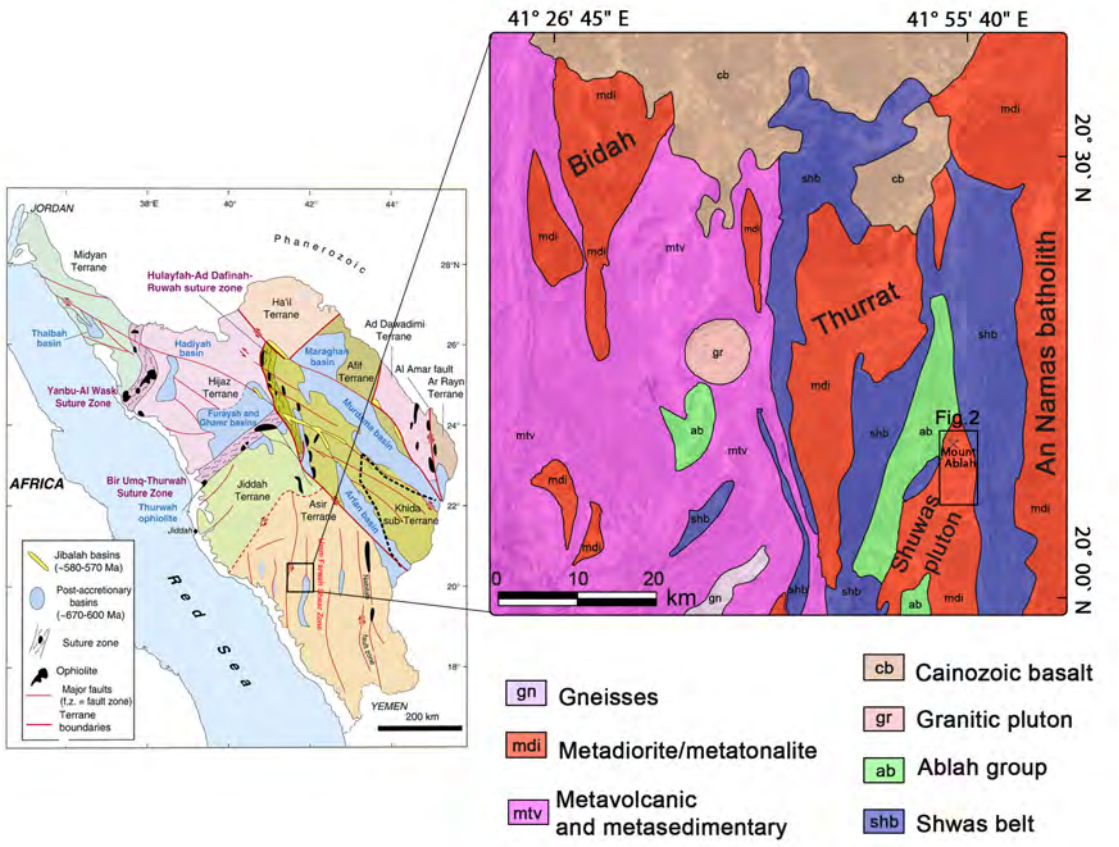

Figure 4.1: Regional Geological map shows main geological units in the study area (modified after Marzouki et al., 1982). The location map shows the major tectonic terranes and the suture zones in the Arabian Shield (modified after Stern and Johnson, 2010).

Voluminous magmatism occurred throughout the Neoproterozoic and into the Cambrian but was particularly extensive between 870–540 Ma (Robinson, Foden, and Collins, 2015). The later, post-orogenic, intrusions contain many alkali plutons that are known sources of critical minerals and metals such as Sn, W, Mo, Nb, rare-earth elements (REE), Y and Be, and other base and precious metals (Cu, Zn, Au). Thus far, over 400 individual occurrences of these precious metals and critical mineral commodities have been identified in association with felsic intrusions in the Arabian Shield (Agar, 1992;

Johnson, 2006; Marzouki et al., 1982; Nehlig et al., 1999). A high fluid/rock ratio associated with these felsic intrusions, and subsequent hydrothermal alterations, could be a key factor for several mineralisation types and can be used as an exploration guide for hydrothermal mineralisation in the surrounding areas. Circulating fluids along faults and shear zones within pre-existing rocks can enhance mineral dissolution, element transport, mineral precipitation and rock deformation, depending on the temporal and spatial variations in temperature, pressure and element activities (Ahmed and Surour, 2016). Thus, understanding the evolution and timing of these felsic intrusions is important to understand the origin, genesis and spatial distribution of the above metal commodities in the Arabian Shield, which in turn will be beneficial for future exploration of these critical resources.

The Rb-Sr isotope system can be used to date the timing and temporal relation between the felsic intrusions and associated mineralisations because the latter commonly contain K- and Rb-rich minerals such as micas and feldspars. The recent development of novel *in-situ* Rb-Sr dating by a laser ablation (LA) coupled with an inductively coupled plasma - tandem mass spectrometer (ICP-MS/MS) offers a rapid and cost-efficient dating approach for K- and Rb-rich silicate minerals (Hogmalm et al., 2017). Although a more established laser-based U-Pb dating can be used as well to constrain the timing of mineralisation, certain limitations of the latter technique make the Rb-Sr method preferable. Specifically, the accessory minerals with high U to Pb ratios such as zircon and monazite could be rare in the quartz veins and associated alterations because these minerals have a closure temperature of Pb diffusion >800 °C (Cherniak and Watson, 2001; McFarlane and Mark Harrison, 2006). In contrast, apatite, that is a common accessory phase in mineralised and hydrothermal systems can be however easily reset during the hydrothermal events (Kirkland et al., 2018) which makes the age constrain via U-Pb dating of apatite problematic. Thus, this study focuses on novel *in-situ* Rb-Sr dating of abundant and K and Rb-rich silicate minerals such as micas and feldspars in a hydrothermal system.

In the present work, we investigate the temporal relation between Umm Farwah major Shear zone and Ablah mineralisations by constraining the paragenetic sequence and timing of felsic intrusions, the greisen and the Cu-Au mineralisation in the Shuwas pluton via *in-situ* Rb–Sr dating of K-rich minerals such as micas and feldspar. Using the LA-ICPMS/MS technique for the Rb-Sr system allowed dating of both the country rocks (i.e., metadiorite) and the mineralisation zone (i.e., pegmatite, quartz-vein related alteration zone and greisen) using the LA-ICP-MS/MS. As the Ablah Cu-Au mineralisation is located within a major structure in the southern part of the Arabian Shield, this work

provides new information about the timing and nature of geological events associated with deformation in this area. Following other recent pioneering studies that used LA-ICP-MS/MS approach for dating of mineral systems and metallogenesis (Olierook et al., 2020; Şengün et al., 2019; Tillberg et al., 2020), this work demonstrates the advantage of this novel and rapid *in-situ* Rb–Sr dating by LA-ICP-MS/MS to better constrain the timing, and thus plausible genetic models, for economic mineralisation in the Arabian Shield, with implications for future and improved exploration strategies (Armistead et al., 2020; Hogmalm et al., 2017; Redaa et al., 2021; Li et al., 2020).

4.2 Geological background

The tectonic-thermal evolution of the Saudi part of the Arabian-Nubian Shield occurred mainly in the Neoproterozoic, between ca. 870–540 Ma, in three main stages, including: (1) the formation of island arcs mostly at the floor of Mozambique Ocean, (2) the collision and accretion of these arcs with each other and with pre-existing continental fragments during the closure of the Mozambique Ocean and the subsequent collision of Neoproterozoic India with these terranes to form this part of Gondwana, and (3) the formation and the development of terrestrial and marine post-amalgamation basins, associated with post-accretion magmatism (Collins et al., 2021; Johnson and Woldehaimanot, 2003; Merdith et al., 2021; Nettle et al., 2014; Robinson et al., 2014; Robinson, Foden, and Collins, 2015; Stern and Johnson, 2010; Stoeser and Frost, 2006). Recently, it has been suggested that the margins of the Arabian-Nubian Shield extend to include Tonian rocks in Oman, Pakistan and NW India (Alessio et al., 2018; Blades et al., 2020; Collins et al., 2021), as well as Stenian and Tonian juvenile rocks beneath the Sahara of Chad and Sudan (Blades et al., 2021; Şengör et al., 2020). In Saudi Arabia, the development of the Arabian Shield was accompanied by several magmatic and predominantly felsic intrusion events that ranged in composition from I–S to A-type granites, but also included mafic and tholeiite-like magmatic products (Robinson, Foden, and Collins, 2015). These intrusion events form four temporal groups, based on their crystallisation ages. These are (1) intrusions associated with island arcs (ca. 845 Ma), (2) syn-collisional intrusions (ca. 710 Ma), (3) post-tectonic intrusions (ca. 620 Ma), and (4) anorogenic intrusions (> 600 Ma) (Robinson et al., 2014; Robinson, Foden, and Collins, 2015). Each of these intrusion events was formed due to different igneous processes, where those that occurred during the subduction and amalgamation (between ca. 845–600 Ma) involved contaminated MORB-/arc-tholeiite-like magmatic products

(Robinson, Foden, and Collins, 2015), while the younger and post-tectonic magmatism are characterized by tonalite-trondhjemite-granodiorite (TTG) and granite (monzogranite, syenogranite). Finally, the anorogenic magmatism is dominated by alkali-feldspar and alkali granite (Johnson et al., 2011). These different magmatic products indicate changing sources of magma beneath the Arabian Shield, ranging from depleted mantle to a more enriched mantle source with limited crust–mantle interaction, the latter is more dominant from ca. 600 Ma due to the change of tectonic settings and processes (Robinson et al., 2014; Robinson, Foden, and Collins, 2015).

The copper–gold mineralisation in the Ablah area is hosted in essentially pegmatite that intrudes metadiorite/metatonalite, which forms a part of the Shuwas pluton (Moufti, 2001) (Figure 4.1). The age of the Shuwas pluton has not been investigated directly but has been estimated by correlating the pluton with other supposedly equivalent units including Dhuqiyah igneous complex, and Buwwah suite, which includes Dhara, Bidah, Tharad/Thurrat plutons, as well as Baljurashi and Al Bayda batholiths (Johnson, 2005; Johnson, 2006 and references therein). There is a considerable variability in reported crystallisation ages of these rocks, but the most reliable ages suggest the emplacement of Buwwah suite between 855 Ma and 815 Ma (see Figure 4.2, and Johnson, 2005 and references therein). The Shuwas pluton intrudes the Qirsha and Khutnah formations (known also as Shwas belt Johnson, 2006 and Jiddah group (Greenwood, 1975)) that formed as an intra-oceanic island arc volcanosedimentary unit (Figure 4.1). The formations (Shwas belt) include sheared and altered volcanic flows and pyroclastic rocks that have tholeiitic and calc-alkalic compositions (Moufti, 2001 and references therein). Their age was estimated using a Rb–Sr errorchron at 721 $\pm$ 55 Ma (Bokhari and Kramers, 1981). This age overlaps the reported age for Tharad pluton 744 $\pm$ 22 Ma (Marzouki et al., 1982) that is located to the northwest of the formations (Figure 4.1). However, Johnson, 2006 argued that the age of the Shwas belt should be older than 815 Ma (Figure 4.3) relying on the contact between the formations and the An Namas batholith (Figure 4.1) as the latter was dated using Rb–Sr whole rock at 837 $\pm$ 55 Ma (Johnson, 2006 and references therein).

The Umm Farwah regional Shear Zone extends 200 km N–S across the Asir terrane (Figure 4.1). It deformed both the Shwas belt and the metadiorite/metatonalite igneous complexes that intrude the belt. The shear zone and the metadiorite/metatonalite are intruded by A-type granitoid bodies (syenite and syenogranite) and several aplitic dykes that may have intruded during deformation (Moufti, 2001) (Figure 4.2). The syenite and the syenogranite were dated previously by the whole-rock Rb–Sr approach that yielded isochron ages of 617 $\pm$ 17 Ma and 605 $\pm$ 5 Ma (Figure 4.3) with relatively low initial

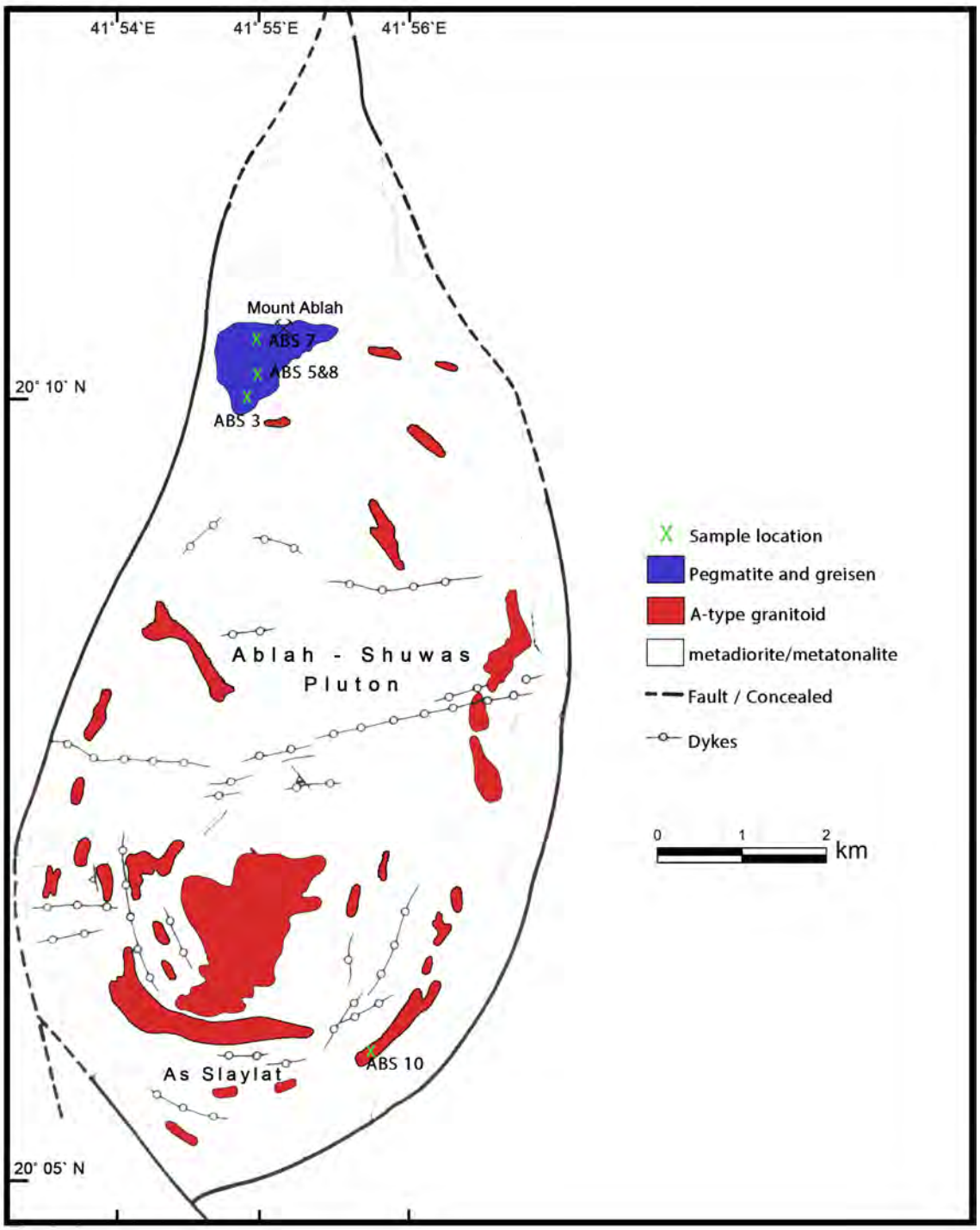

Figure 4.2: Geological map of Shuwas pluton showing the main geological units in the study area, and sampling locations (modified after Moufti, 2001).

$^{87}Sr/^{86}Sr$ ratios of 0.7035 and 0.7038, respectively (Moufti, 2001). Based on these ages, Johnson, 2006 suggested that the brittle-ductile deformation of the Umm Farwah shear zone occurred as late as 605 Ma (Figure 4.3).

In addition to the syenite and the syenogranite, a pegmatitic unit (known as Mount Ablah) intruded the metadiorite/metatonalite exposed in the north-western part of the Shuwas pluton (Figure 4.2). Mount Ablah consists of pegmatitic feldspar and quartz that is highly brecciated (Figure 4.4A) and cross-cut by several quartz veins that are surrounded by sericitized alteration zones (Figure 4.4B). It is also capped with a greisen deposit that presents as a massive muscovite-fluorite body (Figure 4.4B) (Jackson, 1986; Salimo, 2015). Mount Ablah has been historically exploited for copper and gold, and although it also contains appreciable Nb, Zr, REE, F and other precious metals; these have not been exploited to date (Jackson, 1986). Several exploratory boreholes were drilled in the area by the Saudi Arabian Mining Company (Ma'aden), that yielded gold grades that ranged between 0.37 and 25.37 g/t, with highest gold grades concentrated around the brecciated quartz veins in the alteration zone (Salimo, 2015).

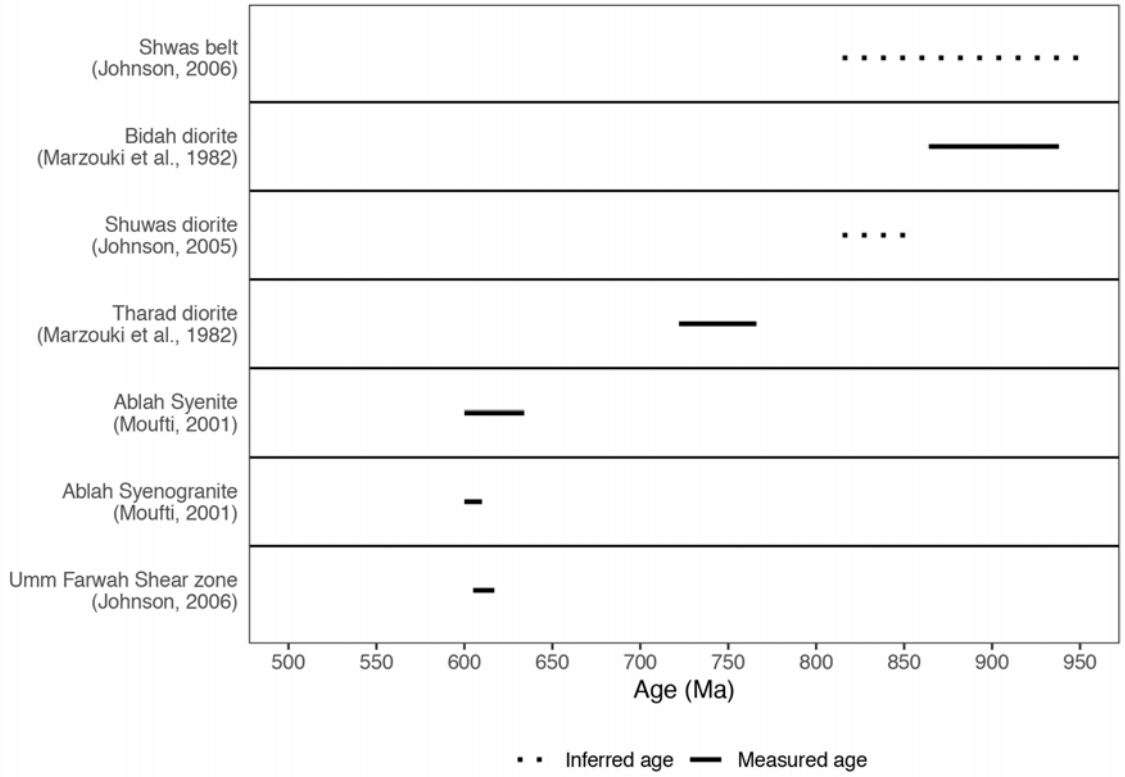

Figure 4.3: The published ages for the main unites and events in Mount Ablah area.

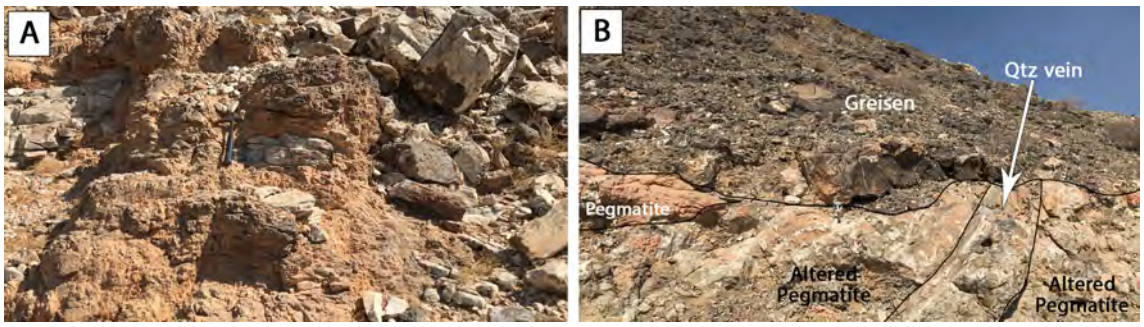

Figure 4.4: Field photographs show (A) the brecciated quartz and feldspar in Mount Ablah, and (B) shows the field relation between pegmatite, quartz vein, altered pegmatite that hosted the Cu-Au mineralisation, and greisen.

4.3 Methodology

4.3.1 Sample selection and preparation

Representative samples of metadiorite (ABS 13), syenogranite (ABS 10), partially altered pegmatite (ABS 5 and ABS 8), altered pegmatite (ABS 3), and greisen (ABS 7) were collected from the Shuwas Pluton and Mount Ablah area. The samples were analysed *in-situ* for major element and Rb–Sr dating to investigate the ages and temporal evolution of the Mount Ablah Cu-Au mineralisation with respect to the crystallisation ages of the host rocks (i.e., Shuwas pluton).

The metadiorite sample (ABS 13) was collected from the depth of 28.77 meters from a core (No. ABD 4), which was drilled by Ma'aden company on the foothill of Mount Ablah. The sample was mounted in the epoxy resin, then polished for *in-situ* Rb–Sr analysis by the LA-ICP-MS/MS. Sample ABS 10 was collected from a surface outcrop of syenogranite that intruded into the metadiorite/metatonalite of the Shuwas pluton and is exposed at 20°05' 58.17" N and 041°55' 42.01" E. (Figure 4.2). Feldspars were separated from this sample (ABS 10), mounted, and polished for Rb–Sr analysis by the LA-ICP-MS/MS. Four samples (ABS 3, ABS 5, ABS 7 and ABS 8) were acquired from the Mount Ablah outcrop, and their locations are illustrated in Figure 4.2. The partially altered pegmatite samples (ABS 5 and ABS 8) were acquired from the Ablah pegmatite within a few meters of the alteration zone to investigate the effect of the quartz veinlet generating hydrothermal system on the samples. ABS 3 was collected from the alteration zone in pegmatite around the quartz veinlets/pipe. Finally, ABS 7 was extracted from the greisen that forms the top of the pegmatite system. These samples (ABS 3, ABS 5, ABS 7 and ABS 8) were prepared as thin-polished sections to be analysed for major elements by a scanning electron microscope (SEM), and for the *in-situ* Rb–Sr dating on

the LA-ICP-MS/MS.

4.3.2 Petrography and mineral mapping

The partially altered pegmatite (ABS 5 and ABS 8), altered pegmatite (ABS 3), and the greisen (ABS 7) samples were investigated using a petrographic microscope at the University of Adelaide to identify major rock forming K-bearing minerals such as micas and feldspars. Thin-sections were inspected before and after the *in-situ* Rb–Sr analysis by LA-ICP MS/MS to record the ablated spot positions for each mineral phase. In addition, sample ABS 5 was chosen for quantitative mineral mapping to characterise the main K-bearing minerals in this sample, using an FEI Teneo LoVac field emission scanning electron microscope (SEM) equipped with dual Bruker XFlash Series 6 energy dispersive X-ray spectroscopy (EDS) detectors at Macquarie University to better characterise the main K-bearing minerals in this sample. High-resolution BSE images and mineral maps of several regions of interest were collected at 10 mm working distance and 15 kV accelerating voltage. BSE image tile sets (100 nm pixel resolution) and EDS spectra (1.5 μm step size, 8 ms acquisition time) for mineral mapping were collected sequentially using the FEI Maps Mineralogy software, followed by classification of the individual EDS spectrum using the FEI Nanomin software (Rafiei et al., 2020). Further elemental mapping and semi-quantitative major element fingerprinting of distinct muscovite classes in samples ABS 3, ABS 7 and ABS 8 were achieved using an FEI Quanta 450 high-resolution field emission SEM equipped with EDS detector at The University of Adelaide.

4.3.3 *In-situ* Rb–Sr age dating of K-rich minerals

$^{87}Rb/^{86}Sr$ and $^{87}Sr/^{86}Sr$ isotope ratios of selected K-bearing minerals from metadiorite (ABS 13), syenogranite (ABS 10), partially altered pegmatite (ABS 5 and ABS 8), altered pegmatite (ABS 3) and greisen (ABS 7) were analysed using a LA-ICP-MS/MS to perform the *in-situ* Rb–Sr dating of these minerals. The *in-situ* Rb–Sr dating was conducted at the University of Adelaide using an Agilent 8900 ICP-MS/MS instrument, coupled with a RESOlution ArF excimer (193nm) laser system, following the approach detailed in Redaa et al., 2021. Briefly, the key parameters and analytical conditions of our LA-ICP-MS/MS setup are listed in Table 4.A in the supplementary materials (SM). All measured $^{87}Rb/^{86}Sr$ and $^{87}Sr/^{86}Sr$ data were first processed in Iolite4 (Paton et al., 2011), using a customised data reduction algorithm described in Redaa et al., 2021; and subsequently the Rb–Sr isochron ages were calculated using IsoplotR (Vermeesch, 2018).

A phlogopite pressed nano-powder pellet (Mica-Mg-NP), described in Garbe-Schönberg and Müller, 2014 and Hogmalm et al., 2017, was used in this study as the primary reference material to correct for elemental fractionation effects and the instrumental drift (see also Redaa et al., 2021). In addition, two natural minerals were used as a secondary reference material to monitor the LA-ICP-MS/MS performance following the approaches described elsewhere (Armistead et al., 2020; Redaa et al., 2021; Li et al., 2020). These minerals are phlogopite (MDC) and glauconite (GL-O), and the former was sourced from the same location as Mica-Mg-NP (Bekily, Madagascar) whereas the latter is a well-known reference material distributed by Association Nationale de la Recherche Technique (ANRT (Govindaraju, 1995). MDC yielded an accurate age of 520 $\pm$ 18 Ma and GL-O also yielded an acceptable age of 93 $\pm$ 4 Ma (see Figure 4.2.A in the supplementary material), and both of these ages are within 0.2% of accuracy from the expected or published ages for these mineral standards (Charbit, Guillou, and Turpin, 1998; Derkowski et al., 2009; Hogmalm et al., 2017). Such agreement in turn indicates that there were no significant matrix effects biasing the accuracy of Rb-Sr age for the above mineral standards (GL-O and MDC). Consequently, any matrix-effects on acquired Rb-Sr ages for investigated micas, using Mica-Mg-NP as a reference, are negligible. However, unlike for micas, there might potentially be some effects on Rb-Sr ages of investigated feldspars due to the lack of suitable matrix-matched reference materials for feldspars, which thus warrants further investigation. Although this uncertainty for feldspar is currently unconstrained, it is likely within 3 %, as observed for other non-matrix matched silicate minerals analysed via *in-situ* Rb-Sr dating technique (Redaa et al., 2021). Therefore, the above uncertainty has been taken into account when discussing the Rb-Sr age data from feldspars and their geological context and implications.

4.4 Results

4.4.1 Petrography and elemental maps

Pegmatite and altered pegmatite

Partially altered pegmatite samples (ABS 5 and ABS 8) mainly consist of medium subhedral and anhedral crystals of orthoclase, quartz, and muscovite in addition to rutile as accessory mineral. Small quartz veinlets cut across the samples, with orthoclase crystals around the veinlets showing alteration to sericite. Muscovite in samples ABS 5 and ABS 8 has two modes of occurrence; Group I: large euhedral/subhedral crystals located within

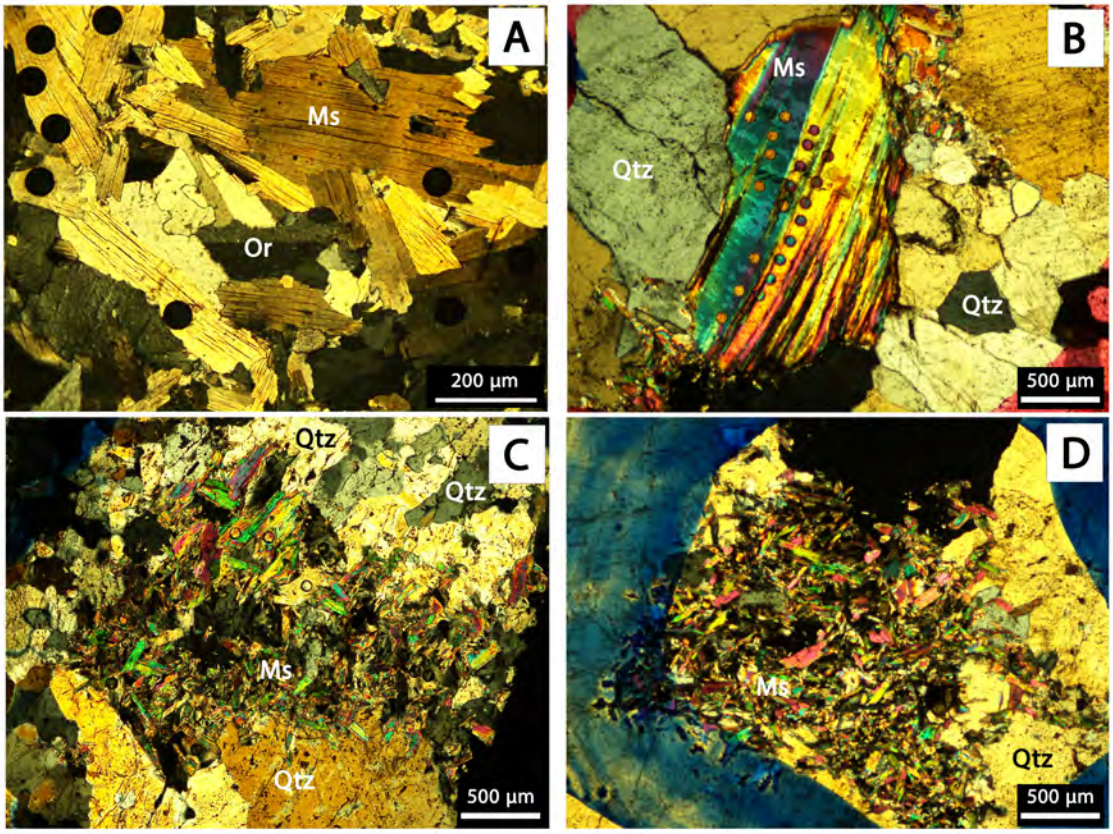

Figure 4.5: Photomicrographs of partially altered pegmatite showing the different muscovite phases: (A-B) Large crystals of the primary muscovite (Ms, Group I), quartz (Qtz) and orthoclase (Or) and (C-D) the muscovite cluster (Ms, Group II) formed after orthoclase and concentrated around the quartz vein (Qtz). The small/black circles are the inherited pits of the laser ablation during the *in-situ* analysis by the LA-ICP-MS/MS.

the 'pristine' zone of the samples (Figure 4.5A and Figure 4.5B), and Group II: fine aggregates of subhedra/anhedral crystals associated with sericite in the alteration zone (Figure 4.5C and Figure 4.5D). The SEM-EDS/ Nanomin mineral maps obtained for the partially altered pegmatite (sample ABS 5) confirmed that orthoclase and muscovite are the main K-bearing phases in the sample, and rutile is present as an accessory mineral (Figure 4.6). The low-count EDS spectra collected for mineral mapping do not show obvious differences in chemical compositions between Group I and Group II muscovite (Figure 4.6), although longer counting times for elemental mapping on the FEI Quanta 450 revealed a higher Fe content in Group I muscovite relative to Group II muscovite (Figure 4.7). The altered pegmatite (ABS 3) was also investigated by the petrographic microscope, and results show that the sample is highly sericitized, and it is composed mainly of muscovite (Group II), orthoclase, and quartz with quartz veinlets.

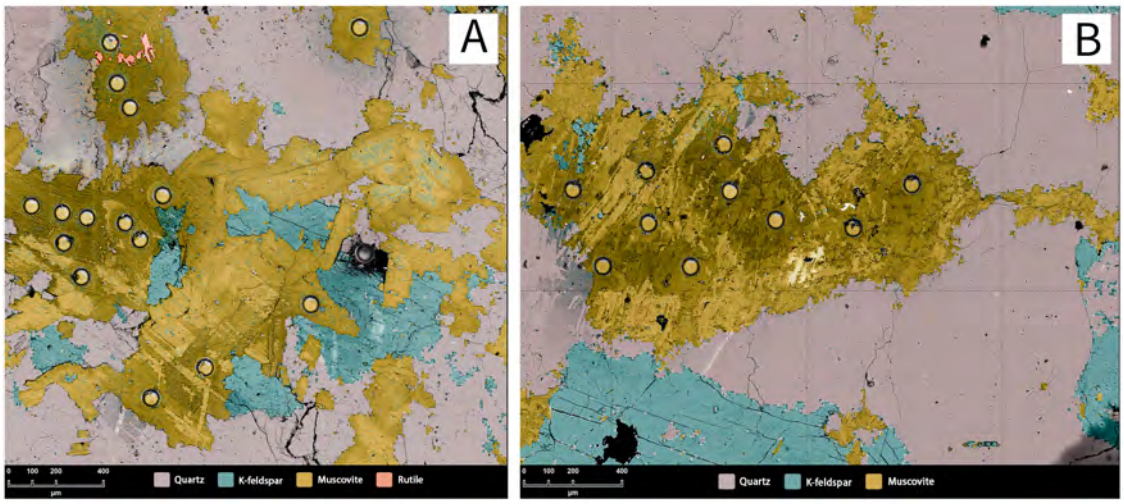

Figure 4.6: Nanomin images show the main K-bearing phases in pegmatite. (A) the large muscovite crystals among orthoclase and quartz with a minor presence of rutile. (B) shows a muscovite cluster formed after orthoclase along the cracks with remnant of orthoclase inside the cluster.

The greisen

Sample ABS 7 was extracted from the greisen located at the top of Ablah pegmatite. The mineralogical composition of the sample was investigated under the petrographic microscope, and the result shows that medium to fine subhedral and anhedral crystals of muscovite are the major component of the sample with small amount of coarse altered orthoclase, fluorite, and quartz. Both groups of muscovite (Group I and Group II) are also present in the greisen, and they were widespread in the samples.

4.4.2 Elemental composition of muscovite

Semi-quantitative analyses were conducted on selected muscovite grains on the partially altered pegmatite (ABS 8), altered pegmatite (ABS 3) and the greisen (ABS 7) using the Quanta 450 SEM. The SEM images (Figure 4.7) confirmed the petrographic results that muscovite in pegmatite and in the greisen has two forms, the large muscovite (Group I, Figure 4.7A) and the fine aggregate muscovite (Group II, Figure 4.7B). The major element concentrations in muscovite including K, Al, Si, O and Fe were analysed by energy dispersive X-ray spectroscopy, and the results, listed in Table. 4.B in the Supplementary Material, showed that concentrations of K, Al and Si were similar between the two muscovite groups. However, muscovite of Group I contained slightly higher Fe compared to Group II as indicated from the intensity map in Figure 4.7. Thus, K, Fe and Al were plotted in a ternary diagram to better characterise these two groups of muscovites (Figure 4.8), and the results show that there is a correlation between

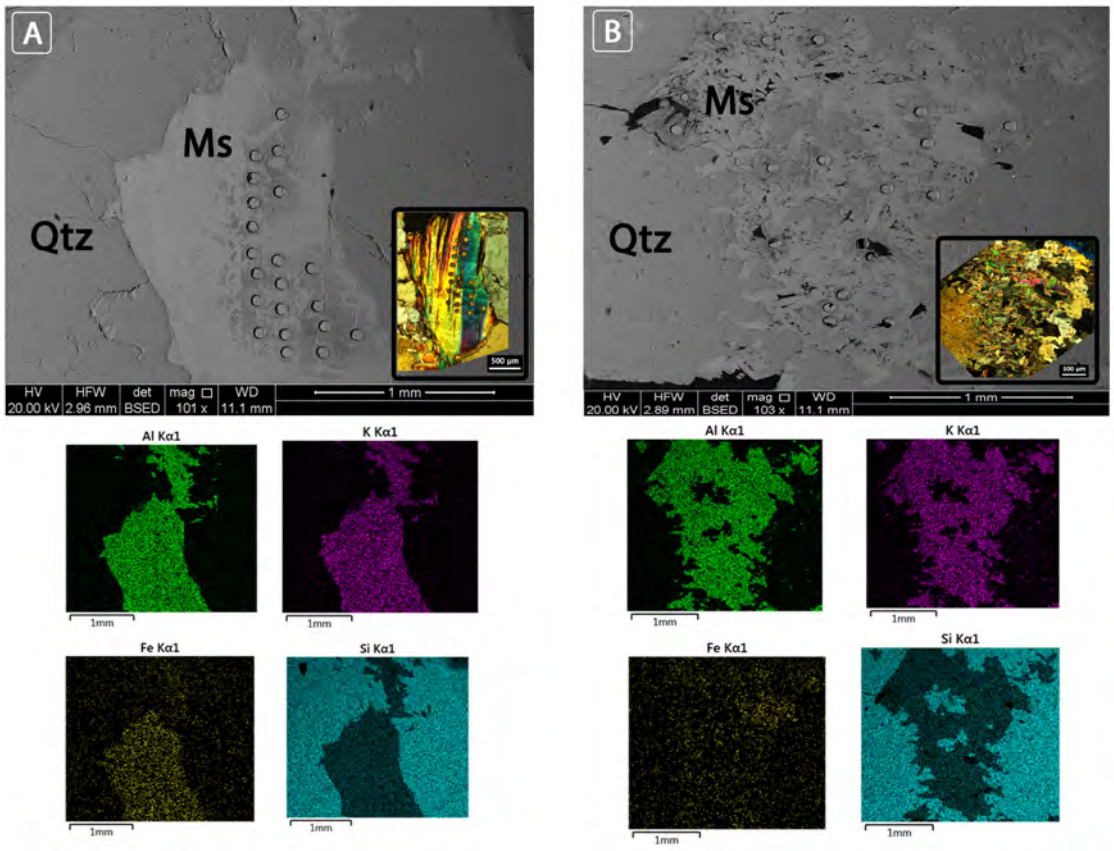

Figure 4.7: EM image with microscpic (xpl) images, and elemental maps for muscoivte of (A) Group I and (B) Group II obtined via the Quanta 450 SEM equipped with x-ray detector.

the three components specifically Fe decreases with increasing K and Al (Figure 4.8B). Therefore, the studied muscovites can be characterised and separated into two groups (i.e., Group I and Group II) based on their Fe abundances. Overall, muscovite of Group I has higher Fe (ranged between 2.75 and 5.8 wt%) compared to muscovite of Group II (Figure 4.8B), which have Fe content ranges between 0.27 and 2.03 wt%.

4.4.3 *In-situ* Rb–Sr geochronology of K-rich minerals

K-feldspars

K-feldspars from the metadiorite (ABS 10), syenogranite (ABS 13), partially altered pegmatite (ABS 5 and ABS 8) and altered pegmatite (ABS 3) were analysed using the *in-situ* Rb–Sr dating method as described in the section 4.3.3. The metadiorite sample (ABS 13) yielded an isochron age of 658 $\pm$ 34 Ma with unexpectedly unradiogenic initial ratio of 0.67 $\pm$ 0.15. Due to the large uncertainty in the calculated age and in the initial $^{87}Sr/^{86}Sr$ ratio, the model age of sample ABS 13 was calculated

at 651 ± 5 Ma, using the initial ratio of 0.70246 (Figure 4.9A) that was reported for Bidah metadiorite-metatonalite pluton (see Figure 4.1 and Marzouki et al., 1982) which previously correlated with the Shuwas metadiorite (sample ABS 13) (Johnson, 2006). Additional uncertainty of 3% was added to the Rb-Sr age of sample ABS 13, yielding 651 ± 20 Ma, because there was no suitable feldspar mineral standard that could be used in this study to monitor the impact of matrix-effect on the accuracy of analysed orthoclase. The above uncertainty of 3% reflects the overall impact of matrix-effects during *in-situ* Rb-Sr dating of silicate minerals, as quantified in the recent study by Redaa et al., 2021. The K-feldspars of the syenogranite (ABS 10) yielded an isochron age of 633 ± 84 Ma with low initial $^{87}Sr/^{86}Sr$ ratio of 0.7012 ±0.0037 (Figure 4.9B) that overlaps within the uncertainty the previously reported initial $^{87}Sr/^{86}Sr$ for Ablah granitoids (0.70365 ± 0.00015) by Moufti, 2001. The large uncertainty in the isochron age of this syenogranite is due to low Rb content and thus generally less radiogenic $^{87}Sr/^{86}Sr$ values in the analysed feldspars (see Figure 4.9B). Orthoclase of partially altered pegmatite (samples ABS 5 and ABS 8) and the altered pegmatite (ABS 3) yielded younger ages ranged between 571 and 527 (Figure 4.9C-E) Ma with high initial $^{87}Sr/^{86}Sr$ ratio for samples ABS 3 (0.733 ± 0.025) and ABS 5 (0.777 ± 0.050). However, orthoclase of sample ABS 8 yielded lower initial $^{87}Sr/^{86}Sr$ ratio with high uncertainty (0.576 ± 0.150), thus the model age of the sample was calculated at 571 ± 9 Ma (Figure 4.9E), using the initial $^{87}Sr/^{86}Sr$ ratio of 0.777 ± 0.050 obtained from orthoclase of the other partially

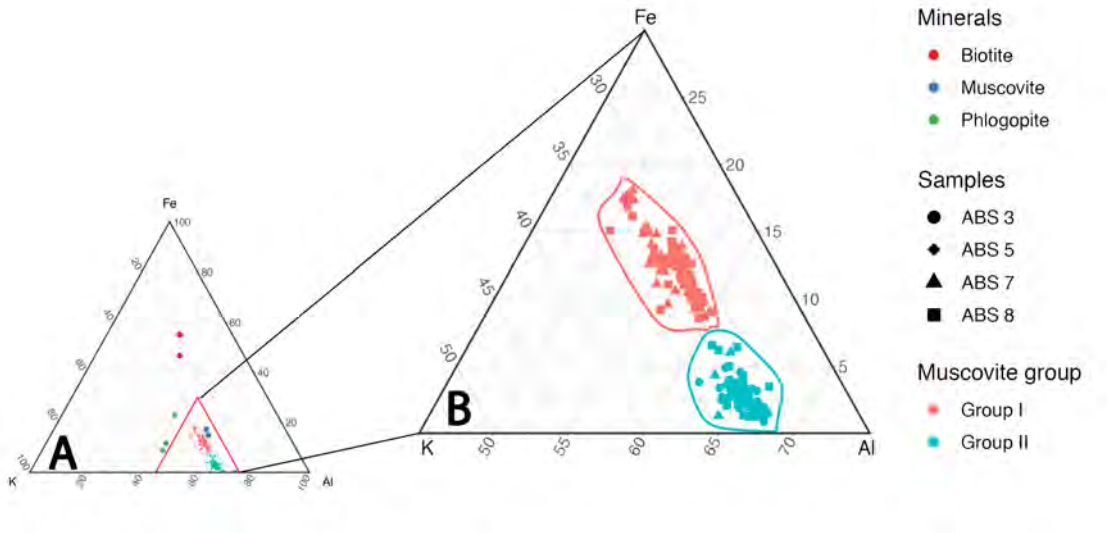

Figure 4.8: Ternary diagrams of K, Fe and Al in muscovite. (A) shows the composition of Ablah muscovite (obtained via the Quanta 450) comparing with other mica minerals including biotite, phlogopite and muscovite. Data sources for other mica minerals (used as references) are listed in table 4.C in the supplementary materials. (B) illustrates the differences in muscovite elemental compositions (obtained via the Quanta 450) between Group I and Group II.

altered pegmatite (ABS 5).

Group I muscovite

Group I muscovite was *in-situ* dated in the partially altered pegmatite (samples ABS 5 and ABS 8), and greisen (ABS 7). Group I muscovite of samples ABS 5 and ABS 8 yielded isochron ages of 625 ± 19 Ma and 611 ± 9 Ma with initial $^{87}Sr/^{86}Sr$ of 0.702 ± 0.099 and 0.704 ± 0.030, respectively (Figure 4.9E and H). In the greisen (ABS 7), Group I muscovite yielded an isochron age of 636 ± 5 Ma but with low initial $^{87}Sr/^{86}Sr$ ratio (0.699 ± 0.018). Thus, the obtained isochron line was anchored to the initial $^{87}Sr/^{86}Sr$ ratio of 0.702 ± 0.099 that obtained from sample ABS 5, and the model age of sample ABS 7 calculated at 626 ± 2 Ma (Figure 4.9G). Thus, we can conclude that the age of Group I muscovite in the partially altered pegmatite and the greisen ranges between 626 Ma and 611 Ma.

Group II muscovite

Muscovite of Group II was dated in the partially altered pegmatite (samples ABS 5 and ABS 8), altered pegmatite (ABS 3) and greisen (ABS 7) (Figure 4.9I-L). Overall, the Group II muscovite yielded younger ages comparing to Group I muscovite, ranging between 601 Ma and 560 Ma (Figure 4.9). Group II muscovite in samples ABS 5 and ABS 7 yielded similar ages determined at 598 ± 14 Ma and 601 ± 12 Ma with initial $^{87}Sr/^{86}Sr$ ratios of 0.707 ± 0.061 and 0.705 ± 0.029, respectively (Figure 4.9J and K). However, muscovite (Group II) in sample ABS 3 yielded younger age (560 ± 23 Ma) with higher initial $^{87}Sr/^{86}Sr$ ratio of 0.730 ± 0.084 (Figure 4.9I). Finally, Group II muscovite in sample ABS 8 yielded an isochron age of 608 ± 25 Ma, but with low $^{87}Sr/^{86}Sr$ ratio (0.639 ±0.058), thus the model age of the sample was calculated at 581 ± 8 Ma by anchoring the isochron to the same initial $^{87}Sr/^{86}Sr$ ratio (0.707) obtained from the other partially altered pegmatite sample (ABS 5) (Figure 4.9L).

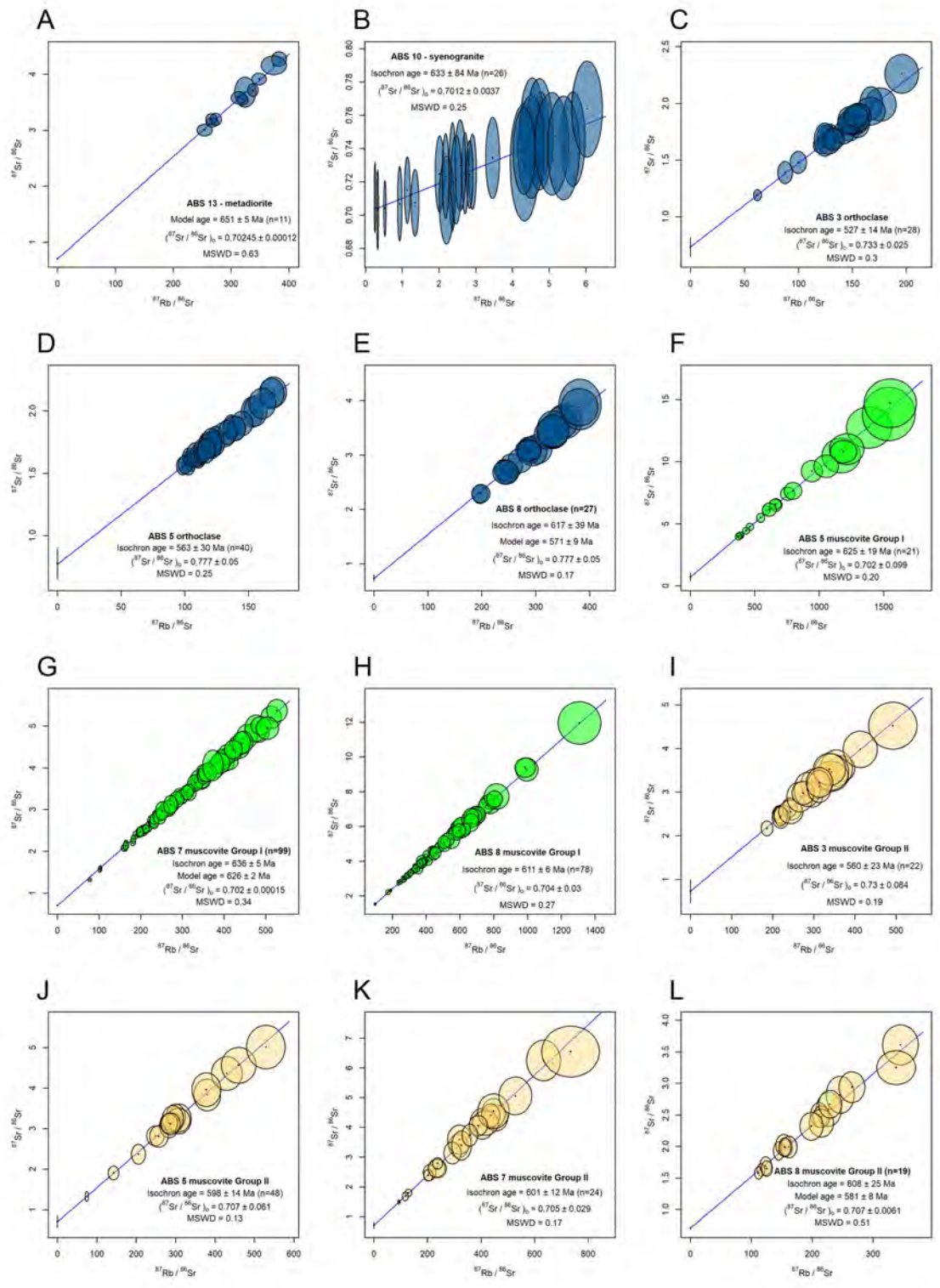

Figure 4.9: Rb–Sr isochron diagrams for orthoclase (blue), Group I muscovite(green), and Group II muscovite (orange) of samples ABS 13, ABS 10, ABS 3, ABS 5, ABS 8.

4.5 Discussion

4.5.1 Classification of muscovite in Ablah mineralisation

The results show that muscovite in investigated samples can be classified into two groups with distinct genetic origins and formed at different times. Group I muscovite seems to be a primary phase associated with the crystallisation of the Ablah pegmatite between the period of 626 Ma to 611 Ma, and it is texturally and chemically distinctive from Group II muscovite. The Group II muscovite seems to be formed due to alteration processes that occurred at two different times. The first alteration process is the greisenisation that occurred at 601 $\pm$ 12 Ma and formed the Group II muscovite in samples ABS 5 and ABS 7 and characterised by low initial $^{87}Sr/^{86}Sr$ ratio (0.707). The second alteration event occurred at 556 $\pm$ 23 Ma, and it is genetically different from the greisen as indicated from the high initial $^{87}Sr/^{86}Sr$ ratio obtained from the alteration zone in pegmatite (sample ABS 3, see Figure 4.9l). This alteration zone is associated with quartz veins that may reflect hydrothermal circulation that formed the Cu-Au mineralisation in Mount Ablah.

4.5.2 Magmatic evolution of the Mount Ablah area: Constraints from *in-situ* Rb–Sr dating

Mount Ablah pegmatite and A-type granitoids (including the syenogranite (ABS 10)) are intruded into the metadiorite that was suggested to be emplaced in the lower Neoproterozoic (Tonian) period between 855 Ma and 815 Ma (Johnson, 2005; Johnson, 2006). Thus, the much younger *in-situ* Rb–Sr age of 651 $\pm$ 20 Ma for the metadiorite sample (ABS 13) could reflect the timing of later (Cryogenian) isotopic disturbance and/or recrystallisation due to the development of Umm Farwah Shear zone. The timing of the Umm Farwah Shear zone was presumed to be as young as 605 Ma (Johnson et al., 2011) based on the whole-rock Rb–Sr age of A-type granitoids intruded in the Shuwas pluton (Figure 4.2). However, the Cryogenian age of the metadiorite (sample ABS 13) suggests that the Shuwas pluton was affected by brittle-ductile deformation associated with the development of the shear zone, which could have been initiated at ca. 651 $\pm$ 20 Ma. This would suggest that the shear zone is linked to the Pan-African tectonism in the south of the Arabian Shield (Genna et al., 1999).

The development of the Umm Farwah shear zone was associated with partial melting and crustal fusion that is believed to have produced the granitoids exposed in the Shuwas pluton as shown in Figure 4.2 (Moufti, 2001). The *in-situ* Rb–Sr dating of the

syenogranite constrained in this study at 633 ± 84 Ma (Figure 4.9B), with a large uncertainty due to the low and not very radiogenic $^{87}Sr/^{86}Sr$ ratios in the analysed feldspars. Although this large uncertainty makes the *in-situ* Rb–Sr age of syenogranite rather poorly constrained, the mean of the age of 633 Ma is close to other published ages for granitoids in the Ablah area (i.e., 617 ± 17 Ma for syenite, and 605 ± 5 Ma for syenogranite (Moufti, 2001)). This in turn implies that the partial melting, associated with Umm Farwah shear zone, and the formation of syenogranite probably started at around 633 Ma or during the Cryogenian/Ediacaran transition, with the following 'cooling phase' allowing isotopic closure lasting up to 25 Ma until ca.605 Ma.

4.5.3 Paragenetic sequence of the Mount Ablah Cu-Au mineralisation

The Mount Ablah pegmatite contains two types of mineralisation which are the greisen and the Cu-Au mineralisation in the alteration zone in pegmatite. The greisen in Mount Ablah is considered a source for fluorite and yttrium (Jackson, 1986) whereas the Cu and Au are mostly concentrated in the quartz-associated alteration zones in the pegmatite (Salimo, 2015). Our *in-situ* Rb–Sr data indicated that pegmatite emplacement occurred between 626 and 611 Ma as indicated from Group I muscovite in the partially altered pegmatite (ABS 5 and ABS 8). This age is in agreement with the age of most of the post-tectonic intrusions in the Arabian Shield whose ages scatter around 620 Ma (Robinson et al., 2014), and it overlaps the crystallisation age inferred from the syenogranite (sample ABS 10) at 633 ± 84 Ma, which seems to indicate that the pegmatite was formed at around the same time as the syenogranite and probably from the same or related magma sources. Subsequently, the greisenisation process occurred at 601 ± 12 Ma as indicated by the Group II muscovite in the greisen (sample ABS 7). Noticeably, the age of the greisen is in agreement with the lower limit of the magmatic process that formed the A-type granitoids (605 ± 5 Ma) in the Shuwas pluton (Moufti, 2001) and Mount Ablah pegmatite (625 ± 19 Ma), which could indicate that the greisen was formed from residual magmatic fluids rich in volatiles, specifically fluorine. This can explain the presence of economic fluorite deposit in the Mount Ablah (Peterková and Dolejš, 2019; Smirnov, 2015). In addition, this is also supported by agreement in the initial $^{87}Sr/^{86}Sr$ ratio between Group II muscovite in the greisen (sample ABS 7) and from feldspars in the syenogranite (ABS 10) and Group I muscovite in the pegmatite (sample ABS 5). Later, the Mount Ablah pegmatite was affected by a later stage of alteration events that form the Cu-Au mineralisation. This is insinuated by data from

Group II muscovite in altered pegmatite (ABS 3) and from orthoclase which seem to record the timing of these later stage events between 574 and 530 Ma (Figure 4.10). The younger ages for orthoclase comparing with the primary Group I muscovite indicate that Rb-Sr of orthoclase was diffused during the alteration process whereas muscovite was more resistant to alteration. This indicates that the predominant temperature during the alteration event was between 475 and 500 °C as this range lies close or above the closure temperature of orthoclase (Giletti, 1990) but lower than the closure temperature of muscovite (Dodson, 1973).

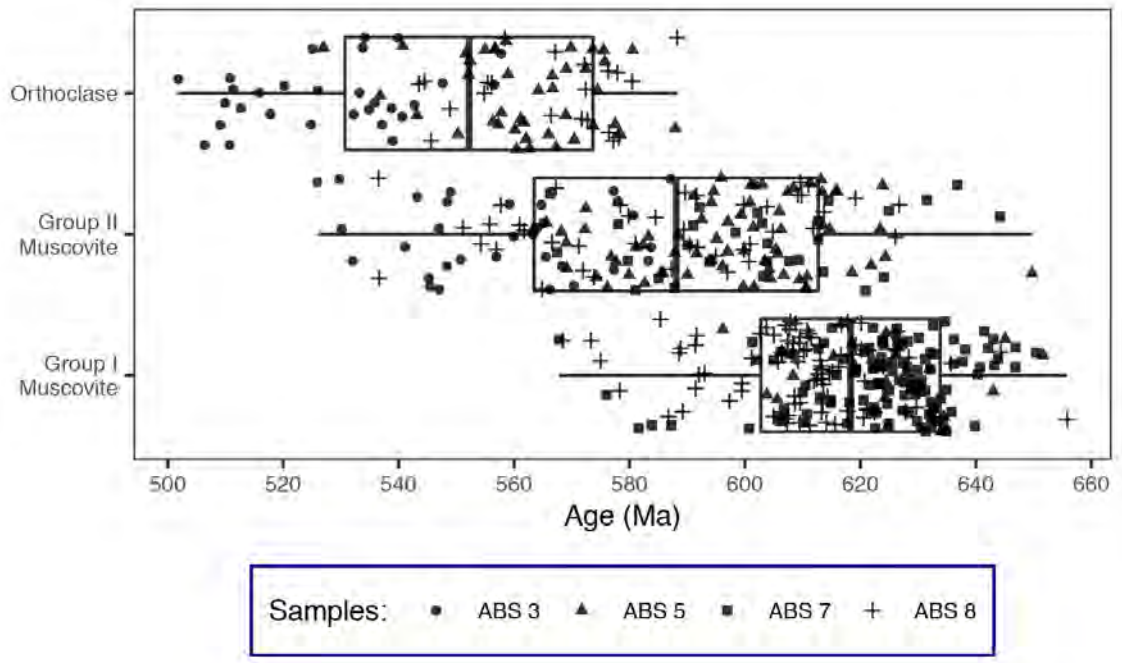

Figure 4.10: Boxplot diagram shows the Rb-Sr age distribution of orthoclase, Group I muscovite and Group II muscovite in the samples ABS 3, ABS 5, ABS 7 and ABS 8. The box illustrates the mean of the ages and standard deviation.

4.6 Conclusions

The *in-situ* Rb–Sr dating of K-bearing minerals such as muscovite and K-feldspar, coupled with published geochronological data from the Mount Ablah area including the Shuwas pluton, allows us to constrain the ages of these mineral sequences with implications for the timing of multiple events affecting the study area. Using the *in-situ* Rb-Sr dating technique, we were able to:

- Constrain, for the first time, the timing of the development of Umm Farwah Shear Zone at 651 $\pm$ 20 Ma helps us to understand the development of the southern part

of the Arabian Shield as the shear zone is a major structure in the Asir terrane.

- Determine the timing of emplacement of Ablah pegmatite at 625 $\pm$ 19 Ma.
- Constrain the timing of the greisenisation process that formed the greisen deposit between 613 Ma and 589 Ma.
- Constrain the timing of alteration event that formed the Cu-Au mineralisation in Mount Ablah between 580 Ma and 530 Ma.

4.7 Acknowledgement

The authors thank the Saudi Arabian Mining Company (Ma'aden) and Mr. Zaid Al Moald for providing access to the core samples of Mount Ablah. We also thank King Abdulaziz University and Prof. Hesham Harbi for facilitating the field trip to the study area. Adelaide Microscopy and Mr. Ken Neubauer are thanked for assistance in the SEM analysis. Additional thanks go to the iolite team specifically to Bence Paul and Joe Petrus for providing a licence for iolite4 software. Finally, we would also like to thank the editor and two reviewers (Prof. Yehia H. Dawood and an anonymous reviewer) for their constructive comments and criticism, which improved the overall quality of this study.

References

Agar, R A (1992). "The tectono-metallogenic evolution of the Arabian Shield". In: *Precambrian Research* 58.1-4, pp. 169–194.

Ahmed, Ahmed Hassan and Adel Abdullah Surour (2016). "Fluid-related modifications of Cr-spinel and olivine from ophiolitic peridotites by contact metamorphism of granitic intrusions in the Ablah area, Saudi Arabia". In: *Journal of Asian Earth Sciences* 122, pp. 58–79.

Alessio, Brandon L, Morgan L Blades, George Murray, Benjamin Thorpe, Alan S Collins, David E Kelsey, John Foden, Justin Payne, Salah Al-Khirbash, and Fred Jourdan (2018). "Origin and tectonic evolution of the NE basement of Oman: a window into the Neoproterozoic accretionary growth of India?" In: *Geological Magazine* 155.5, pp. 1150–1174.

Armistead, Sheree E, Alan S Collins, Ahmad Redaa, Gilby Jepson, Jack Gillespie, Sarah Gilbert, Morgan L Blades, John D Foden, and Théodore Razakamanana (2020). "Structural evolution and medium-temperature thermochronology of central Madagascar: implications for Gondwana amalgamation". In: *Journal of the Geological Society* 177, pp. 784–798.

Blades, M L, B L Alessio, A S Collins, J Foden, J L Payne, S Glorie, P Holden, B Thorpe, and S Al-Khirbash (2020). "Unravelling the Neoproterozoic accretionary history of Oman, using an array of isotopic systems in zircon". In: *Journal of the Geological Society* 177.2, p. 357.

Blades, M L, A S Collins, J L Payne, J D Foden, K Stüwe, M Hassan, and T Abu-Alam (2021). "Age and Hafnium Isotope Evolution of Sudanese Butana and Chad Illuminates the Stenian to Ediacaran Evolution of the Southeast Sahara Metacraton". In: *Precambrian Research* In press.

Bokhari, F Y and J D Kramers (1981). "Island arc character and late Precambrian age of volcanics at Wadi Shwas, Hijaz, Saudi Arabia: geochemical and Sr and Nd isotopic evidence". In: *Earth and Planetary Science Letters* 54.3, pp. 409–422.

Charbit, S, H Guillou, and L Turpin (1998). "Cross calibration of K–Ar standard minerals using an unspiked Ar measurement technique". In: *Chemical Geology* 150.1, pp. 147–159.

Cherniak, D J and E B Watson (2001). "Pb diffusion in zircon". In: *Chemical Geology* 172.1, pp. 5–24.

Collins, Alan S, Morgan L Blades, and Andrew S Merdith (2021). "Chapter 8: The Arabian Nubian Shield within the Neoproterozoic Plate Tectonic Circuit". In: *The Geology of the Arabian-Nubian Shield*. Ed. by Zakaria. Hamimi, Abdel-Rahman. Fowler, Jean-Paul. Liégeois, Alan S Collins, Mohamed G Abdelsalam, and Mohamed Abd El-Wahed. Springer.

Collins, Alan S, Morgan L Blades, Andrew S Merdith, and John D Foden (2021). "Closure of the Proterozoic Mozambique Ocean was instigated by a late Tonian plate reorganization event". In: *Communications Earth & Environment* 2.1, p. 75.

Collins, Alan S and Sergei A Pisarevsky (2005). "Amalgamating eastern Gondwana: The evolution of the Circum-Indian Orogens". In: *Earth-Science Reviews* 71.3, pp. 229–270.

Derkowski, Arkadiusz, Jan Srodon, Wojciech Franus, Peter Uhlík, Grzegorz Banas Michałand Zielinski, Maria Caplovicova, Małgorzata Franus, Michał Banas, Grzegorz Zielinski, Maria Caplovicova, and Małgorzata Franus (2009). "Partial dissolution of glauconitic samples: implications for the methodology of K-Ar and Rb-Sr dating". In: *Clays and Clay Minerals* 57.5, pp. 531–554.

Dodson, Martin H (1973). "Closure Temperature in Cooling Geochronological and Petrological Systems". In: *Contributions to Mineralogy and Petrology* 40.3, pp. 259–274.

Garbe-Schönberg, Dieter and Samuel Müller (2014). "Nano-particulate pressed powder tablets for LA-ICP-MS". In: *Journal of Analytical Atomic Spectrometry* 29.6, pp. 990–1000.

Genna, Antonin, Catherine Guerrot, Yves Deschamps, Pierre Nehlig, and Mohammed Shanti (1999). "Les formations Ablah d'Arabie Saoudite (datation et implication géologique)". In: *Comptes Rendus de l'Académie des Sciences-Series IIA-Earth and Planetary Science* 329.9, pp. 661–667.

Giletti, B j (1990). "Rb and Sr diffusion in alkali feldspars, with implications for cooling histories of rocks". In: *Geochimica et Cosmochimica Acta* 55.5, pp. 1331–1343.

Govindaraju, K (1995). "1995 Working values with confidence limits for twenty-six CRPG, ANRT and IWG-GIT geostandards". In: *Geostandards Newsletter* 19.s1, pp. 1–32.

Greenwood, W R (1975). *Geology of Al 'Aqiq quadrangle, sheet 20/41D, Kingdom of Saudi Arabia*. Tech. rep. Jeddah: Saudi Arabian Directorate General of Mineral Resources.

Hogmalm, K. Johan, Thomas Zack, Andreas K. O. Karlsson, Axel S. L. Sjöqvist, and Dieter Garbe-Schönberg (2017). "In situ Rb-Sr and K-Ca dating by LA-ICP-MS/MS: an evaluation of N^2O and SF^6 as reaction gases". In: *Journal of Analytical Atomic Spectrometry* 32.2, pp. 305–313.

Jackson, Norman J (1986). "Mineralization associated with felsic plutonic rocks in the Arabian Shield". In: *Journal of African Earth Sciences (1983)* 4, pp. 213–227.

Johnson, P R (2006). *Explanatory notes to the map of Proterozoic geology of western Saudi Arabia*. Tech. rep. Jeddah.

Johnson, P R, A Andresen, A S Collins, A R Fowler, H Fritz, W Ghebreab, T Kusky, and R J Stern (2011). "Late Cryogenian–Ediacaran history of the Arabian–Nubian Shield: A review of depositional, plutonic, structural, and tectonic events in the closing stages of the northern East African Orogen". In: *Journal of African Earth Sciences* 61.3, pp. 167–232.

Johnson, P R and B Woldehaimanot (2003). *Development of the Arabian-Nubian Shield: Perspectives on accretion and deformation in the northern East African Orogen and the assembly of Gondwana*.

Johnson, Peter R (2005). *Proterozoic geology of western Saudi Arabia, West-central sheet, (Amended September 2005), notes on Proterozoic stratigraphy*. Tech. rep. Jeddah.

Kirkland, C L, C Yakymchuk, K Szilas, N Evans, J Hollis, B McDonald, and N J Gardiner (2018). "Apatite: a U-Pb thermochronometer or geochronometer?" In: *Lithos* 318-319, pp. 143–157.

Li, Shan-Shan, M Santosh, Juraj Farkaš, Ahmad Redaa, Sohini Ganguly, Sung Won Kim, Cun Zhang, Sarah Gilbert, and Thomas Zack (2020). "Coupled U-Pb and Rb-Sr laser ablation geochronology trace Archean to Proterozoic crustal evolution in the Dharwar Craton, India". In: *Precambrian Research* 343, p. 105709.

Marzouki, F M H, N J Jackson, C R Ramsay, and D P F Darbyshire (1982). "Composition, age and origin of two proterozoic diorite—tonalite complexes in the Arabian shield". In: *Precambrian Research* 19.1, pp. 31–50.

McFarlane, Christopher R M and T Mark Harrison (2006). "Pb-diffusion in monazite: Constraints from a high-T contact aureole setting". In: *Earth and Planetary Science Letters* 250.1, pp. 376–384.

Merdith, Andrew S, Simon E Williams, Alan S Collins, Michael G Tetley, Jacob A Mulder, Morgan L Blades, Alexander Young, Sheree E Armistead, John Cannon, Sabin Zahirovic, and R Dietmar Müller (2021). "Extending full-plate tectonic models into deep time: Linking the Neoproterozoic and the Phanerozoic". In: *Earth-Science Reviews* 214, p. 103477.

Moufti, M (2001). "Age, geochemistry and origin of peraluminous A-type granitoids of the Ablah-Shuwas pluton, Ablah Graben Arabian Shield". In: *Acta Mineralogica–Petrographica* 42.2001, pp. 5–20.

Nehlig, P, I Salpeteur, F Asfirane, V Bouchot, J M Eberlé, and A Genna (1999). "The Mineral Potential of the Arabian Shield: A reassessment". In: *Proceedings of the IUGS/UNESCO Meeting on the "Base and Precious Metal Deposits in the Arabian Shield", Jeddah, November*, pp. 12–19.

Nettle, David, Galen P Halverson, Grant M Cox, Alan S Collins, Mark Schmitz, James Gehling, Peter R Johnson, and Khalid Kadi (2014). "A middle–late Ediacaran volcanosedimentary record from the eastern Arabian-Nubian shield". In: *Terra Nova* 26.2, pp. 120–129.

Olierook, Hugo K H, Kai Rankenburg, Stanislav Ulrich, Christopher L Kirkland, Noreen J Evans, Stephen Brown, Brent I A McInnes, Alexander Prent, Jack Gillespie, and Bradley McDonald (2020). "Resolving multiple geological events using in situ Rb–Sr geochronology: implications for metallogenesis at Tropicana, Western Australia". In: *Geochronology* 2.2, pp. 283–303.

Paton, Chad, John Hellstrom, Bence Paul, Jon Woodhead, and Janet Hergt (2011). "Iolite: Freeware for the visualisation and processing of mass spectrometric data". In: *Journal of Analytical Atomic Spectrometry* 26.12, pp. 2508–2518.

Peterková, Tereza and David Dolejš (2019). "Magmatic-hydrothermal transition of Mo-W-mineralized granite-pegmatite-greisen system recorded by trace elements in quartz: Krupka district, Eastern Krušné hory/Erzgebirge". In: *Chemical Geology* 523, pp. 179–202.

Rafiei, Mehrnoush, Stefan Lhr, Andre Baldermann, Richard Webster, and Charlie Kong (2020). "Quantitative petrographic differentiation of detrital vs diagenetic clay minerals in marine sedimentary sequences: Implications for the rise of biotic soils". In: *Precambrian Research* 350, p. 105948.

Redaa, Ahmad, Juraj Farkašš, Sarah Gilbert, Alan S. Collins, Benjamin Wade, stefan Löhr, Thomas Zack, and Dieter Garbe-Schönberg (2021). "Assessment of elemental fractionation and matrix effects during in-situ Rb–Sr dating of phlogopite by LA-ICP-MS/MS: Implications for the accuracy and precision of mineral ages". In: *Journal of Analytical Atomic Spectrometry* 36, pp. 322–344.

Robinson, F A, J D Foden, and A S Collins (2015). "Geochemical and isotopic constraints on island arc, synorogenic, post-orogenic and anorogenic granitoids in the Arabian Shield, Saudi Arabia". In: *Lithos* 220–223, pp. 97–115.

Robinson, F A, J D Foden, A S Collins, and J L Payne (2014). "Arabian Shield magmatic cycles and their relationship with Gondwana assembly: Insights from zircon U–Pb and Hf isotopes". In: *Earth and Planetary Science Letters* 408.0, pp. 207–225.

Salimo, Luckmore (2015). *Al Hajar Project - Preliminary review of Ablah prospect*. Tech. rep. Jeddah: Ma'aden Gold and Base Metals Co.

Smirnov, S Z (2015). "The fluid regime of crystallization of water-saturated granitic and pegmatitic magmas: a physicochemical analysis". In: *Russian Geology and geophysics* 56.9, pp. 1292–1307.

Stern, Robert J (2002). "Crustal evolution in the East African Orogen: a neodymium isotopic perspective". In: *Journal of African Earth Sciences* 34.3, pp. 109–117.

Stern, Robert J and Peter Johnson (2010). "Continental lithosphere of the Arabian Plate: A geologic, petrologic, and geophysical synthesis". In: *Earth-Science Reviews* 101.1, pp. 29–67.

Stoeser, Douglas B and Carol D Frost (2006). "Nd, Pb, Sr, and O isotopic characterization of Saudi Arabian Shield terranes". In: *Chemical Geology* 226.3–4, pp. 163–188.

Tillberg, Mikael, Henrik Drake, Thomas Zack, Ellen Kooijman, Martin J Whitehouse, and Mats E Åström (2020). "In situ Rb-Sr dating of slickenfibres in deep crystalline basement faults". In: *Scientific Reports* 10.1, pp. 1–13.

Vermeesch, Pieter (2018). "IsoplotR: A free and open toolbox for geochronology". In: *Geoscience Frontiers* 9, pp. 1479–1493.

Şengör, A M Celâl, Nalan Lom, Cengiz Zabcı, Gürsel Sunal, and Tayfun Öner (2020). "Reconstructing orogens without biostratigraphy: The Saharides and continental growth during the final assembly of Gondwana-Land". In: *Proceedings of the National Academy of Sciences* 117.51, p. 32278.

Şengün, Fırat, Viktor Bertrandsson Erlandsson, Johan Hogmalm, and Thomas Zack (2019). "In situ Rb-Sr dating of K-bearing minerals from the orogenic Akçaabat gold deposit in the Menderes Massif, Western Anatolia, Turkey". In: *Journal of Asian Earth Sciences* 185, p. 104048.

CHAPTER 5

Summary of the thesis research outcomes and directions for future studies

This PhD thesis aimed to develop a novel *in-situ* Rb-Sr dating of selected silicate minerals (micas, feldspars, clays) done by the LA-ICP-MS/MS to be further validated and utilised for applications in earth sciences. The main focus of the thesis was to assess the factors (i.e., analytical parameters and reference materials) that affect the accuracy and precision of *in-situ* Rb-Sr dating technique and acquired 'ages', which was accomplished by testing a number of mineral reference materials (nano-powders and fused glasses) to minimise the impact of such analytical issues and limitations. Furthermore, this thesis also applied the newly developed *in-situ* Rb-Sr dating approach to constrain the timing of copper-gold mineralisation and its link to local/regional geological (igneous, tectonic/metamorphic and alteration) events based on a case study in Saudi Arabia, which targeted and dated suitable silicate minerals (K-rich micas, K-feldspars) associated with the Cu-Au mineralisation in the Mount Ablah area in the Southern Arabian Shield. The following sections and conclusions highlight the main outcomes of this thesis and its individual components (chapters), with suggestion on research directions for future studies to further validate and improve *in-situ* Rb-Sr dating by a single and/or multi-collector LA-ICP-MS/MS.

5.1 The current state and limitations of the *in-situ* Rb-Sr dating by the LA-ICP-MS/MS

LA-ICP-MS/MS is a novel development in the analytical techniques for Rb-Sr isotopic ratio measurements and geochronology, which significantly reduces the required time for sample preparation and chemical separation of rubidium (^{87}Rb) from strontium (^{87}Sr) to resolve their isobaric interference. The analysis can be performed in either solutions or solid materials, and for the latter at micro-scale level using a laser ablation (LA) system. However, due to elemental fractionation and matrix effects (i.e., non-matched samples and standards), the impact of the above effects on the accuracy of obtained Rb-Sr ages can be about 3-7% for single-collector LA-ICP-MS/MS applications. As shown by results and data presented in this thesis, such matrix effects could be reduced or minimised by normalising the measured Rb-Sr isotopic data to a suitable matrix-matched reference materials (preferably a mineral-specific nano-powder pellet), but thus far the availability of such suitable reference materials remains rather limited to certain minerals, which thus posing the main challenge for more robust and frequent application of *in-situ* Rb-Sr dating. Thus, further work on developing well-characterised reference materials for *in-situ* Rb-Sr dating by the LA-ICP-MS/MS is necessary to expand the utility of this technique

in earth sciences. As shown by results and tests done in this thesis, this problem and limitation can be partly addressed and resolved by analysing a secondary reference mineral (e.g., GL-O glauconite and/or MDC phlogopite) with known ages and chemical/mineral composition, allowing matrix-matching with the samples of interest (i.e., micas, clays) to monitor data quality and acquired Rb-Sr ages. Results of this thesis also showed that down-hole fractionation (DHF) can also affect the accuracy and precision of *in-situ* Rb-Sr analysis and dating by LA-ICP-MS/MS. Such DHF phenomena and effects could vary with different laser wavelengths, and LA spot size, causing time- and depth-dependent variations in measured $^{87}Rb/^{86}Sr$ isotopic ratios during and/or between the analytical sessions, but these DHF effects do not affect significantly $^{87}Sr/^{86}Sr$ ratios. Considering these effects and analytical artifacts on measured $^{87}Rb/^{86}Sr$ ratios, raw data needs to be collected systematically (using consistent LA parameters and spacing) and also processed carefully to minimise the impact of DHF. This can be done by selecting the representative part of the spectrum or intensity (i.e., Rb(cps)/ Sr(cps)) during the data processing (i.e., via iolite software), and using such approach systematically for both samples and standards. Nevertheless, further work is required to develop and validate other suitable approaches and methods to minimise these matrix and DHF effects that impact the Rb-Sr dating applications so a full potential of this novel geochronological tool can be untapped and realised by future studies.

5.2 New reference materials for improved *in-situ* Rb-Sr dating of silicate minerals by LA-ICP-MS/MS

The current practice to calibrate or normalise Rb-Sr data acquired via LA-ICP-MS/MS is to use the reported $^{87}Rb/^{86}Sr$ and $^{87}Sr/^{86}Sr$ ratios of mineral reference materials to obtain or calculate representative 'correction factors' which are then applied to data acquired from unknown samples of the same or similar mineralogical and chemical composition (i.e., the concept of matrix-matching). Alternatively, $^{87}Rb/^{86}Sr$ and $^{87}Sr/^{86}Sr$ can be also quantified following Hogmalm et al., 2017 approach, which involves calculating the expected $^{87}Rb/^{86}Sr$ ratios of a given RM using measured $^{87}Sr/^{86}Sr$ ratios over multiple sessions and normalised to NIST 610, the expected age of the RM and its assumed initial $^{87}Sr/^{86}Sr$ ratio along with the decay constant of $1.3972 \pm 0.0045 \times 10^{-11}$ for the Rb-Sr system (Villa et al., 2015).

In this thesis and following the above approach, an additional and new glauconite nano-powder standard GL-O-NP was tested and used as a reference material to normalise Rb-Sr isotopic data of glauconite grains (GL-O), and the produced ages were within 1% of accuracy of the expected stratigraphic age (99.6 Ma) for this internationally-recognised glauconite reference material. This excellent agreement suggests that the acquired $^{87}Rb/^{86}Sr$ ratio of GL-O-NP of 34.56 $\pm$ 1.52 (data from this thesis) can be used along with the published $^{87}Sr/^{86}Sr$ ratio of GL-O of 0.7535 $\pm$ 0.001 (Govindaraju, 1995; Odin, 1976), which overlaps within the uncertainty of measured $^{87}Sr/^{86}Sr$ ratios in this thesis (0.7548 $\pm$ 0.015), to normalise Rb-Sr isotopic ratios of unknown glauconite samples to yield reliable Rb-Sr ages via LA-ICP-MS/MS approach. This reference material is also most likely suitable to calibrate Rb-Sr isotopic data of glauconite and phlogopite.

Biotite nano-powder standard Mica-Fe-NP was also investigated in this thesis to test its homogeneity and robustness for *in-situ* Rb-Sr dating and data normalisation for unknown biotites. Results yielded $^{87}Rb/^{86}Sr$ and $^{87}Sr/^{86}Sr$ ratios of a Mica-Fe-NP of 1687.32 $\pm$ 67.69 and 8.036 $\pm$ 0.057, respectively; and these values were used to normalise Rb-Sr isotopic data of well-characterised and dated MDC (phlogopite) and GL-O (glauconite) natural minerals. However, data normalised to Mica-Fe-NP yielded ages for MDC and GL-O that were rather inaccurate (4-5% off) from the expected ages, which is likely due to the matrix effect (i.e., non-matched chemical compositions of the above micas). Thus, further testing of Mica-Fe-NP in needed, specifically applied to dating of biotite samples, to validate the suitability of this reference material for *in-situ* Rb-Sr biotite dating.

Finally, K-feldspar nano-powder reference material FK-N-NP was also investigated in this thesis, as a potential mineral standard for *in-situ* Rb-Sr dating of feldspars. However, due to lack of published data (i.e., Rb-Sr ages or ratios) from this mineral standard, it was problematic to correctly quantify accurate $^{87}Rb/^{86}Sr$ and $^{87}Sr/^{86}Sr$ values for this mineral standard and thus to calculate the corresponding correction factors. Thus, the measured Rb-Sr isotope data from FK-N-NP were normalised to non-matched reference material (i.e., Mica-Mg-NP and GL-O-NP), but such results yielded highly variable Rb-Sr ages for FK-N-NP ranging between 475 and 550 Ma, depending on the standard used (Mica-Mg-NP and GL-O-NP). Further work is therefore needed on FK-N-NP to accurately constrain its $^{87}Rb/^{86}Sr$ and $^{87}Sr/^{86}Sr$ values as this mineral standard can potentially be used in future as a reference material for *in-situ* Rb-Sr dating of K-feldspar minerals. The research potential of *in-situ* Rb-Sr dating of feldspar or single grains is also illustrated by recent study of Bevan et al., 2021 who used both multi-collector and single-collector

LA-ICP MS/MS approaches to generate Rb-Sr ages from feldspar minerals, which could be applied for problems relevant to igneous and metamorphic geology and/or studies targeting detrital feldspars in sedimentary rock archives.

5.3 *In-situ* Rb-Sr dating as a geochronological tool to constrain the timing for genesis of Cu-Au mineralisation

Mineralisation and alteration zones (i.e., halos around ore deposits) usually contain a great abundance of K-bearing minerals such as newly formed feldspar, 'white micas' and/or sericite that are all suitable for *in-situ* Rb-Sr dating. Therefore, constraining the Rb-Sr ages of these secondary minerals associated with ore bodies could provide insight into the timing and genesis of the mineralisation. In this thesis, we targeted a case study involving the Cu-Au mineralisation and greisen deposit located in the Mount Ablah, in the southern part of the Arabian Shield, Saudi Arabia. The Mount Ablah is exposed in the central part of Umm Farwah Shear zone that extends ~200 km N–S across the Asir terrane. Representative rock samples were collected from the outcrops and drill cores affected by the above shear zone, and from post-tectonic intrusion units, and Cu-Au mineralisation zone. *In-situ* Rb-Sr analysis was conducted on two phases of muscovite and K-feldspar hosted in these collected rocks. The application of *in-situ* Rb-Sr dating via LA-ICP-MS/MS to constrain the 'ages' of the above mineral phases can yield information on the timing of development of Umm Farwah Shear zone, as well as emplacement of post-tectonic intrusions, and associated alterations processes that led to the formation of the Cu-Au mineralisation and greisen at the studied site. The results of this thesis suggest that the development of Umm Farwah shear zone occurred at 651 ± 20 Ma, followed by the emplacement of Mount Ablah pegmatite dated at 625 ± 19 Ma. Subsequently, the greisenisation of local igneous rocks took a place between 613 Ma and 589 Ma, followed by a reactivation that forms the Cu-Au mineralisation in the Mount Ablah which was dated between 580 Ma and 530 Ma.

References

Bevan, Dan, Christopher D Coath, Jamie Lewis, Johannes Schwieters, Nicholas Lloyd, Grant Craig, Henning Wehrs, and Tim Elliott (2021). "In situ Rb–Sr dating by collision cell, multicollection inductively-coupled plasma mass-spectrometry with pre-cell mass-filter,(CC-MC-ICPMS/MS)". In: *Journal of Analytical Atomic Spectrometry* 36.5, pp. 917–931.

Govindaraju, K (1995). "1995 Working values with confidence limits for twenty-six CRPG, ANRT and IWG-GIT geostandards". In: *Geostandards Newsletter* 19.s1, pp. 1–32.

Hogmalm, K. Johan, Thomas Zack, Andreas K. O. Karlsson, Axel S. L. Sjöqvist, and Dieter Garbe-Schönberg (2017). "In situ Rb-Sr and K-Ca dating by LA-ICP-MS/MS: an evaluation of N^2O and SF^6 as reaction gases". In: *Journal of Analytical Atomic Spectrometry* 32.2, pp. 305–313.

Odin, G S (1976). "Glauconite GL-O, interlaboratory standard for radiochronometric analysis". In: *Analusis* 4.6, pp. 287–291.

Villa, I M, P De Bièvre, N E Holden, and P R Renne (2015). "IUPAC-IUGS recommendation on the half life of ^{87}Rb". In: *Geochimica et Cosmochimica Acta* 164, pp. 382–385.

CHAPTER 6

Appendices

Chapter 2 Table 2.A Raw $^{87}Rb/^{86}Sr$ and $^{87}Sr/^{86}Sr$ ratios of Mica-Mg-NP reference material analysed by LA ICP-MS/MS over multiple Sessions using either a 193 nm or 213 nm laser ablation system

Table 2.A: Raw $^{87}Rb/^{86}Sr$ and $^{87}Sr/^{86}Sr$ ratios of Mica-Mg-NP-powder reference material analysed by LA ICP-MS/MS over multiple Sessions using either a 193 nm or 213 nm laser ablation system

spot	$^{87}Rb/^{86}Sr$	2SE	$^{87}Sr/^{86}Sr$	2SE	Session	LA	spot	$^{87}Rb/^{86}Sr$	2SE	$^{87}Sr/^{86}Sr$	2SE	Session	LA
1-Mica Mg P	133.3	1.3	1.881	0.024	Session 1	213nm	MicaMg - 15.d	153.3	1.1	1.893	0.013	Session 1	193nm
3-Mica Mg P	136.8	1.9	1.9	0.021	Session 1	213nm	MicaMg - 16.d	156.5	1.3	1.899	0.017	Session 1	193nm
4-Mica Mg P	132.4	1.7	1.883	0.024	Session 1	213nm	MicaMg - 17.d	154.6	1.2	1.901	0.014	Session 1	193nm
21-Mica Mg P	138	1.8	1.908	0.023	Session 1	213nm	MicaMg - 18.d	154.6	1.2	1.89	0.014	Session 1	193nm
22-Mica Mg P	141.5	2.2	1.892	0.02	Session 1	213nm	Mica-Mg - 1	160.8	1.7	1.888	0.021	Session 2	193nm
23-Mica Mg P	138.4	1.8	1.899	0.02	Session 1	213nm	Mica-Mg - 2	165.1	1.3	1.9	0.016	Session 2	193nm
24-Mica Mg P	141	1.7	1.894	0.015	Session 1	213nm	Mica-Mg - 3	163	1.5	1.907	0.016	Session 2	193nm
41-Mica Mg P	137.2	2.2	1.885	0.023	Session 1	213nm	Mica-Mg - 4	163.8	2	1.91	0.024	Session 2	193nm
42-Mica Mg P	137.4	1.9	1.886	0.022	Session 1	213nm	Mica-Mg - 5	167.5	1.4	1.902	0.017	Session 2	193nm
43-Mica Mg P	142.6	2.2	1.91	0.024	Session 1	213nm	Mica-Mg - 6	166.7	1.4	1.909	0.014	Session 2	193nm
44-Mica Mg P	139	1.6	1.91	0.021	Session 1	213nm	Mica-Mg - 7	164.4	1.9	1.894	0.022	Session 2	193nm
60-Mica Mg P	144.1	2.7	1.905	0.02	Session 1	213nm	Mica-Mg - 8	165.6	1.4	1.905	0.016	Session 2	193nm
61-Mica Mg P	137.3	1.8	1.908	0.021	Session 1	213nm	Mica-Mg - 9	159.5	1.3	1.905	0.014	Session 2	193nm
62-Mica Mg P	142.8	2.2	1.897	0.021	Session 1	213nm	Mica-Mg - 10	162.6	1.4	1.912	0.016	Session 2	193nm
MicaMg - 1.d	160.7	1.3	1.903	0.015	Session 1	193nm	Mica-Mg - 11	159.9	1.7	1.902	0.014	Session 2	193nm
MicaMg - 2.d	163	1.2	1.896	0.014	Session 1	193nm	Mica-Mg - 12	162	1.5	1.891	0.016	Session 2	193nm
MicaMg - 3.d	156.8	1.2	1.893	0.016	Session 1	193nm	Mica-Mg - 13	159.1	1.6	1.89	0.016	Session 2	193nm
MicaMg - 4.d	160	1.2	1.884	0.014	Session 1	193nm	Mica-Mg - 14	160.5	1.6	1.89	0.017	Session 2	193nm
MicaMg - 5.d	160.2	1.2	1.893	0.015	Session 1	193nm	Mica-Mg - 15	163.1	1.4	1.907	0.016	Session 2	193nm
MicaMg - 6.d	157.1	1.1	1.895	0.014	Session 1	193nm	Mica-Mg - 16	163.4	1.5	1.897	0.015	Session 2	193nm
MicaMg - 7.d	155.3	1.1	1.899	0.013	Session 1	193nm	Mica-Mg - 17	163.7	1.2	1.903	0.013	Session 2	193nm
MicaMg - 8.d	157.9	1.2	1.914	0.015	Session 1	193nm	Mica-Mg - 18	164.6	1.4	1.891	0.015	Session 2	193nm
MicaMg - 9.d	157	1.1	1.889	0.015	Session 1	193nm	Mica-Mg - 19	153.7	1.5	1.908	0.019	Session 2	193nm
MicaMg - 10.d	154.4	1.1	1.908	0.015	Session 1	193nm	Mica-Mg - 20	161.9	1.3	1.89	0.016	Session 2	193nm
MicaMg - 11.d	157.6	1.4	1.917	0.015	Session 1	193nm	Mica-Mg - 21	160	1.6	1.906	0.014	Session 2	193nm
MicaMg - 12.d	155.6	1.1	1.884	0.012	Session 1	193nm	Mica-Mg - 22	162.3	1.3	1.91	0.016	Session 2	193nm

Continued on next page

Table 2.A Raw $^{87}Rb/^{86}Sr$ and $^{87}Sr/^{86}Sr$ ratios of Mica-Mg-NP-powder reference material analysed by LA ICP-MS/MS over multiple Sessions using either a 193 nm or 213 nm laser ablation system

Continued from previous page

spot	$^{87}Rb/^{86}Sr$	2SE	$^{87}Sr/^{86}Sr$	2SE	Session	LA	spot	$^{87}Rb/^{86}Sr$	2SE	$^{87}Sr/^{86}Sr$	2SE	Session	LA
MicaMg - 13.d	156.2	1.2	1.893	0.014	Session 1	193nm	Mica-Mg - 23	162.7	1.4	1.914	0.014	Session 2	193nm
MicaMg - 14.d	153.8	1.1	1.876	0.016	Session 1	193nm	Mica-Mg - 24	158	1.4	1.907	0.016	Session 2	193nm
Mica-Mg - 25	157.7	1.5	1.908	0.015	Session 2	193nm	MicaMgp - 15	145.3	1.2	1.873	0.011	Session 2	213nm
Mica-Mg - 26	157.8	1.5	1.905	0.015	Session 2	193nm	MicaMgp - 25	149.2	1.2	1.883	0.01	Session 2	213nm
Mica-Mg - 27	157.4	1.2	1.9	0.016	Session 2	193nm	MicaMgp - 26	145.4	1.3	1.88	0.01	Session 2	213nm
Mica-Mg - 28	158.9	1.4	1.909	0.014	Session 2	193nm	MicaMgp - 27	142.4	1	1.874	0.01	Session 2	213nm
Mica-Mg - 29	160.6	1.3	1.9	0.015	Session 2	193nm	MicaMgp - 34	146.8	1.1	1.875	0.01	Session 2	213nm
Mica-Mg - 30	159.9	1.1	1.895	0.013	Session 2	193nm	MicaMgp - 35	145	1.3	1.891	0.011	Session 2	213nm
Mica-Mg - 31	161.8	1.4	1.908	0.015	Session 2	193nm	MicaMgp - 36	146.19	0.99	1.872	0.01	Session 2	213nm
Mica-Mg - 32	159.5	1.3	1.911	0.017	Session 2	193nm	MicaMgp - 37	140.9	1	1.864	0.011	Session 2	213nm
Mica-Mg - 33	158.6	1.2	1.899	0.013	Session 2	193nm	MicaMgp - 38	143.1	1.1	1.879	0.01	Session 2	213nm
Mica-Mg - 34	155.6	1.2	1.896	0.014	Session 2	193nm	MicaMgp - 39	144.3	1.1	1.878	0.011	Session 2	213nm
Mica-Mg - 35	156	1.1	1.9	0.013	Session 2	193nm	Mica-Mg - 1	164.5	1.6	1.892	0.021	Session 3	193nm
Mica-Mg - 36	158	1.6	1.905	0.015	Session 2	193nm	Mica-Mg - 2	168.1	1.4	1.908	0.017	Session 3	193nm
Mica-Mg - 37	161.8	1.4	1.902	0.016	Session 2	193nm	Mica-Mg - 3	168.3	1.4	1.916	0.018	Session 3	193nm
Mica-Mg - 38	161.6	1.5	1.901	0.016	Session 2	193nm	Mica-Mg - 4	164.4	1.8	1.885	0.018	Session 3	193nm
Mica-Mg - 39	161.6	1.3	1.916	0.016	Session 2	193nm	Mica-Mg - 5	164.3	1.5	1.91	0.018	Session 3	193nm
Mica-Mg - 40	159.4	1.4	1.909	0.017	Session 2	193nm	Mica-Mg - 6	164.4	1.3	1.899	0.016	Session 3	193nm
Mica-Mg - 41	156.1	2.1	1.893	0.014	Session 2	193nm	Mica-Mg - 7	161.4	1.4	1.905	0.015	Session 3	193nm
Mica-Mg - 42	154.4	1.4	1.884	0.014	Session 2	193nm	Mica-Mg - 8	158.4	1.5	1.897	0.016	Session 3	193nm
Mica-Mg - 43	157.2	1.3	1.903	0.019	Session 2	193nm	Mica-Mg - 9	164	1.7	1.918	0.016	Session 3	193nm
Mica-Mg - 44	157.4	1.4	1.893	0.016	Session 2	193nm	Mica-Mg - 10	163.7	1.5	1.905	0.016	Session 3	193nm
Mica-Mg - 45	160.3	1.5	1.908	0.016	Session 2	193nm	Mica-Mg - 11	162.6	2.2	1.917	0.023	Session 3	193nm
Mica-Mg - 46	167.2	1.5	1.891	0.02	Session 2	193nm	Mica-Mg - 12	163.6	1.4	1.914	0.019	Session 3	193nm
Mica-Mg - 47	169.9	1.4	1.913	0.017	Session 2	193nm	Mica-Mg - 13	164	1.5	1.907	0.016	Session 3	193nm
Mica-Mg - 48	166.1	1.3	1.903	0.014	Session 2	193nm	Mica-Mg - 14	164.7	1.7	1.905	0.018	Session 3	193nm
MicaMgp - 1	148.1	1.3	1.8809	0.0099	Session 2	213nm	Mica-Mg - 15	161.6	1.4	1.914	0.015	Session 3	193nm
MicaMgp - 2	139.79	0.96	1.878	0.01	Session 2	213nm	Mica-Mg - 16	162.6	1.3	1.905	0.017	Session 3	193nm

Continued on next page

Table 2.A Raw $^{87}Rb/^{86}Sr$ and $^{87}Sr/^{86}Sr$ ratios of Mica-Mg-NP-powder reference material analysed by LA ICP-MS/MS over multiple Sessions using either a 193 nm or 213 nm laser ablation system

Continued from previous page

spot	$^{87}Rb/^{86}Sr$	2SE	$^{87}Sr/^{86}Sr$	2SE	Session	LA	spot	$^{87}Rb/^{86}Sr$	2SE	$^{87}Sr/^{86}Sr$	2SE	Session	LA
MicaMgp - 3	151.8	1.3	1.8766	0.0095	Session 2	213nm	Mica-Mg - 17	160.8	1.7	1.912	0.015	Session 3	193nm
MicaMgp - 13	142	1	1.8699	0.0092	Session 2	213nm	Mica-Mg - 18	157.2	1.5	1.894	0.016	Session 3	193nm
MicaMgp - 14	149.1	1.5	1.879	0.012	Session 2	213nm	Mica-Mg - 19	159.8	1.4	1.904	0.016	Session 3	193nm
Mica-Mg - 20	158.8	1.5	1.894	0.014	Session 3	193nm	Mica-Mg - 25	153.6	1.1	1.902	0.013	Session 4	193nm
Mica-Mg - 21	160	1.6	1.909	0.016	Session 3	193nm	Mica-Mg - 26	155.5	1.1	1.892	0.012	Session 4	193nm
Mica-Mg - 22	163.9	1.7	1.903	0.017	Session 3	193nm	Mica-Mg - 27	156.6	1.3	1.895	0.012	Session 4	193nm
Mica-Mg - 23	164.4	2.2	1.921	0.025	Session 3	193nm	Mica-Mg - 28	154.8	1.4	1.908	0.013	Session 4	193nm
Mica-Mg - 24	160.5	1.5	1.902	0.017	Session 3	193nm	Mica-Mg - 29	157.7	1.1	1.908	0.012	Session 4	193nm
Mica-Mg - 1	168.4	1.4	1.888	0.015	Session 4	193nm	Mica-Mg - 30	156	1.1	1.902	0.012	Session 4	193nm
Mica-Mg - 2	159.5	1.1	1.908	0.015	Session 4	193nm	Mica-Mg - 31	154.7	1.1	1.892	0.013	Session 4	193nm
Mica-Mg - 3	159.1	1.3	1.898	0.017	Session 4	193nm	Mica-Mg - 32	156.5	1.3	1.909	0.014	Session 4	193nm
Mica-Mg - 4	160.7	1.1	1.901	0.012	Session 4	193nm	Mica-Mg - 33	155.8	1	1.901	0.011	Session 4	193nm
Mica-Mg - 5	156.2	1.3	1.889	0.014	Session 4	193nm	Mica-Mg - 34	172.2	1.7	1.909	0.021	Session 4	193nm
Mica-Mg - 6	155.7	1.3	1.905	0.013	Session 4	193nm	Mica-Mg - 35	153.4	1.2	1.88	0.013	Session 4	193nm
Mica-Mg - 7	159.2	1.2	1.899	0.012	Session 4	193nm	Mica-Mg - 36	154.5	1.3	1.909	0.012	Session 4	193nm
Mica-Mg - 8	156.5	1.3	1.9	0.014	Session 4	193nm	Mica-Mg - 37	155.82	0.97	1.901	0.011	Session 4	193nm
Mica-Mg - 9	155.7	1	1.904	0.011	Session 4	193nm	Mica-Mg - 38	160.4	1.2	1.911	0.015	Session 4	193nm
Mica-Mg - 10	159.6	1.1	1.906	0.011	Session 4	193nm	Mica-Mg - 39	163.7	1.2	1.903	0.013	Session 4	193nm
Mica-Mg - 11	155	1.2	1.905	0.011	Session 4	193nm	Mica-Mg - 40	164.7	1.2	1.901	0.014	Session 4	193nm
Mica-Mg - 12	168.6	1.2	1.916	0.014	Session 4	193nm	Mica-Mg - 41	162.8	1.3	1.9	0.013	Session 4	193nm
Mica-Mg - 13	153.7	1.2	1.902	0.011	Session 4	193nm	Mica-Mg - 42	162.9	1.6	1.894	0.014	Session 4	193nm
Mica-Mg - 14	157.4	1.2	1.905	0.013	Session 4	193nm	Mica-Mg - 43	158.7	1.4	1.882	0.015	Session 4	193nm
Mica-Mg - 15	156.1	1.2	1.902	0.012	Session 4	193nm	Mica-Mg - 44	159.9	1.6	1.891	0.013	Session 4	193nm
Mica-Mg - 16	153	1.2	1.893	0.012	Session 4	193nm	Mica-Mg - 45	168.7	1.3	1.889	0.013	Session 4	193nm
Mica-Mg - 17	157	0.93	1.897	0.011	Session 4	193nm	Mica-Mg - 46	163.2	1.4	1.897	0.015	Session 4	193nm
Mica-Mg - 18	153.3	1	1.89	0.013	Session 4	193nm	Mica-Mg - 47	155.1	1	1.9	0.012	Session 4	193nm
Mica-Mg - 19	155.2	1.2	1.901	0.011	Session 4	193nm	Mica-Mg - 48	166.9	1.1	1.905	0.013	Session 4	193nm
Mica-Mg - 20	156.2	1.2	1.899	0.013	Session 4	193nm	Mica-Mg - 49	161.8	1.2	1.903	0.014	Session 4	193nm

Continued on next page

Table 2.A Raw $^{87}Rb/^{86}Sr$ and $^{87}Sr/^{86}Sr$ ratios of Mica-Mg-NP-powder reference material analysed by LA ICP-MS/MS over multiple Sessions using either a 193 nm or 213 nm laser ablation system

Continued from previous page

spot	$^{87}Rb/^{86}Sr$	2SE	$^{87}Sr/^{86}Sr$	2SE	Session	LA	spot	$^{87}Rb/^{86}Sr$	2SE	$^{87}Sr/^{86}Sr$	2SE	Session	LA
Mica-Mg - 21	155.7	1.4	1.896	0.013	Session 4	193nm	Mica-Mg - 50	161.5	1.2	1.898	0.011	Session 4	193nm
Mica-Mg - 22	156.7	1.1	1.904	0.012	Session 4	193nm	Mica-Mg - 51	160.8	1.5	1.898	0.013	Session 4	193nm
Mica-Mg - 23	166.1	1.3	1.901	0.014	Session 4	193nm	Mica-Mg - 1	162.3	1.6	1.919	0.016	Session 5	193nm
Mica-Mg - 24	155.6	1	1.892	0.011	Session 4	193nm	Mica-Mg - 2	156.3	1.3	1.891	0.015	Session 5	193nm
Mica-Mg - 3	154.5	1.4	1.911	0.015	Session 5	193nm	Mica-Mg - 32	152.8	1.6	1.898	0.013	Session 5	193nm
Mica-Mg - 4	156.7	1.6	1.908	0.014	Session 5	193nm	Mica-Mg - 33	149.7	1.4	1.908	0.015	Session 5	193nm
Mica-Mg - 5	155.1	1.4	1.892	0.015	Session 5	193nm	Mica-Mg - 34	156.8	1.7	1.901	0.015	Session 5	193nm
Mica-Mg - 6	160.4	1.5	1.911	0.019	Session 5	193nm	Mica-Mg - 35	157.1	1.3	1.9	0.016	Session 5	193nm
Mica-Mg - 7	158.9	1.4	1.917	0.017	Session 5	193nm	Mica-Mg - 36	157.5	1.6	1.905	0.015	Session 5	193nm
Mica-Mg - 8	156.9	1.5	1.912	0.018	Session 5	193nm	Mica-Mg - 1	166.9	1.4	1.893	0.02	Session 6	193nm
Mica-Mg - 9	157.8	1.8	1.895	0.016	Session 5	193nm	Mica-Mg - 2	166.4	2.2	1.887	0.028	Session 6	193nm
Mica-Mg - 10	159	1.7	1.889	0.015	Session 5	193nm	Mica-Mg - 3	169.1	1.4	1.901	0.019	Session 6	193nm
Mica-Mg - 11	155.8	1.3	1.894	0.015	Session 5	193nm	Mica-Mg - 4	165.1	1.3	1.907	0.018	Session 6	193nm
Mica-Mg - 12	156.8	1.5	1.888	0.016	Session 5	193nm	Mica-Mg - 5	163.3	1.3	1.904	0.018	Session 6	193nm
Mica-Mg - 13	155.6	1.5	1.909	0.016	Session 5	193nm	Mica-Mg - 6	159.1	1.5	1.9	0.022	Session 6	193nm
Mica-Mg - 14	150.2	1.6	1.887	0.015	Session 5	193nm	Mica-Mg - 7	167.9	1.8	1.906	0.026	Session 6	193nm
Mica-Mg - 15	155.2	1.4	1.892	0.018	Session 5	193nm	Mica-Mg - 8	170.8	1.4	1.91	0.014	Session 6	193nm
Mica-Mg - 16	159.8	1.6	1.924	0.018	Session 5	193nm	Mica-Mg - 9	171.2	1.5	1.919	0.018	Session 6	193nm
Mica-Mg - 17	158.7	1.5	1.905	0.016	Session 5	193nm	Mica-Mg - 10	168	1.7	1.881	0.021	Session 6	193nm
Mica-Mg - 18	158.4	1.3	1.911	0.014	Session 5	193nm	Mica-Mg - 11	162.7	2	1.895	0.02	Session 6	193nm
Mica-Mg - 19	154.3	1.5	1.894	0.016	Session 5	193nm	Mica-Mg - 12	162.1	1.2	1.901	0.015	Session 6	193nm
Mica-Mg - 20	155.4	1.3	1.9	0.015	Session 5	193nm	Mica-Mg - 13	169	1.9	1.929	0.017	Session 6	193nm
Mica-Mg - 21	155	1.4	1.899	0.016	Session 5	193nm	Mica-Mg - 14	165	1.4	1.903	0.016	Session 6	193nm
Mica-Mg - 22	155.1	1.5	1.915	0.019	Session 5	193nm	Mica-Mg - 15	167	1.7	1.88	0.018	Session 6	193nm
Mica-Mg - 23	150.8	1.1	1.902	0.016	Session 5	193nm	Mica-Mg - 16	167.1	1.8	1.902	0.018	Session 6	193nm
Mica-Mg - 24	153.6	2.1	1.91	0.024	Session 5	193nm	Mica-Mg - 17	162.6	1.4	1.896	0.016	Session 6	193nm
Mica-Mg - 25	154.4	1.2	1.892	0.015	Session 5	193nm	Mica-Mg - 18	163.9	1.4	1.903	0.019	Session 6	193nm
Mica-Mg - 26	154.6	1.2	1.902	0.016	Session 5	193nm	Mica-Mg - 19	160.8	1.5	1.88	0.016	Session 6	193nm

Continued on next page

Table 2.A Raw $^{87}Rb/^{86}Sr$ and $^{87}Sr/^{86}Sr$ ratios of Mica-Mg-NP-powder reference material analysed by LA ICP-MS/MS over multiple Sessions using either a 193 nm or 213 nm laser ablation system

Continued from previous page

spot	$^{87}Rb/^{86}Sr$	2SE	$^{87}Sr/^{86}Sr$	2SE	Session	LA	spot	$^{87}Rb/^{86}Sr$	2SE	$^{87}Sr/^{86}Sr$	2SE	Session	LA
Mica-Mg - 27	156.6	1.5	1.893	0.018	Session 5	193nm	Mica-Mg - 20	152.8	1.7	1.879	0.02	Session 6	193nm
Mica-Mg - 28	155.9	1.5	1.892	0.018	Session 5	193nm	Mica-Mg - 21	157	1.2	1.929	0.017	Session 6	193nm
Mica-Mg - 29	156.2	1.6	1.915	0.017	Session 5	193nm	Mica-Mg - 22	157.3	1.2	1.908	0.015	Session 6	193nm
Mica-Mg - 30	156.3	1.4	1.896	0.018	Session 5	193nm	Mica-Mg - 23	160.5	1.5	1.911	0.017	Session 6	193nm
Mica-Mg - 31	154	1.6	1.906	0.02	Session 5	193nm	Mica-Mg - 24	159.7	1.4	1.903	0.016	Session 6	193nm
Mica-Mg - 25	158.5	1.2	1.906	0.016	Session 6	193nm	Mica-Mg - 54	155.5	1.9	1.89	0.021	Session 6	193nm
Mica-Mg - 26	158.6	1.2	1.903	0.016	Session 6	193nm	Mica-Mg - 55	154.4	1.5	1.906	0.02	Session 6	193nm
Mica-Mg - 27	158.4	1.3	1.89	0.018	Session 6	193nm	Mica-Mg - 56	153.7	1.3	1.899	0.015	Session 6	193nm
Mica-Mg - 28	157.8	1.2	1.899	0.015	Session 6	193nm	Mica-Mg - 57	154.6	1.3	1.912	0.017	Session 6	193nm
Mica-Mg - 29	157.5	1.5	1.906	0.016	Session 6	193nm	Mica-Mg - 58	152.3	1.1	1.896	0.014	Session 6	193nm
Mica-Mg - 30	154.3	1	1.904	0.013	Session 6	193nm	Mica-Mg - 59	151.15	0.96	1.902	0.014	Session 6	193nm
Mica-Mg - 31	153.7	1.5	1.902	0.016	Session 6	193nm	Mica-Mg - 60	152.4	1.3	1.908	0.017	Session 6	193nm
Mica-Mg - 32	158.9	1.4	1.898	0.013	Session 6	193nm	Mica-Mg - 61	152.3	1.4	1.913	0.019	Session 6	193nm
Mica-Mg - 33	158.9	1.4	1.887	0.015	Session 6	193nm	Mica-Mg - 62	151.5	1.4	1.886	0.019	Session 6	193nm
Mica-Mg - 34	159.4	1.2	1.902	0.015	Session 6	193nm	Mica-Mg - 63	149.5	1.6	1.888	0.021	Session 6	193nm
Mica-Mg - 35	157.9	1.3	1.898	0.014	Session 6	193nm	Mica-Mg - 64	155.3	1.2	1.898	0.015	Session 6	193nm
Mica-Mg - 36	152.4	1.8	1.897	0.02	Session 6	193nm	Mica-Mg - 65	151.5	1.2	1.881	0.018	Session 6	193nm
Mica-Mg - 37	156	1.3	1.906	0.016	Session 6	193nm	Mica-Mg - 66	152.8	1.1	1.904	0.014	Session 6	193nm
Mica-Mg - 38	154.3	1.2	1.9	0.015	Session 6	193nm	Mica-Mg - 67	150.4	1.3	1.894	0.014	Session 6	193nm
Mica-Mg - 39	153.9	1.6	1.914	0.026	Session 6	193nm	Mica-Mg - 1	156.6	1.9	1.899	0.024	Session 7	193nm
Mica-Mg - 40	151.9	1.3	1.882	0.016	Session 6	193nm	Mica-Mg - 2	159.3	1.8	1.89	0.022	Session 7	193nm
Mica-Mg - 41	153.9	1.5	1.872	0.019	Session 6	193nm	Mica-Mg - 3	162.1	1.6	1.906	0.022	Session 7	193nm
Mica-Mg - 42	156	1.3	1.899	0.019	Session 6	193nm	Mica-Mg - 4	165.2	1.4	1.908	0.02	Session 7	193nm
Mica-Mg - 43	158	1.4	1.899	0.015	Session 6	193nm	Mica-Mg - 5	160.9	1.6	1.905	0.02	Session 7	193nm
Mica-Mg - 44	155.2	1.5	1.892	0.018	Session 6	193nm	Mica-Mg - 6	156.2	2	1.898	0.024	Session 7	193nm
Mica-Mg - 45	155	1.4	1.888	0.014	Session 6	193nm	Mica-Mg - 7	159.7	1.5	1.912	0.019	Session 7	193nm
Mica-Mg - 46	151.9	1.3	1.896	0.014	Session 6	193nm	Mica-Mg - 8	156.6	2	1.87	0.024	Session 7	193nm
Mica-Mg - 47	152	1.2	1.909	0.014	Session 6	193nm	Mica-Mg - 9	159.1	1.7	1.872	0.026	Session 7	193nm

Continued on next page

Table 2.A Raw $^{87}Rb/^{86}Sr$ and $^{87}Sr/^{86}Sr$ ratios of Mica-Mg-NP-powder reference material analysed by LA ICP-MS/MS over multiple Sessions using either a 193 nm or 213 nm laser ablation system

Continued from previous page

spot	$^{87}Rb/^{86}Sr$	2SE	$^{87}Sr/^{86}Sr$	2SE	Session	LA	spot	$^{87}Rb/^{86}Sr$	2SE	$^{87}Sr/^{86}Sr$	2SE	Session	LA
Mica-Mg - 48	151.7	1.3	1.879	0.017	Session 6	193nm	Mica-Mg - 10	156.7	1.6	1.87	0.022	Session 7	193nm
Mica-Mg - 49	152	1.3	1.914	0.017	Session 6	193nm	Mica-Mg - 11	156.2	1.8	1.907	0.022	Session 7	193nm
Mica-Mg - 50	152.2	1.5	1.895	0.015	Session 6	193nm	Mica-Mg - 12	154.4	1.9	1.889	0.026	Session 7	193nm
Mica-Mg - 51	153.8	1	1.893	0.015	Session 6	193nm	Mica-Mg - 13	154.5	1.8	1.864	0.021	Session 7	193nm
Mica-Mg - 52	157.5	1.2	1.925	0.015	Session 6	193nm	Mica-Mg - 14	155.6	1.7	1.889	0.022	Session 7	193nm
Mica-Mg - 53	157.3	1.4	1.898	0.015	Session 6	193nm	Mica-Mg - 15	154.6	1.7	1.902	0.022	Session 7	193nm
Mica-Mg - 16	154.1	1.6	1.915	0.027	Session 7	193nm	Mica-Mg - 9	159.4	1.7	1.885	0.019	Session 8	193nm
Mica-Mg - 17	155.5	1.8	1.897	0.026	Session 7	193nm	Mica-Mg - 10	160.8	1.8	1.871	0.023	Session 8	193nm
Mica-Mg - 18	154.3	1.7	1.894	0.023	Session 7	193nm	Mica-Mg - 11	158.7	1.6	1.89	0.019	Session 8	193nm
Mica-Mg - 19	155	1.9	1.912	0.024	Session 7	193nm	Mica-Mg - 12	156	1.4	1.877	0.02	Session 8	193nm
Mica-Mg - 20	156.2	2.3	1.905	0.021	Session 7	193nm	Mica-Mg - 13	159.1	1.6	1.918	0.02	Session 8	193nm
Mica-Mg - 21	151.8	1.4	1.887	0.019	Session 7	193nm	Mica-Mg - 14	155	2.1	1.884	0.021	Session 8	193nm
Mica-Mg - 22	156.1	1.9	1.901	0.021	Session 7	193nm	Mica-Mg - 15	155.2	1.9	1.904	0.023	Session 8	193nm
Mica-Mg - 23	152.9	1.9	1.915	0.026	Session 7	193nm	Mica-Mg - 16	157.4	1.9	1.903	0.023	Session 8	193nm
Mica-Mg - 24	150	1.7	1.897	0.022	Session 7	193nm	Mica-Mg - 17	153.8	2.1	1.905	0.027	Session 8	193nm
Mica-Mg - 25	154.7	1.9	1.889	0.023	Session 7	193nm	Mica-Mg - 18	156.7	2.2	1.884	0.026	Session 8	193nm
Mica-Mg - 26	150.3	1.5	1.899	0.021	Session 7	193nm	Mica-Mg - 19	161	2	1.925	0.029	Session 8	193nm
Mica-Mg - 27	149.6	1.5	1.892	0.021	Session 7	193nm	Mica-Mg - 20	157	1.8	1.915	0.027	Session 8	193nm
Mica-Mg - 28	154.4	1.7	1.9	0.022	Session 7	193nm	Mica-Mg - 21	159.6	1.9	1.906	0.021	Session 8	193nm
Mica-Mg - 29	158.4	2.1	1.908	0.021	Session 7	193nm	Mica-Mg - 22	155.3	2	1.896	0.029	Session 8	193nm
Mica-Mg - 30	154.9	1.8	1.92	0.027	Session 7	193nm	Mica-Mg - 23	153.9	2	1.878	0.025	Session 8	193nm
Mica-Mg - 31	154.2	1.6	1.881	0.021	Session 7	193nm	Mica-Mg - 24	154.8	2.5	1.912	0.023	Session 8	193nm
Mica-Mg - 32	154	2	1.893	0.024	Session 7	193nm	Mica-Mg - 25	149.5	1.9	1.897	0.031	Session 8	193nm
Mica-Mg - 33	152.2	1.6	1.913	0.026	Session 7	193nm	Mica-Mg - 26	153.8	1.7	1.888	0.022	Session 8	193nm
Mica-Mg - 34	151.8	1.7	1.884	0.022	Session 7	193nm	Mica-Mg - 27	152	1.6	1.887	0.024	Session 8	193nm
Mica-Mg - 35	152.2	1.9	1.897	0.023	Session 7	193nm	Mica-Mg - 28	155.1	1.5	1.891	0.02	Session 8	193nm
Mica-Mg - 36	154.2	1.9	1.912	0.018	Session 7	193nm	Mica-Mg - 29	154.9	2.1	1.881	0.034	Session 8	193nm
Mica-Mg - 37	150.8	1.6	1.92	0.022	Session 7	193nm	Mica-Mg - 30	154.2	2	1.898	0.027	Session 8	193nm

Continued on next page

Table 2.A Raw $^{87}Rb/^{86}Sr$ and $^{87}Sr/^{86}Sr$ ratios of Mica-Mg-NP-powder reference material analysed by LA ICP-MS/MS over multiple Sessions using either a 193 nm or 213 nm laser ablation system

Continued from previous page

spot	$^{87}Rb/^{86}Sr$	2SE	$^{87}Sr/^{86}Sr$	2SE	Session	LA	spot	$^{87}Rb/^{86}Sr$	2SE	$^{87}Sr/^{86}Sr$	2SE	Session	LA
Mica-Mg - 38	153.5	2	1.875	0.029	Session 7	193nm	Mica-Mg - 31	154	2	1.9	0.029	Session 8	193nm
Mica-Mg - 39	156.5	1.6	1.899	0.021	Session 7	193nm	Mica-Mg - 32	153.8	2.2	1.879	0.031	Session 8	193nm
Mica-Mg - 1	161.5	1.5	1.894	0.019	Session 8	193nm	Mica-Mg - 33	151.2	2	1.9	0.026	Session 8	193nm
Mica-Mg - 2	156.9	1.6	1.892	0.019	Session 8	193nm	Mica-Mg - 34	152.7	2	1.895	0.021	Session 8	193nm
Mica-Mg - 3	157.1	1.5	1.918	0.021	Session 8	193nm	Mica-Mg - 35	150.3	1.7	1.88	0.017	Session 8	193nm
Mica-Mg - 4	158	1.8	1.891	0.02	Session 8	193nm	Mica-Mg - 36	154.7	1.8	1.903	0.023	Session 8	193nm
Mica-Mg - 5	156.1	1.6	1.853	0.025	Session 8	193nm	Mica-Mg - 37	151.6	1.5	1.886	0.021	Session 8	193nm
Mica-Mg - 6	161.7	2	1.896	0.021	Session 8	193nm	Mica-Mg - 38	152.3	1.7	1.892	0.018	Session 8	193nm
Mica-Mg - 7	163.6	1.9	1.907	0.02	Session 8	193nm	Mica-Mg - 39	149.3	1.8	1.876	0.022	Session 8	193nm
Mica-Mg - 8	163	1.6	1.905	0.018	Session 8	193nm							

Table 2.B: $^{87}Rb/^{86}Sr$ and $^{87}Sr/^{86}Sr$ isotopic ratios for MDC analysed by LA-ICP-MS/MS over multiple sessions and normalised to Mica-Mg-NP reference material, using either a 193 nm or 213 nm laser ablation system.

spot	$^{87}Rb/^{86}Sr$	2SE	$^{87}Sr/^{86}Sr$	2SE	Session	LA	spot	$^{87}Rb/^{86}Sr$	2SE	$^{87}Sr/^{86}Sr$	2SE	Session	LA
MDC - 1	41.2	0.32	1.0356	0.0078	Session 1	213nm	MDC Mica - 6	39.53	0.26	1.0325	0.0071	Session 2	193nm
MDC - 2	43.65	0.4	1.0453	0.0096	Session 1	213nm	MDC Mica - 7	40	0.31	1.0319	0.0069	Session 2	193nm
MDC - 3	43.66	0.47	1.033	0.0084	Session 1	213nm	MDC Mica - 8	39.69	0.29	1.0353	0.0067	Session 2	193nm
MDC - 13	41.49	0.28	1.0294	0.008	Session 1	213nm	MDC Mica - 9	39.27	0.27	1.0308	0.0058	Session 2	193nm
MDC - 14	44.95	0.5	1.023	0.011	Session 1	213nm	MDC Mica - 10	39.3	0.32	1.0224	0.0067	Session 2	193nm
MDC - 15	44.83	0.58	1.0276	0.0096	Session 1	213nm	MDC Mica - 11	39.13	0.27	1.0302	0.0068	Session 2	193nm
MDC - 25	43.21	0.49	1.0344	0.0076	Session 1	213nm	MDC Mica - 12	38.93	0.29	1.0239	0.0069	Session 2	193nm
MDC - 26	42.83	0.44	1.0347	0.007	Session 1	213nm	MDC Mica - 13	40.1	0.32	1.0314	0.0067	Session 2	193nm
MDC - 27	44.02	0.48	1.0299	0.0082	Session 1	213nm	MDC Mica - 14	39.71	0.32	1.0384	0.0062	Session 2	193nm
MDC - 34	43.46	0.48	1.0324	0.0088	Session 1	213nm	MDC Mica - 15	39.44	0.3	1.0312	0.0061	Session 2	193nm
MDC - 35	43.76	0.51	1.0381	0.009	Session 1	213nm	MDC Mica - 16	39.7	0.26	1.0208	0.0065	Session 2	193nm
MDC - 36	44.07	0.5	1.0433	0.0094	Session 1	213nm	MDC Mica - 17	39.34	0.28	1.0298	0.0072	Session 2	193nm
MDC - 37	43.42	0.34	1.0331	0.0073	Session 1	213nm	MDC Mica - 18	39.37	0.29	1.0301	0.0068	Session 2	193nm
MDC - 38	45.21	0.62	1.0425	0.008	Session 1	213nm	MDC Mica - 19	39.69	0.3	1.0257	0.0065	Session 2	193nm
MDC - 39	45.08	0.6	1.0208	0.0086	Session 1	213nm	MDC Mica - 20	39.9	0.31	1.0325	0.0067	Session 2	193nm
MDC-mineral - 1.d	40.79	0.3	1.0324	0.007	Session 1	193nm	MDC Mica - 21	40.71	0.34	1.0267	0.008	Session 2	193nm
MDC-mineral - 2.d	41.83	0.28	1.0326	0.0082	Session 1	193nm	MDC Mica - 22	39.64	0.27	1.0219	0.0072	Session 2	193nm
MDC-mineral - 3.d	41.32	0.28	1.0313	0.0074	Session 1	193nm	MDC Mica - 23	40.39	0.3	1.0309	0.0078	Session 2	193nm
MDC-mineral - 4.d	41.27	0.3	1.036	0.0074	Session 1	193nm	MDC Mica - 24	39.17	0.31	1.0265	0.0064	Session 2	193nm
MDC-mineral - 5.d	41.8	0.27	1.0406	0.0069	Session 1	193nm	MDC Mica - 25	39.36	0.28	1.0281	0.0065	Session 2	193nm
MDC-mineral - 6.d	41.64	0.35	1.0384	0.0076	Session 1	193nm	MDC Mica - 26	39.49	0.3	1.0353	0.0066	Session 2	193nm
MDC-mineral - 7.d	41.8	0.28	1.036	0.0064	Session 1	193nm	MDC Mica - 27	39.36	0.33	1.0298	0.0067	Session 2	193nm
MDC-mineral - 8.d	41.99	0.28	1.0285	0.0071	Session 1	193nm	MDC Mica - 28	40.29	0.28	1.0341	0.0072	Session 2	193nm
MDC-mineral - 9.d	41.82	0.31	1.0254	0.0073	Session 1	193nm	MDC Mica - 29	39.88	0.29	1.0277	0.0069	Session 2	193nm
MDC-mineral - 10.d	41.79	0.32	1.0354	0.007	Session 1	193nm	MDC Mica - 30	40.25	0.34	1.0306	0.0064	Session 2	193nm
MDC-mineral - 11.d	42.37	0.3	1.0326	0.0074	Session 1	193nm	MDC Mica - 31	40.19	0.38	1.0373	0.0062	Session 2	193nm

Continued on next page

Table 2.B $^{87}Rb/^{86}Sr$ and $^{87}Sr/^{86}Sr$ isotopic ratios for MDC analysed by LA-ICP-MS/MS over multiple sessions and normalised to Mica-Mg-NP reference material, using either a 193 nm or 213 nm laser ablation system

Continued from previous page

spot	$^{87}Rb/^{86}Sr$	2SE	$^{87}Sr/^{86}Sr$	2SE	Session	LA	spot	$^{87}Rb/^{86}Sr$	2SE	$^{87}Sr/^{86}Sr$	2SE	Session	LA
MDC-mineral - 12.d	42.11	0.35	1.024	0.0078	Session 1	193nm	MDC Mica - 32	41.16	0.37	1.0315	0.0072	Session 2	193nm
MDC Mica - 1	38.38	0.36	1.0303	0.0073	Session 2	193nm	MDC Mica - 33	40.31	0.35	1.0295	0.007	Session 2	193nm
MDC Mica - 2	38.52	0.33	1.034	0.0079	Session 2	193nm	MDC Mica - 34	39.38	0.28	1.0236	0.0064	Session 2	193nm
MDC Mica - 3	38.51	0.28	1.0308	0.0059	Session 2	193nm	MDC Mica - 35	39.24	0.3	1.0246	0.0064	Session 2	193nm
MDC Mica - 4	39.67	0.29	1.0342	0.0078	Session 2	193nm	MDC Mica - 36	38.74	0.33	1.0238	0.0067	Session 2	193nm
MDC Mica - 5	39.25	0.28	1.028	0.0084	Session 2	193nm	MDC Mica - 38	39.49	0.28	1.0197	0.0072	Session 2	193nm
MDC Mica - 39	40.44	0.36	1.025	0.0076	Session 2	193nm	MDC Mica - 8	40.4	0.28	1.0258	0.0074	Session 3	193nm
MDC Mica - 40	39.61	0.3	1.0302	0.0065	Session 2	193nm	MDC Mica - 9	40.61	0.31	1.031	0.0077	Session 3	193nm
MDC Mica - 41	39.42	0.29	1.0216	0.0056	Session 2	193nm	MDC Mica - 10	40.53	0.28	1.0231	0.0073	Session 3	193nm
MDC Mica - 42	39.24	0.29	1.0193	0.0066	Session 2	193nm	MDC Mica - 11	40.46	0.27	1.0268	0.0081	Session 3	193nm
MDC Mica - 43	39.9	0.3	1.0309	0.0058	Session 2	193nm	MDC Mica - 12	39.64	0.25	1.0313	0.0077	Session 3	193nm
MDC Mica - 44	40.41	0.28	1.0342	0.0059	Session 2	193nm	MDC Mica - 13	40.03	0.25	1.0282	0.0077	Session 3	193nm
MDC Mica - 45	40.65	0.31	1.0281	0.0059	Session 2	193nm	MDC Mica - 14	40.42	0.32	1.0254	0.0074	Session 3	193nm
MDC Mica - 46	41.11	0.3	1.0275	0.0062	Session 2	193nm	MDC Mica - 15	40.61	0.31	1.0197	0.0081	Session 3	193nm
MDC Mica - 47	41.02	0.35	1.033	0.0068	Session 2	193nm	MDC Mica - 16	40.54	0.28	1.0204	0.008	Session 3	193nm
MDC Mica - 48	41.15	0.39	1.0362	0.007	Session 2	193nm	MDC Mica - 17	41.59	0.3	1.0269	0.0079	Session 3	193nm
5-MDS mica	45.38	0.48	1.055	0.015	Session 2	213nm	MDC Mica - 18	41.75	0.37	1.0328	0.0076	Session 3	193nm
6-MDS mica	44.81	0.38	1.0485	0.0071	Session 2	213nm	MDC Mica - 19	41.87	0.36	1.0279	0.0081	Session 3	193nm
7-MDS mica	45.16	0.4	1.05	0.011	Session 2	213nm	MDC Mica - 20	41.16	0.32	1.0289	0.0086	Session 3	193nm
8-MDS mica	45.28	0.35	1.05	0.01	Session 2	213nm	MDC Mica - 21	41.91	0.27	1.0298	0.0087	Session 3	193nm
25-MDS mica	43.8	0.47	1.032	0.0063	Session 2	213nm	MDC Mica - 22	41.61	0.38	1.0265	0.0074	Session 3	193nm
26-MDS mica	42.91	0.49	1.0413	0.009	Session 2	213nm	MDC Mica - 23	40.8	0.32	1.0308	0.0074	Session 3	193nm
27-MDS mica	42.77	0.38	1.031	0.017	Session 2	213nm	MDC Mica - 24	41.88	0.44	1.0299	0.0086	Session 3	193nm
28-MDS mica	43.52	0.41	1.037	0.011	Session 2	213nm	MDCMICA - 1	40.66	0.29	1.0225	0.0077	Session 3	193nm
45-MDS mica	45.74	0.48	1.0492	0.0097	Session 2	213nm	MDCMICA - 2	40.33	0.32	1.0349	0.0072	Session 3	193nm
46-MDS mica	45.51	0.45	1.056	0.014	Session 2	213nm	MDCMICA - 3	40.62	0.33	1.036	0.011	Session 3	193nm
47-MDS mica	45.11	0.47	1.0501	0.009	Session 2	213nm	MDC - 1	41.2	0.3	1.0361	0.0084	Session 4	193nm
48-MDS mica	46.17	0.61	1.052	0.012	Session 2	213nm	MDC - 2	39.69	0.21	1.0269	0.0062	Session 4	193nm

Continued on next page

Table 2.B $^{87}Rb/^{86}Sr$ and $^{87}Sr/^{86}Sr$ isotopic ratios for MDC analysed by LA-ICP-MS/MS over multiple sessions and normalised to Mica-Mg-NP reference material, using either a 193 nm or 213 nm laser ablation system

Continued from previous page

spot	$^{87}Rb/^{86}Sr$	2SE	$^{87}Sr/^{86}Sr$	2SE	Session	LA	spot	$^{87}Rb/^{86}Sr$	2SE	$^{87}Sr/^{86}Sr$	2SE	Session	LA
63-MDS mica	42.53	0.44	1.032	0.0095	Session 2	213nm	MDC - 3	40.69	0.26	1.0208	0.0081	Session 4	193nm
64-MDS mica	42.76	0.44	1.024	0.013	Session 2	213nm	MDC - 4	40.48	0.35	1.0359	0.0066	Session 4	193nm
65-MDS mica	43.12	0.51	1.034	0.011	Session 2	213nm	MDC - 5	40.49	0.24	1.0315	0.0063	Session 4	193nm
66-MDS mica	42.76	0.42	1.027	0.012	Session 2	213nm	MDC - 6	39.96	0.26	1.033	0.0082	Session 4	193nm
MDC Mica - 1	38.15	0.4	1.0297	0.0084	Session 3	193nm	MDC - 7	40.33	0.29	1.0342	0.0066	Session 4	193nm
MDC Mica - 2	38.87	0.31	1.0311	0.0079	Session 3	193nm	MDC - 8	40.08	0.27	1.0388	0.0066	Session 4	193nm
MDC Mica - 3	38.58	0.27	1.0276	0.007	Session 3	193nm	MDC - 9	39.98	0.26	1.034	0.0062	Session 4	193nm
MDC Mica - 4	39.89	0.28	1.0292	0.0079	Session 3	193nm	MDC - 10	39.74	0.27	1.0317	0.006	Session 4	193nm
MDC Mica - 5	40.35	0.26	1.0345	0.0081	Session 3	193nm	MDC - 11	40.23	0.3	1.0329	0.0052	Session 4	193nm
MDC Mica - 6	40.11	0.27	1.0323	0.0064	Session 3	193nm	MDC - 12	39.96	0.29	1.034	0.0064	Session 4	193nm
MDC Mica - 7	41.11	0.31	1.04	0.0074	Session 3	193nm	MDC - 13	40.75	0.31	1.0338	0.0063	Session 4	193nm
MDC - 14	40.13	0.33	1.0333	0.0067	Session 4	193nm	MDC - 47	41.51	0.39	1.0428	0.0074	Session 4	193nm
MDC - 15	40.45	0.41	1.0304	0.0061	Session 4	193nm	MDC - 48	40.41	0.29	1.0339	0.007	Session 4	193nm
MDC - 16	39.58	0.34	1.031	0.0056	Session 4	193nm	MDC - 49	39.92	0.3	1.0316	0.0052	Session 4	193nm
MDC - 17	41.42	0.4	1.0279	0.0069	Session 4	193nm	MDC - 50	40.2	0.39	1.0274	0.0056	Session 4	193nm
MDC - 18	41.54	0.34	1.0385	0.0089	Session 4	193nm	MDC - 51	40.6	0.41	1.0267	0.0057	Session 4	193nm
MDC - 19	42.15	0.3	1.0442	0.0072	Session 4	193nm	MDC 1 - 1	43.26	0.27	1.0513	0.0073	Session 4	193nm
MDC - 20	41.97	0.25	1.0383	0.0083	Session 4	193nm	MDC 1 - 2	42.46	0.27	1.0462	0.0071	Session 4	193nm
MDC - 21	41.46	0.3	1.0385	0.008	Session 4	193nm	MDC 1 - 3	42.3	0.26	1.0517	0.0066	Session 4	193nm
MDC - 22	40.9	0.26	1.0357	0.0064	Session 4	193nm	MDC 1 - 4	42.36	0.27	1.0453	0.0058	Session 4	193nm
MDC - 23	40.67	0.27	1.0282	0.0081	Session 4	193nm	MDC 1 - 5	42.84	0.28	1.0544	0.0065	Session 4	193nm
MDC - 24	40.83	0.33	1.0358	0.0063	Session 4	193nm	MDC 1 - 6	43.29	0.24	1.0481	0.0063	Session 4	193nm
MDC - 25	41.07	0.35	1.0346	0.0069	Session 4	193nm	MDC 1 - 7	43.23	0.26	1.0531	0.0071	Session 4	193nm
MDC - 26	40.86	0.33	1.0307	0.0074	Session 4	193nm	MDC 1 - 8	42.58	0.25	1.0545	0.0062	Session 4	193nm
MDC - 27	40.74	0.29	1.0316	0.0073	Session 4	193nm	MDC 1 - 9	42.74	0.26	1.0557	0.0066	Session 4	193nm
MDC - 28	40.41	0.3	1.03	0.0072	Session 4	193nm	MDC 1 - 10	42.93	0.27	1.065	0.0065	Session 4	193nm
MDC - 29	40.91	0.34	1.029	0.0068	Session 4	193nm	MDC 2 - 1	41.56	0.35	1.0416	0.0062	Session 4	193nm
MDC - 30	40.81	0.28	1.0337	0.0065	Session 4	193nm	MDC 2 - 2	40.83	0.29	1.0371	0.007	Session 4	193nm

Continued on next page

Table 2.B $^{87}Rb/^{86}Sr$ and $^{87}Sr/^{86}Sr$ isotopic ratios for MDC analysed by LA-ICP-MS/MS over multiple sessions and normalised to Mica-Mg-NP reference material, using either a 193 nm or 213 nm laser ablation system

Continued from previous page

spot	$^{87}Rb/^{86}Sr$	2SE	$^{87}Sr/^{86}Sr$	2SE	Session	LA	spot	$^{87}Rb/^{86}Sr$	2SE	$^{87}Sr/^{86}Sr$	2SE	Session	LA
MDC - 31	40.86	0.32	1.0273	0.0065	Session 4	193nm	MDC 2 - 3	40.56	0.31	1.0386	0.0062	Session 4	193nm
MDC - 32	41.96	0.47	1.0335	0.0089	Session 4	193nm	MDC 2 - 4	40.5	0.27	1.0344	0.0059	Session 4	193nm
MDC - 33	42.27	0.44	1.0314	0.0057	Session 4	193nm	MDC 2 - 5	40.25	0.27	1.0387	0.0056	Session 4	193nm
MDC - 34	41.03	0.35	1.0341	0.0057	Session 4	193nm	MDC 2 - 6	40.45	0.3	1.0343	0.0061	Session 4	193nm
MDC - 35	41.24	0.35	1.0317	0.0069	Session 4	193nm	MDC 2 - 7	40.88	0.3	1.0308	0.0057	Session 4	193nm
MDC - 36	40.9	0.38	1.0391	0.0074	Session 4	193nm	MDC 2 - 8	42.3	0.29	1.0425	0.0073	Session 4	193nm
MDC - 37	40.34	0.38	1.0285	0.007	Session 4	193nm	MDC 2 - 9	41.3	0.32	1.0404	0.0063	Session 4	193nm
MDC - 38	40.75	0.36	1.0339	0.0075	Session 4	193nm	MDC 2 - 10	40.17	0.29	1.0369	0.0058	Session 4	193nm
MDC - 39	39.86	0.31	1.0235	0.0064	Session 4	193nm	MDC 3 - 1	41.58	0.26	1.0385	0.0072	Session 4	193nm
MDC - 40	40.01	0.35	1.0325	0.0079	Session 4	193nm	MDC 3 - 2	41.43	0.26	1.0358	0.0084	Session 4	193nm
MDC - 41	40.95	0.43	1.0188	0.0098	Session 4	193nm	MDC 3 - 3	41.45	0.23	1.0354	0.0073	Session 4	193nm
MDC - 42	41.01	0.36	1.0237	0.0096	Session 4	193nm	MDC 3 - 4	41.65	0.26	1.0417	0.0071	Session 4	193nm
MDC - 43	40.92	0.43	1.0366	0.0076	Session 4	193nm	MDC 3 - 5	41.24	0.28	1.0394	0.0078	Session 4	193nm
MDC - 44	41.47	0.39	1.0363	0.0077	Session 4	193nm	MDC 3 - 6	41.12	0.25	1.0406	0.0064	Session 4	193nm
MDC - 45	40.74	0.35	1.0364	0.0067	Session 4	193nm	MDC 3 - 7	41.62	0.32	1.037	0.0075	Session 4	193nm
MDC - 46	41.5	0.41	1.0402	0.008	Session 4	193nm	MDC 3 - 8	41.5	0.31	1.0369	0.0073	Session 4	193nm
MDC 3 - 9	41.94	0.26	1.0403	0.008	Session 4	193nm	MDC - 27	40.29	0.45	1.0311	0.0081	Session 5	193nm
MDC 3 - 10	41.6	0.33	1.0434	0.0072	Session 4	193nm	MDC - 28	40.56	0.49	1.0367	0.0079	Session 5	193nm
MDC 4 - 1	43.92	0.26	1.0265	0.0068	Session 4	193nm	MDC - 29	40.69	0.46	1.0378	0.0064	Session 5	193nm
MDC 4 - 2	42.86	0.32	1.0409	0.0079	Session 4	193nm	MDC - 30	40.65	0.51	1.0328	0.0071	Session 5	193nm
MDC 4 - 3	43.88	0.28	1.0441	0.0089	Session 4	193nm	MDC - 31	41.52	0.39	1.0262	0.0072	Session 5	193nm
MDC 4 - 4	44.2	0.27	1.0426	0.0076	Session 4	193nm	MDC - 32	41.99	0.49	1.0346	0.0091	Session 5	193nm
MDC 4 - 5	41.93	0.26	1.0361	0.0071	Session 4	193nm	MDC - 33	42.02	0.34	1.0304	0.0084	Session 5	193nm
MDC 4 - 6	42.6	0.27	1.0493	0.0067	Session 4	193nm	MDC - 34	41.63	0.43	1.0314	0.0076	Session 5	193nm
MDC 4 - 7	43.42	0.3	1.0405	0.0076	Session 4	193nm	MDC - 35	41.59	0.41	1.0285	0.0083	Session 5	193nm
MDC 4 - 8	44.59	0.35	1.0503	0.0081	Session 4	193nm	MDC - 36	41.72	0.35	1.041	0.0076	Session 5	193nm
MDC 4 - 9	43.57	0.33	1.0403	0.0096	Session 4	193nm	MDC - 37	41.93	0.38	1.0376	0.0086	Session 5	193nm
MDC 4 - 10	44.76	0.35	1.0395	0.0079	Session 4	193nm	MDC - 38	42	0.37	1.0362	0.0088	Session 5	193nm

Continued on next page

Table 2.B $^{87}Rb/^{86}Sr$ and $^{87}Sr/^{86}Sr$ isotopic ratios for MDC analysed by LA-ICP-MS/MS over multiple sessions and normalised to Mica-Mg-NP reference material, using either a 193 nm or 213 nm laser ablation system

Continued from previous page

spot	$^{87}Rb/^{86}Sr$	2SE	$^{87}Sr/^{86}Sr$	2SE	Session	LA	spot	$^{87}Rb/^{86}Sr$	2SE	$^{87}Sr/^{86}Sr$	2SE	Session	LA
MDC 5 - 1	41.39	0.25	1.0299	0.0065	Session 4	193nm	MDC - 39	41.32	0.46	1.0302	0.0072	Session 5	193nm
MDC 5 - 2	42.13	0.28	1.0381	0.0071	Session 4	193nm	MDC - 40	41.75	0.42	1.0392	0.008	Session 5	193nm
MDC 5 - 3	41.92	0.28	1.0386	0.0057	Session 4	193nm	MDC - 41	42.06	0.4	1.0303	0.0086	Session 5	193nm
MDC 5 - 4	41.32	0.27	1.0396	0.0067	Session 4	193nm	MDC - 42	41.78	0.4	1.036	0.0068	Session 5	193nm
MDC 5 - 5	41.17	0.25	1.0396	0.0068	Session 4	193nm	MDC - 43	41.2	0.4	1.026	0.0063	Session 5	193nm
MDC 5 - 6	40.87	0.28	1.0345	0.0063	Session 4	193nm	MDC - 44	41.65	0.42	1.0416	0.0069	Session 5	193nm
MDC 5 - 7	41.59	0.3	1.0397	0.0073	Session 4	193nm	MDC - 45	41.06	0.44	1.0347	0.0083	Session 5	193nm
MDC 5 - 8	41.64	0.27	1.0398	0.0067	Session 4	193nm	MDC - 46	41.47	0.52	1.0353	0.0073	Session 5	193nm
MDC 5 - 9	41.92	0.27	1.0363	0.0071	Session 4	193nm	MDC - 47	41.87	0.55	1.0427	0.0063	Session 5	193nm
MDC 5 - 10	42.13	0.27	1.0465	0.0069	Session 4	193nm	MDC - 48	41.46	0.5	1.0376	0.0069	Session 5	193nm
MDC - 16	39.37	0.36	1.0249	0.0072	Session 5	193nm	MDC - 49	40.28	0.32	1.0248	0.0079	Session 5	193nm
MDC - 17	39.86	0.31	1.0219	0.0074	Session 5	193nm	MDC - 50	41.1	0.33	1.0345	0.0086	Session 5	193nm
MDC - 18	40.66	0.33	1.031	0.0082	Session 5	193nm	MDC - 51	41.47	0.39	1.0339	0.0093	Session 5	193nm
MDC - 19	40.39	0.4	1.0276	0.0075	Session 5	193nm	MDC - 1	40.46	0.37	1.0363	0.0058	Session 6	193nm
MDC - 20	40.4	0.36	1.0354	0.0072	Session 5	193nm	MDC - 2	40.19	0.37	1.0387	0.0066	Session 6	193nm
MDC - 21	40.49	0.34	1.0228	0.0093	Session 5	193nm	MDC - 3	39.89	0.36	1.0324	0.0062	Session 6	193nm
MDC - 22	40.44	0.4	1.0301	0.0072	Session 5	193nm	MDC - 4	45.34	0.28	1.0659	0.0072	Session 6	193nm
MDC - 23	40.35	0.35	1.0271	0.0069	Session 5	193nm	MDC - 5	44.46	0.25	1.0593	0.0072	Session 6	193nm
MDC - 24	40.76	0.35	1.0377	0.0073	Session 5	193nm	MDC - 6	45.28	0.36	1.0648	0.0076	Session 6	193nm
MDC - 25	39.81	0.49	1.028	0.0073	Session 5	193nm	MDC - 7	41	0.28	1.0393	0.0074	Session 6	193nm
MDC - 26	40.03	0.49	1.0216	0.0071	Session 5	193nm	MDC - 8	40.62	0.25	1.0201	0.0072	Session 6	193nm
MDC - 9	40.65	0.25	1.0151	0.0072	Session 6	193nm	MDC - 42	41.03	0.48	1.0435	0.0057	Session 6	193nm
MDC - 10	40.2	0.27	1.0166	0.0064	Session 6	193nm	MDC - 43	40.68	0.41	1.035	0.0059	Session 6	193nm
MDC - 11	40.61	0.32	1.0141	0.006	Session 6	193nm	MDC - 44	40.71	0.44	1.044	0.0062	Session 6	193nm
MDC - 12	40.73	0.34	1.0332	0.0071	Session 6	193nm	MDC - 45	40.66	0.4	1.0313	0.006	Session 6	193nm
MDC - 13	40.32	0.36	1.021	0.0055	Session 6	193nm	MDC - 46	40.58	0.45	1.0367	0.0062	Session 6	193nm
MDC - 14	40.19	0.42	1.0183	0.0061	Session 6	193nm	MDC - 47	40.21	0.43	1.0382	0.0061	Session 6	193nm
MDC - 15	40.08	0.47	1.0246	0.0063	Session 6	193nm	MDC - 48	40.92	0.47	1.0398	0.0062	Session 6	193nm

Continued on next page

Table 2.B $^{87}Rb/^{86}Sr$ and $^{87}Sr/^{86}Sr$ isotopic ratios for MDC analysed by LA-ICP-MS/MS over multiple sessions and normalised to Mica-Mg-NP reference material, using either a 193 nm or 213 nm laser ablation system

Continued from previous page

spot	$^{87}Rb/^{86}Sr$	2SE	$^{87}Sr/^{86}Sr$	2SE	Session	LA	spot	$^{87}Rb/^{86}Sr$	2SE	$^{87}Sr/^{86}Sr$	2SE	Session	LA
MDC - 16	40.25	0.38	1.0267	0.0066	Session 6	193nm	MDC - 49	40.91	0.43	1.0438	0.0066	Session 6	193nm
MDC - 17	40.35	0.38	1.0189	0.006	Session 6	193nm	MDC - 50	40.53	0.38	1.0402	0.0057	Session 6	193nm
MDC - 18	40.29	0.45	1.0421	0.0066	Session 6	193nm	MDC - 51	40.35	0.38	1.0308	0.0059	Session 6	193nm
MDC - 19	39.99	0.41	1.0343	0.0069	Session 6	193nm	MDC - 52	39.92	0.45	1.0298	0.0064	Session 6	193nm
MDC - 20	40.02	0.41	1.0323	0.0066	Session 6	193nm	MDC - 53	40.03	0.37	1.0333	0.0063	Session 6	193nm
MDC - 21	40.9	0.45	1.0273	0.0069	Session 6	193nm	MDC - 54	40.26	0.45	1.0376	0.006	Session 6	193nm
MDC - 22	40.69	0.44	1.0251	0.0061	Session 6	193nm	MDC - 55	40.4	0.45	1.0348	0.0059	Session 6	193nm
MDC - 23	40.6	0.39	1.0367	0.0068	Session 6	193nm	MDC - 56	39.59	0.41	1.0331	0.0058	Session 6	193nm
MDC - 24	40.42	0.39	1.0318	0.0056	Session 6	193nm	MDC - 57	40	0.43	1.0353	0.0057	Session 6	193nm
MDC - 25	39.93	0.42	1.0367	0.0059	Session 6	193nm	MDC - 58	39.86	0.41	1.0338	0.006	Session 6	193nm
MDC - 26	40.15	0.39	1.0399	0.0065	Session 6	193nm	MDC - 59	39.29	0.53	1.0374	0.006	Session 6	193nm
MDC - 27	40.3	0.44	1.0289	0.0064	Session 6	193nm	MDC - 60	40.01	0.4	1.0409	0.0065	Session 6	193nm
MDC - 28	40.05	0.38	1.026	0.0068	Session 6	193nm	MDC - 61	40.22	0.44	1.0433	0.0058	Session 6	193nm
MDC - 29	40.44	0.41	1.0332	0.0063	Session 6	193nm	MDC - 62	40.15	0.42	1.0355	0.0062	Session 6	193nm
MDC - 30	40.15	0.4	1.0264	0.0061	Session 6	193nm	MDC - 63	40.41	0.41	1.0414	0.0057	Session 6	193nm
MDC - 31	40.5	0.39	1.0403	0.0063	Session 6	193nm	MDC - 64	40.63	0.41	1.04	0.0058	Session 6	193nm
MDC - 32	40.09	0.45	1.032	0.006	Session 6	193nm	MDC - 65	39.86	0.42	1.0348	0.0054	Session 6	193nm
MDC - 33	40.42	0.41	1.0301	0.0057	Session 6	193nm	MDC - 66	40.14	0.47	1.0338	0.0064	Session 6	193nm
MDC - 34	40.53	0.42	1.0375	0.0059	Session 6	193nm	MDC - 67	39.76	0.46	1.034	0.0065	Session 6	193nm
MDC - 35	40.56	0.38	1.0403	0.0056	Session 6	193nm	MDC - 68	39.83	0.41	1.0397	0.0067	Session 6	193nm
MDC - 36	40.47	0.47	1.0361	0.0063	Session 6	193nm	MDC - 69	39.76	0.43	1.0319	0.0065	Session 6	193nm
MDC - 37	40.6	0.46	1.0366	0.0057	Session 6	193nm	MDC - 1	40.45	0.32	1.041	0.01	Session 7	193nm
MDC - 38	40.78	0.35	1.0304	0.0063	Session 6	193nm	MDC - 2	40.13	0.28	1.047	0.01	Session 7	193nm
MDC - 39	40.64	0.41	1.0291	0.0065	Session 6	193nm	MDC - 3	40	0.24	1.0395	0.0081	Session 7	193nm
MDC - 40	40.9	0.45	1.0321	0.0057	Session 6	193nm	MDC - 4	39.84	0.28	1.034	0.01	Session 7	193nm
MDC - 41	40.77	0.46	1.037	0.0053	Session 6	193nm	MDC - 5	39.85	0.28	1.0313	0.0089	Session 7	193nm
MDC - 6	39.34	0.27	1.0328	0.0074	Session 7	193nm	MDC - 39	39.5	0.29	1.0311	0.008	Session 7	193nm
MDC - 7	39.73	0.29	1.033	0.011	Session 7	193nm	MDC - 1	40.58	0.28	1.0269	0.0082	Session 8	193nm

Continued on next page

Table 2.B $^{87}Rb/^{86}Sr$ and $^{87}Sr/^{86}Sr$ isotopic ratios for MDC analysed by LA-ICP-MS/MS over multiple sessions and normalised to Mica-Mg-NP reference material, using either a 193 nm or 213 nm laser ablation system

Continued from previous page

spot	$^{87}Rb/^{86}Sr$	2SE	$^{87}Sr/^{86}Sr$	2SE	Session	LA	spot	$^{87}Rb/^{86}Sr$	2SE	$^{87}Sr/^{86}Sr$	2SE	Session	LA
MDC - 8	39.72	0.36	1.033	0.014	Session 7	193nm	MDC - 2	40.44	0.33	1.0184	0.0097	Session 8	193nm
MDC - 9	39.69	0.29	1.028	0.0086	Session 7	193nm	MDC - 3	40.83	0.26	1.0377	0.0075	Session 8	193nm
MDC - 10	39.61	0.27	1.0379	0.0072	Session 7	193nm	MDC - 4	40.99	0.32	1.0324	0.0079	Session 8	193nm
MDC - 11	40.08	0.3	1.0323	0.0091	Session 7	193nm	MDC - 5	41.71	0.36	1.045	0.011	Session 8	193nm
MDC - 12	40.32	0.36	1.041	0.01	Session 7	193nm	MDC - 6	41.49	0.32	1.0394	0.0099	Session 8	193nm
MDC - 13	39.09	0.3	1.0403	0.0077	Session 7	193nm	MDC - 7	40.48	0.35	1.0333	0.0079	Session 8	193nm
MDC - 14	38.96	0.33	1.029	0.01	Session 7	193nm	MDC - 8	41.43	0.35	1.0415	0.0082	Session 8	193nm
MDC - 15	39.06	0.24	1.0303	0.0088	Session 7	193nm	MDC - 9	41.37	0.36	1.0279	0.0095	Session 8	193nm
MDC - 16	39.27	0.25	1.0402	0.008	Session 7	193nm	MDC - 10	41.42	0.35	1.035	0.0093	Session 8	193nm
MDC - 17	39.27	0.35	1.04	0.01	Session 7	193nm	MDC - 11	41.5	0.34	1.038	0.01	Session 8	193nm
MDC - 18	38.77	0.29	1.0357	0.0085	Session 7	193nm	MDC - 12	41.48	0.33	1.04	0.0081	Session 8	193nm
MDC - 19	39.24	0.31	1.036	0.0095	Session 7	193nm	MDC - 13	41.68	0.32	1.0451	0.0084	Session 8	193nm
MDC - 20	39.1	0.26	1.0401	0.0098	Session 7	193nm	MDC - 14	40.76	0.3	1.0336	0.0064	Session 8	193nm
MDC - 21	39.36	0.29	1.0392	0.0095	Session 7	193nm	MDC - 15	40.65	0.27	1.0301	0.0089	Session 8	193nm
MDC - 22	39.3	0.25	1.0395	0.0086	Session 7	193nm	MDC - 16	40.65	0.28	1.0405	0.0071	Session 8	193nm
MDC - 23	39.67	0.36	1.04	0.011	Session 7	193nm	MDC - 17	41.2	0.32	1.0366	0.0091	Session 8	193nm
MDC - 24	39.52	0.41	1.036	0.01	Session 7	193nm	MDC - 18	41.28	0.34	1.0309	0.0086	Session 8	193nm
MDC - 25	39.14	0.24	1.0267	0.0084	Session 7	193nm	MDC - 19	40.84	0.37	1.0357	0.0079	Session 8	193nm
MDC - 26	39.81	0.35	1.0389	0.0092	Session 7	193nm	MDC - 20	40.83	0.43	1.0291	0.009	Session 8	193nm
MDC - 27	40.47	0.4	1.03	0.013	Session 7	193nm	MDC - 21	41.1	0.42	1.038	0.009	Session 8	193nm
MDC - 28	39.64	0.33	1.0513	0.0082	Session 7	193nm	MDC - 22	41.93	0.4	1.0261	0.0084	Session 8	193nm
MDC - 29	39.24	0.3	1.0287	0.0095	Session 7	193nm	MDC - 23	41.77	0.39	1.0503	0.0066	Session 8	193nm
MDC - 30	38.9	0.32	1.0267	0.0095	Session 7	193nm	MDC - 24	42.13	0.45	1.0481	0.0085	Session 8	193nm
MDC - 31	39.08	0.27	1.0376	0.0086	Session 7	193nm	MDC - 25	41.66	0.41	1.0413	0.0087	Session 8	193nm
MDC - 32	40.16	0.38	1.031	0.012	Session 7	193nm	MDC - 26	41.89	0.39	1.0326	0.009	Session 8	193nm
MDC - 33	39.14	0.32	1.0287	0.009	Session 7	193nm	MDC - 27	41.11	0.39	1.0306	0.0086	Session 8	193nm
MDC - 34	39.16	0.32	1.0222	0.0095	Session 7	193nm	MDC - 28	40.52	0.29	1.0355	0.0079	Session 8	193nm
MDC - 35	38.71	0.29	1.0303	0.0077	Session 7	193nm	MDC - 29	40.75	0.41	1.0285	0.0085	Session 8	193nm

Continued on next page

Table 2.B $^{87}Rb/^{86}Sr$ and $^{87}Sr/^{86}Sr$ isotopic ratios for MDC analysed by LA-ICP-MS/MS over multiple sessions and normalised to Mica-Mg-NP reference material, using either a 193 nm or 213 nm laser ablation system

Continued from previous page

spot	$^{87}Rb/^{86}Sr$	2SE	$^{87}Sr/^{86}Sr$	2SE	Session	LA	spot	$^{87}Rb/^{86}Sr$	2SE	$^{87}Sr/^{86}Sr$	2SE	Session	LA
MDC - 36	37.94	0.28	1.0242	0.0086	Session 7	193nm	MDC - 30	41.77	0.43	1.034	0.0082	Session 8	193nm
MDC - 37	37.87	0.26	1.0304	0.0076	Session 7	193nm	MDC - 31	40.27	0.34	1.0251	0.0081	Session 8	193nm
MDC - 38	38.07	0.34	1.0266	0.0076	Session 7	193nm	MDC - 32	41.65	0.35	1.0387	0.0079	Session 8	193nm
MDC - 33	41.49	0.5	1.0388	0.0087	Session 8	193nm	MDC - 37	41.23	0.35	1.0412	0.0083	Session 8	193nm
MDC - 34	40.56	0.44	1.0313	0.0067	Session 8	193nm	MDC - 38	41.36	0.42	1.0323	0.0082	Session 8	193nm
MDC - 35	41.28	0.36	1.0362	0.0098	Session 8	193nm	MDC - 39	42.16	0.33	1.0412	0.009	Session 8	193nm
MDC - 36	41.57	0.42	1.0381	0.0078	Session 8	193nm							

Table 2.C: $^{87}Rb/^{86}Sr$ and $^{87}Sr/^{86}Sr$ isotopic ratios for MDC analysed by the LA-ICP-MS/MS using either a 193 nm or 213 nm laser ablation system and normalised to NIST 610 reference material

spot	$^{87}Rb/^{86}Sr$	2SE	$^{87}Sr/^{86}Sr$	2SE	LA
MDCtest - 1	47.57	0.35	1.0298	0.0084	193nm
MDCtest - 3	47.39	0.43	1.031	0.013	193nm
MDCtest - 4	46.26	0.34	1.0202	0.0091	193nm
MDCtest - 5	46.67	0.34	1.0256	0.0091	193nm
MDCtest - 6	46.58	0.34	1.0219	0.0086	193nm
MDCtest - 7	46.21	0.38	1.0313	0.0091	193nm
MDCtest - 8	46.44	0.31	1.0189	0.0092	193nm
MDCtest - 9	47.06	0.36	1.0179	0.0095	193nm
MDCtest - 10	47.46	0.34	1.0323	0.0095	193nm
MDCtest - 11	47.33	0.34	1.0292	0.0089	193nm
MDCtest - 12	47.61	0.32	1.036	0.011	193nm
MDCtest - 13	47.12	0.38	1.0275	0.009	193nm
MDCtest - 14	47.71	0.34	1.0378	0.0068	193nm
MDCtest - 15	47.56	0.35	1.0354	0.0079	193nm
MDCtest - 16	47.43	0.42	1.026	0.012	193nm
MDCtest - 17	48.04	0.42	1.0222	0.0091	193nm
MDCtest - 18	48.1	0.45	1.0228	0.009	193nm
MDCtest - 19	49.09	0.45	1.0321	0.0088	193nm
MDCtest - 2	46.56	0.35	1.0257	0.009	193nm
MDCtest - 20	49.15	0.45	1.0352	0.0078	193nm
MDCtest - 1	50.67	0.56	1.069	0.011	213nm
MDCtest - 3	51.89	0.51	1.068	0.01	213nm
MDCtest - 4	53.63	0.84	1.0703	0.0088	213nm
MDCtest - 5	53.51	0.81	1.054	0.012	213nm
MDCtest - 6	53.6	1.1	1.066	0.012	213nm
MDCtest - 7	53.32	0.79	1.0645	0.0088	213nm
MDCtest - 8	54	1.1	1.066	0.012	213nm
MDCtest - 9	55.3	1.3	1.07	0.011	213nm
MDCtest - 10	54.9	1	1.073	0.013	213nm
MDCtest - 11	53.19	0.89	1.0631	0.0095	213nm
MDCtest - 12	52.63	0.84	1.0635	0.0092	213nm
MDCtest - 13	51.38	0.47	1.06	0.01	213nm
MDCtest - 14	51.69	0.76	1.057	0.012	213nm
MDCtest - 15	51.85	0.61	1.0597	0.009	213nm
MDCtest - 16	52.1	1	1.058	0.011	213nm
MDCtest - 17	53.58	0.91	1.0702	0.009	213nm
MDCtest - 18	53.38	0.75	1.0708	0.0095	213nm
MDCtest - 19	53.03	0.88	1.072	0.011	213nm
MDCtest - 2	51.53	0.43	1.071	0.01	213nm
MDCtest - 20	52.61	0.83	1.0532	0.0097	213nm

Table 2.D: Rb-Sr isotopic ratios of NIST 610 and MDC using 'line raster' sampling approach with the 193nm laser (74 µm diameter). All data is normalised to Mica-Mg-NP reference material.

Line number	$^{87}Rb/^{86}Sr$	2SE	$^{87}Sr/^{86}Sr$	2SE
NIST610line - 1	2.0688	0.0041	0.7106	0.001
NIST610line - 2	2.0859	0.0036	0.71067	0.00086
NIST610line - 3	2.0932	0.0041	0.7104	0.0011
NIST610line - 4	2.1184	0.0035	0.71007	0.00099
NIST610line - 5	2.1259	0.0038	0.71147	0.00097
NIST610line - 6	2.1161	0.0033	0.71067	0.00091
NIST610line - 7	2.1354	0.0037	0.7094	0.001
NIST610line - 8	2.1413	0.0039	0.71044	0.00093
NIST610line - 9	2.145	0.0036	0.70936	0.00089
NIST610line - 10	2.1464	0.0036	0.70847	0.00096
MDC line - 1	37.24	0.14	1.0377	0.0051
MDC line - 2	36.68	0.14	1.032	0.005
MDC line - 3	36.59	0.17	1.0369	0.0053
MDC line - 4	36.75	0.14	1.0351	0.0056
MDC line - 5	36.46	0.18	1.0412	0.0052
MDC line - 6	36.29	0.18	1.0326	0.007
MDC line - 7	36.67	0.18	1.0352	0.005
MDC line - 8	36.4	0.14	1.0281	0.0056
MDC line - 9	36.7	0.14	1.0334	0.0043
MDC line - 10	36.78	0.16	1.0407	0.0055

Table 2.E: Rb-Sr isotopic ratios of Mic-Mg-NP and MDC using 'line raster' sampling approach with the 193nm laser (74 µm diameter). All data is normalised to NIST 610 reference material.

Line number	$^{87}Rb/^{86}Sr$	2SE	$^{87}Sr/^{86}Sr$	2SE
MicaMgline - 1	167.4	1.2	1.849	0.015
MicaMgline - 2	168.3	1.5	1.855	0.014
MicaMgline - 3	168.8	1.4	1.853	0.012
MicaMgline - 4	168.6	1.5	1.853	0.016
MicaMgline - 5	169.7	1.1	1.847	0.014
MicaMgline - 6	171.9	1.1	1.849	0.01
MicaMgline - 7	168.9	1.2	1.852	0.012
MicaMgline - 8	173.4	1.3	1.841	0.011
MicaMgline - 9	171.9	1.3	1.855	0.012
MicaMgline - 10	172.4	1.2	1.86	0.013
MDCline - 1	40.98	0.15	1.0371	0.0051
MDCline - 2	40.26	0.19	1.0363	0.0053
MDCline - 3	40.44	0.15	1.0345	0.0056
MDCline - 4	40.12	0.2	1.0406	0.0052
MDCline - 5	39.93	0.19	1.032	0.007
MDCline - 6	40.35	0.2	1.0345	0.005
MDCline - 7	40.05	0.16	1.0274	0.0056
MDCline - 8	40.39	0.16	1.0327	0.0043
MDCline - 9	40.47	0.17	1.0401	0.0055
MDCline - 10	40.36	0.15	1.0313	0.005

Table 2.F: Rb-Sr ratios of NIST 610 analysed by the LA-ICP-MS/MS over multiple Sessions using the 193 nm laser systems and normalised to Mica Mg-NP reference material.

spot	$^{87}Rb/^{86}Sr$	2SE	$^{87}Sr/^{86}Sr$	2SE	Session	LA	spot	$^{87}Rb/^{86}Sr$	2SE	$^{87}Sr/^{86}Sr$	2SE	Session	LA
NIST610 - 1	1.9973	0.0054	0.7125	0.0014	Session 1	193nm	NIST610 - 21	1.9649	0.0077	0.7095	0.0017	Session 2	193nm
NIST610 - 2	1.9904	0.0049	0.7109	0.0012	Session 1	193nm	NIST610 - 22	1.9595	0.0075	0.7089	0.0017	Session 2	193nm
NIST610 - 3	2.0093	0.0051	0.7116	0.0012	Session 1	193nm	NIST610 - 23	1.9677	0.0069	0.709	0.0015	Session 2	193nm
NIST610 - 4	2.0005	0.0056	0.7113	0.0013	Session 1	193nm	NIST610 - 24	1.9621	0.0078	0.7098	0.0023	Session 2	193nm
NIST610 - 5	2.0149	0.0049	0.7112	0.0013	Session 1	193nm	NIST610 - 25	1.9681	0.0078	0.7092	0.0018	Session 2	193nm
NIST610 - 6	2.0064	0.0055	0.7126	0.0013	Session 1	193nm	NIST610 - 26	1.9641	0.0076	0.7084	0.0017	Session 2	193nm
NIST610 - 7	2.0293	0.0053	0.7106	0.0013	Session 1	193nm	NIST610 - 27	1.973	0.0083	0.7095	0.0019	Session 2	193nm
NIST610 - 8	2.025	0.0055	0.7116	0.0012	Session 1	193nm	NIST610 - 28	1.9737	0.007	0.7091	0.0016	Session 2	193nm
NIST610 - 9	2.0458	0.0054	0.7101	0.0013	Session 1	193nm	NIST610 - 29	1.9777	0.008	0.7104	0.0021	Session 2	193nm
NIST610 - 10	2.0304	0.0061	0.7113	0.0013	Session 1	193nm	NIST610 - 30	1.9786	0.0073	0.7091	0.0018	Session 2	193nm
NIST610 - 11	2.069	0.0061	0.7117	0.0013	Session 1	193nm	NIST610 - 31	1.9829	0.0075	0.7087	0.0016	Session 2	193nm
NIST610 - 12	2.0529	0.0058	0.7113	0.0014	Session 1	193nm	NIST610 - 32	1.9732	0.008	0.7113	0.0037	Session 2	193nm
NIST610 - 1	1.8944	0.0096	0.71	0.0022	Session 2	193nm	NIST610 - 1	1.8711	0.007	0.7083	0.0021	Session 3	193nm
NIST610 - 2	1.9021	0.0081	0.7085	0.002	Session 2	193nm	NIST610 - 2	1.8687	0.0081	0.7087	0.0019	Session 3	193nm
NIST610 - 3	1.9218	0.0084	0.7099	0.0019	Session 2	193nm	NIST610 - 3	1.9346	0.0082	0.7085	0.0021	Session 3	193nm
NIST610 - 4	1.9198	0.0078	0.7105	0.0019	Session 2	193nm	NIST610 - 4	1.9261	0.0074	0.7092	0.0019	Session 3	193nm
NIST610 - 5	1.9322	0.0085	0.7099	0.0024	Session 2	193nm	NIST610 - 5	1.965	0.0074	0.7072	0.0017	Session 3	193nm
NIST610 - 6	1.9303	0.0084	0.7118	0.0038	Session 2	193nm	NIST610 - 6	1.9557	0.0087	0.7115	0.0038	Session 3	193nm
NIST610 - 7	1.9405	0.0089	0.7094	0.0018	Session 2	193nm	NIST610 - 7	1.9424	0.0078	0.707	0.0018	Session 3	193nm
NIST610 - 8	1.9374	0.0085	0.7103	0.0016	Session 2	193nm	NIST610 - 8	1.9397	0.0068	0.7088	0.0019	Session 3	193nm
NIST610 - 9	1.9526	0.0071	0.7089	0.0017	Session 2	193nm	NIST610 - 9	1.9593	0.0076	0.7078	0.0018	Session 3	193nm
NIST610 - 10	1.9369	0.0078	0.7087	0.0018	Session 2	193nm	NIST610 - 10	1.9561	0.0084	0.7082	0.0018	Session 3	193nm
NIST610 - 11	1.9452	0.0083	0.7094	0.0016	Session 2	193nm	NIST610 - 11	1.9951	0.0083	0.7071	0.0019	Session 3	193nm
NIST610 - 12	1.9462	0.0077	0.7096	0.0018	Session 2	193nm	NIST610 - 12	1.9844	0.0083	0.7085	0.002	Session 3	193nm
NIST610 - 13	1.9558	0.0079	0.7088	0.0018	Session 2	193nm	NIST610 - 13	1.9879	0.0087	0.7083	0.0019	Session 3	193nm
NIST610 - 14	1.9487	0.0079	0.712	0.003	Session 2	193nm	NIST610 - 14	1.9859	0.0079	0.7083	0.0019	Session 3	193nm

Continued on next page

Table 2.F Rb-Sr ratios of NIST 610 analysed by the LA-ICP-MS/MS over multiple Sessions using the 193 nm laser systems and normalised to Mica Mg-NP reference material.

Continued from previous page

spot	$^{87}Rb/^{86}Sr$	2SE	$^{87}Sr/^{86}Sr$	2SE	Session	LA	spot	$^{87}Rb/^{86}Sr$	2SE	$^{87}Sr/^{86}Sr$	2SE	Session	LA
NIST610 - 15	1.9607	0.0075	0.7085	0.0018	Session 2	193nm	NIST610 - 15	1.9591	0.0088	0.7082	0.002	Session 3	193nm
NIST610 - 16	1.9503	0.0081	0.7086	0.0018	Session 2	193nm	NIST610 - 16	1.9647	0.0082	0.7089	0.0019	Session 3	193nm
NIST610 - 17	1.964	0.0077	0.7082	0.0015	Session 2	193nm	NIST610 - 17	1.9687	0.0074	0.7104	0.002	Session 3	193nm
NIST610 - 18	1.959	0.0071	0.7091	0.0015	Session 2	193nm	NIST610 - 18	1.9589	0.0074	0.7078	0.0019	Session 3	193nm
NIST610 - 19	1.9601	0.0074	0.7099	0.0022	Session 2	193nm	NIST610 - 1	1.9795	0.0061	0.7113	0.0014	Session 4	193nm
NIST610 - 20	1.9552	0.0078	0.7095	0.002	Session 2	193nm	NIST610 - 2	1.9773	0.0057	0.7115	0.0012	Session 4	193nm
NIST610 - 3	1.991	0.006	0.7106	0.0013	Session 4	193nm	NIST610 - 2	2.0247	0.0074	0.7085	0.0018	Session 5	193nm
NIST610 - 4	1.9884	0.0058	0.7112	0.0013	Session 4	193nm	NIST610 - 3	2.0453	0.0076	0.7096	0.0019	Session 5	193nm
NIST610 - 5	1.9973	0.0059	0.7119	0.0012	Session 4	193nm	NIST610 - 4	2.0304	0.0075	0.7095	0.0016	Session 5	193nm
NIST610 - 6	1.9949	0.0061	0.7111	0.0015	Session 4	193nm	NIST610 - 5	2.0385	0.0076	0.7093	0.0018	Session 5	193nm
NIST610 - 7	2.0003	0.006	0.7106	0.0014	Session 4	193nm	NIST610 - 6	2.0381	0.0074	0.7105	0.0016	Session 5	193nm
NIST610 - 8	1.9946	0.0067	0.7116	0.0013	Session 4	193nm	NIST610 - 7	2.0454	0.0075	0.7101	0.0018	Session 5	193nm
NIST610 - 9	1.997	0.0062	0.7114	0.0015	Session 4	193nm	NIST610 - 8	2.0363	0.0072	0.7115	0.0016	Session 5	193nm
NIST610 - 10	1.9902	0.0064	0.7116	0.0013	Session 4	193nm	NIST610 - 9	2.0502	0.0075	0.7099	0.0017	Session 5	193nm
NIST610 - 11	1.9973	0.0065	0.7108	0.0014	Session 4	193nm	NIST610 - 10	2.0475	0.0068	0.7103	0.0016	Session 5	193nm
NIST610 - 12	1.9951	0.0067	0.7117	0.0015	Session 4	193nm	NIST610 - 11	2.0482	0.0073	0.7087	0.0018	Session 5	193nm
NIST610 - 13	1.9957	0.0071	0.7114	0.0014	Session 4	193nm	NIST610 - 12	2.0451	0.0081	0.7099	0.0014	Session 5	193nm
NIST610 - 14	1.9961	0.0059	0.71	0.0013	Session 4	193nm	NIST610 - 13	2.0426	0.0066	0.7097	0.0017	Session 5	193nm
NIST610 - 15	1.9968	0.0062	0.7107	0.0015	Session 4	193nm	NIST610 - 14	2.0381	0.0073	0.7111	0.0015	Session 5	193nm
NIST610 - 16	2.0011	0.0062	0.7106	0.0013	Session 4	193nm	NIST610 - 15	2.0449	0.0071	0.7097	0.0017	Session 5	193nm
NIST610 - 17	1.9924	0.0059	0.7115	0.0013	Session 4	193nm	NIST610 - 16	2.0385	0.0069	0.7094	0.0017	Session 5	193nm
NIST610 - 18	1.9896	0.0063	0.7102	0.0014	Session 4	193nm	NIST610 - 17	2.0418	0.0078	0.7085	0.0018	Session 5	193nm
NIST610 - 19	1.9957	0.0059	0.7115	0.0012	Session 4	193nm	NIST610 - 18	2.0432	0.008	0.7105	0.0018	Session 5	193nm
NIST610 - 20	1.9918	0.0058	0.7108	0.0014	Session 4	193nm	NIST610 - 19	2.0327	0.0075	0.7102	0.0015	Session 5	193nm
NIST610 - 21	1.996	0.0056	0.711	0.0013	Session 4	193nm	NIST610 - 20	2.0324	0.0068	0.71	0.002	Session 5	193nm
NIST610 - 22	1.9854	0.0067	0.7095	0.0013	Session 4	193nm	NIST610 - 21	2.0323	0.0079	0.7106	0.0017	Session 5	193nm
NIST610 - 23	1.9897	0.0066	0.7096	0.0013	Session 4	193nm	NIST610 - 22	2.0374	0.007	0.7106	0.0017	Session 5	193nm
NIST610 - 24	1.9796	0.0066	0.7111	0.0012	Session 4	193nm	NIST610 - 23	2.0324	0.0077	0.7097	0.0018	Session 5	193nm

Continued on next page

Table 2.F Rb-Sr ratios of NIST 610 analysed by the LA-ICP-MS/MS over multiple Sessions using the 193 nm laser systems and normalised to Mica Mg-NP reference material.

Continued from previous page

spot	$^{87}Rb/^{86}Sr$	2SE	$^{87}Sr/^{86}Sr$	2SE	Session	LA	spot	$^{87}Rb/^{86}Sr$	2SE	$^{87}Sr/^{86}Sr$	2SE	Session	LA
NIST610 - 25	1.9921	0.0062	0.7114	0.0013	Session 4	193nm	NIST610 - 24	2.0281	0.0081	0.7107	0.0018	Session 5	193nm
NIST610 - 26	1.9843	0.0061	0.7103	0.0012	Session 4	193nm	NIST610 - 1	1.9742	0.0063	0.7101	0.0015	Session 6	193nm
NIST610 - 27	1.9867	0.0063	0.7097	0.0013	Session 4	193nm	NIST610 - 2	2.03	0.0062	0.7109	0.0018	Session 6	193nm
NIST610 - 28	1.9859	0.0067	0.7107	0.0012	Session 4	193nm	NIST610 - 3	1.9942	0.0068	0.7112	0.0015	Session 6	193nm
NIST610 - 29	1.9905	0.0065	0.7112	0.0014	Session 4	193nm	NIST610 - 4	2.0079	0.0058	0.7089	0.0012	Session 6	193nm
NIST610 - 30	1.9794	0.0062	0.711	0.0013	Session 4	193nm	NIST610 - 5	2.0167	0.0067	0.7092	0.0017	Session 6	193nm
NIST610 - 31	1.9835	0.0066	0.7099	0.0014	Session 4	193nm	NIST610 - 6	2.0136	0.006	0.7086	0.0016	Session 6	193nm
NIST610 - 32	1.9706	0.0066	0.7106	0.0014	Session 4	193nm	NIST610 - 7	1.9985	0.0056	0.7102	0.0015	Session 6	193nm
NIST610 - 33	1.983	0.0068	0.71	0.0015	Session 4	193nm	NIST610 - 8	2.0049	0.0061	0.709	0.0013	Session 6	193nm
NIST610 - 34	1.9818	0.0063	0.7109	0.0014	Session 4	193nm	NIST610 - 9	2.0049	0.0066	0.71	0.0013	Session 6	193nm
NIST610 - 1	2.0342	0.008	0.7107	0.0016	Session 5	193nm	NIST610 - 10	2.0107	0.0058	0.7087	0.0014	Session 6	193nm
NIST610 - 11	2.0148	0.0066	0.7117	0.0014	Session 6	193nm	NIST610 - 3	1.948	0.0055	0.7099	0.0019	Session 7	193nm
NIST610 - 12	2.0112	0.0073	0.7105	0.0013	Session 6	193nm	NIST610 - 4	1.9547	0.0055	0.7082	0.0017	Session 7	193nm
NIST610 - 13	2.016	0.0064	0.7101	0.0012	Session 6	193nm	NIST610 - 5	1.9502	0.0055	0.7092	0.0017	Session 7	193nm
NIST610 - 14	2.0016	0.0059	0.7105	0.0012	Session 6	193nm	NIST610 - 6	1.9429	0.0071	0.7077	0.002	Session 7	193nm
NIST610 - 15	2.0066	0.0063	0.7107	0.0013	Session 6	193nm	NIST610 - 7	1.9409	0.0043	0.7104	0.0019	Session 7	193nm
NIST610 - 16	2.0032	0.0064	0.7093	0.0014	Session 6	193nm	NIST610 - 8	1.9475	0.0058	0.7094	0.0019	Session 7	193nm
NIST610 - 17	2.017	0.0065	0.7112	0.0014	Session 6	193nm	NIST610 - 9	1.9455	0.0078	0.7083	0.0016	Session 7	193nm
NIST610 - 18	2.0144	0.0064	0.7101	0.0015	Session 6	193nm	NIST610 - 10	1.9384	0.0065	0.7085	0.0016	Session 7	193nm
NIST610 - 19	2.0081	0.0066	0.7111	0.0015	Session 6	193nm	NIST610 - 11	1.9533	0.0061	0.7097	0.0021	Session 7	193nm
NIST610 - 20	2.0146	0.0073	0.7118	0.0013	Session 6	193nm	NIST610 - 12	1.9436	0.0065	0.7097	0.0023	Session 7	193nm
NIST610 - 21	2.0159	0.0073	0.7102	0.0014	Session 6	193nm	NIST610 - 13	1.9329	0.0051	0.7089	0.0015	Session 7	193nm
NIST610 - 22	2.0093	0.0071	0.7104	0.0014	Session 6	193nm	NIST610 - 14	1.934	0.0055	0.7097	0.0021	Session 7	193nm
NIST610 - 23	2.0145	0.0057	0.7098	0.0014	Session 6	193nm	NIST610 - 15	1.9402	0.006	0.7087	0.002	Session 7	193nm
NIST610 - 24	2.005	0.0066	0.7086	0.0015	Session 6	193nm	NIST610 - 16	1.9212	0.0058	0.71	0.002	Session 7	193nm
NIST610 - 25	2.0083	0.0068	0.7109	0.0013	Session 6	193nm	NIST610 - 17	1.9356	0.0074	0.7087	0.0018	Session 7	193nm
NIST610 - 25	1.9938	0.0074	0.7095	0.0018	Session 6	193nm	NIST610 - 18	1.9445	0.0063	0.7095	0.002	Session 7	193nm
NIST610 - 26	1.9999	0.0066	0.7109	0.0014	Session 6	193nm	NIST610 - 19	1.9262	0.0063	0.7099	0.0013	Session 7	193nm

Continued on next page

Table 2.F Rb-Sr ratios of NIST 610 analysed by the LA-ICP-MS/MS over multiple Sessions using the 193 nm laser systems and normalised to Mica Mg-NP reference material.

Continued from previous page

spot	$^{87}Rb/^{86}Sr$	2SE	$^{87}Sr/^{86}Sr$	2SE	Session	LA	spot	$^{87}Rb/^{86}Sr$	2SE	$^{87}Sr/^{86}Sr$	2SE	Session	LA
NIST610 - 27	2.0088	0.0061	0.7115	0.0014	Session 6	193nm	NIST610 - 20	1.9297	0.006	0.7076	0.0015	Session 7	193nm
NIST610 - 28	2.0058	0.006	0.7095	0.0013	Session 6	193nm	NIST610 - 21	1.9359	0.0049	0.7091	0.0016	Session 7	193nm
NIST610 - 29	2.0107	0.0064	0.7096	0.0013	Session 6	193nm	NIST610 - 22	1.9507	0.0073	0.707	0.0021	Session 7	193nm
NIST610 - 30	2.0092	0.0061	0.7118	0.0014	Session 6	193nm	NIST610 - 23	1.9368	0.0062	0.7092	0.0017	Session 7	193nm
NIST610 - 31	2.0071	0.0067	0.7126	0.0014	Session 6	193nm	NIST610 - 24	1.9367	0.0063	0.7098	0.0017	Session 7	193nm
NIST610 - 32	2.0024	0.0071	0.7119	0.0013	Session 6	193nm	NIST610 - 25	1.9459	0.0056	0.711	0.0015	Session 7	193nm
NIST610 - 33	2.0045	0.0065	0.7109	0.0014	Session 6	193nm	NIST610 - 26	1.9432	0.0054	0.709	0.0019	Session 7	193nm
NIST610 - 34	2.0001	0.0057	0.7109	0.0013	Session 6	193nm	NIST610 - 1	1.9786	0.0072	0.7102	0.0022	Session 8	193nm
NIST610 - 35	2.0054	0.0061	0.7104	0.0014	Session 6	193nm	NIST610 - 2	1.9866	0.0049	0.7087	0.002	Session 8	193nm
NIST610 - 36	2.0001	0.0064	0.7091	0.0014	Session 6	193nm	NIST610 - 3	2.0099	0.0076	0.7109	0.0027	Session 8	193nm
NIST610 - 37	2.0011	0.0059	0.7118	0.0013	Session 6	193nm	NIST610 - 4	2.0085	0.007	0.7101	0.0016	Session 8	193nm
NIST610 - 38	1.9988	0.0071	0.7104	0.0013	Session 6	193nm	NIST610 - 5	2.0018	0.0064	0.7083	0.002	Session 8	193nm
NIST610 - 39	1.9904	0.0067	0.7093	0.0013	Session 6	193nm	NIST610 - 6	2.0018	0.0058	0.7108	0.0019	Session 8	193nm
NIST610 - 40	1.9909	0.0074	0.7097	0.0012	Session 6	193nm	NIST610 - 7	2.0126	0.0078	0.7103	0.002	Session 8	193nm
NIST610 - 1	1.9465	0.0066	0.7096	0.002	Session 7	193nm	NIST610 - 8	2.0201	0.0071	0.7102	0.0021	Session 8	193nm
NIST610 - 2	1.945	0.0059	0.71	0.0021	Session 7	193nm	NIST610 - 9	2.0142	0.0061	0.7106	0.0016	Session 8	193nm
NIST610 - 10	2.0224	0.0065	0.7094	0.0021	Session 8	193nm	NIST610 - 19	1.9985	0.0062	0.7105	0.0016	Session 8	193nm
NIST610 - 11	2.0051	0.0071	0.7071	0.0025	Session 8	193nm	NIST610 - 20	2.0036	0.0066	0.7102	0.0018	Session 8	193nm
NIST610 - 12	2.0153	0.0077	0.7122	0.002	Session 8	193nm	NIST610 - 21	2.007	0.0062	0.7088	0.0014	Session 8	193nm
NIST610 - 13	2.003	0.0069	0.7089	0.0018	Session 8	193nm	NIST610 - 22	2.0076	0.0082	0.7103	0.0019	Session 8	193nm
NIST610 - 14	2.0097	0.0063	0.7134	0.0018	Session 8	193nm	NIST610 - 23	2.0016	0.0062	0.71	0.0019	Session 8	193nm
NIST610 - 15	2.0163	0.0067	0.711	0.002	Session 8	193nm	NIST610 - 24	2.0066	0.0064	0.711	0.0019	Session 8	193nm
NIST610 - 16	2.0033	0.0057	0.7101	0.0018	Session 8	193nm	NIST610 - 25	2.0104	0.0071	0.7102	0.0023	Session 8	193nm
NIST610 - 17	2.0035	0.0078	0.7093	0.0019	Session 8	193nm	NIST610 - 26	2.0082	0.0073	0.7091	0.0021	Session 8	193nm
NIST610 - 18	2.0134	0.0078	0.7107	0.002	Session 8	193nm							

Figure 2.A: Rb-Sr isochrons of MDC phlogopite from each individual analytical session. In figures (A-H) $^{87}Rb/^{86}Sr$ and $^{87}Sr/^{86}Sr$ ratios were obtained by the 193nm laser while (I and J) show data that obtained by the 213nm laser. The initial $^{87}Sr/^{86}Sr$ ratio was fixed at 0.72607.

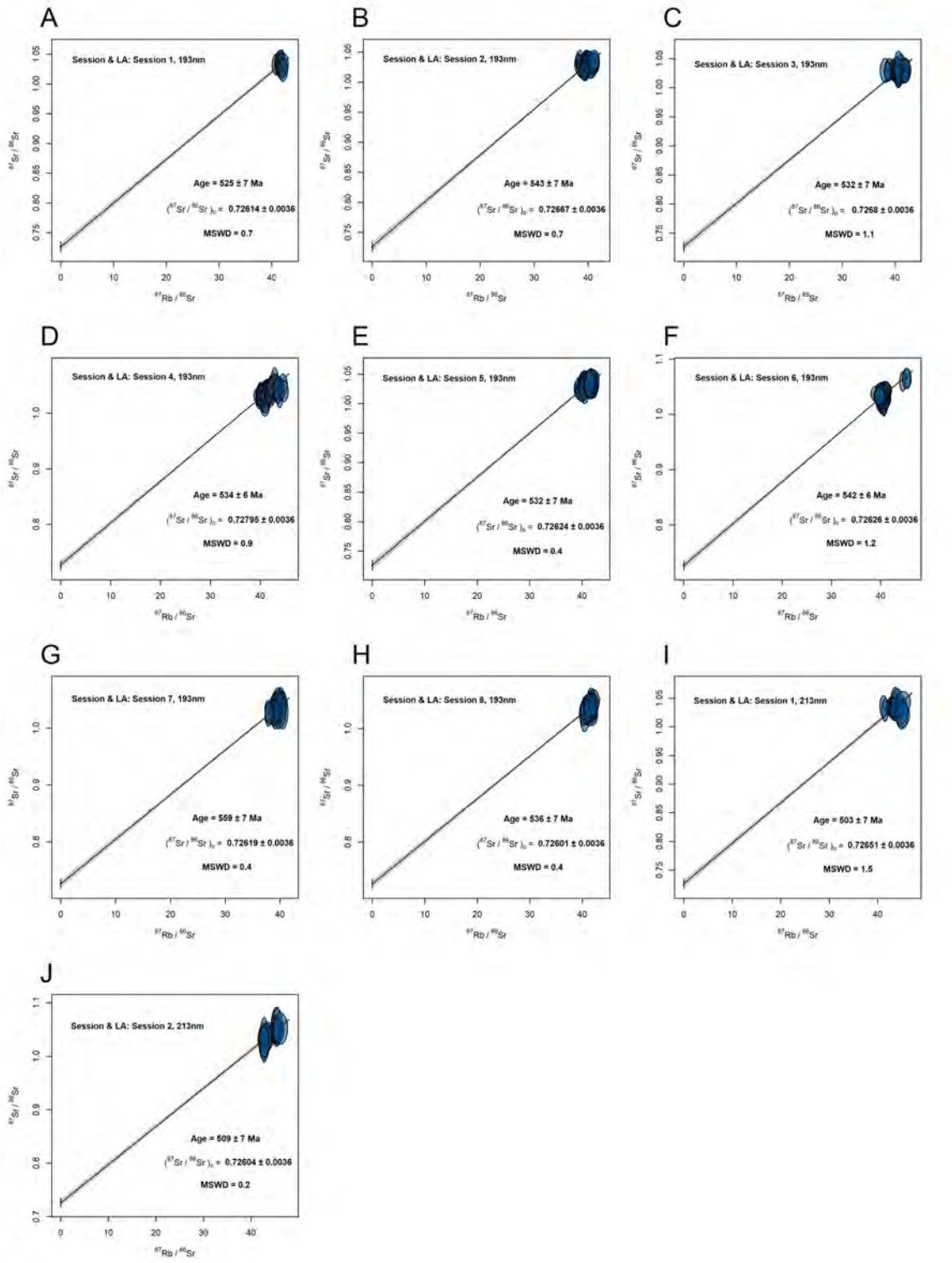

Table 3.A: Rb and Sr concentrations of RMs analysed by LA-ICP-MS/MS.

Spot Id	Rb (ppm)	2SE	Sr (ppm)	2SE	Sample name	Spot Id	Rb (ppm)	2SE	Sr (ppm)	2SE	Sample name
Mica Mg - 1.d	1366	25	22.3	0.4	Mica-Mg-NP	Mica Mg - 28.d	1408	19	20.4	0.3	Mica-Mg-NP
Mica Mg - 2.d	1389	22	21.6	0.3	Mica-Mg-NP	Mica Mg - 29.d	1429	23	20.2	0.3	Mica-Mg-NP
Mica Mg - 3.d	1403	22	21.5	0.3	Mica-Mg-NP	Mica Mg - 30.d	1440	22	20.5	0.3	Mica-Mg-NP
Mica Mg - 4.d	1396	22	20.9	0.3	Mica-Mg-NP	Mica Mg - 31.d	1433	22	20.1	0.3	Mica-Mg-NP
Mica Mg - 5.d	1407	23	21.2	0.3	Mica-Mg-NP	Mica Mg - 32.d	1422	23	20.0	0.3	Mica-Mg-NP
Mica Mg - 6.d	1408	26	21.1	0.4	Mica-Mg-NP	Mica Mg - 33.d	1412	27	19.9	0.4	Mica-Mg-NP
Mica Mg - 7.d	1430	23	21.4	0.3	Mica-Mg-NP	Mica Mg - 34.d	1449	33	20.3	0.5	Mica-Mg-NP
Mica Mg - 8.d	1393	21	20.6	0.4	Mica-Mg-NP	Mica Mg - 35.d	1423	23	20.5	0.3	Mica-Mg-NP
Mica Mg - 9.d	1415	20	20.8	0.3	Mica-Mg-NP	Mica Mg - 36.d	1425	25	20.1	0.3	Mica-Mg-NP
Mica Mg - 10.d	1428	25	20.7	0.3	Mica-Mg-NP	Mica Mg - 37.d	1451	30	20.3	0.4	Mica-Mg-NP
Mica Mg - 11.d	1416	18	20.5	0.2	Mica-Mg-NP	Mica Mg - 38.d	1422	30	20.4	0.4	Mica-Mg-NP
Mica Mg - 12.d	1416	22	20.5	0.3	Mica-Mg-NP	Mica Mg - 39.d	1420	31	20.1	0.4	Mica-Mg-NP
Mica Mg - 13.d	1392	21	20.1	0.3	Mica-Mg-NP	Mica Mg glass - 1.d	792	5	30.6	0.2	Mica-Mg G1
Mica Mg - 14.d	1394	23	20.4	0.3	Mica-Mg-NP	Mica Mg glass - 2.d	798	5	24.5	0.2	Mica-Mg G1
Mica Mg - 15.d	1432	24	20.8	0.3	Mica-Mg-NP	Mica Mg glass - 3.d	732	5	21.9	0.2	Mica-Mg G1
Mica Mg - 16.d	1376	30	20.7	0.4	Mica-Mg-NP	Mica Mg glass - 4.d	755	7	22.3	0.2	Mica-Mg G1
Mica Mg - 17.d	1402	24	20.3	0.3	Mica-Mg-NP	Mica Mg glass - 5.d	863	7	21.2	0.2	Mica-Mg G1
Mica Mg - 18.d	1414	19	20.5	0.4	Mica-Mg-NP	Mica Mg glass - 6.d	725	10	21.6	0.3	Mica-Mg G1
Mica Mg - 19.d	1449	19	20.4	0.3	Mica-Mg-NP	Mica Mg glass - 7.d	826	6	21.5	0.2	Mica-Mg G1
Mica Mg - 20.d	1431	26	20.1	0.4	Mica-Mg-NP	Mica Mg glass - 8.d	742	9	22.1	0.2	Mica-Mg G1
Mica Mg - 21.d	1398	13	20.3	0.2	Mica-Mg-NP	Mica Mg glass - 9.d	1139	22	20.5	0.3	Mica-Mg G1
Mica Mg - 22.d	1404	19	20.1	0.3	Mica-Mg-NP	Mica Mg glass - 10.d	881	8	20.7	0.2	Mica-Mg G1
Mica Mg - 23.d	1418	19	20.0	0.3	Mica-Mg-NP	Mica Mg glass - 11.d	955	13	23.0	0.3	Mica-Mg G1
Mica Mg - 24.d	1398	20	19.7	0.3	Mica-Mg-NP	Mica Fe g 1 - 1.d	2404	13	3.5	0.1	Mica-Fe G1
Mica Mg - 25.d	1421	39	20.5	0.4	Mica-Mg-NP	Mica Fe g 1 - 2.d	2293	22	3.0	0.1	Mica-Fe G1
Mica Mg - 26.d	1392	23	19.9	0.4	Mica-Mg-NP	Mica Fe g 1 - 3.d	2352	17	3.4	0.1	Mica-Fe G1
Mica Mg - 27.d	1397	22	20.4	0.4	Mica-Mg-NP	Mica Fe g 1 - 4.d	2594	21	3.0	0.1	Mica-Fe G1

Continued on next page

Table 3.A Rb and Sr concentrations of RMs analysed by LA-ICP-MS/MS

Continued from previous page

Spot Id	Rb (ppm)	2SE	Sr (ppm)	2SE	Sample name	Spot Id	Rb (ppm)	2SE	Sr (ppm)	2SE	Sample name
Mica Fe g 1 - 5.d	2338	40	2.6	0.1	Mica-Fe G1	Mica Fe P - 14.d	2596	68	3.1	0.1	Mica-Fe-NP
Mica Fe g 1 - 6.d	2641	38	3.3	0.1	Mica-Fe G1	Mica Fe P - 15.d	2535	68	3.2	0.1	Mica-Fe-NP
Mica Fe g 1 - 7.d	2509	29	3.3	0.1	Mica-Fe G1	Mica Fe P - 16.d	2670	44	3.2	0.1	Mica-Fe-NP
Mica Fe g 1 - 8.d	2342	61	2.6	0.1	Mica-Fe G1	Mica Fe P - 17.d	2551	61	3.2	0.1	Mica-Fe-NP
Mica Fe g 1 - 9.d	2072	31	3.7	0.1	Mica-Fe G1	Mica Fe P - 18.d	2566	62	2.9	0.1	Mica-Fe-NP
Mica Fe g 1 - 10.d	2590	30	3.1	0.1	Mica-Fe G1	Mica Fe P - 19.d	2628	66	3.5	0.1	Mica-Fe-NP
Mica Fe g 2 - 1.d	2362	13	3.5	0.1	Mica-Fe G2	Mica Fe P - 20.d	2571	64	3.2	0.1	Mica-Fe-NP
Mica Fe g 2 - 2.d	2111	12	2.7	0.0	Mica-Fe G2	GLO G 1 - 1.d	296	2	5.8	0.1	GL-O G1
Mica Fe g 2 - 3.d	2016	13	2.7	0.1	Mica-Fe G2	GLO G 1 - 2.d	276	1	13.6	0.2	GL-O G1
Mica Fe g 2 - 4.d	2204	17	3.2	0.0	Mica-Fe G2	GLO G 1 - 3.d	258	3	13.4	0.4	GL-O G1
Mica Fe g 2 - 5.d	2007	26	2.5	0.1	Mica-Fe G2	GLO G 1 - 4.d	230	2	13.8	0.2	GL-O G1
Mica Fe g 2 - 6.d	2199	20	2.6	0.1	Mica-Fe G2	GLO G 1 - 5.d	222	2	17.7	0.1	GL-O G1
Mica Fe g 2 - 7.d	2199	25	2.8	0.1	Mica-Fe G2	GLO G 1 - 6.d	199	2	66.8	0.5	GL-O G1
Mica Fe g 2 - 8.d	2137	20	3.3	0.1	Mica-Fe G2	GLO G 1 - 7.d	207	2	16.0	0.1	GL-O G1
Mica Fe g 2 - 9.d	2147	17	3.9	0.1	Mica-Fe G2	GLO G 1 - 8.d	190	1	24.9	0.2	GL-O G1
Mica Fe g 2 - 10.d	2274	39	3.1	0.1	Mica-Fe G2	GLO G 1 - 9.d	222	2	12.2	0.1	GL-O G1
Mica Fe g 2 - 11.d	2138	41	2.9	0.1	Mica-Fe G2	GLO G 1 - 10.d	247	2	7.0	0.1	GL-O G1
Mica Fe g 2 - 12.d	1918	37	2.6	0.1	Mica-Fe G2	GLO G 1 - 11.d	252	1	6.1	0.1	GL-O G1
Mica Fe g 2 - 13.d	2220	38	3.3	0.1	Mica-Fe G2	GLO G 1 - 12.d	248	2	6.2	0.1	GL-O G1
Mica Fe g 2 - 14.d	1905	35	2.6	0.1	Mica-Fe G2	GLO G 1 - 13.d	310	2	7.0	0.1	GL-O G1
Mica Fe P - 1.d	2840	24	3.1	0.1	Mica-Fe-NP	GLO G 1 - 14.d	239	2	12.1	0.1	GL-O G1
Mica Fe P - 2.d	2766	28	3.2	0.1	Mica-Fe-NP	GLO G 1 - 15.d	250	2	7.0	0.1	GL-O G1
Mica Fe P - 3.d	2771	21	3.3	0.1	Mica-Fe-NP	GLO G 1 - 16.d	260	2	6.0	0.1	GL-O G1
Mica Fe P - 4.d	2747	29	3.1	0.1	Mica-Fe-NP	GLO G 1 - 17.d	225	2	8.6	0.1	GL-O G1
Mica Fe P - 5.d	2653	41	3.3	0.1	Mica-Fe-NP	GLO G 1 - 18.d	232	2	7.3	0.1	GL-O G1
Mica Fe P - 6.d	2689	36	3.4	0.1	Mica-Fe-NP	GLO G 1 - 19.d	263	2	4.7	0.1	GL-O G1
Mica Fe P - 7.d	2639	51	3.2	0.1	Mica-Fe-NP	GLO G 1 - 20.d	244	2	5.8	0.1	GL-O G1
Mica Fe P - 8.d	2646	58	3.1	0.1	Mica-Fe-NP	GLO G 2 - 1.d	287	2	5.0	0.1	GL-O G2

Continued on next page

Table 3.A Rb and Sr concentrations of RMs analysed by LA-ICP-MS/MS

Continued from previous page

Spot Id	Rb (ppm)	2SE	Sr (ppm)	2SE	Sample name	Spot Id	Rb (ppm)	2SE	Sr (ppm)	2SE	Sample name
Mica Fe P - 9.d	2616	66	3.1	0.1	Mica-Fe-NP	GLO G 2 - 2.d	264	1	5.5	0.1	GL-O G3
Mica Fe P - 10.d	2612	73	3.2	0.1	Mica-Fe-NP	GLO G 2 - 3.d	201	1	37.0	0.2	GL-O G4
Mica Fe P - 11.d	2649	47	3.5	0.1	Mica-Fe-NP	GLO G 2 - 4.d	212	1	40.2	0.2	GL-O G5
Mica Fe P - 12.d	2568	70	3.1	0.1	Mica-Fe-NP	GLO G 2 - 5.d	194	1	51.8	0.6	GL-O G6
Mica Fe P - 13.d	2548	75	3.0	0.1	Mica-Fe-NP	GLO G 2 - 6.d	212	2	31.8	0.5	GL-O G7
GLO G 2 - 7.d	221	1	12.1	0.1	GL-O G8	GLO M - 21.d	250	3	3.9	0.1	GL-O glauconite
GLO G 2 - 8.d	204	1	8.9	0.1	GL-O G9	GLO M - 22.d	263	3	4.6	0.1	GL-O glauconite
GLO G 2 - 9.d	221	2	5.6	0.1	GL-O G10	GLO M - 23.d	293	3	6.0	0.1	GL-O glauconite
GLO G 2 - 10.d	229	2	5.4	0.1	GL-O G11	GLO M - 24.d	276	3	4.6	0.1	GL-O glauconite
GLO G 2 - 11.d	181	2	69.2	1.6	GL-O G12	GLO M - 25.d	261	2	4.7	0.1	GL-O glauconite
GLO G 2 - 12.d	254	2	5.2	0.1	GL-O G13	GLO M - 26.d	264	3	3.6	0.0	GL-O glauconite
GLO G 2 - 13.d	264	1	13.6	0.1	GL-O G14	GLO M - 27.d	259	2	4.2	0.1	GL-O glauconite
GLO G 2 - 14.d	194	2	62.2	1.0	GL-O G15	GLO M - 29.d	248	2	4.6	0.1	GL-O glauconite
GLO G 2 - 15.d	244	3	7.3	0.1	GL-O G16	GLO M - 30.d	249	2	4.5	0.0	GL-O glauconite
GLO G 2 - 16.d	186	2	20.3	0.3	GL-O G17	GLO M - 31.d	240	2	3.7	0.0	GL-O glauconite
GLO G 2 - 17.d	215	1	5.5	0.1	GL-O G18	GLO M - 33.d	250	2	5.5	0.1	GL-O glauconite
GLO G 2 - 18.d	268	2	4.8	0.1	GL-O G19	GLO M - 34.d	297	3	4.8	0.0	GL-O glauconite
GLO M - 1.d	257	2	4.7	0.1	GL-O glauconite	GLO M - 35.d	291	3	4.5	0.0	GL-O glauconite
GLO M - 2.d	340	4	7.2	0.1	GL-O glauconite	GLO M - 37.d	274	3	4.9	0.0	GL-O glauconite
GLO M - 4.d	262	2	4.7	0.1	GL-O glauconite	GLO M - 38.d	268	2	4.8	0.1	GL-O glauconite
GLO M - 6.d	325	3	5.7	0.1	GL-O glauconite	GLO M - 40.d	305	3	5.3	0.1	GL-O glauconite
GLO M - 7.d	293	3	5.3	0.1	GL-O glauconite	GLO M - 42.d	283	3	4.8	0.1	GL-O glauconite
GLO M - 8.d	275	3	4.8	0.1	GL-O glauconite	FK G1 - 1.d	870	14	28.2	0.3	FK-N G1
GLO M - 9.d	323	3	4.6	0.1	GL-O glauconite	FK G1 - 2.d	837	8	31.3	0.3	FK-N G1
GLO M - 10.d	305	3	7.7	0.2	GL-O glauconite	FK G1 - 3.d	825	5	28.6	0.2	FK-N G1
GLO M - 11.d	336	4	5.1	0.1	GL-O glauconite	FK G1 - 4.d	840	6	29.1	0.2	FK-N G1
GLO M - 12.d	242	3	4.7	0.0	GL-O glauconite	FK G1 - 5.d	835	10	28.7	0.4	FK-N G1
GLO M - 13.d	339	3	6.7	0.1	GL-O glauconite	FK G1 - 6.d	829	7	26.7	0.3	FK-N G1

Continued on next page

Table 3.A Rb and Sr concentrations of RMs analysed by LA-ICP-MS/MS

Continued from previous page

Spot Id	Rb (ppm)	2SE	Sr (ppm)	2SE	Sample name	Spot Id	Rb (ppm)	2SE	Sr (ppm)	2SE	Sample name
GLO M - 14.d	261	2	4.3	0.0	GL-O glauconite	FK G1 - 7.d	836	7	32.4	0.3	FK-N G1
GLO M - 15.d	272	2	5.2	0.1	GL-O glauconite	FK G1 - 8.d	850	6	27.2	0.2	FK-N G1
GLO M - 16.d	274	3	4.7	0.1	GL-O glauconite	FK G1 - 9.d	852	9	30.7	0.3	FK-N G1
GLO M - 18.d	232	2	4.9	0.0	GL-O glauconite	FK G1 - 10.d	849	6	27.3	0.2	FK-N G1
GLO M - 20.d	328	4	6.5	0.1	GL-O glauconite	FK G1 - 11.d	838	7	31.9	0.3	FK-N G1
FK G1 - 12.d	845	8	30.8	0.3	FK-N G1	KF Powder - 4.d	875	31	28.3	0.9	FK-N-NP
FK G1 - 13.d	833	8	28.7	0.3	FK-N G1	KF Powder - 5.d	915	32	27.5	0.9	FK-N-NP
FK G1 - 14.d	855	8	28.7	0.2	FK-N G1	KF Powder - 6.d	887	24	28.0	0.7	FK-N-NP
FK G1 - 15.d	833	8	29.1	0.3	FK-N G1	KF Powder - 7.d	889	23	28.1	0.9	FK-N-NP
FK G1 - 16.d	837	10	29.0	0.4	FK-N G1	KF Powder - 8.d	883	29	27.8	0.8	FK-N-NP
FK G1 - 17.d	840	8	29.7	0.3	FK-N G1	KF Powder - 9.d	900	24	28.9	0.7	FK-N-NP
FK G1 - 18.d	841	12	31.7	0.5	FK-N G1	KF Powder - 10.d	881	22	27.4	0.7	FK-N-NP
FK G1 - 19.d	827	9	27.8	0.3	FK-N G1	KF Powder - 11.d	889	28	27.2	0.9	FK-N-NP
FK G1 - 20.d	871	8	26.2	0.2	FK-N G1	KF Powder - 12.d	851	17	27.2	0.6	FK-N-NP
FK G1 - 21.d	851	17	27.0	0.5	FK-N G2	KF Powder - 13.d	894	27	28.6	0.8	FK-N-NP
FK G2 - 1.d	826	8	34.0	0.3	FK-N G2	KF Powder - 14.d	896	24	28.3	0.7	FK-N-NP
FK G2 - 2.d	854	10	29.5	0.3	FK-N G2	KF Powder - 15.d	871	24	28.7	0.8	FK-N-NP
FK G2 - 3.d	819	8	30.1	0.3	FK-N G2	KF Powder - 16.d	901	26	28.6	0.8	FK-N-NP
FK G2 - 4.d	801	6	32.7	0.3	FK-N G2	KF Powder - 17.d	873	25	27.8	0.8	FK-N-NP
FK G2 - 5.d	755	6	23.9	0.2	FK-N G2	KF Powder - 18.d	898	23	28.1	0.6	FK-N-NP
FK G2 - 6.d	804	7	24.2	0.2	FK-N G2	KF Powder - 19.d	879	27	28.7	0.8	FK-N-NP
FK G2 - 7.d	832	8	26.2	0.3	FK-N G2	KF Powder - 20.d	887	24	27.6	0.8	FK-N-NP
FK G2 - 8.d	800	7	23.9	0.2	FK-N G2	KF Powder - 21.d	889	21	29.2	0.7	FK-N-NP
FK G2 - 9.d	849	8	26.8	0.3	FK-N G2	GL-O np - 1.d	235	3	17.3	0.3	GL-O-NP
FK G2 - 10.d	807	6	31.1	0.3	FK-N G2	GL-O np - 2.d	236	2	17.4	0.3	GL-O-NP
FK G2 - 11.d	836	7	28.2	0.3	FK-N G2	GL-O np - 3.d	234	3	17.3	0.2	GL-O-NP
FK G2 - 12.d	833	8	31.9	0.4	FK-N G2	GL-O np - 4.d	66	1	4.8	0.1	GL-O-NP
FK G2 - 13.d	853	17	29.6	0.5	FK-N G2	GL-O np - 5.d	236	2	17.3	0.2	GL-O-NP

Continued on next page

Table 3.A Rb and Sr concentrations of RMs analysed by LA-ICP-MS/MS

Continued from previous page

Spot Id	Rb (ppm)	2SE	Sr (ppm)	2SE	Sample name	Spot Id	Rb (ppm)	2SE	Sr (ppm)	2SE	Sample name
FK G2 - 14.d	873	15	29.5	0.3	FK-N G2	GL-O np - 6.d	235	2	17.1	0.2	GL-O-NP
FK G2 - 15.d	833	9	32.9	0.3	FK-N G2	GL-O np - 7.d	237	2	17.5	0.2	GL-O-NP
FK G2 - 16.d	840	8	33.3	0.3	FK-N G2	GL-O np - 8.d	238	2	17.5	0.3	GL-O-NP
FK G2 - 17.d	751	6	19.6	0.2	FK-N G2	GL-O np - 9.d	238	2	17.5	0.2	GL-O-NP
FK G2 - 18.d	808	12	28.6	0.4	FK-N G2	GL-O np - 10.d	236	2	17.5	0.2	GL-O-NP
FK G2 - 19.d	859	12	30.5	0.4	FK-N G2	GL-O np - 11.d	241	3	17.8	0.3	GL-O-NP
FK G2 - 20.d	796	7	27.8	0.3	FK-N G2	GL-O np - 12.d	237	3	17.6	0.2	GL-O-NP
KF Powder - 1.d	901	31	27.7	0.8	FK-N-NP	GL-O np - 13.d	242	3	18.3	0.3	GL-O-NP
KF Powder - 2.d	899	24	29.3	0.9	FK-N-NP	GL-O np - 14.d	238	3	17.9	0.3	GL-O-NP
KF Powder - 3.d	881	24	27.8	0.8	FK-N-NP	GL-O np - 15.d	239	3	17.9	0.2	GL-O-NP
GL-O np - 16.d	240	3	18.0	0.2	GL-O-NP	GL-O np - 47.d	242	3	18.4	0.3	GL-O-NP
GL-O np - 17.d	238	3	17.9	0.2	GL-O-NP	GL-O np - 48.d	242	3	18.6	0.2	GL-O-NP
GL-O np - 18.d	239	3	17.7	0.3	GL-O-NP	GL-O np - 49.d	241	4	18.0	0.3	GL-O-NP
GL-O np - 19.d	237	3	17.2	0.2	GL-O-NP	GL-O np - 50.d	244	3	17.9	0.2	GL-O-NP
GL-O np - 20.d	240	3	17.8	0.2	GL-O-NP	GL-O np - 51.d	243	2	18.2	0.2	GL-O-NP
GL-O np - 21.d	240	3	17.8	0.2	GL-O-NP	GL-O np - 52.d	242	3	18.3	0.2	GL-O-NP
GL-O np - 22.d	237	3	17.3	0.2	GL-O-NP	GL-O np - 53.d	242	3	18.1	0.2	GL-O-NP
GL-O np - 23.d	240	3	18.0	0.3	GL-O-NP	GL-O np - 54.d	242	3	17.9	0.3	GL-O-NP
GL-O np - 24.d	240	3	17.9	0.2	GL-O-NP	GL-O np - 55.d	243	3	18.0	0.3	GL-O-NP
GL-O np - 25.d	241	3	18.1	0.2	GL-O-NP	GL-O np - 56.d	241	3	17.9	0.3	GL-O-NP
GL-O np - 26.d	238	3	17.8	0.3	GL-O-NP	GL-O np - 57.d	241	3	18.2	0.3	GL-O-NP
GL-O np - 27.d	239	3	17.9	0.3	GL-O-NP	GL-O np - 58.d	244	3	17.9	0.3	GL-O-NP
GL-O np - 28.d	239	3	18.0	0.2	GL-O-NP	GL-O np - 59.d	245	3	18.1	0.2	GL-O-NP
GL-O np - 29.d	243	3	18.2	0.3	GL-O-NP	GL-O np - 60.d	242	3	17.5	0.2	GL-O-NP
GL-O np - 30.d	241	2	18.0	0.2	GL-O-NP	GL-O np - 61.d	244	2	18.5	0.3	GL-O-NP
GL-O np - 31.d	240	2	18.1	0.2	GL-O-NP	GL-O np - 62.d	241	3	17.9	0.2	GL-O-NP
GL-O np - 32.d	240	3	18.5	0.3	GL-O-NP	GL-O np - 63.d	242	3	18.0	0.2	GL-O-NP
GL-O np - 33.d	240	3	18.1	0.3	GL-O-NP	GL-O np - 64.d	241	4	18.2	0.3	GL-O-NP

Continued on next page

Table 3.A Rb and Sr concentrations of RMs analysed by LA-ICP-MS/MS

Continued from previous page

Spot Id	Rb (ppm)	2SE	Sr (ppm)	2SE	Sample name	Spot Id	Rb (ppm)	2SE	Sr (ppm)	2SE	Sample name
GL-O np - 34.d	242	3	18.4	0.3	GL-O-NP	GL-O np - 65.d	240	3	18.3	0.2	GL-O-NP
GL-O np - 35.d	239	3	18.2	0.2	GL-O-NP	GL-O np - 66.d	238	3	18.3	0.3	GL-O-NP
GL-O np - 36.d	239	3	18.2	0.2	GL-O-NP	GL-O np - 67.d	240	3	18.1	0.2	GL-O-NP
GL-O np - 37.d	239	3	18.0	0.3	GL-O-NP	GL-O np - 68.d	242	3	17.6	0.3	GL-O-NP
GL-O np - 38.d	238	3	18.2	0.3	GL-O-NP	GL-O np - 69.d	244	3	18.5	0.3	GL-O-NP
GL-O np - 39.d	241	3	18.1	0.3	GL-O-NP	GL-O np - 70.d	243	3	18.1	0.3	GL-O-NP
GL-O np - 40.d	244	3	18.2	0.3	GL-O-NP	GL-O np - 71.d	242	3	17.9	0.2	GL-O-NP
GL-O np - 41.d	242	3	17.9	0.2	GL-O-NP	GL-O np - 72.d	242	3	18.1	0.2	GL-O-NP
GL-O np - 42.d	243	3	18.1	0.2	GL-O-NP	GL-O np - 73.d	243	3	18.1	0.3	GL-O-NP
GL-O np - 43.d	240	3	17.9	0.2	GL-O-NP	GL-O np - 74.d	240	3	17.9	0.3	GL-O-NP
GL-O np - 44.d	242	3	18.2	0.2	GL-O-NP	GL-O np - 75.d	240	3	18.0	0.3	GL-O-NP
GL-O np - 45.d	242	3	18.3	0.3	GL-O-NP	GL-O np - 76.d	243	3	18.5	0.3	GL-O-NP
GL-O np - 46.d	245	3	18.2	0.2	GL-O-NP						

Table 3.B: Rb-Sr isotopic ratios calibrated versus NIST 610 glass.

Spot	Raw $^{87}Sr/^{86}Sr$	2SE	Raw $^{87}Rb/^{86}Sr$	2SE	Calibrated $^{87}Rb/^{86}Sr$	2SE	Calibrated $^{87}Sr/^{86}Sr$	2SE	Sample	Type	Session	Date
Mic-Mg - 1.d	1.879	0.015	144.11	1.09	189.72	1.43	1.843	0.015	Mica-Mg	NP	S1	171103
Mic-Mg - 2.d	1.889	0.013	145.91	0.93	191.68	1.22	1.852	0.013	Mica-Mg	NP	S1	171103
Mic-Mg - 3.d	1.907	0.014	147.49	1.15	193.54	1.51	1.871	0.014	Mica-Mg	NP	S1	171103
Mic-Mg - 4.d	1.900	0.014	148.33	1.10	191.46	1.42	1.864	0.013	Mica-Mg	NP	S1	171103
Mic-Mg - 5.d	1.870	0.014	144.49	1.05	186.33	1.35	1.834	0.014	Mica-Mg	NP	S1	171103
Mic-Mg - 7.d	1.887	0.016	147.52	1.19	188.33	1.52	1.850	0.015	Mica-Mg	NP	S1	171103
Mic-Mg - 8.d	1.896	0.014	143.66	1.61	183.33	2.05	1.859	0.014	Mica-Mg	NP	S1	171103
Mic-Mg - 9.d	1.889	0.016	146.37	1.40	186.73	1.79	1.852	0.016	Mica-Mg	NP	S1	171103
Mic-Mg - 10.d	1.896	0.016	146.07	1.35	185.85	1.72	1.859	0.015	Mica-Mg	NP	S1	171103
Mic-Mg - 12.d	1.882	0.015	143.52	1.40	182.56	1.78	1.845	0.015	Mica-Mg	NP	S1	171103
Mic-Mg - 13.d	1.881	0.014	146.55	1.24	185.99	1.57	1.844	0.014	Mica-Mg	NP	S1	171103
Mic-Mg - 14.d	1.888	0.013	152.25	1.58	193.20	2.01	1.851	0.012	Mica-Mg	NP	S1	171103
Mic-Mg - 15.d	1.897	0.012	145.83	1.50	185.03	1.90	1.860	0.012	Mica-Mg	NP	S1	171103
Mic-Mg - 16.d	1.894	0.013	144.19	1.18	182.92	1.50	1.857	0.013	Mica-Mg	NP	S1	171103
Mic-Mg - 17.d	1.885	0.012	143.51	1.07	182.06	1.36	1.848	0.012	Mica-Mg	NP	S1	171103
Mic-Mg - 18.d	1.898	0.012	142.79	0.94	181.14	1.20	1.861	0.011	Mica-Mg	NP	S1	171103
Mic-Mg - 19.d	1.897	0.014	139.34	1.12	176.57	1.42	1.860	0.014	Mica-Mg	NP	S1	171103
Mic-Mg - 20.d	1.893	0.015	144.93	1.39	183.62	1.76	1.855	0.015	Mica-Mg	NP	S1	171103
Mic-Mg - 21.d	1.893	0.014	143.30	1.25	181.52	1.59	1.856	0.014	Mica-Mg	NP	S1	171103
Mic-Mg - 22.d	1.898	0.013	144.69	1.16	182.72	1.46	1.861	0.013	Mica-Mg	NP	S1	171103
Mic-Mg - 23.d	1.880	0.014	144.48	1.75	182.43	2.22	1.843	0.014	Mica-Mg	NP	S1	171103
Mic-Mg - 24.d	1.880	0.014	145.26	1.65	183.37	2.09	1.843	0.014	Mica-Mg	NP	S1	171103
Mic-Mg - 25.d	1.877	0.011	145.58	1.27	183.39	1.60	1.840	0.011	Mica-Mg	NP	S1	171103
Mic-Mg - 26.d	1.870	0.013	143.17	1.34	180.34	1.69	1.833	0.012	Mica-Mg	NP	S1	171103
Mic-Mg - 27.d	1.885	0.013	144.47	1.36	181.96	1.71	1.848	0.012	Mica-Mg	NP	S1	171103
Mic-Mg - 28.d	1.881	0.014	146.76	1.58	184.71	1.99	1.844	0.014	Mica-Mg	NP	S1	171103
Mic-Mg - 29.d	1.880	0.014	143.62	1.30	180.75	1.64	1.843	0.014	Mica-Mg	NP	S1	171103

Continued on next page

Table 3.B Rb-Sr isotopic ratios calibrated versus NIST 610 glass

Continued from previous page

Spot	Raw $^{87}Sr/^{86}Sr$	2SE	Raw $^{87}Rb/^{86}Sr$	2SE	Calibrated $^{87}Rb/^{86}Sr$	2SE	Calibrated $^{87}Sr/^{86}Sr$	2SE	Sample	Type	Session	Date
Mic-Mg - 30.d	1.891	0.014	144.50	1.44	181.85	1.81	1.854	0.014	Mica-Mg	NP	S1	171103
Mic-Mg - 31.d	1.887	0.014	145.82	1.31	183.26	1.65	1.850	0.013	Mica-Mg	NP	S1	171103
Mic-Mg - 32.d	1.889	0.015	143.48	1.26	180.30	1.58	1.852	0.015	Mica-Mg	NP	S1	171103
Mic-Mg - 33.d	1.900	0.013	143.48	1.01	180.29	1.27	1.863	0.013	Mica-Mg	NP	S1	171103
Mic-Mg - 34.d	1.876	0.012	143.12	1.20	179.73	1.51	1.840	0.012	Mica-Mg	NP	S1	171103
Mic-Mg - 35.d	1.876	0.012	143.07	1.17	179.68	1.47	1.840	0.012	Mica-Mg	NP	S1	171103
Mic-Mg - 36.d	1.899	0.014	143.28	1.09	179.95	1.37	1.862	0.014	Mica-Mg	NP	S1	171103
Mic-Mg - 37.d	1.885	0.014	144.35	1.34	181.76	1.69	1.848	0.013	Mica-Mg	NP	S1	171103
Mic-Mg - 38.d	1.883	0.014	143.39	1.30	180.58	1.64	1.846	0.014	Mica-Mg	NP	S1	171103
Mic-Mg - 39.d	1.886	0.014	143.39	1.19	180.62	1.50	1.849	0.014	Mica-Mg	NP	S1	171103
MicaMg - 1.d	1.929	0.033	146.15	2.31	167.62	2.65	1.869	0.032	Mica-Mg	NP	S2	210916
MicaMg - 2.d	1.946	0.033	147.05	2.45	168.66	2.81	1.886	0.032	Mica-Mg	NP	S2	210916
MicaMg - 3.d	1.943	0.032	145.57	2.03	166.98	2.33	1.883	0.031	Mica-Mg	NP	S2	210916
MicaMg - 4.d	1.899	0.032	145.25	2.39	167.16	2.76	1.843	0.031	Mica-Mg	NP	S2	210916
MicaMg - 5.d	1.913	0.037	151.46	2.74	174.32	3.15	1.857	0.036	Mica-Mg	NP	S2	210916
MicaMg - 6.d	1.939	0.029	145.67	2.17	167.66	2.50	1.882	0.028	Mica-Mg	NP	S2	210916
MicaMg - 7.d	1.910	0.035	149.30	2.27	172.06	2.62	1.852	0.034	Mica-Mg	NP	S2	210916
MicaMg - 8.d	1.888	0.032	144.50	2.15	166.53	2.48	1.831	0.031	Mica-Mg	NP	S2	210916
MicaMg - 9.d	1.919	0.033	147.17	2.16	169.61	2.48	1.861	0.032	Mica-Mg	NP	S2	210916
MicaMg - 10.d	1.906	0.033	145.63	2.25	167.81	2.59	1.849	0.032	Mica-Mg	NP	S2	210916
MicaMg - 11.d	1.935	0.033	147.01	2.36	169.41	2.72	1.877	0.032	Mica-Mg	NP	S2	210916
MicaMg - 12.d	1.931	0.036	148.57	2.43	171.20	2.80	1.873	0.035	Mica-Mg	NP	S2	210916
MicaMg - 13.d	1.948	0.033	146.51	2.68	168.59	3.08	1.886	0.032	Mica-Mg	NP	S2	210916
MicaMg - 14.d	1.908	0.032	143.14	2.03	164.70	2.33	1.847	0.031	Mica-Mg	NP	S2	210916
MicaMg - 15.d	1.888	0.030	144.35	2.01	166.09	2.31	1.828	0.029	Mica-Mg	NP	S2	210916
MicaMg - 16.d	1.926	0.029	146.01	2.18	167.74	2.50	1.865	0.028	Mica-Mg	NP	S2	210916
MicaMg - 17.d	1.940	0.030	145.04	2.47	166.62	2.83	1.880	0.029	Mica-Mg	NP	S2	210916
MicaMg - 18.d	1.961	0.034	147.09	2.29	168.97	2.64	1.899	0.033	Mica-Mg	NP	S2	210916

Continued on next page

Table 3.B Rb-Sr isotopic ratios calibrated versus NIST 610 glass

Continued from previous page

Spot	Raw $^{87}Sr/^{86}Sr$	2SE	Raw $^{87}Rb/^{86}Sr$	2SE	Calibrated $^{87}Rb/^{86}Sr$	2SE	Calibrated $^{87}Sr/^{86}Sr$	2SE	Sample	Type	Session	Date
MicaMg - 19.d	1.901	0.035	144.55	2.19	165.97	2.51	1.843	0.034	Mica-Mg	NP	S2	210916
MicaMg - 20.d	1.887	0.036	147.10	2.44	168.90	2.80	1.830	0.035	Mica-Mg	NP	S2	210916
MicaMg - 21.d	1.926	0.037	148.26	2.56	170.23	2.94	1.868	0.036	Mica-Mg	NP	S2	210916
MicaMg - 22.d	1.913	0.030	148.82	2.59	170.99	2.97	1.856	0.029	Mica-Mg	NP	S2	210916
MicaMg - 23.d	1.912	0.033	145.51	2.38	167.20	2.74	1.855	0.032	Mica-Mg	NP	S2	210916
MicaMg - 24.d	1.911	0.028	143.27	2.13	164.63	2.44	1.855	0.027	Mica-Mg	NP	S2	210916
MicaMg - 25.d	1.927	0.033	145.92	2.36	167.86	2.72	1.873	0.032	Mica-Mg	NP	S2	210916
MicaMg - 26.d	1.923	0.031	145.62	2.22	167.53	2.56	1.869	0.030	Mica-Mg	NP	S2	210916
MicaMg - 27.d	1.915	0.032	144.63	2.25	166.40	2.59	1.862	0.032	Mica-Mg	NP	S2	210916
MicaMg - 28.d	1.933	0.039	148.77	2.56	171.22	2.94	1.874	0.038	Mica-Mg	NP	S2	210916
MicaMg - 29.d	1.913	0.032	143.97	1.98	165.70	2.28	1.855	0.031	Mica-Mg	NP	S2	210916
MicaMg - 30.d	1.920	0.037	145.42	2.51	167.37	2.89	1.861	0.036	Mica-Mg	NP	S2	210916
MicaMg - 31.d	1.928	0.034	145.76	2.23	167.82	2.56	1.871	0.033	Mica-Mg	NP	S2	210916
MicaMg - 32.d	1.930	0.031	147.45	2.40	169.77	2.77	1.873	0.030	Mica-Mg	NP	S2	210916
MicaMg - 33.d	1.900	0.036	143.13	2.64	164.79	3.04	1.844	0.035	Mica-Mg	NP	S2	210916
MicaMg - 34.d	1.924	0.030	145.04	2.11	167.16	2.43	1.867	0.029	Mica-Mg	NP	S2	210916
MicaMg - 35.d	1.896	0.035	145.35	2.25	167.52	2.59	1.840	0.034	Mica-Mg	NP	S2	210916
MicaMg - 36.d	1.925	0.033	146.44	2.39	168.77	2.75	1.868	0.032	Mica-Mg	NP	S2	210916
MicaMg - 37.d	1.906	0.030	144.79	2.09	166.96	2.41	1.846	0.029	Mica-Mg	NP	S2	210916
MicaMg - 38.d	1.920	0.035	147.51	2.26	170.09	2.60	1.860	0.034	Mica-Mg	NP	S2	210916
MicaMg - 39.d	1.919	0.030	145.80	2.26	168.12	2.61	1.858	0.029	Mica-Mg	NP	S2	210916
MicaMg - 40.d	1.928	0.030	144.46	2.13	166.54	2.46	1.866	0.029	Mica-Mg	NP	S2	210916
MicaMg - 41.d	1.913	0.035	142.69	2.02	164.50	2.33	1.852	0.033	Mica-Mg	NP	S2	210916
MicaMg - 42.d	1.905	0.031	148.21	2.41	170.85	2.78	1.844	0.030	Mica-Mg	NP	S2	210916
MicaMg - 43.d	1.944	0.034	144.84	2.01	166.89	2.32	1.887	0.033	Mica-Mg	NP	S2	210916
MicaMg - 44.d	1.951	0.038	147.07	2.40	169.45	2.76	1.895	0.037	Mica-Mg	NP	S2	210916
MicaMg - 45.d	1.900	0.029	144.08	2.16	166.01	2.49	1.845	0.029	Mica-Mg	NP	S2	210916
MicaMg - 46.d	1.932	0.034	148.45	2.19	170.93	2.52	1.872	0.033	Mica-Mg	NP	S2	210916

Continued on next page

Table 3.B Rb-Sr isotopic ratios calibrated versus NIST 610 glass

Continued from previous page

Spot	Raw $^{87}Sr/^{86}Sr$	2SE	Raw $^{87}Rb/^{86}Sr$	2SE	Calibrated $^{87}Rb/^{86}Sr$	2SE	Calibrated $^{87}Sr/^{86}Sr$	2SE	Sample	Type	Session	Date
MicaMg - 47.d	1.887	0.028	144.68	2.08	166.59	2.40	1.827	0.027	Mica-Mg	NP	S2	210916
MicaMg - 48.d	1.930	0.033	146.19	2.22	168.32	2.56	1.870	0.032	Mica-Mg	NP	S2	210916
MicaMg - 49.d	1.908	0.033	146.81	2.07	168.97	2.39	1.847	0.032	Mica-Mg	NP	S2	210916
MicaMg - 50.d	1.899	0.030	145.22	2.64	167.14	3.04	1.838	0.029	Mica-Mg	NP	S2	210916
MicaMg - 51.d	1.925	0.031	148.76	2.38	171.21	2.74	1.864	0.030	Mica-Mg	NP	S2	210916
MicaMg - 1.d	1.921	0.039	145.80	2.61	168.53	3.01	1.864	0.038	Mica-Mg	NP	S3	210917
MicaMg - 2.d	1.927	0.034	147.42	2.14	170.40	2.47	1.870	0.033	Mica-Mg	NP	S3	210917
MicaMg - 3.d	1.922	0.032	146.99	2.26	169.91	2.61	1.865	0.031	Mica-Mg	NP	S3	210917
MicaMg - 4.d	1.938	0.039	146.93	2.39	169.96	2.77	1.880	0.037	Mica-Mg	NP	S3	210917
MicaMg - 5.d	1.933	0.035	148.57	2.33	172.04	2.69	1.875	0.034	Mica-Mg	NP	S3	210917
MicaMg - 6.d	1.920	0.033	147.92	2.35	171.30	2.72	1.863	0.032	Mica-Mg	NP	S3	210917
MicaMg - 7.d	1.922	0.039	148.01	2.51	171.46	2.91	1.865	0.038	Mica-Mg	NP	S3	210917
MicaMg - 8.d	1.884	0.030	144.52	1.97	167.43	2.28	1.827	0.029	Mica-Mg	NP	S3	210917
MicaMg - 9.d	1.905	0.030	145.98	2.29	169.12	2.65	1.848	0.029	Mica-Mg	NP	S3	210917
MicaMg - 10.d	1.946	0.037	146.02	2.10	169.20	2.43	1.888	0.036	Mica-Mg	NP	S3	210917
MicaMg - 11.d	1.921	0.034	148.72	2.27	172.34	2.63	1.863	0.033	Mica-Mg	NP	S3	210917
MicaMg - 12.d	1.908	0.034	147.78	2.17	171.24	2.51	1.850	0.033	Mica-Mg	NP	S3	210917
MicaMg - 13.d	1.930	0.028	145.33	2.13	168.43	2.47	1.872	0.028	Mica-Mg	NP	S3	210917
MicaMg - 14.d	1.950	0.034	147.97	2.23	171.48	2.58	1.891	0.033	Mica-Mg	NP	S3	210917
MicaMg - 15.d	1.923	0.032	145.82	2.06	169.00	2.39	1.865	0.031	Mica-Mg	NP	S3	210917
MicaMg - 16.d	1.929	0.041	145.16	2.41	168.24	2.79	1.871	0.040	Mica-Mg	NP	S3	210917
MicaMg - 17.d	1.912	0.034	146.89	2.18	170.24	2.53	1.854	0.033	Mica-Mg	NP	S3	210917
MicaMg - 18.d	1.905	0.036	148.71	2.40	172.35	2.79	1.847	0.035	Mica-Mg	NP	S3	210917
MicaMg - 19.d	1.936	0.035	152.31	2.60	176.48	3.01	1.878	0.034	Mica-Mg	NP	S3	210917
MicaMg - 20.d	1.916	0.035	149.26	2.28	172.95	2.65	1.858	0.034	Mica-Mg	NP	S3	210917
MicaMg - 21.d	1.960	0.039	152.98	2.54	177.26	2.94	1.901	0.038	Mica-Mg	NP	S3	210917
MicaMg - 22.d	1.925	0.035	152.61	2.40	176.78	2.78	1.867	0.033	Mica-Mg	NP	S3	210917
MicaMg - 23.d	1.922	0.032	153.01	2.52	177.24	2.91	1.864	0.031	Mica-Mg	NP	S3	210917

Continued on next page

Table 3.B Rb-Sr isotopic ratios calibrated versus NIST 610 glass

Continued from previous page

Spot	Raw $^{87}Sr/^{86}Sr$	2SE	Raw $^{87}Rb/^{86}Sr$	2SE	Calibrated $^{87}Rb/^{86}Sr$	2SE	Calibrated $^{87}Sr/^{86}Sr$	2SE	Sample	Type	Session	Date
MicaMg - 24.d	1.903	0.034	149.35	2.39	172.99	2.77	1.845	0.033	Mica-Mg	NP	S3	210917
MicaMg - 25.d	1.878	0.031	149.40	2.35	172.99	2.72	1.822	0.030	Mica-Mg	NP	S3	210917
MicaMg - 26.d	1.932	0.039	151.56	2.45	175.48	2.84	1.874	0.037	Mica-Mg	NP	S3	210917
MicaMg - 27.d	1.922	0.037	151.11	2.54	174.97	2.94	1.864	0.035	Mica-Mg	NP	S3	210917
MicaMg - 28.d	1.921	0.033	151.76	2.45	175.66	2.84	1.863	0.032	Mica-Mg	NP	S3	210917
MicaMg - 29.d	1.913	0.035	149.80	2.23	173.39	2.58	1.855	0.034	Mica-Mg	NP	S3	210917
MicaMg - 30.d	1.903	0.035	149.12	2.51	172.60	2.91	1.845	0.034	Mica-Mg	NP	S3	210917
MicaMg - 31.d	1.987	0.043	154.07	2.59	178.28	3.00	1.927	0.042	Mica-Mg	NP	S3	210917
MicaMg - 32.d	1.923	0.037	150.07	2.49	173.65	2.88	1.864	0.036	Mica-Mg	NP	S3	210917
MicaMg - 33.d	1.922	0.035	151.77	2.31	175.61	2.67	1.864	0.034	Mica-Mg	NP	S3	210917
MicaMg - 34.d	1.928	0.035	153.66	2.46	177.77	2.85	1.870	0.034	Mica-Mg	NP	S3	210917
MicaMg - 35.d	1.931	0.039	151.99	2.48	175.85	2.87	1.872	0.037	Mica-Mg	NP	S3	210917
MicaMg - 36.d	1.886	0.036	151.28	2.45	175.02	2.84	1.829	0.035	Mica-Mg	NP	S3	210917
MicaMg - 37.d	1.932	0.033	153.83	2.38	177.95	2.75	1.873	0.032	Mica-Mg	NP	S3	210917
MicaMg - 38.d	1.927	0.038	150.71	2.54	174.34	2.94	1.868	0.037	Mica-Mg	NP	S3	210917
MicaMg - 39.d	1.914	0.035	153.21	2.65	177.24	3.07	1.856	0.033	Mica-Mg	NP	S3	210917
MicaMg - 40.d	1.933	0.042	155.81	2.63	180.24	3.05	1.874	0.041	Mica-Mg	NP	S3	210917
MicaMg - 41.d	1.901	0.033	154.04	2.72	178.18	3.14	1.843	0.032	Mica-Mg	NP	S3	210917
MicaMg - 42.d	1.935	0.037	156.32	2.67	180.82	3.09	1.876	0.036	Mica-Mg	NP	S3	210917
MicaMg - 43.d	1.933	0.038	157.47	2.87	182.16	3.33	1.874	0.037	Mica-Mg	NP	S3	210917
MicaMg - 44.d	1.943	0.036	155.26	2.26	179.60	2.61	1.884	0.035	Mica-Mg	NP	S3	210917
MicaMg - 45.d	1.924	0.033	145.94	1.95	168.82	2.25	1.865	0.032	Mica-Mg	NP	S3	210917
MicaMg - 46.d	1.946	0.034	148.84	2.35	172.21	2.71	1.886	0.033	Mica-Mg	NP	S3	210917
MicaMg - 47.d	1.906	0.036	150.01	2.45	173.57	2.83	1.848	0.035	Mica-Mg	NP	S3	210917
MicaMg - 48.d	1.953	0.037	146.28	2.58	169.25	2.99	1.894	0.036	Mica-Mg	NP	S3	210917
MicaMg - 49.d	1.927	0.035	144.60	2.35	167.36	2.72	1.868	0.034	Mica-Mg	NP	S3	210917
MicaMg - 50.d	1.904	0.035	147.63	2.37	170.88	2.74	1.846	0.034	Mica-Mg	NP	S3	210917
MicaMg - 51.d	1.920	0.036	147.81	2.20	171.08	2.54	1.861	0.035	Mica-Mg	NP	S3	210917

Continued on next page

Table 3.B Rb-Sr isotopic ratios calibrated versus NIST 610 glass

Continued from previous page

Spot	Raw $^{87}Sr/^{86}Sr$	2SE	Raw $^{87}Rb/^{86}Sr$	2SE	Calibrated $^{87}Rb/^{86}Sr$	2SE	Calibrated $^{87}Sr/^{86}Sr$	2SE	Sample	Type	Session	Date
MicaMg - 52.d	1.914	0.034	146.22	2.31	169.32	2.67	1.855	0.032	Mica-Mg	NP	S3	210917
MicaMg - 53.d	1.908	0.037	146.16	2.55	169.25	2.96	1.849	0.036	Mica-Mg	NP	S3	210917
MicaMg - 54.d	1.934	0.036	148.61	2.44	172.10	2.83	1.874	0.035	Mica-Mg	NP	S3	210917
MicaMg - 55.d	1.901	0.031	144.21	2.22	167.09	2.57	1.842	0.030	Mica-Mg	NP	S3	210917
MicaMg - 56.d	1.898	0.035	142.60	2.25	165.23	2.61	1.839	0.034	Mica-Mg	NP	S3	210917
MicaMg - 57.d	1.921	0.032	146.01	2.24	169.19	2.60	1.863	0.031	Mica-Mg	NP	S3	210917
MicaMg - 58.d	1.966	0.038	145.69	2.45	168.95	2.84	1.906	0.036	Mica-Mg	NP	S3	210917
MicaMg - 59.d	1.905	0.033	142.95	2.01	165.78	2.33	1.847	0.032	Mica-Mg	NP	S3	210917
MicaMg - 60.d	1.934	0.033	148.13	2.08	171.78	2.42	1.874	0.032	Mica-Mg	NP	S3	210917
Mica Mg - 1.d	1.870	0.031	128.53	2.46	149.63	2.87	1.847	0.031	Mica-Mg	NP	S4	190802
Mica Mg - 2.d	1.880	0.028	137.67	1.81	160.27	2.10	1.858	0.028	Mica-Mg	NP	S4	190802
Mica Mg - 3.d	1.857	0.024	141.96	2.25	165.27	2.62	1.835	0.024	Mica-Mg	NP	S4	190802
Mica Mg - 4.d	1.873	0.023	142.20	1.62	165.55	1.88	1.851	0.023	Mica-Mg	NP	S4	190802
Mica Mg - 5.d	1.891	0.026	143.28	1.76	166.80	2.04	1.868	0.026	Mica-Mg	NP	S4	190802
Mica Mg - 6.d	1.894	0.030	146.24	2.31	170.25	2.69	1.872	0.029	Mica-Mg	NP	S4	190802
Mica Mg - 7.d	1.853	0.026	144.84	1.83	168.62	2.13	1.830	0.026	Mica-Mg	NP	S4	190802
Mica Mg - 8.d	1.867	0.021	144.85	1.63	168.64	1.89	1.845	0.021	Mica-Mg	NP	S4	190802
Mica Mg - 9.d	1.877	0.024	146.47	1.83	170.52	2.13	1.855	0.024	Mica-Mg	NP	S4	190802
Mica Mg - 10.d	1.894	0.025	150.66	2.03	175.40	2.36	1.871	0.025	Mica-Mg	NP	S4	190802
Mica Mg - 11.d	1.883	0.025	150.12	2.07	174.77	2.41	1.861	0.025	Mica-Mg	NP	S4	190802
Mica Mg - 12.d	1.889	0.025	148.18	1.76	172.51	2.05	1.866	0.025	Mica-Mg	NP	S4	190802
Mica Mg - 13.d	1.848	0.025	146.46	1.99	170.50	2.31	1.826	0.025	Mica-Mg	NP	S4	190802
Mica Mg - 14.d	1.878	0.026	147.28	1.83	171.47	2.14	1.855	0.026	Mica-Mg	NP	S4	190802
Mica Mg - 15.d	1.886	0.034	146.58	2.27	170.65	2.64	1.863	0.033	Mica-Mg	NP	S4	190802
Mica Mg - 16.d	1.829	0.032	141.67	2.15	164.93	2.50	1.807	0.031	Mica-Mg	NP	S4	190802
Mica Mg - 17.d	1.879	0.027	147.14	2.00	171.30	2.33	1.856	0.027	Mica-Mg	NP	S4	190802
Mica Mg - 18.d	1.888	0.023	147.15	2.10	171.31	2.45	1.866	0.023	Mica-Mg	NP	S4	190802
Mica Mg - 19.d	1.881	0.027	153.07	2.16	178.20	2.52	1.859	0.027	Mica-Mg	NP	S4	190802

Continued on next page

Table 3.B Rb-Sr isotopic ratios calibrated versus NIST 610 glass

Continued from previous page

Spot	Raw $^{87}Sr/^{86}Sr$	2SE	Raw $^{87}Rb/^{86}Sr$	2SE	Calibrated $^{87}Rb/^{86}Sr$	2SE	Calibrated $^{87}Sr/^{86}Sr$	2SE	Sample	Type	Session	Date
Mica Mg - 20.d	1.860	0.027	151.20	2.08	176.03	2.42	1.838	0.027	Mica-Mg	NP	S4	190802
Mica Mg - 21.d	1.877	0.025	149.17	1.68	173.67	1.96	1.855	0.025	Mica-Mg	NP	S4	190802
Mica Mg - 22.d	1.881	0.025	149.88	1.53	174.49	1.78	1.859	0.025	Mica-Mg	NP	S4	190802
Mica Mg - 23.d	1.864	0.026	149.90	1.87	174.52	2.18	1.842	0.026	Mica-Mg	NP	S4	190802
Mica Mg - 24.d	1.870	0.022	149.35	1.50	173.87	1.75	1.848	0.021	Mica-Mg	NP	S4	190802
Mica Mg - 25.d	1.864	0.031	129.21	1.99	150.43	2.32	1.842	0.031	Mica-Mg	NP	S4	190802
Mica Mg - 26.d	1.863	0.025	148.29	1.95	172.63	2.27	1.840	0.025	Mica-Mg	NP	S4	190802
Mica Mg - 27.d	1.873	0.029	147.05	1.98	171.19	2.31	1.850	0.029	Mica-Mg	NP	S4	190802
Mica Mg - 28.d	1.880	0.023	148.81	1.79	173.25	2.09	1.858	0.023	Mica-Mg	NP	S4	190802
Mica Mg - 29.d	1.871	0.030	148.22	2.32	172.56	2.70	1.849	0.029	Mica-Mg	NP	S4	190802
Mica Mg - 30.d	1.885	0.025	150.13	2.07	174.78	2.41	1.862	0.025	Mica-Mg	NP	S4	190802
Mica Mg - 31.d	1.867	0.027	150.00	2.09	174.63	2.43	1.844	0.027	Mica-Mg	NP	S4	190802
Mica Mg - 32.d	1.878	0.025	151.04	2.29	175.84	2.66	1.855	0.025	Mica-Mg	NP	S4	190802
Mica Mg - 33.d	1.883	0.027	151.96	1.97	176.91	2.29	1.860	0.026	Mica-Mg	NP	S4	190802
Mica Mg - 34.d	1.878	0.026	153.94	2.50	179.22	2.91	1.855	0.026	Mica-Mg	NP	S4	190802
Mica Mg - 35.d	1.874	0.025	148.77	1.78	173.20	2.07	1.851	0.025	Mica-Mg	NP	S4	190802
Mica Mg - 36.d	1.881	0.025	152.38	2.01	177.40	2.33	1.858	0.025	Mica-Mg	NP	S4	190802
Mica Mg - 37.d	1.872	0.025	149.86	2.36	174.47	2.75	1.850	0.024	Mica-Mg	NP	S4	190802
Mica Mg - 38.d	1.878	0.029	150.53	2.33	175.25	2.72	1.856	0.029	Mica-Mg	NP	S4	190802
Mica Mg - 39.d	1.892	0.029	151.36	2.43	176.22	2.83	1.870	0.029	Mica-Mg	NP	S4	190802
Mica-Fe - 1.d	7.407	0.168	1630.48	40.24	2056.41	50.76	7.261	0.165	Mica-Fe	NP	S1	171103
Mica-Fe - 2.d	7.520	0.159	1618.92	33.35	2041.51	42.06	7.372	0.155	Mica-Fe	NP	S1	171103
Mica-Fe - 3.d	7.961	0.138	1696.06	31.00	2138.48	39.09	7.805	0.136	Mica-Fe	NP	S1	171103
Mica-Fe - 4.d	7.839	0.137	1615.57	28.17	2036.76	35.52	7.685	0.135	Mica-Fe	NP	S1	171103
Mica-Fe - 5.d	8.138	0.153	1677.13	32.06	2114.05	40.42	7.978	0.150	Mica-Fe	NP	S1	171103
Mica-Fe - 6.d	8.251	0.152	1677.05	27.33	2113.70	34.44	8.089	0.149	Mica-Fe	NP	S1	171103
Mica-Fe - 7.d	8.304	0.137	1703.10	32.42	2146.30	40.86	8.141	0.134	Mica-Fe	NP	S1	171103
Mica-Fe - 8.d	8.301	0.164	1678.41	35.94	2114.97	45.29	8.138	0.161	Mica-Fe	NP	S1	171103

Continued on next page

Table 3.B Rb-Sr isotopic ratios calibrated versus NIST 610 glass

Continued from previous page

Spot	Raw $^{87}Sr/^{86}Sr$	2SE	Raw $^{87}Rb/^{86}Sr$	2SE	Calibrated $^{87}Rb/^{86}Sr$	2SE	Calibrated $^{87}Sr/^{86}Sr$	2SE	Sample	Type	Session	Date
Mica-Fe - 9.d	8.171	0.163	1589.99	38.57	2003.36	48.59	8.010	0.160	Mica-Fe	NP	S1	171103
Mica-Fe - 10.d	7.655	0.160	1508.65	33.54	1900.67	42.25	7.505	0.157	Mica-Fe	NP	S1	171103
MicaFe-NP - 1.d	8.020	0.330	1661.28	65.78	1912.40	75.72	7.760	0.319	Mica-Fe	NP	S2	210916
MicaFe-NP - 2.d	8.618	0.372	1767.30	64.96	2034.42	74.78	8.338	0.360	Mica-Fe	NP	S2	210916
MicaFe-NP - 3.d	7.774	0.364	1552.85	71.84	1787.55	82.69	7.521	0.352	Mica-Fe	NP	S2	210916
MicaFe-NP - 4.d	8.511	0.413	1718.69	80.77	1978.43	92.97	8.235	0.399	Mica-Fe	NP	S2	210916
MicaFe-NP - 5.d	8.551	0.345	1739.39	68.15	2002.23	78.45	8.274	0.333	Mica-Fe	NP	S2	210916
MicaFe-NP - 6.d	8.965	0.359	1811.85	72.16	2085.63	83.06	8.674	0.347	Mica-Fe	NP	S2	210916
MicaFe-NP - 7.d	8.015	0.284	1614.39	53.50	1858.31	61.58	7.755	0.275	Mica-Fe	NP	S2	210916
MicaFe-NP - 8.d	8.196	0.322	1577.13	57.80	1815.41	66.54	7.929	0.311	Mica-Fe	NP	S2	210916
MicaFe-NP - 9.d	8.295	0.323	1627.89	59.52	1873.83	68.51	8.026	0.313	Mica-Fe	NP	S2	210916
MicaFe-NP - 10.d	7.948	0.306	1531.83	56.73	1763.23	65.30	7.690	0.296	Mica-Fe	NP	S2	210916
MicaFe-NP - 11.d	7.906	0.274	1550.79	53.13	1785.04	61.15	7.650	0.265	Mica-Fe	NP	S2	210916
MicaFe-NP - 12.d	8.129	0.310	1614.30	62.17	1858.14	71.56	7.865	0.300	Mica-Fe	NP	S2	210916
MicaFe-NP - 13.d	8.494	0.349	1680.29	71.05	1934.08	81.78	8.218	0.337	Mica-Fe	NP	S2	210916
MicaFe-NP - 14.d	7.904	0.310	1553.17	57.99	1787.74	66.75	7.648	0.300	Mica-Fe	NP	S2	210916
MicaFe-NP - 15.d	8.145	0.416	1590.53	81.89	1830.74	94.26	7.881	0.403	Mica-Fe	NP	S2	210916
MicaFe-NP - 16.d	8.401	0.368	1634.37	59.01	1881.19	67.92	8.130	0.356	Mica-Fe	NP	S2	210916
MicaFe-NP - 17.d	8.100	0.272	1593.10	51.70	1833.67	59.51	7.838	0.264	Mica-Fe	NP	S2	210916
MicaFe-NP - 18.d	8.147	0.302	1589.39	56.70	1829.39	65.26	7.884	0.292	Mica-Fe	NP	S2	210916
MicaFe-NP - 19.d	8.451	0.393	1685.46	73.79	1939.95	84.94	8.179	0.380	Mica-Fe	NP	S2	210916
MicaFe-NP - 20.d	10.157	0.671	2029.81	133.13	2336.28	153.23	9.830	0.650	Mica-Fe	NP	S2	210916
MICA FE - 1.d	7.936	0.370	1607.53	67.91	1860.23	78.59	7.695	0.359	Mica-Fe	NP	S3	210917
MICA FE - 2.d	8.431	0.314	1696.34	64.26	1962.99	74.37	8.175	0.304	Mica-Fe	NP	S3	210917
MICA FE - 3.d	8.488	0.355	1672.41	64.63	1935.29	74.78	8.230	0.344	Mica-Fe	NP	S3	210917
MICA FE - 4.d	7.871	0.320	1529.83	57.72	1770.29	66.80	7.632	0.311	Mica-Fe	NP	S3	210917
MICA FE - 5.d	7.992	0.439	1586.53	90.21	1835.88	104.39	7.749	0.426	Mica-Fe	NP	S3	210917
MICA FE - 6.d	9.131	0.451	1846.96	85.44	2137.23	98.86	8.854	0.437	Mica-Fe	NP	S3	210917

Continued on next page

Table 3.B Rb-Sr isotopic ratios calibrated versus NIST 610 glass

Continued from previous page

Spot	Raw $^{87}Sr/^{86}Sr$	2SE	Raw $^{87}Rb/^{86}Sr$	2SE	Calibrated $^{87}Rb/^{86}Sr$	2SE	Calibrated $^{87}Sr/^{86}Sr$	2SE	Sample	Type	Session	Date
MICA FE - 7.d	8.834	0.380	1775.16	68.87	2054.05	79.68	8.566	0.368	Mica-Fe	NP	S3	210917
MICA FE - 8.d	9.575	0.399	1942.80	79.02	2248.01	91.43	9.284	0.387	Mica-Fe	NP	S3	210917
MICA FE - 9.d	8.261	0.270	1630.23	47.65	1886.32	55.14	8.010	0.262	Mica-Fe	NP	S3	210917
MICA FE - 10.d	8.550	0.333	1697.17	64.51	1963.77	74.64	8.290	0.323	Mica-Fe	NP	S3	210917
MICA FE - 11.d	8.195	0.319	1658.35	60.44	1918.84	69.94	7.946	0.309	Mica-Fe	NP	S3	210917
MICA FE - 12.d	8.029	0.337	1646.10	67.41	1904.66	78.00	7.785	0.327	Mica-Fe	NP	S3	210917
MICA FE - 13.d	8.098	0.333	1643.62	67.86	1901.78	78.51	7.852	0.323	Mica-Fe	NP	S3	210917
MICA FE - 14.d	8.164	0.327	1643.45	63.97	1901.58	74.02	7.916	0.318	Mica-Fe	NP	S3	210917
MICA FE - 15.d	8.411	0.311	1744.42	66.59	2018.39	77.05	8.155	0.301	Mica-Fe	NP	S3	210917
MICA FE - 16.d	7.525	0.355	1473.24	69.54	1704.61	80.46	7.297	0.344	Mica-Fe	NP	S3	210917
MICA FE - 17.d	8.186	0.305	1610.37	59.19	1863.26	68.48	7.937	0.296	Mica-Fe	NP	S3	210917
MICA FE - 18.d	8.433	0.373	1700.78	73.07	1967.86	84.54	8.177	0.361	Mica-Fe	NP	S3	210917
MICA FE - 19.d	8.180	0.325	1638.39	57.34	1895.67	66.35	7.931	0.315	Mica-Fe	NP	S3	210917
MICA FE - 20.d	8.136	0.338	1641.68	59.79	1899.46	69.17	7.889	0.328	Mica-Fe	NP	S3	210917
MICA FE - 21.d	8.420	0.474	1674.14	83.14	1937.01	96.20	8.165	0.460	Mica-Fe	NP	S3	210917
MICA FE - 22.d	10.550	0.501	2182.45	97.92	2525.13	113.29	10.230	0.486	Mica-Fe	NP	S3	210917
MICA FE - 23.d	9.705	0.456	2056.36	108.40	2379.22	125.42	9.410	0.442	Mica-Fe	NP	S3	210917
MICA FE - 24.d	8.580	0.347	1736.11	68.24	2008.68	78.96	8.320	0.337	Mica-Fe	NP	S3	210917
MICA FE - 25.d	8.370	0.315	1696.69	67.89	1963.07	78.55	8.115	0.305	Mica-Fe	NP	S3	210917
MICA FE - 26.d	7.794	0.330	1583.88	66.74	1832.54	77.21	7.557	0.320	Mica-Fe	NP	S3	210917
MICA FE - 27.d	7.389	0.331	1468.95	63.10	1699.55	73.00	7.164	0.321	Mica-Fe	NP	S3	210917
MICA FE - 28.d	8.106	0.301	1642.33	59.35	1900.14	68.67	7.859	0.292	Mica-Fe	NP	S3	210917
MICA FE - 29.d	8.341	0.309	1655.13	63.19	1914.94	73.11	8.088	0.299	Mica-Fe	NP	S3	210917
MICA FE - 30.d	8.041	0.387	1628.42	85.38	1884.03	98.79	7.796	0.375	Mica-Fe	NP	S3	210917
Mica Fe P - 1.d	8.131	0.258	1948.76	58.51	2268.74	68.12	8.034	0.255	Mica-Fe	NP	S4	190802
Mica Fe P - 2.d	7.801	0.244	1798.64	51.93	2093.97	60.46	7.708	0.241	Mica-Fe	NP	S4	190802
Mica Fe P - 3.d	7.982	0.229	1845.55	54.93	2148.58	63.95	7.887	0.227	Mica-Fe	NP	S4	190802
Mica Fe P - 4.d	8.130	0.252	1863.91	55.68	2169.95	64.82	8.033	0.249	Mica-Fe	NP	S4	190802

Continued on next page

Table 3.B Rb-Sr isotopic ratios calibrated versus NIST 610 glass

Continued from previous page

Spot	Raw $^{87}Sr/^{86}Sr$	2SE	Raw $^{87}Rb/^{86}Sr$	2SE	Calibrated $^{87}Rb/^{86}Sr$	2SE	Calibrated $^{87}Sr/^{86}Sr$	2SE	Sample	Type	Session	Date
Mica Fe P - 5.d	7.994	0.229	1707.09	44.33	1987.38	51.61	7.899	0.227	Mica-Fe	NP	S4	190802
Mica Fe P - 6.d	7.494	0.193	1678.17	39.52	1953.72	46.01	7.405	0.191	Mica-Fe	NP	S4	190802
Mica Fe P - 7.d	7.883	0.198	1752.94	48.67	2040.77	56.66	7.789	0.196	Mica-Fe	NP	S4	190802
Mica Fe P - 8.d	8.344	0.245	1799.14	47.09	2094.54	54.83	8.245	0.242	Mica-Fe	NP	S4	190802
Mica Fe P - 9.d	8.323	0.205	1826.97	47.87	2126.94	55.73	8.224	0.203	Mica-Fe	NP	S4	190802
Mica Fe P - 10.d	8.131	0.188	1758.59	44.96	2047.34	52.34	8.034	0.186	Mica-Fe	NP	S4	190802
Mica Fe P - 11.d	7.485	0.268	1692.72	57.48	1970.65	66.92	7.396	0.265	Mica-Fe	NP	S4	190802
Mica Fe P - 12.d	8.271	0.217	1803.42	52.52	2099.53	61.14	8.173	0.215	Mica-Fe	NP	S4	190802
Mica Fe P - 13.d	8.563	0.261	1871.07	58.56	2178.28	68.17	8.461	0.258	Mica-Fe	NP	S4	190802
Mica Fe P - 14.d	8.253	0.250	1790.24	56.48	2084.19	65.76	8.155	0.247	Mica-Fe	NP	S4	190802
Mica Fe P - 15.d	7.819	0.192	1654.65	39.40	1926.34	45.86	7.725	0.190	Mica-Fe	NP	S4	190802
Mica Fe P - 16.d	8.093	0.223	1775.25	48.39	2066.74	56.34	7.997	0.220	Mica-Fe	NP	S4	190802
Mica Fe P - 17.d	8.231	0.225	1767.52	51.05	2057.73	59.44	8.133	0.223	Mica-Fe	NP	S4	190802
Mica Fe P - 18.d	8.948	0.252	1902.81	59.18	2215.24	68.90	8.842	0.249	Mica-Fe	NP	S4	190802
Mica Fe P - 19.d	7.462	0.214	1601.17	47.52	1864.07	55.32	7.373	0.212	Mica-Fe	NP	S4	190802
Mica Fe P - 20.d	8.053	0.247	1750.25	48.91	2037.63	56.95	7.957	0.244	Mica-Fe	NP	S4	190802
GLO-nano-S - 1.d	0.789	0.013	32.84	0.40	39.55	0.48	0.762	0.013	GL-O	NP	S1	200206
GLO-nano-S - 2.d	0.780	0.013	31.92	0.35	38.45	0.42	0.754	0.012	GL-O	NP	S1	200206
GLO-nano-S - 3.d	0.778	0.011	32.65	0.36	39.33	0.44	0.751	0.011	GL-O	NP	S1	200206
GLO-nano-S - 4.d	0.764	0.011	29.42	0.34	35.44	0.41	0.738	0.011	GL-O	NP	S1	200206
GLO-nano-S - 5.d	0.792	0.014	32.58	0.45	39.25	0.54	0.765	0.013	GL-O	NP	S1	200206
GLO-nano-S - 6.d	0.774	0.012	31.82	0.37	38.34	0.44	0.748	0.012	GL-O	NP	S1	200206
GLO-nano-S - 7.d	0.792	0.012	32.22	0.39	38.81	0.48	0.765	0.012	GL-O	NP	S1	200206
GLO-nano-S - 8.d	0.781	0.012	33.05	0.44	39.82	0.53	0.754	0.012	GL-O	NP	S1	200206
GLO-nano-S - 9.d	0.788	0.012	32.30	0.41	38.91	0.49	0.761	0.012	GL-O	NP	S1	200206
GLO-nano-S - 10.d	0.795	0.012	32.68	0.39	39.37	0.47	0.767	0.012	GL-O	NP	S1	200206
GLO-nano-S - 11.d	0.783	0.013	32.17	0.43	38.75	0.52	0.756	0.013	GL-O	NP	S1	200206
GLO-nano-S - 12.d	0.793	0.012	32.24	0.39	38.83	0.46	0.766	0.012	GL-O	NP	S1	200206

Continued on next page

Table 3.B Rb-Sr isotopic ratios calibrated versus NIST 610 glass

Continued from previous page

Spot	Raw $^{87}Sr/^{86}Sr$	2SE	Raw $^{87}Rb/^{86}Sr$	2SE	Calibrated $^{87}Rb/^{86}Sr$	2SE	Calibrated $^{87}Sr/^{86}Sr$	2SE	Sample	Type	Session	Date
GLO-nano-S - 13.d	0.785	0.012	31.67	0.33	38.15	0.40	0.758	0.012	GL-O	NP	S1	200206
GLO-nano-S - 14.d	0.776	0.012	31.72	0.36	38.21	0.44	0.749	0.012	GL-O	NP	S1	200206
GLO-nano-S - 15.d	0.775	0.012	31.68	0.38	38.17	0.46	0.748	0.012	GL-O	NP	S1	200206
GLO-nano-S - 16.d	0.772	0.011	32.00	0.41	38.55	0.50	0.745	0.011	GL-O	NP	S1	200206
GLO-nano-S - 17.d	0.779	0.012	32.08	0.41	38.64	0.49	0.752	0.012	GL-O	NP	S1	200206
GLO-nano-S - 18.d	0.787	0.011	32.31	0.38	38.92	0.46	0.760	0.011	GL-O	NP	S1	200206
GLO-nano-S - 19.d	0.773	0.011	31.84	0.34	38.36	0.41	0.747	0.011	GL-O	NP	S1	200206
GLO-nano-S - 20.d	0.775	0.013	32.04	0.51	38.59	0.62	0.749	0.013	GL-O	NP	S1	200206
GLO-nano - 1.d	0.783	0.013	33.08	0.53	39.85	0.64	0.756	0.013	GL-O	NP	S1	200206
GLO-nano - 2.d	0.783	0.013	31.46	0.43	37.89	0.52	0.756	0.013	GL-O	NP	S1	200206
GLO-nano - 3.d	0.788	0.014	32.85	0.41	39.58	0.49	0.761	0.013	GL-O	NP	S1	200206
GLO-nano - 4.d	0.776	0.012	31.75	0.44	38.25	0.53	0.750	0.012	GL-O	NP	S1	200206
GLO-nano - 5.d	0.784	0.013	33.35	0.50	40.18	0.60	0.757	0.012	GL-O	NP	S1	200206
GLO-nano - 6.d	0.796	0.015	34.30	0.64	41.32	0.77	0.769	0.014	GL-O	NP	S1	200206
GLO-nano - 7.d	0.790	0.014	31.98	0.42	38.52	0.51	0.763	0.013	GL-O	NP	S1	200206
GLO-nano - 8.d	0.786	0.012	32.61	0.37	39.29	0.44	0.759	0.011	GL-O	NP	S1	200206
GLO-nano - 9.d	0.787	0.011	32.67	0.38	39.35	0.46	0.760	0.010	GL-O	NP	S1	200206
GLO-nano - 10.d	0.789	0.013	32.86	0.45	39.58	0.54	0.762	0.012	GL-O	NP	S1	200206
GLO-nano - 11.d	0.777	0.013	31.63	0.37	38.10	0.45	0.750	0.012	GL-O	NP	S1	200206
GLO-nano - 12.d	0.782	0.012	31.45	0.43	37.89	0.52	0.755	0.011	GL-O	NP	S1	200206
GLO-nano - 13.d	0.777	0.011	32.12	0.38	38.69	0.45	0.750	0.010	GL-O	NP	S1	200206
GLO-nano - 14.d	0.776	0.012	31.47	0.42	37.90	0.50	0.750	0.011	GL-O	NP	S1	200206
GLO-nano - 15.d	0.766	0.013	31.06	0.40	37.42	0.48	0.740	0.012	GL-O	NP	S1	200206
GLO-nano - 16.d	0.780	0.012	32.42	0.42	39.05	0.51	0.753	0.012	GL-O	NP	S1	200206
GLO-nano - 17.d	0.787	0.010	31.82	0.37	38.34	0.44	0.760	0.010	GL-O	NP	S1	200206
GLO-nano - 18.d	0.787	0.011	32.69	0.41	39.38	0.49	0.760	0.011	GL-O	NP	S1	200206
GLO-nano - 19.d	0.775	0.012	32.12	0.39	38.69	0.47	0.749	0.012	GL-O	NP	S1	200206
GLO-nano - 20.d	0.776	0.011	31.51	0.39	37.96	0.47	0.749	0.010	GL-O	NP	S1	200206

Continued on next page

Table 3.B Rb-Sr isotopic ratios calibrated versus NIST 610 glass

Continued from previous page

Spot	Raw $^{87}Sr/^{86}Sr$	2SE	Raw $^{87}Rb/^{86}Sr$	2SE	Calibrated $^{87}Rb/^{86}Sr$	2SE	Calibrated $^{87}Sr/^{86}Sr$	2SE	Sample	Type	Session	Date
GLO-nano - 21.d	0.783	0.012	31.45	0.34	37.89	0.41	0.756	0.011	GL-O	NP	S1	200206
GLO-nano - 22.d	0.777	0.011	31.60	0.47	38.07	0.57	0.750	0.011	GL-O	NP	S1	200206
GLO-nano - 23.d	0.773	0.012	32.97	0.45	39.72	0.55	0.746	0.011	GL-O	NP	S1	200206
GLO-nano - 24.d	0.792	0.012	32.13	0.41	38.71	0.49	0.765	0.012	GL-O	NP	S1	200206
GLO-nano - 25.d	0.777	0.011	31.25	0.35	37.65	0.42	0.751	0.011	GL-O	NP	S1	200206
GLO-nano - 26.d	0.783	0.012	31.45	0.39	37.88	0.47	0.756	0.012	GL-O	NP	S1	200206
GLO-NP - 1.d	0.777	0.016	32.24	0.52	36.98	0.60	0.753	0.016	GL-O	NP	S2	210916
GLO-NP - 2.d	0.775	0.017	32.56	0.49	37.36	0.56	0.751	0.016	GL-O	NP	S2	210916
GLO-NP - 3.d	0.765	0.014	32.10	0.54	36.95	0.62	0.743	0.014	GL-O	NP	S2	210916
GLO-NP - 4.d	0.780	0.018	32.27	0.53	37.14	0.61	0.758	0.017	GL-O	NP	S2	210916
GLO-NP - 5.d	0.793	0.015	32.16	0.42	37.06	0.49	0.769	0.014	GL-O	NP	S2	210916
GLO-NP - 6.d	0.783	0.016	32.86	0.54	37.87	0.63	0.759	0.015	GL-O	NP	S2	210916
GLO-NP - 7.d	0.778	0.017	31.94	0.50	36.81	0.58	0.755	0.017	GL-O	NP	S2	210916
GLO-NP - 8.d	0.789	0.016	32.79	0.47	37.78	0.55	0.766	0.016	GL-O	NP	S2	210916
GLO-NP - 9.d	0.784	0.016	31.59	0.49	36.34	0.56	0.759	0.016	GL-O	NP	S2	210916
GLO-NP - 10.d	0.772	0.015	32.90	0.46	37.86	0.53	0.747	0.015	GL-O	NP	S2	210916
GLO-NP - 11.d	0.794	0.018	32.96	0.55	37.86	0.64	0.769	0.017	GL-O	NP	S2	210916
GLO-NP - 12.d	0.786	0.015	32.82	0.49	37.70	0.56	0.762	0.015	GL-O	NP	S2	210916
GLO-NP - 13.d	0.772	0.015	31.83	0.43	36.55	0.49	0.748	0.015	GL-O	NP	S2	210916
GLO-NP - 14.d	0.766	0.015	32.33	0.43	37.13	0.50	0.743	0.014	GL-O	NP	S2	210916
GLO-NP - 15.d	0.770	0.016	31.58	0.52	36.29	0.60	0.747	0.016	GL-O	NP	S2	210916
GLO-NP - 16.d	0.786	0.017	33.15	0.52	38.09	0.60	0.763	0.017	GL-O	NP	S2	210916
GLO-NP - 17.d	0.785	0.016	32.41	0.46	37.28	0.53	0.763	0.016	GL-O	NP	S2	210916
GLO-NP - 18.d	0.777	0.015	32.13	0.59	36.96	0.68	0.755	0.015	GL-O	NP	S2	210916
GLO-NP - 19.d	0.787	0.016	32.38	0.53	37.26	0.61	0.763	0.016	GL-O	NP	S2	210916
GLO-NP - 20.d	0.789	0.017	32.43	0.50	37.33	0.58	0.765	0.016	GL-O	NP	S2	210916
GLO-NP - 21.d	0.776	0.017	32.41	0.56	37.32	0.64	0.753	0.016	GL-O	NP	S2	210916
GLO-NP - 22.d	0.766	0.016	31.94	0.51	36.77	0.59	0.743	0.015	GL-O	NP	S2	210916

Continued on next page

Table 3.B Rb-Sr isotopic ratios calibrated versus NIST 610 glass

Continued from previous page

Spot	Raw $^{87}Sr/^{86}Sr$	2SE	Raw $^{87}Rb/^{86}Sr$	2SE	Calibrated $^{87}Rb/^{86}Sr$	2SE	Calibrated $^{87}Sr/^{86}Sr$	2SE	Sample	Type	Session	Date
GLO-NP - 23.d	0.775	0.016	31.83	0.46	36.69	0.53	0.752	0.016	GL-O	NP	S2	210916
GLO-NP - 24.d	0.775	0.014	32.41	0.55	37.36	0.63	0.752	0.014	GL-O	NP	S2	210916
GLO-NP - 25.d	0.785	0.015	32.72	0.46	37.73	0.53	0.761	0.015	GL-O	NP	S2	210916
GLO-NP - 26.d	0.789	0.014	30.67	0.63	35.37	0.73	0.764	0.013	GL-O	NP	S2	210916
GLO-NP - 27.d	0.788	0.014	32.52	0.51	37.49	0.59	0.762	0.014	GL-O	NP	S2	210916
GLO-NP - 28.d	0.783	0.016	32.46	0.55	37.42	0.63	0.758	0.016	GL-O	NP	S2	210916
GLO-NP - 29.d	0.773	0.015	33.76	0.53	38.90	0.61	0.751	0.015	GL-O	NP	S2	210916
GLO-NP - 30.d	0.791	0.015	32.60	0.51	37.57	0.59	0.768	0.015	GL-O	NP	S2	210916
GLO-NP - 31.d	0.785	0.015	32.73	0.44	37.68	0.51	0.760	0.015	GL-O	NP	S2	210916
GLO-NP - 32.d	0.777	0.016	31.59	0.52	36.37	0.60	0.752	0.015	GL-O	NP	S2	210916
GLO-NP - 33.d	0.768	0.015	31.57	0.45	36.34	0.52	0.744	0.015	GL-O	NP	S2	210916
GLO-NP - 34.d	0.776	0.016	32.49	0.57	37.39	0.65	0.752	0.015	GL-O	NP	S2	210916
GLO nano - 1.d	0.785	0.018	30.15	0.58	34.91	0.67	0.761	0.017	GL-O	NP	S3	210917
GLO nano - 2.d	0.772	0.017	30.24	0.48	35.01	0.55	0.748	0.017	GL-O	NP	S3	210917
GLO nano - 3.d	0.788	0.016	30.89	0.43	35.77	0.50	0.764	0.015	GL-O	NP	S3	210917
GLO nano - 4.d	0.784	0.017	31.56	0.59	36.55	0.68	0.760	0.016	GL-O	NP	S3	210917
GLO nano - 5.d	0.775	0.015	30.45	0.52	35.26	0.60	0.751	0.015	GL-O	NP	S3	210917
GLO nano - 6.d	0.766	0.016	30.89	0.50	35.78	0.58	0.743	0.015	GL-O	NP	S3	210917
GLO nano - 7.d	0.773	0.014	29.42	0.48	34.07	0.55	0.749	0.014	GL-O	NP	S3	210917
GLO nano - 8.d	0.772	0.016	30.17	0.50	34.94	0.58	0.749	0.015	GL-O	NP	S3	210917
GLO nano - 9.d	0.771	0.015	30.59	0.51	35.42	0.59	0.748	0.015	GL-O	NP	S3	210917
GLO nano - 10.d	0.789	0.015	31.86	0.55	36.90	0.64	0.765	0.015	GL-O	NP	S3	210917
GLO nano - 11.d	0.773	0.014	30.95	0.47	35.85	0.55	0.749	0.013	GL-O	NP	S3	210917
GLO nano - 12.d	0.784	0.016	31.60	0.52	36.60	0.61	0.760	0.015	GL-O	NP	S3	210917
GLO nano - 13.d	0.777	0.015	31.76	0.50	36.78	0.58	0.753	0.014	GL-O	NP	S3	210917
GLO nano - 14.d	0.787	0.014	31.66	0.43	36.67	0.50	0.763	0.013	GL-O	NP	S3	210917
GLO nano - 15.d	0.790	0.017	31.11	0.46	36.04	0.54	0.766	0.016	GL-O	NP	S3	210917
GLO nano - 16.d	0.763	0.015	30.91	0.46	35.81	0.53	0.739	0.014	GL-O	NP	S3	210917

Continued on next page

Table 3.B Rb-Sr isotopic ratios calibrated versus NIST 610 glass

Continued from previous page

Spot	Raw $^{87}Sr/^{86}Sr$	2SE	Raw $^{87}Rb/^{86}Sr$	2SE	Calibrated $^{87}Rb/^{86}Sr$	2SE	Calibrated $^{87}Sr/^{86}Sr$	2SE	Sample	Type	Session	Date
GLO nano - 17.d	0.789	0.015	32.52	0.48	37.67	0.55	0.765	0.015	GL-O	NP	S3	210917
GLO nano - 18.d	0.779	0.014	32.03	0.49	37.11	0.56	0.755	0.013	GL-O	NP	S3	210917
GLO nano - 19.d	0.788	0.017	32.38	0.59	37.51	0.69	0.763	0.016	GL-O	NP	S3	210917
GLO nano - 20.d	0.778	0.016	31.44	0.44	36.42	0.51	0.754	0.016	GL-O	NP	S3	210917
GLO nano - 21.d	0.769	0.014	31.55	0.57	36.55	0.66	0.746	0.013	GL-O	NP	S3	210917
GLO nano - 22.d	0.777	0.016	31.61	0.48	36.61	0.55	0.753	0.015	GL-O	NP	S3	210917
GLO nano - 23.d	0.775	0.016	31.73	0.49	36.75	0.57	0.751	0.015	GL-O	NP	S3	210917
GLO nano - 24.d	0.776	0.015	31.71	0.48	36.73	0.55	0.752	0.014	GL-O	NP	S3	210917
GLO nano - 25.d	0.770	0.016	31.44	0.47	36.43	0.55	0.746	0.015	GL-O	NP	S3	210917
GLO nano - 26.d	0.782	0.015	32.67	0.47	37.85	0.55	0.758	0.015	GL-O	NP	S3	210917
GLO nano - 27.d	0.762	0.016	31.64	0.51	36.66	0.59	0.738	0.015	GL-O	NP	S3	210917
GLO nano - 28.d	0.767	0.016	31.24	0.50	36.20	0.57	0.744	0.016	GL-O	NP	S3	210917
GLO nano - 29.d	0.757	0.015	30.87	0.50	35.76	0.58	0.734	0.014	GL-O	NP	S3	210917
GLO nano - 30.d	0.785	0.017	31.70	0.50	36.73	0.58	0.761	0.017	GL-O	NP	S3	210917
FK-N C3 - 1.d	1.238	0.010	66.67	0.79	84.38	1.00	1.213	0.010	FK-N	NP	S1	171103
FK-N C3 - 2.d	1.240	0.010	66.66	0.62	84.33	0.79	1.215	0.009	FK-N	NP	S1	171103
FK-N C3 - 3.d	1.246	0.011	67.49	0.62	85.38	0.78	1.222	0.010	FK-N	NP	S1	171103
FK-N C3 - 4.d	1.245	0.011	66.91	0.74	84.62	0.94	1.221	0.011	FK-N	NP	S1	171103
FK-N C3 - 5.d	1.242	0.009	70.29	0.72	88.88	0.91	1.218	0.009	FK-N	NP	S1	171103
FK-N C3 - 6.d	1.223	0.009	62.65	0.67	79.20	0.85	1.199	0.009	FK-N	NP	S1	171103
FK-N C3 - 7.d	1.234	0.010	67.41	0.70	85.21	0.88	1.210	0.009	FK-N	NP	S1	171103
FK-N C3 - 8.d	1.234	0.009	68.46	0.96	86.50	1.21	1.210	0.009	FK-N	NP	S1	171103
FK-N C3 - 9.d	1.230	0.010	66.97	0.76	84.61	0.96	1.206	0.010	FK-N	NP	S1	171103
FK-N C3 - 10.d	1.237	0.010	67.97	0.62	85.86	0.79	1.213	0.010	FK-N	NP	S1	171103
FK-N-NP - 1.d	1.232	0.023	66.22	1.35	76.26	1.56	1.195	0.022	FK-N	NP	S2	210916
FK-N-NP - 2.d	1.259	0.029	70.89	1.77	81.64	2.04	1.221	0.028	FK-N	NP	S2	210916
FK-N-NP - 3.d	1.243	0.023	65.02	1.07	74.88	1.23	1.205	0.022	FK-N	NP	S2	210916
FK-N-NP - 4.d	1.259	0.024	68.25	1.50	78.60	1.73	1.220	0.023	FK-N	NP	S2	210916

Continued on next page

Table 3.B Rb-Sr isotopic ratios calibrated versus NIST 610 glass

Continued from previous page

Spot	Raw $^{87}Sr/^{86}Sr$	2SE	Raw $^{87}Rb/^{86}Sr$	2SE	Calibrated $^{87}Rb/^{86}Sr$	2SE	Calibrated $^{87}Sr/^{86}Sr$	2SE	Sample	Type	Session	Date
FK-N-NP - 5.d	1.253	0.021	69.22	1.49	79.71	1.71	1.215	0.021	FK-N	NP	S2	210916
FK-N-NP - 6.d	1.249	0.022	67.30	1.42	77.50	1.63	1.211	0.021	FK-N	NP	S2	210916
FK-N-NP - 7.d	1.250	0.021	63.11	1.21	72.68	1.39	1.212	0.021	FK-N	NP	S2	210916
FK-N-NP - 8.d	1.262	0.021	69.41	1.40	79.93	1.61	1.223	0.020	FK-N	NP	S2	210916
FK-N-NP - 9.d	1.230	0.022	64.90	1.42	74.73	1.63	1.192	0.021	FK-N	NP	S2	210916
FK-N-NP - 10.d	1.245	0.020	65.03	1.31	74.88	1.50	1.207	0.020	FK-N	NP	S2	210916
FK-N-NP - 11.d	1.264	0.019	68.17	1.14	78.49	1.31	1.225	0.018	FK-N	NP	S2	210916
FK-N-NP - 12.d	1.259	0.022	66.71	1.18	76.80	1.36	1.219	0.021	FK-N	NP	S2	210916
FK-N-NP - 13.d	1.244	0.024	67.55	1.38	77.77	1.59	1.204	0.023	FK-N	NP	S2	210916
FK-N-NP - 14.d	1.266	0.020	66.11	1.27	76.11	1.46	1.225	0.019	FK-N	NP	S2	210916
FK-N-NP - 15.d	1.268	0.024	69.36	1.62	79.85	1.86	1.228	0.024	FK-N	NP	S2	210916
FK-N-NP - 16.d	1.276	0.023	68.45	1.41	78.80	1.62	1.235	0.022	FK-N	NP	S2	210916
FK-N-NP - 17.d	1.270	0.027	68.09	1.58	78.39	1.82	1.229	0.026	FK-N	NP	S2	210916
FK-N-NP - 18.d	1.245	0.021	66.58	1.15	76.64	1.33	1.205	0.021	FK-N	NP	S2	210916
FK-N-NP - 19.d	1.270	0.027	68.59	1.36	78.96	1.57	1.228	0.026	FK-N	NP	S2	210916
FK-N-NP - 20.d	1.260	0.023	68.50	1.46	78.85	1.68	1.219	0.022	FK-N	NP	S2	210916
KSP FK-N - 1.d	1.266	0.024	66.35	1.22	76.85	1.42	1.228	0.024	FK-N	NP	S3	210917
KSP FK-N - 2.d	1.225	0.020	62.86	1.16	72.82	1.35	1.188	0.020	FK-N	NP	S3	210917
KSP FK-N - 3.d	1.254	0.025	64.90	1.35	75.18	1.57	1.217	0.024	FK-N	NP	S3	210917
KSP FK-N - 4.d	1.243	0.022	69.48	1.38	80.49	1.59	1.206	0.022	FK-N	NP	S3	210917
KSP FK-N - 5.d	1.246	0.021	65.66	1.18	76.06	1.36	1.208	0.021	FK-N	NP	S3	210917
KSP FK-N - 6.d	1.250	0.026	68.54	1.31	79.40	1.52	1.212	0.025	FK-N	NP	S3	210917
KSP FK-N - 7.d	1.249	0.020	64.92	1.32	75.21	1.53	1.212	0.019	FK-N	NP	S3	210917
KSP FK-N - 8.d	1.251	0.024	69.06	1.46	80.01	1.69	1.213	0.024	FK-N	NP	S3	210917
KSP FK-N - 9.d	1.258	0.024	67.41	1.22	78.10	1.41	1.220	0.023	FK-N	NP	S3	210917
KSP FK-N - 10.d	1.268	0.022	67.77	1.34	78.51	1.56	1.230	0.021	FK-N	NP	S3	210917
KSP FK-N - 11.d	1.242	0.026	65.71	1.69	76.13	1.96	1.204	0.026	FK-N	NP	S3	210917
KSP FK-N - 12.d	1.262	0.026	72.32	1.60	83.79	1.85	1.224	0.025	FK-N	NP	S3	210917

Continued on next page

Table 3.B Rb-Sr isotopic ratios calibrated versus NIST 610 glass

Continued from previous page

Spot	Raw $^{87}Sr/^{86}Sr$	2SE	Raw $^{87}Rb/^{86}Sr$	2SE	Calibrated $^{87}Rb/^{86}Sr$	2SE	Calibrated $^{87}Sr/^{86}Sr$	2SE	Sample	Type	Session	Date
KSP FK-N - 13.d	1.262	0.025	68.22	1.36	79.04	1.58	1.224	0.024	FK-N	NP	S3	210917
KSP FK-N - 14.d	1.254	0.023	64.78	1.19	75.05	1.38	1.216	0.022	FK-N	NP	S3	210917
KSP FK-N - 15.d	1.279	0.024	68.80	1.41	79.71	1.63	1.241	0.023	FK-N	NP	S3	210917
KSP FK-N - 16.d	1.249	0.024	68.30	1.54	79.14	1.79	1.212	0.024	FK-N	NP	S3	210917
KSP FK-N - 17.d	1.270	0.026	68.88	1.36	79.80	1.57	1.232	0.025	FK-N	NP	S3	210917
KSP FK-N - 18.d	1.251	0.024	67.94	1.52	78.72	1.76	1.213	0.024	FK-N	NP	S3	210917
KSP FK-N - 19.d	1.268	0.029	67.78	1.38	78.53	1.59	1.230	0.028	FK-N	NP	S3	210917
KSP FK-N - 20.d	1.247	0.023	68.07	1.32	78.87	1.53	1.209	0.022	FK-N	NP	S3	210917
KSP FK-N - 21.d	1.255	0.024	69.30	1.39	80.29	1.61	1.217	0.023	FK-N	NP	S3	210917
KSP FK-N - 22.d	1.273	0.026	72.37	1.43	83.85	1.66	1.234	0.025	FK-N	NP	S3	210917
KSP FK-N - 23.d	1.236	0.023	65.60	1.34	76.01	1.55	1.199	0.023	FK-N	NP	S3	210917
KSP FK-N - 24.d	1.245	0.022	67.86	1.50	78.63	1.74	1.207	0.021	FK-N	NP	S3	210917
KSP FK-N - 25.d	1.263	0.022	64.48	1.12	74.71	1.30	1.225	0.022	FK-N	NP	S3	210917
KSP FK-N - 26.d	1.261	0.023	68.48	1.35	79.35	1.57	1.223	0.022	FK-N	NP	S3	210917
KSP FK-N - 27.d	1.231	0.022	68.27	1.35	79.10	1.57	1.194	0.022	FK-N	NP	S3	210917
KSP FK-N - 28.d	1.251	0.025	66.85	1.32	77.45	1.53	1.213	0.025	FK-N	NP	S3	210917
KSP FK-N - 29.d	1.267	0.025	68.21	1.62	79.03	1.88	1.229	0.025	FK-N	NP	S3	210917
KF Powder - 1.csv	1.219	0.017	68.37	1.13	79.60	1.31	1.205	0.017	FK-N	NP	S4	190802
KF Powder - 2.csv	1.219	0.014	65.27	0.76	75.98	0.88	1.205	0.014	FK-N	NP	S4	190802
KF Powder - 3.csv	1.230	0.014	67.35	0.86	78.40	1.00	1.215	0.014	FK-N	NP	S4	190802
KF Powder - 4.csv	1.243	0.014	66.86	0.90	77.84	1.05	1.228	0.013	FK-N	NP	S4	190802
KF Powder - 5.csv	1.223	0.017	69.13	0.98	80.49	1.14	1.208	0.017	FK-N	NP	S4	190802
KF Powder - 6.csv	1.235	0.016	67.64	0.80	78.75	0.93	1.220	0.016	FK-N	NP	S4	190802
KF Powder - 7.csv	1.227	0.016	66.43	0.80	77.34	0.93	1.213	0.015	FK-N	NP	S4	190802
KF Powder - 8.csv	1.215	0.014	67.43	0.82	78.51	0.96	1.201	0.014	FK-N	NP	S4	190802
KF Powder - 9.csv	1.215	0.014	66.08	0.81	76.93	0.95	1.200	0.014	FK-N	NP	S4	190802
KF Powder - 10.csv	1.222	0.014	68.15	0.99	79.35	1.15	1.207	0.014	FK-N	NP	S4	190802
KF Powder - 11.csv	1.247	0.017	68.92	0.87	80.24	1.01	1.232	0.017	FK-N	NP	S4	190802

Continued on next page

Table 3.B Rb-Sr isotopic ratios calibrated versus NIST 610 glass

Continued from previous page

Spot	Raw $^{87}Sr/^{86}Sr$	2SE	Raw $^{87}Rb/^{86}Sr$	2SE	Calibrated $^{87}Rb/^{86}Sr$	2SE	Calibrated $^{87}Sr/^{86}Sr$	2SE	Sample	Type	Session	Date
KF Powder - 12.csv	1.234	0.014	67.38	0.68	78.44	0.79	1.220	0.014	FK-N	NP	S4	190802
KF Powder - 13.csv	1.216	0.013	65.88	0.92	76.70	1.07	1.202	0.013	FK-N	NP	S4	190802
KF Powder - 14.csv	1.224	0.015	67.16	0.94	78.18	1.10	1.209	0.015	FK-N	NP	S4	190802
KF Powder - 15.csv	1.229	0.013	64.92	0.81	75.58	0.95	1.215	0.013	FK-N	NP	S4	190802
KF Powder - 16.csv	1.227	0.015	66.20	1.02	77.07	1.19	1.212	0.015	FK-N	NP	S4	190802
KF Powder - 17.csv	1.218	0.013	66.48	0.72	77.39	0.84	1.203	0.013	FK-N	NP	S4	190802
KF Powder - 18.csv	1.231	0.013	67.95	0.75	79.11	0.87	1.217	0.012	FK-N	NP	S4	190802
KF Powder - 19.csv	1.230	0.013	64.93	0.93	75.59	1.08	1.216	0.013	FK-N	NP	S4	190802
KF Powder - 20.csv	1.235	0.016	68.22	0.87	79.42	1.02	1.220	0.015	FK-N	NP	S4	190802
KF Powder - 21.csv	1.225	0.015	65.62	0.89	76.39	1.03	1.211	0.015	FK-N	NP	S4	190802
BCR - 1.d	0.718	0.002	0.37	0.00	0.48	0.00	0.704	0.002	BCR-2G	G	S1	171103
BCR - 2.d	0.720	0.002	0.35	0.00	0.46	0.00	0.706	0.002	BCR-2G	G	S1	171103
BCR - 3.d	0.720	0.003	0.35	0.00	0.45	0.00	0.706	0.003	BCR-2G	G	S1	171103
BCR - 4.d	0.719	0.002	0.35	0.00	0.45	0.00	0.705	0.002	BCR-2G	G	S1	171103
BCR - 5.d	0.718	0.003	0.35	0.00	0.44	0.00	0.704	0.002	BCR-2G	G	S1	171103
BCR - 6.d	0.717	0.003	0.35	0.00	0.45	0.00	0.703	0.003	BCR-2G	G	S1	171103
BCR - 7.d	0.719	0.003	0.35	0.00	0.44	0.00	0.705	0.003	BCR-2G	G	S1	171103
BCR - 8.d	0.718	0.003	0.35	0.00	0.45	0.00	0.704	0.003	BCR-2G	G	S1	171103
BCR - 9.d	0.719	0.003	0.35	0.00	0.45	0.01	0.705	0.003	BCR-2G	G	S1	171103
BCR - 10.d	0.720	0.003	0.36	0.00	0.45	0.00	0.706	0.003	BCR-2G	G	S1	171103
BCR - 11.d	0.717	0.003	0.36	0.00	0.45	0.01	0.703	0.003	BCR-2G	G	S1	171103
BCR - 12.d	0.717	0.003	0.35	0.00	0.44	0.00	0.703	0.003	BCR-2G	G	S1	171103
BCR - 13.d	0.721	0.002	0.35	0.00	0.44	0.00	0.707	0.002	BCR-2G	G	S1	171103
BCR - 14.d	0.720	0.003	0.35	0.00	0.45	0.00	0.706	0.003	BCR-2G	G	S1	171103
BCR - 15.d	0.719	0.003	0.35	0.00	0.44	0.00	0.705	0.003	BCR-2G	G	S1	171103
BCR - 16.d	0.717	0.003	0.35	0.00	0.44	0.00	0.703	0.003	BCR-2G	G	S1	171103
BCR - 17.d	0.719	0.002	0.36	0.00	0.45	0.00	0.705	0.002	BCR-2G	G	S1	171103
BCR - 18.d	0.719	0.002	0.35	0.00	0.45	0.00	0.705	0.002	BCR-2G	G	S1	171103

Continued on next page

Table 3.B Rb-Sr isotopic ratios calibrated versus NIST 610 glass

Continued from previous page

Spot	Raw $^{87}Sr/^{86}Sr$	2SE	Raw $^{87}Rb/^{86}Sr$	2SE	Calibrated $^{87}Rb/^{86}Sr$	2SE	Calibrated $^{87}Sr/^{86}Sr$	2SE	Sample	Type	Session	Date
BCR - 19.d	0.720	0.003	0.35	0.00	0.44	0.00	0.706	0.003	BCR-2G	G	S1	171103
BCR - 20.d	0.718	0.003	0.35	0.00	0.44	0.00	0.704	0.003	BCR-2G	G	S1	171103
BCR - 21.d	0.719	0.003	0.35	0.00	0.44	0.00	0.705	0.003	BCR-2G	G	S1	171103
BCR - 22.d	0.718	0.003	0.35	0.00	0.44	0.00	0.704	0.003	BCR-2G	G	S1	171103
BCR - 23.d	0.718	0.003	0.35	0.00	0.43	0.01	0.704	0.003	BCR-2G	G	S1	171103
BCR - 24.d	0.721	0.002	0.34	0.00	0.43	0.00	0.707	0.002	BCR-2G	G	S1	171103
BCR - 25.d	0.718	0.003	0.34	0.00	0.43	0.00	0.704	0.003	BCR-2G	G	S1	171103
BCR - 26.d	0.718	0.002	0.34	0.00	0.42	0.00	0.704	0.002	BCR-2G	G	S1	171103
BCR - 1.d	0.731	0.003	0.36	0.00	0.44	0.00	0.706	0.003	BCR-2G	G	S2	200206
BCR - 2.d	0.730	0.003	0.35	0.00	0.43	0.00	0.705	0.003	BCR-2G	G	S2	200206
BCR - 3.d	0.731	0.003	0.36	0.00	0.43	0.00	0.706	0.003	BCR-2G	G	S2	200206
BCR - 4.d	0.732	0.004	0.35	0.00	0.43	0.00	0.707	0.003	BCR-2G	G	S2	200206
BCR - 5.d	0.732	0.004	0.36	0.00	0.43	0.00	0.707	0.003	BCR-2G	G	S2	200206
BCR - 6.d	0.731	0.004	0.35	0.00	0.42	0.00	0.706	0.004	BCR-2G	G	S2	200206
BCR - 7.d	0.729	0.004	0.35	0.00	0.42	0.00	0.704	0.004	BCR-2G	G	S2	200206
BCR - 8.d	0.727	0.003	0.35	0.00	0.43	0.00	0.702	0.003	BCR-2G	G	S2	200206
BCR - 9.d	0.731	0.004	0.36	0.00	0.43	0.00	0.706	0.004	BCR-2G	G	S2	200206
BCR - 10.d	0.732	0.004	0.36	0.00	0.43	0.00	0.707	0.004	BCR-2G	G	S2	200206
BCR - 11.d	0.729	0.003	0.35	0.00	0.42	0.00	0.704	0.003	BCR-2G	G	S2	200206
BCR - 12.d	0.733	0.004	0.34	0.00	0.41	0.00	0.708	0.003	BCR-2G	G	S2	200206
BCR - 13.d	0.728	0.004	0.35	0.00	0.42	0.00	0.703	0.004	BCR-2G	G	S2	200206
BCR - 14.d	0.732	0.005	0.34	0.00	0.41	0.00	0.707	0.004	BCR-2G	G	S2	200206
BCR - 15.d	0.731	0.004	0.35	0.00	0.42	0.00	0.706	0.004	BCR-2G	G	S2	200206
BCR - 16.d	0.729	0.005	0.34	0.00	0.41	0.00	0.704	0.004	BCR-2G	G	S2	200206
BCR - 17.d	0.728	0.005	0.34	0.00	0.41	0.00	0.703	0.005	BCR-2G	G	S2	200206
BCR - 18.d	0.731	0.004	0.35	0.00	0.42	0.00	0.706	0.004	BCR-2G	G	S2	200206
BCR - 19.d	0.731	0.005	0.35	0.00	0.42	0.00	0.705	0.004	BCR-2G	G	S2	200206
BCR - 20.d	0.735	0.004	0.35	0.00	0.42	0.00	0.710	0.004	BCR-2G	G	S2	200206

Continued on next page

Table 3.B Rb-Sr isotopic ratios calibrated versus NIST 610 glass

Continued from previous page

Spot	Raw $^{87}Sr/^{86}Sr$	2SE	Raw $^{87}Rb/^{86}Sr$	2SE	Calibrated $^{87}Rb/^{86}Sr$	2SE	Calibrated $^{87}Sr/^{86}Sr$	2SE	Sample	Type	Session	Date
BCR - 21.d	0.728	0.005	0.34	0.00	0.42	0.00	0.703	0.005	BCR-2G	G	S2	200206
BCR - 22.d	0.727	0.005	0.34	0.00	0.41	0.00	0.702	0.005	BCR-2G	G	S2	200206
BCR - 23.d	0.733	0.004	0.34	0.00	0.42	0.00	0.707	0.004	BCR-2G	G	S2	200206
BCR - 24.d	0.733	0.004	0.34	0.00	0.41	0.00	0.708	0.004	BCR-2G	G	S2	200206
BCR - 25.d	0.731	0.004	0.34	0.00	0.42	0.00	0.706	0.004	BCR-2G	G	S2	200206
BCR - 26.d	0.730	0.003	0.34	0.00	0.41	0.00	0.705	0.003	BCR-2G	G	S2	200206
BCR - 1.d	0.731	0.005	0.37	0.00	0.42	0.00	0.708	0.005	BCR-2G	G	S3	210916
BCR - 2.d	0.728	0.005	0.36	0.00	0.41	0.00	0.705	0.005	BCR-2G	G	S3	210916
BCR - 3.d	0.726	0.004	0.36	0.00	0.41	0.00	0.705	0.004	BCR-2G	G	S3	210916
BCR - 4.d	0.730	0.004	0.35	0.00	0.40	0.00	0.708	0.004	BCR-2G	G	S3	210916
BCR - 5.d	0.725	0.005	0.36	0.00	0.41	0.00	0.703	0.005	BCR-2G	G	S3	210916
BCR - 6.d	0.731	0.005	0.35	0.00	0.41	0.00	0.709	0.004	BCR-2G	G	S3	210916
BCR - 7.d	0.731	0.005	0.36	0.00	0.41	0.00	0.709	0.004	BCR-2G	G	S3	210916
BCR - 8.d	0.730	0.005	0.35	0.00	0.40	0.00	0.708	0.005	BCR-2G	G	S3	210916
BCR - 9.d	0.725	0.005	0.35	0.00	0.40	0.00	0.702	0.005	BCR-2G	G	S3	210916
BCR - 10.d	0.724	0.004	0.36	0.00	0.41	0.01	0.701	0.004	BCR-2G	G	S3	210916
BCR - 11.d	0.727	0.005	0.36	0.00	0.41	0.00	0.705	0.005	BCR-2G	G	S3	210916
BCR - 12.d	0.724	0.004	0.35	0.00	0.40	0.00	0.702	0.004	BCR-2G	G	S3	210916
BCR - 13.d	0.726	0.005	0.35	0.00	0.41	0.00	0.704	0.005	BCR-2G	G	S3	210916
BCR - 14.d	0.724	0.005	0.35	0.00	0.41	0.00	0.702	0.004	BCR-2G	G	S3	210916
BCR - 15.d	0.729	0.006	0.35	0.00	0.41	0.01	0.708	0.006	BCR-2G	G	S3	210916
BCR - 16.d	0.723	0.005	0.35	0.00	0.41	0.00	0.702	0.005	BCR-2G	G	S3	210916
BCR - 17.d	0.730	0.005	0.35	0.00	0.41	0.00	0.710	0.005	BCR-2G	G	S3	210916
BCR - 18.d	0.725	0.005	0.35	0.00	0.40	0.00	0.705	0.005	BCR-2G	G	S3	210916
BCR - 19.d	0.730	0.004	0.35	0.00	0.40	0.01	0.707	0.004	BCR-2G	G	S3	210916
BCR - 20.d	0.723	0.005	0.36	0.00	0.41	0.01	0.700	0.005	BCR-2G	G	S3	210916
BCR - 21.d	0.724	0.005	0.35	0.00	0.41	0.00	0.703	0.004	BCR-2G	G	S3	210916
BCR - 22.d	0.727	0.005	0.35	0.00	0.41	0.01	0.705	0.005	BCR-2G	G	S3	210916

Continued on next page

Table 3.B Rb-Sr isotopic ratios calibrated versus NIST 610 glass

Continued from previous page

Spot	Raw $^{87}Sr/^{86}Sr$	2SE	Raw $^{87}Rb/^{86}Sr$	2SE	Calibrated $^{87}Rb/^{86}Sr$	2SE	Calibrated $^{87}Sr/^{86}Sr$	2SE	Sample	Type	Session	Date
BCR - 23.d	0.725	0.005	0.35	0.00	0.41	0.00	0.703	0.005	BCR-2G	G	S3	210916
BCR - 24.d	0.725	0.004	0.35	0.00	0.40	0.01	0.703	0.004	BCR-2G	G	S3	210916
BCR - 25.d	0.727	0.006	0.36	0.00	0.41	0.00	0.704	0.006	BCR-2G	G	S3	210916
BCR - 26.d	0.725	0.005	0.35	0.00	0.40	0.00	0.702	0.005	BCR-2G	G	S3	210916
BCR - 27.d	0.724	0.006	0.36	0.00	0.41	0.00	0.701	0.005	BCR-2G	G	S3	210916
BCR - 28.d	0.726	0.005	0.35	0.00	0.40	0.01	0.703	0.005	BCR-2G	G	S3	210916
BCR - 29.d	0.729	0.005	0.35	0.00	0.40	0.00	0.708	0.005	BCR-2G	G	S3	210916
BCR - 30.d	0.727	0.005	0.35	0.00	0.41	0.00	0.706	0.005	BCR-2G	G	S3	210916
BCR - 31.d	0.728	0.005	0.35	0.00	0.40	0.00	0.705	0.004	BCR-2G	G	S3	210916
BCR - 32.d	0.728	0.005	0.35	0.00	0.40	0.01	0.705	0.005	BCR-2G	G	S3	210916
BCR - 33.d	0.727	0.005	0.36	0.00	0.41	0.01	0.704	0.005	BCR-2G	G	S3	210916
BCR - 34.d	0.731	0.005	0.36	0.00	0.41	0.01	0.708	0.005	BCR-2G	G	S3	210916
BCR - 1.d	0.715	0.003	0.37	0.00	0.43	0.00	0.706	0.003	BCR-2G	G	S4	190802
BCR - 2.d	0.710	0.004	0.37	0.00	0.43	0.00	0.702	0.004	BCR-2G	G	S4	190802
BCR - 3.d	0.712	0.004	0.37	0.00	0.43	0.00	0.703	0.004	BCR-2G	G	S4	190802
BCR - 4.d	0.713	0.004	0.37	0.00	0.43	0.00	0.705	0.004	BCR-2G	G	S4	190802
BCR - 5.d	0.715	0.004	0.36	0.00	0.42	0.00	0.706	0.003	BCR-2G	G	S4	190802
BCR - 6.d	0.715	0.004	0.37	0.00	0.43	0.00	0.707	0.004	BCR-2G	G	S4	190802
BCR - 7.d	0.719	0.004	0.37	0.00	0.43	0.00	0.710	0.004	BCR-2G	G	S4	190802
BCR - 8.d	0.718	0.004	0.36	0.00	0.42	0.00	0.709	0.004	BCR-2G	G	S4	190802
BCR - 9.d	0.715	0.005	0.37	0.00	0.43	0.00	0.706	0.005	BCR-2G	G	S4	190802
BCR - 10.d	0.713	0.004	0.37	0.00	0.43	0.00	0.704	0.004	BCR-2G	G	S4	190802
BCR - 11.d	0.713	0.004	0.35	0.00	0.41	0.00	0.705	0.004	BCR-2G	G	S4	190802
BCR - 12.d	0.716	0.006	0.35	0.00	0.41	0.01	0.707	0.006	BCR-2G	G	S4	190802
BCR - 13.d	0.711	0.006	0.36	0.01	0.42	0.01	0.702	0.006	BCR-2G	G	S4	190802
BCR - 14.d	0.710	0.006	0.36	0.01	0.42	0.01	0.702	0.006	BCR-2G	G	S4	190802
BCR - 15.d	0.713	0.005	0.35	0.00	0.41	0.00	0.704	0.005	BCR-2G	G	S4	190802
BCR - 16.d	0.716	0.004	0.35	0.00	0.41	0.00	0.707	0.004	BCR-2G	G	S4	190802

Continued on next page

Table 3.B Rb-Sr isotopic ratios calibrated versus NIST 610 glass

Continued from previous page

Spot	Raw $^{87}Sr/^{86}Sr$	2SE	Raw $^{87}Rb/^{86}Sr$	2SE	Calibrated $^{87}Rb/^{86}Sr$	2SE	Calibrated $^{87}Sr/^{86}Sr$	2SE	Sample	Type	Session	Date
BCR - 17.d	0.714	0.004	0.35	0.00	0.41	0.00	0.706	0.004	BCR-2G	G	S4	190802
BCR - 18.d	0.715	0.006	0.36	0.01	0.41	0.01	0.707	0.006	BCR-2G	G	S4	190802
BCR - 19.d	0.716	0.005	0.35	0.00	0.41	0.01	0.708	0.005	BCR-2G	G	S4	190802
BCR - 20.d	0.712	0.005	0.35	0.00	0.41	0.00	0.703	0.005	BCR-2G	G	S4	190802
BCR - 21.d	0.710	0.004	0.35	0.00	0.41	0.00	0.701	0.004	BCR-2G	G	S4	190802
BCR - 22.d	0.715	0.006	0.36	0.00	0.42	0.01	0.707	0.006	BCR-2G	G	S4	190802
BCR - 23.d	0.711	0.006	0.36	0.01	0.42	0.01	0.703	0.006	BCR-2G	G	S4	190802
BCR - 24.d	0.712	0.006	0.36	0.01	0.42	0.01	0.704	0.006	BCR-2G	G	S4	190802
BCR - 25.d	0.716	0.006	0.35	0.01	0.41	0.01	0.707	0.006	BCR-2G	G	S4	190802
BCR - 26.d	0.709	0.006	0.35	0.00	0.41	0.01	0.701	0.006	BCR-2G	G	S4	190802
FK G1 - 1.d	1.246	0.028	70.25	1.63	81.79	1.89	1.231	0.028	FK-N	G1	S4	190802
FK G1 - 2.d	1.182	0.018	58.29	0.75	67.86	0.88	1.168	0.018	FK-N	G1	S4	190802
FK G1 - 3.d	1.254	0.015	62.55	0.73	72.82	0.85	1.239	0.014	FK-N	G1	S4	190802
FK G1 - 4.d	1.225	0.019	62.87	0.85	73.19	0.99	1.211	0.019	FK-N	G1	S4	190802
FK G1 - 5.d	1.238	0.017	63.49	0.74	73.91	0.86	1.223	0.017	FK-N	G1	S4	190802
FK G1 - 6.d	1.284	0.020	68.12	1.00	79.31	1.16	1.269	0.020	FK-N	G1	S4	190802
FK G1 - 7.d	1.211	0.015	56.26	0.62	65.50	0.72	1.197	0.015	FK-N	G1	S4	190802
FK G1 - 8.d	1.272	0.017	68.24	0.80	79.45	0.93	1.257	0.017	FK-N	G1	S4	190802
FK G1 - 9.d	1.237	0.013	59.88	0.61	69.71	0.71	1.222	0.013	FK-N	G1	S4	190802
FK G1 - 10.d	1.245	0.020	66.91	0.84	77.90	0.98	1.231	0.020	FK-N	G1	S4	190802
FK G1 - 11.d	1.215	0.016	57.27	0.54	66.67	0.63	1.200	0.016	FK-N	G1	S4	190802
FK G1 - 12.d	1.245	0.014	59.77	0.80	69.59	0.93	1.231	0.014	FK-N	G1	S4	190802
FK G1 - 13.d	1.231	0.017	61.85	0.67	72.01	0.78	1.216	0.017	FK-N	G1	S4	190802
FK G1 - 14.d	1.249	0.018	64.75	0.99	75.38	1.15	1.234	0.018	FK-N	G1	S4	190802
FK G1 - 15.d	1.215	0.016	61.84	0.62	71.99	0.72	1.200	0.016	FK-N	G1	S4	190802
FK G1 - 16.d	1.229	0.020	62.97	0.86	73.31	1.00	1.214	0.020	FK-N	G1	S4	190802
FK G1 - 17.d	1.219	0.019	62.42	0.91	72.67	1.06	1.204	0.019	FK-N	G1	S4	190802
FK G1 - 18.d	1.193	0.017	58.09	0.89	67.63	1.03	1.178	0.017	FK-N	G1	S4	190802

Continued on next page

Table 3.B Rb-Sr isotopic ratios calibrated versus NIST 610 glass

Continued from previous page

Spot	Raw $^{87}Sr/^{86}Sr$	2SE	Raw $^{87}Rb/^{86}Sr$	2SE	Calibrated $^{87}Rb/^{86}Sr$	2SE	Calibrated $^{87}Sr/^{86}Sr$	2SE	Sample	Type	Session	Date
FK G1 - 19.d	1.252	0.015	65.80	0.85	76.61	0.99	1.237	0.015	FK-N	G1	S4	190802
FK G1 - 20.d	1.268	0.018	70.26	0.76	81.80	0.89	1.253	0.018	FK-N	G1	S4	190802
FK G1 - 21.d	1.251	0.022	69.36	1.27	80.75	1.48	1.237	0.021	FK-N	G1	S4	190802
FK G2 - 1.d	1.236	0.024	53.50	0.91	62.28	1.06	1.221	0.023	FK-N	G2	S4	190802
FK G2 - 2.d	1.222	0.019	62.40	0.89	72.65	1.04	1.208	0.018	FK-N	G2	S4	190802
FK G2 - 3.d	1.300	0.022	59.11	0.72	68.81	0.84	1.284	0.022	FK-N	G2	S4	190802
FK G2 - 4.d	1.241	0.014	53.27	0.55	62.01	0.64	1.226	0.014	FK-N	G2	S4	190802
FK G2 - 5.d	1.204	0.021	67.88	0.97	79.03	1.13	1.189	0.020	FK-N	G2	S4	190802
FK G2 - 6.d	1.242	0.016	70.91	0.87	82.56	1.01	1.228	0.016	FK-N	G2	S4	190802
FK G2 - 7.d	1.282	0.019	67.39	0.91	78.46	1.05	1.267	0.019	FK-N	G2	S4	190802
FK G2 - 8.d	1.316	0.021	72.95	0.93	84.93	1.08	1.300	0.021	FK-N	G2	S4	190802
FK G2 - 9.d	1.293	0.019	69.13	1.10	80.48	1.28	1.278	0.019	FK-N	G2	S4	190802
FK G2 - 10.d	1.231	0.017	55.63	0.65	64.77	0.75	1.216	0.017	FK-N	G2	S4	190802
FK G2 - 11.d	1.258	0.016	64.61	0.69	75.22	0.80	1.243	0.016	FK-N	G2	S4	190802
FK G2 - 12.d	1.229	0.017	56.38	0.68	65.64	0.80	1.214	0.017	FK-N	G2	S4	190802
FK G2 - 13.d	1.203	0.019	61.40	1.12	71.48	1.30	1.189	0.019	FK-N	G2	S4	190802
FK G2 - 14.d	1.229	0.018	65.17	1.27	75.87	1.48	1.215	0.018	FK-N	G2	S4	190802
FK G2 - 15.d	1.254	0.019	55.61	0.87	64.74	1.01	1.239	0.019	FK-N	G2	S4	190802
FK G2 - 16.d	1.188	0.015	54.89	0.67	63.90	0.78	1.174	0.015	FK-N	G2	S4	190802
FK G2 - 17.d	1.222	0.021	82.70	0.84	96.27	0.98	1.207	0.021	FK-N	G2	S4	190802
FK G2 - 18.d	1.224	0.018	61.00	0.90	71.01	1.05	1.210	0.018	FK-N	G2	S4	190802
FK G2 - 19.d	1.209	0.014	60.31	0.69	70.21	0.80	1.195	0.014	FK-N	G2	S4	190802
FK G2 - 20.d	1.217	0.015	61.30	0.66	71.37	0.77	1.203	0.015	FK-N	G2	S4	190802
GLO M - 1.d	0.882	0.020	119.04	2.16	138.58	2.52	0.872	0.020	GL-O	NGr	S4	190802
GLO M - 2.d	0.861	0.024	99.16	1.98	115.44	2.31	0.850	0.023	GL-O	NGr	S4	190802
GLO M - 4.d	0.916	0.024	120.73	2.23	140.55	2.60	0.905	0.024	GL-O	NGr	S4	190802
GLO M - 6.d	0.901	0.018	120.85	1.78	140.69	2.08	0.890	0.017	GL-O	NGr	S4	190802
GLO M - 7.d	0.895	0.021	118.12	2.25	137.52	2.62	0.884	0.020	GL-O	NGr	S4	190802

Continued on next page

Table 3.B Rb-Sr isotopic ratios calibrated versus NIST 610 glass

Continued from previous page

Spot	Raw $^{87}Sr/^{86}Sr$	2SE	Raw $^{87}Rb/^{86}Sr$	2SE	Calibrated $^{87}Rb/^{86}Sr$	2SE	Calibrated $^{87}Sr/^{86}Sr$	2SE	Sample	Type	Session	Date
GLO M - 8.d	0.882	0.025	126.29	2.31	147.02	2.69	0.871	0.024	GL-O	NGr	S4	190802
GLO M - 9.d	0.955	0.031	152.87	3.66	177.98	4.26	0.944	0.030	GL-O	NGr	S4	190802
GLO M - 10.d	0.856	0.020	85.18	1.70	99.17	1.98	0.845	0.020	GL-O	NGr	S4	190802
GLO M - 11.d	0.949	0.022	144.57	2.48	168.30	2.89	0.938	0.022	GL-O	NGr	S4	190802
GLO M - 12.d	0.868	0.028	110.40	2.18	128.53	2.54	0.857	0.028	GL-O	NGr	S4	190802
GLO M - 13.d	0.893	0.021	108.49	2.27	126.30	2.65	0.883	0.021	GL-O	NGr	S4	190802
GLO M - 14.d	0.917	0.024	131.54	2.67	153.13	3.11	0.906	0.024	GL-O	NGr	S4	190802
GLO M - 15.d	0.878	0.023	112.41	1.95	130.86	2.27	0.868	0.022	GL-O	NGr	S4	190802
GLO M - 16.d	0.889	0.024	124.76	2.30	145.24	2.67	0.878	0.024	GL-O	NGr	S4	190802
GLO M - 18.d	0.862	0.016	100.47	1.50	116.97	1.74	0.852	0.016	GL-O	NGr	S4	190802
GLO M - 20.d	0.871	0.019	107.77	1.54	125.47	1.79	0.860	0.019	GL-O	NGr	S4	190802
GLO M - 21.d	0.890	0.029	137.64	2.77	160.24	3.22	0.879	0.029	GL-O	NGr	S4	190802
GLO M - 22.d	0.883	0.022	122.52	2.37	142.64	2.75	0.873	0.022	GL-O	NGr	S4	190802
GLO M - 23.d	0.873	0.020	105.30	1.76	122.59	2.05	0.863	0.020	GL-O	NGr	S4	190802
GLO M - 24.d	0.931	0.020	129.76	2.20	151.07	2.56	0.920	0.019	GL-O	NGr	S4	190802
GLO M - 25.d	0.890	0.019	117.70	1.77	137.03	2.06	0.879	0.019	GL-O	NGr	S4	190802
GLO M - 26.d	0.939	0.027	161.83	3.98	188.40	4.63	0.927	0.027	GL-O	NGr	S4	190802
GLO M - 27.d	0.905	0.026	131.58	2.19	153.18	2.55	0.894	0.026	GL-O	NGr	S4	190802
GLO M - 29.d	0.882	0.018	114.50	1.81	133.30	2.11	0.871	0.018	GL-O	NGr	S4	190802
GLO M - 30.d	0.899	0.029	121.20	2.94	141.10	3.43	0.888	0.028	GL-O	NGr	S4	190802
GLO M - 31.d	0.936	0.031	142.19	3.29	165.54	3.83	0.925	0.030	GL-O	NGr	S4	190802
GLO M - 33.d	0.848	0.018	96.15	1.44	111.94	1.68	0.838	0.018	GL-O	NGr	S4	190802
GLO M - 34.d	0.915	0.022	133.37	2.38	155.26	2.78	0.905	0.021	GL-O	NGr	S4	190802
GLO M - 35.d	0.910	0.022	137.27	2.83	159.81	3.29	0.899	0.022	GL-O	NGr	S4	190802
GLO M - 36.d	0.833	0.021	76.52	1.55	89.08	1.81	0.823	0.020	GL-O	NGr	S4	190802
GLO M - 37.d	0.893	0.025	116.72	2.27	135.88	2.64	0.883	0.024	GL-O	NGr	S4	190802
GLO M - 38.d	0.887	0.023	118.72	2.26	138.21	2.63	0.876	0.023	GL-O	NGr	S4	190802
GLO M - 40.d	0.911	0.028	125.65	2.38	146.28	2.77	0.900	0.027	GL-O	NGr	S4	190802

Continued on next page

Table 3.B Rb-Sr isotopic ratios calibrated versus NIST 610 glass

Continued from previous page

Spot	Raw $^{87}Sr/^{86}Sr$	2SE	Raw $^{87}Rb/^{86}Sr$	2SE	Calibrated $^{87}Rb/^{86}Sr$	2SE	Calibrated $^{87}Sr/^{86}Sr$	2SE	Sample	Type	Session	Date
GLO M - 42.d	0.922	0.023	127.92	1.92	148.93	2.23	0.911	0.023	GL-O	NGr	S4	190802
GLO G 1 - 1.d	0.889	0.035	120.95	3.15	140.81	3.67	0.879	0.034	GL-O	G1	S4	190802
GLO G 1 - 2.d	0.804	0.021	48.10	0.83	56.00	0.97	0.795	0.021	GL-O	G1	S4	190802
GLO G 1 - 3.d	0.785	0.020	48.66	1.15	56.65	1.34	0.775	0.020	GL-O	G1	S4	190802
GLO G 1 - 4.d	0.773	0.014	36.56	0.56	42.57	0.65	0.764	0.014	GL-O	G1	S4	190802
GLO G 1 - 5.d	0.748	0.011	26.98	0.27	31.41	0.32	0.739	0.011	GL-O	G1	S4	190802
GLO G 1 - 6.d	0.730	0.007	6.60	0.06	7.69	0.07	0.721	0.007	GL-O	G1	S4	190802
GLO G 1 - 7.d	0.762	0.015	27.94	0.37	32.53	0.43	0.753	0.014	GL-O	G1	S4	190802
GLO G 1 - 8.d	0.744	0.011	16.53	0.18	19.25	0.21	0.735	0.011	GL-O	G1	S4	190802
GLO G 1 - 9.d	0.782	0.014	39.50	0.56	45.98	0.66	0.773	0.014	GL-O	G1	S4	190802
GLO G 1 - 10.d	0.836	0.020	78.37	1.59	91.24	1.85	0.826	0.020	GL-O	G1	S4	190802
GLO G 1 - 11.d	0.850	0.026	89.42	1.76	104.10	2.05	0.840	0.025	GL-O	G1	S4	190802
GLO G 1 - 12.d	0.854	0.019	85.01	1.48	98.96	1.72	0.844	0.018	GL-O	G1	S4	190802
GLO G 1 - 13.d	0.891	0.023	96.52	2.07	112.37	2.41	0.881	0.023	GL-O	G1	S4	190802
GLO G 1 - 14.d	0.795	0.017	44.29	0.81	51.56	0.94	0.785	0.017	GL-O	G1	S4	190802
GLO G 1 - 15.d	0.813	0.014	77.87	1.07	90.66	1.25	0.803	0.014	GL-O	G1	S4	190802
GLO G 1 - 16.d	0.857	0.021	93.51	1.66	108.86	1.93	0.847	0.021	GL-O	G1	S4	190802
GLO G 1 - 17.d	0.790	0.018	55.99	0.85	65.19	0.99	0.780	0.017	GL-O	G1	S4	190802
GLO G 1 - 18.d	0.813	0.017	68.82	1.07	80.12	1.24	0.803	0.016	GL-O	G1	S4	190802
GLO G 1 - 19.d	0.920	0.028	122.28	3.13	142.36	3.64	0.909	0.027	GL-O	G1	S4	190802
GLO G 1 - 20.d	0.859	0.021	91.98	1.78	107.08	2.07	0.848	0.021	GL-O	G1	S4	190802
GLO G 2 - 1.d	0.894	0.027	123.15	2.26	143.37	2.63	0.883	0.027	GL-O	G2	S4	190802
GLO G 2 - 2.d	0.873	0.022	102.24	1.82	119.02	2.12	0.862	0.022	GL-O	G2	S4	190802
GLO G 2 - 3.d	0.731	0.007	11.72	0.09	13.64	0.11	0.723	0.007	GL-O	G2	S4	190802
GLO G 2 - 4.d	0.741	0.006	11.17	0.12	13.01	0.14	0.733	0.006	GL-O	G2	S4	190802
GLO G 2 - 5.d	0.727	0.007	8.05	0.06	9.37	0.07	0.718	0.007	GL-O	G2	S4	190802
GLO G 2 - 6.d	0.741	0.010	15.21	0.27	17.71	0.31	0.732	0.009	GL-O	G2	S4	190802
GLO G 2 - 7.d	0.782	0.015	40.15	0.64	46.75	0.74	0.773	0.015	GL-O	G2	S4	190802

Continued on next page

Table 3.B Rb-Sr isotopic ratios calibrated versus NIST 610 glass

Continued from previous page

Spot	Raw $^{87}Sr/^{86}Sr$	2SE	Raw $^{87}Rb/^{86}Sr$	2SE	Calibrated $^{87}Rb/^{86}Sr$	2SE	Calibrated $^{87}Sr/^{86}Sr$	2SE	Sample	Type	Session	Date
GLO G 2 - 8.d	0.796	0.018	50.52	0.84	58.81	0.97	0.786	0.017	GL-O	G2	S4	190802
GLO G 2 - 9.d	0.815	0.022	85.67	1.57	99.74	1.82	0.806	0.022	GL-O	G2	S4	190802
GLO G 2 - 10.d	0.866	0.023	92.54	1.77	107.74	2.06	0.856	0.022	GL-O	G2	S4	190802
GLO G 2 - 11.d	0.721	0.007	5.83	0.13	6.78	0.15	0.713	0.007	GL-O	G2	S4	190802
GLO G 2 - 12.d	0.883	0.024	110.20	2.33	128.29	2.72	0.873	0.024	GL-O	G2	S4	190802
GLO G 2 - 13.d	0.774	0.012	41.28	0.48	48.06	0.56	0.764	0.012	GL-O	G2	S4	190802
GLO G 2 - 14.d	0.732	0.006	6.57	0.15	7.65	0.17	0.723	0.006	GL-O	G2	S4	190802
GLO G 2 - 15.d	0.836	0.034	78.68	2.54	91.60	2.96	0.826	0.034	GL-O	G2	S4	190802
GLO G 2 - 16.d	0.748	0.010	20.21	0.28	23.52	0.32	0.739	0.010	GL-O	G2	S4	190802
GLO G 2 - 17.d	0.842	0.021	85.45	1.45	99.48	1.68	0.832	0.020	GL-O	G2	S4	190802
GLO G 2 - 18.d	0.919	0.026	120.27	2.27	140.02	2.65	0.908	0.026	GL-O	G2	S4	190802
Mica Fe g 1 - 1.d	8.322	0.243	1456.12	42.55	1695.21	49.54	8.222	0.240	Mica-Fe	G1	S4	190802
Mica Fe g 1 - 2.d	9.553	0.369	1761.25	68.03	2050.43	79.20	9.439	0.365	Mica-Fe	G1	S4	190802
Mica Fe g 1 - 3.d	9.375	0.321	1652.11	57.57	1923.38	67.02	9.263	0.317	Mica-Fe	G1	S4	190802
Mica Fe g 1 - 4.d	8.268	0.248	1495.70	43.55	1741.29	50.71	8.170	0.245	Mica-Fe	G1	S4	190802
Mica Fe g 1 - 5.d	8.530	0.281	1693.05	56.13	1971.03	65.35	8.429	0.278	Mica-Fe	G1	S4	190802
Mica Fe g 1 - 6.d	8.818	0.259	1774.13	55.25	2065.43	64.32	8.713	0.255	Mica-Fe	G1	S4	190802
Mica Fe g 1 - 7.d	8.648	0.249	1694.40	53.72	1972.61	62.54	8.545	0.246	Mica-Fe	G1	S4	190802
Mica Fe g 1 - 8.d	8.023	0.244	1360.01	42.45	1583.31	49.42	7.928	0.241	Mica-Fe	G1	S4	190802
Mica Fe g 1 - 9.d	8.238	0.242	1233.10	33.12	1435.57	38.56	8.140	0.240	Mica-Fe	G1	S4	190802
Mica Fe g 1 - 10.d	9.064	0.265	1593.81	50.44	1855.51	58.72	8.956	0.262	Mica-Fe	G1	S4	190802
Mica Fe g 1 - 11.d	8.967	0.289	1633.13	52.27	1901.27	60.85	8.860	0.286	Mica-Fe	G1	S4	190802
Mica Fe g 1 - 12.d	8.254	0.267	1638.31	65.22	1907.31	75.93	8.155	0.264	Mica-Fe	G1	S4	190802
Mica Fe g 1 - 13.d	8.532	0.262	1473.51	39.72	1715.46	46.24	8.431	0.259	Mica-Fe	G1	S4	190802
Mica Fe g 1 - 14.d	8.832	0.279	1631.02	43.18	1898.82	50.27	8.726	0.276	Mica-Fe	G1	S4	190802
Mica Fe g 2 - 1.d	8.907	0.312	1527.80	51.68	1778.65	60.17	8.801	0.309	Mica-Fe	G2	S4	190802
Mica Fe g 2 - 2.d	9.077	0.308	1721.66	56.28	2004.35	65.52	8.969	0.304	Mica-Fe	G2	S4	190802
Mica Fe g 2 - 3.d	8.238	0.340	1438.50	51.49	1674.70	59.95	8.140	0.336	Mica-Fe	G2	S4	190802

Continued on next page

Table 3.B Rb-Sr isotopic ratios calibrated versus NIST 610 glass

Continued from previous page

Spot	Raw $^{87}Sr/^{86}Sr$	2SE	Raw $^{87}Rb/^{86}Sr$	2SE	Calibrated $^{87}Rb/^{86}Sr$	2SE	Calibrated $^{87}Sr/^{86}Sr$	2SE	Sample	Type	Session	Date
Mica Fe g 2 - 4.d	8.775	0.282	1843.73	62.30	2146.46	72.53	8.670	0.279	Mica-Fe	G2	S4	190802
Mica Fe g 2 - 6.d	8.406	0.288	1959.01	77.12	2280.67	89.79	8.306	0.284	Mica-Fe	G2	S4	190802
Mica Fe g 2 - 7.d	8.548	0.334	1696.63	69.56	1975.20	80.98	8.446	0.330	Mica-Fe	G2	S4	190802
Mica Fe g 2 - 8.d	8.850	0.364	2268.82	85.26	2641.34	99.26	8.744	0.360	Mica-Fe	G2	S4	190802
Mica Fe g 2 - 9.d	8.442	0.272	1229.58	40.83	1431.47	47.54	8.341	0.269	Mica-Fe	G2	S4	190802
Mica Fe g 2 - 10.d	8.074	0.350	1781.66	88.35	2074.20	102.86	7.978	0.345	Mica-Fe	G2	S4	190802
Mica Mg glass - 2.d	1.718	0.022	69.62	0.76	81.05	0.89	1.698	0.022	Mica-Mg	G1	S4	190802
Mica Mg glass - 3.d	1.894	0.029	73.20	0.88	85.21	1.02	1.871	0.028	Mica-Mg	G1	S4	190802
Mica Mg glass - 4.d	1.839	0.024	72.51	0.83	84.42	0.97	1.817	0.024	Mica-Mg	G1	S4	190802
Mica Mg glass - 5.d	1.894	0.026	87.21	1.20	101.53	1.40	1.872	0.026	Mica-Mg	G1	S4	190802
Mica Mg glass - 6.d	1.885	0.025	72.04	0.93	83.86	1.08	1.863	0.025	Mica-Mg	G1	S4	190802
Mica Mg glass - 7.d	1.903	0.026	82.85	0.90	96.45	1.04	1.881	0.026	Mica-Mg	G1	S4	190802
Mica Mg glass - 8.d	1.881	0.027	72.50	1.01	84.41	1.17	1.859	0.027	Mica-Mg	G1	S4	190802
Mica Mg glass - 9.d	1.867	0.031	117.23	2.10	136.48	2.44	1.845	0.030	Mica-Mg	G1	S4	190802
Mica Mg glass - 10.d	1.890	0.024	91.93	1.52	107.03	1.77	1.868	0.024	Mica-Mg	G1	S4	190802
Mica Mg glass - 11.d	1.872	0.036	81.93	1.53	95.38	1.78	1.850	0.035	Mica-Mg	G1	S4	190802
GL-O np - 1.d	31.825	0.406	0.78	0.01	38.47	0.49	0.759	0.014	GL-O	NP	S5	200323
GL-O np - 2.d	31.566	0.498	0.77	0.01	38.15	0.60	0.748	0.012	GL-O	NP	S5	200323
GL-O np - 3.d	31.611	0.416	0.78	0.01	38.21	0.50	0.755	0.015	GL-O	NP	S5	200323
GL-O np - 5.d	31.649	0.398	0.77	0.01	38.26	0.48	0.749	0.011	GL-O	NP	S5	200323
GL-O np - 6.d	32.114	0.370	0.77	0.01	38.82	0.45	0.745	0.012	GL-O	NP	S5	200323
GL-O np - 7.d	31.798	0.419	0.78	0.01	38.44	0.51	0.757	0.012	GL-O	NP	S5	200323
GL-O np - 8.d	31.802	0.454	0.77	0.01	38.44	0.55	0.749	0.014	GL-O	NP	S5	200323
GL-O np - 9.d	31.411	0.396	0.77	0.01	37.97	0.48	0.747	0.013	GL-O	NP	S5	200323
GL-O np - 10.d	31.572	0.391	0.77	0.01	38.16	0.47	0.749	0.012	GL-O	NP	S5	200323
GL-O np - 11.d	31.514	0.400	0.77	0.01	38.09	0.48	0.747	0.011	GL-O	NP	S5	200323
GL-O np - 12.d	30.968	0.357	0.77	0.01	37.43	0.43	0.745	0.011	GL-O	NP	S5	200323
GL-O np - 13.d	31.000	0.479	0.77	0.01	37.47	0.58	0.752	0.012	GL-O	NP	S5	200323

Continued on next page

Table 3.B Rb-Sr isotopic ratios calibrated versus NIST 610 glass

Continued from previous page

Spot	Raw $^{87}Sr/^{86}Sr$	2SE	Raw $^{87}Rb/^{86}Sr$	2SE	Calibrated $^{87}Rb/^{86}Sr$	2SE	Calibrated $^{87}Sr/^{86}Sr$	2SE	Sample	Type	Session	Date
GL-O np - 14.d	30.769	0.488	0.78	0.01	37.19	0.59	0.759	0.012	GL-O	NP	S5	200323
GL-O np - 15.d	31.019	0.402	0.77	0.01	37.49	0.49	0.748	0.012	GL-O	NP	S5	200323
GL-O np - 16.d	31.426	0.488	0.78	0.01	37.99	0.59	0.756	0.014	GL-O	NP	S5	200323
GL-O np - 17.d	31.272	0.444	0.78	0.01	37.80	0.54	0.762	0.012	GL-O	NP	S5	200323
GL-O np - 18.d	31.746	0.393	0.78	0.01	38.37	0.48	0.759	0.012	GL-O	NP	S5	200323
GL-O np - 19.d	32.303	0.388	0.78	0.01	39.05	0.47	0.759	0.014	GL-O	NP	S5	200323
GL-O np - 20.d	31.407	0.401	0.79	0.01	37.96	0.48	0.763	0.013	GL-O	NP	S5	200323
GL-O np - 21.d	31.793	0.400	0.78	0.01	38.43	0.48	0.760	0.013	GL-O	NP	S5	200323
GL-O np - 22.d	32.076	0.432	0.78	0.01	38.77	0.52	0.757	0.013	GL-O	NP	S5	200323
GL-O np - 23.d	31.119	0.339	0.78	0.01	37.62	0.41	0.756	0.011	GL-O	NP	S5	200323
GL-O np - 24.d	31.790	0.379	0.79	0.01	38.43	0.46	0.766	0.012	GL-O	NP	S5	200323
GL-O np - 25.d	31.203	0.402	0.78	0.01	37.72	0.49	0.759	0.011	GL-O	NP	S5	200323
GL-O np - 26.d	31.346	0.377	0.78	0.01	37.89	0.46	0.759	0.012	GL-O	NP	S5	200323
GL-O np - 27.d	31.322	0.420	0.78	0.01	37.86	0.51	0.756	0.012	GL-O	NP	S5	200323
GL-O np - 28.d	30.889	0.387	0.77	0.01	37.34	0.47	0.749	0.012	GL-O	NP	S5	200323
GL-O np - 29.d	31.381	0.423	0.78	0.01	37.93	0.51	0.759	0.011	GL-O	NP	S5	200323
GL-O np - 30.d	31.551	0.433	0.77	0.01	38.14	0.52	0.750	0.012	GL-O	NP	S5	200323
GL-O np - 31.d	30.762	0.406	0.78	0.01	37.18	0.49	0.757	0.013	GL-O	NP	S5	200323
GL-O np - 32.d	30.608	0.357	0.79	0.01	37.00	0.43	0.765	0.013	GL-O	NP	S5	200323
GL-O np - 33.d	31.119	0.421	0.78	0.01	37.61	0.51	0.758	0.015	GL-O	NP	S5	200323
GL-O np - 34.d	30.682	0.352	0.78	0.01	37.09	0.43	0.758	0.012	GL-O	NP	S5	200323
GL-O np - 35.d	30.597	0.386	0.78	0.01	36.98	0.47	0.754	0.013	GL-O	NP	S5	200323
GL-O np - 36.d	30.776	0.422	0.79	0.01	37.20	0.51	0.764	0.013	GL-O	NP	S5	200323
GL-O np - 37.d	30.945	0.295	0.78	0.01	37.40	0.36	0.757	0.011	GL-O	NP	S5	200323
GL-O np - 38.d	30.692	0.394	0.77	0.01	37.10	0.48	0.752	0.012	GL-O	NP	S5	200323
GL-O np - 39.d	31.401	0.397	0.79	0.01	37.96	0.48	0.762	0.011	GL-O	NP	S5	200323
GL-O np - 40.d	31.316	0.374	0.78	0.01	37.85	0.45	0.755	0.013	GL-O	NP	S5	200323
GL-O np - 41.d	31.151	0.348	0.77	0.01	37.65	0.42	0.748	0.013	GL-O	NP	S5	200323

Continued on next page

Table 3.B Rb-Sr isotopic ratios calibrated versus NIST 610 glass

Continued from previous page

Spot	Raw $^{87}Sr/^{86}Sr$	2SE	Raw $^{87}Rb/^{86}Sr$	2SE	Calibrated $^{87}Rb/^{86}Sr$	2SE	Calibrated $^{87}Sr/^{86}Sr$	2SE	Sample	Type	Session	Date
GL-O np - 42.d	31.651	0.404	0.78	0.01	38.26	0.49	0.754	0.012	GL-O	NP	S5	200323
GL-O np - 43.d	31.077	0.325	0.77	0.01	37.56	0.39	0.752	0.012	GL-O	NP	S5	200323
GL-O np - 44.d	30.726	0.383	0.78	0.01	37.14	0.46	0.759	0.013	GL-O	NP	S5	200323
GL-O np - 45.d	31.087	0.425	0.78	0.01	37.58	0.51	0.759	0.012	GL-O	NP	S5	200323
GL-O np - 46.d	31.346	0.404	0.77	0.01	37.89	0.49	0.749	0.012	GL-O	NP	S5	200323
GL-O np - 47.d	30.882	0.392	0.78	0.01	37.33	0.47	0.754	0.012	GL-O	NP	S5	200323
GL-O np - 48.d	30.474	0.369	0.78	0.01	36.83	0.45	0.757	0.011	GL-O	NP	S5	200323
GL-O np - 49.d	31.358	0.415	0.78	0.01	37.90	0.50	0.756	0.011	GL-O	NP	S5	200323
GL-O np - 50.d	31.474	0.416	0.78	0.01	38.04	0.50	0.753	0.012	GL-O	NP	S5	200323
GL-O np - 51.d	31.617	0.409	0.78	0.01	38.22	0.49	0.761	0.012	GL-O	NP	S5	200323
GL-O np - 52.d	31.169	0.384	0.78	0.01	37.67	0.46	0.754	0.012	GL-O	NP	S5	200323
GL-O np - 53.d	31.006	0.386	0.76	0.01	37.48	0.47	0.737	0.012	GL-O	NP	S5	200323
GL-O np - 54.d	31.391	0.440	0.78	0.01	37.94	0.53	0.758	0.012	GL-O	NP	S5	200323
GL-O np - 55.d	31.465	0.390	0.77	0.01	38.03	0.47	0.750	0.013	GL-O	NP	S5	200323
GL-O np - 56.d	31.411	0.440	0.77	0.01	37.97	0.53	0.750	0.012	GL-O	NP	S5	200323
GL-O np - 57.d	31.641	0.419	0.80	0.01	38.25	0.51	0.775	0.011	GL-O	NP	S5	200323
GL-O np - 58.d	31.693	0.437	0.77	0.01	38.31	0.53	0.747	0.012	GL-O	NP	S5	200323
GL-O np - 59.d	31.459	0.422	0.77	0.01	38.03	0.51	0.743	0.012	GL-O	NP	S5	200323
GL-O np - 60.d	32.141	0.411	0.78	0.02	38.85	0.50	0.759	0.015	GL-O	NP	S5	200323
GL-O np - 61.d	31.142	0.516	0.78	0.01	37.64	0.62	0.761	0.013	GL-O	NP	S5	200323
GL-O np - 62.d	31.729	0.463	0.78	0.01	38.35	0.56	0.760	0.014	GL-O	NP	S5	200323
GL-O np - 63.d	31.529	0.395	0.78	0.01	38.11	0.48	0.759	0.011	GL-O	NP	S5	200323
GL-O np - 64.d	31.014	0.469	0.79	0.01	37.49	0.57	0.765	0.014	GL-O	NP	S5	200323
GL-O np - 65.d	30.494	0.378	0.77	0.01	36.86	0.46	0.748	0.011	GL-O	NP	S5	200323
GL-O np - 66.d	30.615	0.397	0.77	0.01	37.01	0.48	0.750	0.012	GL-O	NP	S5	200323
GL-O np - 67.d	30.564	0.356	0.76	0.01	36.94	0.43	0.736	0.012	GL-O	NP	S5	200323
GL-O np - 68.d	32.300	0.418	0.79	0.01	39.04	0.51	0.764	0.013	GL-O	NP	S5	200323
GL-O np - 69.d	30.411	0.378	0.77	0.01	36.76	0.46	0.751	0.012	GL-O	NP	S5	200323

Continued on next page

Table 3.B Rb-Sr isotopic ratios calibrated versus NIST 610 glass

Continued from previous page

Spot	Raw $^{87}Sr/^{86}Sr$	2SE	Raw $^{87}Rb/^{86}Sr$	2SE	Calibrated $^{87}Rb/^{86}Sr$	2SE	Calibrated $^{87}Sr/^{86}Sr$	2SE	Sample	Type	Session	Date
GL-O np - 70.d	31.311	0.359	0.77	0.01	37.85	0.43	0.746	0.012	GL-O	NP	S5	200323
GL-O np - 71.d	31.882	0.404	0.79	0.01	38.54	0.49	0.763	0.012	GL-O	NP	S5	200323
GL-O np - 72.d	30.707	0.365	0.78	0.01	37.12	0.44	0.756	0.012	GL-O	NP	S5	200323
GL-O np - 73.d	31.467	0.437	0.78	0.01	38.04	0.53	0.761	0.013	GL-O	NP	S5	200323
GL-O np - 74.d	31.122	0.408	0.78	0.01	37.62	0.49	0.757	0.011	GL-O	NP	S5	200323
GL-O np - 75.d	31.119	0.405	0.77	0.01	37.62	0.49	0.745	0.012	GL-O	NP	S5	200323
GL-O np - 76.d	30.841	0.370	0.77	0.01	37.28	0.45	0.748	0.011	GL-O	NP	S5	200323

Table 3.C: Rb-Sr isotopic ratios of MDC, GLO and FK-N-NP calibrated versus different RM.

Spot	Sample	Session	RM	$^{87}Rb/^{86}Sr$	2SE	$^{87}Sr/^{86}Sr$	2SE
MDC - 1.d	Session 1	MDC	Mica-Mg-NP	41.15	0.42	1.031	0.012
MDC - 2.d	Session 1	MDC	Mica-Mg-NP	40.77	0.39	1.031	0.012
MDC - 3.d	Session 1	MDC	Mica-Mg-NP	40.41	0.42	1.036	0.011
MDC - 4.d	Session 1	MDC	Mica-Mg-NP	40.80	0.44	1.038	0.011
MDC - 5.d	Session 1	MDC	Mica-Mg-NP	41.10	0.42	1.039	0.012
MDC - 6.d	Session 1	MDC	Mica-Mg-NP	40.83	0.46	1.039	0.012
MDC - 7.d	Session 1	MDC	Mica-Mg-NP	40.77	0.47	1.027	0.011
MDC - 8.d	Session 1	MDC	Mica-Mg-NP	40.94	0.39	1.029	0.011
MDC - 9.d	Session 1	MDC	Mica-Mg-NP	40.67	0.48	1.033	0.011
MDC - 10.d	Session 1	MDC	Mica-Mg-NP	40.65	0.40	1.021	0.011
MDC - 11.d	Session 1	MDC	Mica-Mg-NP	40.09	0.48	1.037	0.011
MDC - 12.d	Session 1	MDC	Mica-Mg-NP	40.87	0.51	1.042	0.011
MDC - 13.d	Session 1	MDC	Mica-Mg-NP	41.03	0.57	1.029	0.011
MDC - 14.d	Session 1	MDC	Mica-Mg-NP	40.89	0.52	1.039	0.012
MDC - 15.d	Session 1	MDC	Mica-Mg-NP	41.12	0.56	1.032	0.010
MDC - 16.d	Session 1	MDC	Mica-Mg-NP	41.43	0.52	1.039	0.011
MDC - 17.d	Session 1	MDC	Mica-Mg-NP	41.33	0.59	1.036	0.010
MDC - 18.d	Session 1	MDC	Mica-Mg-NP	41.13	0.45	1.036	0.011
MDC - 19.d	Session 1	MDC	Mica-Mg-NP	40.77	0.44	1.030	0.010
MDC - 20.d	Session 1	MDC	Mica-Mg-NP	40.66	0.50	1.033	0.012
MDC - 1.d	Session 2	MDC	Mica-Mg-NP	41.19	0.49	1.036	0.014
MDC - 2.d	Session 2	MDC	Mica-Mg-NP	41.02	0.55	1.024	0.013
MDC - 3.d	Session 2	MDC	Mica-Mg-NP	40.62	0.49	1.013	0.014
MDC - 4.d	Session 2	MDC	Mica-Mg-NP	40.91	0.48	1.029	0.014
MDC - 5.d	Session 2	MDC	Mica-Mg-NP	41.24	0.55	1.033	0.014
MDC - 6.d	Session 2	MDC	Mica-Mg-NP	41.07	0.48	1.027	0.015
MDC - 7.d	Session 2	MDC	Mica-Mg-NP	40.58	0.48	1.031	0.014
MDC - 8.d	Session 2	MDC	Mica-Mg-NP	41.87	0.51	1.024	0.015
MDC - 9.d	Session 2	MDC	Mica-Mg-NP	42.08	0.61	1.042	0.014
MDC - 10.d	Session 2	MDC	Mica-Mg-NP	41.24	0.47	1.021	0.012
MDC - 11.d	Session 2	MDC	Mica-Mg-NP	41.71	0.52	1.029	0.014
MDC - 12.d	Session 2	MDC	Mica-Mg-NP	41.15	0.50	1.034	0.015
MDC - 13.d	Session 2	MDC	Mica-Mg-NP	41.62	0.59	1.029	0.015
MDC - 14.d	Session 2	MDC	Mica-Mg-NP	41.49	0.53	1.043	0.014
MDC - 15.d	Session 2	MDC	Mica-Mg-NP	40.77	0.52	1.013	0.014
MDC - 16.d	Session 2	MDC	Mica-Mg-NP	42.12	0.59	1.029	0.016
MDC - 17.d	Session 2	MDC	Mica-Mg-NP	41.63	0.65	1.024	0.015
MDC - 18.d	Session 2	MDC	Mica-Mg-NP	41.39	0.53	1.016	0.014
MDC - 19.d	Session 2	MDC	Mica-Mg-NP	41.95	0.59	1.020	0.015
MDC - 20.d	Session 2	MDC	Mica-Mg-NP	42.46	0.61	1.047	0.014
MDC - 1.d	Session 3	MDC	Mica-Mg-NP	46.16	0.66	1.078	0.015
MDC - 2.d	Session 3	MDC	Mica-Mg-NP	45.38	0.53	1.063	0.013

Continued on next page

Continued from previous page

Spot	Sample	Session	RM	$^{87}Rb/^{86}Sr$	2SE	$^{87}Sr/^{86}Sr$	2SE
MDC - 3.d	Session 3	MDC	Mica-Mg-NP	44.20	0.67	1.053	0.017
MDC - 4.d	Session 3	MDC	Mica-Mg-NP	44.12	0.63	1.047	0.015
MDC - 5.d	Session 3	MDC	Mica-Mg-NP	44.45	0.62	1.051	0.016
MDC - 6.d	Session 3	MDC	Mica-Mg-NP	43.93	0.58	1.061	0.014
MDC - 7.d	Session 3	MDC	Mica-Mg-NP	43.75	0.58	1.051	0.015
MDC - 8.d	Session 3	MDC	Mica-Mg-NP	43.49	0.65	1.053	0.015
MDC - 9.d	Session 3	MDC	Mica-Mg-NP	43.42	0.60	1.050	0.013
MDC - 10.d	Session 3	MDC	Mica-Mg-NP	43.27	0.56	1.048	0.014
MDC - 11.d	Session 3	MDC	Mica-Mg-NP	46.03	0.77	1.073	0.021
MDC - 12.d	Session 3	MDC	Mica-Mg-NP	46.46	0.74	1.072	0.019
MDC - 13.d	Session 3	MDC	Mica-Mg-NP	46.21	0.74	1.085	0.019
MDC - 14.d	Session 3	MDC	Mica-Mg-NP	45.31	0.76	1.073	0.020
MDC - 15.d	Session 3	MDC	Mica-Mg-NP	44.23	0.64	1.047	0.015
MDC - 16.d	Session 3	MDC	Mica-Mg-NP	45.17	0.61	1.071	0.016
MDC - 17.d	Session 3	MDC	Mica-Mg-NP	44.17	0.56	1.059	0.014
MDC - 18.d	Session 3	MDC	Mica-Mg-NP	43.85	0.63	1.055	0.014
MDC - 19.d	Session 3	MDC	Mica-Mg-NP	43.65	0.60	1.061	0.015
MDC - 20.d	Session 3	MDC	Mica-Mg-NP	44.02	0.59	1.079	0.016
MDC - 21.d	Session 3	MDC	Mica-Mg-NP	43.32	0.56	1.058	0.015
MDC - 22.d	Session 3	MDC	Mica-Mg-NP	43.24	0.62	1.072	0.015
MDC - 23.d	Session 3	MDC	Mica-Mg-NP	44.10	0.72	1.071	0.017
MDC - 24.d	Session 3	MDC	Mica-Mg-NP	43.40	0.63	1.048	0.014
MDC - 25.d	Session 3	MDC	Mica-Mg-NP	43.27	0.90	1.034	0.022
MDC - 26.d	Session 3	MDC	Mica-Mg-NP	44.26	0.52	1.057	0.015
MDC - 27.d	Session 3	MDC	Mica-Mg-NP	44.59	0.62	1.063	0.016
MDC - 28.d	Session 3	MDC	Mica-Mg-NP	43.54	0.58	1.059	0.016
MDC - 29.d	Session 3	MDC	Mica-Mg-NP	44.01	0.59	1.073	0.016
MDC - 30.d	Session 3	MDC	Mica-Mg-NP	43.05	0.64	1.061	0.016
MDC - 1.d	Session 2	MDC	Mica-Fe-NP	38.55	0.45	1.034	0.014
MDC - 2.d	Session 2	MDC	Mica-Fe-NP	38.38	0.51	1.021	0.013
MDC - 3.d	Session 2	MDC	Mica-Fe-NP	38.01	0.46	1.010	0.014
MDC - 4.d	Session 2	MDC	Mica-Fe-NP	38.28	0.45	1.027	0.013
MDC - 5.d	Session 2	MDC	Mica-Fe-NP	38.59	0.52	1.031	0.014
MDC - 6.d	Session 2	MDC	Mica-Fe-NP	38.43	0.45	1.024	0.014
MDC - 7.d	Session 2	MDC	Mica-Fe-NP	37.97	0.45	1.028	0.014
MDC - 8.d	Session 2	MDC	Mica-Fe-NP	39.18	0.48	1.021	0.015
MDC - 9.d	Session 2	MDC	Mica-Fe-NP	39.37	0.57	1.039	0.014
MDC - 10.d	Session 2	MDC	Mica-Fe-NP	38.58	0.44	1.018	0.012
MDC - 11.d	Session 2	MDC	Mica-Fe-NP	39.02	0.49	1.026	0.014
MDC - 12.d	Session 2	MDC	Mica-Fe-NP	38.50	0.47	1.031	0.015
MDC - 13.d	Session 2	MDC	Mica-Fe-NP	38.93	0.55	1.027	0.015
MDC - 14.d	Session 2	MDC	Mica-Fe-NP	38.82	0.50	1.040	0.014
MDC - 15.d	Session 2	MDC	Mica-Fe-NP	38.14	0.48	1.010	0.014
MDC - 16.d	Session 2	MDC	Mica-Fe-NP	39.40	0.56	1.026	0.016

Continued on next page

Continued from previous page

Spot	Sample	Session	RM	$^{87}Rb/^{86}Sr$	2SE	$^{87}Sr/^{86}Sr$	2SE
MDC - 17.d	Session 2	MDC	Mica-Fe-NP	38.94	0.60	1.021	0.015
MDC - 18.d	Session 2	MDC	Mica-Fe-NP	38.72	0.50	1.013	0.014
MDC - 19.d	Session 2	MDC	Mica-Fe-NP	39.24	0.55	1.017	0.015
MDC - 20.d	Session 2	MDC	Mica-Fe-NP	39.72	0.57	1.044	0.014
MDC - 1.d	Session 3	MDC	Mica-Fe-NP	43.38	0.62	1.070	0.015
MDC - 2.d	Session 3	MDC	Mica-Fe-NP	42.65	0.50	1.055	0.013
MDC - 3.d	Session 3	MDC	Mica-Fe-NP	41.53	0.63	1.045	0.017
MDC - 4.d	Session 3	MDC	Mica-Fe-NP	41.46	0.59	1.039	0.015
MDC - 5.d	Session 3	MDC	Mica-Fe-NP	41.77	0.59	1.043	0.016
MDC - 6.d	Session 3	MDC	Mica-Fe-NP	41.28	0.55	1.053	0.014
MDC - 7.d	Session 3	MDC	Mica-Fe-NP	41.11	0.55	1.043	0.015
MDC - 8.d	Session 3	MDC	Mica-Fe-NP	40.86	0.61	1.045	0.015
MDC - 9.d	Session 3	MDC	Mica-Fe-NP	40.80	0.57	1.042	0.013
MDC - 10.d	Session 3	MDC	Mica-Fe-NP	40.66	0.53	1.040	0.014
MDC - 11.d	Session 3	MDC	Mica-Fe-NP	43.25	0.72	1.065	0.021
MDC - 12.d	Session 3	MDC	Mica-Fe-NP	43.66	0.69	1.064	0.019
MDC - 13.d	Session 3	MDC	Mica-Fe-NP	43.42	0.70	1.077	0.018
MDC - 14.d	Session 3	MDC	Mica-Fe-NP	42.57	0.71	1.064	0.020
MDC - 15.d	Session 3	MDC	Mica-Fe-NP	41.56	0.60	1.039	0.015
MDC - 16.d	Session 3	MDC	Mica-Fe-NP	42.44	0.57	1.063	0.015
MDC - 17.d	Session 3	MDC	Mica-Fe-NP	41.50	0.53	1.051	0.014
MDC - 18.d	Session 3	MDC	Mica-Fe-NP	41.20	0.59	1.047	0.014
MDC - 19.d	Session 3	MDC	Mica-Fe-NP	41.01	0.56	1.053	0.015
MDC - 20.d	Session 3	MDC	Mica-Fe-NP	41.37	0.55	1.071	0.016
MDC - 21.d	Session 3	MDC	Mica-Fe-NP	40.70	0.53	1.050	0.015
MDC - 22.d	Session 3	MDC	Mica-Fe-NP	40.63	0.58	1.064	0.015
MDC - 23.d	Session 3	MDC	Mica-Fe-NP	41.44	0.68	1.063	0.017
MDC - 24.d	Session 3	MDC	Mica-Fe-NP	40.78	0.59	1.040	0.014
MDC - 25.d	Session 3	MDC	Mica-Fe-NP	40.66	0.84	1.026	0.022
MDC - 26.d	Session 3	MDC	Mica-Fe-NP	41.59	0.48	1.049	0.015
MDC - 27.d	Session 3	MDC	Mica-Fe-NP	41.90	0.58	1.055	0.016
MDC - 28.d	Session 3	MDC	Mica-Fe-NP	40.92	0.55	1.051	0.016
MDC - 29.d	Session 3	MDC	Mica-Fe-NP	41.35	0.56	1.065	0.016
MDC - 30.d	Session 3	MDC	Mica-Fe-NP	40.45	0.60	1.053	0.015
MDC - 1.d	Session 1	MDC	GL-O-NP	42.47	0.43	1.030	0.012
MDC - 2.d	Session 1	MDC	GL-O-NP	42.09	0.40	1.029	0.012
MDC - 3.d	Session 1	MDC	GL-O-NP	41.71	0.44	1.034	0.011
MDC - 4.d	Session 1	MDC	GL-O-NP	42.11	0.45	1.036	0.011
MDC - 5.d	Session 1	MDC	GL-O-NP	42.42	0.43	1.037	0.012
MDC - 6.d	Session 1	MDC	GL-O-NP	42.14	0.48	1.037	0.012
MDC - 7.d	Session 1	MDC	GL-O-NP	42.08	0.49	1.025	0.011
MDC - 8.d	Session 1	MDC	GL-O-NP	42.25	0.40	1.027	0.011
MDC - 9.d	Session 1	MDC	GL-O-NP	41.98	0.49	1.032	0.011
MDC - 10.d	Session 1	MDC	GL-O-NP	41.95	0.42	1.019	0.011

Continued on next page

Continued from previous page

Spot	Sample	Session	RM	$^{87}Rb/^{86}Sr$	2SE	$^{87}Sr/^{86}Sr$	2SE
MDC - 11.d	Session 1	MDC	GL-O-NP	41.38	0.50	1.035	0.011
MDC - 12.d	Session 1	MDC	GL-O-NP	42.19	0.53	1.040	0.011
MDC - 13.d	Session 1	MDC	GL-O-NP	42.35	0.59	1.027	0.011
MDC - 14.d	Session 1	MDC	GL-O-NP	42.21	0.54	1.037	0.012
MDC - 15.d	Session 1	MDC	GL-O-NP	42.44	0.57	1.030	0.010
MDC - 16.d	Session 1	MDC	GL-O-NP	42.76	0.53	1.037	0.011
MDC - 17.d	Session 1	MDC	GL-O-NP	42.66	0.61	1.034	0.010
MDC - 18.d	Session 1	MDC	GL-O-NP	42.46	0.47	1.034	0.011
MDC - 19.d	Session 1	MDC	GL-O-NP	42.09	0.46	1.028	0.010
MDC - 20.d	Session 1	MDC	GL-O-NP	41.96	0.51	1.031	0.012
MDC - 1.d	Session 2	MDC	GL-O-NP	41.40	0.49	1.040	0.014
MDC - 2.d	Session 2	MDC	GL-O-NP	41.21	0.55	1.027	0.013
MDC - 3.d	Session 2	MDC	GL-O-NP	40.80	0.49	1.016	0.014
MDC - 4.d	Session 2	MDC	GL-O-NP	41.09	0.49	1.033	0.014
MDC - 5.d	Session 2	MDC	GL-O-NP	41.41	0.56	1.037	0.014
MDC - 6.d	Session 2	MDC	GL-O-NP	41.22	0.48	1.030	0.015
MDC - 7.d	Session 2	MDC	GL-O-NP	40.72	0.48	1.034	0.014
MDC - 8.d	Session 2	MDC	GL-O-NP	42.01	0.51	1.026	0.015
MDC - 9.d	Session 2	MDC	GL-O-NP	42.21	0.61	1.044	0.014
MDC - 10.d	Session 2	MDC	GL-O-NP	41.35	0.48	1.023	0.012
MDC - 11.d	Session 2	MDC	GL-O-NP	41.75	0.52	1.030	0.014
MDC - 12.d	Session 2	MDC	GL-O-NP	41.18	0.50	1.034	0.015
MDC - 13.d	Session 2	MDC	GL-O-NP	41.64	0.59	1.030	0.015
MDC - 14.d	Session 2	MDC	GL-O-NP	41.51	0.53	1.043	0.014
MDC - 15.d	Session 2	MDC	GL-O-NP	40.78	0.52	1.013	0.014
MDC - 16.d	Session 2	MDC	GL-O-NP	42.13	0.59	1.029	0.016
MDC - 17.d	Session 2	MDC	GL-O-NP	41.64	0.65	1.023	0.015
MDC - 18.d	Session 2	MDC	GL-O-NP	41.40	0.53	1.015	0.014
MDC - 19.d	Session 2	MDC	GL-O-NP	41.95	0.59	1.019	0.015
MDC - 20.d	Session 2	MDC	GL-O-NP	42.46	0.61	1.046	0.014
MDC - 1.d	Session 3	MDC	GL-O-NP	48.92	0.70	1.081	0.015
MDC - 2.d	Session 3	MDC	GL-O-NP	48.10	0.56	1.066	0.013
MDC - 3.d	Session 3	MDC	GL-O-NP	46.84	0.71	1.056	0.017
MDC - 4.d	Session 3	MDC	GL-O-NP	46.76	0.67	1.049	0.015
MDC - 5.d	Session 3	MDC	GL-O-NP	47.11	0.66	1.054	0.016
MDC - 6.d	Session 3	MDC	GL-O-NP	46.56	0.62	1.064	0.014
MDC - 7.d	Session 3	MDC	GL-O-NP	46.37	0.62	1.054	0.015
MDC - 8.d	Session 3	MDC	GL-O-NP	46.09	0.69	1.056	0.015
MDC - 9.d	Session 3	MDC	GL-O-NP	46.02	0.64	1.053	0.013
MDC - 10.d	Session 3	MDC	GL-O-NP	45.86	0.60	1.051	0.014
MDC - 11.d	Session 3	MDC	GL-O-NP	48.78	0.82	1.075	0.021
MDC - 12.d	Session 3	MDC	GL-O-NP	49.24	0.78	1.075	0.020
MDC - 13.d	Session 3	MDC	GL-O-NP	48.97	0.79	1.088	0.019
MDC - 14.d	Session 3	MDC	GL-O-NP	48.02	0.80	1.075	0.020

Continued on next page

Continued from previous page

Spot	Sample	Session	RM	$^{87}Rb/^{86}Sr$	2SE	$^{87}Sr/^{86}Sr$	2SE
MDC - 15.d	Session 3	MDC	GL-O-NP	46.87	0.68	1.049	0.015
MDC - 16.d	Session 3	MDC	GL-O-NP	47.87	0.64	1.074	0.016
MDC - 17.d	Session 3	MDC	GL-O-NP	46.81	0.60	1.062	0.014
MDC - 18.d	Session 3	MDC	GL-O-NP	46.47	0.67	1.058	0.014
MDC - 19.d	Session 3	MDC	GL-O-NP	46.26	0.64	1.064	0.015
MDC - 20.d	Session 3	MDC	GL-O-NP	46.66	0.62	1.082	0.016
MDC - 21.d	Session 3	MDC	GL-O-NP	45.91	0.60	1.060	0.015
MDC - 22.d	Session 3	MDC	GL-O-NP	45.83	0.65	1.075	0.015
MDC - 23.d	Session 3	MDC	GL-O-NP	46.74	0.76	1.073	0.017
MDC - 24.d	Session 3	MDC	GL-O-NP	45.99	0.66	1.051	0.014
MDC - 25.d	Session 3	MDC	GL-O-NP	45.86	0.95	1.036	0.022
MDC - 26.d	Session 3	MDC	GL-O-NP	46.91	0.55	1.059	0.015
MDC - 27.d	Session 3	MDC	GL-O-NP	47.26	0.65	1.066	0.016
MDC - 28.d	Session 3	MDC	GL-O-NP	46.15	0.62	1.062	0.016
MDC - 29.d	Session 3	MDC	GL-O-NP	46.64	0.63	1.076	0.016
MDC - 30.d	Session 3	MDC	GL-O-NP	45.63	0.68	1.064	0.016
GLO-G - 1.d	Session 1	GL-O	Mica-Mg-NP	216.73	5.51	0.980	0.029
GLO-G - 2.d	Session 1	GL-O	Mica-Mg-NP	168.61	3.91	0.922	0.028
GLO-G - 3.d	Session 1	GL-O	Mica-Mg-NP	208.87	6.96	1.015	0.036
GLO-G - 4.d	Session 1	GL-O	Mica-Mg-NP	137.54	5.29	0.893	0.044
GLO-G - 5.d	Session 1	GL-O	Mica-Mg-NP	215.28	6.43	1.024	0.035
GLO-G - 6.d	Session 1	GL-O	Mica-Mg-NP	173.30	4.66	0.944	0.033
GLO-G - 7.d	Session 1	GL-O	Mica-Mg-NP	144.54	3.34	0.920	0.028
GLO-G - 8.d	Session 1	GL-O	Mica-Mg-NP	188.85	4.13	0.967	0.028
GLO-G - 9.d	Session 1	GL-O	Mica-Mg-NP	146.19	2.95	0.930	0.025
GLO-G - 11.d	Session 1	GL-O	Mica-Mg-NP	136.04	3.18	0.927	0.029
GLO-G - 12.d	Session 1	GL-O	Mica-Mg-NP	100.86	1.86	0.837	0.024
GLO-G - 14.d	Session 1	GL-O	Mica-Mg-NP	130.83	2.39	0.895	0.022
GLO-G - 15.d	Session 1	GL-O	Mica-Mg-NP	178.07	4.20	0.953	0.033
GLO-G - 16.d	Session 1	GL-O	Mica-Mg-NP	132.33	2.63	0.892	0.025
GLO-G - 17.d	Session 1	GL-O	Mica-Mg-NP	144.01	2.67	0.908	0.023
GLO-G - 18.d	Session 1	GL-O	Mica-Mg-NP	147.23	3.27	0.938	0.028
GLO-G - 19.d	Session 1	GL-O	Mica-Mg-NP	153.71	3.18	0.928	0.024
GLO-G - 20.d	Session 1	GL-O	Mica-Mg-NP	137.91	2.95	0.918	0.025
GLO - 3.d	Session 2	GL-O	Mica-Mg-NP	133.42	4.73	0.883	0.033
GLO - 4.d	Session 2	GL-O	Mica-Mg-NP	190.25	5.44	0.970	0.036
GLO - 5.d	Session 2	GL-O	Mica-Mg-NP	137.36	3.47	0.894	0.036
GLO - 6.d	Session 2	GL-O	Mica-Mg-NP	132.92	3.20	0.888	0.032
GLO - 7.d	Session 2	GL-O	Mica-Mg-NP	182.65	5.51	0.969	0.037
GLO - 9.d	Session 2	GL-O	Mica-Mg-NP	137.76	4.16	0.855	0.034
GLO - 10.d	Session 2	GL-O	Mica-Mg-NP	155.80	4.42	0.908	0.034
GLO - 11.d	Session 2	GL-O	Mica-Mg-NP	155.31	4.15	0.937	0.033
GLO - 12.d	Session 2	GL-O	Mica-Mg-NP	148.78	3.50	0.914	0.029
GLO - 13.d	Session 2	GL-O	Mica-Mg-NP	111.99	2.48	0.874	0.028

Continued on next page

Continued from previous page

Spot	Sample	Session	RM	$^{87}Rb/^{86}Sr$	2SE	$^{87}Sr/^{86}Sr$	2SE
GLO - 14.d	Session 2	GL-O	Mica-Mg-NP	161.40	5.02	0.944	0.034
GLO - 16.d	Session 2	GL-O	Mica-Mg-NP	174.85	6.21	0.983	0.041
GLO - 18.d	Session 2	GL-O	Mica-Mg-NP	111.06	4.11	0.874	0.032
GLO - 19.d	Session 2	GL-O	Mica-Mg-NP	174.95	3.87	0.956	0.035
GLO - 1.d	Session 3	GL-O	Mica-Mg-NP	143.39	6.75	0.929	0.039
GLO - 6.d	Session 3	GL-O	Mica-Mg-NP	164.24	6.25	0.946	0.039
GLO - 7.d	Session 3	GL-O	Mica-Mg-NP	151.31	5.33	0.934	0.040
GLO - 8.d	Session 3	GL-O	Mica-Mg-NP	196.92	6.59	0.944	0.038
GLO - 11.d	Session 3	GL-O	Mica-Mg-NP	155.65	5.12	0.945	0.039
GLO - 12.d	Session 3	GL-O	Mica-Mg-NP	182.27	4.64	0.974	0.036
GLO - 13.d	Session 3	GL-O	Mica-Mg-NP	182.41	4.80	0.978	0.038
GLO - 14.d	Session 3	GL-O	Mica-Mg-NP	186.14	5.19	0.971	0.043
GLO - 15.d	Session 3	GL-O	Mica-Mg-NP	151.76	5.02	0.897	0.035
GLO - 16.d	Session 3	GL-O	Mica-Mg-NP	164.55	4.94	0.940	0.039
GLO - 17.d	Session 3	GL-O	Mica-Mg-NP	212.69	6.53	1.040	0.045
GLO - 18.d	Session 3	GL-O	Mica-Mg-NP	201.39	5.66	0.994	0.033
GLO - 19.d	Session 3	GL-O	Mica-Mg-NP	202.30	6.02	1.019	0.045
GLO - 20.d	Session 3	GL-O	Mica-Mg-NP	224.82	8.92	1.020	0.044
GLO - 21.d	Session 3	GL-O	Mica-Mg-NP	216.02	8.21	1.024	0.050
GLO - 22.d	Session 3	GL-O	Mica-Mg-NP	154.51	5.97	0.899	0.034
GLO - 23.d	Session 3	GL-O	Mica-Mg-NP	183.27	6.03	0.972	0.039
GLO - 25.d	Session 3	GL-O	Mica-Mg-NP	164.90	5.90	0.991	0.048
GLO - 3.d	Session 2	GL-O	Mica-Fe-NP	124.89	4.43	0.881	0.033
GLO - 4.d	Session 2	GL-O	Mica-Fe-NP	178.08	5.09	0.967	0.036
GLO - 5.d	Session 2	GL-O	Mica-Fe-NP	128.57	3.25	0.891	0.036
GLO - 6.d	Session 2	GL-O	Mica-Fe-NP	124.41	2.99	0.886	0.032
GLO - 7.d	Session 2	GL-O	Mica-Fe-NP	170.96	5.15	0.966	0.037
GLO - 9.d	Session 2	GL-O	Mica-Fe-NP	128.94	3.89	0.853	0.034
GLO - 10.d	Session 2	GL-O	Mica-Fe-NP	145.82	4.14	0.905	0.034
GLO - 11.d	Session 2	GL-O	Mica-Fe-NP	145.36	3.89	0.934	0.033
GLO - 12.d	Session 2	GL-O	Mica-Fe-NP	139.24	3.27	0.911	0.029
GLO - 13.d	Session 2	GL-O	Mica-Fe-NP	104.81	2.32	0.872	0.028
GLO - 14.d	Session 2	GL-O	Mica-Fe-NP	151.05	4.70	0.941	0.034
GLO - 16.d	Session 2	GL-O	Mica-Fe-NP	163.63	5.81	0.980	0.041
GLO - 18.d	Session 2	GL-O	Mica-Fe-NP	103.93	3.84	0.871	0.032
GLO - 19.d	Session 2	GL-O	Mica-Fe-NP	163.71	3.62	0.954	0.035
GLO - 1.d	Session 3	GL-O	Mica-Fe-NP	134.73	6.34	0.922	0.039
GLO - 6.d	Session 3	GL-O	Mica-Fe-NP	154.33	5.87	0.939	0.039
GLO - 7.d	Session 3	GL-O	Mica-Fe-NP	142.18	5.01	0.927	0.040
GLO - 8.d	Session 3	GL-O	Mica-Fe-NP	185.03	6.19	0.937	0.037
GLO - 11.d	Session 3	GL-O	Mica-Fe-NP	146.25	4.81	0.938	0.038
GLO - 12.d	Session 3	GL-O	Mica-Fe-NP	171.27	4.36	0.966	0.036
GLO - 13.d	Session 3	GL-O	Mica-Fe-NP	171.40	4.51	0.970	0.038
GLO - 14.d	Session 3	GL-O	Mica-Fe-NP	174.91	4.88	0.964	0.043

Continued on next page

Continued from previous page

Spot	Sample	Session	RM	$^{87}Rb/^{86}Sr$	2SE	$^{87}Sr/^{86}Sr$	2SE
GLO - 15.d	Session 3	GL-O	Mica-Fe-NP	142.60	4.72	0.890	0.035
GLO - 16.d	Session 3	GL-O	Mica-Fe-NP	154.62	4.64	0.933	0.039
GLO - 17.d	Session 3	GL-O	Mica-Fe-NP	199.85	6.14	1.033	0.045
GLO - 18.d	Session 3	GL-O	Mica-Fe-NP	189.24	5.32	0.986	0.032
GLO - 19.d	Session 3	GL-O	Mica-Fe-NP	190.09	5.65	1.011	0.044
GLO - 20.d	Session 3	GL-O	Mica-Fe-NP	211.25	8.38	1.012	0.043
GLO - 21.d	Session 3	GL-O	Mica-Fe-NP	202.98	7.71	1.016	0.050
GLO - 22.d	Session 3	GL-O	Mica-Fe-NP	145.18	5.61	0.892	0.034
GLO - 23.d	Session 3	GL-O	Mica-Fe-NP	172.21	5.67	0.964	0.038
GLO - 25.d	Session 3	GL-O	Mica-Fe-NP	154.95	5.54	0.983	0.048
GLO-G - 1.d	Session 1	GL-O	GL-O-NP	223.70	5.69	0.978	0.029
GLO-G - 2.d	Session 1	GL-O	GL-O-NP	174.04	4.04	0.920	0.027
GLO-G - 3.d	Session 1	GL-O	GL-O-NP	215.58	7.18	1.013	0.036
GLO-G - 4.d	Session 1	GL-O	GL-O-NP	141.97	5.46	0.891	0.044
GLO-G - 5.d	Session 1	GL-O	GL-O-NP	222.21	6.64	1.022	0.035
GLO-G - 6.d	Session 1	GL-O	GL-O-NP	178.87	4.81	0.942	0.033
GLO-G - 7.d	Session 1	GL-O	GL-O-NP	149.19	3.44	0.918	0.028
GLO-G - 8.d	Session 1	GL-O	GL-O-NP	194.93	4.26	0.965	0.028
GLO-G - 9.d	Session 1	GL-O	GL-O-NP	150.89	3.05	0.928	0.025
GLO-G - 11.d	Session 1	GL-O	GL-O-NP	140.42	3.29	0.926	0.029
GLO-G - 12.d	Session 1	GL-O	GL-O-NP	104.10	1.92	0.836	0.024
GLO-G - 14.d	Session 1	GL-O	GL-O-NP	135.04	2.46	0.893	0.022
GLO-G - 15.d	Session 1	GL-O	GL-O-NP	183.80	4.34	0.951	0.033
GLO-G - 16.d	Session 1	GL-O	GL-O-NP	136.59	2.72	0.890	0.025
GLO-G - 17.d	Session 1	GL-O	GL-O-NP	148.65	2.75	0.907	0.023
GLO-G - 18.d	Session 1	GL-O	GL-O-NP	151.97	3.37	0.936	0.028
GLO-G - 19.d	Session 1	GL-O	GL-O-NP	158.65	3.28	0.926	0.024
GLO-G - 20.d	Session 1	GL-O	GL-O-NP	142.34	3.04	0.916	0.025
GLO - 3.d	Session 2	GL-O	GL-O-NP	134.38	4.77	0.887	0.033
GLO - 4.d	Session 2	GL-O	GL-O-NP	191.62	5.48	0.974	0.036
GLO - 5.d	Session 2	GL-O	GL-O-NP	138.35	3.50	0.898	0.036
GLO - 6.d	Session 2	GL-O	GL-O-NP	133.87	3.22	0.893	0.032
GLO - 7.d	Session 2	GL-O	GL-O-NP	183.95	5.55	0.973	0.037
GLO - 9.d	Session 2	GL-O	GL-O-NP	138.72	4.19	0.859	0.034
GLO - 10.d	Session 2	GL-O	GL-O-NP	156.87	4.45	0.912	0.034
GLO - 11.d	Session 2	GL-O	GL-O-NP	156.36	4.18	0.941	0.033
GLO - 12.d	Session 2	GL-O	GL-O-NP	149.76	3.52	0.918	0.029
GLO - 13.d	Session 2	GL-O	GL-O-NP	112.71	2.50	0.878	0.029
GLO - 14.d	Session 2	GL-O	GL-O-NP	162.42	5.05	0.948	0.034
GLO - 16.d	Session 2	GL-O	GL-O-NP	175.90	6.25	0.987	0.041
GLO - 18.d	Session 2	GL-O	GL-O-NP	111.68	4.13	0.877	0.032
GLO - 19.d	Session 2	GL-O	GL-O-NP	175.89	3.89	0.960	0.035
GLO - 1.d	Session 3	GL-O	GL-O-NP	151.97	7.15	0.931	0.039
GLO - 6.d	Session 3	GL-O	GL-O-NP	174.07	6.62	0.948	0.039

Continued on next page

Continued from previous page

Spot	Sample	Session	RM	$^{87}Rb/^{86}Sr$	2SE	$^{87}Sr/^{86}Sr$	2SE
GLO - 7.d	Session 3	GL-O	GL-O-NP	160.36	5.65	0.937	0.041
GLO - 8.d	Session 3	GL-O	GL-O-NP	208.70	6.98	0.946	0.038
GLO - 11.d	Session 3	GL-O	GL-O-NP	164.96	5.42	0.947	0.039
GLO - 12.d	Session 3	GL-O	GL-O-NP	193.18	4.92	0.976	0.036
GLO - 13.d	Session 3	GL-O	GL-O-NP	193.32	5.09	0.980	0.038
GLO - 14.d	Session 3	GL-O	GL-O-NP	197.28	5.50	0.973	0.043
GLO - 15.d	Session 3	GL-O	GL-O-NP	160.84	5.32	0.899	0.035
GLO - 16.d	Session 3	GL-O	GL-O-NP	174.39	5.23	0.942	0.039
GLO - 17.d	Session 3	GL-O	GL-O-NP	225.41	6.92	1.043	0.045
GLO - 18.d	Session 3	GL-O	GL-O-NP	213.44	6.00	0.996	0.033
GLO - 19.d	Session 3	GL-O	GL-O-NP	214.41	6.38	1.022	0.045
GLO - 20.d	Session 3	GL-O	GL-O-NP	238.27	9.46	1.023	0.044
GLO - 21.d	Session 3	GL-O	GL-O-NP	228.94	8.70	1.027	0.050
GLO - 22.d	Session 3	GL-O	GL-O-NP	163.76	6.33	0.901	0.034
GLO - 23.d	Session 3	GL-O	GL-O-NP	194.23	6.39	0.974	0.039
GLO - 25.d	Session 3	GL-O	GL-O-NP	174.77	6.25	0.993	0.048
FK-N C3 - 1.d	Session 1	FK-N-NP	Mica-Mg-NP	71.67	0.85	1.219	0.010
FK-N C3 - 2.d	Session 1	FK-N-NP	Mica-Mg-NP	71.65	0.67	1.221	0.009
FK-N C3 - 3.d	Session 1	FK-N-NP	Mica-Mg-NP	72.55	0.67	1.228	0.010
FK-N C3 - 4.d	Session 1	FK-N-NP	Mica-Mg-NP	71.92	0.80	1.227	0.011
FK-N C3 - 5.d	Session 1	FK-N-NP	Mica-Mg-NP	75.56	0.78	1.224	0.009
FK-N C3 - 6.d	Session 1	FK-N-NP	Mica-Mg-NP	67.34	0.72	1.205	0.009
FK-N C3 - 7.d	Session 1	FK-N-NP	Mica-Mg-NP	72.47	0.75	1.216	0.009
FK-N C3 - 8.d	Session 1	FK-N-NP	Mica-Mg-NP	73.59	1.03	1.216	0.009
FK-N C3 - 9.d	Session 1	FK-N-NP	Mica-Mg-NP	71.99	0.82	1.212	0.010
FK-N C3 - 10.d	Session 1	FK-N-NP	Mica-Mg-NP	73.07	0.67	1.219	0.010
FK-N-NP - 1.d	Session 2	FK-N-NP	Mica-Mg-NP	70.60	1.44	1.197	0.022
FK-N-NP - 2.d	Session 2	FK-N-NP	Mica-Mg-NP	75.57	1.89	1.223	0.028
FK-N-NP - 3.d	Session 2	FK-N-NP	Mica-Mg-NP	69.32	1.14	1.207	0.022
FK-N-NP - 4.d	Session 2	FK-N-NP	Mica-Mg-NP	72.76	1.60	1.223	0.023
FK-N-NP - 5.d	Session 2	FK-N-NP	Mica-Mg-NP	73.79	1.59	1.217	0.021
FK-N-NP - 6.d	Session 2	FK-N-NP	Mica-Mg-NP	71.74	1.51	1.213	0.022
FK-N-NP - 7.d	Session 2	FK-N-NP	Mica-Mg-NP	67.27	1.29	1.215	0.021
FK-N-NP - 8.d	Session 2	FK-N-NP	Mica-Mg-NP	73.98	1.49	1.226	0.020
FK-N-NP - 9.d	Session 2	FK-N-NP	Mica-Mg-NP	69.17	1.51	1.194	0.021
FK-N-NP - 10.d	Session 2	FK-N-NP	Mica-Mg-NP	69.31	1.39	1.210	0.020
FK-N-NP - 11.d	Session 2	FK-N-NP	Mica-Mg-NP	72.65	1.21	1.228	0.018
FK-N-NP - 12.d	Session 2	FK-N-NP	Mica-Mg-NP	71.07	1.26	1.223	0.021
FK-N-NP - 13.d	Session 2	FK-N-NP	Mica-Mg-NP	71.96	1.47	1.209	0.024
FK-N-NP - 14.d	Session 2	FK-N-NP	Mica-Mg-NP	70.43	1.35	1.229	0.019
FK-N-NP - 15.d	Session 2	FK-N-NP	Mica-Mg-NP	73.89	1.72	1.232	0.024
FK-N-NP - 16.d	Session 2	FK-N-NP	Mica-Mg-NP	72.92	1.50	1.240	0.022
FK-N-NP - 17.d	Session 2	FK-N-NP	Mica-Mg-NP	72.54	1.69	1.234	0.026
FK-N-NP - 18.d	Session 2	FK-N-NP	Mica-Mg-NP	70.92	1.23	1.210	0.021

Continued on next page

Continued from previous page

Spot	Sample	Session	RM	$^{87}Rb/^{86}Sr$	2SE	$^{87}Sr/^{86}Sr$	2SE
FK-N-NP - 19.d	Session 2	FK-N-NP	Mica-Mg-NP	73.06	1.45	1.233	0.026
FK-N-NP - 20.d	Session 2	FK-N-NP	Mica-Mg-NP	72.96	1.55	1.224	0.022
KSP FK-N - 1.d	Session 3	FK-N-NP	Mica-Mg-NP	69.14	1.28	1.225	0.024
KSP FK-N - 2.d	Session 3	FK-N-NP	Mica-Mg-NP	65.51	1.21	1.185	0.020
KSP FK-N - 3.d	Session 3	FK-N-NP	Mica-Mg-NP	67.64	1.41	1.214	0.024
KSP FK-N - 4.d	Session 3	FK-N-NP	Mica-Mg-NP	72.41	1.43	1.203	0.022
KSP FK-N - 5.d	Session 3	FK-N-NP	Mica-Mg-NP	68.43	1.23	1.205	0.020
KSP FK-N - 6.d	Session 3	FK-N-NP	Mica-Mg-NP	71.43	1.36	1.209	0.025
KSP FK-N - 7.d	Session 3	FK-N-NP	Mica-Mg-NP	67.66	1.38	1.209	0.019
KSP FK-N - 8.d	Session 3	FK-N-NP	Mica-Mg-NP	71.97	1.52	1.210	0.024
KSP FK-N - 9.d	Session 3	FK-N-NP	Mica-Mg-NP	70.25	1.27	1.217	0.023
KSP FK-N - 10.d	Session 3	FK-N-NP	Mica-Mg-NP	70.62	1.40	1.226	0.021
KSP FK-N - 11.d	Session 3	FK-N-NP	Mica-Mg-NP	68.48	1.76	1.201	0.026
KSP FK-N - 12.d	Session 3	FK-N-NP	Mica-Mg-NP	75.37	1.67	1.221	0.025
KSP FK-N - 13.d	Session 3	FK-N-NP	Mica-Mg-NP	71.10	1.42	1.221	0.024
KSP FK-N - 14.d	Session 3	FK-N-NP	Mica-Mg-NP	67.51	1.24	1.213	0.022
KSP FK-N - 15.d	Session 3	FK-N-NP	Mica-Mg-NP	71.70	1.47	1.238	0.023
KSP FK-N - 16.d	Session 3	FK-N-NP	Mica-Mg-NP	71.18	1.61	1.209	0.024
KSP FK-N - 17.d	Session 3	FK-N-NP	Mica-Mg-NP	71.78	1.42	1.229	0.025
KSP FK-N - 18.d	Session 3	FK-N-NP	Mica-Mg-NP	70.80	1.59	1.210	0.024
KSP FK-N - 19.d	Session 3	FK-N-NP	Mica-Mg-NP	70.64	1.43	1.227	0.028
KSP FK-N - 20.d	Session 3	FK-N-NP	Mica-Mg-NP	70.94	1.38	1.206	0.022
KSP FK-N - 21.d	Session 3	FK-N-NP	Mica-Mg-NP	72.21	1.45	1.214	0.023
KSP FK-N - 22.d	Session 3	FK-N-NP	Mica-Mg-NP	75.42	1.49	1.231	0.025
KSP FK-N - 23.d	Session 3	FK-N-NP	Mica-Mg-NP	68.37	1.39	1.196	0.023
KSP FK-N - 24.d	Session 3	FK-N-NP	Mica-Mg-NP	70.72	1.57	1.204	0.021
KSP FK-N - 25.d	Session 3	FK-N-NP	Mica-Mg-NP	67.19	1.17	1.222	0.022
KSP FK-N - 26.d	Session 3	FK-N-NP	Mica-Mg-NP	71.37	1.41	1.220	0.022
KSP FK-N - 27.d	Session 3	FK-N-NP	Mica-Mg-NP	71.14	1.41	1.191	0.022
KSP FK-N - 28.d	Session 3	FK-N-NP	Mica-Mg-NP	69.66	1.38	1.210	0.024
KSP FK-N - 29.d	Session 3	FK-N-NP	Mica-Mg-NP	71.08	1.69	1.226	0.025
FK-N C3 - 1.d	Session 1	FK-N-NP	Mica-Fe-NP	67.42	0.80	1.257	0.010
FK-N C3 - 2.d	Session 1	FK-N-NP	Mica-Fe-NP	67.40	0.63	1.259	0.010
FK-N C3 - 3.d	Session 1	FK-N-NP	Mica-Fe-NP	68.25	0.63	1.265	0.011
FK-N C3 - 4.d	Session 1	FK-N-NP	Mica-Fe-NP	67.65	0.75	1.264	0.011
FK-N C3 - 5.d	Session 1	FK-N-NP	Mica-Fe-NP	71.08	0.73	1.262	0.009
FK-N C3 - 6.d	Session 1	FK-N-NP	Mica-Fe-NP	63.35	0.68	1.242	0.010
FK-N C3 - 7.d	Session 1	FK-N-NP	Mica-Fe-NP	68.17	0.70	1.253	0.010
FK-N C3 - 8.d	Session 1	FK-N-NP	Mica-Fe-NP	69.22	0.97	1.253	0.009
FK-N C3 - 9.d	Session 1	FK-N-NP	Mica-Fe-NP	67.72	0.77	1.249	0.010
FK-N C3 - 10.d	Session 1	FK-N-NP	Mica-Fe-NP	68.73	0.63	1.256	0.010
FK-N-NP - 1.d	Session 2	FK-N-NP	Mica-Fe-NP	66.18	1.35	1.191	0.022
FK-N-NP - 2.d	Session 2	FK-N-NP	Mica-Fe-NP	70.85	1.77	1.216	0.028
FK-N-NP - 3.d	Session 2	FK-N-NP	Mica-Fe-NP	64.98	1.07	1.201	0.022

Continued on next page

Continued from previous page

Spot	Sample	Session	RM	$^{87}Rb/^{86}Sr$	2SE	$^{87}Sr/^{86}Sr$	2SE
FK-N-NP - 4.d	Session 2	FK-N-NP	Mica-Fe-NP	68.21	1.50	1.217	0.023
FK-N-NP - 5.d	Session 2	FK-N-NP	Mica-Fe-NP	69.18	1.49	1.211	0.020
FK-N-NP - 6.d	Session 2	FK-N-NP	Mica-Fe-NP	67.26	1.41	1.207	0.021
FK-N-NP - 7.d	Session 2	FK-N-NP	Mica-Fe-NP	63.08	1.21	1.208	0.020
FK-N-NP - 8.d	Session 2	FK-N-NP	Mica-Fe-NP	69.37	1.40	1.219	0.020
FK-N-NP - 9.d	Session 2	FK-N-NP	Mica-Fe-NP	64.86	1.42	1.188	0.021
FK-N-NP - 10.d	Session 2	FK-N-NP	Mica-Fe-NP	64.99	1.31	1.204	0.019
FK-N-NP - 11.d	Session 2	FK-N-NP	Mica-Fe-NP	68.13	1.14	1.222	0.018
FK-N-NP - 12.d	Session 2	FK-N-NP	Mica-Fe-NP	66.67	1.18	1.217	0.021
FK-N-NP - 13.d	Session 2	FK-N-NP	Mica-Fe-NP	67.51	1.38	1.202	0.023
FK-N-NP - 14.d	Session 2	FK-N-NP	Mica-Fe-NP	66.07	1.27	1.223	0.019
FK-N-NP - 15.d	Session 2	FK-N-NP	Mica-Fe-NP	69.32	1.62	1.226	0.024
FK-N-NP - 16.d	Session 2	FK-N-NP	Mica-Fe-NP	68.41	1.41	1.233	0.022
FK-N-NP - 17.d	Session 2	FK-N-NP	Mica-Fe-NP	68.05	1.58	1.228	0.026
FK-N-NP - 18.d	Session 2	FK-N-NP	Mica-Fe-NP	66.54	1.15	1.204	0.021
FK-N-NP - 19.d	Session 2	FK-N-NP	Mica-Fe-NP	68.55	1.36	1.227	0.026
FK-N-NP - 20.d	Session 2	FK-N-NP	Mica-Fe-NP	68.46	1.46	1.218	0.022
KSP FK-N - 1.d	Session 3	FK-N-NP	Mica-Fe-NP	64.97	1.20	1.216	0.024
KSP FK-N - 2.d	Session 3	FK-N-NP	Mica-Fe-NP	61.56	1.14	1.176	0.020
KSP FK-N - 3.d	Session 3	FK-N-NP	Mica-Fe-NP	63.56	1.32	1.204	0.024
KSP FK-N - 4.d	Session 3	FK-N-NP	Mica-Fe-NP	68.04	1.35	1.194	0.021
KSP FK-N - 5.d	Session 3	FK-N-NP	Mica-Fe-NP	64.30	1.15	1.196	0.020
KSP FK-N - 6.d	Session 3	FK-N-NP	Mica-Fe-NP	67.12	1.28	1.200	0.025
KSP FK-N - 7.d	Session 3	FK-N-NP	Mica-Fe-NP	63.57	1.29	1.199	0.019
KSP FK-N - 8.d	Session 3	FK-N-NP	Mica-Fe-NP	67.63	1.43	1.201	0.023
KSP FK-N - 9.d	Session 3	FK-N-NP	Mica-Fe-NP	66.01	1.19	1.208	0.023
KSP FK-N - 10.d	Session 3	FK-N-NP	Mica-Fe-NP	66.36	1.32	1.217	0.021
KSP FK-N - 11.d	Session 3	FK-N-NP	Mica-Fe-NP	64.34	1.66	1.192	0.025
KSP FK-N - 12.d	Session 3	FK-N-NP	Mica-Fe-NP	70.82	1.57	1.212	0.025
KSP FK-N - 13.d	Session 3	FK-N-NP	Mica-Fe-NP	66.80	1.33	1.211	0.024
KSP FK-N - 14.d	Session 3	FK-N-NP	Mica-Fe-NP	63.43	1.17	1.204	0.022
KSP FK-N - 15.d	Session 3	FK-N-NP	Mica-Fe-NP	67.37	1.38	1.228	0.023
KSP FK-N - 16.d	Session 3	FK-N-NP	Mica-Fe-NP	66.88	1.51	1.200	0.024
KSP FK-N - 17.d	Session 3	FK-N-NP	Mica-Fe-NP	67.45	1.33	1.219	0.025
KSP FK-N - 18.d	Session 3	FK-N-NP	Mica-Fe-NP	66.53	1.49	1.201	0.023
KSP FK-N - 19.d	Session 3	FK-N-NP	Mica-Fe-NP	66.37	1.35	1.217	0.028
KSP FK-N - 20.d	Session 3	FK-N-NP	Mica-Fe-NP	66.66	1.29	1.197	0.022
KSP FK-N - 21.d	Session 3	FK-N-NP	Mica-Fe-NP	67.86	1.36	1.205	0.023
KSP FK-N - 22.d	Session 3	FK-N-NP	Mica-Fe-NP	70.87	1.40	1.222	0.025
KSP FK-N - 23.d	Session 3	FK-N-NP	Mica-Fe-NP	64.24	1.31	1.187	0.022
KSP FK-N - 24.d	Session 3	FK-N-NP	Mica-Fe-NP	66.46	1.47	1.195	0.021
KSP FK-N - 25.d	Session 3	FK-N-NP	Mica-Fe-NP	63.14	1.10	1.213	0.021
KSP FK-N - 26.d	Session 3	FK-N-NP	Mica-Fe-NP	67.06	1.33	1.211	0.022
KSP FK-N - 27.d	Session 3	FK-N-NP	Mica-Fe-NP	66.85	1.32	1.182	0.022

Continued on next page

Continued from previous page

Spot	Sample	Session	RM	$^{87}Rb/^{86}Sr$	2SE	$^{87}Sr/^{86}Sr$	2SE
KSP FK-N - 28.d	Session 3	FK-N-NP	Mica-Fe-NP	65.46	1.30	1.201	0.024
KSP FK-N - 29.d	Session 3	FK-N-NP	Mica-Fe-NP	66.79	1.59	1.216	0.024
FK-N-NP - 1.d	Session 2	FK-N-NP	GL-O-NP	70.12	1.43	1.189	0.022
FK-N-NP - 2.d	Session 2	FK-N-NP	GL-O-NP	75.12	1.88	1.214	0.028
FK-N-NP - 3.d	Session 2	FK-N-NP	GL-O-NP	68.95	1.14	1.199	0.022
FK-N-NP - 4.d	Session 2	FK-N-NP	GL-O-NP	72.42	1.60	1.215	0.023
FK-N-NP - 5.d	Session 2	FK-N-NP	GL-O-NP	73.50	1.58	1.209	0.020
FK-N-NP - 6.d	Session 2	FK-N-NP	GL-O-NP	71.51	1.50	1.205	0.021
FK-N-NP - 7.d	Session 2	FK-N-NP	GL-O-NP	67.11	1.28	1.207	0.020
FK-N-NP - 8.d	Session 2	FK-N-NP	GL-O-NP	73.86	1.49	1.218	0.020
FK-N-NP - 9.d	Session 2	FK-N-NP	GL-O-NP	69.10	1.51	1.187	0.021
FK-N-NP - 10.d	Session 2	FK-N-NP	GL-O-NP	69.29	1.39	1.203	0.019
FK-N-NP - 11.d	Session 2	FK-N-NP	GL-O-NP	72.68	1.21	1.221	0.018
FK-N-NP - 12.d	Session 2	FK-N-NP	GL-O-NP	71.57	1.27	1.219	0.021
FK-N-NP - 13.d	Session 2	FK-N-NP	GL-O-NP	72.51	1.48	1.204	0.023
FK-N-NP - 14.d	Session 2	FK-N-NP	GL-O-NP	71.00	1.36	1.225	0.019
FK-N-NP - 15.d	Session 2	FK-N-NP	GL-O-NP	74.52	1.74	1.228	0.024
FK-N-NP - 16.d	Session 2	FK-N-NP	GL-O-NP	73.58	1.51	1.236	0.022
FK-N-NP - 17.d	Session 2	FK-N-NP	GL-O-NP	73.23	1.70	1.231	0.026
FK-N-NP - 18.d	Session 2	FK-N-NP	GL-O-NP	71.63	1.24	1.207	0.021
FK-N-NP - 19.d	Session 2	FK-N-NP	GL-O-NP	73.82	1.47	1.230	0.026
FK-N-NP - 20.d	Session 2	FK-N-NP	GL-O-NP	73.75	1.57	1.221	0.022
KSP FK-N - 1.d	Session 3	FK-N-NP	GL-O-NP	73.28	1.35	1.228	0.024
KSP FK-N - 2.d	Session 3	FK-N-NP	GL-O-NP	69.43	1.28	1.188	0.020
KSP FK-N - 3.d	Session 3	FK-N-NP	GL-O-NP	71.69	1.49	1.217	0.024
KSP FK-N - 4.d	Session 3	FK-N-NP	GL-O-NP	76.74	1.52	1.206	0.022
KSP FK-N - 5.d	Session 3	FK-N-NP	GL-O-NP	72.52	1.30	1.208	0.021
KSP FK-N - 6.d	Session 3	FK-N-NP	GL-O-NP	75.70	1.45	1.212	0.025
KSP FK-N - 7.d	Session 3	FK-N-NP	GL-O-NP	71.71	1.46	1.212	0.019
KSP FK-N - 8.d	Session 3	FK-N-NP	GL-O-NP	76.28	1.61	1.213	0.024
KSP FK-N - 9.d	Session 3	FK-N-NP	GL-O-NP	74.46	1.34	1.220	0.023
KSP FK-N - 10.d	Session 3	FK-N-NP	GL-O-NP	74.85	1.48	1.230	0.021
KSP FK-N - 11.d	Session 3	FK-N-NP	GL-O-NP	72.57	1.87	1.204	0.026
KSP FK-N - 12.d	Session 3	FK-N-NP	GL-O-NP	79.88	1.77	1.224	0.025
KSP FK-N - 13.d	Session 3	FK-N-NP	GL-O-NP	75.35	1.50	1.224	0.024
KSP FK-N - 14.d	Session 3	FK-N-NP	GL-O-NP	71.55	1.32	1.216	0.022
KSP FK-N - 15.d	Session 3	FK-N-NP	GL-O-NP	75.99	1.55	1.241	0.023
KSP FK-N - 16.d	Session 3	FK-N-NP	GL-O-NP	75.44	1.70	1.212	0.024
KSP FK-N - 17.d	Session 3	FK-N-NP	GL-O-NP	76.07	1.50	1.232	0.025
KSP FK-N - 18.d	Session 3	FK-N-NP	GL-O-NP	75.04	1.68	1.213	0.024
KSP FK-N - 19.d	Session 3	FK-N-NP	GL-O-NP	74.86	1.52	1.230	0.028
KSP FK-N - 20.d	Session 3	FK-N-NP	GL-O-NP	75.18	1.46	1.209	0.022
KSP FK-N - 21.d	Session 3	FK-N-NP	GL-O-NP	76.54	1.53	1.217	0.023
KSP FK-N - 22.d	Session 3	FK-N-NP	GL-O-NP	79.93	1.58	1.234	0.025

Continued on next page

Table 3.C Rb-Sr isotopic ratios of MDC, GLO and FK-N-NP calibrated versus different RM

Continued from previous page

Spot	Sample	Session	RM	$^{87}Rb/^{86}Sr$	2SE	$^{87}Sr/^{86}Sr$	2SE
KSP FK-N - 23.d	Session 3	FK-N-NP	GL-O-NP	72.46	1.48	1.199	0.023
KSP FK-N - 24.d	Session 3	FK-N-NP	GL-O-NP	74.96	1.66	1.207	0.021
KSP FK-N - 25.d	Session 3	FK-N-NP	GL-O-NP	71.21	1.24	1.225	0.022
KSP FK-N - 26.d	Session 3	FK-N-NP	GL-O-NP	75.64	1.50	1.223	0.022
KSP FK-N - 27.d	Session 3	FK-N-NP	GL-O-NP	75.40	1.49	1.194	0.022
KSP FK-N - 28.d	Session 3	FK-N-NP	GL-O-NP	73.83	1.46	1.213	0.025
KSP FK-N - 29.d	Session 3	FK-N-NP	GL-O-NP	75.33	1.79	1.229	0.025

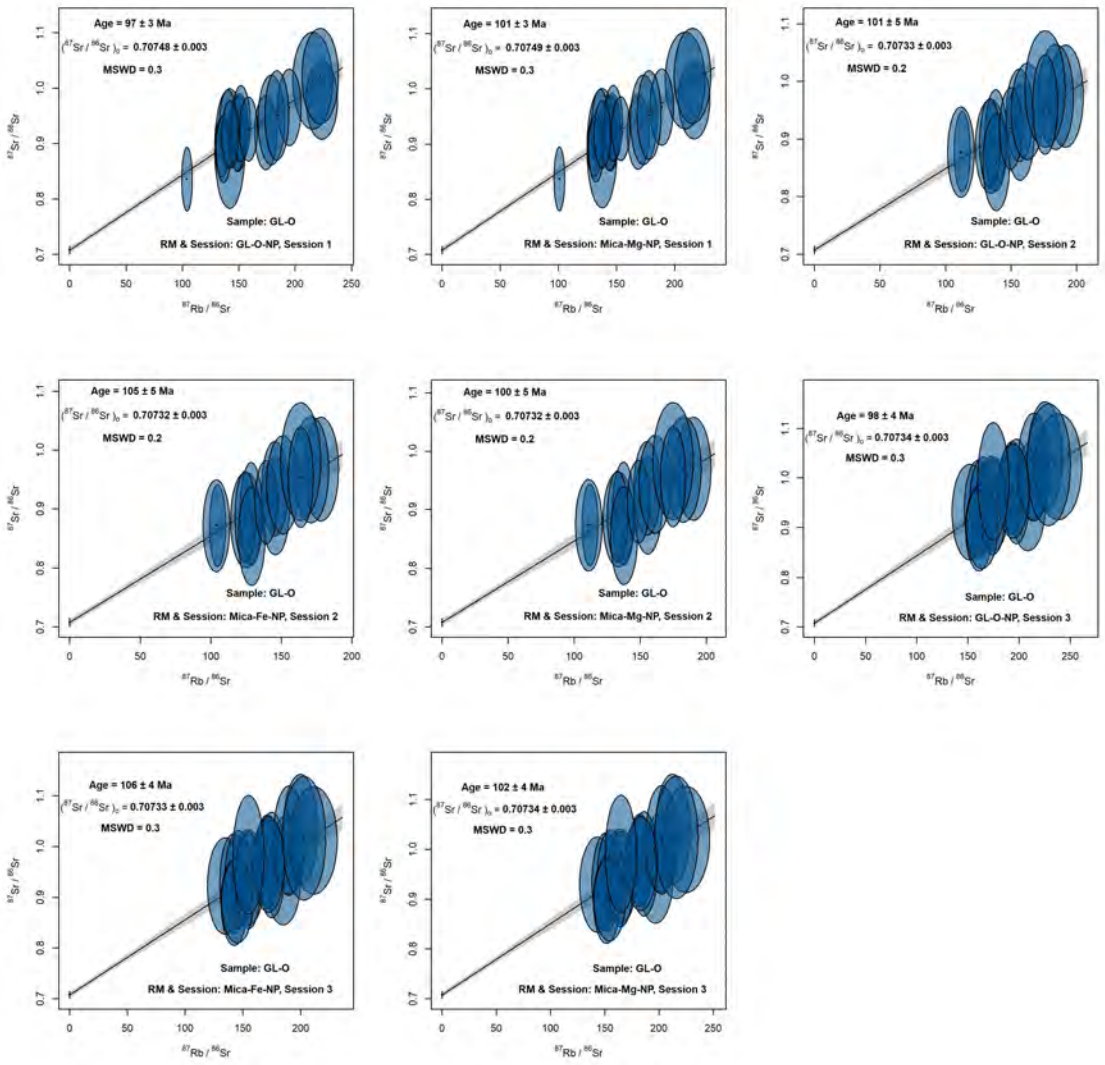

Figure 3.A: Isochron diagrams of GL-O analysed in different sessions and calibrated versus different RMs.

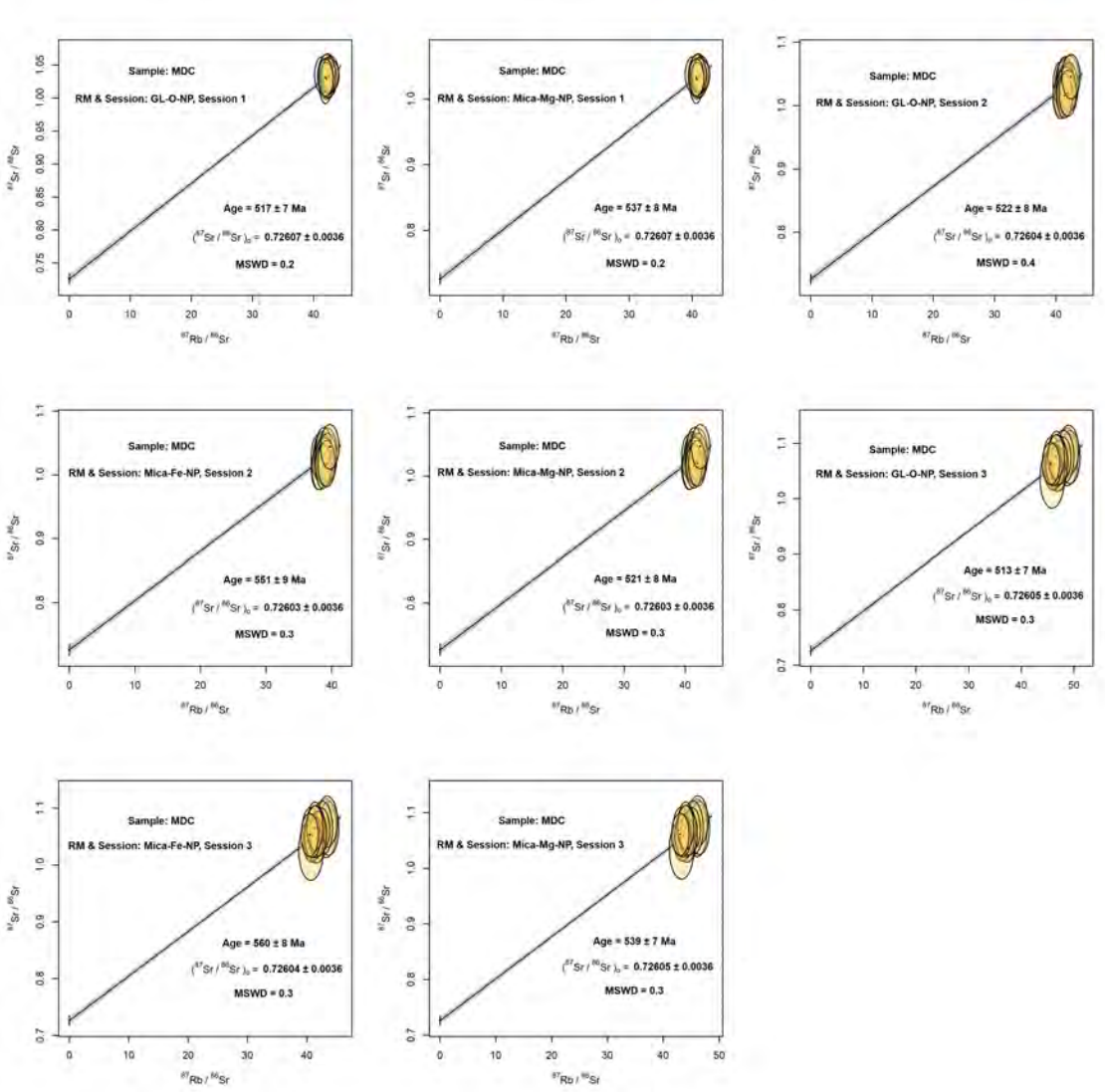

Figure 3.B: Isochron diagrams of MDC analysed in different sessions and calibrated versus different RMs.

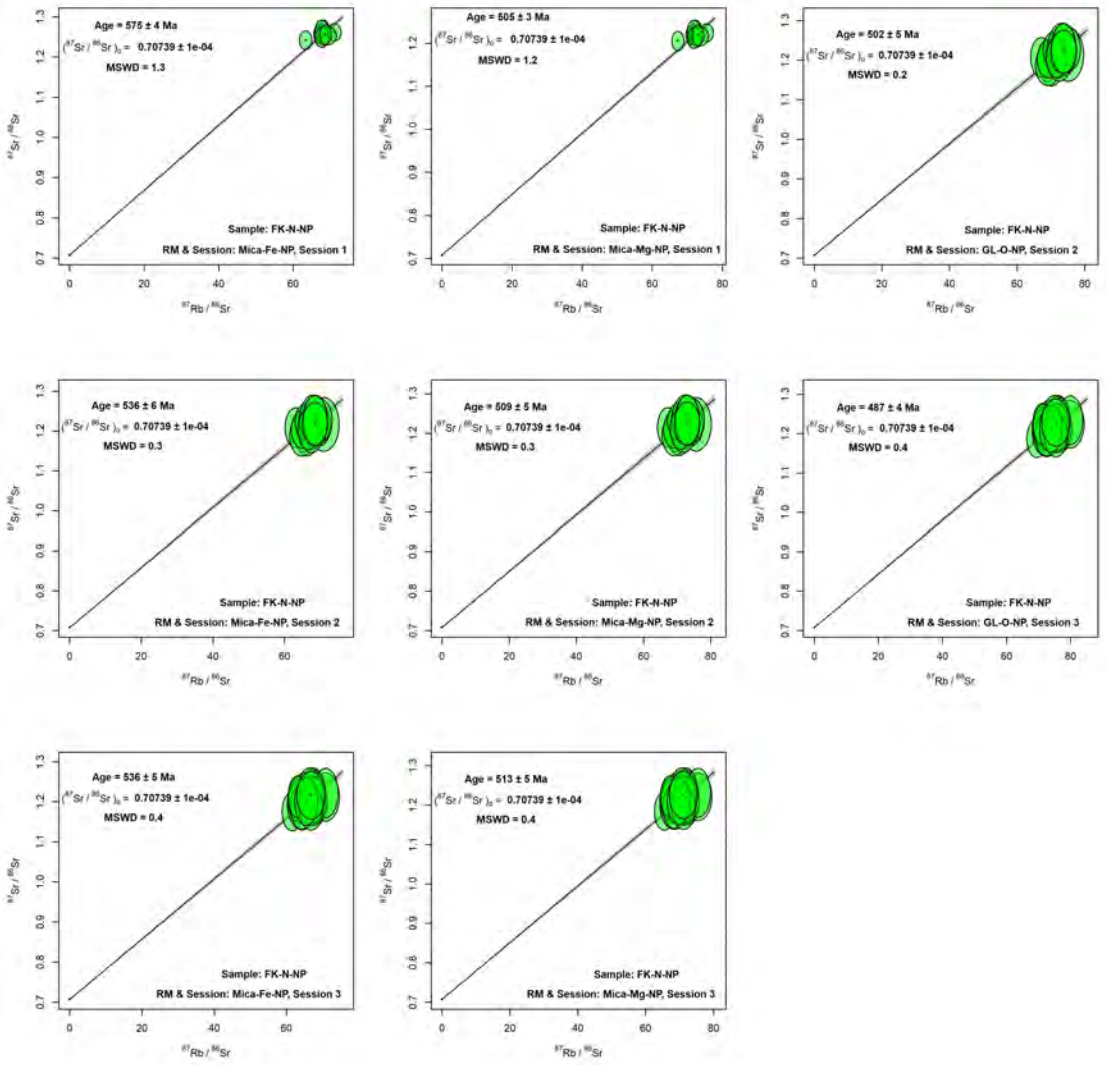

Figure 3.C: Isochron diagrams of FK-N-NP analysed in different sessions and calibrated versus different RMs.

Table 4.A: Settings of laser ablation and ICP-MS/MS.

	Units	
Laser parameters		
He carrier gas	ml/min	350
Ar carrier gas	ml/min	1050
N2 addition	ml/min	3.5
Spot size	μm	74
Repetition Rate	Hz	5
Fluence	J/cm^2	3.5
Sample Chamber		S155 large format
ICP-MS/MS		
Plasma Parameters		
RF Power	W	1350
Sample Depth	mm	5
Lens Parameters		
Extract 1	V	-0.5
Extract 2	V	-145
Omega Bias	V	-60
Omega Lens	V	7
Q1 entrance	V	1.5
Q1 exit	V	-2
Cell focus	V	-2
Cell entrance	V	-90
Cell exit	V	-120
Deflect	V	-11
Plate bias	V	-80
Q1 Parameters		
Q1 bias	V	-2
Q1 prefilter bias	V	-10
Q1 postfilter bias	V	-7
Cell Parameters		
N_2O flow rate	mL/min	0.35
OctP Bias	V	-24
Axial acceleration	V	2
OctP RF	V	180
Energy discrimination	V	-8
Q2 Parameters		
Q2 Bias	V	-32

Table 4.B: Semi-quantitative elemental composition of muscovite minerals acquired via X-ray spectroscopy attached with the Quanta 450 SEM

sample	Spectrum.Label	Si (wt%)	Al (wt%)	K (wt%)	Fe (wt%)	Mg (wt%)	O (wt%)
ABS 3	Spectrum 1	22.7	19.74	9.58	1.01	0.18	46.78
ABS 3	Spectrum 4	22.22	20.61	9.74	0.4	NA	47.03
ABS 3	Spectrum 5	22.88	19.54	9.59	0.82	0.24	46.93
ABS 3	Spectrum 6	22.25	20.44	9.52	0.52	NA	47.27
ABS 3	Spectrum 7	22.85	19.97	9.5	1.02	0.17	46.33
ABS 3	Spectrum 8	23.86	20.55	10.07	0.95	0.22	44.19
ABS 3	Spectrum 9	22.8	20	9.62	0.67	0.16	46.6
ABS 3	Spectrum 10	23.27	21.68	10.66	0.41	NA	43.81
ABS 3	Spectrum 13	22.58	20.39	9.58	0.48	NA	46.97
ABS 3	Spectrum 14	23.02	20.93	9.75	0.5	NA	45.64
ABS 3	Spectrum 15	23.15	19.37	9.5	1.05	0.3	46.63
ABS 3	Spectrum 17	24.15	21.48	10.76	0.62	NA	42.99
ABS 3	Spectrum 18	22.47	19.63	9.65	0.78	0.22	47.25
ABS 3	Spectrum 19	22.49	20.24	9.47	0.62	NA	47.17
ABS 3	Spectrum 20	22.59	20.46	9.48	0.57	0.12	46.62
ABS 3	Spectrum 21	22.25	20.9	9.78	0.27	NA	46.43
ABS 3	Spectrum 22	22.32	20.5	9.92	0.61	NA	46.65
ABS 3	Spectrum 23	22.06	20.54	9.59	0.52	NA	47.16
ABS 3	Spectrum 24	22.47	20.62	9.74	0.43	0.15	46.59
ABS 3	Spectrum 25	22.71	20.51	9.51	0.59	NA	46.68
ABS 3	Spectrum 26	22.33	20.5	9.43	0.45	NA	47.28
ABS 3	Spectrum 32	23.74	20.3	10.22	0.88	0.24	44.62
ABS 3	Spectrum 34	22.9	20.5	9.94	0.81	NA	45.85
ABS 3	Spectrum 35	24.22	21.24	11.18	1.14	NA	42.21
ABS 3	Spectrum 36	22.81	19.72	9.61	1.16	0.17	46.54
ABS 3	Spectrum 37	23.39	19.79	9.68	1.41	0.28	45.44
ABS 3	Spectrum 38	22.57	20.6	9.59	0.52	NA	46.72
ABS 3	Spectrum 39	23.06	19.91	9.92	1.05	0.23	45.82
ABS 3	Spectrum 40	22.91	19.8	9.74	0.65	0.26	46.65
ABS 3	Spectrum 42	22.69	20.2	9.63	0.61	0.16	46.72
ABS 3	Spectrum 48	23.03	20.1	9.76	0.65	0.2	46.25
ABS 3	Spectrum 49	23.02	20.05	9.41	0.96	NA	46.55
ABS 3	Spectrum 50	22.59	20.82	9.77	0.44	NA	46.37
ABS 3	Spectrum 54	22.75	20.78	9.82	0.46	NA	46.19
ABS 3	Spectrum 55	22.4	20.87	9.95	0.47	NA	46.32
ABS 3	Spectrum 56	23.21	19.8	9.74	1	0.23	46.02
ABS 3	Spectrum 59	22.9	19.92	9.7	0.73	0.2	46.56
ABS 3	Spectrum 60	22.83	19.83	9.69	1.16	0.17	46.32
ABS 3	Spectrum 61	22.84	20.59	9.79	0.7	NA	46.08
ABS 3	Spectrum 62	24.2	19.93	10.18	1.55	0.31	43.84
ABS 3	Spectrum 63	22.95	20.15	9.83	0.86	0.15	46.05
ABS 3	Spectrum 64	23.71	20.49	10.41	0.98	0.25	44.17

Continued on next page

Table 4.B Semi-quantitative elemental composition of muscovite minerals acquired via X-ray spectroscopy attached with the Quanta 450 SEM

Continued from previous page

sample	Spectrum.Label	Si (wt%)	Al (wt%)	K (wt%)	Fe (wt%)	Mg (wt%)	O (wt%)
ABS 3	Spectrum 66	24.9	20.98	9.9	0.76	0.26	43.2
ABS 3	Spectrum 70	24.86	20.96	11.69	1.3	0.2	40.74
ABS 3	Spectrum 71	22.42	20.43	9.61	0.58	0.14	46.69
ABS 3	Spectrum 72	23.35	20.51	10.03	0.83	0.13	45.15
ABS 3	Spectrum 73	23.05	20.47	9.94	0.77	0.16	45.6
ABS 3	Spectrum 74	24.44	20.75	10.91	0.81	0.22	42.88
ABS 3	Spectrum 75	24.22	19.92	9.88	1.18	0.23	44.57
ABS 3	Spectrum 77	22.94	20.23	9.76	0.85	NA	46.21
ABS 3	Spectrum 78	23.66	20.68	9.81	0.61	NA	45.23
ABS 3	Spectrum 79	22.5	21.06	10.02	0.52	NA	45.9
ABS 3	Spectrum 80	23.2	20.93	9.96	0.57	NA	45.35
ABS 3	Spectrum 81	24.75	20.68	10.49	1.01	0.28	42.79
ABS 3	Spectrum 90	22.5	19.54	9.78	0.78	NA	47.39
ABS 3	Spectrum 91	22.97	20.18	10.59	0.86	NA	45.39
ABS 3	Spectrum 92	22.36	19.81	9.98	0.88	NA	46.98
ABS 3	Spectrum 93	22.9	20.23	10.24	0.86	NA	45.77
ABS 3	Spectrum 94	23.43	20.32	10.53	0.76	NA	44.96
ABS 3	Spectrum 95	22.11	19.84	9.72	1.12	NA	47.21
ABS 3	Spectrum 96	24.06	20.51	9.95	0.71	NA	44.76
ABS 7	Spectrum 72	24.09	21.59	11.56	0.44	NA	41.57
ABS 7	Spectrum 74	24.77	20.87	10.73	0.89	NA	41.75
ABS 7	Spectrum 76	23.71	18.77	10.23	3.21	NA	44.07
ABS 7	Spectrum 77	22.82	20.78	10.58	1.09	NA	44.73
ABS 7	Spectrum 84	21.21	20.28	9.84	0.43	NA	46.57
ABS 7	Spectrum 88	22.37	20.07	10.2	1.21	NA	44.39
ABS 7	Spectrum 1	22.92	18.03	10.17	3.97	NA	44.92
ABS 7	Spectrum 2	22.73	16.48	10.03	4.33	0.84	45.6
ABS 7	Spectrum 3	23.62	16.11	10.2	5.8	0.9	42.98
ABS 7	Spectrum 4	23.4	15.73	10.07	5.41	1.21	44.18
ABS 7	Spectrum 5	23.46	15.45	9.94	5.44	1.29	44.43
ABS 7	Spectrum 6	23.84	15.51	10.16	5.41	1.26	43.82
ABS 7	Spectrum 7	22.62	18.16	10.19	3.85	NA	45.19
ABS 7	Spectrum 8	22.13	17.51	9.78	3.89	NA	46.69
ABS 7	Spectrum 9	22.46	16.22	9.9	4.59	0.85	45.97
ABS 7	Spectrum 11	22.42	18.14	10.01	3.53	NA	45.9
ABS 7	Spectrum 12	23.17	18.26	10.36	4.2	NA	44.02
ABS 7	Spectrum 13	23.33	18.66	10.43	3.72	NA	43.86
ABS 7	Spectrum 14	22.97	18.2	10.01	3.93	0.17	44.72
ABS 7	Spectrum 15	23.33	16.87	10.12	4	1.37	44.3
ABS 7	Spectrum 31	22.55	16.19	9.63	3.57	1.44	46.62
ABS 7	Spectrum 32	21.91	18.09	9.83	3.32	NA	46.85
ABS 7	Spectrum 33	22.43	15.88	9.56	3.94	1.52	46.68
ABS 7	Spectrum 34	22.5	16.14	9.17	3.66	1.29	44.26
ABS 7	Spectrum 35	22.74	16.51	9.74	3.6	1.45	45.96

Continued on next page

Table 4.B Semi-quantitative elemental composition of muscovite minerals acquired via X-ray spectroscopy attached with the Quanta 450 SEM

Continued from previous page

sample	Spectrum.Label	Si (wt%)	Al (wt%)	K (wt%)	Fe (wt%)	Mg (wt%)	O (wt%)
ABS 7	Spectrum 36	22.67	16.41	9.57	3.71	1.46	46.18
ABS 7	Spectrum 37	22.09	15.91	9.51	3.5	1.48	44.41
ABS 7	Spectrum 38	23.21	16.07	9.81	3.84	1.6	45.48
ABS 7	Spectrum 39	23.2	16.72	9.91	4.05	1.33	44.79
ABS 7	Spectrum 40	22.59	14.97	9.62	5.19	1.19	43.76
ABS 7	Spectrum 41	22.12	15.72	9.6	3.83	1.53	45.62
ABS 7	Spectrum 42	22.18	15.45	9.61	4.36	1.47	45.42
ABS 7	Spectrum 43	22.89	16.3	9.81	3.84	1.56	45.59
ABS 7	Spectrum 44	22.86	15.91	9.67	3.79	1.53	46.24
ABS 7	Spectrum 45	22.46	16.31	9.72	4.52	0.8	46.19
ABS 7	Spectrum 46	23.47	15.99	9.67	3.93	1.51	45.43
ABS 7	Spectrum 47	22.78	15.58	9.64	4.52	1.35	46.12
ABS 7	Spectrum 48	22.48	17.85	9.97	3.43	NA	46.28
ABS 7	Spectrum 49	22.65	16.49	9.62	3.87	1.27	46.09
ABS 7	Spectrum 51	22.99	15.83	9.63	3.19	1.7	46.66
ABS 7	Spectrum 52	22.51	16.19	9.73	3.74	1.52	46.32
ABS 7	Spectrum 54	21.51	16.85	9.28	4.22	NA	46.5
ABS 7	Spectrum 55	21.5	17.27	9.52	4.03	NA	45.93
ABS 7	Spectrum 56	21.54	17.22	9.81	4.11	NA	45.73
ABS 7	Spectrum 57	21.76	17.19	9.64	3.84	NA	45.99
ABS 7	Spectrum 58	21.56	17.3	9.6	3.75	NA	46.17
ABS 7	Spectrum 59	21.91	17.53	9.78	3.83	NA	45.26
ABS 7	Spectrum 60	23.26	15.51	9.82	5.33	1.33	43.13
ABS 7	Spectrum 62	21.9	17.56	9.92	3.88	NA	45.19
ABS 7	Spectrum 63	22.17	16	9.5	3.71	1.4	45.6
ABS 7	Spectrum 64	23.13	16.28	10.07	3.79	1.49	43.99
ABS 7	Spectrum 65	22.77	16.41	9.72	2.78	1.34	45.34
ABS 7	Spectrum 66	21.43	17.25	9.62	3.8	NA	46.3
ABS 7	Spectrum 67	22.04	15.79	9.68	4.61	0.89	45.45
ABS 7	Spectrum 68	22.82	15.09	9.77	5.31	1.35	45.66
ABS 7	Spectrum 69	21.3	17.33	9.64	3.95	NA	46.17
ABS 7	Spectrum 70	21.66	17.38	9.72	3.8	NA	45.88
ABS 7	Spectrum 71	21.34	17.38	9.6	4.03	NA	45.99
ABS 7	Spectrum 16	21.29	19.65	9.65	1.03	NA	46.72
ABS 7	Spectrum 17	22.5	19.47	10.05	1.09	NA	45.29
ABS 7	Spectrum 18	22.09	19.98	9.97	1.92	NA	46.04
ABS 7	Spectrum 21	21.43	20.35	9.82	0.43	NA	46.42
ABS 7	Spectrum 22	22.46	18.19	9.74	2.88	NA	46.21
ABS 7	Spectrum 23	22.51	18.29	9.64	3.02	NA	46.05
ABS 7	Spectrum 24	23.56	18.59	10.69	3.47	NA	43.69
ABS 7	Spectrum 25	23.56	21.13	11.2	1.46	NA	42.4
ABS 7	Spectrum 26	22.44	18.54	10.1	2.91	NA	46.01
ABS 7	Spectrum 29	22.34	18.15	10.04	3.3	NA	46.18
ABS 8	Spectrum 1	23.02	18.42	10.01	3.79	NA	44.75

Continued on next page

Table 4.B Semi-quantitative elemental composition of muscovite minerals acquired via X-ray spectroscopy attached with the Quanta 450 SEM

Continued from previous page

sample	Spectrum.Label	Si (wt%)	Al (wt%)	K (wt%)	Fe (wt%)	Mg (wt%)	O (wt%)
ABS 8	Spectrum 3	22.76	18.5	10.02	3.39	NA	45.33
ABS 8	Spectrum 4	22.57	16.34	9.87	4.17	0.81	46.25
ABS 8	Spectrum 5	22.58	17.37	10.08	3.95	0.37	45.65
ABS 8	Spectrum 6	22.54	18.49	10.17	3.21	NA	45.58
ABS 8	Spectrum 15	23.52	19.32	10.24	2.82	NA	44.09
ABS 8	Spectrum 16	22.43	17.61	10.03	4.3	NA	45.62
ABS 8	Spectrum 17	22.4	17.35	9.57	4.04	NA	46.64
ABS 8	Spectrum 18	23.08	18.36	10.5	4.39	NA	43.68
ABS 8	Spectrum 19	22.85	17.86	10.18	4.13	NA	44.99
ABS 8	Spectrum 20	22.78	17.84	10.08	4.29	NA	45.02
ABS 8	Spectrum 21	23.68	18.76	10.54	3.85	NA	43.17
ABS 8	Spectrum 22	23.29	18.34	10.21	4.11	NA	44.06
ABS 8	Spectrum 23	21.73	17.17	9.24	3.81	NA	48.04
ABS 8	Spectrum 24	22.43	17.88	10	4.19	NA	45.51
ABS 8	Spectrum 25	20.91	19.14	8.62	1	NA	50.33
ABS 8	Spectrum 26	22.77	19.84	9.65	2.02	NA	45.72
ABS 8	Spectrum 28	22.75	17.96	9.9	3.8	NA	45.59
ABS 8	Spectrum 29	24.33	17.24	10.14	4.1	NA	44.18
ABS 8	Spectrum 30	23.95	18.2	10.68	3.6	NA	43.57
ABS 8	Spectrum 32	21.99	17.09	9.63	4.75	NA	46.53
ABS 8	Spectrum 74	24	18.07	9.88	4.16	NA	43.88
ABS 8	Spectrum 76	23.24	18.31	10.09	3.84	NA	44.52
ABS 8	Spectrum 77	22.99	17.72	9.98	4.24	NA	45.07
ABS 8	Spectrum 78	23.42	18.36	10.41	4.77	NA	43.04
ABS 8	Spectrum 79	23.37	20.31	9.86	1.36	NA	45.09
ABS 8	Spectrum 80	22.74	21.1	10.28	0.65	NA	45.22
ABS 8	Spectrum 81	22.97	21.35	10.09	0.48	NA	45.11
ABS 8	Spectrum 82	23.07	18.91	10.3	3.09	NA	44.62
ABS 8	Spectrum 83	23.06	18	10.25	4.68	NA	44.02
ABS 8	Spectrum 84	24.88	16.9	11.7	5.07	1.33	40.13
ABS 8	Spectrum 86	23.43	18.3	10.16	4.34	NA	43.77
ABS 8	Spectrum 88	23.15	18.19	10.15	3.9	NA	44.61
ABS 8	Spectrum 89	22.57	20.89	10.24	0.94	NA	45.36
ABS 8	Spectrum 90	23.19	17.61	9.58	3.24	NA	46.38
ABS 8	Spectrum 91	23.4	18.66	10.2	3.43	NA	44.32
ABS 8	Spectrum 92	22.83	21.25	9.93	0.37	NA	45.62
ABS 8	Spectrum 35	23.98	19.01	10.08	3.27	NA	43.65
ABS 8	Spectrum 37	22.85	18.66	9.86	3.23	NA	45.4
ABS 8	Spectrum 39	23.67	21.28	10.48	0.72	NA	43.85
ABS 8	Spectrum 40	23.43	18.62	10.08	3.65	NA	44.22
ABS 8	Spectrum 41	24.75	19.03	10.3	2.75	NA	43.17
ABS 8	Spectrum 42	24.85	21.18	10.55	0.73	NA	42.68
ABS 8	Spectrum 43	22.02	18.41	9.53	2.79	NA	47.24
ABS 8	Spectrum 45	22.56	20.8	10.45	0.69	NA	45.5

Continued on next page

Table 4.B Semi-quantitative elemental composition of muscovite minerals acquired via X-ray spectroscopy attached with the Quanta 450 SEM

Continued from previous page

sample	Spectrum.Label	Si (wt%)	Al (wt%)	K (wt%)	Fe (wt%)	Mg (wt%)	O (wt%)
ABS 8	Spectrum 46	23.33	15.67	10.03	4.94	1.21	44.83
ABS 8	Spectrum 47	22.62	17.8	9.97	4.43	NA	45.18
ABS 8	Spectrum 48	22.46	20.31	10.32	1.26	NA	45.65
ABS 8	Spectrum 49	23.05	18.14	10.03	3.49	NA	45.28
ABS 8	Spectrum 51	22.81	18.46	9.86	3.32	NA	45.56
ABS 8	Spectrum 52	22.7	19.49	9.84	1.54	NA	46.44
ABS 8	Spectrum 53	24.83	19.2	11.68	3.13	0.53	40.64
ABS 8	Spectrum 54	24.48	21.59	10.79	0.87	NA	42.28
ABS 8	Spectrum 55	22.87	17.99	9.88	4.18	NA	45.08
ABS 8	Spectrum 56	23.09	17.89	9.95	3.86	NA	45.2
ABS 8	Spectrum 57	23.16	17.8	10.09	4.52	NA	44.44
ABS 8	Spectrum 58	22.95	18.65	10.07	3.28	NA	45.06
ABS 8	Spectrum 59	22.83	18.95	9.98	2.03	0.4	45.8
ABS 8	Spectrum 60	24.75	16.56	10.74	5.54	1.25	41.17
ABS 8	Spectrum 61	23.16	17.93	10.19	3.97	NA	44.75
ABS 8	Spectrum 62	22.8	16.98	9.4	3.88	NA	46.94
ABS 8	Spectrum 93	22.16	20.74	10.13	0.71	NA	46.25
ABS 8	Spectrum 94	22.32	18.54	9.58	1.86	NA	47.7
ABS 8	Spectrum 95	24.72	21.93	11.39	0.7	NA	41.26
ABS 8	Spectrum 96	23.91	21.96	10.92	0.45	NA	42.75
ABS 8	Spectrum 97	22.74	21.28	10.27	0.66	NA	45.06
ABS 8	Spectrum 98	23.16	19.32	10.34	3.12	NA	44.06
ABS 8	Spectrum 101	22.61	21.38	10.29	0.4	NA	45.32

Table 4.C: Rb-Sr isotopic ratios and ages of investigated samples acquired by LA-ICP-MS/MS

Spot number	Samples	Mineral	$^{87}Rb/^{86}Sr$	2SE	$^{87}Sr/^{86}Sr$	2SE	Age(Ma)
ABS-3 fracture fine - 1	ABS 3	Muscovite	368.0	13.0	3.54	0.12	550
ABS-3 fracture fine - 10	ABS 3	Muscovite	428.0	25.0	3.93	0.22	537
ABS-3 fracture fine - 11	ABS 3	Muscovite	241.0	14.0	2.64	0.13	573
ABS-3 fracture fine - 12	ABS 3	Muscovite	246.9	9.5	2.61	0.10	550
ABS-3 fracture fine - 13	ABS 3	Muscovite	298.0	10.0	2.95	0.12	537
ABS-3 fracture fine - 14	ABS 3	Muscovite	186.2	5.8	2.17	0.07	561
ABS-3 fracture fine - 15	ABS 3	Muscovite	215.3	6.5	2.49	0.08	591
ABS-3 fracture fine - 16	ABS 3	Muscovite	492.0	24.0	4.52	0.22	553
ABS-3 fracture fine - 17	ABS 3	Muscovite	717.0	44.0	6.25	0.37	552
ABS-3 fracture fine - 18	ABS 3	Muscovite	223.6	8.5	2.49	0.09	570
ABS-3 fracture fine - 20	ABS 3	Muscovite	288.0	15.0	2.86	0.13	534
ABS-3 fracture fine - 21	ABS 3	Muscovite	289.0	16.0	3.04	0.15	576
ABS-3 fracture fine - 22	ABS 3	Muscovite	241.3	7.2	2.65	0.09	575
ABS-3 fracture fine - 23	ABS 3	Muscovite	355.0	16.0	3.55	0.17	572
ABS-3 fracture fine - 24	ABS 3	Muscovite	219.5	8.4	2.42	0.10	557
ABS-3 fracture fine - 4	ABS 3	Muscovite	619.0	38.0	5.64	0.36	569
ABS-3 fracture fine - 5	ABS 3	Muscovite	413.0	17.0	3.98	0.17	566
ABS-3 fracture fine - 6	ABS 3	Muscovite	219.4	6.6	2.45	0.09	567
ABS-3 fracture fine - 7	ABS 3	Muscovite	244.0	12.0	2.55	0.11	540
ABS-3 fracture fine - 8	ABS 3	Muscovite	306.0	17.0	3.10	0.14	558
ABS-3 fracture fine - 9	ABS 3	Muscovite	342.0	17.0	3.36	0.14	554
ABS-3 mica fine2 - 10	ABS 3	Muscovite	303.0	14.0	3.19	0.14	585
ABS-3 mica fine2 - 11	ABS 3	Muscovite	323.0	18.0	3.32	0.22	577
ABS-3 mica fine2 - 12	ABS 3	Muscovite	343.0	17.0	3.46	0.17	573
ABS-3 mica fine2 - 13	ABS 3	Muscovite	257.0	13.0	2.82	0.14	587
ABS-3 mica fine2 - 14	ABS 3	Muscovite	330.0	17.0	3.26	0.15	552
ABS-3 mica fine2 - 15	ABS 3	Muscovite	266.0	13.0	2.89	0.14	586
ABS-3 mica fine2 - 16	ABS 3	Muscovite	284.0	13.0	3.06	0.16	591
ABS-3 mica fine2 - 17	ABS 3	Muscovite	338.0	16.0	3.52	0.15	594
ABS-3 mica fine2 - 6	ABS 3	Muscovite	351.0	26.0	3.70	0.24	608
ABS-3 mica fine2 - 7	ABS 3	Muscovite	274.0	11.0	2.98	0.11	592
ABS-3 mica fine2 - 8	ABS 3	Muscovite	313.0	12.0	3.13	0.15	553
ABS-3 mica fine2 - 9	ABS 3	Muscovite	314.0	13.0	3.22	0.14	571
ABS-3 feldspar - 1	ABS 3	Orthoclase	131.8	4.5	1.69	0.04	534
ABS-3 feldspar - 11	ABS 3	Orthoclase	147.6	4.1	1.79	0.05	525
ABS-3 feldspar - 12	ABS 3	Orthoclase	154.5	4.6	1.82	0.05	515
ABS-3 feldspar - 14	ABS 3	Orthoclase	141.8	4.0	1.74	0.04	521
ABS-3 feldspar - 16	ABS 3	Orthoclase	176.1	5.9	1.99	0.06	521
ABS-3 feldspar - 3	ABS 3	Orthoclase	153.4	4.6	1.83	0.04	524
ABS-3 feldspar - 6	ABS 3	Orthoclase	150.3	4.5	1.82	0.04	530
ABS-3 feldspar - 8	ABS 3	Orthoclase	121.8	3.3	1.63	0.03	542
ABS-3 feldspar - 9	ABS 3	Orthoclase	127.9	4.4	1.65	0.04	528

Continued on next page

Table 4.C Rb-Sr isotopic ratios and ages of investigated samples acquired by LA-ICP-MS/MS

Continued from previous page

Spot number	Samples	Mineral	$^{87}Rb/^{86}Sr$	2SE	$^{87}Sr/^{86}Sr$	2SE	Age(Ma)
ABS-3 feldspar1 - 1	ABS 3	Orthoclase	195.6	6.4	2.26	0.07	567
ABS-3 feldspar1 - 10	ABS 3	Orthoclase	149.0	3.8	1.82	0.04	534
ABS-3 feldspar1 - 11	ABS 3	Orthoclase	128.5	3.5	1.72	0.04	564
ABS-3 feldspar1 - 12	ABS 3	Orthoclase	148.6	4.1	1.85	0.04	550
ABS-3 feldspar1 - 13	ABS 3	Orthoclase	167.3	4.3	2.00	0.06	552
ABS-3 feldspar1 - 14	ABS 3	Orthoclase	147.8	4.6	1.85	0.05	553
ABS-3 feldspar1 - 15	ABS 3	Orthoclase	153.9	7.0	1.90	0.06	554
ABS-3 feldspar1 - 16	ABS 3	Orthoclase	99.9	3.1	1.48	0.04	554
ABS-3 feldspar1 - 17	ABS 3	Orthoclase	124.9	3.1	1.71	0.04	574
ABS-3 feldspar1 - 18	ABS 3	Orthoclase	119.1	4.9	1.63	0.04	555
ABS-3 feldspar1 - 19	ABS 3	Orthoclase	87.7	2.8	1.39	0.04	558
ABS-3 feldspar1 - 2	ABS 3	Orthoclase	124.4	4.0	1.68	0.06	560
ABS-3 feldspar1 - 20	ABS 3	Orthoclase	153.7	4.3	1.88	0.04	546
ABS-3 feldspar1 - 3	ABS 3	Orthoclase	166.5	5.7	1.93	0.05	525
ABS-3 feldspar1 - 4	ABS 3	Orthoclase	132.2	3.7	1.68	0.04	527
ABS-3 feldspar1 - 6	ABS 3	Orthoclase	155.9	4.0	1.90	0.04	547
ABS-3 feldspar1 - 7	ABS 3	Orthoclase	155.5	4.8	1.88	0.05	539
ABS-3 feldspar1 - 8	ABS 3	Orthoclase	144.9	3.5	1.82	0.04	549
ABS-3 feldspar1 - 9	ABS 3	Orthoclase	153.1	4.6	1.89	0.04	552
ABS-3 orthoclase1 - 1	ABS 3	Muscovite	176.9	4.9	2.03	0.06	535
ABS-3 orthoclase1 - 10	ABS 3	Muscovite	141.5	5.0	1.79	0.05	547
ABS-3 orthoclase1 - 11	ABS 3	Muscovite	169.7	4.6	2.02	0.05	553
ABS-3 orthoclase1 - 12	ABS 3	Muscovite	159.1	3.9	1.92	0.05	545
ABS-3 orthoclase1 - 13	ABS 3	Muscovite	163.0	6.3	1.98	0.06	558
ABS-3 orthoclase1 - 14	ABS 3	Muscovite	128.9	3.2	1.71	0.04	557
ABS-3 orthoclase1 - 15	ABS 3	Muscovite	118.3	3.7	1.61	0.03	546
ABS-3 orthoclase1 - 16	ABS 3	Muscovite	109.2	2.3	1.59	0.03	579
ABS-3 orthoclase1 - 2	ABS 3	Muscovite	196.3	6.5	2.16	0.07	529
ABS-3 orthoclase1 - 3	ABS 3	Muscovite	152.2	3.8	1.88	0.04	551
ABS-3 orthoclase1 - 4	ABS 3	Muscovite	157.4	4.7	1.87	0.05	528
ABS-3 orthoclase1 - 5	ABS 3	Muscovite	91.6	2.8	1.41	0.03	550
ABS-3 orthoclase1 - 6	ABS 3	Muscovite	158.6	4.4	1.89	0.05	533
ABS-3 orthoclase1 - 7	ABS 3	Muscovite	108.6	2.5	1.51	0.03	529
ABS-3 orthoclase1 - 8	ABS 3	Muscovite	157.5	4.3	1.90	0.05	542
ABS-3 orthoclase1 - 9	ABS 3	Muscovite	159.8	4.5	1.95	0.05	556
ABS-5-1 fine mica - 1	ABS 5	Muscovite	380.0	14.0	3.83	0.16	586
ABS-5-1 fine mica - 10	ABS 5	Muscovite	531.0	25.0	5.24	0.25	609
ABS-5-1 fine mica - 12	ABS 5	Muscovite	446.0	18.0	4.37	0.18	586
ABS-5-1 fine mica - 13	ABS 5	Muscovite	589.0	26.0	5.76	0.27	612
ABS-5-1 fine mica - 14	ABS 5	Muscovite	522.0	29.0	5.21	0.30	615
ABS-5-1 fine mica - 15	ABS 5	Muscovite	614.0	30.0	5.94	0.29	608
ABS-5-1 fine mica - 16	ABS 5	Muscovite	521.0	28.0	4.89	0.28	573
ABS-5-1 fine mica - 17	ABS 5	Muscovite	440.0	18.0	4.45	0.19	607
ABS-5-1 fine mica - 18	ABS 5	Muscovite	402.0	20.0	4.18	0.22	616

Continued on next page

Table 4.C Rb-Sr isotopic ratios and ages of investigated samples acquired by LA-ICP-MS/MS

Continued from previous page

Spot number	Samples	Mineral	$^{87}Rb/^{86}Sr$	2SE	$^{87}Sr/^{86}Sr$	2SE	Age(Ma)
ABS-5-1 fine mica - 2	ABS 5	Muscovite	523.0	33.0	5.16	0.33	607
ABS-5-1 fine mica - 20	ABS 5	Muscovite	430.0	16.0	4.36	0.17	606
ABS-5-1 fine mica - 21	ABS 5	Muscovite	346.0	15.0	3.64	0.16	605
ABS-5-1 fine mica - 22	ABS 5	Muscovite	536.0	32.0	5.40	0.34	624
ABS-5-1 fine mica - 23	ABS 5	Muscovite	248.5	9.1	2.82	0.10	607
ABS-5-1 fine mica - 5	ABS 5	Muscovite	283.0	12.0	3.07	0.14	596
ABS-5-1 fine mica - 6	ABS 5	Muscovite	408.0	21.0	4.15	0.23	602
ABS-5-1 fine mica - 7	ABS 5	Muscovite	310.0	12.0	3.24	0.15	583
ABS-5-1 fine mica - 8	ABS 5	Muscovite	360.0	15.0	3.99	0.18	650
ABS-5-1 fine mica - 9	ABS 5	Muscovite	515.0	32.0	4.87	0.29	577
ABS-5-2 fine mica - 1	ABS 5	Muscovite	526.0	31.0	4.97	0.27	578
ABS-5-2 fine mica - 10	ABS 5	Muscovite	607.0	30.0	5.83	0.34	602
ABS-5-2 fine mica - 2	ABS 5	Muscovite	794.0	50.0	7.57	0.50	616
ABS-5-2 fine mica - 3	ABS 5	Muscovite	465.0	19.0	4.44	0.20	573
ABS-5-2 fine mica - 4	ABS 5	Muscovite	531.0	24.0	5.22	0.24	606
ABS-5-2 fine mica - 5	ABS 5	Muscovite	830.0	39.0	7.69	0.41	600
ABS-5-2 fine mica - 7	ABS 5	Muscovite	717.0	48.0	6.98	0.54	624
ABS-5-2 fine mica - 8	ABS 5	Muscovite	787.0	42.0	7.45	0.39	611
ABS-5-2 fine mica - 9	ABS 5	Muscovite	778.0	38.0	7.13	0.36	589
ABS-5-3 fine mica - 1	ABS 5	Muscovite	790.0	36.0	7.60	0.35	622
ABS-5-3 fine mica - 11	ABS 5	Muscovite	205.5	7.3	2.37	0.10	578
ABS-5-3 fine mica - 12	ABS 5	Muscovite	300.0	10.0	3.29	0.13	614
ABS-5-3 fine mica - 13	ABS 5	Muscovite	732.0	34.0	7.12	0.33	625
ABS-5-3 fine mica - 15	ABS 5	Muscovite	758.0	55.0	7.03	0.46	595
ABS-5-3 fine mica - 18	ABS 5	Muscovite	1170.0	61.0	10.49	0.57	596
ABS-5-3 fine mica - 19	ABS 5	Muscovite	1387.0	72.0	12.75	0.68	619
ABS-5-3 fine mica - 20	ABS 5	Muscovite	1213.0	55.0	11.01	0.51	606
ABS-5-3 fine mica - 21	ABS 5	Muscovite	1188.0	42.0	10.81	0.37	606
ABS-5-3 fine mica - 3	ABS 5	Muscovite	410.0	20.0	3.96	0.19	566
ABS-5-3 fine mica - 5	ABS 5	Muscovite	238.0	11.0	2.67	0.11	589
ABS-5-3 fine mica - 8	ABS 5	Muscovite	371.0	18.0	3.88	0.21	610
ABS-5-4 large mica - 1	ABS 5	Muscovite	663.0	20.0	6.51	0.21	624
ABS-5-4 large mica - 10	ABS 5	Muscovite	390.0	10.0	4.07	0.11	615
ABS-5-4 large mica - 12	ABS 5	Muscovite	755.0	23.0	7.42	0.22	634
ABS-5-4 large mica - 13	ABS 5	Muscovite	943.0	34.0	9.24	0.35	645
ABS-5-4 large mica - 14	ABS 5	Muscovite	545.0	13.0	5.48	0.15	625
ABS-5-4 large mica - 15	ABS 5	Muscovite	796.0	28.0	7.65	0.28	622
ABS-5-4 large mica - 16	ABS 5	Muscovite	1054.0	39.0	9.63	0.37	604
ABS-5-4 large mica - 17	ABS 5	Muscovite	1539.0	84.0	13.84	0.88	608
ABS-5-4 large mica - 18	ABS 5	Muscovite	1552.0	83.0	14.71	0.80	643
ABS-5-4 large mica - 2	ABS 5	Muscovite	462.0	12.0	4.75	0.12	624
ABS-5-4 large mica - 3	ABS 5	Muscovite	432.0	11.0	4.44	0.11	616
ABS-5-4 large mica - 4	ABS 5	Muscovite	589.0	13.0	6.09	0.15	652
ABS-5-4 large mica - 5	ABS 5	Muscovite	659.0	19.0	6.57	0.17	634

Continued on next page

Table 4.C Rb-Sr isotopic ratios and ages of investigated samples acquired by LA-ICP-MS/MS

Continued from previous page

Spot number	Samples	Mineral	$^{87}Rb/^{86}Sr$	2SE	$^{87}Sr/^{86}Sr$	2SE	Age(Ma)
ABS-5-4 large mica - 6	ABS 5	Muscovite	382.3	9.4	4.02	0.09	618
ABS-5-4 large mica - 7	ABS 5	Muscovite	389.0	10.0	4.13	0.09	628
ABS-5-4 large mica - 8	ABS 5	Muscovite	612.0	22.0	6.13	0.22	632
ABS-5-4 large mica - 9	ABS 5	Muscovite	373.0	10.0	3.97	0.12	624
ABS-5-5 fine mica - 1	ABS 5	Muscovite	378.0	15.0	3.96	0.17	614
ABS-5-5 fine mica - 10	ABS 5	Muscovite	283.5	9.9	3.07	0.12	595
ABS-5-5 fine mica - 11	ABS 5	Muscovite	375.0	17.0	3.67	0.17	564
ABS-5-5 fine mica - 12	ABS 5	Muscovite	291.0	11.0	3.14	0.10	597
ABS-5-5 fine mica - 13	ABS 5	Muscovite	307.0	12.0	3.21	0.12	582
ABS-5-5 fine mica - 14	ABS 5	Muscovite	257.3	9.6	2.81	0.11	584
ABS-5-5 fine mica - 15	ABS 5	Muscovite	309.0	14.0	3.17	0.12	569
ABS-5-5 fine mica - 16	ABS 5	Muscovite	197.0	12.0	2.28	0.11	570
ABS-5-5 fine mica - 17	ABS 5	Muscovite	347.0	16.0	3.65	0.17	605
ABS-5-5 fine mica - 18	ABS 5	Muscovite	293.0	11.0	3.25	0.13	619
ABS-5-5 fine mica - 19	ABS 5	Muscovite	359.0	44.0	3.70	0.49	595
ABS-5-5 fine mica - 2	ABS 5	Muscovite	507.0	23.0	5.05	0.23	611
ABS-5-5 fine mica - 21	ABS 5	Muscovite	282.7	9.1	3.13	0.10	612
ABS-5-5 fine mica - 22	ABS 5	Muscovite	287.0	10.0	3.12	0.11	600
ABS-5-5 fine mica - 3	ABS 5	Muscovite	413.0	19.0	4.19	0.20	602
ABS-5-5 fine mica - 4	ABS 5	Muscovite	281.0	12.0	2.95	0.14	570
ABS-5-5 fine mica - 5	ABS 5	Muscovite	579.0	35.0	5.50	0.34	590
ABS-5-5 fine mica - 6	ABS 5	Muscovite	422.0	17.0	4.21	0.16	592
ABS-5-5 fine mica - 7	ABS 5	Muscovite	433.0	20.0	4.25	0.21	584
ABS-5-5 fine mica - 8	ABS 5	Muscovite	405.0	18.0	3.97	0.19	575
ABS-5-5 fine mica - 9	ABS 5	Muscovite	460.0	18.0	4.56	0.18	598
ABS-5-6 mica- - 1	ABS 5	Muscovite	690.0	29.0	6.43	0.28	592
ABS-5-6 mica- - 4	ABS 5	Muscovite	339.0	15.0	3.56	0.18	601
ABS-5-7 fine miac - 1	ABS 5	Muscovite	529.0	20.0	5.01	0.22	580
ABS-5-7 fine miac - 2	ABS 5	Muscovite	74.5	1.8	1.33	0.05	599
ABS-5-7 fine miac - 3	ABS 5	Muscovite	419.0	25.0	4.19	0.23	593
ABS-5-7 fine miac - 4	ABS 5	Muscovite	142.2	5.5	1.91	0.07	605
ABS-5-7 fine miac - 5	ABS 5	Muscovite	242.0	13.0	2.79	0.13	614
ABS-5-6 feldspar - 1	ABS 5	Orthoclase	103.5	2.0	1.61	0.03	624
ABS-5-6 feldspar - 13	ABS 5	Orthoclase	152.8	3.5	1.99	0.05	600
ABS-5-6 feldspar - 14	ABS 5	Orthoclase	116.8	2.6	1.72	0.03	620
ABS-5-6 feldspar - 15	ABS 5	Orthoclase	131.0	3.7	1.81	0.04	602
ABS-5-6 feldspar - 16	ABS 5	Orthoclase	122.4	2.7	1.75	0.04	609
ABS-5-6 feldspar - 17	ABS 5	Orthoclase	136.6	2.7	1.87	0.04	609
ABS-5-6 feldspar - 18	ABS 5	Orthoclase	155.5	4.7	2.02	0.06	603
ABS-5-6 feldspar - 19	ABS 5	Orthoclase	117.0	2.5	1.72	0.04	619
ABS-5-6 feldspar - 20	ABS 5	Orthoclase	117.0	2.5	1.73	0.04	625
ABS-5-6 feldspar - 21	ABS 5	Orthoclase	119.7	2.5	1.72	0.04	605
ABS-5-6 feldspar - 22	ABS 5	Orthoclase	111.6	1.9	1.65	0.03	604
ABS-5-6 feldspar - 23	ABS 5	Orthoclase	104.1	2.1	1.59	0.03	607

Continued on next page

Table 4.C Rb-Sr isotopic ratios and ages of investigated samples acquired by LA-ICP-MS/MS

Continued from previous page

Spot number	Samples	Mineral	$^{87}Rb/^{86}Sr$	2SE	$^{87}Sr/^{86}Sr$	2SE	Age(Ma)
ABS-5-6 feldspar - 24	ABS 5	Orthoclase	98.1	1.9	1.56	0.03	622
ABS-5-6 feldspar - 25	ABS 5	Orthoclase	169.5	4.2	2.15	0.05	608
ABS-5-6 feldspar - 26	ABS 5	Orthoclase	155.4	3.7	2.00	0.05	595
ABS-5-6 feldspar - 27	ABS 5	Orthoclase	103.4	2.2	1.63	0.03	638
ABS-5-6 feldspar - 28	ABS 5	Orthoclase	107.3	2.7	1.62	0.03	609
ABS-5-6 feldspar - 29	ABS 5	Orthoclase	124.2	2.5	1.78	0.04	618
ABS-5-6 feldspar - 3	ABS 5	Orthoclase	110.5	2.6	1.64	0.04	604
ABS-5-6 feldspar - 30	ABS 5	Orthoclase	102.8	2.1	1.56	0.03	594
ABS-5-6 feldspar - 4	ABS 5	Orthoclase	100.2	2.2	1.57	0.03	616
ABS-5-6 feldspar - 5	ABS 5	Orthoclase	112.7	2.3	1.66	0.04	605
ABS-5-6 feldspar - 6	ABS 5	Orthoclase	121.2	3.3	1.73	0.04	604
ABS-5-6 feldspar - 8	ABS 5	Orthoclase	108.7	3.0	1.65	0.04	620
ABS-5-7 feldspar - 1	ABS 5	Orthoclase	124.3	2.8	1.74	0.04	594
ABS-5-7 feldspar - 10	ABS 5	Orthoclase	117.3	2.7	1.69	0.03	599
ABS-5-7 feldspar - 11	ABS 5	Orthoclase	168.0	4.0	2.14	0.05	609
ABS-5-7 feldspar - 12	ABS 5	Orthoclase	113.6	2.8	1.68	0.04	613
ABS-5-7 feldspar - 13	ABS 5	Orthoclase	149.2	4.7	1.90	0.05	572
ABS-5-7 feldspar - 14	ABS 5	Orthoclase	160.7	4.3	2.06	0.05	602
ABS-5-7 feldspar - 15	ABS 5	Orthoclase	145.0	3.4	1.90	0.04	588
ABS-5-7 feldspar - 16	ABS 5	Orthoclase	138.8	3.6	1.86	0.04	594
ABS-5-7 feldspar - 2	ABS 5	Orthoclase	140.3	2.9	1.86	0.04	587
ABS-5-7 feldspar - 3	ABS 5	Orthoclase	139.8	4.3	1.87	0.05	595
ABS-5-7 feldspar - 4	ABS 5	Orthoclase	113.9	2.2	1.67	0.03	605
ABS-5-7 feldspar - 5	ABS 5	Orthoclase	133.4	2.9	1.83	0.04	602
ABS-5-7 feldspar - 6	ABS 5	Orthoclase	121.0	3.3	1.74	0.05	610
ABS-5-7 feldspar - 7	ABS 5	Orthoclase	134.6	5.3	1.86	0.06	612
ABS-5-7 feldspar - 8	ABS 5	Orthoclase	116.7	2.8	1.68	0.04	596
ABS-5-7 feldspar - 9	ABS 5	Orthoclase	150.7	4.1	1.92	0.04	575
ABS-7-1 large mica - 10	ABS 7	Muscovite	103.6	1.1	1.59	0.03	610
ABS-7-1 large mica - 11	ABS 7	Muscovite	243.6	6.6	2.87	0.06	634
ABS-7-1 large mica - 12	ABS 7	Muscovite	280.2	4.5	3.21	0.06	637
ABS-7-1 large mica - 13	ABS 7	Muscovite	309.0	5.3	3.40	0.05	622
ABS-7-1 large mica - 14	ABS 7	Muscovite	252.1	3.6	2.96	0.04	638
ABS-7-1 large mica - 15	ABS 7	Muscovite	226.6	4.3	2.74	0.05	640
ABS-7-1 large mica - 16	ABS 7	Muscovite	269.7	5.5	3.07	0.06	625
ABS-7-1 large mica - 17	ABS 7	Muscovite	297.3	6.2	3.30	0.07	622
ABS-7-1 large mica - 18	ABS 7	Muscovite	206.0	3.3	2.51	0.03	625
ABS-7-1 large mica - 19	ABS 7	Muscovite	306.3	4.8	3.40	0.05	627
ABS-7-1 large mica - 2	ABS 7	Muscovite	101.4	1.5	1.57	0.03	609
ABS-7-1 large mica - 20	ABS 7	Muscovite	260.0	10.0	3.00	0.10	629
ABS-7-1 large mica - 21	ABS 7	Muscovite	351.4	7.1	3.91	0.07	650
ABS-7-1 large mica - 22	ABS 7	Muscovite	395.9	6.9	4.28	0.07	644
ABS-7-1 large mica - 23	ABS 7	Muscovite	336.6	6.0	3.68	0.07	630
ABS-7-1 large mica - 24	ABS 7	Muscovite	309.3	5.3	3.43	0.06	628

Continued on next page

Table 4.C Rb-Sr isotopic ratios and ages of investigated samples acquired by LA-ICP-MS/MS

Continued from previous page

Spot number	Samples	Mineral	$^{87}Rb/^{86}Sr$	2SE	$^{87}Sr/^{86}Sr$	2SE	Age(Ma)
ABS-7-1 large mica - 3	ABS 7	Muscovite	259.9	6.1	2.99	0.06	627
ABS-7-1 large mica - 4	ABS 7	Muscovite	293.8	6.5	3.34	0.07	639
ABS-7-1 large mica - 5	ABS 7	Muscovite	432.5	8.7	4.53	0.10	630
ABS-7-1 large mica - 6	ABS 7	Muscovite	195.1	2.9	2.41	0.03	623
ABS-7-1 large mica - 7	ABS 7	Muscovite	230.0	3.3	2.79	0.04	646
ABS-7-1 large mica - 8	ABS 7	Muscovite	165.0	2.1	2.20	0.03	646
ABS-7-1 large mica - 9	ABS 7	Muscovite	339.3	5.6	3.69	0.06	627
ABS-7-1 large mica bright - 1	ABS 7	Muscovite	205.0	3.8	2.49	0.05	621
ABS-7-1 large mica bright - 11	ABS 7	Muscovite	324.2	5.6	3.56	0.06	628
ABS-7-1 large mica bright - 12	ABS 7	Muscovite	371.7	7.5	4.00	0.07	632
ABS-7-1 large mica bright - 13	ABS 7	Muscovite	195.8	2.9	2.44	0.04	632
ABS-7-1 large mica bright - 2	ABS 7	Muscovite	256.5	4.5	2.97	0.05	630
ABS-7-1 large mica bright - 3	ABS 7	Muscovite	187.3	2.4	2.39	0.04	642
ABS-7-1 large mica bright - 4	ABS 7	Muscovite	286.5	4.8	3.23	0.05	628
ABS-7-1 large mica bright - 5	ABS 7	Muscovite	357.6	5.4	3.87	0.06	631
ABS-7-1 large mica bright - 7	ABS 7	Muscovite	348.0	11.0	3.74	0.10	622
ABS-7-1 large mica bright - 8	ABS 7	Muscovite	243.9	4.3	2.86	0.05	630
ABS-7-2 fine mica - 1	ABS 7	Muscovite	77.6	1.7	1.32	0.02	566
ABS-7-2 fine mica - 10	ABS 7	Muscovite	404.0	19.0	4.12	0.21	603
ABS-7-2 fine mica - 11	ABS 7	Muscovite	236.0	12.0	2.63	0.12	582
ABS-7-2 fine mica - 12	ABS 7	Muscovite	316.0	15.0	3.38	0.16	604
ABS-7-2 fine mica - 14	ABS 7	Muscovite	243.3	3.6	2.87	0.04	634
ABS-7-2 fine mica - 15	ABS 7	Muscovite	280.4	5.5	3.19	0.07	632
ABS-7-2 fine mica - 2	ABS 7	Muscovite	596.0	37.0	5.83	0.40	613
ABS-7-2 fine mica - 4	ABS 7	Muscovite	128.3	5.0	1.80	0.05	609
ABS-7-2 fine mica - 5	ABS 7	Muscovite	319.0	18.0	3.59	0.20	645
ABS-7-2 fine mica - 6	ABS 7	Muscovite	207.5	9.6	2.48	0.11	610
ABS-7-2 fine mica - 7	ABS 7	Muscovite	203.1	7.0	2.39	0.08	592
ABS-7-2 fine mica - 8	ABS 7	Muscovite	293.0	13.0	3.14	0.15	593
ABS-7-2 fine mica - 9	ABS 7	Muscovite	168.0	11.0	2.17	0.09	622
ABS-7-3 fine mica - 1	ABS 7	Muscovite	455.0	18.0	4.32	0.18	567
ABS-7-3 fine mica - 10	ABS 7	Muscovite	332.0	12.0	3.52	0.12	605
ABS-7-3 fine mica - 11	ABS 7	Muscovite	446.0	18.0	4.48	0.20	603
ABS-7-3 fine mica - 13	ABS 7	Muscovite	416.0	20.0	4.15	0.17	590
ABS-7-3 fine mica - 14	ABS 7	Muscovite	479.0	12.0	4.85	0.10	617
ABS-7-3 fine mica - 15	ABS 7	Muscovite	411.0	19.0	4.29	0.16	622
ABS-7-3 fine mica - 16	ABS 7	Muscovite	344.0	10.0	3.73	0.10	627
ABS-7-3 fine mica - 19	ABS 7	Muscovite	436.0	14.0	4.40	0.16	604
ABS-7-3 fine mica - 2	ABS 7	Muscovite	236.0	14.0	2.62	0.13	579
ABS-7-3 fine mica - 3	ABS 7	Muscovite	446.0	24.0	4.54	0.24	613
ABS-7-3 fine mica - 4	ABS 7	Muscovite	495.0	20.0	5.15	0.19	640
ABS-7-3 fine mica - 5	ABS 7	Muscovite	401.0	13.0	4.28	0.13	635
ABS-7-3 fine mica - 6	ABS 7	Muscovite	528.0	25.0	5.06	0.26	588
ABS-7-3 fine mica - 7	ABS 7	Muscovite	237.6	7.6	2.79	0.08	626

Continued on next page

Table 4.C Rb-Sr isotopic ratios and ages of investigated samples acquired by LA-ICP-MS/MS

Continued from previous page

Spot number	Samples	Mineral	$^{87}Rb/^{86}Sr$	2SE	$^{87}Sr/^{86}Sr$	2SE	Age(Ma)
ABS-7-3 fine mica - 8	ABS 7	Muscovite	633.0	26.0	6.25	0.28	624
ABS-7-3 fine mica - 9	ABS 7	Muscovite	116.9	4.4	1.68	0.06	595
ABS-7-4 fine mica - 10	ABS 7	Muscovite	455.0	10.0	4.75	0.12	634
ABS-7-4 fine mica - 11	ABS 7	Muscovite	479.0	33.0	4.83	0.31	614
ABS-7-4 fine mica - 12	ABS 7	Muscovite	93.4	1.8	1.49	0.03	600
ABS-7-4 fine mica - 14	ABS 7	Muscovite	206.6	4.9	2.51	0.05	623
ABS-7-4 fine mica - 15	ABS 7	Muscovite	501.0	17.0	4.79	0.16	581
ABS-7-4 fine mica - 17	ABS 7	Muscovite	327.0	15.0	3.39	0.20	586
ABS-7-4 fine mica - 19	ABS 7	Muscovite	345.0	19.0	3.49	0.18	576
ABS-7-4 fine mica - 3	ABS 7	Muscovite	218.8	3.2	2.59	0.05	614
ABS-7-4 fine mica - 4	ABS 7	Muscovite	202.3	3.1	2.49	0.04	629
ABS-7-4 fine mica - 5	ABS 7	Muscovite	477.0	11.0	4.95	0.13	634
ABS-7-4 fine mica - 6	ABS 7	Muscovite	662.0	48.0	6.09	0.49	580
ABS-7-4 fine mica - 7	ABS 7	Muscovite	376.0	15.0	3.80	0.14	587
ABS-7-4 fine mica - 8	ABS 7	Muscovite	389.0	14.0	4.06	0.14	615
ABS-7-4 fine mica - 9	ABS 7	Muscovite	358.0	12.0	3.74	0.15	604
ABS-7-5- - 1	ABS 7	Muscovite	383.0	6.8	4.10	0.09	632
ABS-7-5- - 10	ABS 7	Muscovite	266.5	6.3	3.03	0.07	622
ABS-7-5- - 11	ABS 7	Muscovite	209.7	3.6	2.52	0.04	617
ABS-7-5- - 14	ABS 7	Muscovite	228.8	4.1	2.69	0.05	619
ABS-7-5- - 15	ABS 7	Muscovite	276.7	5.1	3.15	0.06	630
ABS-7-5- - 16	ABS 7	Muscovite	436.0	10.0	4.47	0.10	616
ABS-7-5- - 17	ABS 7	Muscovite	407.0	7.5	4.28	0.08	626
ABS-7-5- - 18	ABS 7	Muscovite	346.4	7.2	3.68	0.07	612
ABS-7-5- - 19	ABS 7	Muscovite	734.0	44.0	6.55	0.35	568
ABS-7-5- - 2	ABS 7	Muscovite	316.3	6.7	3.41	0.08	610
ABS-7-5- - 20	ABS 7	Muscovite	331.3	7.5	3.64	0.08	632
ABS-7-5- - 22	ABS 7	Muscovite	297.8	5.8	3.31	0.07	624
ABS-7-5- - 23	ABS 7	Muscovite	403.8	8.4	4.14	0.09	607
ABS-7-5- - 24	ABS 7	Muscovite	446.3	9.2	4.61	0.11	624
ABS-7-5- - 25	ABS 7	Muscovite	513.0	10.0	5.21	0.11	626
ABS-7-5- - 26	ABS 7	Muscovite	488.3	9.7	5.01	0.09	628
ABS-7-5- - 27	ABS 7	Muscovite	407.0	11.0	4.14	0.08	602
ABS-7-5- - 28	ABS 7	Muscovite	264.0	5.8	3.01	0.05	623
ABS-7-5- - 29	ABS 7	Muscovite	527.0	10.0	5.37	0.11	631
ABS-7-5- - 3	ABS 7	Muscovite	350.2	6.0	3.78	0.07	626
ABS-7-5- - 30	ABS 7	Muscovite	258.6	4.2	2.96	0.05	622
ABS-7-5- - 31	ABS 7	Muscovite	315.6	5.6	3.47	0.06	625
ABS-7-5- - 32	ABS 7	Muscovite	353.4	7.5	3.84	0.07	632
ABS-7-5- - 33	ABS 7	Muscovite	311.0	6.2	3.41	0.07	620
ABS-7-5- - 34	ABS 7	Muscovite	248.8	4.7	2.90	0.05	629
ABS-7-5- - 35	ABS 7	Muscovite	380.9	8.0	3.99	0.09	615
ABS-7-5- - 36	ABS 7	Muscovite	276.5	6.1	3.10	0.06	618
ABS-7-5- - 38	ABS 7	Muscovite	504.0	11.0	4.95	0.11	600

Continued on next page

Table 4.C Rb-Sr isotopic ratios and ages of investigated samples acquired by LA-ICP-MS/MS

Continued from previous page

Spot number	Samples	Mineral	$^{87}Rb/^{86}Sr$	2SE	$^{87}Sr/^{86}Sr$	2SE	Age(Ma)
ABS-7-5- - 4	ABS 7	Muscovite	244.1	3.9	2.86	0.05	629
ABS-7-5- - 5	ABS 7	Muscovite	405.7	7.4	4.27	0.07	626
ABS-7-5- - 6	ABS 7	Muscovite	381.4	6.5	4.06	0.08	627
ABS-7-5- - 7	ABS 7	Muscovite	421.0	8.9	4.36	0.08	619
ABS-7-5- - 9	ABS 7	Muscovite	394.0	13.0	4.20	0.12	632
ABS-7-6 L mica - 1	ABS 7	Muscovite	181.1	2.6	2.23	0.04	601
ABS-7-6 L mica - 10	ABS 7	Muscovite	211.2	3.0	2.55	0.04	623
ABS-7-6 L mica - 11	ABS 7	Muscovite	198.3	3.0	2.45	0.03	628
ABS-7-6 L mica - 12	ABS 7	Muscovite	196.9	3.4	2.46	0.05	636
ABS-7-6 L mica - 13	ABS 7	Muscovite	199.1	3.5	2.47	0.05	632
ABS-7-6 L mica - 14	ABS 7	Muscovite	252.9	4.5	2.96	0.06	636
ABS-7-6 L mica - 15	ABS 7	Muscovite	182.0	2.3	2.29	0.04	621
ABS-7-6 L mica - 16	ABS 7	Muscovite	162.5	2.5	2.10	0.04	612
ABS-7-6 L mica - 17	ABS 7	Muscovite	158.6	2.5	2.08	0.03	618
ABS-7-6 L mica - 18	ABS 7	Muscovite	232.0	4.7	2.70	0.05	613
ABS-7-6 L mica - 19	ABS 7	Muscovite	247.3	4.0	2.87	0.06	624
ABS-7-6 L mica - 2	ABS 7	Muscovite	164.3	2.7	2.14	0.04	623
ABS-7-6 L mica - 20	ABS 7	Muscovite	232.1	4.4	2.69	0.06	610
ABS-7-6 L mica - 3	ABS 7	Muscovite	398.1	8.6	4.20	0.09	626
ABS-7-6 L mica - 4	ABS 7	Muscovite	441.6	8.8	4.60	0.11	629
ABS-7-6 L mica - 5	ABS 7	Muscovite	406.2	8.7	4.31	0.10	633
ABS-7-6 L mica - 6	ABS 7	Muscovite	422.0	8.8	4.44	0.09	631
ABS-7-6 L mica - 7	ABS 7	Muscovite	390.2	9.6	4.11	0.10	622
ABS-7-6 L mica - 8	ABS 7	Muscovite	360.3	8.9	3.89	0.09	630
ABS-7-6 L mica - 9	ABS 7	Muscovite	213.0	3.7	2.54	0.04	614
ABS-7-7 mica - 10	ABS 7	Muscovite	331.0	12.0	3.69	0.14	643
ABS-7-7 mica - 11	ABS 7	Muscovite	286.1	6.8	3.24	0.08	632
ABS-7-7 mica - 12	ABS 7	Muscovite	232.1	4.3	2.77	0.05	634
ABS-7-7 mica - 13	ABS 7	Muscovite	265.4	7.9	3.03	0.08	625
ABS-7-7 mica - 14	ABS 7	Muscovite	245.6	6.4	2.85	0.08	623
ABS-7-7 mica - 15	ABS 7	Muscovite	251.3	6.5	2.97	0.09	643
ABS-7-7 mica - 16	ABS 7	Muscovite	271.5	6.5	3.12	0.09	634
ABS-7-7 mica - 17	ABS 7	Muscovite	251.2	9.9	2.89	0.13	620
ABS-7-7 mica - 4	ABS 7	Muscovite	304.0	12.0	3.40	0.10	632
ABS-7-7 mica - 5	ABS 7	Muscovite	373.0	10.0	4.06	0.15	641
ABS-8-1 mica - 1	ABS 8	Muscovite	338.0	7.8	3.65	0.09	621
ABS-8-1 mica - 2	ABS 8	Muscovite	267.1	6.0	3.00	0.07	613
ABS-8-1 mica - 3	ABS 8	Muscovite	408.0	12.0	4.29	0.14	626
ABS-8-1 mica - 4	ABS 8	Muscovite	508.0	30.0	5.38	0.31	656
ABS-8-1 mica - 5	ABS 8	Muscovite	368.2	7.8	3.94	0.09	626
ABS-8-1 mica - 6	ABS 8	Muscovite	433.0	9.9	4.62	0.10	644
ABS-8-1 mica - 7	ABS 8	Muscovite	397.9	7.4	4.17	0.10	621
ABS-8-1 mica - 8	ABS 8	Muscovite	570.0	14.0	5.73	0.14	628
ABS-8-2 mica - 10	ABS 8	Muscovite	352.0	11.0	3.56	0.12	578

Continued on next page

Table 4.C Rb-Sr isotopic ratios and ages of investigated samples acquired by LA-ICP-MS/MS

Continued from previous page

Spot number	Samples	Mineral	$^{87}Rb/^{86}Sr$	2SE	$^{87}Sr/^{86}Sr$	2SE	Age(Ma)
ABS-8-2 mica - 11	ABS 8	Muscovite	386.2	7.3	4.06	0.08	619
ABS-8-2 mica - 12	ABS 8	Muscovite	227.3	8.4	2.59	0.11	592
ABS-8-2 mica - 2	ABS 8	Muscovite	686.0	22.0	6.54	0.21	606
ABS-8-2 mica - 3	ABS 8	Muscovite	475.0	23.0	4.65	0.26	592
ABS-8-2 mica - 4	ABS 8	Muscovite	123.7	4.0	1.69	0.06	568
ABS-8-2 mica - 5	ABS 8	Muscovite	387.0	11.0	4.00	0.09	607
ABS-8-2 mica - 6	ABS 8	Muscovite	1135.0	67.0	10.68	0.67	626
ABS-8-2 mica - 7	ABS 8	Muscovite	345.0	12.0	3.61	0.13	600
ABS-8-2 mica - 8	ABS 8	Muscovite	250.0	13.0	2.66	0.15	558
ABS-8-2 mica - 9	ABS 8	Muscovite	2180.0	120.0	19.40	1.10	611
ABS-8-3 mica - 10	ABS 8	Muscovite	411.0	10.0	4.01	0.10	573
ABS-8-3 mica - 11	ABS 8	Muscovite	363.6	6.0	3.84	0.07	615
ABS-8-3 mica - 12	ABS 8	Muscovite	278.0	5.6	3.08	0.06	609
ABS-8-3 mica - 6	ABS 8	Muscovite	1680.0	120.0	14.50	1.00	585
ABS-8-3 mica - 7	ABS 8	Muscovite	759.0	34.0	7.26	0.30	616
ABS-8-3 mica - 8	ABS 8	Muscovite	602.0	24.0	5.87	0.22	612
ABS-8-3 mica - 9	ABS 8	Muscovite	332.6	6.2	3.56	0.07	612
ABS-8-4 mica - 1	ABS 8	Muscovite	897.0	44.0	8.51	0.41	620
ABS-8-4 mica - 4	ABS 8	Muscovite	606.0	18.0	6.01	0.21	624
ABS-8-5 mica - 1	ABS 8	Muscovite	560.0	15.0	5.58	0.16	621
ABS-8-5 mica - 10	ABS 8	Muscovite	246.1	9.5	2.82	0.12	613
ABS-8-5 mica - 11	ABS 8	Muscovite	211.6	5.9	2.50	0.08	605
ABS-8-5 mica - 12	ABS 8	Muscovite	239.0	14.0	2.75	0.15	610
ABS-8-5 mica - 13	ABS 8	Muscovite	205.9	9.4	2.48	0.10	615
ABS-8-5 mica - 14	ABS 8	Muscovite	174.2	5.4	2.22	0.06	620
ABS-8-5 mica - 15	ABS 8	Muscovite	175.3	7.4	2.23	0.09	620
ABS-8-5 mica - 16	ABS 8	Muscovite	145.1	3.6	1.93	0.06	602
ABS-8-5 mica - 17	ABS 8	Muscovite	96.7	2.0	1.53	0.03	609
ABS-8-5 mica - 18	ABS 8	Muscovite	1598.0	99.0	13.90	0.91	589
ABS-8-5 mica - 19	ABS 8	Muscovite	537.0	29.0	5.43	0.28	627
ABS-8-5 mica - 2	ABS 8	Muscovite	383.0	16.0	3.79	0.15	574
ABS-8-5 mica - 20	ABS 8	Muscovite	153.5	5.4	2.02	0.07	611
ABS-8-5 mica - 21	ABS 8	Muscovite	373.0	13.0	3.97	0.15	624
ABS-8-5 mica - 22	ABS 8	Muscovite	216.0	17.0	2.54	0.14	606
ABS-8-5 mica - 23	ABS 8	Muscovite	338.0	13.0	3.25	0.11	537
ABS-8-5 mica - 24	ABS 8	Muscovite	445.0	12.0	4.38	0.13	589
ABS-8-5 mica - 25	ABS 8	Muscovite	370.2	7.8	3.85	0.09	606
ABS-8-5 mica - 26	ABS 8	Muscovite	585.0	13.0	5.70	0.14	609
ABS-8-5 mica - 27	ABS 8	Muscovite	302.1	5.4	3.30	0.07	612
ABS-8-5 mica - 28	ABS 8	Muscovite	996.0	27.0	9.28	0.27	614
ABS-8-5 mica - 29	ABS 8	Muscovite	777.0	25.0	7.30	0.23	605
ABS-8-5 mica - 3	ABS 8	Muscovite	156.5	4.4	1.98	0.06	581
ABS-8-5 mica - 30	ABS 8	Muscovite	986.0	25.0	9.39	0.23	628
ABS-8-5 mica - 31	ABS 8	Muscovite	441.2	9.0	4.64	0.10	636

Continued on next page

Table 4.C Rb-Sr isotopic ratios and ages of investigated samples acquired by LA-ICP-MS/MS

Continued from previous page

Spot number	Samples	Mineral	$^{87}Rb/^{86}Sr$	2SE	$^{87}Sr/^{86}Sr$	2SE	Age(Ma)
ABS-8-5 mica - 32	ABS 8	Muscovite	477.0	11.0	4.77	0.10	608
ABS-8-5 mica - 33	ABS 8	Muscovite	480.0	12.0	4.82	0.12	611
ABS-8-5 mica - 34	ABS 8	Muscovite	378.8	7.4	3.95	0.08	611
ABS-8-5 mica - 35	ABS 8	Muscovite	292.4	6.2	3.21	0.07	611
ABS-8-5 mica - 36	ABS 8	Muscovite	380.1	7.1	3.95	0.08	609
ABS-8-5 mica - 37	ABS 8	Muscovite	319.9	6.2	3.47	0.06	616
ABS-8-5 mica - 38	ABS 8	Muscovite	699.0	20.0	6.72	0.19	613
ABS-8-5 mica - 39	ABS 8	Muscovite	784.0	22.0	7.41	0.17	610
ABS-8-5 mica - 4	ABS 8	Muscovite	458.0	28.0	4.51	0.28	592
ABS-8-5 mica - 5	ABS 8	Muscovite	116.0	2.6	1.63	0.04	569
ABS-8-5 mica - 6	ABS 8	Muscovite	587.0	43.0	5.74	0.45	611
ABS-8-5 mica - 8	ABS 8	Muscovite	215.0	5.7	2.47	0.07	586
ABS-8-5 mica - 9	ABS 8	Muscovite	266.0	12.0	2.95	0.13	602
ABS-8-5 mica 1F - 1	ABS 8	Muscovite	365.0	8.2	3.91	0.08	626
ABS-8-5 mica 1F - 2	ABS 8	Muscovite	325.6	6.5	3.45	0.07	601
ABS-8-5 mica 1F - 3	ABS 8	Muscovite	701.0	18.0	6.77	0.17	617
ABS-8-5 mica 1F - 4	ABS 8	Muscovite	756.0	19.0	7.21	0.17	613
ABS-8-5 mica 1F - 5	ABS 8	Muscovite	512.0	12.0	5.01	0.11	599
ABS-8-6 mica - 1	ABS 8	Muscovite	372.0	12.0	3.85	0.10	603
ABS-8-6 mica - 10	ABS 8	Muscovite	708.0	18.0	6.66	0.19	600
ABS-8-6 mica - 11	ABS 8	Muscovite	578.0	12.0	5.63	0.13	607
ABS-8-6 mica - 12	ABS 8	Muscovite	688.0	29.0	6.58	0.29	609
ABS-8-6 mica - 13	ABS 8	Muscovite	508.0	15.0	4.93	0.15	593
ABS-8-6 mica - 18	ABS 8	Muscovite	281.3	5.0	3.10	0.06	607
ABS-8-6 mica - 19	ABS 8	Muscovite	306.3	4.8	3.31	0.06	606
ABS-8-6 mica - 2	ABS 8	Muscovite	243.8	4.6	2.83	0.05	622
ABS-8-6 mica - 20	ABS 8	Muscovite	360.9	6.5	3.81	0.08	613
ABS-8-6 mica - 21	ABS 8	Muscovite	381.5	8.0	3.96	0.08	608
ABS-8-6 mica - 22	ABS 8	Muscovite	265.6	6.3	2.93	0.06	597
ABS-8-6 mica - 23	ABS 8	Muscovite	2470.0	140.0	20.40	1.20	568
ABS-8-6 mica - 24	ABS 8	Muscovite	1172.0	89.0	10.40	0.78	590
ABS-8-6 mica - 3	ABS 8	Muscovite	339.5	9.3	3.58	0.09	604
ABS-8-6 mica - 4	ABS 8	Muscovite	291.2	8.6	3.19	0.07	609
ABS-8-6 mica - 5	ABS 8	Muscovite	443.0	10.0	4.55	0.11	619
ABS-8-6 mica - 6	ABS 8	Muscovite	376.7	8.7	3.97	0.09	618
ABS-8-6 mica - 7	ABS 8	Muscovite	161.9	5.4	1.99	0.07	566
ABS-8-6 mica - 8	ABS 8	Muscovite	612.0	22.0	6.00	0.22	617
ABS-8-6 mica - 9	ABS 8	Muscovite	817.0	30.0	7.73	0.30	613
ABS-8-7 mica V - 10	ABS 8	Muscovite	455.0	13.0	4.48	0.14	592
ABS-8-7 mica V - 11	ABS 8	Muscovite	1650.0	99.0	14.92	0.91	614
ABS-8-7 mica V - 12	ABS 8	Muscovite	311.6	6.8	3.36	0.07	608
ABS-8-7 mica V - 13	ABS 8	Muscovite	246.3	4.4	2.81	0.06	609
ABS-8-7 mica V - 14	ABS 8	Muscovite	235.9	4.3	2.76	0.06	621
ABS-8-7 mica V - 15	ABS 8	Muscovite	550.0	20.0	5.25	0.21	589

Continued on next page

Table 4.C Rb-Sr isotopic ratios and ages of investigated samples acquired by LA-ICP-MS/MS

Continued from previous page

Spot number	Samples	Mineral	$^{87}Rb/^{86}Sr$	2SE	$^{87}Sr/^{86}Sr$	2SE	Age(Ma)
ABS-8-7 mica V - 16	ABS 8	Muscovite	661.0	21.0	6.41	0.20	615
ABS-8-7 mica V - 26	ABS 8	Muscovite	544.0	24.0	5.22	0.21	592
ABS-8-7 mica V - 27	ABS 8	Muscovite	363.6	7.6	3.88	0.09	623
ABS-8-7 mica V - 28	ABS 8	Muscovite	682.0	20.0	6.57	0.18	613
ABS-8-7 mica V - 29	ABS 8	Muscovite	958.0	39.0	8.66	0.33	592
ABS-8-7 mica V - 30	ABS 8	Muscovite	908.0	44.0	8.48	0.42	610
ABS-8-7 mica V - 31	ABS 8	Muscovite	1308.0	52.0	11.96	0.50	613
ABS-8-7 mica V - 32	ABS 8	Muscovite	578.0	18.0	5.61	0.16	605
ABS-8-7 mica V - 33	ABS 8	Muscovite	805.0	19.0	7.59	0.19	610
ABS-8-7 mica V - 34	ABS 8	Muscovite	280.7	5.6	3.12	0.06	613
ABS-8-7 mica V - 35	ABS 8	Muscovite	307.9	6.1	3.33	0.08	608
ABS-8-7 mica V - 36	ABS 8	Muscovite	772.0	40.0	7.06	0.34	587
ABS-8-7 mica V - 37	ABS 8	Muscovite	188.9	2.9	2.32	0.04	610
ABS-8-7 mica V - 38	ABS 8	Muscovite	666.0	18.0	6.59	0.19	630
ABS-8-7 mica V - 4	ABS 8	Muscovite	475.0	23.0	4.40	0.22	555
ABS-8-7 mica V - 6	ABS 8	Muscovite	666.0	18.0	6.23	0.21	591
ABS-8-7 mica V - 7	ABS 8	Muscovite	1561.0	85.0	14.14	0.73	613
ABS-8-7 mica V - 8	ABS 8	Muscovite	525.0	16.0	5.23	0.16	614
ABS-8-8 mica - 1	ABS 8	Muscovite	263.0	12.0	2.91	0.14	598
ABS-8-8 mica - 11	ABS 8	Muscovite	484.0	25.0	4.59	0.26	572
ABS-8-8 mica - 12	ABS 8	Muscovite	112.0	2.7	1.58	0.04	558
ABS-8-8 mica - 13	ABS 8	Muscovite	125.3	3.8	1.65	0.05	539
ABS-8-8 mica - 14	ABS 8	Muscovite	215.1	8.2	2.37	0.09	552
ABS-8-8 mica - 15	ABS 8	Muscovite	155.1	4.0	1.99	0.06	591
ABS-8-8 mica - 16	ABS 8	Muscovite	633.0	12.0	5.81	0.15	575
ABS-8-8 mica - 17	ABS 8	Muscovite	594.0	16.0	5.77	0.16	608
ABS-8-8 mica - 18	ABS 8	Muscovite	506.0	15.0	5.09	0.15	618
ABS-8-8 mica - 19	ABS 8	Muscovite	294.0	19.0	3.02	0.14	562
ABS-8-8 mica - 2	ABS 8	Muscovite	225.0	11.0	2.48	0.13	563
ABS-8-8 mica - 20	ABS 8	Muscovite	271.0	12.0	2.94	0.13	588
ABS-8-8 mica - 3	ABS 8	Muscovite	339.0	17.0	3.47	0.21	582
ABS-8-8 mica - 4	ABS 8	Muscovite	164.0	11.0	1.99	0.11	559
ABS-8-8 mica - 5	ABS 8	Muscovite	229.4	7.7	2.67	0.09	611
ABS-8-8 mica - 6	ABS 8	Muscovite	349.0	20.0	3.62	0.19	596
ABS-8-8 mica - 7	ABS 8	Muscovite	265.3	8.7	2.94	0.10	601
ABS-8-8 mica - 8	ABS 8	Muscovite	829.0	36.0	7.35	0.32	572
ABS-8-8 mica - 9	ABS 8	Muscovite	198.8	7.8	2.32	0.09	580
ABS-8-3 feldspar - 1	ABS 8	Orthoclase	303.0	11.0	3.11	0.11	566
ABS-8-3 feldspar - 10	ABS 8	Orthoclase	248.3	7.5	2.67	0.07	565
ABS-8-3 feldspar - 11	ABS 8	Orthoclase	196.4	5.9	2.28	0.07	572
ABS-8-3 feldspar - 2	ABS 8	Orthoclase	354.0	13.0	3.62	0.13	587
ABS-8-3 feldspar - 3	ABS 8	Orthoclase	288.1	9.2	3.09	0.10	590
ABS-8-3 feldspar - 4	ABS 8	Orthoclase	254.6	8.7	2.80	0.09	587
ABS-8-3 feldspar - 5	ABS 8	Orthoclase	294.0	11.0	3.07	0.11	574

Continued on next page

Table 4.C Rb-Sr isotopic ratios and ages of investigated samples acquired by LA-ICP-MS/MS

Continued from previous page

Spot number	Samples	Mineral	$^{87}Rb/^{86}Sr$	2SE	$^{87}Sr/^{86}Sr$	2SE	Age(Ma)
ABS-8-3 feldspar - 6	ABS 8	Orthoclase	245.8	8.5	2.69	0.09	576
ABS-8-3 feldspar - 7	ABS 8	Orthoclase	240.3	7.0	2.72	0.08	598
ABS-8-3 feldspar - 8	ABS 8	Orthoclase	285.7	9.5	3.09	0.08	595
ABS-8-3 feldspar - 9	ABS 8	Orthoclase	198.1	6.8	2.29	0.07	571
ABS-8-4 feldspar - 1	ABS 8	Orthoclase	331.0	12.0	3.41	0.12	583
ABS-8-4 feldspar - 10	ABS 8	Orthoclase	347.0	12.0	3.59	0.12	593
ABS-8-4 feldspar - 2	ABS 8	Orthoclase	322.0	10.0	3.38	0.11	592
ABS-8-4 feldspar - 3	ABS 8	Orthoclase	271.0	9.2	2.90	0.09	578
ABS-8-4 feldspar - 4	ABS 8	Orthoclase	332.0	12.0	3.47	0.14	594
ABS-8-4 feldspar - 5	ABS 8	Orthoclase	382.0	16.0	3.93	0.19	602
ABS-8-4 feldspar - 6	ABS 8	Orthoclase	332.0	12.0	3.44	0.12	587
ABS-8-4 feldspar - 7	ABS 8	Orthoclase	381.0	14.0	3.88	0.14	594
ABS-8-4 feldspar - 8	ABS 8	Orthoclase	244.3	9.9	2.68	0.09	577
ABS-8-4 feldspar - 9	ABS 8	Orthoclase	286.7	8.9	3.08	0.08	591
ABS-8-2 mica - 1	ABS 8	Muscovite	375.0	13.0	3.81	0.16	590
ABS-8-3 mica - 1	ABS 8	Muscovite	207.6	8.6	2.41	0.08	586
ABS-8-3 mica - 2	ABS 8	Muscovite	235.6	8.7	2.53	0.08	553
ABS-8-3 mica - 3	ABS 8	Muscovite	310.0	11.0	3.20	0.11	574
ABS-8-3 mica - 4	ABS 8	Muscovite	245.2	7.4	2.63	0.08	560
ABS-8-3 mica - 5	ABS 8	Muscovite	233.7	6.9	2.61	0.08	581
AB10-K1 - 1.d	ABS 10	Orthoclase	2.7	0.0	0.73	0.01	567
AB10-K1 - 2.d	ABS 10	Orthoclase	2.4	0.0	0.72	0.01	588
AB10-K1 - 3.d	ABS 10	Orthoclase	2.9	0.0	0.73	0.01	551
AB10-K1 - 4.d	ABS 10	Orthoclase	4.8	0.1	0.75	0.01	645
AB10-K1 - 5.d	ABS 10	Orthoclase	2.8	0.0	0.72	0.01	523
AB10-K3 - 1.d	ABS 10	Orthoclase	2.0	0.1	0.72	0.01	742
AB10-K4 - 1.d	ABS 10	Orthoclase	4.5	0.1	0.75	0.01	750
AB10-K4 - 2.d	ABS 10	Orthoclase	5.6	0.1	0.75	0.01	532
AB10-K4 - 4.d	ABS 10	Orthoclase	4.3	0.2	0.73	0.01	464
AB10-K4 - 5.d	ABS 10	Orthoclase	3.5	0.1	0.73	0.01	633
AB10-K5 - 1.d	ABS 10	Orthoclase	0.3	0.0	0.70	0.01	-76
AB10-K5 - 3.d	ABS 10	Orthoclase	0.9	0.0	0.71	0.01	250
AB10-K5 - 5.d	ABS 10	Orthoclase	1.3	0.0	0.71	0.01	201
AB10-K6 - 1.d	ABS 10	Orthoclase	4.7	0.2	0.75	0.01	676
AB10-K6 - 2.d	ABS 10	Orthoclase	0.3	0.0	0.71	0.01	1897
AB10-K6 - 3.d	ABS 10	Orthoclase	2.2	0.1	0.71	0.01	176
AB10-K6 - 4.d	ABS 10	Orthoclase	4.5	0.1	0.74	0.01	590
AB10-K6 - 5.d	ABS 10	Orthoclase	5.1	0.2	0.74	0.01	552
AB10-K7 - 1.d	ABS 10	Orthoclase	2.6	0.1	0.73	0.01	724
AB10-K7 - 2.d	ABS 10	Orthoclase	5.4	0.2	0.74	0.01	485
AB10-K7 - 4.d	ABS 10	Orthoclase	2.2	0.0	0.72	0.01	647
AB10-K7 - 5.d	ABS 10	Orthoclase	0.5	0.0	0.70	0.01	55
AB10-K8 - 1.d	ABS 10	Orthoclase	2.5	0.1	0.72	0.01	512
AB10-K8 - 2.d	ABS 10	Orthoclase	1.1	0.0	0.72	0.01	714

Continued on next page

Table 4.C Rb-Sr isotopic ratios and ages of investigated samples acquired by LA-ICP-MS/MS

Continued from previous page

Spot number	Samples	Mineral	$^{87}Rb/^{86}Sr$	2SE	$^{87}Sr/^{86}Sr$	2SE	Age(Ma)
AB10-K8 - 4.d	ABS 10	Orthoclase	4.3	0.1	0.74	0.01	573
AB10-K8 - 5.d	ABS 10	Orthoclase	6.0	0.2	0.76	0.01	709
ABS13 - 1	ABS 13	Orthoclase	348.4	5.1	3.92	0.04	657
ABS13 - 2	ABS 13	Orthoclase	382.7	5.3	4.27	0.05	664
ABS13 - 3	ABS 13	Orthoclase	373.8	9.0	4.16	0.07	659
ABS13 - 4	ABS 13	Orthoclase	254.2	5.4	3.00	0.04	645
ABS13 - 5	ABS 13	Orthoclase	324.3	7.5	3.68	0.11	654
ABS13 - 6	ABS 13	Orthoclase	337.7	3.7	3.72	0.05	636
ABS13 - 7	ABS 13	Orthoclase	267.5	4.5	3.14	0.04	650
ABS13 - 8	ABS 13	Orthoclase	319.3	4.1	3.55	0.04	634
ABS13 - 9	ABS 13	Orthoclase	313.0	5.4	3.58	0.05	655
ABS13 - 10	ABS 13	Orthoclase	273.5	4.0	3.19	0.05	649
ABS13 - 11	ABS 13	Orthoclase	265.9	3.9	3.20	0.04	669

Published work as journal articles and conference abstracts

JAAS

ROYAL SOCIETY OF CHEMISTRY

PAPER

Cite this: *J. Anal. At. Spectrom.*, 2021, **36**, 322

Assessment of elemental fractionation and matrix effects during *in situ* Rb–Sr dating of phlogopite by LA-ICP-MS/MS: implications for the accuracy and precision of mineral ages†

Ahmad Redaa, *[ab] Juraj Farkaš,[a] Sarah Gilbert,[c] Alan S. Collins,[a] Ben Wade,[c] Stefan Löhr,[d] Thomas Zack[ae] and Dieter Garbe-Schönberg[f]

Laser-ablation inductively-coupled plasma tandem mass-spectrometry (LA-ICP-MS/MS) allows for rapid and interference free analyses of Rb and Sr isotopes, permitting *in situ* Rb–Sr dating of minerals. However, the general lack of matrix matched reference materials remains one of its main obstacles, affecting both precision and accuracy. This study systematically investigates the impact of matrix effects and down-hole fractionation (DHF) on the *in situ* Rb–Sr ages of an igneous phlogopite mineral (MDC) analysed by an ICP-MS/MS using two different LA systems: (i) a RESOlution ArF (193 nm) excimer and (ii) a NWR (213 nm) Nd-YAG laser system. A phlogopite reference material (Mica-Mg), originating from the same location as the MDC, was prepared as a pressed nano-powder pellet (NP) and used in this study as a primary reference material. The results revealed that the accuracy of the Rb–Sr ages is typically within about 3% (for 70% of analysed samples), but occasionally higher ranging between 4 to 8% (*ca.* 30% of cases). We hypothesize that the above bias and uncertainty in the Rb–Sr ages are related to matrix effects between Mica-Mg-NP and MDC, due to their specific ablation characteristics and different physical properties. In addition, the elemental fractionation effects observed in this study for $^{87}Rb/^{86}Sr$ are also dependent on laser wavelength (*i.e.*, 193 nm *vs.* 213 nm). Hence, developing an improved nano-powder reference material, or a mineral or glass with better matrix matching to natural phlogopite minerals would be desirable to further improve the accuracy of *in situ* Rb–Sr dating. Currently, regular monitoring of secondary and matrix-matched reference minerals such as the MDC phlogopite can be used to assess and evaluate the accuracy of *in situ* Rb–Sr dating of phlogopite, yielding ages within accuracy of *ca.* 3% or better.

Received 20th June 2020
Accepted 5th November 2020

DOI: 10.1039/d0ja00299b

rsc.li/jaas

1. Introduction

The Rb–Sr geochronological technique is a well-established dating tool used to constrain the crystallisation and/or cooling ages of igneous minerals and rocks, and the timing of alteration events or processes such as metamorphism, metasomatism and diagenesis.[1–3] Rubidium has two naturally occurring isotopes, ^{85}Rb and ^{87}Rb. The latter undergoes beta decay to form radiogenic ^{87}Sr with a decay constant of $1.3972 \pm 0.0045 \times 10^{-11}$ per year.[4] To establish the age of geological materials *via* the Rb–Sr dating method, the measured $^{87}Rb/^{86}Sr$ and $^{87}Sr/^{86}Sr$ ratios (*i.e.*, from co-genetic minerals or whole rock samples) are cross-plotted to define an isochron; the slope of which is a function of age. Historically, $^{87}Rb/^{86}Sr$ and $^{87}Sr/^{86}Sr$ isotopic ratios were measured by thermal ionisation mass spectrometry (TIMS) or more recently *via* multi collector inductively coupled plasma mass spectrometry (MC-ICP-MS).[5–7] These approaches, however, require isotopic spiking and time-consuming chemical separation of Rb and Sr from the sample matrix for precise ratio determination *via* eluent chromatography.[8] Uncertainties associated with the gravimetric calibration of isotope spikes remain the dominant source of error on the accuracy of ages calculated *via* TIMS and MC-ICP-MS, with typical errors on Rb–Sr ages determined by the above techniques below 1%, and for more recent studies as low as 0.1–0.2%.[9]

The chemical separation of Rb from Sr for conventional TIMS and MC-ICP-MS approaches is required to resolve isobaric interference between ^{87}Rb and ^{87}Sr. Importantly, the recent development of tandem ICP mass spectrometers (ICP-MS/MS),

[a]*Department of Earth Sciences, University of Adelaide, Adelaide, Australia. E-mail: areda@kau.edu.sa*
[b]*Faculty of Earth Sciences, King Abdulaziz University, Jeddah, Saudi Arabia*
[c]*Adelaide Microscopy, University of Adelaide, Australia*
[d]*Department of Earth and Planetary Sciences, Macquarie University, Sydney, Australia*
[e]*Department of Earth Sciences, University of Gothenburg, Gothenburg, Sweden*
[f]*Institute of Geosciences, Kiel University, Kiel, Germany*

† Electronic supplementary information (ESI) available. See DOI: 10.1039/d0ja00299b

equipped with a reaction/collision cell located between two quadrupoles (Q1 and Q2) and coupled with a laser-ablation (LA) system, allows for *in situ* Rb–Sr dating of geological materials at the micro-scale level.[10–12] Using such a setup, the first quadrupole (Q1) can be set independently to allow only isotopes with a mass-to-charge ratio of 87 ($^{87}Rb^+$ and $^{87}Sr^+$ in this case) to enter the reaction cell of the ICP-MS/MS system. The cell can be filled with reaction gases such as O_2 or N_2O gas,[10–16] as both react with $^{87}Sr^+$ ions to form $^{87}Sr^{16}O^+$ with typical efficiencies and yields around 85–99%.[11,12,17] In contrast, $^{87}Rb^+$ is unreactive with the above reaction gases, and, thus, such distinct behaviour of Rb and Sr ions with O_2 and N_2O gases allow for interference-free measurements of ^{87}Sr abundances as a 'mass-shifted' [$^{87}Sr^{16}O^+$] reaction product with a mass of 103 amu.

Hence, coupling the ICP-MS/MS with a laser ablation (LA) system and using a suitable reaction gas allows for targeted analysis of samples at the 50–100 μm scale, making *in situ* Rb–Sr dating of minerals possible.[11,12,17–21] An additional advantage of LA-ICP-MS/MS over conventional TIMS or MC-ICP-MS based Rb–Sr dating techniques is that *in situ* dating can be done rapidly and with minimal sample preparation, as mounted minerals and/or polished rock chips can be used. However, the accuracy and precision of this technique can be affected by several factors including the laser wavelength and frequency, and the external reference materials used for calibration (matrix effect).[17] Elemental fractionation effects, and the current lack of matrix-matched reference materials, coupled with using a single-collector design of ICP-MS/MS, remain the main limitations in terms of accuracy and precision for *in situ* dating purposes.[22–29]

The mechanism and impact of elemental fractionation during LA-ICP-MS analysis have been studied in detail for other element/isotope systems,[22–29] and these effects are related to phenomena such as (i) the laser–sample interaction, (ii) aerosol formation and transportation, and (iii) ionisation of aerosols in the ICP. Also, elemental fractionation effects are most pronounced for element pairs where one element volatilises more readily than the other (more refractory) element under certain conditions,[23,30] which is a common feature for pairs such as U/Pb, Rb/Sr and K/Ca.[11,29] These effects can be further magnified if a sample and reference material have different physical and chemical properties that translate into different ablation rates and elemental fractionation patterns.[26,27] Nevertheless, the influence of elemental fractionation on the accuracy and precision of the LA-ICP-MS/MS analysis can be controlled by (i) filtering the produced aerosol, (ii) calibration against matrix matched reference materials, and (iii) strictly controlled and monitored analytical conditions.[23,25–27,29–33]

To date, only a limited number of well-characterised reference materials are available for *in situ* Rb–Sr dating and $^{87}Sr/^{86}Sr$ isotopic analysis by LA-ICP-MS/MS. These include phlogopite Mica-Mg (Centre de Recherches Pétrographiques et Géochimiques (CRPG)),[34,35] and synthetic glasses NIST SRM 610,[12,36] which have been used in several previous studies.[12,17,19–21] The original CRPG Mica-Mg has been processed into nano-particulate pressed powder pellets[37] (Mica-Mg-NP) and was validated by measuring its $^{87}Sr/^{86}Sr$ ratios *via* LA-ICP-MS/MS and calibrating it against NIST 610. The $^{87}Rb/^{86}Sr$ ratio was then calculated based on the mean of reported crystallisation ages (*i.e.* using Rb–Sr phlogopite and U–Pb zircon) in the Bekily area (from which this phlogopite sample/standard originated), which is constrained at 519.4 ± 6.5 Ma with an initial $^{87}Sr/^{86}Sr$ ratio of 0.72607 ± 0.0007 (see Hogmalm *et al.*, (2017) for details).[12]

In this study, we investigate the fractionation of Rb from Sr in natural and nano-powder phlogopite (MDC and Mica-Mg-NP) and synthetic glass NIST 610 during LA-ICP-MS/MS analysis and its overall effect on the accuracy and precision of *in situ* Rb–Sr isochron ages. Specifically, this study compares ablation properties, down-hole fractionation (DHF) patterns and matrix effects between MDC, Mica-Mg-NP phlogopites (both sourced from the Ampandrandava mine, Bekily area, Madagascar) and the synthetic glass NIST 610 and their effects on the precision and accuracy of acquired *in situ* Rb–Sr ages of phlogopite. In addition, two different LA systems were used in this study, specifically: (i) a RESOlution ArF (193 nm) excimer laser and (ii) a NWR (213 nm) Nd-YAG laser. A better understanding of the above processes and associated effects is critical to further improve the precision and accuracy of this novel geochronological tool, and results of this study provide new insights into these complex phenomena and how to monitor and tackle these analytical challenges for *in situ* Rb–Sr dating applications.

2. Materials and methods

2.1. Investigated materials

This study investigates and compares DHF, ablation properties and matrix effects between three types of materials, including: (i) a natural igneous phlogopite mineral (MDC), (ii) the Mica-Mg-NP phlogopite reference material (supplied by J. Hogmalm and T. Zack),[12] and (iii) the synthetic glass NIST 610. The natural MDC

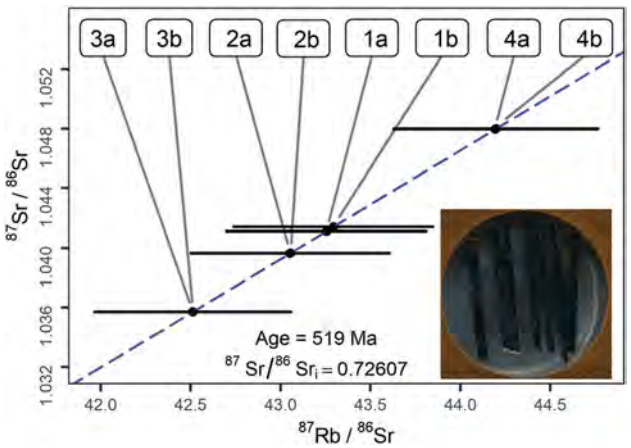

Fig. 1 A theoretical Rb–Sr isochron of MDC based on $^{87}Sr/^{86}Sr$ data acquired by TIMS and the calculated $^{87}Rb/^{86}Sr$ ratios (see eqn (2)), corresponding to an age of 519 Ma. The results show the spread of the data along the theoretical isochron, reflecting the natural variation in $^{87}Rb/^{86}Sr$ and $^{87}Sr/^{86}Sr$ ratios of the MDC sample, most likely linked to minor inhomogeneity in elemental Rb/Sr ratios within the studied phlogopite crystal flakes.

Table 1 The expected values of $^{87}Rb/^{86}Sr$ and $^{87}Sr/^{86}Sr$ ratios for investigated materials.[12,36,38] Note that the reported uncertainties are represented in 2σ (*i.e.*, 95% confidence intervals)

Material	$^{87}Rb/^{86}Sr$	$^{87}Sr/^{86}Sr$	Age (Ma)
Mica-Mg-NP	154.6 ± 1.93	1.8525 ± 0.0024	519.4 ± 6.5 Ma
NIST 610 (glass)	2.3300	0.709699 ± 0.000018	N/A
MDC (phlogopite mineral)	N/A	N/A	519.4 ± 6.5 Ma

phlogopite, with flakes large enough to be mounted and analysed by the LA-ICP-MS/MS, was sourced from the same area (Bekily, Madagascar) as the Mica-Mg reference material. In our experiment, four larger flakes of MDC were mounted into resin, with cleavage planes perpendicular to the polished sample-mount surface (see the image inset in Fig. 1), and these flakes were treated in this study as unknown samples. For *in situ* Rb–Sr dating, both Mica-Mg-NP and NIST 610 were used as the primary reference materials and MDC was used as secondary reference material. Based on published data, the expected $^{87}Rb/^{86}Sr$ and $^{87}Sr/^{86}Sr$ ratios and corresponding Rb–Sr ages of the above investigated reference materials are summarised in Table 1.

2.2. TIMS analysis – Sr isotopic composition of MDC

High-precision measurements of $^{87}Sr/^{86}Sr$ ratios of the MDC phlogopite were obtained *via* thermal ionisation mass spectrometry (TIMS) using a Phoenix IsotopX TIMS instrument and clean-laboratory procedures established at the Metal Isotope Group (MIG) facilities in the Department of Earth Sciences at the University of Adelaide (for details see Shao *et al.*, 2018).[39] In brief, four aliquots of MDC phlogopite flakes were digested in a mixture of HF-HNO_3 acid, and then evaporated and re-dissolved in 4 mL 8 M nitric acid. Following this step, two 1 mL aliquots from each sample were passed through cation-exchange columns and subsequently analysed for $^{87}Sr/^{86}Sr$ ratios. Strontium extraction and purification was carried out using Bio-Spin columns filled with 200 μL of Eichrom Sr resin. Measured $^{87}Sr/^{86}Sr$ ratios were internally normalised to a $^{86}Sr/^{88}Sr$ ratio of 0.1194 using an exponential mass fractionation correction.[40] The NIST SRM 987 reference material was used as the primary standard to monitor and assess data quality and reproducibility. The above analytical procedure yielded a typical $^{87}Sr/^{86}Sr$ external reproducibility of ±0.000015 (2σ), and a total procedural Sr blank was on the order of *ca.* 100 pg. The latter is negligible as it represents <0.1% of the total amount of Sr processed through the columns for each sample, as a typical sample size was about 500 ng of Sr. Only the Sr isotope ratios (*i.e.*, $^{87}Sr/^{86}Sr$) of MDC flakes were analysed in this study by TIMS, and the other desirable elemental ratio ($^{87}Rb/^{86}Sr$) was not measured *via* TIMS due to the lack of gravimetrically calibrated Sr and Rb single spikes in the MIG laboratories.

2.3. LA-ICP-MS/MS instrumentation and analytical set-up

All *in situ* Rb–Sr analyses were conducted at Adelaide Microscopy, University of Adelaide, Australia. An Agilent 8900 ICP-MS/MS instrument, coupled with a laser ablation (LA) system, was used to determine simultaneously both $^{87}Rb/^{86}Sr$ and $^{87}Sr/^{86}Sr$ ratios of the studied samples and reference materials. Two different laser systems were used, specifically (i) a RESOlution ArF excimer (193 nm) and (ii) a NWR213 Nd-YAG (213 nm) system. Each laser was coupled to the ICP-MS/MS with the same length of interface tubing, and included a Squid mixing device (Laurin Technic). The instrumental setup and tuning parameters of the ICP-MS/MS are summarised in Table 2. All samples were ablated in a He atmosphere and mixed with Ar as the carrier gas to the ICP, with 3.5 mL min^{-1} of N_2 added before the

Table 2 Instrumental parameters for two laser ablation systems (193 nm and 213 nm) and the ICP-MS/MS (Agilent 8900), used in this study

	Units	ArF 193 nm	NWR213 (213 nm)
Laser parameters			
He carrier gas	mL min^{-1}	350	700
Ar carrier gas	mL min^{-1}	1050	880
N_2 addition	mL min^{-1}	3.5	3.5
Spot size	μm	74	75
Repetition rate	Hz	5	5
Fluence	J cm^{-2}	3.5	10
Sample chamber		S155 large format	TV2
ICP-MS/MS			
Plasma parameters			
RF Power	W	1350	1350
Sample depth	mm	4	4
Lens parameters			
Extract 1	V	−2.0	−1.0
Extract 2	V	−150	−140
Omega bias	V	75	50
Omega lens	V	7.0	7.0
Q1 entrance	V	2.0	1.0
Q1 exit	V	−1.0	−1.0
Cell focus	V	−2.0	4.0
Cell entrance	V	−100	−80
Cell exit	V	−150	−150
Deflect	V	−10	−10
Plate bias	V	−80	−90
Q1 parameters			
Q1 bias	V	−2.0	−1.0
Q1 prefilter bias	V	−9.0	−9.0
Q1 postfilter bias	V	−10	−10
Cell parameters			
N_2O flow rate	mL min^{-1}	0.37	0.37
OctP bias	V	−23	−23
Axial acceleration	V	2.0	2.0
OctP RF	V	180	180
Energy discrimination	V	−10	−10
Q2 parameters			
Q2 bias	V	−33	−33

ICP torch to enhance the signal sensitivity,[41] and using N_2O reaction gas to separate ^{87}Sr from ^{87}Rb.

2.4. Optimising analytical conditions for LA-ICP MS/MS

The carrier gas flow rates (He, Ar & N_2) and plasma conditions were tuned daily in normal 'no-gas' mode (*i.e.* no gas in the reaction cell), using the NIST 612 glass, and parameters optimized (i) to minimise oxide production (<0.2% ThO/Th), (ii) ensure efficient ionisation of the aerosol in the plasma (U/Th ratio < 1.05),[32] and (iii) high element sensitivity. The reaction gas (N_2O) flow rate was optimised at 0.37 mL min^{-1} to achieve the highest sensitivity for both on-mass Rb (85 and 87 *m*/*z*), as well as mass shifted Sr reaction product ions (*e.g.* $[^{88}Sr^{16}O^+]$ at 104 *m*/*z*). A preliminary test showed almost complete conversion of ^{88}Sr ions (close to ~99% yield) with N_2O to form $[^{88}Sr^{16}O^+]$, with no detectable reaction of ^{85}Rb occurring (<0.00001% reaction). In addition, the efficiency of the reaction did not change with different matrices (*i.e.* glass reference material *vs.* nano-powder *vs.* natural phlogopite mineral) and thus our analytical setup was able to effectively separate ^{87}Sr (*via* $^{87}Sr^{16}O^+$) from ^{87}Rb for the purposes of *in situ* Rb–Sr dating.

2.5. Sampling strategy and data processing

In this study, we analysed Mica-Mg-NP as a primary reference material/standard to correct for drift and instrument mass-bias, and the above standard was measured after every 20 unknown samples. Data measured with the 193 nm LA system, were collected over eight individual analytical sessions, which were spread over a 10 month period to evaluate the long-term stability and reproducibility of *in situ* Rb–Sr ages. In addition to 'spot' analyses (see parameters in Table 2), line scans or 'raster' analyses were also performed using the following LA settings: 74 μm beam diameter, fluence of 3.5 J cm^{-2}, repetition rate of 10 Hz and scan speed of 7.4 μm s^{-1}. Analyses conducted on the 213 nm LA system were carried out over two separate analytical sessions using a spot size of 75 μm (laser parameters are available in Table 2).

All data collected in this study *via* LA-ICP MS/MS were processed using the Iolite 3 software.[42] A customised data reduction algorithm was programmed for the purpose of *in situ* Rb–Sr dating, which includes the following steps: (1) calculation of the average background-subtracted ^{85}Rb, ^{86}Sr and ^{87}Sr count per second (cps) from signals collected on masses 85, 102, and 103 amu, respectively; (2) a conversion of ^{85}Rb cps signal to ^{87}Rb cps based on the natural abundance of Rb isotopes (where $^{87}Rb = {}^{85}Rb \times 0.38562$);[9,43] (3) calculation of the raw and interference-free $^{87}Sr/^{86}Sr$ and $^{87}Rb/^{86}Sr$ ratios; and (4) drift corrected normalisation of the ratios using correction factors obtained by dividing the measured $^{87}Sr/^{86}Sr$ and $^{87}Rb/^{86}Sr$ ratios of reference materials, by their expected ratios (see data in Table 1). Since Rb was measured in analog mode during all sessions for all samples (MDC, NIST 610 and Mica-Mg-NP), no additional correction for the Pulse–Analog (P/A) factor was required. Finally, the plotting of processed and normalised data ($^{87}Sr/^{86}Sr$ and $^{87}Rb/^{86}Sr$ ratios) in conventional isochron plots, and the calculation of corresponding Rb–Sr ages and the Sr isotope initial ratios, was performed using IsoplotR.[44]

2.6. Three-dimensional (3D) imaging and analysis of laser ablation craters

The shape and morphology of laser craters can provide valuable information about laser–sample interactions and specific ablation rates of the studied materials. A laser scanning confocal microscope (LSCM) was used to characterise the morphology of the produced LA craters in the investigated samples. The laser craters were imaged using an Olympus LEXT OLS5000-SAF 3D LSCM at Adelaide Microscopy, University of Adelaide. The images were acquired with a x50/0.60NA lens, and the measurements of crater depths and geometry were performed using the Olympus Data Analysis Application software.

2.7. BSE imaging

High-resolution backscatter electron (BSE) images covering the entire mineral mount or pressed powder pellet were collected to characterise (1) morphology of laser craters, (2) distribution of ejecta material, (3) impact of laser damage on subsequent analyses, and also (4) to investigate possible grain-size heterogeneity in the Mica-Mg-NP. Samples were carbon coated after completion of the laser experiments and imaged using a FEI Teneo LoVac Field Emission Scanning Electron Microscope (FE-SEM) at Macquarie University (13 mm working distance, 15 kV accelerating voltage). BSE image tile sets covering the entire sample (~450 nm pixel resolution) and smaller higher resolution regions of interest (~45 nm pixel resolution) were collected and stitched together using FEI Maps Mineralogy software.

3. Results

3.1. TIMS analysis of MDC

To indirectly constrain the expected $^{87}Rb/^{86}Sr$ ratios of the MDC phlogopite (assuming its crystallisation age of 519.4 ± 6.5 Ma),[12] subsamples of the mounted MDC flakes were analysed *via* TIMS for high-precision $^{87}Sr/^{86}Sr$ ratios.

The measured $^{87}Sr/^{86}Sr$ ratio can be substituted into the conventional Rb–Sr geochronology equation below to calculate the expected $^{87}Rb/^{86}Sr$ ratio:[4]

$$\left(\frac{^{87}Sr}{^{86}Sr}\right)_p = \left(\frac{^{87}Sr}{^{86}Sr}\right)_i + \left(\frac{^{87}Rb}{^{86}Sr}\right)_p \times \left(e^{\lambda t} - 1\right) \quad (1)$$

where $(^{87}Sr/^{86}Sr)_p$ and $(^{87}Rb/^{86}Sr)_p$ are the 'present-day' measured isotope compositions, $(^{87}Sr/^{86}Sr)_i$ is the 'initial' $^{87}Sr/^{86}Sr$ ratio in a sample which has been estimated for Mica-Mg-NP phlogopite by previous studies at 0.72607 ± 0.0007,[12] λ is the ^{87}Rb decay constant of 1.3972 ± 0.0045 × 10^{-11} per year,[4] and t is the crystallisation age (in years) of MDC and/or Mica-Mg-NP constrained at 519.4 ± 6.5 Ma.[12] The above equation (eqn (1)) can then re-arranged to solve for the expected $^{87}Rb/^{86}Sr$ ratio (see below):

$$\left(\frac{^{87}Rb}{^{86}Sr}\right)_p = \left(\frac{\left(\frac{^{87}Sr}{^{86}Sr}\right)_p - \left(\frac{^{87}Sr}{^{86}Sr}\right)_i}{\left(e^{\lambda t} - 1\right)}\right) \quad (2)$$

Using the TIMS measured $(^{87}Sr/^{86}Sr)_p$ ratios (see data in Table 3), the calculated $^{87}Rb/^{86}Sr$ ratios for MDC sample yield a range from 42.51 to 44.20 (Table 3). Note that the stated uncertainties for these $^{87}Rb/^{86}Sr$ ratios were calculated using the following equation for a combined uncertainty:

$$\left(\frac{^{87}Rb}{^{86}Sr}\right)_{error\%} = \left(\frac{\sqrt{(a\%)^2 + (b\%)^2 + (c\%)^2 + (d\%)^2} \times \left(\frac{^{87}Rb}{^{86}Sr}\right)}{100}\right) \quad (3)$$

where a is the analytical uncertainty (2σ) of $(^{87}Sr/^{86}Sr)_p$ acquired by TIMS, b is the uncertainty of $(^{87}Sr/^{86}Sr)_I$ as stated in Hogmalm *et al.* (2017),[12] c is the uncertainty in the Rb–Sr decay constant,[4] and d is the uncertainty in the expected age of MDC 519.4 ± 6.5 Ma.[12]

The TIMS data show variations in measured present-day $^{87}Sr/^{86}Sr$ ratios, and thus a corresponding spread is also observed for the calculated $^{87}Rb/^{86}Sr$ ratios of MDC (see eqn (2); Fig. 1). This spread of data along the theoretical Rb–Sr isochron, defined by a crystallisation age of 519.4 Ma and an initial $^{87}Sr/^{86}Sr$ of 0.72607 (see also Table 1), is thus due to the natural variation of Rb and Sr concentrations in the MDC flakes.

Table 3 Measured $^{87}Sr/^{86}Sr$ ratios of MDC flakes analysed by TIMS and calculated (theoretical) $^{87}Rb/^{86}Sr$ ratios based on an assumed age of 519.4 Ma for MDC, using an initial $^{87}Sr/^{86}Sr$ ratio of 0.72607. The reported errors represent 2σ uncertainties (*i.e.*, 95% confidence intervals)

Sample ID	$^{87}Sr/^{86}Sr$ (TIMS)	2σ	$^{87}Rb/^{86}Sr$ (theoretical)	2σ
MDC-1a	1.041116	0.000003	43.26	0.56
MDC-1b	1.041399	0.000004	43.29	0.56
MDC-2a	1.039637	0.000004	43.05	0.56
MDC-2b	1.039656	0.000004	43.05	0.56
MDC-3a	1.035708	0.000004	42.51	0.55
MDC-3b	1.035696	0.000004	42.51	0.55
MDC-4a	1.047962	0.000014	44.20	0.57
MDC-4b	1.047992	0.000004	44.20	0.57
Average	1.041145	0.009477	43.26	1.30

3.2. Reproducibility of $^{87}Rb/^{86}Sr$ and $^{87}Sr/^{86}Sr$ ratios in the igneous phlogopite

3.2.1. LA spot analyses. In order to examine the reproducibility and robustness of *in situ* Rb–Sr isochron ages, the Mica-Mg-NP, MDC and NIST 610 data were compared from 10 individual sessions (eight analysed *via* 193 nm laser and two *via* 213 nm laser), each consisting of approx. 20–40 individual LA spot analyses.

The raw $^{87}Rb/^{86}Sr$ and $^{87}Sr/^{86}Sr$ ratios for Mica-Mg-NP obtained by the 193 nm and 213 nm laser systems are presented in Fig. 2, and Table 4 in the Appendix. The raw $^{87}Sr/^{86}Sr$ ratios were consistent within their respective analytical errors (*i.e.*, internal reproducibility), and the measured Sr isotope data did not show significant variations from session to session, and/or drift during an individual analytical session (Fig. 2A). In contrast, the raw $^{87}Rb/^{86}Sr$ ratio varied significantly during a single session, and also from session to session (see Fig. 2B).

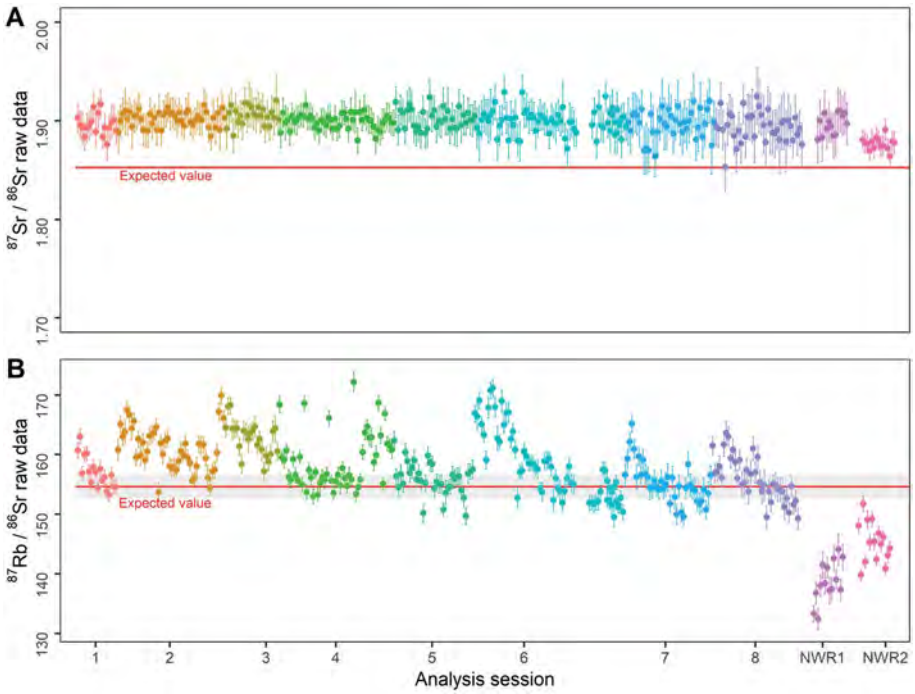

Fig. 2 Long-term and within-session reproducibility of raw (A) $^{87}Sr/^{86}Sr$ and (B) $^{87}Rb/^{86}Sr$ ratios of Mica-Mg-NP over multiple analytical sessions using two laser systems. Data labelled 1 to 8 were obtained with the 193 nm laser whereas NWR refers to 213 nm laser and the numbers refer to analytical session. Note that there is more variation in the $^{87}Rb/^{86}Sr$ ratios within the analytical session compared to the $^{87}Sr/^{86}Sr$ ratios.

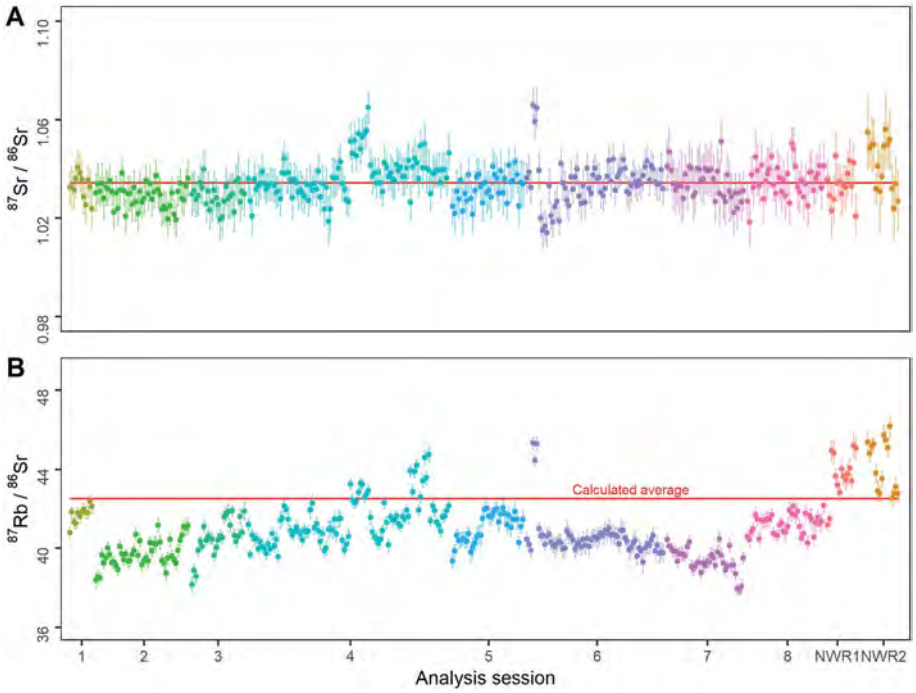

Fig. 3 (A) $^{87}Sr/^{86}Sr$ and (B) $^{87}Rb/^{86}Sr$ isotopic ratios of MDC analysed over ten sessions, normalised to Mica-Mg-NP. The first eight sessions of data were collected using the 193 nm laser whereas NWR1 and 2 refers to data obtained with the 213 nm laser. The red line in (A) shows the $^{87}Sr/^{86}Sr$ average of all acquired data, and in (B) shows the expected $^{87}Rb/^{86}Sr$ calculated from the $^{87}Sr/^{86}Sr$ average in A, with most of the measured $^{87}Rb/^{86}Sr$ data lower than that this expected value, which corresponds to older calculated ages.

The $^{87}Rb/^{86}Sr$ and $^{87}Sr/^{86}Sr$ ratios of MDC, normalised to Mica-Mg-NP, also vary from session to session (see Fig. 3, and data in Table 5 in the Appendix). The $^{87}Sr/^{86}Sr$ ratios of MDC are more robust and less variable from session to session (or within the session) compared to the $^{87}Rb/^{86}Sr$ ratios (see Fig. 3). However, some of the $^{87}Sr/^{86}Sr$ data from MDC yielded more radiogenic values (*e.g.* data collected during sessions 4 and 6, Fig. 3A). Overall, the normalised $^{87}Rb/^{86}Sr$ ratios of MDC displayed more variation than the $^{87}Sr/^{86}Sr$ ratios, often exhibiting a detectable increasing trend in $^{87}Rb/^{86}Sr$ over the course of an individual analytical session (see Fig. 3B). Accordingly, when plotted as an isochron, these variations translate to an excessive spread in $^{87}Rb/^{86}Sr$ ratios along the *x*-axis (Fig. 4A).

The calculated ages for MDC analysed *via* 193 nm laser during the eight sessions tend to give systematically older Rb–Sr ages than the expected age of 519.4 ± 6.5 Ma. About 70% of the calculated ages are falling within 3.2% accuracy (Fig. 4A), whereas the remaining data (*ca.* 30% of runs from the sessions 2, 6 and 7) showed less accurate results, with ages that are 4 to 7.7% older than the expected age (see Fig. 4B). However, the

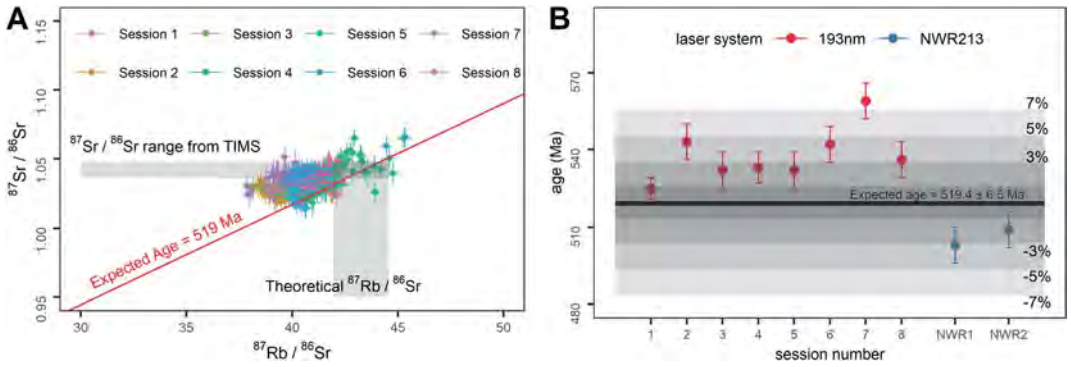

Fig. 4 (A) A Rb–Sr isochron diagram for MDC obtained over eight sessions using the 193 nm laser, producing generally higher variation of $^{87}Rb/^{86}Sr$ ratios along the *x*-axis, compared to $^{87}Sr/^{86}Sr$ data. The grey rectangles represent the range of $^{87}Sr/^{86}Sr$ acquired by TIMS and the calculated $^{87}Rb/^{86}Sr$ ratios of MDC (see Section 3.1.). The red line represents the isochron line of the expected age for MDC of 519 Ma. For more detailed data from each analytical session, see Fig. 12 in the Appendix. (B) Variation in the calculated average age of MDC from session to session obtained using the 193 nm and 213 nm laser systems. The black rectangle represents the expected age of MDC of 519.4 ± 6.5 Ma,[12] and the lighter grey areas show the error range in percentage.

internal precision of all calculated Rb–Sr ages for MDC is less than 1.4% (Fig. 12 in the Appendix).

Two analytical sessions were also conducted with the 213 nm laser to assess the laser wavelength-dependent effects on Rb/Sr elemental fractionation during LA-ICP-MS/MS. The analyses yielded ages of 503 ± 7 Ma and 509 ± 7 Ma (Fig. 4B), which are thus 1.9 and 3.1% younger than the expected age of 519.4 ± 6.5 Ma,[12] respectively.

MDC was also normalised using NIST 610 glass as a reference material for data collected with the 193 nm and 213 nm laser systems to further investigate the effects of non-matrix matched reference materials on *in situ* Rb–Sr dating. The results are listed in Table 6 in the Appendix. The data acquired *via* the 193 nm and 213 nm laser resulted in a calculated age of 455 ± 6 Ma and 456 ± 6 Ma for MDC, respectively, which are thus significantly (up to 12%) younger than the expected age of 519.4 ± 6.5 Ma (Fig. 5), and hence considerably less accurate than when normalised to the chemically-matched phlogopite Mica-Mg-NP standard (see data in Fig. 4B). Such inconsistency in ages is due to a larger offset in $^{87}Rb/^{86}Sr$ ratios (measured *vs.* expected) rather than uncertainty in $^{87}Sr/^{86}Sr$, as the latter is less effected by matrix match effect.

3.2.2. Line rasters analysis. A line raster analytical approach was also adopted to investigate its impacts on elemental fractionation and measured $^{87}Rb/^{86}Sr$ ratios. Ten raster lines were ablated in each material (using the 193 nm laser system), including Mica-Mg-NP, MDC and NIST610, and the data were normalised to Mica-Mg-NP (see Fig. 6, and data in Appendix Table 7) and also to NIST 610 (see Table 8 in the Appendix). The time-resolved $^{87}Rb/^{86}Sr$ ratios of MDC and NIST 610 were relatively stable. However, Mica-Mg-NP signals were generally noisier with larger variability in $^{87}Rb/^{86}Sr$ ratios (Fig. 6).

The Rb–Sr age of MDC phlogopite acquired *via* the line raster approach yielded an age of 601 ± 8 Ma when normalised to Mica-Mg-NP and an age of 545 ± 8 Ma when normalised to NIST 610 (Fig. 7), which are about 15% and 5% older than the expected age of this phlogopite (519.4 ± 6.5 Ma),[12] respectively. This inconsistency in the Rb–Sr age is primary controlled by the offset between the expected and measured $^{87}Rb/^{86}Sr$ ratios, depending on which reference material was used for the normalisation. The $^{87}Rb/^{86}Sr$ ratios of MDC were about 13% lower relative to the expected ratio when data were normalised to Mica-Mg nano-powder (Table 7 in the Appendix), and they were 6% lower when data were normalised to NIST 610 (Table 8 in the Appendix). In contrast the $^{87}Sr/^{86}Sr$ ratios varied by less than 0.7%, which is within the internal error for this data set.

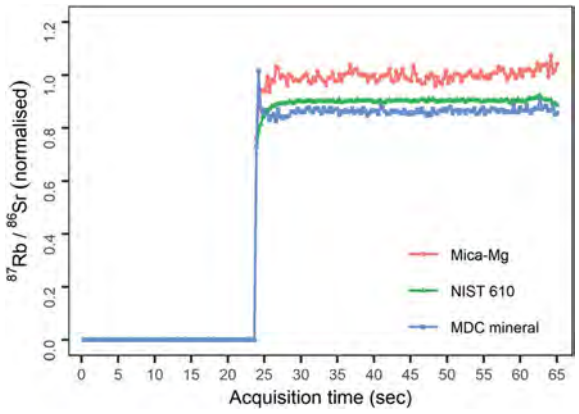

Fig. 6 Average of $^{87}Rb/^{86}Sr$ ratios of Mica-Mg-NP, MDC and NIST610 (normalised to Mica-Mg-NP and its expected values (Table 1), acquired from 10 line rasters using the 193 nm laser with a 74 μm beam diameter and scan speed of 7.4 μm s^{-1}.

3.3. Reproducibility of NIST 610 using the 193 nm laser system

The NIST 610 glass reference material was analysed over eight sessions as discussed previously. The average ratios are displayed in Fig. 8, with source data listed in Table 9 in the

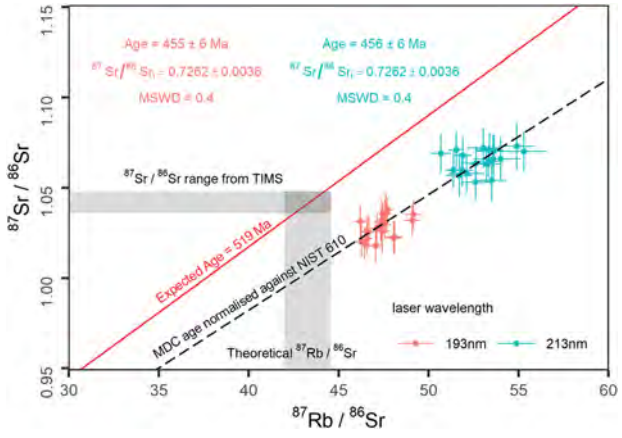

Fig. 5 A Rb–Sr isochron age for MDC, where $^{87}Rb/^{86}Sr$ and $^{87}Sr/^{86}Sr$ ratios were normalised to a non-matrix matched NIST 610 glass. The red and blue points represent the 193 nm and 213 nm laser wavelengths respectively, and the red line illustrates the expected isochron and/or age for MDC phlogopite (519 Ma),[12] and the gray rectangles illustrate the range of $^{87}Rb/^{86}Sr$ and $^{87}Sr/^{86}Sr$ ratios constrained *via* TIMS data (see Section 3.1.).

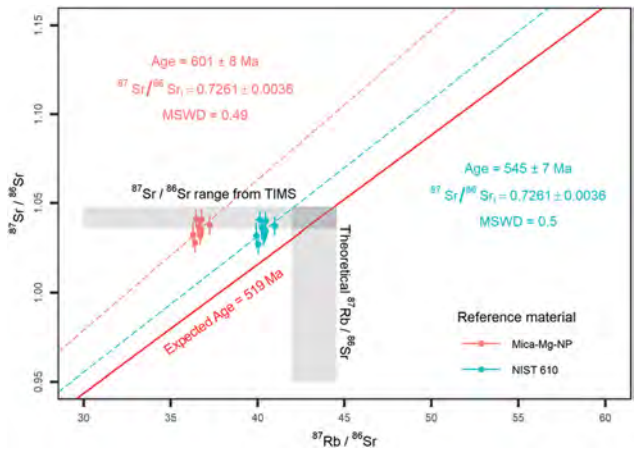

Fig. 7 Rb–Sr age of MDC acquired from line rasters using the 193 nm laser. The red line illustrates the expected isochron age of MDC (519.4 ± 6.5 Ma)[12] and the gray rectangles shows the range of $^{87}Rb/^{86}Sr$ and $^{87}Sr/^{86}Sr$ ratios constrained *via* TIMS data (see also Section 3.1.). The colour of points shows the reference material that was used for normalisation.

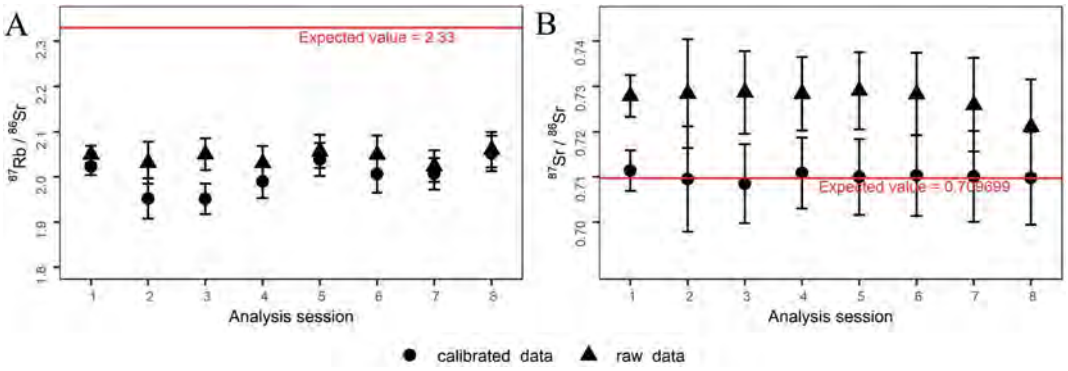

Fig. 8 The average raw and calibrated ratios of NIST 610 analysed with the 193 nm laser over eight different sessions. (A) Diagram shows significant offset in $^{87}Rb/^{86}Sr$ from the expected value, and the calibrated $^{87}Rb/^{86}Sr$ values showed more variation from session to session compared to the raw ratios. (B) $^{87}Sr/^{86}Sr$ of NIST 610 overlap the expected value of 0.709699 ± 0.000018 after the normalisation or calibration against Mica-Mg-NP.

Appendix. The $^{87}Rb/^{86}Sr$ and $^{87}Sr/^{86}Sr$ raw ratios showed limited variation within the sessions (after correction of instrumental drift) with an internal precision ranging between 0.33% and 0.69% (1σ), and between 0.09% and 0.18% (1σ), respectively. The data were normalised to Mica-Mg-NP, but the raw $^{87}Rb/^{86}Sr$ ratios were more consistent from session to session (1σ = 0.66%) compared to the normalised ratios (1σ = 1.84%). The normalised $^{87}Rb/^{86}Sr$ ratios show a significant offset being 13% to 18% lower than the expected ratio of 2.33 (see Hogmalm *et al.*, 2017).[12] In contrast, the variation of raw $^{87}Sr/^{86}Sr$ ratios for NIST 610 between the sessions was 0.36% (1σ) but improved to 0.12% after normalisation, with normalised values falling within the expected range 0.709699 ± 0.000018 (see Woodhead and Hergt (2001)[36] and (Fig. 8)).

3.4. Down hole fractionation effects on $^{87}Rb/^{86}Sr$ ratios

3.4.1. 193 nm laser. The $^{87}Rb/^{86}Sr$ ratios of Mica-Mg-NP, MDC, and NIST 610 were collected using the 193 nm laser system over a period of *ca.* 40 seconds (sec) for 30 individual LA spot analyses in each material, and data were then averaged and normalised to Mica-Mg-NP (Fig. 9A). The results show that the DHF profiles for $^{87}Rb/^{86}Sr$ vary with time during the ablation, and these profiles are also sample-specific.

Both MDC and NIST 610 display a progressively increasing trend in $^{87}Rb/^{86}Sr$ ratios, with MDC being steeper. In contrast, the Mica-Mg-NP has a more complex DHF pattern, where $^{87}Rb/^{86}Sr$ ratios gradually rise over the first *ca.* 10 s but then systematically decrease during an interval from *ca.* 15 to 35 s, and eventually flatten out over the last *ca.* 5 s (Fig. 9A). In contrast, no detectable DHF effects were observed for the radiogenic $^{87}Sr/^{86}Sr$ ratios in any of the above materials.

3.4.2. 213 nm laser. The DHF profiles for $^{87}Rb/^{86}Sr$ were also investigated using the 213 nm laser with a spot size of 75 μm (Fig. 9B). These DHF profiles for Mica-Mg-NP, MDC and NIST 610 were different compared to those measured with the 193 nm laser (compare Fig. 9A and B). Specifically, $^{87}Rb/^{86}Sr$ ratios of MDC increased gradually during the first 5 seconds and then flattened out towards the end of the acquisition. For NIST 610, the $^{87}Rb/^{86}Sr$ ratios increased continuously following a linear trend, whereas data from the Mica-Mg-NP gradually decreased (Fig. 9B).

3.5. Evaluation of ablation characteristics of different materials: MDC, Mica-Mg-NP and NIST 610

3.5.1. Laser profilometry analysis. The ablation craters in MDC phlogopite, Mica-Mg-NP, and NIST 610 glass were imaged *via* the laser scanning confocal microscope (LSCM) to

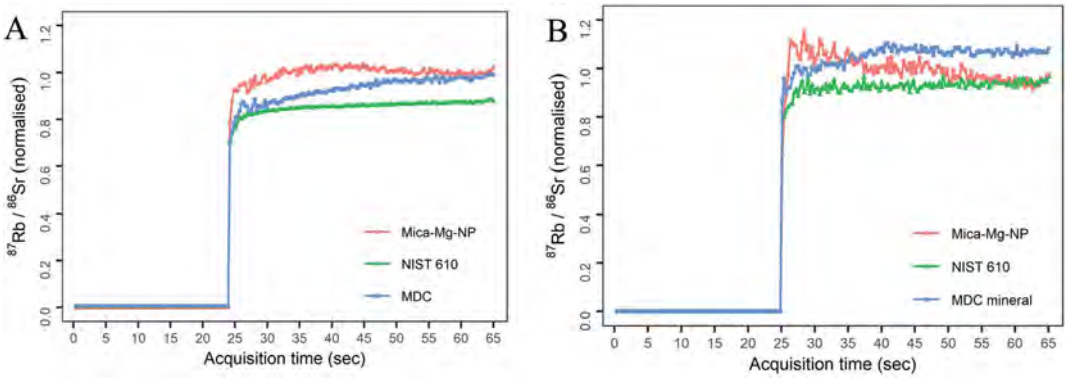

Fig. 9 The DHF profiles for $^{87}Rb/^{86}Sr$ ratios of Mica-Mg-NP, MDC and NIST 610 obtained with (A) the193 nm laser and 74 μm laser beam and (B) with the 213 nm laser, and 75 μm laser beam; all data are normalised to Mica-Mg-NP and its expected $^{87}Rb/^{86}Sr$ value (see data in Table 1).

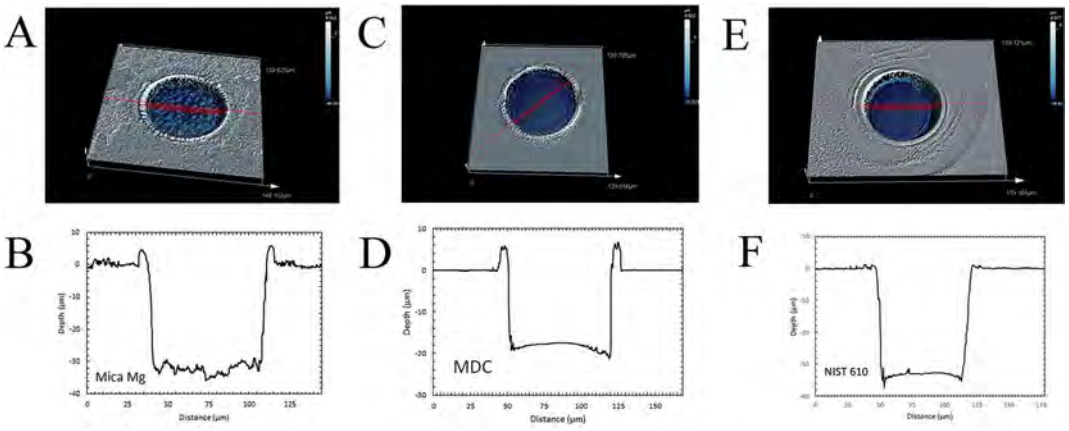

Fig. 10 Laser profilometry images of the laser ablation crater and the DHF profiles illustrating the differences between (A and B) Mica-Mg-NP, (C and D) MDC and (E and F) NIST 610 in terms of crater morphology.

characterise the different ablation properties of these different materials and to assess and calculate the crater 'depths', which, in turn, can be used to quantify absolute ablation rates (*e.g.*, nanometres per a pulse) of the different materials.

The craters in the Mica-Mg-NP show an elevated crater rim and a very uneven and irregular base (Fig. 10A and B). Calculated ablation rates for the Mica-Mg-NP varied among individual craters, with the crater depths ranging from *ca.* 33.5 μm to 39 μm, giving an average ablation rate of ~181 nm per pulse.

The LA craters in MDC also display high rims, but have very smooth convex bases and tend to be much shallower with an average ablation rate of about 90 nm per pulse (Fig. 10C and D). This is almost 50% lower than the ablation rate of Mica-Mg-NP.

Finally, the NIST 610 glass exhibits very similar crater morphologies to those observed in the MDC, with a typically smooth and convex base, but with almost flat crater rims (Fig. 10E and F). The average ablation rate in NIST 610 glass is about 155 nm per pulse, which is closer to that observed in Mica-Mg NP than MDC. Overall, the crater dimensions and morphologies of NIST 610 and MDC materials were relatively constant and reproducible from spot to spot, unlike the craters observed in Mica-Mg-NP, which showed more spatial variation.

3.5.2. High-resolution backscatter electron (BSE) imaging. The Mica-Mg-NP was imaged by scanning electron microscopy to investigate the homogeneity of particle sizes within the pellet, and to assess the physical damage of the NP material after the LA analysis. Backscatter electron images show that there is a considerable degree of heterogeneity in the particle sizes within the pellet, and larger μm-scale fragments of phlogopite (up to 15–20 μm in diameter) were occasionally observed at the surface of the pellet but also in the subsurface (Fig. 11A and B, respectively).

In addition, the craters in Mica-Mg-NP ablated using both 213 nm and 193 nm lasers were also imaged to inspect the impact of the laser wavelength on the NP pellet. There are noticeable differences in the friability and physical damage of the craters induced by different lasers (Fig. 11C and D). Specifically, the 213 nm laser produced uneven craters with a more friable texture. The uneven energy distribution in the 213 nm laser beam is apparent, where one side of the crater tended to be ablated more than the other (Fig. 11D). The base of the 213 nm craters were relatively flat comparing to those produced by the 193 nm laser that have a more irregular base with a granular texture (Fig. 11C) as described in the previous section.

The ejecta blankets around the craters also varied between the different laser systems. The 213 nm laser produced a thicker

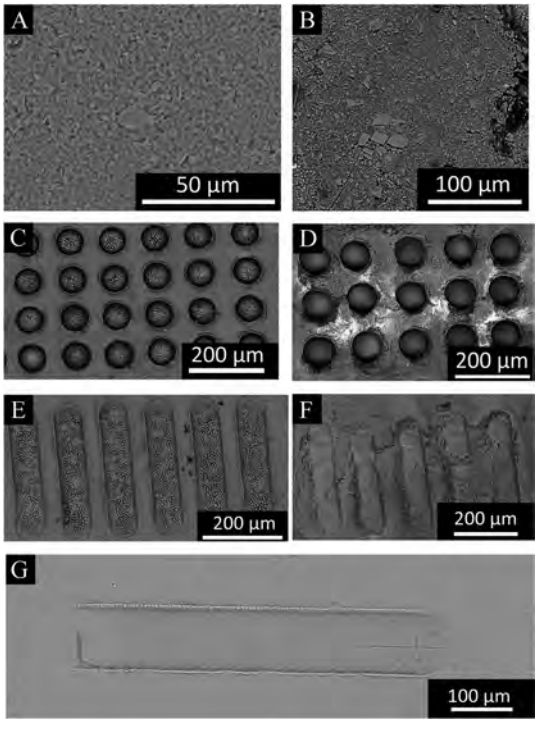

Fig. 11 The BSE images of (A) the surface and (B) subsurface of Mica-Mg-NP from the chipped edge of the pellet, illustrating the variation in particles sizes, which range from a dominant nano-powder (<1 μm), to occasionally larger particles (>10 μm). (C) Laser craters within Mica-Mg-NP produced by 193 nm laser and (D) 213 nm laser system. (E) Lines raster ablated on Mica-Mg-NP by the 193 nm laser system and (F) the 213 nm laser system. (G) Lines raster ablated on MDC by the 193 nm laser system.

and uneven deposit around the craters, with the ejected material extending further around the craters (Fig. 11D), compared to the ejecta produced by the 193 nm laser (Fig. 11C).

The trenches produced by the line raster were also imaged. The 193 nm laser produced lines in MDC with a flat base and only a small amount of ejecta around the ablated area (Fig. 11G). In contrast, the lines produced in Mica-Mg-NP showed an irregular base with ejecta accumulated at the edges of the trenches (Fig. 11E). However, the 213 nm laser was much more destructive in Mica-Mg-NP, and it produced trenches with uneven texture and crumbled edges, separated by areas exhibiting extensive physical damage (Fig. 11F).

4. Discussion

4.1. Ablation characteristics of MDC and Mica-Mg-NP

Considering presumably identical, or very similar, major element compositions of MDC and Mica-Mg-NP phlogopites (both originating from the same Bekily area of Madagascar), it is likely that the observed differences in elemental Rb/Sr fractionation patterns between these two materials (*i.e.*, nano-powder *vs.* natural mineral flakes) are related to their different ablation properties. The friable and granular nature of the nano-powder material (Mica-Mg-NP) is thus likely responsible for the specific ablation characteristics and texture observed at the base of craters in Mica-Mg-NP, compared to the flat-base craters in the natural mineral MDC (see Section 3.5.1.). It is therefore not surprising that these two phlogopite materials, MDC and Mica-Mg-NP, have also very different ablation rates and associated DHF patterns for the $^{87}Rb/^{86}Sr$ ratios. The shapes and depths of the ablated craters in Mica-Mg-NP were also different from spot to spot. This is likely related to the fact that Mica-Mg phlogopite is a difficult mineral to pulverize due to its flaky nature and perfect cleavage, hence, it is not an ideal material for the preparation of equi-granular nano-pellets with constant porosity and ablation characteristics. This can thus explain the observed results and internal variability in ablation characteristics across the Mica-Mg-NP pellet (*e.g.*, due to its variable porosity, compaction, and particle size, see Fig. 11).In addition, it is also possible that some of the observed variability in measured $^{87}Rb/^{86}Sr$ ratios in analysed phlogopites could also arise from the positioning and spacing of LA spots within the Mica-Mg-NP reference material. When a sequence of LA spots were performed using an evenly spaced array, the previously ablated craters were observed to have an effect on the Rb/Sr ratio, and caused the apparent 'drift' seen in some runs (Fig. 2B), which then biased the corrected MDC ages. Possible factors to consider are the potential for physical damage to the material from the previous LA spots especially in the nano-powder pellet (Fig. 11C and D), re-ablation of the ejecta blanket from previous spots (see Košler *et al.*, 2005)[45] or effects of gas flow turbulence from previously ablated craters. The exact physical processes involved require further investigation, but preliminary work indicates that Rb/Sr ratios are more sensitive to these effects than other element pairs (such as U/Pb), and consistency of spot spacing is an important consideration to minimise Rb/Sr fractionation in Mica-Mg-NP.

4.2. The Rb/Sr elemental fractionation effects

The apparent session to session variation in *in situ* Rb–Sr ages of MDC (Fig. 4B) is most likely related to a higher variability in the $^{87}Rb/^{86}Sr$ ratios within, and between sessions from Mica-Mg-NP. Less variability in the calculated age for MDC is seen when it is normalised to the NIST 610 (Fig. 5); however, matrix effects (due to chemical differences with respect to MDC) are greater for this glass standard, relative to Mica-Mg-NP.

The higher variability in $^{87}Rb/^{86}Sr$ ratios between materials analysed, compared to $^{87}Sr/^{86}Sr$, indicates that elemental fractionation effects are occurring between Rb and Sr during the LA-ICP-MS/MS analysis. Commonly, during the ablation, element-signal intensities of refractory elements (*e.g.*, Sr, Ca, U) decrease more rapidly compared to more volatile elements (*e.g.*, Rb, K, Pb).[46] Thus ratios of volatile to refractory elements (*e.g.* $^{208}Pb/^{238}U$) generally display increasing trends during the analysis, as the aerosol size distribution decreases with time and these smaller particles are more enriched in the volatile elements.[46] Such anticipated increase in $^{87}Rb/^{86}Sr$ ratios during the ablation was indeed observed for MDC when it was ablated by the 193 nm laser but when the sample ablated with the 213 nm laser, the measured $^{87}Rb/^{86}Sr$ increased during the first 15 seconds and became constant afterward (see Section 3.4., Fig. 9B). NIST 610 showed slightly increase in the measured $^{87}Rb/^{86}Sr$ during the first few seconds and stabilised during the rest of ablation time (Fig. 9). However, data from Mica-Mg-NP (acquired using both the 213 nm and 193 nm lasers (Fig. 9)) show a more complex DHF pattern that suggests that other processes, apart from volatilisation effects, are also occurring.

We speculate that the observed Rb/Sr fractionation trends for Mica-Mg-NP (see Section 3.4.) are partly related to variable aerosol particle size distribution during the ablation.[47] The BSE images show a degree of heterogeneity in the grain sizes within the Mica-Mg-NP pellet (ranging from nm to μm sizes, see Section 3.5.2.), which may cause the variable ablation observed between craters due to differences in compaction or differential ablation of these larger particles. We speculate that some original mineral particles may also be incorporated in the aerosol stream reaching the ICP due to mechanical disintegration of the pellet (*e.g.*, linked to physical damage around the lines and craters, see Fig. 11C–F). These processes and physical/ablation characteristics of the phlogopite nano-powder pellet could partly explain the observed variation in raw $^{87}Rb/^{86}Sr$ ratios of Mica-Mg-NP within the sessions and from session to session (Section 3.2.1.). Accordingly, the distribution of aerosol size produced during the ablation might have varied from spot to spot, influencing the Rb/Sr elemental fractionation and the corresponding $^{87}Rb/^{86}Sr$ ratios. Although, DHF has been studied extensively for the U–Pb system in a number of minerals,[29,48,49] further and more systematic investigations are needed to better understand the impact of DHF effects on the accuracy and precision for *in situ* Rb–Sr dating.

4.3. Laser-wavelength dependent effects on Rb/Sr elemental fractionation

Rb/Sr elemental fractionation occurs in both 213 nm and 193 nm laser systems, and it seems to be relatively consistent for

NIST 610, but more complicated for Mica-Mg-NP and MDC (see Section 3.4.). The DHF pattern for Rb/Sr observed in NIST 610 does not significantly change between the two different laser wavelengths, which explains the consistency of the calculated Rb–Sr ages for MDC when normalised to NIST 610 (for data analysed by both LA systems; see Fig. 5). In contrast, the increased physical damage around the ablated areas observed in Mica-Mg-NP analysed with the 213 nm laser (see also Section 3.5.2.) is likely partly responsible for the very different DHF pattern for Mica-Mg-NP (see the decreasing of the Rb/Sr ratio with time, Fig. 9B). Such marked differences in Mica-Mg-NP DHF patterns produced by two LA systems (Fig. 9) can in part account for the observed systematic offsets in the calculated Rb–Sr ages for MDC (normalised to Mica-Mg-NP). The 193 nm laser tends to produce ages that are generally older compared to ages acquired *via* the 213 nm laser system (Fig. 4B). These laser specific differences are further amplified by the fact that no DHF correction has been applied for $^{87}Rb/^{86}Sr$ data during processing, as the DHF in the Mica-Mg-NP reference material is not transferable to the samples.

This indicates there are laser specific effects on the accuracy of the *in situ* Rb–Sr ages, especially when the nano-powder is used as a primary reference material for normalisation, which thus needs to be taken into account and carefully evaluated by future studies.

4.4. Matrix effects and their impact on *in situ* Rb–Sr ages

Matrix effects caused by differences in chemical composition between phlogopites (MDC, Mica-Mg-NP) and NIST 610 glass and their ablation characteristic are most apparent for line rasters due to constant ablation over time (*i.e.*, minimum or no DHF present).[50] The Rb–Sr age of MDC obtained by normalising the line raster data against Mica-Mg-NP was less accurate than the age obtained when normalising to NIST 610 (Fig. 7). This suggests that the difference in ablation characteristics between MDC and Mica-Mg-NP has more influence on the accuracy than the difference in chemical composition between MDC and NIST 610. For spot analyses, the DHF increases the $^{87}Rb/^{86}Sr$ ratio with time, which, in this case, offsets some of the observed matrix effects between MDC, NIST 610 and Mica-Mg-NP since the DHF was steepest for MDC. The overall impact of matrix effects is dependent on a combination of the physical properties of ablated materials, laser wavelength, chemical composition of materials, ablation mode and analytical setup, and it may thus vary considerably and should be assessed and monitored closely.

4.5. Implications for the accuracy of *in situ* Rb–Sr ages of phlogopite (MDC)

Assuming that the $^{87}Sr/^{86}Sr$ initial ratio is identical for MDC and Mica-Mg materials, the overall accuracy of our LA-ICP-MS/MS method and acquired Rb–Sr age for MDC were typically within 3% and occasionally up to 8% (see Section 3.2. and Fig. 4B). Considering that MDC and Mica-Mg-NP phlogopites were both sourced from the same area (Bekily, Madagascar), we assume that these materials should have also identical Rb–Sr ages. However, they are unlikely to have the same Rb and Sr concentrations and will also have different $^{87}Rb/^{86}Sr$ and $^{87}Sr/^{86}Sr$ ratios. In this study, the ages of MDC were all calculated using an assumed initial $^{87}Sr/^{86}Sr$ ratio of 0.72607 ± 0.0007, as reported for Mica-Mg phlogopite.[12] One possibility for the age discrepancies (between acquired and expected ages) could be related to potential natural variation in MDC, and differences in the initial $^{87}Sr/^{86}Sr$ of MDC *vs.* Mica-Mg-NP phlogopites. The initial $^{87}Sr/^{86}Sr$ ratio used in this study for MDC and Mica-Mg-NP was constrained based on published $^{87}Rb/^{86}Sr$ and $^{87}Sr/^{86}Sr$ data of two samples from Bekily area (15 527 and 15 529),[51] each containing phlogopite and diopside mineral pairs, which were used to construct Rb–Sr isochron and the Sr initial (see Hogmalm *et al.* (2017) for details).[12] Calculating the initial $^{87}Sr/^{86}Sr$ ratios separately for these two phlogopite–diopside pairs[51] yielded the Sr initials of 0.72585 and 0.72625, respectively, with an average of ~0.7261. Changing the Sr isotope initial ratio of MDC from 0.72607 (used in this study, and adopted from Hogmalm *et al.* (2017)[12]) to a lower value of 0.72585 (*i.e.*, the minimum estimate) or a higher initial of 0.72625 (the maximum based on the above mineral pair data[51]) would only have a minor impact on the calculated Rb–Sr ages of MDC (for all analysed sessions). Specifically, the recalculated age of MDC would change only by 0.09% (for a minimum value) and 0.04% (for the maximum Sr initial), which thus have a very minor effect on the overall accuracy. The initial $^{87}Sr/^{86}Sr$ of the analysed MDC would have to be significantly more radiogenic (>0.73) than the above reported maximum (0.72625) to reconcile the systematically older Rb–Sr ages for MDC acquired in this study using 193 nm laser (see Fig. 4B). Such more radiogenic initial $^{87}Sr/^{86}Sr$ ratios up to 0.74239 were reported for other pegmatitic rocks (syenite) within the Beraketa shear zone in which the Bekily area is located.[51] Using a much more radiogenic initial ratio (0.73311) for our MDC data, measured by 193 nm laser, which would be within the range of published Sr initials for syenite,[51] would yield an average age of ~520 Ma, which would thus be in agreement with the expected age of 519.4 ± 6.5 Ma;[12] corresponding to about 2.3% improvement in the overall accuracy relative to data acquired with the assumed Sr initial of 0.72607 (Hogmalm *et al.* (2017)).[12] However, using such hypothetical and highly radiogenic Sr initial of ~0.73311 for MDC is in our view not well justified due to the fact that this high Sr initial is derived based on the analysis of syenite and not phlogopite data (*i.e.*, phlogopite–diopside pairs).[51]

Regardless of the initial Sr ratio used it would not reconcile the observed session-to-session variability in ages measured for MDC. We conclude that the variation in apparent Rb–Sr ages for MDC (see Fig. 4B), are related to the variable elemental fractionation and ablation characteristics of Mica-Mg-NP relative to the natural mineral (MDC). At present, Mica-Mg-NP is the most commonly available nano-powder reference material for *in situ* LA-ICP-MS/MS Rb–Sr dating of phlogopite, but additional secondary mineral standards of known age are required for more accurate Rb–Sr age determination. Such approach using a secondary mineral standard enables proper assessment of

data quality and a possible age-offset correction, if required (see Armistead *et al.* (2020) and Li *et al.* (2020)).[20,21]

5. Conclusions

In situ Rb–Sr dating *via* LA-ICP-MS/MS still faces certain analytical challenges which currently limits its wider applications and accuracy for age determination. The main challenges include (i) sample-specific Rb–Sr elemental fractionation effects, (ii) different ablation properties between nano-powder standards and natural minerals, and (iii) a lack of matrix-matched reference materials. All of the above have an impact on the measured $^{87}Rb/^{86}Sr$ ratios but have minimum effects on measured $^{87}Sr/^{86}Sr$ ratios, which were more reproducible for all studied materials (Mica-Mg-NP, MDC phlogopite mineral, and NIST 610 glass), using both 193 nm and 213 nm laser systems.

For phlogopite dating, the Mica-Mg-NP is currently the best nano-powder reference material that is available, but it is still not ideal due to observed differences in ablation rates, crater shapes, and DHF patterns compared to the natural phlogopite mineral (MDC). Therefore, further investigation is required to constrain the sources and mechanisms of $^{87}Rb/^{86}Sr$ fractionation during *in situ* Rb–Sr dating. In addition, developing more reliable and matrix matched reference materials for phlogopite, and other rock-forming K-rich minerals, is needed.

With the current reference materials available for *in situ* Rb–Sr dating, we recommend regular analysis of a secondary matrix-matched mineral standard (such as MDC-phlogopite, Högsbo-muscovite,[12] *etc.*) to assess the accuracy of the calculated *in situ* Rb–Sr ages. With this method we have shown that ages are achievable within an accuracy of about 3%, which can however be further improved to about 1% (*i.e.*, typical internal precision), if an unknown sample and the mineral standard have identical ablation properties and chemical compositions, thus minimising the impact from DHF and matrix effects.

Alternatively, one can calculate an age-offset correction factor derived from the secondary mineral standard which can be then applied to unknown samples. Such approach has been used recently to successfully date micas *via in situ* Rb–Sr technique in a range of geological settings to better understand the tectonic and geological history of our planet.[20,21]

Appendix

Table 4 Raw $^{87}Rb/^{86}Sr$ and $^{87}Sr/^{86}Sr$ isotopic ratios of Mica-Mg-NP-powder reference material analysed by LA ICP-MS/MS over multiple Sessions using either a 193 nm or 213 nm laser ablation system (see a column labelled as LA)

Spot	$^{87}Rb/^{86}Sr$	2σ	$^{87}Sr/^{86}Sr$	2σ	Session	LA	Spot	$^{87}Rb/^{86}Sr$	2σ	$^{87}Sr/^{86}Sr$	2σ	Session	LA
MicaMg-1.d	160.7	1.3	1.903	0.015	Session 1	193 nm	Mica-Mg-15	163.1	1.4	1.907	0.016	Session 2	193 nm
MicaMg-2.d	163	1.2	1.896	0.014	Session 1	193 nm	Mica-Mg-16	163.4	1.5	1.897	0.015	Session 2	193 nm
MicaMg-3.d	156.8	1.2	1.893	0.016	Session 1	193 nm	Mica-Mg-17	163.7	1.2	1.903	0.013	Session 2	193 nm
MicaMg-4.d	160	1.2	1.884	0.014	Session 1	193 nm	Mica-Mg-18	164.6	1.4	1.891	0.015	Session 2	193 nm
MicaMg-5.d	160.2	1.2	1.893	0.015	Session 1	193 nm	Mica-Mg-19	153.7	1.5	1.908	0.019	Session 2	193 nm
MicaMg-6.d	157.1	1.1	1.895	0.014	Session 1	193 nm	Mica-Mg-20	161.9	1.3	1.89	0.016	Session 2	193 nm
MicaMg-7.d	155.3	1.1	1.899	0.013	Session 1	193 nm	Mica-Mg-21	160	1.6	1.906	0.014	Session 2	193 nm
MicaMg-8.d	157.9	1.2	1.914	0.015	Session 1	193 nm	Mica-Mg-22	162.3	1.3	1.91	0.016	Session 2	193 nm
MicaMg-9.d	157	1.1	1.889	0.015	Session 1	193 nm	Mica-Mg-23	162.7	1.4	1.914	0.014	Session 2	193 nm
MicaMg-10.d	154.4	1.1	1.908	0.015	Session 1	193 nm	Mica-Mg-24	158	1.4	1.907	0.016	Session 2	193 nm
MicaMg-11.d	157.6	1.4	1.917	0.015	Session 1	193 nm	Mica-Mg-25	157.7	1.5	1.908	0.015	Session 2	193 nm
MicaMg-12.d	155.6	1.1	1.884	0.012	Session 1	193 nm	Mica-Mg-26	157.8	1.5	1.905	0.015	Session 2	193 nm
MicaMg-13.d	156.2	1.2	1.893	0.014	Session 1	193 nm	Mica-Mg-27	157.4	1.2	1.9	0.016	Session 2	193 nm
MicaMg-14.d	153.8	1.1	1.876	0.016	Session 1	193 nm	Mica-Mg-28	158.9	1.4	1.909	0.014	Session 2	193 nm
MicaMg-15.d	153.3	1.1	1.893	0.013	Session 1	193 nm	Mica-Mg-29	160.6	1.3	1.9	0.015	Session 2	193 nm
MicaMg-16.d	156.5	1.3	1.899	0.017	Session 1	193 nm	Mica-Mg-30	159.9	1.1	1.895	0.013	Session 2	193 nm
MicaMg-17.d	154.6	1.2	1.901	0.014	Session 1	193 nm	Mica-Mg-31	161.8	1.4	1.908	0.015	Session 2	193 nm
MicaMg-18.d	154.6	1.2	1.89	0.014	Session 1	193 nm	Mica-Mg-32	159.5	1.3	1.911	0.017	Session 2	193 nm
Mica-Mg-1	160.8	1.7	1.888	0.021	Session 2	193 nm	Mica-Mg-33	158.6	1.2	1.899	0.013	Session 2	193 nm
Mica-Mg-2	165.1	1.3	1.9	0.016	Session 2	193 nm	Mica-Mg-34	155.6	1.2	1.896	0.014	Session 2	193 nm
Mica-Mg-3	163	1.5	1.907	0.016	Session 2	193 nm	Mica-Mg-35	156	1.1	1.9	0.013	Session 2	193 nm
Mica-Mg-4	163.8	2	1.91	0.024	Session 2	193 nm	Mica-Mg-36	158	1.6	1.905	0.015	Session 2	193 nm
Mica-Mg-5	167.5	1.4	1.902	0.017	Session 2	193 nm	Mica-Mg-37	161.8	1.4	1.902	0.016	Session 2	193 nm
Mica-Mg-6	166.7	1.4	1.909	0.014	Session 2	193 nm	Mica-Mg-38	161.6	1.5	1.901	0.016	Session 2	193 nm
Mica-Mg-7	164.4	1.9	1.894	0.022	Session 2	193 nm	Mica-Mg-39	161.6	1.3	1.916	0.016	Session 2	193 nm
Mica-Mg-8	165.6	1.4	1.905	0.016	Session 2	193 nm	Mica-Mg-40	159.4	1.4	1.909	0.017	Session 2	193 nm
Mica-Mg-9	159.5	1.3	1.905	0.014	Session 2	193 nm	Mica-Mg-41	156.1	2.1	1.893	0.014	Session 2	193 nm
Mica-Mg-10	162.6	1.4	1.912	0.016	Session 2	193 nm	Mica-Mg-42	154.4	1.4	1.884	0.014	Session 2	193 nm
Mica-Mg-11	159.9	1.7	1.902	0.014	Session 2	193 nm	Mica-Mg-43	157.2	1.3	1.903	0.019	Session 2	193 nm
Mica-Mg-12	162	1.5	1.891	0.016	Session 2	193 nm	Mica-Mg-44	157.4	1.4	1.893	0.016	Session 2	193 nm

Table 4 (*Contd.*)

Spot	$^{87}Rb/^{86}Sr$	2σ	$^{87}Sr/^{86}Sr$	2σ	Session	LA	Spot	$^{87}Rb/^{86}Sr$	2σ	$^{87}Sr/^{86}Sr$	2σ	Session	LA
Mica-Mg-13	159.1	1.6	1.89	0.016	Session 2	193 nm	Mica-Mg-45	160.3	1.5	1.908	0.016	Session 2	193 nm
Mica-Mg-14	160.5	1.6	1.89	0.017	Session 2	193 nm	Mica-Mg-46	167.2	1.5	1.891	0.02	Session 2	193 nm
Mica-Mg-47	169.9	1.4	1.913	0.017	Session 2	193 nm	Mica-Mg-8	156.5	1.3	1.9	0.014	Session 4	193 nm
Mica-Mg-48	166.1	1.3	1.903	0.014	Session 2	193 nm	Mica-Mg-9	155.7	1	1.904	0.011	Session 4	193 nm
Mica-Mg-1	164.5	1.6	1.892	0.021	Session 3	193 nm	Mica-Mg-10	159.6	1.1	1.906	0.011	Session 4	193 nm
Mica-Mg-2	168.1	1.4	1.908	0.017	Session 3	193 nm	Mica-Mg-11	155	1.2	1.905	0.011	Session 4	193 nm
Mica-Mg-3	168.3	1.4	1.916	0.018	Session 3	193 nm	Mica-Mg-12	168.6	1.2	1.916	0.014	Session 4	193 nm
Mica-Mg-4	164.4	1.8	1.885	0.018	Session 3	193 nm	Mica-Mg-13	153.7	1.2	1.902	0.011	Session 4	193 nm
Mica-Mg-5	164.3	1.5	1.91	0.018	Session 3	193 nm	Mica-Mg-14	157.4	1.2	1.905	0.013	Session 4	193 nm
Mica-Mg-6	164.4	1.3	1.899	0.016	Session 3	193 nm	Mica-Mg-15	156.1	1.2	1.902	0.012	Session 4	193 nm
Mica-Mg-7	161.4	1.4	1.905	0.015	Session 3	193 nm	Mica-Mg-16	153	1.2	1.893	0.012	Session 4	193 nm
Mica-Mg-8	158.4	1.5	1.897	0.016	Session 3	193 nm	Mica-Mg-17	157	0.93	1.897	0.011	Session 4	193 nm
Mica-Mg-9	164	1.7	1.918	0.016	Session 3	193 nm	Mica-Mg-18	153.3	1	1.89	0.013	Session 4	193 nm
Mica-Mg-10	163.7	1.5	1.905	0.016	Session 3	193 nm	Mica-Mg-19	155.2	1.2	1.901	0.011	Session 4	193 nm
Mica-Mg-11	162.6	2.2	1.917	0.023	Session 3	193 nm	Mica-Mg-20	156.2	1.2	1.899	0.013	Session 4	193 nm
Mica-Mg-12	163.6	1.4	1.914	0.019	Session 3	193 nm	Mica-Mg-21	155.7	1.4	1.896	0.013	Session 4	193 nm
Mica-Mg-13	164	1.5	1.907	0.016	Session 3	193 nm	Mica-Mg-22	156.7	1.1	1.904	0.012	Session 4	193 nm
Mica-Mg-14	164.7	1.7	1.905	0.018	Session 3	193 nm	Mica-Mg-23	166.1	1.3	1.901	0.014	Session 4	193 nm
Mica-Mg-15	161.6	1.4	1.914	0.015	Session 3	193 nm	Mica-Mg-24	155.6	1	1.892	0.011	Session 4	193 nm
Mica-Mg-16	162.6	1.3	1.905	0.017	Session 3	193 nm	Mica-Mg-25	153.6	1.1	1.902	0.013	Session 4	193 nm
Mica-Mg-17	160.8	1.7	1.912	0.015	Session 3	193 nm	Mica-Mg-26	155.5	1.1	1.892	0.012	Session 4	193 nm
Mica-Mg-18	157.2	1.5	1.894	0.016	Session 3	193 nm	Mica-Mg-27	156.6	1.3	1.895	0.012	Session 4	193 nm
Mica-Mg-19	159.8	1.4	1.904	0.016	Session 3	193 nm	Mica-Mg-28	154.8	1.4	1.908	0.013	Session 4	193 nm
Mica-Mg-20	158.8	1.5	1.894	0.014	Session 3	193 nm	Mica-Mg-29	157.7	1.1	1.908	0.012	Session 4	193 nm
Mica-Mg-21	160	1.6	1.909	0.016	Session 3	193 nm	Mica-Mg-30	156	1.1	1.902	0.012	Session 4	193 nm
Mica-Mg-22	163.9	1.7	1.903	0.017	Session 3	193 nm	Mica-Mg-31	154.7	1.1	1.892	0.013	Session 4	193 nm
Mica-Mg-23	164.4	2.2	1.921	0.025	Session 3	193 nm	Mica-Mg-32	156.5	1.3	1.909	0.014	Session 4	193 nm
Mica-Mg-24	160.5	1.5	1.902	0.017	Session 3	193 nm	Mica-Mg-33	155.8	1	1.901	0.011	Session 4	193 nm
Mica-Mg-1	168.4	1.4	1.888	0.015	Session 4	193 nm	Mica-Mg-34	172.2	1.7	1.909	0.021	Session 4	193 nm
Mica-Mg-2	159.5	1.1	1.908	0.015	Session 4	193 nm	Mica-Mg-35	153.4	1.2	1.88	0.013	Session 4	193 nm
Mica-Mg-3	159.1	1.3	1.898	0.017	Session 4	193 nm	Mica-Mg-36	154.5	1.3	1.909	0.012	Session 4	193 nm
Mica-Mg-4	160.7	1.1	1.901	0.012	Session 4	193 nm	Mica-Mg-37	155.82	0.97	1.901	0.011	Session 4	193 nm
Mica-Mg-5	156.2	1.3	1.889	0.014	Session 4	193 nm	Mica-Mg-38	160.4	1.2	1.911	0.015	Session 4	193 nm
Mica-Mg-6	155.7	1.3	1.905	0.013	Session 4	193 nm	Mica-Mg-39	163.7	1.2	1.903	0.013	Session 4	193 nm
Mica-Mg-7	159.2	1.2	1.899	0.012	Session 4	193 nm	Mica-Mg-40	164.7	1.2	1.901	0.014	Session 4	193 nm
Mica-Mg-41	162.8	1.3	1.9	0.013	Session 4	193 nm	Mica-Mg-23	150.8	1.1	1.902	0.016	Session 5	193 nm
Mica-Mg-42	162.9	1.6	1.894	0.014	Session 4	193 nm	Mica-Mg-24	153.6	2.1	1.91	0.024	Session 5	193 nm
Mica-Mg-43	158.7	1.4	1.882	0.015	Session 4	193 nm	Mica-Mg-25	154.4	1.2	1.892	0.015	Session 5	193 nm
Mica-Mg-44	159.9	1.6	1.891	0.013	Session 4	193 nm	Mica-Mg-26	154.6	1.2	1.902	0.016	Session 5	193 nm
Mica-Mg-45	168.7	1.3	1.889	0.013	Session 4	193 nm	Mica-Mg-27	156.6	1.5	1.893	0.018	Session 5	193 nm
Mica-Mg-46	163.2	1.4	1.897	0.015	Session 4	193 nm	Mica-Mg-28	155.9	1.5	1.892	0.018	Session 5	193 nm
Mica-Mg-47	155.1	1	1.9	0.012	Session 4	193 nm	Mica-Mg-29	156.2	1.6	1.915	0.017	Session 5	193 nm
Mica-Mg-48	166.9	1.1	1.905	0.013	Session 4	193 nm	Mica-Mg-30	156.3	1.4	1.896	0.018	Session 5	193 nm
Mica-Mg-49	161.8	1.2	1.903	0.014	Session 4	193 nm	Mica-Mg-31	154	1.6	1.906	0.02	Session 5	193 nm
Mica-Mg-50	161.5	1.2	1.898	0.011	Session 4	193 nm	Mica-Mg-32	152.8	1.6	1.898	0.013	Session 5	193 nm
Mica-Mg-51	160.8	1.5	1.898	0.013	Session 4	193 nm	Mica-Mg-33	149.7	1.4	1.908	0.015	Session 5	193 nm
Mica-Mg-1	162.3	1.6	1.919	0.016	Session 5	193 nm	Mica-Mg-34	156.8	1.7	1.901	0.015	Session 5	193 nm
Mica-Mg-2	156.3	1.3	1.891	0.015	Session 5	193 nm	Mica-Mg-35	157.1	1.3	1.9	0.016	Session 5	193 nm
Mica-Mg-3	154.5	1.4	1.911	0.015	Session 5	193 nm	Mica-Mg-36	157.5	1.6	1.905	0.015	Session 5	193 nm
Mica-Mg-4	156.7	1.6	1.908	0.014	Session 5	193 nm	Mica-Mg-1	166.9	1.4	1.893	0.02	Session 6	193 nm
Mica-Mg-5	155.1	1.4	1.892	0.015	Session 5	193 nm	Mica-Mg-2	166.4	2.2	1.887	0.028	Session 6	193 nm
Mica-Mg-6	160.4	1.5	1.911	0.019	Session 5	193 nm	Mica-Mg-3	169.1	1.4	1.901	0.019	Session 6	193 nm
Mica-Mg-7	158.9	1.4	1.917	0.017	Session 5	193 nm	Mica-Mg–4	165.1	1.3	1.907	0.018	Session 6	193 nm
Mica-Mg-8	156.9	1.5	1.912	0.018	Session 5	193 nm	Mica-Mg-5	163.3	1.3	1.904	0.018	Session 6	193 nm
Mica-Mg-9	157.8	1.8	1.895	0.016	Session 5	193 nm	Mica-Mg-6	159.1	1.5	1.9	0.022	Session 6	193 nm
Mica-Mg-10	159	1.7	1.889	0.015	Session 5	193 nm	Mica-Mg-7	167.9	1.8	1.906	0.026	Session 6	193 nm
Mica-Mg-11	155.8	1.3	1.894	0.015	Session 5	193 nm	Mica-Mg-8	170.8	1.4	1.91	0.014	Session 6	193 nm
Mica-Mg-12	156.8	1.5	1.888	0.016	Session 5	193 nm	Mica-Mg-9	171.2	1.5	1.919	0.018	Session 6	193 nm
Mica-Mg-13	155.6	1.5	1.909	0.016	Session 5	193 nm	Mica-Mg-10	168	1.7	1.881	0.021	Session 6	193 nm
Mica-Mg-14	150.2	1.6	1.887	0.015	Session 5	193 nm	Mica-Mg-11	162.7	2	1.895	0.02	Session 6	193 nm
Mica-Mg-15	155.2	1.4	1.892	0.018	Session 5	193 nm	Mica-Mg-12	162.1	1.2	1.901	0.015	Session 6	193 nm
Mica-Mg-16	159.8	1.6	1.924	0.018	Session 5	193 nm	Mica-Mg-13	169	1.9	1.929	0.017	Session 6	193 nm

Table 4 (*Contd.*)

Spot	$^{87}Rb/^{86}Sr$	2σ	$^{87}Sr/^{86}Sr$	2σ	Session	LA	Spot	$^{87}Rb/^{86}Sr$	2σ	$^{87}Sr/^{86}Sr$	2σ	Session	LA
Mica-Mg-17	158.7	1.5	1.905	0.016	Session 5	193 nm	Mica-Mg-14	165	1.4	1.903	0.016	Session 6	193 nm
Mica-Mg-18	158.4	1.3	1.911	0.014	Session 5	193 nm	Mica-Mg-15	167	1.7	1.88	0.018	Session 6	193 nm
Mica-Mg-19	154.3	1.5	1.894	0.016	Session 5	193 nm	Mica-Mg-16	167.1	1.8	1.902	0.018	Session 6	193 nm
Mica-Mg-20	155.4	1.3	1.9	0.015	Session 5	193 nm	Mica-Mg-17	162.6	1.4	1.896	0.016	Session 6	193 nm
Mica-Mg-21	155	1.4	1.899	0.016	Session 5	193 nm	Mica-Mg-18	163.9	1.4	1.903	0.019	Session 6	193 nm
Mica-Mg-22	155.1	1.5	1.915	0.019	Session 5	193 nm	Mica-Mg-19	160.8	1.5	1.88	0.016	Session 6	193 nm
Mica-Mg-20	152.8	1.7	1.879	0.02	Session 6	193 nm	Mica-Mg-53	157.3	1.4	1.898	0.015	Session 6	193 nm
Mica-Mg-21	157	1.2	1.929	0.017	Session 6	193 nm	Mica-Mg-54	155.5	1.9	1.89	0.021	Session 6	193 nm
Mica-Mg-22	157.3	1.2	1.908	0.015	Session 6	193 nm	Mica-Mg-55	154.4	1.5	1.906	0.02	Session 6	193 nm
Mica-Mg-23	160.5	1.5	1.911	0.017	Session 6	193 nm	Mica-Mg-56	153.7	1.3	1.899	0.015	Session 6	193 nm
Mica-Mg-24	159.7	1.4	1.903	0.016	Session 6	193 nm	Mica-Mg-57	154.6	1.3	1.912	0.017	Session 6	193 nm
Mica-Mg-25	158.5	1.2	1.906	0.016	Session 6	193 nm	Mica-Mg-58	152.3	1.1	1.896	0.014	Session 6	193 nm
Mica-Mg-26	158.6	1.2	1.903	0.016	Session 6	193 nm	Mica-Mg-59	151.15	0.96	1.902	0.014	Session 6	193 nm
Mica-Mg-27	158.4	1.3	1.89	0.018	Session 6	193 nm	Mica-Mg-60	152.4	1.3	1.908	0.017	Session 6	193 nm
Mica-Mg-28	157.8	1.2	1.899	0.015	Session 6	193 nm	Mica-Mg-61	152.3	1.4	1.913	0.019	Session 6	193 nm
Mica-Mg-29	157.5	1.5	1.906	0.016	Session 6	193 nm	Mica-Mg-62	151.5	1.4	1.886	0.019	Session 6	193 nm
Mica-Mg-30	154.3	1	1.904	0.013	Session 6	193 nm	Mica-Mg-63	149.5	1.6	1.888	0.021	Session 6	193 nm
Mica-Mg-31	153.7	1.5	1.902	0.016	Session 6	193 nm	Mica-Mg-64	155.3	1.2	1.898	0.015	Session 6	193 nm
Mica-Mg-32	158.9	1.4	1.898	0.013	Session 6	193 nm	Mica-Mg-65	151.5	1.2	1.881	0.018	Session 6	193 nm
Mica-Mg-33	158.9	1.4	1.887	0.015	Session 6	193 nm	Mica-Mg-66	152.8	1.1	1.904	0.014	Session 6	193 nm
Mica-Mg-34	159.4	1.2	1.902	0.015	Session 6	193 nm	Mica-Mg-67	150.4	1.3	1.894	0.014	Session 6	193 nm
Mica-Mg-35	157.9	1.3	1.898	0.014	Session 6	193 nm	Mica-Mg-1	156.6	1.9	1.899	0.024	Session 7	193 nm
Mica-Mg-36	152.4	1.8	1.897	0.02	Session 6	193 nm	Mica-Mg-2	159.3	1.8	1.89	0.022	Session 7	193 nm
Mica-Mg-37	156	1.3	1.906	0.016	Session 6	193 nm	Mica-Mg-3	162.1	1.6	1.906	0.022	Session 7	193 nm
Mica-Mg-38	154.3	1.2	1.9	0.015	Session 6	193 nm	Mica-Mg-4	165.2	1.4	1.908	0.02	Session 7	193 nm
Mica-Mg-39	153.9	1.6	1.914	0.026	Session 6	193 nm	Mica-Mg-5	160.9	1.6	1.905	0.02	Session 7	193 nm
Mica-Mg-40	151.9	1.3	1.882	0.016	Session 6	193 nm	Mica-Mg-6	156.2	2	1.898	0.024	Session 7	193 nm
Mica-Mg-41	153.9	1.5	1.872	0.019	Session 6	193 nm	Mica-Mg-7	159.7	1.5	1.912	0.019	Session 7	193 nm
Mica-Mg-42	156	1.3	1.899	0.019	Session 6	193 nm	Mica-Mg-8	156.6	2	1.87	0.024	Session 7	193 nm
Mica-Mg-43	158	1.4	1.899	0.015	Session 6	193 nm	Mica-Mg-9	159.1	1.7	1.872	0.026	Session 7	193 nm
Mica-Mg-44	155.2	1.5	1.892	0.018	Session 6	193 nm	Mica-Mg-10	156.7	1.6	1.87	0.022	Session 7	193 nm
Mica-Mg-45	155	1.4	1.888	0.014	Session 6	193 nm	Mica-Mg-11	156.2	1.8	1.907	0.022	Session 7	193 nm
Mica-Mg-46	151.9	1.3	1.896	0.014	Session 6	193 nm	Mica-Mg-12	154.4	1.9	1.889	0.026	Session 7	193 nm
Mica-Mg-47	152	1.2	1.909	0.014	Session 6	193 nm	Mica-Mg-13	154.5	1.8	1.864	0.021	Session 7	193 nm
Mica-Mg-48	151.7	1.3	1.879	0.017	Session 6	193 nm	Mica-Mg-14	155.6	1.7	1.889	0.022	Session 7	193 nm
Mica-Mg-49	152	1.3	1.914	0.017	Session 6	193 nm	Mica-Mg-15	154.6	1.7	1.902	0.022	Session 7	193 nm
Mica-Mg-50	152.2	1.5	1.895	0.015	Session 6	193 nm	Mica-Mg-16	154.1	1.6	1.915	0.027	Session 7	193 nm
Mica-Mg-51	153.8	1	1.893	0.015	Session 6	193 nm	Mica-Mg-17	155.5	1.8	1.897	0.026	Session 7	193 nm
Mica-Mg-52	157.5	1.2	1.925	0.015	Session 6	193 nm	Mica-Mg-18	154.3	1.7	1.894	0.023	Session 7	193 nm
Mica-Mg-19	155	1.9	1.912	0.024	Session 7	193 nm	Mica-Mg-13	159.1	1.6	1.918	0.02	Session 8	193 nm
Mica-Mg-20	156.2	2.3	1.905	0.021	Session 7	193 nm	Mica-Mg-14	155	2.1	1.884	0.021	Session 8	193 nm
Mica-Mg-21	151.8	1.4	1.887	0.019	Session 7	193 nm	Mica-Mg-15	155.2	1.9	1.904	0.023	Session 8	193 nm
Mica-Mg-22	156.1	1.9	1.901	0.021	Session 7	193 nm	Mica-Mg-16	157.4	1.9	1.903	0.023	Session 8	193 nm
Mica-Mg-23	152.9	1.9	1.915	0.026	Session 7	193 nm	Mica-Mg-17	153.8	2.1	1.905	0.027	Session 8	193 nm
Mica-Mg-24	150	1.7	1.897	0.022	Session 7	193 nm	Mica-Mg-18	156.7	2.2	1.884	0.026	Session 8	193 nm
Mica-Mg-25	154.7	1.9	1.889	0.023	Session 7	193 nm	Mica-Mg-19	161	2	1.925	0.029	Session 8	193 nm
Mica-Mg-26	150.3	1.5	1.899	0.021	Session 7	193 nm	Mica-Mg-20	157	1.8	1.915	0.027	Session 8	193 nm
Mica-Mg-27	149.6	1.5	1.892	0.021	Session 7	193 nm	Mica-Mg-21	159.6	1.9	1.906	0.021	Session 8	193 nm
Mica-Mg-28	154.4	1.7	1.9	0.022	Session 7	193 nm	Mica-Mg-22	155.3	2	1.896	0.029	Session 8	193 nm
Mica-Mg-29	158.4	2.1	1.908	0.021	Session 7	193 nm	Mica-Mg-23	153.9	2	1.878	0.025	Session 8	193 nm
Mica-Mg-30	154.9	1.8	1.92	0.027	Session 7	193 nm	Mica-Mg-24	154.8	2.5	1.912	0.023	Session 8	193 nm
Mica-Mg-31	154.2	1.6	1.881	0.021	Session 7	193 nm	Mica-Mg-25	149.5	1.9	1.897	0.031	Session 8	193 nm
Mica-Mg-32	154	2	1.893	0.024	Session 7	193 nm	Mica-Mg-26	153.8	1.7	1.888	0.022	Session 8	193 nm
Mica-Mg-33	152.2	1.6	1.913	0.026	Session 7	193 nm	Mica-Mg-27	152	1.6	1.887	0.024	Session 8	193 nm
Mica-Mg-34	151.8	1.7	1.884	0.022	Session 7	193 nm	Mica-Mg-28	155.1	1.5	1.891	0.02	Session 8	193 nm
Mica-Mg-35	152.2	1.9	1.897	0.023	Session 7	193 nm	Mica-Mg-29	154.9	2.1	1.881	0.034	Session 8	193 nm
Mica-Mg-36	154.2	1.9	1.912	0.018	Session 7	193 nm	Mica-Mg-30	154.2	2	1.898	0.027	Session 8	193 nm
Mica-Mg-37	150.8	1.6	1.92	0.022	Session 7	193 nm	Mica-Mg-31	154	2	1.9	0.029	Session 8	193 nm
Mica-Mg-38	153.5	2	1.875	0.029	Session 7	193 nm	Mica-Mg-32	153.8	2.2	1.879	0.031	Session 8	193 nm
Mica-Mg-39	156.5	1.6	1.899	0.021	Session 7	193 nm	Mica-Mg-33	151.2	2	1.9	0.026	Session 8	193 nm
Mica-Mg-1	161.5	1.5	1.894	0.019	Session 8	193 nm	Mica-Mg-34	152.7	2	1.895	0.021	Session 8	193 nm
Mica-Mg-2	156.9	1.6	1.892	0.019	Session 8	193 nm	Mica-Mg-35	150.3	1.7	1.88	0.017	Session 8	193 nm
Mica-Mg-3	157.1	1.5	1.918	0.021	Session 8	193 nm	Mica-Mg-36	154.7	1.8	1.903	0.023	Session 8	193 nm

Table 4 (*Contd.*)

Spot	$^{87}Rb/^{86}Sr$	2σ	$^{87}Sr/^{86}Sr$	2σ	Session	LA	Spot	$^{87}Rb/^{86}Sr$	2σ	$^{87}Sr/^{86}Sr$	2σ	Session	LA
Mica-Mg-4	158	1.8	1.891	0.02	Session 8	193 nm	Mica-Mg-37	151.6	1.5	1.886	0.021	Session 8	193 nm
Mica-Mg-5	156.1	1.6	1.853	0.025	Session 8	193 nm	Mica-Mg-38	152.3	1.7	1.892	0.018	Session 8	193 nm
Mica-Mg-6	161.7	2	1.896	0.021	Session 8	193 nm	Mica-Mg-39	149.3	1.8	1.876	0.022	Session 8	193 nm
Mica-Mg-7	163.6	1.9	1.907	0.02	Session 8	193 nm	1-Mica Mg P	133.3	1.3	1.881	0.024	Session 1	213 nm
Mica-Mg-8	163	1.6	1.905	0.018	Session 8	193 nm	3-Mica Mg P	136.8	1.9	1.9	0.021	Session 1	213 nm
Mica-Mg-9	159.4	1.7	1.885	0.019	Session 8	193 nm	4-Mica Mg P	132.4	1.7	1.883	0.024	Session 1	213 nm
Mica-Mg-10	160.8	1.8	1.871	0.023	Session 8	193 nm	21-Mica Mg P	138	1.8	1.908	0.023	Session 1	213 nm
Mica-Mg-11	158.7	1.6	1.89	0.019	Session 8	193 nm	22-Mica Mg P	141.5	2.2	1.892	0.02	Session 1	213 nm
Mica-Mg-12	156	1.4	1.877	0.02	Session 8	193 nm	23-Mica Mg P	138.4	1.8	1.899	0.02	Session 1	213 nm
24-Mica Mg P	141	1.7	1.894	0.015	Session 1	213 nm	MicaMgp-14	149.1	1.5	1.879	0.012	Session 2	213 nm
41-Mica Mg P	137.2	2.2	1.885	0.023	Session 1	213 nm	MicaMgp-15	145.3	1.2	1.873	0.011	Session 2	213 nm
42-Mica Mg P	137.4	1.9	1.886	0.022	Session 1	213 nm	MicaMgp-25	149.2	1.2	1.883	0.01	Session 2	213 nm
43-Mica Mg P	142.6	2.2	1.91	0.024	Session 1	213 nm	MicaMgp-26	145.4	1.3	1.88	0.01	Session 2	213 nm
44-Mica Mg P	139	1.6	1.91	0.021	Session 1	213 nm	MicaMgp-27	142.4	1	1.874	0.01	Session 2	213 nm
60-Mica Mg P	144.1	2.7	1.905	0.02	Session 1	213 nm	MicaMgp-34	146.8	1.1	1.875	0.01	Session 2	213 nm
61-Mica Mg P	137.3	1.8	1.908	0.021	Session 1	213 nm	MicaMgp-35	145	1.3	1.891	0.011	Session 2	213 nm
62-Mica Mg P	142.8	2.2	1.897	0.021	Session 1	213 nm	MicaMgp-36	146.19	0.99	1.872	0.01	Session 2	213 nm
MicaMgp-1	148.1	1.3	1.8809	0.0099	Session 2	213 nm	MicaMgp-37	140.9	1	1.864	0.011	Session 2	213 nm
MicaMgp-2	139.79	0.96	1.878	0.01	Session 2	213 nm	MicaMgp-38	143.1	1.1	1.879	0.01	Session 2	213 nm
MicaMgp-3	151.8	1.3	1.8766	0.0095	Session 2	213 nm	MicaMgp-39	144.3	1.1	1.878	0.011	Session 2	213 nm
MicaMgp-13	142	1	1.8699	0.0092	Session 2	213 nm							

Table 5 $^{87}Rb/^{86}Sr$ and $^{87}Sr/^{86}Sr$ isotopic ratios for MDC analysed by LA-ICP-MS/MS over multiple sessions and normalised to Mica-Mg-NP reference material, using either a 193 nm or 213 nm laser ablation system (see column labelled: LA)

Spot	$^{87}Rb/^{86}Sr$	2σ	$^{87}Sr/^{86}Sr$	2σ	Session	LA	Spot	$^{87}Rb/^{86}Sr$	2σ	$^{87}Sr/^{86}Sr$	2σ	Session	LA
MDC-mineral-1.d	40.79	0.3	1.0324	0.007	Session 1	193 nm	MDC Mica-33	40.31	0.35	1.0295	0.007	Session 2	193 nm
MDC-mineral-2.d	41.83	0.28	1.0326	0.0082	Session 1	193 nm	MDC Mica-34	39.38	0.28	1.0236	0.0064	Session 2	193 nm
MDC-mineral-3.d	41.32	0.28	1.0313	0.0074	Session 1	193 nm	MDC Mica-35	39.24	0.3	1.0246	0.0064	Session 2	193 nm
MDC-mineral-4.d	41.27	0.3	1.036	0.0074	Session 1	193 nm	MDC Mica-36	38.74	0.33	1.0238	0.0067	Session 2	193 nm
MDC-mineral-5.d	41.8	0.27	1.0406	0.0069	Session 1	193 nm	MDC Mica-38	39.49	0.28	1.0197	0.0072	Session 2	193 nm
MDC-mineral-6.d	41.64	0.35	1.0384	0.0076	Session 1	193 nm	MDC Mica-39	40.44	0.36	1.025	0.0076	Session 2	193 nm
MDC-mineral-7.d	41.8	0.28	1.036	0.0064	Session 1	193 nm	MDC Mica-40	39.61	0.3	1.0302	0.0065	Session 2	193 nm
MDC-mineral-8.d	41.99	0.28	1.0285	0.0071	Session 1	193 nm	MDC Mica-41	39.42	0.29	1.0216	0.0056	Session 2	193 nm
MDC-mineral-9.d	41.82	0.31	1.0254	0.0073	Session 1	193 nm	MDC Mica-42	39.24	0.29	1.0193	0.0066	Session 2	193 nm
MDC-mineral-10.d	41.79	0.32	1.0354	0.007	Session 1	193 nm	MDC Mica-43	39.9	0.3	1.0309	0.0058	Session 2	193 nm
MDC-mineral-11.d	42.37	0.3	1.0326	0.0074	Session 1	193 nm	MDC Mica-44	40.41	0.28	1.0342	0.0059	Session 2	193 nm
MDC-mineral-12.d	42.11	0.35	1.024	0.0078	Session 1	193 nm	MDC Mica-45	40.65	0.31	1.0281	0.0059	Session 2	193 nm
MDC Mica-1	38.38	0.36	1.0303	0.0073	Session 2	193 nm	MDC Mica-46	41.11	0.3	1.0275	0.0062	Session 2	193 nm
MDC Mica-2	38.52	0.33	1.034	0.0079	Session 2	193 nm	MDC Mica-47	41.02	0.35	1.033	0.0068	Session 2	193 nm
MDC Mica-3	38.51	0.28	1.0308	0.0059	Session 2	193 nm	MDC Mica-48	41.15	0.39	1.0362	0.007	Session 2	193 nm
MDC Mica-4	39.67	0.29	1.0342	0.0078	Session 2	193 nm	MDC Mica-1	38.15	0.4	1.0297	0.0084	Session 3	193 nm
MDC Mica-5	39.25	0.28	1.028	0.0084	Session 2	193 nm	MDC Mica-2	38.87	0.31	1.0311	0.0079	Session 3	193 nm
MDC Mica-6	39.53	0.26	1.0325	0.0071	Session 2	193 nm	MDC Mica-3	38.58	0.27	1.0276	0.007	Session 3	193 nm
MDC Mica-7	40	0.31	1.0319	0.0069	Session 2	193 nm	MDC Mica-4	39.89	0.28	1.0292	0.0079	Session 3	193 nm
MDC Mica-8	39.69	0.29	1.0353	0.0067	Session 2	193 nm	MDC Mica-5	40.35	0.26	1.0345	0.0081	Session 3	193 nm
MDC Mica-9	39.27	0.27	1.0308	0.0058	Session 2	193 nm	MDC Mica-6	40.11	0.27	1.0323	0.0064	Session 3	193 nm
MDC Mica-10	39.3	0.32	1.0224	0.0067	Session 2	193 nm	MDC Mica-7	41.11	0.31	1.04	0.0074	Session 3	193 nm
MDC Mica-11	39.13	0.27	1.0302	0.0068	Session 2	193 nm	MDC Mica-8	40.4	0.28	1.0258	0.0074	Session 3	193 nm
MDC Mica-12	38.93	0.29	1.0239	0.0069	Session 2	193 nm	MDC Mica-9	40.61	0.31	1.031	0.0077	Session 3	193 nm
MDC Mica-13	40.1	0.32	1.0314	0.0067	Session 2	193 nm	MDC Mica-10	40.53	0.28	1.0231	0.0073	Session 3	193 nm
MDC Mica-14	39.71	0.32	1.0384	0.0062	Session 2	193 nm	MDC Mica-11	40.46	0.27	1.0268	0.0081	Session 3	193 nm
MDC Mica-15	39.44	0.3	1.0312	0.0061	Session 2	193 nm	MDC Mica-12	39.64	0.25	1.0313	0.0077	Session 3	193 nm
MDC Mica-16	39.7	0.26	1.0208	0.0065	Session 2	193 nm	MDC Mica-13	40.03	0.25	1.0282	0.0077	Session 3	193 nm
MDC Mica-17	39.34	0.28	1.0298	0.0072	Session 2	193 nm	MDC Mica-14	40.42	0.32	1.0254	0.0074	Session 3	193 nm
MDC Mica-18	39.37	0.29	1.0301	0.0068	Session 2	193 nm	MDC Mica-15	40.61	0.31	1.0197	0.0081	Session 3	193 nm
MDC Mica-19	39.69	0.3	1.0257	0.0065	Session 2	193 nm	MDC Mica-16	40.54	0.28	1.0204	0.008	Session 3	193 nm
MDC Mica-20	39.9	0.31	1.0325	0.0067	Session 2	193 nm	MDC Mica-17	41.59	0.3	1.0269	0.0079	Session 3	193 nm

Table 5 (*Contd.*)

Spot	$^{87}Rb/^{86}Sr$	2σ	$^{87}Sr/^{86}Sr$	2σ	Session	LA	Spot	$^{87}Rb/^{86}Sr$	2σ	$^{87}Sr/^{86}Sr$	2σ	Session	LA
MDC Mica-21	40.71	0.34	1.0267	0.008	Session 2	193 nm	MDC Mica-18	41.75	0.37	1.0328	0.0076	Session 3	193 nm
MDC Mica-22	39.64	0.27	1.0219	0.0072	Session 2	193 nm	MDC Mica-19	41.87	0.36	1.0279	0.0081	Session 3	193 nm
MDC Mica-23	40.39	0.3	1.0309	0.0078	Session 2	193 nm	MDC Mica-20	41.16	0.32	1.0289	0.0086	Session 3	193 nm
MDC Mica-24	39.17	0.31	1.0265	0.0064	Session 2	193 nm	MDC Mica-21	41.91	0.27	1.0298	0.0087	Session 3	193 nm
MDC Mica-25	39.36	0.28	1.0281	0.0065	Session 2	193 nm	MDCMICA-1	40.66	0.29	1.0225	0.0077	Session 3	193 nm
MDC Mica-26	39.49	0.3	1.0353	0.0066	Session 2	193 nm	MDCMICA-2	40.33	0.32	1.0349	0.0072	Session 3	193 nm
MDC Mica-27	39.36	0.33	1.0298	0.0067	Session 2	193 nm	MDCMICA-3	40.62	0.33	1.036	0.011	Session 3	193 nm
MDC Mica-28	40.29	0.28	1.0341	0.0072	Session 2	193 nm	MDC Mica-22	41.61	0.38	1.0265	0.0074	Session 3	193 nm
MDC Mica-29	39.88	0.29	1.0277	0.0069	Session 2	193 nm	MDC Mica-23	40.8	0.32	1.0308	0.0074	Session 3	193 nm
MDC Mica-30	40.25	0.34	1.0306	0.0064	Session 2	193 nm	MDC Mica-24	41.88	0.44	1.0299	0.0086	Session 3	193 nm
MDC Mica-31	40.19	0.38	1.0373	0.0062	Session 2	193 nm	MDC-1	41.2	0.3	1.0361	0.0084	Session 4	193 nm
MDC Mica-32	41.16	0.37	1.0315	0.0072	Session 2	193 nm	MDC-2	39.69	0.21	1.0269	0.0062	Session 4	193 nm
MDC-3	40.69	0.26	1.0208	0.0081	Session 4	193 nm	MDC-48	40.41	0.29	1.0339	0.007	Session 4	193 nm
MDC-4	40.48	0.35	1.0359	0.0066	Session 4	193 nm	MDC-49	39.92	0.3	1.0316	0.0052	Session 4	193 nm
MDC-5	40.49	0.24	1.0315	0.0063	Session 4	193 nm	MDC-50	40.2	0.39	1.0274	0.0056	Session 4	193 nm
MDC-6	39.96	0.26	1.033	0.0082	Session 4	193 nm	MDC-51	40.6	0.41	1.0267	0.0057	Session 4	193 nm
MDC-7	40.33	0.29	1.0342	0.0066	Session 4	193 nm	MDC 1-1	43.26	0.27	1.0513	0.0073	Session 4	193 nm
MDC-8	40.08	0.27	1.0388	0.0066	Session 4	193 nm	MDC 1-2	42.46	0.27	1.0462	0.0071	Session 4	193 nm
MDC-9	39.98	0.26	1.034	0.0062	Session 4	193 nm	MDC 1-3	42.3	0.26	1.0517	0.0066	Session 4	193 nm
MDC-10	39.74	0.27	1.0317	0.006	Session 4	193 nm	MDC 1-4	42.36	0.27	1.0453	0.0058	Session 4	193 nm
MDC-11	40.23	0.3	1.0329	0.0052	Session 4	193 nm	MDC 1-5	42.84	0.28	1.0544	0.0065	Session 4	193 nm
MDC-12	39.96	0.29	1.034	0.0064	Session 4	193 nm	MDC 1-6	43.29	0.24	1.0481	0.0063	Session 4	193 nm
MDC-13	40.75	0.31	1.0338	0.0063	Session 4	193 nm	MDC 1-7	43.23	0.26	1.0531	0.0071	Session 4	193 nm
MDC-14	40.13	0.33	1.0333	0.0067	Session 4	193 nm	MDC 1-8	42.58	0.25	1.0545	0.0062	Session 4	193 nm
MDC-15	40.45	0.41	1.0304	0.0061	Session 4	193 nm	MDC 1-9	42.74	0.26	1.0557	0.0066	Session 4	193 nm
MDC-16	39.58	0.34	1.031	0.0056	Session 4	193 nm	MDC 1-10	42.93	0.27	1.065	0.0065	Session 4	193 nm
MDC-17	41.42	0.4	1.0279	0.0069	Session 4	193 nm	MDC 2-1	41.56	0.35	1.0416	0.0062	Session 4	193 nm
MDC-18	41.54	0.34	1.0385	0.0089	Session 4	193 nm	MDC 2-2	40.83	0.29	1.0371	0.007	Session 4	193 nm
MDC-19	42.15	0.3	1.0442	0.0072	Session 4	193 nm	MDC 2-3	40.56	0.31	1.0386	0.0062	Session 4	193 nm
MDC-20	41.97	0.25	1.0383	0.0083	Session 4	193 nm	MDC 2-4	40.5	0.27	1.0344	0.0059	Session 4	193 nm
MDC-21	41.46	0.3	1.0385	0.008	Session 4	193 nm	MDC 2-5	40.25	0.27	1.0387	0.0056	Session 4	193 nm
MDC-22	40.9	0.26	1.0357	0.0064	Session 4	193 nm	MDC 2-6	40.45	0.3	1.0343	0.0061	Session 4	193 nm
MDC-23	40.67	0.27	1.0282	0.0081	Session 4	193 nm	MDC 2-7	40.88	0.3	1.0308	0.0057	Session 4	193 nm
MDC-24	40.83	0.33	1.0358	0.0063	Session 4	193 nm	MDC 2-8	42.3	0.29	1.0425	0.0073	Session 4	193 nm
MDC-25	41.07	0.35	1.0346	0.0069	Session 4	193 nm	MDC 2-9	41.3	0.32	1.0404	0.0063	Session 4	193 nm
MDC-26	40.86	0.33	1.0307	0.0074	Session 4	193 nm	MDC 2-10	40.17	0.29	1.0369	0.0058	Session 4	193 nm
MDC-27	40.74	0.29	1.0316	0.0073	Session 4	193 nm	MDC 3-1	41.58	0.26	1.0385	0.0072	Session 4	193 nm
MDC-28	40.41	0.3	1.03	0.0072	Session 4	193 nm	MDC 3-2	41.43	0.26	1.0358	0.0084	Session 4	193 nm
MDC-29	40.91	0.34	1.029	0.0068	Session 4	193 nm	MDC 3–3	41.45	0.23	1.0354	0.0073	Session 4	193 nm
MDC-30	40.81	0.28	1.0337	0.0065	Session 4	193 nm	MDC 3-4	41.65	0.26	1.0417	0.0071	Session 4	193 nm
MDC-31	40.86	0.32	1.0273	0.0065	Session 4	193 nm	MDC 3-5	41.24	0.28	1.0394	0.0078	Session 4	193 nm
MDC-32	41.96	0.47	1.0335	0.0089	Session 4	193 nm	MDC 3-6	41.12	0.25	1.0406	0.0064	Session 4	193 nm
MDC-33	42.27	0.44	1.0314	0.0057	Session 4	193 nm	MDC 3-7	41.62	0.32	1.037	0.0075	Session 4	193 nm
MDC-34	41.03	0.35	1.0341	0.0057	Session 4	193 nm	MDC 3-8	41.5	0.31	1.0369	0.0073	Session 4	193 nm
MDC-35	41.24	0.35	1.0317	0.0069	Session 4	193 nm	MDC 3-9	41.94	0.26	1.0403	0.008	Session 4	193 nm
MDC-36	40.9	0.38	1.0391	0.0074	Session 4	193 nm	MDC 3-10	41.6	0.33	1.0434	0.0072	Session 4	193 nm
MDC-37	40.34	0.38	1.0285	0.007	Session 4	193 nm	MDC 4-1	43.92	0.26	1.0265	0.0068	Session 4	193 nm
MDC-38	40.75	0.36	1.0339	0.0075	Session 4	193 nm	MDC 4–2	42.86	0.32	1.0409	0.0079	Session 4	193 nm
MDC-39	39.86	0.31	1.0235	0.0064	Session 4	193 nm	MDC 4-3	43.88	0.28	1.0441	0.0089	Session 4	193 nm
MDC-40	40.01	0.35	1.0325	0.0079	Session 4	193 nm	MDC 4-4	44.2	0.27	1.0426	0.0076	Session 4	193 nm
MDC-41	40.95	0.43	1.0188	0.0098	Session 4	193 nm	MDC 4-5	41.93	0.26	1.0361	0.0071	Session 4	193 nm
MDC-42	41.01	0.36	1.0237	0.0096	Session 4	193 nm	MDC 4–6	42.6	0.27	1.0493	0.0067	Session 4	193 nm
MDC-43	40.92	0.43	1.0366	0.0076	Session 4	193 nm	MDC 4-7	43.42	0.3	1.0405	0.0076	Session 4	193 nm
MDC-44	41.47	0.39	1.0363	0.0077	Session 4	193 nm	MDC 4-8	44.59	0.35	1.0503	0.0081	Session 4	193 nm
MDC-45	40.74	0.35	1.0364	0.0067	Session 4	193 nm	MDC 4-9	43.57	0.33	1.0403	0.0096	Session 4	193 nm
MDC-46	41.5	0.41	1.0402	0.008	Session 4	193 nm	MDC 4-10	44.76	0.35	1.0395	0.0079	Session 4	193 nm
MDC-47	41.51	0.39	1.0428	0.0074	Session 4	193 nm	MDC 5–1	41.39	0.25	1.0299	0.0065	Session 4	193 nm

Table 5 (*Contd.*)

Spot	$^{87}Rb/^{86}Sr$	2σ	$^{87}Sr/^{86}Sr$	2σ	Session	LA	Spot	$^{87}Rb/^{86}Sr$	2σ	$^{87}Sr/^{86}Sr$	2σ	Session	LA
MDC 5-2	42.13	0.28	1.0381	0.0071	Session 4	193 nm	MDC-1	40.46	0.37	1.0363	0.0058	Session 6	193 nm
MDC 5-3	41.92	0.28	1.0386	0.0057	Session 4	193 nm	MDC-2	40.19	0.37	1.0387	0.0066	Session 6	193 nm
MDC 5-4	41.32	0.27	1.0396	0.0067	Session 4	193 nm	MDC-3	39.89	0.36	1.0324	0.0062	Session 6	193 nm
MDC 5-5	41.17	0.25	1.0396	0.0068	Session 4	193 nm	MDC-4	45.34	0.28	1.0659	0.0072	Session 6	193 nm
MDC 5-6	40.87	0.28	1.0345	0.0063	Session 4	193 nm	MDC-5	44.46	0.25	1.0593	0.0072	Session 6	193 nm
MDC 5-7	41.59	0.3	1.0397	0.0073	Session 4	193 nm	MDC-6	45.28	0.36	1.0648	0.0076	Session 6	193 nm
MDC 5-8	41.64	0.27	1.0398	0.0067	Session 4	193 nm	MDC-7	41	0.28	1.0393	0.0074	Session 6	193 nm
MDC 5-9	41.92	0.27	1.0363	0.0071	Session 4	193 nm	MDC-8	40.62	0.25	1.0201	0.0072	Session 6	193 nm
MDC 5-10	42.13	0.27	1.0465	0.0069	Session 4	193 nm	MDC-9	40.65	0.25	1.0151	0.0072	Session 6	193 nm
MDC-16	39.37	0.36	1.0249	0.0072	Session 5	193 nm	MDC-10	40.2	0.27	1.0166	0.0064	Session 6	193 nm
MDC-17	39.86	0.31	1.0219	0.0074	Session 5	193 nm	MDC-11	40.61	0.32	1.0141	0.006	Session 6	193 nm
MDC-18	40.66	0.33	1.031	0.0082	Session 5	193 nm	MDC-12	40.73	0.34	1.0332	0.0071	Session 6	193 nm
MDC-19	40.39	0.4	1.0276	0.0075	Session 5	193 nm	MDC-13	40.32	0.36	1.021	0.0055	Session 6	193 nm
MDC-20	40.4	0.36	1.0354	0.0072	Session 5	193 nm	MDC-14	40.19	0.42	1.0183	0.0061	Session 6	193 nm
MDC-21	40.49	0.34	1.0228	0.0093	Session 5	193 nm	MDC-15	40.08	0.47	1.0246	0.0063	Session 6	193 nm
MDC-22	40.44	0.4	1.0301	0.0072	Session 5	193 nm	MDC-16	40.25	0.38	1.0267	0.0066	Session 6	193 nm
MDC-23	40.35	0.35	1.0271	0.0069	Session 5	193 nm	MDC-17	40.35	0.38	1.0189	0.006	Session 6	193 nm
MDC-24	40.76	0.35	1.0377	0.0073	Session 5	193 nm	MDC-18	40.29	0.45	1.0421	0.0066	Session 6	193 nm
MDC-25	39.81	0.49	1.028	0.0073	Session 5	193 nm	MDC-19	39.99	0.41	1.0343	0.0069	Session 6	193 nm
MDC-26	40.03	0.49	1.0216	0.0071	Session 5	193 nm	MDC-20	40.02	0.41	1.0323	0.0066	Session 6	193 nm
MDC-27	40.29	0.45	1.0311	0.0081	Session 5	193 nm	MDC-21	40.9	0.45	1.0273	0.0069	Session 6	193 nm
MDC-28	40.56	0.49	1.0367	0.0079	Session 5	193 nm	MDC-22	40.69	0.44	1.0251	0.0061	Session 6	193 nm
MDC-29	40.69	0.46	1.0378	0.0064	Session 5	193 nm	MDC-23	40.6	0.39	1.0367	0.0068	Session 6	193 nm
MDC-30	40.65	0.51	1.0328	0.0071	Session 5	193 nm	MDC-24	40.42	0.39	1.0318	0.0056	Session 6	193 nm
MDC-31	41.52	0.39	1.0262	0.0072	Session 5	193 nm	MDC-25	39.93	0.42	1.0367	0.0059	Session 6	193 nm
MDC-32	41.99	0.49	1.0346	0.0091	Session 5	193 nm	MDC-26	40.15	0.39	1.0399	0.0065	Session 6	193 nm
MDC-33	42.02	0.34	1.0304	0.0084	Session 5	193 nm	MDC-27	40.3	0.44	1.0289	0.0064	Session 6	193 nm
MDC-34	41.63	0.43	1.0314	0.0076	Session 5	193 nm	MDC-28	40.05	0.38	1.026	0.0068	Session 6	193 nm
MDC-35	41.59	0.41	1.0285	0.0083	Session 5	193 nm	MDC-29	40.44	0.41	1.0332	0.0063	Session 6	193 nm
MDC-36	41.72	0.35	1.041	0.0076	Session 5	193 nm	MDC-30	40.15	0.4	1.0264	0.0061	Session 6	193 nm
MDC-37	41.93	0.38	1.0376	0.0086	Session 5	193 nm	MDC-31	40.5	0.39	1.0403	0.0063	Session 6	193 nm
MDC-38	42	0.37	1.0362	0.0088	Session 5	193 nm	MDC-32	40.09	0.45	1.032	0.006	Session 6	193 nm
MDC-39	41.32	0.46	1.0302	0.0072	Session 5	193 nm	MDC-33	40.42	0.41	1.0301	0.0057	Session 6	193 nm
MDC-40	41.75	0.42	1.0392	0.008	Session 5	193 nm	MDC-34	40.53	0.42	1.0375	0.0059	Session 6	193 nm
MDC-41	42.06	0.4	1.0303	0.0086	Session 5	193 nm	MDC-35	40.56	0.38	1.0403	0.0056	Session 6	193 nm
MDC-42	41.78	0.4	1.036	0.0068	Session 5	193 nm	MDC-36	40.47	0.47	1.0361	0.0063	Session 6	193 nm
MDC-43	41.2	0.4	1.026	0.0063	Session 5	193 nm	MDC-37	40.6	0.46	1.0366	0.0057	Session 6	193 nm
MDC-44	41.65	0.42	1.0416	0.0069	Session 5	193 nm	MDC-38	40.78	0.35	1.0304	0.0063	Session 6	193 nm
MDC-45	41.06	0.44	1.0347	0.0083	Session 5	193 nm	MDC-39	40.64	0.41	1.0291	0.0065	Session 6	193 nm
MDC-46	41.47	0.52	1.0353	0.0073	Session 5	193 nm	MDC-40	40.9	0.45	1.0321	0.0057	Session 6	193 nm
MDC-47	41.87	0.55	1.0427	0.0063	Session 5	193 nm	MDC-41	40.77	0.46	1.037	0.0053	Session 6	193 nm
MDC-48	41.46	0.5	1.0376	0.0069	Session 5	193 nm	MDC-42	41.03	0.48	1.0435	0.0057	Session 6	193 nm
MDC-49	40.28	0.32	1.0248	0.0079	Session 5	193 nm	MDC-43	40.68	0.41	1.035	0.0059	Session 6	193 nm
MDC-50	41.1	0.33	1.0345	0.0086	Session 5	193 nm	MDC-44	40.71	0.44	1.044	0.0062	Session 6	193 nm
MDC-51	41.47	0.39	1.0339	0.0093	Session 5	193 nm	MDC-45	40.66	0.4	1.0313	0.006	Session 6	193 nm
MDC-46	40.58	0.45	1.0367	0.0062	Session 6	193 nm	MDC-22	39.3	0.25	1.0395	0.0086	Session 7	193 nm
MDC-47	40.21	0.43	1.0382	0.0061	Session 6	193 nm	MDC-23	39.67	0.36	1.04	0.011	Session 7	193 nm
MDC-48	40.92	0.47	1.0398	0.0062	Session 6	193 nm	MDC-24	39.52	0.41	1.036	0.01	Session 7	193 nm
MDC-49	40.91	0.43	1.0438	0.0066	Session 6	193 nm	MDC-25	39.14	0.24	1.0267	0.0084	Session 7	193 nm
MDC-50	40.53	0.38	1.0402	0.0057	Session 6	193 nm	MDC-26	39.81	0.35	1.0389	0.0092	Session 7	193 nm
MDC-51	40.35	0.38	1.0308	0.0059	Session 6	193 nm	MDC-27	40.47	0.4	1.03	0.013	Session 7	193 nm
MDC-52	39.92	0.45	1.0298	0.0064	Session 6	193 nm	MDC-28	39.64	0.33	1.0513	0.0082	Session 7	193 nm
MDC-53	40.03	0.37	1.0333	0.0063	Session 6	193 nm	MDC-29	39.24	0.3	1.0287	0.0095	Session 7	193 nm
MDC-54	40.26	0.45	1.0376	0.006	Session 6	193 nm	MDC-30	38.9	0.32	1.0267	0.0095	Session 7	193 nm
MDC-55	40.4	0.45	1.0348	0.0059	Session 6	193 nm	MDC-31	39.08	0.27	1.0376	0.0086	Session 7	193 nm
MDC-56	39.59	0.41	1.0331	0.0058	Session 6	193 nm	MDC-32	40.16	0.38	1.031	0.012	Session 7	193 nm
MDC-57	40	0.43	1.0353	0.0057	Session 6	193 nm	MDC-33	39.14	0.32	1.0287	0.009	Session 7	193 nm
MDC-58	39.86	0.41	1.0338	0.006	Session 6	193 nm	MDC-34	39.16	0.32	1.0222	0.0095	Session 7	193 nm

Table 5 (*Contd.*)

Spot	$^{87}Rb/^{86}Sr$	2σ	$^{87}Sr/^{86}Sr$	2σ	Session	LA	Spot	$^{87}Rb/^{86}Sr$	2σ	$^{87}Sr/^{86}Sr$	2σ	Session	LA
MDC-59	39.29	0.53	1.0374	0.006	Session 6	193 nm	MDC-35	38.71	0.29	1.0303	0.0077	Session 7	193 nm
MDC-60	40.01	0.4	1.0409	0.0065	Session 6	193 nm	MDC-36	37.94	0.28	1.0242	0.0086	Session 7	193 nm
MDC-61	40.22	0.44	1.0433	0.0058	Session 6	193 nm	MDC-37	37.87	0.26	1.0304	0.0076	Session 7	193 nm
MDC-62	40.15	0.42	1.0355	0.0062	Session 6	193 nm	MDC-38	38.07	0.34	1.0266	0.0076	Session 7	193 nm
MDC-63	40.41	0.41	1.0414	0.0057	Session 6	193 nm	MDC-39	39.5	0.29	1.0311	0.008	Session 7	193 nm
MDC-64	40.63	0.41	1.04	0.0058	Session 6	193 nm	MDC-1	40.58	0.28	1.0269	0.0082	Session 8	193 nm
MDC-65	39.86	0.42	1.0348	0.0054	Session 6	193 nm	MDC-2	40.44	0.33	1.0184	0.0097	Session 8	193 nm
MDC-66	40.14	0.47	1.0338	0.0064	Session 6	193 nm	MDC-3	40.83	0.26	1.0377	0.0075	Session 8	193 nm
MDC-67	39.76	0.46	1.034	0.0065	Session 6	193 nm	MDC-4	40.99	0.32	1.0324	0.0079	Session 8	193 nm
MDC-68	39.83	0.41	1.0397	0.0067	Session 6	193 nm	MDC-5	41.71	0.36	1.045	0.011	Session 8	193 nm
MDC-69	39.76	0.43	1.0319	0.0065	Session 6	193 nm	MDC-6	41.49	0.32	1.0394	0.0099	Session 8	193 nm
MDC-1	40.45	0.32	1.041	0.01	Session 7	193 nm	MDC-7	40.48	0.35	1.0333	0.0079	Session 8	193 nm
MDC-2	40.13	0.28	1.047	0.01	Session 7	193 nm	MDC-8	41.43	0.35	1.0415	0.0082	Session 8	193 nm
MDC-3	40	0.24	1.0395	0.0081	Session 7	193 nm	MDC-9	41.37	0.36	1.0279	0.0095	Session 8	193 nm
MDC-4	39.84	0.28	1.034	0.01	Session 7	193 nm	MDC-10	41.42	0.35	1.035	0.0093	Session 8	193 nm
MDC-5	39.85	0.28	1.0313	0.0089	Session 7	193 nm	MDC-11	41.5	0.34	1.038	0.01	Session 8	193 nm
MDC-6	39.34	0.27	1.0328	0.0074	Session 7	193 nm	MDC-12	41.48	0.33	1.04	0.0081	Session 8	193 nm
MDC-7	39.73	0.29	1.033	0.011	Session 7	193 nm	MDC-13	41.68	0.32	1.0451	0.0084	Session 8	193 nm
MDC-8	39.72	0.36	1.033	0.014	Session 7	193 nm	MDC-14	40.76	0.3	1.0336	0.0064	Session 8	193 nm
MDC-9	39.69	0.29	1.028	0.0086	Session 7	193 nm	MDC-15	40.65	0.27	1.0301	0.0089	Session 8	193 nm
MDC-10	39.61	0.27	1.0379	0.0072	Session 7	193 nm	MDC-16	40.65	0.28	1.0405	0.0071	Session 8	193 nm
MDC-11	40.08	0.3	1.0323	0.0091	Session 7	193 nm	MDC-17	41.2	0.32	1.0366	0.0091	Session 8	193 nm
MDC-12	40.32	0.36	1.041	0.01	Session 7	193 nm	MDC-18	41.28	0.34	1.0309	0.0086	Session 8	193 nm
MDC-13	39.09	0.3	1.0403	0.0077	Session 7	193 nm	MDC-19	40.84	0.37	1.0357	0.0079	Session 8	193 nm
MDC-14	38.96	0.33	1.029	0.01	Session 7	193 nm	MDC-20	40.83	0.43	1.0291	0.009	Session 8	193 nm
MDC-15	39.06	0.24	1.0303	0.0088	Session 7	193 nm	MDC-21	41.1	0.42	1.038	0.009	Session 8	193 nm
MDC-16	39.27	0.25	1.0402	0.008	Session 7	193 nm	MDC-22	41.93	0.4	1.0261	0.0084	Session 8	193 nm
MDC-17	39.27	0.35	1.04	0.01	Session 7	193 nm	MDC-23	41.77	0.39	1.0503	0.0066	Session 8	193 nm
MDC-18	38.77	0.29	1.0357	0.0085	Session 7	193 nm	MDC-24	42.13	0.45	1.0481	0.0085	Session 8	193 nm
MDC-19	39.24	0.31	1.036	0.0095	Session 7	193 nm	MDC-25	41.66	0.41	1.0413	0.0087	Session 8	193 nm
MDC-20	39.1	0.26	1.0401	0.0098	Session 7	193 nm	MDC-26	41.89	0.39	1.0326	0.009	Session 8	193 nm
MDC-21	39.36	0.29	1.0392	0.0095	Session 7	193 nm	MDC-27	41.11	0.39	1.0306	0.0086	Session 8	193 nm
MDC-28	40.52	0.29	1.0355	0.0079	Session 8	193 nm	MDC-35	43.76	0.51	1.0381	0.009	Session 1	213 nm
MDC-29	40.75	0.41	1.0285	0.0085	Session 8	193 nm	MDC-36	44.07	0.5	1.0433	0.0094	Session 1	213 nm
MDC-30	41.77	0.43	1.034	0.0082	Session 8	193 nm	MDC-37	43.42	0.34	1.0331	0.0073	Session 1	213 nm
MDC-31	40.27	0.34	1.0251	0.0081	Session 8	193 nm	MDC-38	45.21	0.62	1.0425	0.008	Session 1	213 nm
MDC-32	41.65	0.35	1.0387	0.0079	Session 8	193 nm	MDC-39	45.08	0.6	1.0208	0.0086	Session 1	213 nm
MDC-33	41.49	0.5	1.0388	0.0087	Session 8	193 nm	5-MDS mica	45.38	0.48	1.055	0.015	Session 2	213 nm
MDC-34	40.56	0.44	1.0313	0.0067	Session 8	193 nm	6-MDS mica	44.81	0.38	1.0485	0.0071	Session 2	213 nm
MDC-35	41.28	0.36	1.0362	0.0098	Session 8	193 nm	7-MDS mica	45.16	0.4	1.05	0.011	Session 2	213 nm
MDC-36	41.57	0.42	1.0381	0.0078	Session 8	193 nm	8-MDS mica	45.28	0.35	1.05	0.01	Session 2	213 nm
MDC-37	41.23	0.35	1.0412	0.0083	Session 8	193 nm	25-MDS mica	43.8	0.47	1.032	0.0063	Session 2	213 nm
MDC-38	41.36	0.42	1.0323	0.0082	Session 8	193 nm	26-MDS mica	42.91	0.49	1.0413	0.009	Session 2	213 nm
MDC-39	42.16	0.33	1.0412	0.009	Session 8	193 nm	27-MDS mica	42.77	0.38	1.031	0.017	Session 2	213 nm
MDC-1	41.2	0.32	1.0356	0.0078	Session 1	213 nm	28-MDS mica	43.52	0.41	1.037	0.011	Session 2	213 nm
MDC-13	41.49	0.28	1.0294	0.008	Session 1	213 nm	45-MDS mica	45.74	0.48	1.0492	0.0097	Session 2	213 nm
MDC-14	44.95	0.5	1.023	0.011	Session 1	213 nm	46-MDS mica	45.51	0.45	1.056	0.014	Session 2	213 nm
MDC-15	44.83	0.58	1.0276	0.0096	Session 1	213 nm	47-MDS mica	45.11	0.47	1.0501	0.009	Session 2	213 nm
MDC-2	43.65	0.4	1.0453	0.0096	Session 1	213 nm	48-MDS mica	46.17	0.61	1.052	0.012	Session 2	213 nm
MDC-25	43.21	0.49	1.0344	0.0076	Session 1	213 nm	63-MDS mica	42.53	0.44	1.032	0.0095	Session 2	213 nm
MDC-26	42.83	0.44	1.0347	0.007	Session 1	213 nm	64-MDS mica	42.76	0.44	1.024	0.013	Session 2	213 nm
MDC-27	44.02	0.48	1.0299	0.0082	Session 1	213 nm	65-MDS mica	43.12	0.51	1.034	0.011	Session 2	213 nm
MDC-3	43.66	0.47	1.033	0.0084	Session 1	213 nm	66-MDS mica	42.76	0.42	1.027	0.012	Session 2	213 nm
MDC-34	43.46	0.48	1.0324	0.0088	Session 1	213 nm							

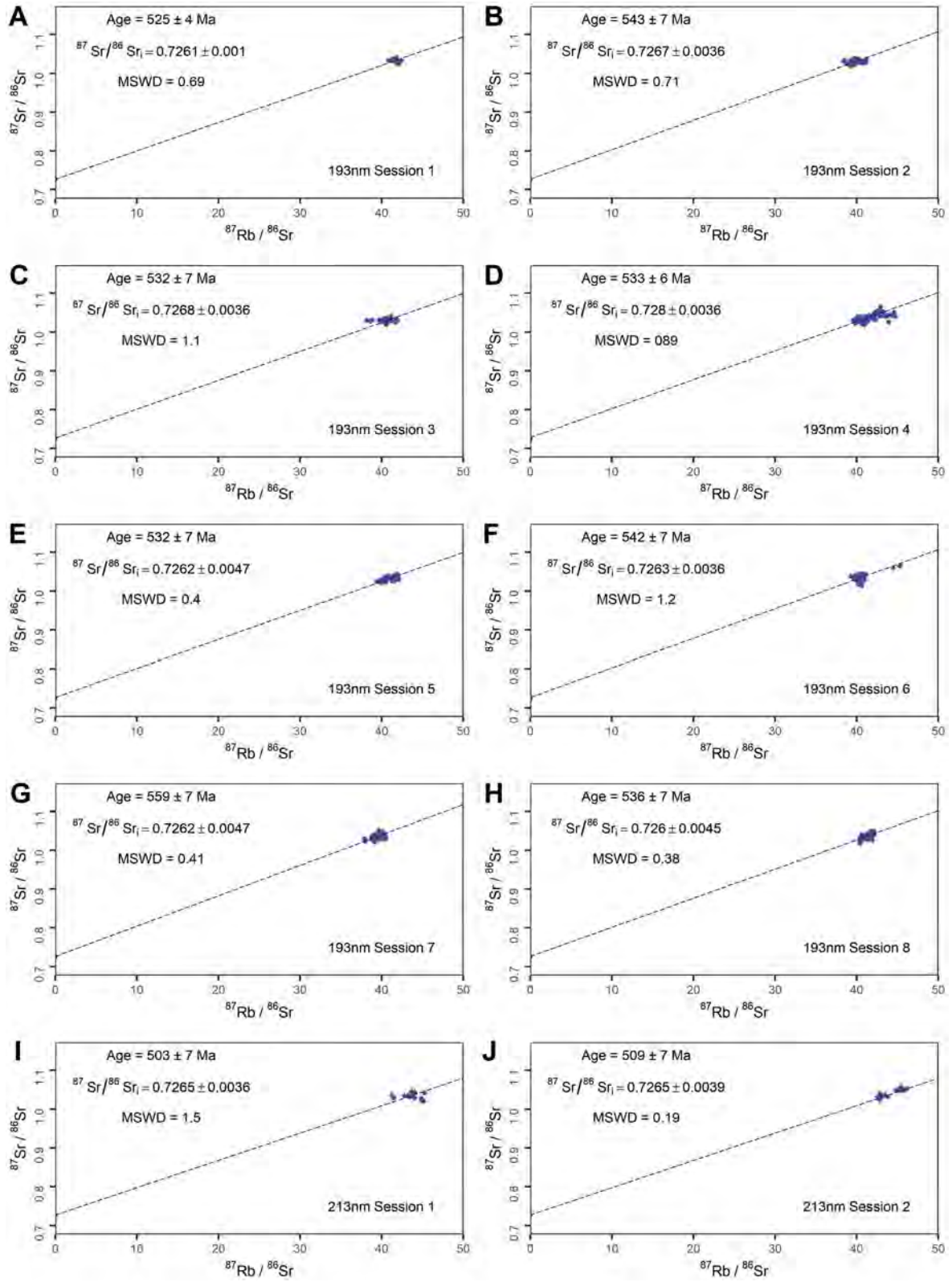

Fig. 12 The Rb/Sr isochron ages of MDC phlogopite from each individual analytical session. (A–H) the $^{87}Rb/^{86}Sr$ and $^{87}Sr/^{86}Sr$ ratios were obtained with the 193 nm laser. (I and J) the $^{87}Rb/^{86}Sr$ and $^{87}Sr/^{86}Sr$ ratios were obtained with the 213 nm laser. The initial $^{87}Sr/^{86}Sr$ ratio was fixed at 0.72607.

Table 6 $^{87}Rb/^{86}Sr$ and $^{87}Sr/^{86}Sr$ isotopic ratios for MDC analysed by and normalised to NIST 610 reference material, using either a 193 nm or 213 nm laser ablation system (see a column labelled as LA)

Spot	$^{87}Rb/^{86}Sr$	2σ	$^{87}Sr/^{86}Sr$	2σ	LA	Spot	$^{87}Rb/^{86}Sr$	2σ	$^{87}Sr/^{86}Sr$	2σ	LA
MDCtest-1	47.57	0.35	1.0298	0.0084	193 nm	MDCtest-1	50.67	0.56	1.069	0.011	213 nm
MDCtest-2	46.56	0.35	1.0257	0.009	193 nm	MDCtest-2	51.53	0.43	1.071	0.01	213 nm
MDCtest-3	47.39	0.43	1.031	0.013	193 nm	MDCtest-3	51.89	0.51	1.068	0.01	213 nm
MDCtest-4	46.26	0.34	1.0202	0.0091	193 nm	MDCtest-4	53.63	0.84	1.0703	0.0088	213 nm
MDCtest-5	46.67	0.34	1.0256	0.0091	193 nm	MDCtest-5	53.51	0.81	1.054	0.012	213 nm
MDCtest-6	46.58	0.34	1.0219	0.0086	193 nm	MDCtest-6	53.6	1.1	1.066	0.012	213 nm
MDCtest-7	46.21	0.38	1.0313	0.0091	193 nm	MDCtest-7	53.32	0.79	1.0645	0.0088	213 nm
MDCtest-8	46.44	0.31	1.0189	0.0092	193 nm	MDCtest-8	54	1.1	1.066	0.012	213 nm
MDCtest-9	47.06	0.36	1.0179	0.0095	193 nm	MDCtest-9	55.3	1.3	1.07	0.011	213 nm
MDCtest-10	47.46	0.34	1.0323	0.0095	193 nm	MDCtest-10	54.9	1	1.073	0.013	213 nm
MDCtest-11	47.33	0.34	1.0292	0.0089	193 nm	MDCtest-11	53.19	0.89	1.0631	0.0095	213 nm
MDCtest-12	47.61	0.32	1.036	0.011	193 nm	MDCtest-12	52.63	0.84	1.0635	0.0092	213 nm
MDCtest-13	47.12	0.38	1.0275	0.009	193 nm	MDCtest-13	51.38	0.47	1.06	0.01	213 nm
MDCtest-14	47.71	0.34	1.0378	0.0068	193 nm	MDCtest-14	51.69	0.76	1.057	0.012	213 nm
MDCtest-15	47.56	0.35	1.0354	0.0079	193 nm	MDCtest-15	51.85	0.61	1.0597	0.009	213 nm
MDCtest-16	47.43	0.42	1.026	0.012	193 nm	MDCtest-16	52.1	1	1.058	0.011	213 nm
MDCtest-17	48.04	0.42	1.0222	0.0091	193 nm	MDCtest-17	53.58	0.91	1.0702	0.009	213 nm
MDCtest-18	48.1	0.45	1.0228	0.009	193 nm	MDCtest-18	53.38	0.75	1.0708	0.0095	213 nm
MDCtest-19	49.09	0.45	1.0321	0.0088	193 nm	MDCtest-19	53.03	0.88	1.072	0.011	213 nm
MDCtest-20	49.15	0.45	1.0352	0.0078	193 nm	MDCtest-20	52.61	0.83	1.0532	0.0097	213 nm

Table 7 Rb-Sr isotopic ratios of NIST 610 and MDC using 'line raster' sampling approach with the 193 nm laser (74 μm diameter). All data is normalised to Mica-Mg-NP reference material

Line number ID	$^{87}Rb/^{86}Sr$	2σ	$^{87}Sr/^{86}Sr$	2σ	Line number ID	$^{87}Rb/^{86}Sr$	2σ	$^{87}Sr/^{86}Sr$	2σ
NIST610line-1	2.0688	0.0041	0.7106	0.001	MDC line-1	37.24	0.14	1.0377	0.0051
NIST610line-2	2.0859	0.0036	0.71067	0.00086	MDC line-2	36.68	0.14	1.032	0.005
NIST610line-3	2.0932	0.0041	0.7104	0.0011	MDC line-3	36.59	0.17	1.0369	0.0053
NIST610line-4	2.1184	0.0035	0.71007	0.00099	MDC line-4	36.75	0.14	1.0351	0.0056
NIST610line-5	2.1259	0.0038	0.71147	0.00097	MDC line-5	36.46	0.18	1.0412	0.0052
NIST610line-6	2.1161	0.0033	0.71067	0.00091	MDC line-6	36.29	0.18	1.0326	0.007
NIST610line-7	2.1354	0.0037	0.7094	0.001	MDC line-7	36.67	0.18	1.0352	0.005
NIST610line-8	2.1413	0.0039	0.71044	0.00093	MDC line-8	36.4	0.14	1.0281	0.0056
NIST610line-9	2.145	0.0036	0.70936	0.00089	MDC line-9	36.7	0.14	1.0334	0.0043
NIST610line-10	2.1464	0.0036	0.70847	0.00096	MDC line-10	36.78	0.16	1.0407	0.0055

Table 8 Rb-Sr isotopic ratios of NIST 610 and MDC using 'line raster' sampling approach with the 193 nm laser (74 μm diameter). All data is normalised to NIST 610 reference material

Line number ID	$^{87}Rb/^{86}Sr$	2σ	$^{87}Sr/^{86}Sr$	2σ	Line number ID	$^{87}Rb/^{86}Sr$	2σ	$^{87}Sr/^{86}Sr$	2σ
MicaMgline-1	167.4	1.2	1.849	0.015	MDCline-1	40.98	0.15	1.0371	0.0051
MicaMgline-2	168.3	1.5	1.855	0.014	MDCline-2	40.26	0.19	1.0363	0.0053
MicaMgline-3	168.8	1.4	1.853	0.012	MDCline-3	40.44	0.15	1.0345	0.0056
MicaMgline-4	168.6	1.5	1.853	0.016	MDCline-4	40.12	0.2	1.0406	0.0052
MicaMgline-5	169.7	1.1	1.847	0.014	MDCline-5	39.93	0.19	1.032	0.007
MicaMgline-6	171.9	1.1	1.849	0.01	MDCline-6	40.35	0.2	1.0345	0.005
MicaMgline-7	168.9	1.2	1.852	0.012	MDCline-7	40.05	0.16	1.0274	0.0056
MicaMgline-8	173.4	1.3	1.841	0.011	MDCline-8	40.39	0.16	1.0327	0.0043
MicaMgline-9	171.9	1.3	1.855	0.012	MDCline-9	40.47	0.17	1.0401	0.0055
MicaMgline-10	172.4	1.2	1.86	0.013	MDCline-10	40.36	0.15	1.0313	0.005

Table 9 Rb-Sr ratios of NIST 610 analysed by the LA-ICP-MS/MS over multiple Sessions using the 193 nm laser systems and normalised to Mica Mg-NP reference material

Spot	$^{87}Rb/^{86}Sr$	2σ	$^{87}Sr/^{86}Sr$	2σ	Session	LA	spot	$^{87}Rb/^{86}Sr$	2σ	$^{87}Sr/^{86}Sr$	2σ	Session	LA
NIST610-1	1.9973	0.0054	0.7125	0.0014	Session 1	193 nm	NIST610-21	1.9649	0.0077	0.7095	0.0017	Session 2	193 nm
NIST610-2	1.9904	0.0049	0.7109	0.0012	Session 1	193 nm	NIST610-22	1.9595	0.0075	0.7089	0.0017	Session 2	193 nm
NIST610-3	2.0093	0.0051	0.7116	0.0012	Session 1	193 nm	NIST610-23	1.9677	0.0069	0.709	0.0015	Session 2	193 nm
NIST610-4	2.0005	0.0056	0.7113	0.0013	Session 1	193 nm	NIST610-24	1.9621	0.0078	0.7098	0.0023	Session 2	193 nm
NIST610-5	2.0149	0.0049	0.7112	0.0013	Session 1	193 nm	NIST610-25	1.9681	0.0078	0.7092	0.0018	Session 2	193 nm
NIST610-6	2.0064	0.0055	0.7126	0.0013	Session 1	193 nm	NIST610-26	1.9641	0.0076	0.7084	0.0017	Session 2	193 nm
NIST610-7	2.0293	0.0053	0.7106	0.0013	Session 1	193 nm	NIST610-27	1.973	0.0083	0.7095	0.0019	Session 2	193 nm
NIST610-8	2.025	0.0055	0.7116	0.0012	Session 1	193 nm	NIST610-28	1.9737	0.007	0.7091	0.0016	Session 2	193 nm
NIST610-9	2.0458	0.0054	0.7101	0.0013	Session 1	193 nm	NIST610-29	1.9777	0.008	0.7104	0.0021	Session 2	193 nm
NIST610-10	2.0304	0.0061	0.7113	0.0013	Session 1	193 nm	NIST610-30	1.9786	0.0073	0.7091	0.0018	Session 2	193 nm
NIST610-11	2.069	0.0061	0.7117	0.0013	Session 1	193 nm	NIST610-31	1.9829	0.0075	0.7087	0.0016	Session 2	193 nm
NIST610-12	2.0529	0.0058	0.7113	0.0014	Session 1	193 nm	NIST610-32	1.9732	0.008	0.7113	0.0037	Session 2	193 nm
NIST610-1	1.8944	0.0096	0.71	0.0022	Session 2	193 nm	NIST610-1	1.8711	0.007	0.7083	0.0021	Session 3	193 nm
NIST610-2	1.9021	0.0081	0.7085	0.002	Session 2	193 nm	NIST610-2	1.8687	0.0081	0.7087	0.0019	Session 3	193 nm
NIST610-3	1.9218	0.0084	0.7099	0.0019	Session 2	193 nm	NIST610-3	1.9346	0.0082	0.7085	0.0021	Session 3	193 nm
NIST610-4	1.9198	0.0078	0.7105	0.0019	Session 2	193 nm	NIST610-4	1.9261	0.0074	0.7092	0.0019	Session 3	193 nm
NIST610-5	1.9322	0.0085	0.7099	0.0024	Session 2	193 nm	NIST610-5	1.965	0.0074	0.7072	0.0017	Session 3	193 nm
NIST610-6	1.9303	0.0084	0.7118	0.0038	Session 2	193 nm	NIST610-6	1.9557	0.0087	0.7115	0.0038	Session 3	193 nm
NIST610-7	1.9405	0.0089	0.7094	0.0018	Session 2	193 nm	NIST610-7	1.9424	0.0078	0.707	0.0018	Session 3	193 nm
NIST610-8	1.9374	0.0085	0.7103	0.0016	Session 2	193 nm	NIST610-8	1.9397	0.0068	0.7088	0.0019	Session 3	193 nm
NIST610-9	1.9526	0.0071	0.7089	0.0017	Session 2	193 nm	NIST610-9	1.9593	0.0076	0.7078	0.0018	Session 3	193 nm
NIST610-10	1.9369	0.0078	0.7087	0.0018	Session 2	193 nm	NIST610-10	1.9561	0.0084	0.7082	0.0018	Session 3	193 nm
NIST610-11	1.9452	0.0083	0.7094	0.0016	Session 2	193 nm	NIST610-11	1.9951	0.0083	0.7071	0.0019	Session 3	193 nm
NIST610-12	1.9462	0.0077	0.7096	0.0018	Session 2	193 nm	NIST610-12	1.9844	0.0083	0.7085	0.002	Session 3	193 nm
NIST610-13	1.9558	0.0079	0.7088	0.0018	Session 2	193 nm	NIST610-13	1.9879	0.0087	0.7083	0.0019	Session 3	193 nm
NIST610-14	1.9487	0.0079	0.712	0.003	Session 2	193 nm	NIST610-14	1.9859	0.0079	0.7083	0.0019	Session 3	193 nm
NIST610-15	1.9607	0.0075	0.7085	0.0018	Session 2	193 nm	NIST610-15	1.9591	0.0088	0.7082	0.002	Session 3	193 nm
NIST610-16	1.9503	0.0081	0.7086	0.0018	Session 2	193 nm	NIST610-16	1.9647	0.0082	0.7089	0.0019	Session 3	193 nm
NIST610-17	1.964	0.0077	0.7082	0.0015	Session 2	193 nm	NIST610-17	1.9687	0.0074	0.7104	0.002	Session 3	193 nm
NIST610-18	1.959	0.0071	0.7091	0.0015	Session 2	193 nm	NIST610-18	1.9589	0.0074	0.7078	0.0019	Session 3	193 nm
NIST610-19	1.9601	0.0074	0.7099	0.0022	Session 2	193 nm	NIST610-1	1.9795	0.0061	0.7113	0.0014	Session 4	193 nm
NIST610-20	1.9552	0.0078	0.7095	0.002	Session 2	193 nm	NIST610-2	1.9773	0.0057	0.7115	0.0012	Session 4	193 nm
NIST610-3	1.991	0.006	0.7106	0.0013	Session 4	193 nm	NIST610-2	2.0247	0.0074	0.7085	0.0018	Session 5	193 nm
NIST610-4	1.9884	0.0058	0.7112	0.0013	Session 4	193 nm	NIST610-3	2.0453	0.0076	0.7096	0.0019	Session 5	193 nm
NIST610-5	1.9973	0.0059	0.7119	0.0012	Session 4	193 nm	NIST610-4	2.0304	0.0075	0.7095	0.0016	Session 5	193 nm
NIST610-6	1.9949	0.0061	0.7111	0.0015	Session 4	193 nm	NIST610-5	2.0385	0.0076	0.7093	0.0018	Session 5	193 nm
NIST610-7	2.0003	0.006	0.7106	0.0014	Session 4	193 nm	NIST610-6	2.0381	0.0074	0.7105	0.0016	Session 5	193 nm
NIST610-8	1.9946	0.0067	0.7116	0.0013	Session 4	193 nm	NIST610-7	2.0454	0.0075	0.7101	0.0018	Session 5	193 nm
NIST610-9	1.997	0.0062	0.7114	0.0015	Session 4	193 nm	NIST610-8	2.0363	0.0072	0.7115	0.0016	Session 5	193 nm
NIST610-10	1.9902	0.0064	0.7116	0.0013	Session 4	193 nm	NIST610-9	2.0502	0.0075	0.7099	0.0017	Session 5	193 nm
NIST610-11	1.9973	0.0065	0.7108	0.0014	Session 4	193 nm	NIST610-10	2.0475	0.0068	0.7103	0.0016	Session 5	193 nm
NIST610-12	1.9951	0.0067	0.7117	0.0015	Session 4	193 nm	NIST610-11	2.0482	0.0073	0.7087	0.0018	Session 5	193 nm
NIST610-13	1.9957	0.0071	0.7114	0.0014	Session 4	193 nm	NIST610-12	2.0451	0.0081	0.7099	0.0014	Session 5	193 nm
NIST610-14	1.9961	0.0059	0.71	0.0013	Session 4	193 nm	NIST610-13	2.0426	0.0066	0.7097	0.0017	Session 5	193 nm
NIST610-15	1.9968	0.0062	0.7107	0.0015	Session 4	193 nm	NIST610-14	2.0381	0.0073	0.7111	0.0015	Session 5	193 nm
NIST610-16	2.0011	0.0062	0.7106	0.0013	Session 4	193 nm	NIST610-15	2.0449	0.0071	0.7097	0.0017	Session 5	193 nm
NIST610-17	1.9924	0.0059	0.7115	0.0013	Session 4	193 nm	NIST610-16	2.0385	0.0069	0.7094	0.0017	Session 5	193 nm
NIST610-18	1.9896	0.0063	0.7102	0.0014	Session 4	193 nm	NIST610-17	2.0418	0.0078	0.7085	0.0018	Session 5	193 nm
NIST610-19	1.9957	0.0059	0.7115	0.0012	Session 4	193 nm	NIST610-18	2.0432	0.008	0.7105	0.0018	Session 5	193 nm
NIST610-20	1.9918	0.0058	0.7108	0.0014	Session 4	193 nm	NIST610-19	2.0327	0.0075	0.7102	0.0015	Session 5	193 nm
NIST610-21	1.996	0.0056	0.711	0.0013	Session 4	193 nm	NIST610-20	2.0324	0.0068	0.71	0.002	Session 5	193 nm
NIST610-22	1.9854	0.0067	0.7095	0.0013	Session 4	193 nm	NIST610-21	2.0323	0.0079	0.7106	0.0017	Session 5	193 nm
NIST610-23	1.9897	0.0066	0.7096	0.0013	Session 4	193 nm	NIST610-22	2.0374	0.007	0.7106	0.0017	Session 5	193 nm
NIST610-24	1.9796	0.0066	0.7111	0.0012	Session 4	193 nm	NIST610-23	2.0324	0.0077	0.7097	0.0018	Session 5	193 nm
NIST610-25	1.9921	0.0062	0.7114	0.0013	Session 4	193 nm	NIST610-24	2.0281	0.0081	0.7107	0.0018	Session 5	193 nm
NIST610-26	1.9843	0.0061	0.7103	0.0012	Session 4	193 nm	NIST610-25	1.9938	0.0074	0.7095	0.0018	Session 6	193 nm
NIST610-27	1.9867	0.0063	0.7097	0.0013	Session 4	193 nm	NIST610-1	1.9742	0.0063	0.7101	0.0015	Session 6	193 nm
NIST610-28	1.9859	0.0067	0.7107	0.0012	Session 4	193 nm	NIST610-2	2.03	0.0062	0.7109	0.0018	Session 6	193 nm
NIST610-29	1.9905	0.0065	0.7112	0.0014	Session 4	193 nm	NIST610-3	1.9942	0.0068	0.7112	0.0015	Session 6	193 nm
NIST610-30	1.9794	0.0062	0.711	0.0013	Session 4	193 nm	NIST610-4	2.0079	0.0058	0.7089	0.0012	Session 6	193 nm
NIST610-31	1.9835	0.0066	0.7099	0.0014	Session 4	193 nm	NIST610-5	2.0167	0.0067	0.7092	0.0017	Session 6	193 nm
NIST610-32	1.9706	0.0066	0.7106	0.0014	Session 4	193 nm	NIST610-6	2.0136	0.006	0.7086	0.0016	Session 6	193 nm

Table 9 (*Contd.*)

Spot	$^{87}Rb/^{86}Sr$	2σ	$^{87}Sr/^{86}Sr$	2σ	Session	LA	spot	$^{87}Rb/^{86}Sr$	2σ	$^{87}Sr/^{86}Sr$	2σ	Session	LA
NIST610-33	1.983	0.0068	0.71	0.0015	Session 4	193 nm	NIST610-7	1.9985	0.0056	0.7102	0.0015	Session 6	193 nm
NIST610-34	1.9818	0.0063	0.7109	0.0014	Session 4	193 nm	NIST610-8	2.0049	0.0061	0.709	0.0013	Session 6	193 nm
NIST610-1	2.0342	0.008	0.7107	0.0016	Session 5	193 nm	NIST610-9	2.0049	0.0066	0.71	0.0013	Session 6	193 nm
NIST610-10	2.0107	0.0058	0.7087	0.0014	Session 6	193 nm	NIST610-3	1.948	0.0055	0.7099	0.0019	Session 7	193 nm
NIST610-11	2.0148	0.0066	0.7117	0.0014	Session 6	193 nm	NIST610-4	1.9547	0.0055	0.7082	0.0017	Session 7	193 nm
NIST610-12	2.0112	0.0073	0.7105	0.0013	Session 6	193 nm	NIST610-5	1.9502	0.0055	0.7092	0.0017	Session 7	193 nm
NIST610-13	2.016	0.0064	0.7101	0.0012	Session 6	193 nm	NIST610-6	1.9429	0.0071	0.7077	0.002	Session 7	193 nm
NIST610-14	2.0016	0.0059	0.7105	0.0012	Session 6	193 nm	NIST610-7	1.9409	0.0043	0.7104	0.0019	Session 7	193 nm
NIST610-15	2.0066	0.0063	0.7107	0.0013	Session 6	193 nm	NIST610-8	1.9475	0.0058	0.7094	0.0019	Session 7	193 nm
NIST610-16	2.0032	0.0064	0.7093	0.0014	Session 6	193 nm	NIST610-9	1.9455	0.0078	0.7083	0.0016	Session 7	193 nm
NIST610-17	2.017	0.0065	0.7112	0.0014	Session 6	193 nm	NIST610-10	1.9384	0.0065	0.7085	0.0016	Session 7	193 nm
NIST610-18	2.0144	0.0064	0.7101	0.0015	Session 6	193 nm	NIST610-11	1.9533	0.0061	0.7097	0.0021	Session 7	193 nm
NIST610-19	2.0081	0.0066	0.7111	0.0015	Session 6	193 nm	NIST610-12	1.9436	0.0065	0.7097	0.0023	Session 7	193 nm
NIST610-20	2.0146	0.0073	0.7118	0.0013	Session 6	193 nm	NIST610-13	1.9329	0.0051	0.7089	0.0015	Session 7	193 nm
NIST610-21	2.0159	0.0073	0.7102	0.0014	Session 6	193 nm	NIST610-14	1.934	0.0055	0.7097	0.0021	Session 7	193 nm
NIST610-22	2.0093	0.0071	0.7104	0.0014	Session 6	193 nm	NIST610-15	1.9402	0.006	0.7087	0.002	Session 7	193 nm
NIST610-23	2.0145	0.0057	0.7098	0.0014	Session 6	193 nm	NIST610-16	1.9212	0.0058	0.71	0.002	Session 7	193 nm
NIST610-24	2.005	0.0066	0.7086	0.0015	Session 6	193 nm	NIST610-17	1.9356	0.0074	0.7087	0.0018	Session 7	193 nm
NIST610-25	2.0083	0.0068	0.7109	0.0013	Session 6	193 nm	NIST610-18	1.9445	0.0063	0.7095	0.002	Session 7	193 nm
NIST610-26	1.9999	0.0066	0.7109	0.0014	Session 6	193 nm	NIST610-19	1.9262	0.0063	0.7099	0.0013	Session 7	193 nm
NIST610-27	2.0088	0.0061	0.7115	0.0014	Session 6	193 nm	NIST610-20	1.9297	0.006	0.7076	0.0015	Session 7	193 nm
NIST610-28	2.0058	0.006	0.7095	0.0013	Session 6	193 nm	NIST610-21	1.9359	0.0049	0.7091	0.0016	Session 7	193 nm
NIST610-29	2.0107	0.0064	0.7096	0.0013	Session 6	193 nm	NIST610-22	1.9507	0.0073	0.707	0.0021	Session 7	193 nm
NIST610-30	2.0092	0.0061	0.7118	0.0014	Session 6	193 nm	NIST610-23	1.9368	0.0062	0.7092	0.0017	Session 7	193 nm
NIST610-31	2.0071	0.0067	0.7126	0.0014	Session 6	193 nm	NIST610-24	1.9367	0.0063	0.7098	0.0017	Session 7	193 nm
NIST610-32	2.0024	0.0071	0.7119	0.0013	Session 6	193 nm	NIST610-25	1.9459	0.0056	0.711	0.0015	Session 7	193 nm
NIST610-33	2.0045	0.0065	0.7109	0.0014	Session 6	193 nm	NIST610-26	1.9432	0.0054	0.709	0.0019	Session 7	193 nm
NIST610-34	2.0001	0.0057	0.7109	0.0013	Session 6	193 nm	NIST610-1	1.9786	0.0072	0.7102	0.0022	Session 8	193 nm
NIST610-35	2.0054	0.0061	0.7104	0.0014	Session 6	193 nm	NIST610-2	1.9866	0.0049	0.7087	0.002	Session 8	193 nm
NIST610-36	2.0001	0.0064	0.7091	0.0014	Session 6	193 nm	NIST610-3	2.0099	0.0076	0.7109	0.0027	Session 8	193 nm
NIST610-37	2.0011	0.0059	0.7118	0.0013	Session 6	193 nm	NIST610-4	2.0085	0.007	0.7101	0.0016	Session 8	193 nm
NIST610-38	1.9988	0.0071	0.7104	0.0013	Session 6	193 nm	NIST610-5	2.0018	0.0064	0.7083	0.002	Session 8	193 nm
NIST610-39	1.9904	0.0067	0.7093	0.0013	Session 6	193 nm	NIST610-6	2.0018	0.0058	0.7108	0.0019	Session 8	193 nm
NIST610-40	1.9909	0.0074	0.7097	0.0012	Session 6	193 nm	NIST610-7	2.0126	0.0078	0.7103	0.002	Session 8	193 nm
NIST610-1	1.9465	0.0066	0.7096	0.002	Session 7	193 nm	NIST610-8	2.0201	0.0071	0.7102	0.0021	Session 8	193 nm
NIST610-2	1.945	0.0059	0.71	0.0021	Session 7	193 nm	NIST610-9	2.0142	0.0061	0.7106	0.0016	Session 8	193 nm
NIST610-10	2.0224	0.0065	0.7094	0.0021	Session 8	193 nm	NIST610-19	1.9985	0.0062	0.7105	0.0016	Session 8	193 nm
NIST610-11	2.0051	0.0071	0.7071	0.0025	Session 8	193 nm	NIST610-20	2.0036	0.0066	0.7102	0.0018	Session 8	193 nm
NIST610-12	2.0153	0.0077	0.7122	0.002	Session 8	193 nm	NIST610-21	2.007	0.0062	0.7088	0.0014	Session 8	193 nm
NIST610-13	2.003	0.0069	0.7089	0.0018	Session 8	193 nm	NIST610-22	2.0076	0.0082	0.7103	0.0019	Session 8	193 nm
NIST610-14	2.0097	0.0063	0.7134	0.0018	Session 8	193 nm	NIST610-23	2.0016	0.0062	0.71	0.0019	Session 8	193 nm
NIST610-15	2.0163	0.0067	0.711	0.002	Session 8	193 nm	NIST610-24	2.0066	0.0064	0.711	0.0019	Session 8	193 nm
NIST610-16	2.0033	0.0057	0.7101	0.0018	Session 8	193 nm	NIST610-25	2.0104	0.0071	0.7102	0.0023	Session 8	193 nm
NIST610-17	2.0035	0.0078	0.7093	0.0019	Session 8	193 nm	NIST610-26	2.0082	0.0073	0.7091	0.0021	Session 8	193 nm
NIST610-18	2.0134	0.0078	0.7107	0.002	Session 8	193 nm							

Conflicts of interest

There are no conflicts of interest to declare.

Acknowledgements

This research was funded *via* the Australian Research Council – ARC Linkage grant LP160101353, and the Mineral Exploration Cooperative Research Centre (MinEx CRC Project 8). Additional financial support was received from Agilent Technologies and the technical assistance of Fred Fryer (Agilent) is also gratefully acknowledged. We also thank Carl Spandler and the three anonymous reviewers for revising the manuscript and for their constructive feedback. Finally, we thank David Bruce for his assistance in analysing the Sr isotope compositions of MDC phlogopite samples by TIMS at the Metal Isotope Group (MIG) facilities at the Department of Earth Sciences, University of Adelaide. This is a MinEx CRC contribution No. 2020/6.

References

1 R. Page, *J. Geol. Soc. Aust.*, 1978, **25**, 141–164.
2 Y. Terakado and S. Nohda, *Chem. Geol.*, 1993, **109**, 69–87.

3 L. E. Nyquist, C.-Y. Shih, F. M. McCubbin, A. R. Santos, C. K. Shearer, Z. X. Peng, P. V. Burger and C. B. Agee, *Meteorit. Planet. Sci.*, 2016, **51**, 483–498.
4 I. M. Villa, P. De Bièvre, N. E. Holden and P. R. Renne, *Geochim. Cosmochim. Acta*, 2015, **164**, 382–385.
5 Y.-h. Yang, H.-f. Zhang, Z.-y. Chu, L.-w. Xie and F.-y. Wu, *Int. J. Mass Spectrom.*, 2010, **290**, 120–126.
6 A. Beranoaguirre, C. Pin, M. E. Sanchez-Lorda, S. García de Madinabeitia and J. I. Gil Ibarguchi, *Int. J. Mass Spectrom.*, 2019, **435**, 234–240.
7 S. i. Nakai, A. N. Halliday, S. E. Kesler, H. D. Jones, J. R. Kyle and T. E. Lane, *Geochim. Cosmochim. Acta*, 1993, **57**, 417–427.
8 D. B. Ward and M. Bell, *Anal. Chim. Acta*, 1990, **229**, 157–162.
9 O. Nebel, in *Encyclopedia of Scientific Dating Methods*, ed. W. Jack Rink and J. W. Thompson, Springer, Netherlands, Dordrecht, 2015, pp. 686–698, DOI: 10.1007/978-94-007-6304-3_116.
10 E. Bolea-Fernandez, S. J. M. Van Malderen, L. Balcaen, M. Resano and F. Vanhaecke, *J. Anal. At. Spectrom.*, 2016, **31**, 464–472.
11 T. Zack and K. J. Hogmalm, *Chem. Geol.*, 2016, **437**, 120–133.
12 K. J. Hogmalm, T. Zack, A. K. O. Karlsson, A. S. L. Sjöqvist and D. Garbe-Schönberg, *J. Anal. At. Spectrom.*, 2017, **32**, 305–313.
13 C. G. Eiden, J. C. Barinaga and W. D. Koppenaal, *J. Anal. At. Spectrom.*, 1999, **14**, 1129–1132.
14 E. Bolea-Fernandez, L. Balcaen, M. Resano and F. Vanhaecke, *J. Anal. At. Spectrom.*, 2015, **31**, 303–310.
15 S. D. Tanner, V. I. Baranov and D. R. Bandura, in *Plasma Source Mass Spectrometry: The New Millennium*, ed. S. D. Tanner and G. Holland, The Royal Society of Chemistry, 2001, pp. 97–98, DOI: 10.1039/9781847551696-00097.
16 D. K. Bohme, *M^+ Chemistry*, http://www.yorku.ca/dkbohme/research/selection_table.html, accessed 02 September, 2020.
17 L. Gorojovsky and O. Alard, *J. Anal. At. Spectrom.*, 2020, **35**(10), 2322–2336.
18 M. Tillberg, H. Drake, T. Zack, J. Hogmalm and M. Åström, *Procedia Earth Planet. Sci.*, 2017, **17**, 464–467.
19 M. Tillberg, H. Drake, T. Zack, E. Kooijman, M. J. Whitehouse and M. E. Åström, *Sci. Rep.*, 2020, **10**, 1–13.
20 S.-S. Li, M. Santosh, J. Farkas, A. Redaa, S. Ganguly, S. W. Kim, C. Zhang, S. Gilbert and T. Zack, *Precambrian Res.*, 2020, **343**, 105709.
21 S. E. Armistead, A. S. Collins, A. Redaa, G. Jepson, J. Gillespie, S. Gilbert, M. L. Blades, J. D. Foden and T. Razakamanana, *J. Geol. Soc.*, 2020, **177**, 784–798.
22 P. Outridge, W. Doherty and D. Gregoire, *Spectrochim. Acta, Part B*, 1997, **52**, 2093–2102.
23 F. Claverie, B. Fernández, C. Pécheyran, J. Alexis and O. F. Donard, *J. Anal. At. Spectrom.*, 2009, **24**, 891–902.
24 S. Zhang, M. He, Z. Yin, E. Zhu, W. Hang and B. Huang, *J. Anal. At. Spectrom.*, 2016, **31**, 358–382.
25 I. Rodushkin, M. D. Axelsson, D. Malinovsky and D. C. Baxter, *J. Anal. At. Spectrom.*, 2002, **17**, 1231–1239.
26 P. Sylvester, in *Laser ablation ICP-MS in the earth sciences: Current practices and outstanding issues*, Mineralogical Association of Canada, 2008, vol. 40, pp. 67–78.
27 C. Agatemor and D. Beauchemin, *Anal. Chim. Acta*, 2011, **706**, 66–83.
28 B. J. Fryer, S. E. Jackson and H. P. Longerich, *Can. Mineral.*, 1995, **33**, 303–312.
29 S. E. Jackson and D. Günther, *J. Anal. At. Spectrom.*, 2003, **18**, 205–212.
30 S. E. Jackson and P. Sylvester, *Signal*, 2008, **10**, 100.
31 A. J. G. Mank and P. R. D. Mason, *J. Anal. At. Spectrom.*, 1999, **14**, 1143–1153.
32 M. Guillong and D. Günther, *J. Anal. At. Spectrom.*, 2002, **17**, 831–837.
33 N. Miliszkiewicz, S. Walas and A. Tobiasz, *J. Anal. At. Spectrom.*, 2015, **30**, 327–338.
34 K. Govindaraju, *Geostand. Geoanal. Res.*, 1979, **3**, 3–24.
35 K. Govindaraju, *Geostand. Newsl.*, 1994, **18**, 1–158.
36 J. D. Woodhead and J. M. Hergt, *Geostand. Newsl.*, 2001, **25**, 261–266.
37 D. Garbe-Schönberg and S. Müller, *J. Anal. At. Spectrom.*, 2014, **29**, 990–1000.
38 M. Elburg, P. Vroon, B. van der Wagt and A. Tchalikian, *Chem. Geol.*, 2005, **223**, 196–207.
39 Y. Shao, J. Farkaš, C. Holmden, L. Mosley, I. Kell-Duivestein, C. Izzo, P. Reis-Santos, J. Tyler, P. Törber and J. Frýda, *Geochim. Cosmochim. Acta*, 2018, **239**, 90–108.
40 A. O. Nier, *Phys. Rev.*, 1938, **54**, 275.
41 Z. Hu, S. Gao, Y. Liu, S. Hu, H. Chen and H. Yuan, *J. Anal. At. Spectrom.*, 2008, **23**, 1093–1101.
42 C. Paton, J. Hellstrom, B. Paul, J. Woodhead and J. Hergt, *J. Anal. At. Spectrom.*, 2011, **26**, 2508–2518.
43 K. Rosman and P. Taylor, *Pure Appl. Chem.*, 1999, **71**, 1593–1607.
44 P. Vermeesch, *Geosci. Front.*, 2018, **9**, 1479–1493.
45 J. Košler, M. Wiedenbeck, R. Wirth, J. Hovorka, P. Sylvester and J. Míková, *J. Anal. At. Spectrom.*, 2005, **20**, 402–409.
46 S. M. Eggins, L. P. J. Kinsley and J. M. G. Shelley, *Appl. Surf. Sci.*, 1998, **127–129**, 278–286.
47 H.-R. Kuhn and D. Günther, *J. Anal. At. Spectrom.*, 2004, **19**, 1158–1164.
48 P. Weis, H. P. Beck and D. Günther, *Anal. Bioanal. Chem.*, 2005, **381**, 212–224.
49 Z. Wang, B. Hattendorf and D. Günther, *J. Am. Soc. Mass Spectrom.*, 2006, **17**, 641–651.
50 S. E. Gilbert, L. V. Danyushevsky, K. Goemann and D. Death, *J. Anal. At. Spectrom.*, 2014, **29**, 1024–1033.
51 G. Morteani, Y. Kostitsyn, H. Gilg, C. Preinfalk and T. Razakamanana, *Int. J. Earth Sci.*, 2013, **102**, 627–645.

Journal of Asian Earth Sciences 224 (2022) 105037

Contents lists available at ScienceDirect

Journal of Asian Earth Sciences

journal homepage: www.elsevier.com/locate/jseaes

Constraints from *in-situ* Rb-Sr dating on the timing of tectono-thermal events in the Umm Farwah shear zone and associated Cu-Au mineralisation in the Southern Arabian Shield, Saudi Arabia

Ahmad Redaa [a,b,*], Juraj Farkaš [a], Ahmed Hassan [b,c], Alan S. Collins [a], Sarah Gilbert [d], Stefan C. Löhr [e]

[a] Department of Earth Sciences and Metal Isotope Group (MIG), University of Adelaide, Adelaide, Australia
[b] Faculty of Earth Sciences, King Abdulaziz University, Jeddah, Saudi Arabia
[c] Department of Geology, Faculty of Science, Helwan University, Cairo, Egypt
[d] Adelaide Microscopy, University of Adelaide, Australia
[e] Department of Earth and Environmental Sciences, Macquarie University, Sydney, Australia

ARTICLE INFO

Keywords:
In-situ Rb-Sr
Arabian shield
Ablah
Umm Farwah shear zone
Rb-Sr dating
Cu-Au mineralisation
ICP-MS/MS

ABSTRACT

Constraining the tectonic history and timing of major shear zone structures in the Arabian Shield is critical for better understanding of the origin, tectonic history and distribution of ore deposits within this Precambrian crystalline crustal block. Here, we used a novel *in-situ* Rb-Sr dating of micas and K-feldspar to constrain the age of the Umm Farwah Shear Zone, which represents a regional tectonic feature that extends about 200 km across the southern part of the Arabian Shield. We also constrain the timing of Mount Ablah mineralisations which are exposed within the Umm Farwah Shear Zone and contains two styles of mineralisations including a greisen and Cu-Au mineralisation. These ore deposits are hosted in a pegmatite body that formed during the development of the Umm Farwah Shear Zone. Two main groups of muscovite (i.e., Group I and Group II) and K-feldspar mineral phases were identified based on ages and elemental variations in the mineralised zone and the host rocks. Results of *in-situ* Rb-Sr dating in the above K-rich minerals show that the Umm Farwah Shear Zone was initiated at ca. 651 Ma, and the emplacement of the Mount Ablah pegmatite occurred between 626 and 611 Ma, followed by the formation of greisen at 601 ± 12 Ma. *In-situ* Rb–Sr data also highlight a younger 'alteration' event occurred at ca. 556 ± 23 Ma, which partially reset the Rb–Sr system in the pegmatite and may thus reflect hydrothermal circulation event or overprint due to formation of Cu-Au mineralisation.

1. Introduction

The Mount Ablah area comprises a pegmatite body composed of orthoclase and quartz, with quartz veins and breccia-associated Cu-Au mineralisation, which is located to the north of the Ablah graben on the western part of Asir terrane in the Arabian Shield (Fig. 1). The Proterozoic basement of Saudi Arabia forms the eastern part of the, largely juvenile, Arabian-Nubian Shield. It is exposed in the western part of the Arabian Peninsula and has been affected by accretionary and collisional orogenesis associated with subduction of the Neoproterozoic Mozambique Ocean (Collins et al., 2021a) and the amalgamation of central Gondwana (Collins et al., 2021b; Collins and Pisarevsky, 2005; Stern, 2002; Stoeser and Frost, 2006).

Voluminous magmatism occurred throughout the Neoproterozoic and into the Cambrian but was particularly extensive between 870 and 540 Ma (Robinson et al., 2015). The later, post-orogenic, intrusions contain many alkali plutons that are known sources of critical minerals and metals such as Sn, W, Mo, Nb, rare-earth elements (REE), Y and Be, and other base and precious metals (Cu, Zn, Au). Thus far, over 400 individual occurrences of these precious metals and critical mineral commodities were identified in association with felsic intrusions in the Arabian Shield (Agar, 1992; Johnson, 2006; Marzouki et al., 1982; Nehlig et al., 1999). The high fluid/rock ratio associated with these felsic intrusions, and subsequent hydrothermal alterations, could be a key factor for several mineralisation types and can be used as an exploration guide for hydrothermal mineralisation in the surrounding

* Corresponding author at: Department of Earth Sciences and Metal Isotope Group (MIG), University of Adelaide, Adelaide, Australia.
E-mail addresses: ahmad.redaa@adelaide.edu.au, areda@kau.edu.sa (A. Redaa).

https://doi.org/10.1016/j.jseaes.2021.105037
Received 8 June 2021; Received in revised form 21 November 2021; Accepted 2 December 2021
Available online 6 December 2021

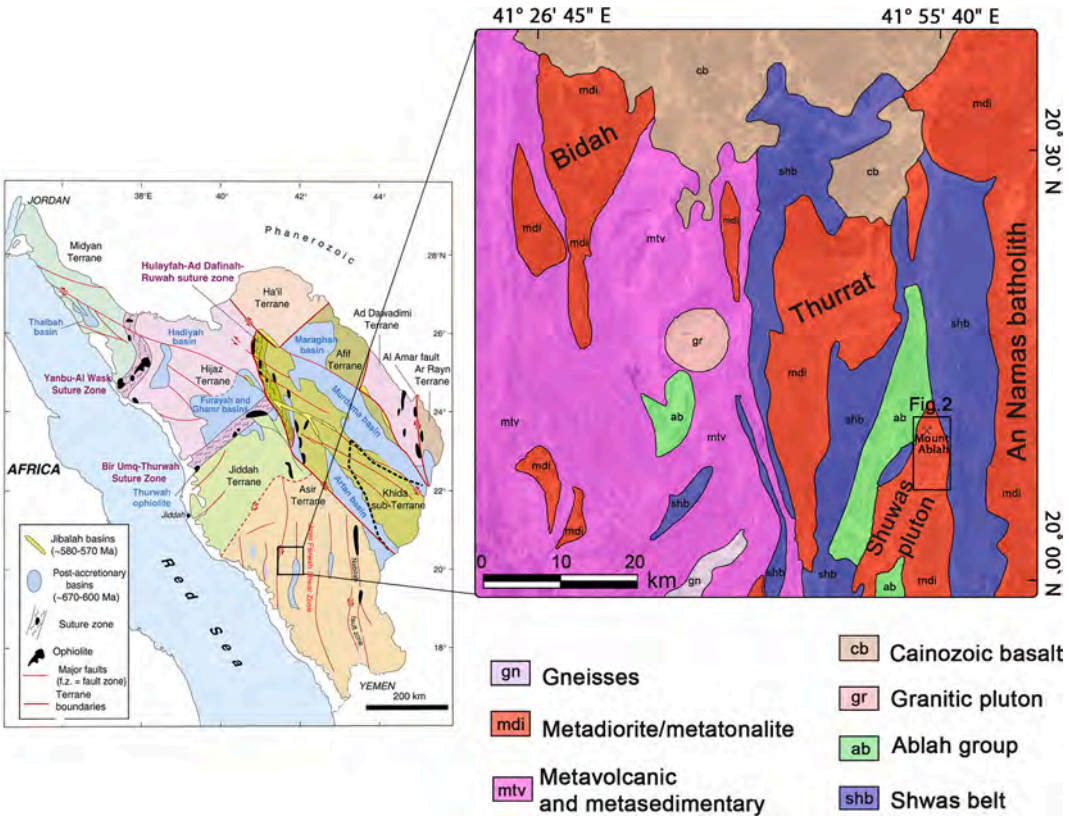

Fig. 1. Regional Geological map shows main geological units in the study area (modified after Marzouki et al. (1982)). The location map shows the major tectonic terranes and the suture zones in the Arabian Shield (modified after Stern and Johnson, 2010).

areas. Circulating fluids along faults and shear zones within pre-existing rocks can enhance mineral dissolution, element transport, mineral precipitation and rock deformation, depending on the temporal and spatial variations in temperature, pressure and element activities (Ahmed and Surour, 2016). Thus, understanding the evolution and timing of these felsic intrusions is important to understand the origin, genesis and spatial distribution of the above metal commodities in the Arabian Shield, which in turn will be beneficial for future exploration of these critical resources.

The Rb-Sr isotope system can be used to date the timing and temporal relation between the felsic intrusions and associated mineralisations because the latter commonly contain K- and Rb-rich minerals such as micas and feldspars. The recent development of novel *in-situ* Rb-Sr dating by a laser ablation (LA) coupled with an inductively coupled plasma - tandem mass spectrometer (ICP-MS/MS) offers a rapid and cost-efficient dating approach for K- and Rb-rich silicate minerals (Hogmalm et al., 2017). Although a more established laser-based U-Pb dating can be used as well to constrain the timing of mineralisation, certain limitations of the latter technique make the Rb-Sr method preferable. Specifically, the accessory minerals with high U to Pb ratios such as zircon and monazite could be rare in the quartz veins and associated alterations because these minerals have a closure temperature of Pb diffusion > 800 °C (Cherniak and Watson, 2001; McFarlane and Mark Harrison, 2006). In contrast, apatite that is a common accessory phase in mineralised and hydrothermal systems can be however easily reset during the hydrothermal events (Kirkland et al., 2018) which makes the age constrain via U-Pb dating of apatite problematic. Thus, this study focuses on novel *in-situ* Rb-Sr dating of abundant and K and Rb-rich silicate minerals such as micas and feldspars in a hydrothermal system.

In the present work, we investigate the temporal relation between Umm Farwah major Shear zone and Ablah mineralisations by constraining the paragenetic sequence and timing of felsic intrusions, the greisen and the Cu-Au mineralisation in the Shuwas pluton via *in-situ* Rb–Sr dating of K-rich minerals such as micas and feldspar. These enabled age dating of both the country rocks (i.e., metadiorite) and the mineralisation zone (i.e., pegmatite, quartz-vein related alteration zone and greisen) using the LA-ICP-MS/MS. As the Ablah Cu-Au mineralisation is located within a major structure in the southern part of the Arabian Shield, this work provides new information about the timing and nature of geological events associated with deformation in this area. Following other recent pioneering studies that used LA-ICP-MS/MS approach for dating of mineral systems and metallogenesis (Olierook et al., 2020; Şengün et al., 2019; Tillberg et al., 2020), this work demonstrates the advantage of this novel and rapid *in-situ* Rb–Sr dating by LA-ICP-MS/MS to better constrain the timing, and thus plausible genetic models, for economic mineralisation in the Arabian Shield, with implications for future and improved exploration strategies (Armistead et al., 2020; Hogmalm et al., 2017; Redaa et al., 2021; Shanshan et al., 2020).

2. Geological background

The tectono-thermal evolution of the Saudi part of the Arabian-Nubian Shield occurred mainly in the Neoproterozoic, between ca. 870–540 Ma, in three main stages, including: (1) the formation of island arcs mostly at the floor of Mozambique Ocean, (2) the collision and accretion of these arcs with each other and with pre-existing continental fragments during the closure of the Mozambique Ocean and the subsequent collision of Neoproterozoic India with these terranes to form this part of Gondwana, and (3) the formation and the development of terrestrial and marine post-amalgamation basins, associated with post-accretion magmatism (Collins et al., 2021a; Johnson and Woldehaimanot, 2003; Merdith et al., 2021; Nettle et al., 2014; Robinson et al., 2015, 2014; Stern and Johnson, 2010; Stoeser and Frost, 2006). Although, recently it has been suggested that the margins of the Arabian-Nubian Shield extend to include Tonian rocks in Oman, Pakistan and NW India (Alessio et al., 2018; Blades et al., 2020; Collins et al., 2021a), as

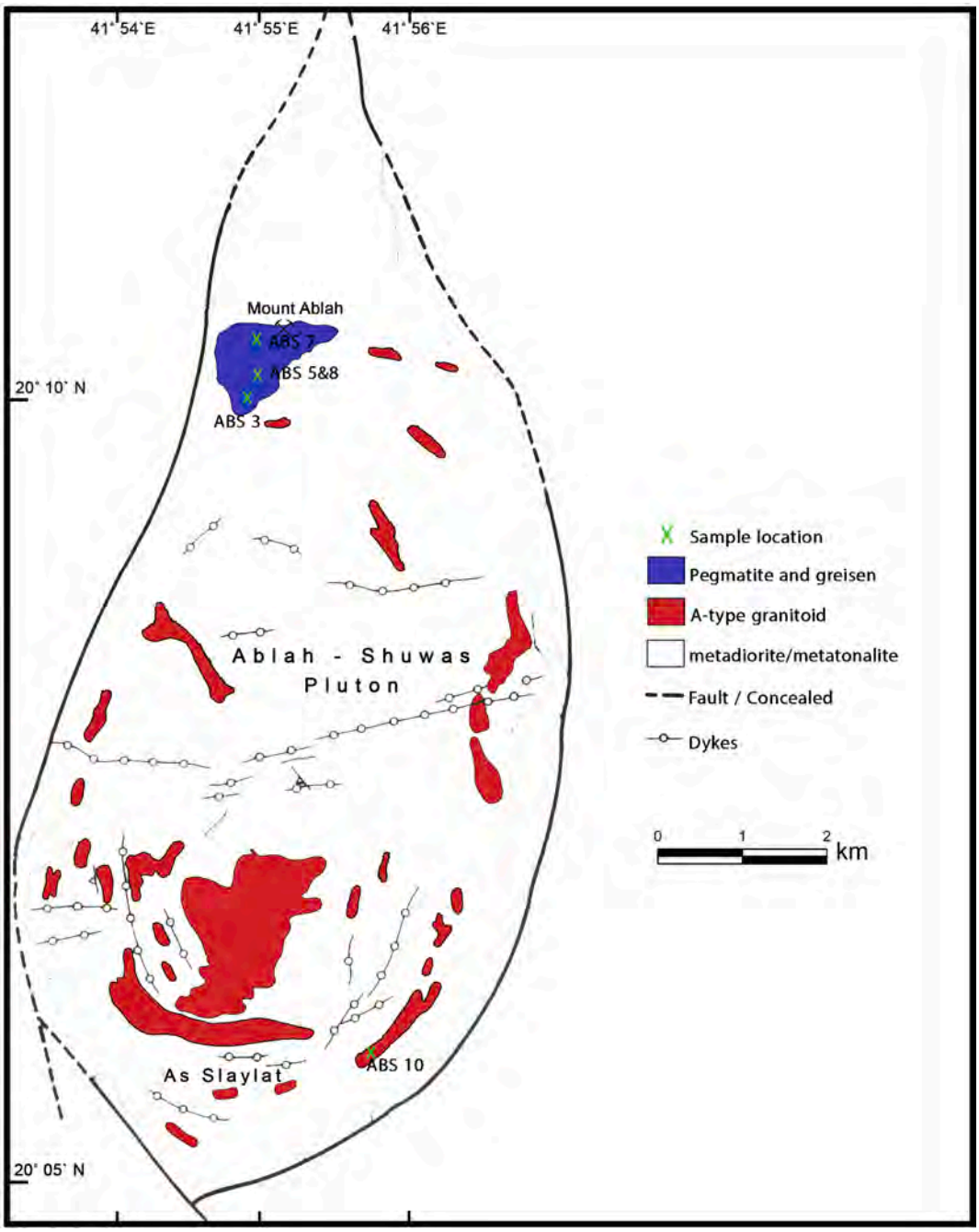

Fig. 2. Geological map of Shuwas pluton showing the main geological units in the study area, and sampling locations (modified after Moufti (2001)).

well as Stenian and Tonian juvenile rocks beneath the Sahara of Chad and Sudan (Blades et al., 2021; Şengör et al., 2020). In Saudi Arabia, the development of the Arabian Shield was accompanied by several magmatic and predominantly felsic intrusion events that ranged in composition from I–S to A-type granites, but included also mafic and tholeiite-like magmatic products (Robinson et al., 2015). These intrusion events form four temporal groups, based on their crystallisation ages. These are (1) intrusions associated with island arcs (ca. 845 Ma), (2) *syn*-collisional intrusions (ca. 710 Ma), (3) post-tectonic intrusions (ca. 620 Ma), and (4) anorogenic intrusions (>600 Ma) (Robinson et al., 2015, 2014). Each of these intrusion events was formed due to different magmatism and igneous processes, where those that occurred during the subduction and amalgamation (between ca. 845–600 Ma) involve contaminated MORB-/arc-tholeiite-like magmatic products (Robinson et al., 2015), while the younger and post-tectonic magmatism are characterized by tonalite-trondhjemite-granodiorite (TTG) and granite (monzogranite, syenogranite). Finally, the anorogenic magmatism is dominated by alkali-feldspar and alkali granite (Johnson et al., 2011). These different magmatic products indicate changing sources of magma beneath the Arabian Shield, ranging from depleted mantle to a more enriched source with limited crust–mantle interaction, the latter are more dominant from ca. 600 Ma due to the change of tectonic settings and processes (Robinson et al., 2015, 2014).

The copper–gold mineralisation in the Ablah area is hosted in essentially pegmatite that intrudes metadiorite/metatonalite, which forms a part of the Shuwas pluton (Moufti, 2001) (Fig. 1). The age of the Shuwas pluton has not been investigated directly but has been estimated by correlating the pluton with other equivalent units including Dhuqiyah igneous complex, and Buwwah suite, which includes Dhara, Bidah, Tharad/Thurrat plutons, as well as Baljurashi and Al Bayda

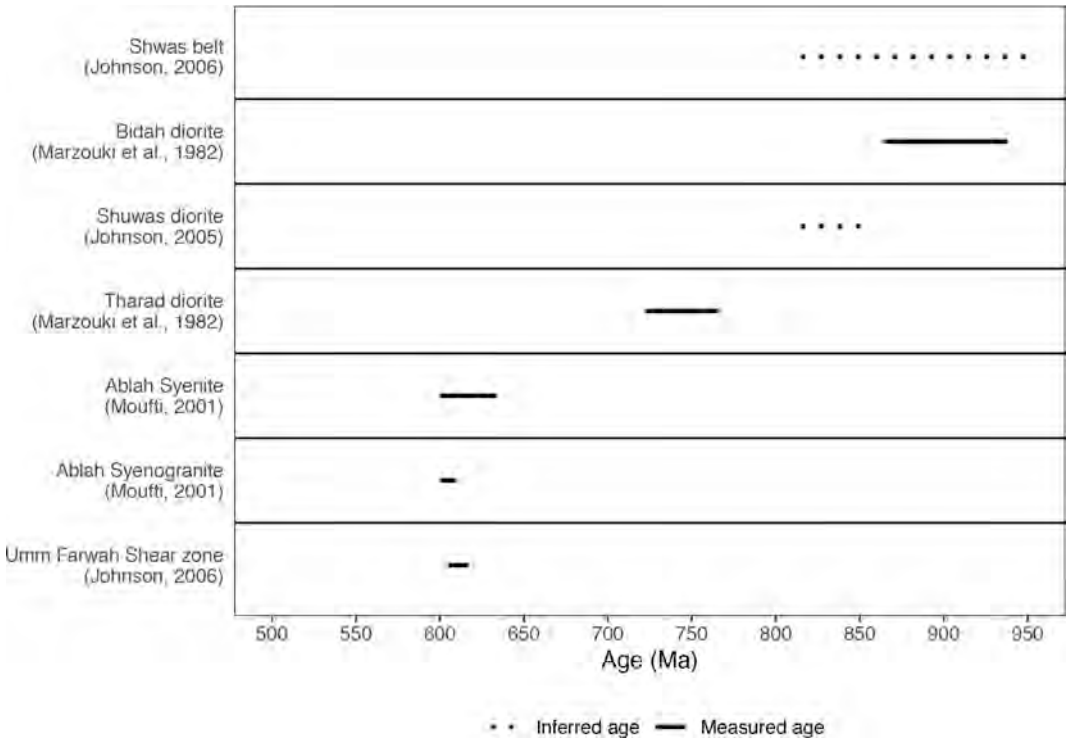

Fig. 3. The published ages for the main unites and events in Mount Ablah area.

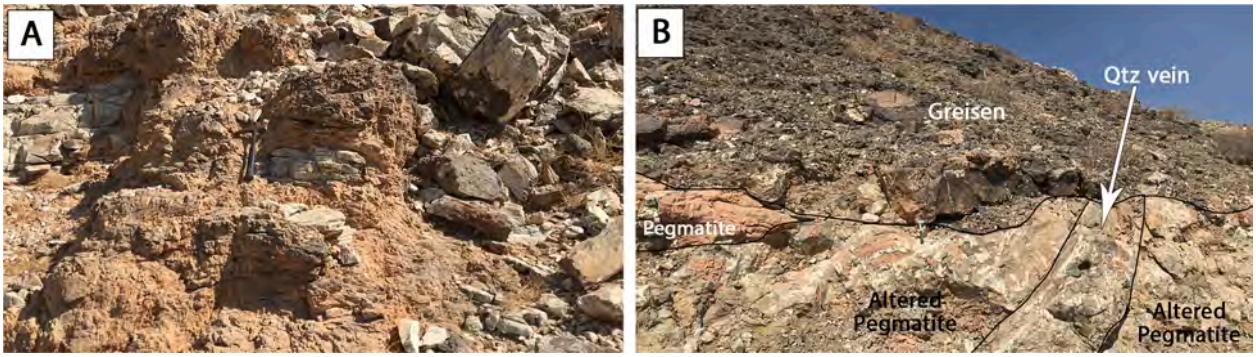

Fig. 4. Field photograph show (A) the brecciated quartz and feldspar in Mount Ablah, and (B) shows the field relation between pegmatite, quartz vein, altered pegmatite that hosted the Cu-Au mineralisation, and greisen.

batholiths (Johnson, 2006, 2005 and references therein). There is a considerable variability in reported crystallisation ages of these rocks, but the most reliable ages suggest the emplacement of Buwwah suite between 855 Ma and 815 Ma (see Fig. 3, and Johnson (2005) and references therein). The Shuwas pluton intrudes the Qirsha and Khutnah formations (known also as Shwas belt (Johnson, 2006) and Jiddah group (Greenwood, 1975)) that formed as an intra-oceanic island arc volcanosedimentary unit (Fig. 1). The formations (Shwas belt) include sheared and altered volcanic flows and pyroclastic rocks that have tholeiitic and calc-alkalic compositions (Moufti, 2001 and references therein). Their age was estimated using a Rb–Sr errorchron at 721 ± 55 Ma (Bokhari and Kramers, 1981). This age overlaps the reported age for Tharad pluton 744 ± 22 Ma (Marzouki et al., 1982) that is located to the northwest of the formations (Fig. 1). However, Johnson (2006) argued that the age of the Shwas belt should be older than 815 Ma (Fig. 3) relying on the contact between the formations and the An Namas batholith (Fig. 1) as the latter was dated using Rb–Sr whole rock at 837 ± 55 Ma (Johnson, 2006 and references therein).

The Umm Farwah reginal Shear Zone extends ~200 km N–S across the Asir terrane (Fig. 1). It deformed both the Shwas belt and the metadiorite/metatonalite igneous complexes that intrude the belt. The shear zone and the metadiorite/metatonalite are intruded by A-type granitoid bodies (syenite and syenogranite) and several aplitic dykes that may have intruded during deformation (Moufti, 2001) (Fig. 2). The syenite and the syenogranite were dated previously by the whole-rock Rb–Sr approach that yielded isochron ages of 617 ± 17 Ma and 605 ± 5 Ma (Fig. 3) with relatively low initial $^{87}Sr/^{86}Sr$ ratios of 0.7035 and 0.7038, respectively (Moufti, 2001). Based on these ages, Johnson et al. (2006) suggested that the brittle-ductile deformation of the Umm Farwah shear zone occurred as late as 605 Ma (Fig. 3).

In addition to the syenite and the syenogranite, a pegmatitic unit (known as Mount Ablah) intruded the metadiorite/metatonalite exposed in the north-western part of the Shuwas pluton (Fig. 2). Mount Ablah consists of pegmatitic feldspar and quartz that is highly brecciated (Fig. 4A) and cross-cut by several quartz veins which are surrounded by sericitized alteration zones (Fig. 4B). It is also capped with a greisen deposit that presents as a massive muscovite-fluorite body (Fig. 4B) (Jackson, 1986; Salimo, 2015). Mount Ablah has been historically

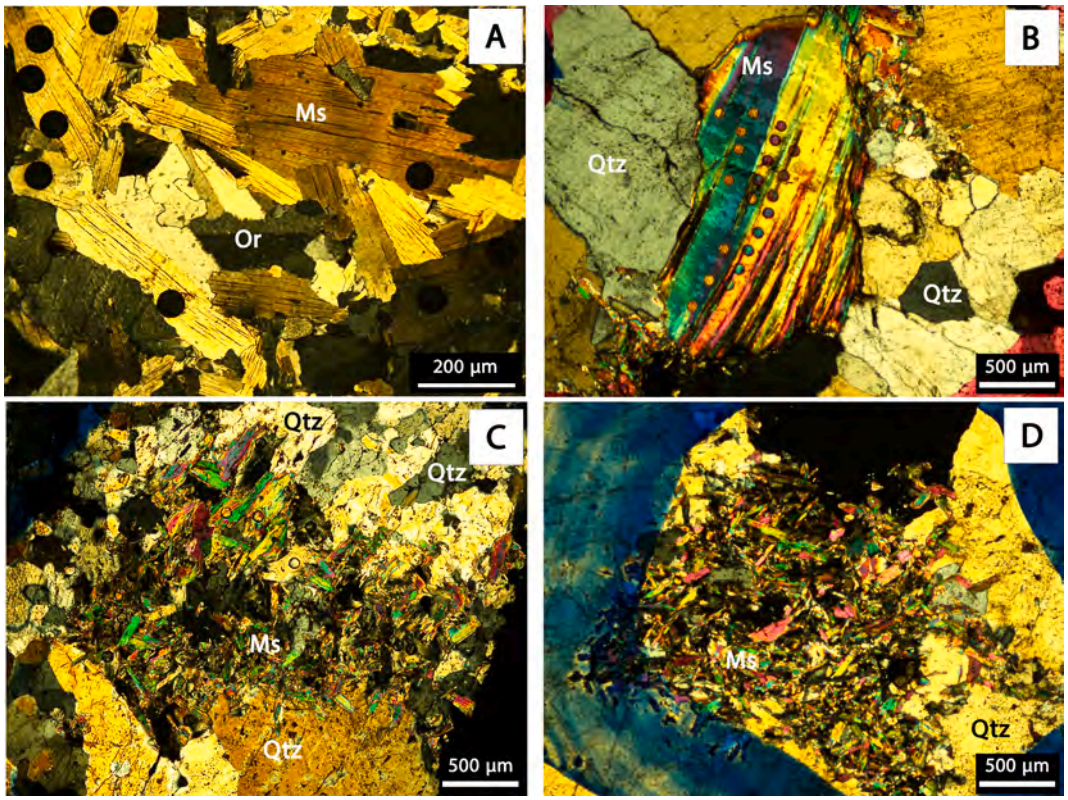

Fig. 5. Photomicrographs of partially altered pegmatite showing the different muscovite phases: (A-B) Large crystals of the primary muscovite (Ms, Group I), quartz (Qtz) and orthoclase (Or) and (C-D) the muscovite cluster (Ms, Group II) formed after orthoclase and concentrated around the quartz vein (Qtz). The small/black circles are the inherited pits of the laser ablation during the in-situ analysis by the LA-ICP-MS/MS.

exploited for copper and gold, and although it also contains appreciable Nb, Zr, REE, F and other precious metals, these have not been exploited to date (Jackson, 1986). Several exploratory boreholes were drilled in the area by the Saudi Arabian Mining Company (Ma'aden), that yielded gold grades that ranged between 0.37 and 25.37 g/t, with highest gold grades concentrated around the brecciated quartz veins in the alteration zone (Salimo, 2015).

3. Methodology

3.1. Sample selection and preparation

Representative samples of metadiorite (ABS 13), syenogranite (ABS 10), partially altered pegmatite (ABS 5 and ABS 8), altered pegmatite (ABS 3), and greisen (ABS 7) were collected from the Shuwas Pluton and Mount Ablah area. The samples were analysed *in-situ* for major element and Rb–Sr dating to investigate the ages and temporal evolution of the Mount Ablah Cu-Au mineralisation with respect to the crystallisation ages of the host rocks (i.e., Shuwas pluton).

The metadiorite sample (ABS 13) was collected from the depth of 28.77 m from a core (No. ABD 4), which was drilled by Ma'aden company on the foothill of Mount Ablah. The sample was mounted in the epoxy resin, then polished for *in-situ* Rb–Sr analysis by the LA-ICP-MS/MS. Sample ABS 10 was collected from a surface outcrop of syenogranite that intruded into the metadiorite/metatonalite of the Shuwas pluton and is exposed at 20° 05′ 58.17″ N and 041° 55′ 42.01″ E. (Fig. 2). Feldspars were separated from this sample (ABS 10), mounted, and polished for Rb–Sr analysis by the LA-ICP-MS/MS. Four samples (ABS 3, ABS 5, ABS 7 and ABS 8) were acquired from the Mount Ablah outcrop, and their locations are illustrated in Fig. 2. The partially altered pegmatite samples (ABS 5 and ABS 8) were acquired from the Ablah pegmatite within a few meters of the alteration zone to investigate the effect of the quartz veinlet generating hydrothermal system on the samples. ABS 3 was collected from the alteration zone in pegmatite around the quartz veinlets/pipe. Finally, ABS 7 was extracted from the greisen that forms the top of the pegmatite system. These samples (ABS 3, ABS 5, ABS 7 and ABS 8) were prepared as thin-polished sections to be analysed for major elements by a scanning electron microscope (SEM), and for the *in-situ* Rb–Sr dating on the LA-ICP-MS/MS.

3.2. Petrography and mineral mapping

The partially altered pegmatite (ABS 5 and ABS 8), altered pegmatite (ABS 3), and the greisen (ABS 7) samples were investigated using a petrographic microscope at the University of Adelaide to identify major rock forming K-bearing minerals such as micas and feldspars. Thin-sections were inspected before and after the *in-situ* Rb–Sr analysis by LA-ICP MS/MS to record the ablated spot positions for each mineral phase. In addition, sample ABS 5 was chosen for quantitative mineral mapping to characterise the main K-bearing minerals in this sample, using an FEI Teneo LoVac field emission scanning electron microscope (SEM) equipped with dual Bruker XFlash Series 6 energy dispersive X-ray spectroscopy (EDS) detectors at Macquarie University to better characterise the main K-bearing minerals in this sample. High-resolution BSE images and mineral maps of several regions of interest were collected at 10 mm working distance and 15 kV accelerating voltage. BSE image tile sets (100 nm pixel resolution) and EDS spectra (1.5 µm step size, 8 ms acquisition time) for mineral mapping were collected sequentially using the FEI Maps Mineralogy software, followed by classification of the individual EDS spectra using the FEI Nanomin software (Rafiei et al., 2020). Further elemental mapping and semi-quantitative major element fingerprinting of distinct muscovite classes in samples ABS 3, ABS 7 and ABS 8 were achieved using an FEI Quanta 450 high-resolution field emission SEM equipped with EDS detector at

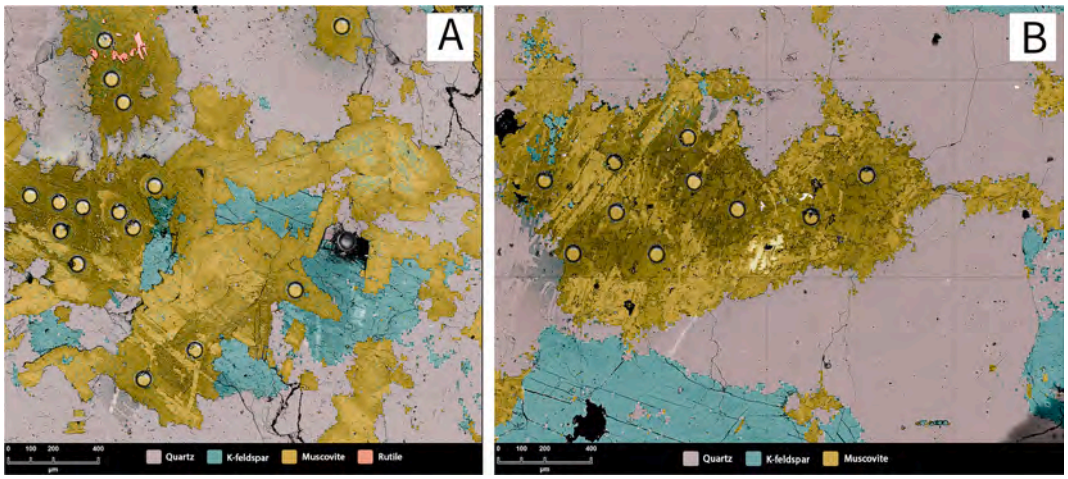

Fig. 6. Nanomin images show the main K-bearing phases in pegmatite. (A) illustrated the large muscovite crystals among orthoclase and quartz with a minor presence of rutile. (B) shows a muscovite cluster formed after orthoclase along the cracks with remnant of orthoclase inside the cluster.

The University of Adelaide.

3.3. In-situ Rb–Sr age dating of K-rich minerals

$^{87}Rb/^{86}Sr$ and $^{87}Sr/^{86}Sr$ isotope ratios of selected K-bearing minerals from metadiorite (ABS 13), syenogranite (ABS 10), partially altered pegmatite (ABS 5 and ABS 8), altered pegmatite (ABS 3) and greisen (ABS 7) were analysed using a LA-ICP-MS/MS to perform the *in-situ* Rb–Sr dating of these minerals. The *in-situ* Rb–Sr dating was conducted at the University of Adelaide using an Agilent 8900 ICP-MS/MS instrument, coupled with a RESOlution ArF excimer (193 nm) laser system, following the approach detailed in Redaa et al. (2021). Briefly, the key parameters and analytical conditions of our LA-ICP-MS/MS setup are listed in Table A in the supplementary materials (SM). All measured $^{87}Rb/^{86}Sr$ and $^{87}Sr/^{86}Sr$ data were first processed in Iolite4 (Paton et al., 2011), using a customised data reduction algorithm described in Redaa

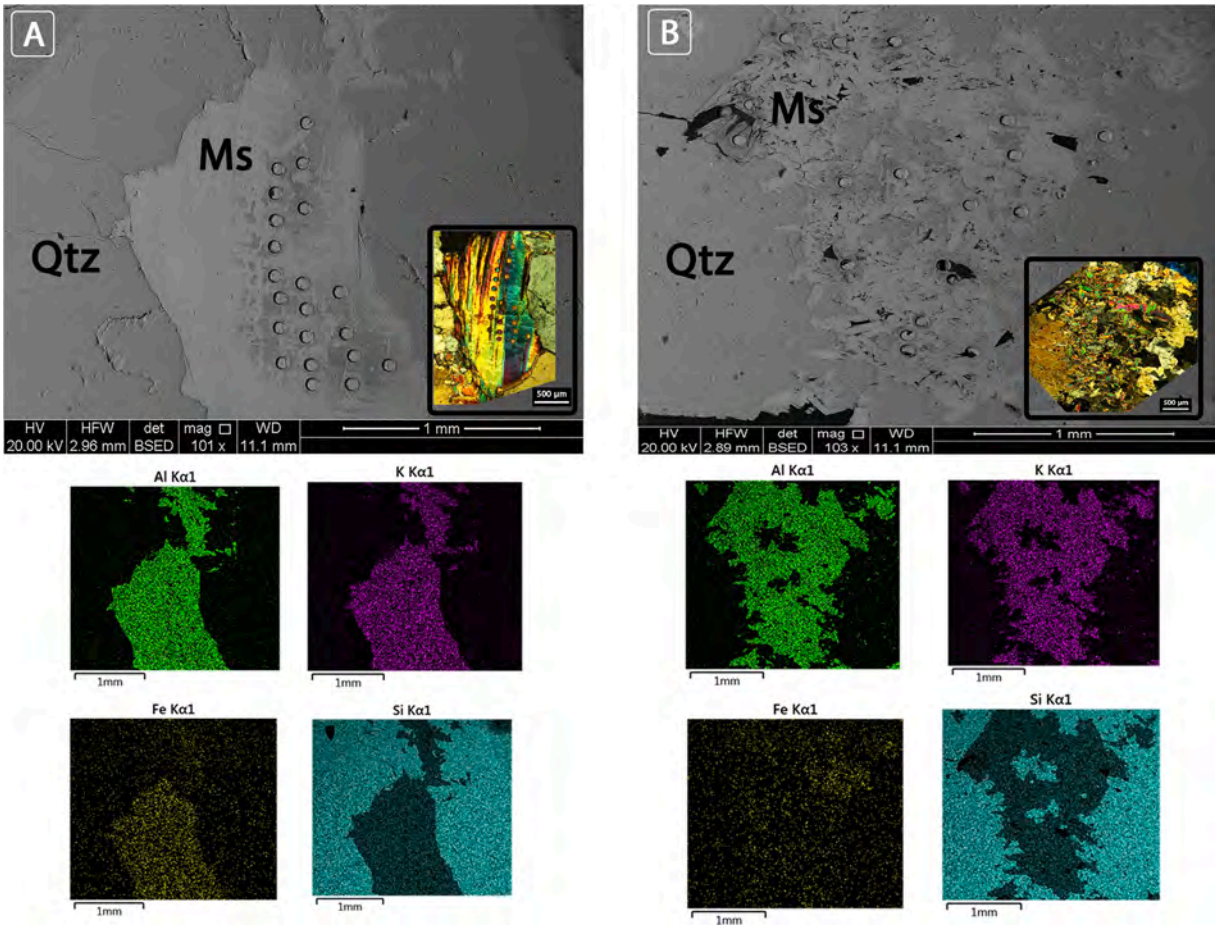

Fig. 7. SEM image with microscpic (xpl) images, and elemental maps for muscoivte of (A) Group I and (B) Group II obtined via the Quanta 450 SEM equipped with x-ray detector.

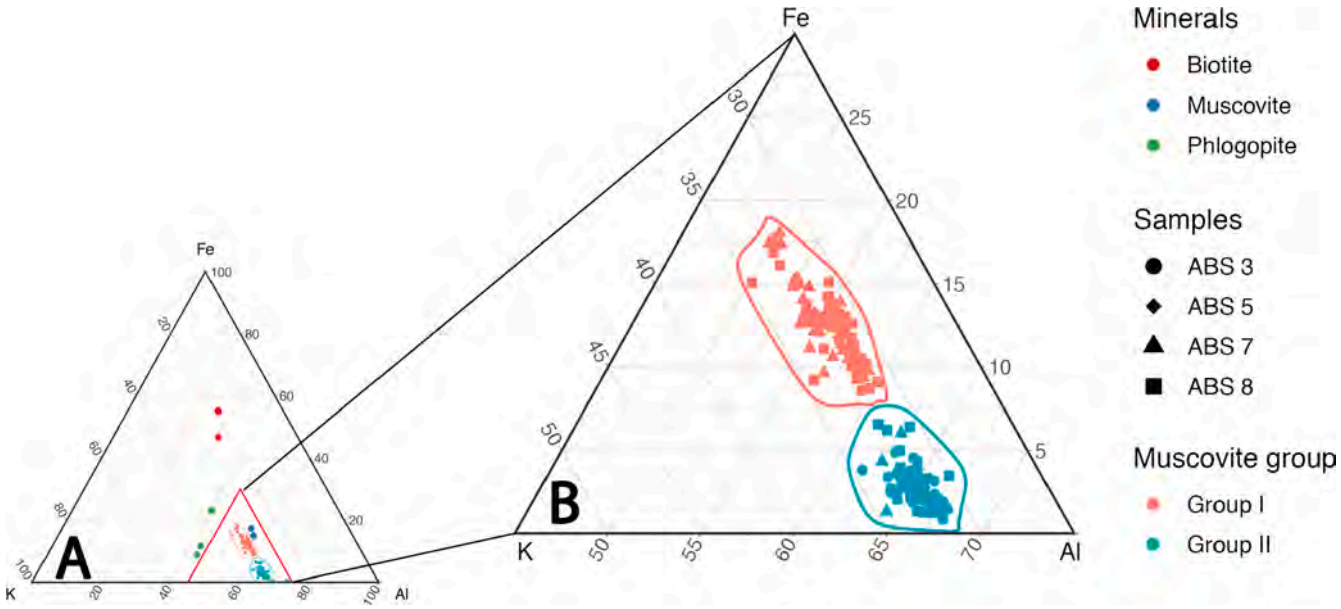

Fig. 8. Ternary diagrams of K, Fe and Al in muscovite. (A) shows the composition of Ablah muscovite (obtained via the Quanta 450) comparing with other mica minerals including biotite, phlogopite and muscovite. Data sources for other mica minerals (used as references) are listed in table C in the supplementary materials. (B) illustrates the differences in muscovite elemental compositions (obtained via the Quanta 450) between Group I and Group II.

et al. (2021); and subsequently the Rb–Sr isochron ages were calculated using IsoplotR (Vermeesch, 2018). A phlogopite pressed nano-powder pellet (Mica-Mg-NP), described in Garbe-Schönberg and Müller (2014) and Hogmalm et al. (2017), was used in this study as the primary reference material to correct for elemental fractionation effects and the instrumental drift (see also Redaa et al., 2021). In addition, two natural minerals were used as a secondary reference material to monitor the LA-ICP-MS/MS performance following the approaches described elsewhere (Armistead et al., 2020; Redaa et al., 2021; Shanshan et al., 2020) These minerals are phlogopite (MDC) and glauconite (GL-O), and the former was sourced from the same location as Mica-Mg-NP (Bekily, Madagascar) whereas the latter is a well-known reference material distributed by Association Nationale de la Recherche Technique (ANRT) (Govindaraju, 1995). MDC yielded an accurate age of 520 ± 18 Ma and GL-O also yielded an acceptable age of 93 ± 4 Ma (see Fig. A in the supplementary material), and both of these ages are within ~0.2% of accuracy from the expected or published ages for these mineral standards (Charbit et al., 1998; Derkowski et al., 2009; Hogmalm et al., 2017). Such agreement in turn indicates that there were no significant matrix effects biasing the accuracy of Rb-Sr age for the above mineral standards (GL-O and MDC). Consequently, any matrix-effects on acquired Rb-Sr ages for investigated micas, using Mica-Mg-NP as a reference, are negligible. However, unlike for micas, there might potentially be some effects on Rb-Sr ages of investigated feldspars due to the lack of suitable matrix-matched reference materials for feldspars, which thus warrants further investigation. Although this uncertainty for feldspar is currently unconstrained, it is likely within 3%, as observed for other non-matrix matched silicate minerals analysed via in-situ Rb-Sr dating technique (Redaa et al., 2021). Therefore, the above uncertainty has been taken into account when discussing the Rb-Sr age data from feldspars and their geological context and implications.

4. Results

4.1. Petrography and elemental maps

4.1.1. Pegmatite and altered pegmatite

Partially altered pegmatite samples (ABS 5 and ABS 8) mainly consist of medium subhedral and anhedral crystals of orthoclase, quartz, and muscovite in addition to rutile as accessory mineral. Small quartz veinlets cut across the samples, with orthoclase crystals around the veinlets showing alteration to sericite. Muscovite in samples ABS 5 and ABS 8 has two modes of occurrence; Group I: large euhedral/subhedral crystals located within the 'pristine' zone of the samples (Fig. 5A and Fig. 5B), and Group II: fine aggregates of subhedral\anhedral crystals associated with sericite in the alteration zone (Fig. 5C and Fig. 5D). The SEM-EDS/ Nanomin mineral maps obtained for the partially altered pegmatite (sample ABS 5) confirmed that orthoclase and muscovite are the main K-bearing phases in the sample, and rutile is present as an accessory mineral (Fig. 6). The low-count EDS spectra collected for mineral mapping do not show obvious differences in chemical compositions between Group I and Group II muscovite (Fig. 6), although longer counting times for elemental mapping on the FEI Quanta 450 reveal a higher Fe content in Group I muscovite relative to Group II muscovite (Fig. 7). The altered pegmatite (ABS 3) was also investigated by the petrographic microscope, and results show that the sample is highly sericitized, and it is composed mainly of muscovite (Group II), orthoclase, and quartz with quartz veinlets.

4.1.2. The greisen

Sample ABS 7 was extracted from the greisen located at the top of Ablah pegmatite. The mineralogical composition of the sample was investigated under the petrographic microscope, and the result shows that medium to fine subhedral and anhedral crystals of muscovite are the major component of the sample with small amount of coarse altered orthoclase, fluorite, and quartz. Both groups of muscovite (Group I and Group II) are also present in the greisen, and they were widespread in the samples.

4.2. Elemental composition of muscovite

Semi-quantitative analyses were conducted on selected muscovite grains on the partially altered pegmatite (ABS 8), altered pegmatite (ABS 3) and the greisen (ABS 7) using the Quanta 450 SEM. The SEM images (Fig. 7) confirmed the petrographic results that muscovite in pegmatite and in the greisen has two forms, the large muscovite (Group I, Fig. 7A) and the fine aggregate muscovite (Group II, Fig. 7B). The major element concentrations in muscovite including K, Al, Si, O and Fe were analysed

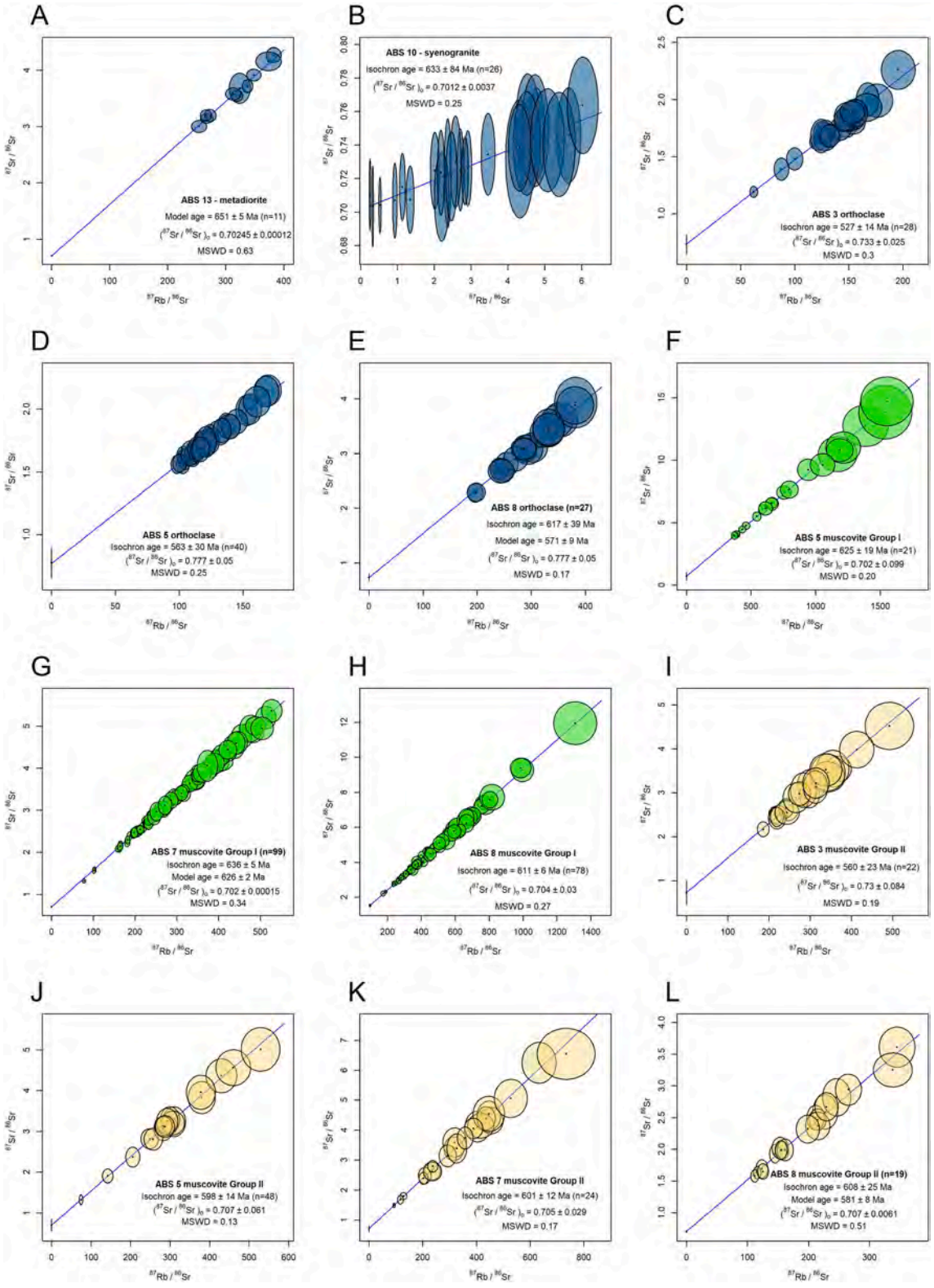

Fig. 9. Rb–Sr isochron diagrams for orthoclase (blue), Group I muscovite(green), and Group II muscovite (orange) of samples ABS 13, ABS 10, ABS 3, ABS 5, ABS 8. (For interpretation of the references to colour in this figure legend, the reader is referred to the web version of this article.)

by energy dispersive X-ray spectroscopy, and the results (listed in Table B in the Supplementary Material showed that concentrations of K, Al and Si were similar between the two muscovite groups. However, muscovite of Group I contained slightly higher Fe compared to Group II as indicated from the intensity map in Fig. 7. Thus, K, Fe and Al were plotted in a ternary diagram to better characterise these two groups of muscovites (Fig. 8), and the results show that there is a correlation between the three components specifically Fe decreases with increasing K and Al (Fig. 8B). Therefore, the studied muscovites can be characterised and separated into two groups (i.e., Group I and Group II) based on their

Fe abundances. Overall, muscovite of Group I has higher Fe (ranged between 2.75 and 5.8 wt%) compared to muscovite of Group II (Fig. 8B), which have Fe content ranges between 0.27 and 2.03 wt%.

4.3. In-situ Rb–Sr geochronology of K-rich minerals

4.3.1. K-feldspars

K-feldspars from the metadiorite (ABS 10), syenogranite (ABS 13), partially altered pegmatite (ABS 5 and ABS 8) and altered pegmatite (ABS 3) were analysed using the *in-situ* Rb–Sr dating method as described in the section 3.3. The metadiorite sample (ABS 13) yielded an isochron age of 658 ± 34 Ma with unexpectedly unradiogenic initial ratio of 0.67 ± 0.15. Due to the large uncertainty in the calculated age and in the initial $^{87}Sr/^{86}Sr$ ratio, the model age of sample ABS 13 was calculated at 651 ± 5 Ma, using the initial ratio of 0.70246 (Fig. 9A) that was reported for Bidah metadiorite-metatonalite pluton (see Fig. 1 and Marzouki et al. (1982)) which previously correlated with the Shuwas metadiorite (sample ABS 13) (Johnson, 2006). Additional uncertainty of 3% was added to the Rb-Sr age of sample ABS 13, yielding 651 ± 20 Ma, because there was no suitable feldspar mineral standard that could be used in this study to monitor the impact of matrix-effect on the accuracy of analysed orthoclase. The above uncertainty of 3% reflects the overall impact of matrix-effects during in-situ Rb-Sr dating of silicate minerals, as quantified in the recent study by Redaa et al. (2021). The K-feldspars of the syenogranite (ABS 10) yielded an isochron age of 633 ± 84 Ma with low initial $^{87}Sr/^{86}Sr$ ratio of 0.7012 ± 0.0037 (Fig. 9B) that overlaps within the uncertainty the previously reported initial $^{87}Sr/^{86}Sr$ for Ablah granitoids (0.70365 ± 0.00015) by Moufti (2001). The large uncertainty in the isochron age of this syenogranite is due to low Rb content and thus generally less radiogenic $^{87}Sr/^{86}Sr$ values in the analysed feldspars (see Fig. 9B). Orthoclase of partially altered pegmatite (samples ABS 5 and ABS 8) and the altered pegmatite (ABS 3) yielded younger ages ranged between 571 and 527 (Fig. 9C-E) Ma with high initial $^{87}Sr/^{86}Sr$ ratio for samples ABS 3 (0.733 ± 0.025) and ABS 5 (0.777 ± 0.050). However, orthoclase of sample ABS 8 yielded lower initial $^{87}Sr/^{86}Sr$ ratio with high uncertainty (0.576 ± 0.150), thus the model age of the sample was calculated at 571 ± 9 Ma (Fig. 9E), using the initial $^{87}Sr/^{86}Sr$ ratio of 0.777 ± 0.050 obtained from orthoclase of the other partially altered pegmatite (ABS 5).

4.3.2. Group I muscovite

Group I muscovite was *in-situ* dated in the partially altered pegmatite (samples ABS 5 and ABS 8), and greisen (ABS 7). Group I muscovite of samples ABS 5 and ABS 8 yielded isochron ages of 625 ± 19 Ma and 611 ± 9 Ma with initial $^{87}Sr/^{86}Sr$ of 0.702 ± 0.099 and 0.704 ± 0.030, respectively (Fig. 9E and H). In the greisen (ABS 7), Group I muscovite yielded an isochron age of 636 ± 5 Ma but with low initial $^{87}Sr/^{86}Sr$ ratio (0.699 ± 0.018). Thus, the obtained isochron line was anchored to the initial $^{87}Sr/^{86}Sr$ ratio of 0.702 ± 0.099 that obtained from sample ABS 5, and the model age of sample ABS 7 calculated at 626 ± 2 Ma (Fig. 9G). Thus, we can conclude that the age of Group I muscovite in the partially altered pegmatite and the greisen ranges between 626 Ma and 611 Ma.

4.3.3. Group II muscovite

Muscovite of Group II was dated in the partially altered pegmatite (samples ABS 5 and ABS 8), altered pegmatite (ABS 3) and greisen (ABS 7) (Fig. 9I-L). Overall, the Group II muscovite yielded younger ages comparing to Group I muscovite, ranging between 601 Ma and 560 Ma (Fig. 9). Group II muscovite in samples ABS 5 and ABS 7 yielded similar ages determined at 598 ± 14 Ma and 601 ± 12 Ma with initial $^{87}Sr/^{86}Sr$ ratios of 0.707 ± 0.061 and 0.705 ± 0.029, respectively (Fig. 9J and K). However, muscovite (Group II) in sample ABS 3 yielded younger age (560 ± 23 Ma) with higher initial $^{87}Sr/^{86}Sr$ ratio of 0.730 ± 0.084 (Fig. 9I). Finally, Group II muscovite in sample ABS 8 yielded an isochron age of 608 ± 25 Ma, but with low $^{87}Sr/^{86}Sr$ ratio (0.639 ± 0.058), thus the model age of the sample was calculated at 581 ± 8 Ma by anchoring the isochron to the same initial $^{87}Sr/^{86}Sr$ ratio (0.707) obtained from the other partially altered pegmatite sample (ABS 5) (Fig. 9L).

5. Discussion

5.1. Classification of muscovite in Ablah mineralisation

The results show that muscovite in investigated samples can be classified into two groups with distinct genetic origins and formed at different times. Group I muscovite seems to be a primary phase associated with the crystallisation of the Ablah pegmatite between the period of 626 Ma to 611 Ma, and it is texturally and chemically distinctive from Group II muscovite. The Group II muscovite seems to be formed due to alteration processes that occurred at two different times. The first alteration process is the greisenisation that occurred at 601 ± 12 Ma and formed the Group II muscovite in samples ABS 5 and ABS 7 and characterised by low initial $^{87}Sr/^{86}Sr$ ratio (~0.707). The second alteration event occurred at 556 ± 23 Ma, and it is genetically different from the greisen as indicated from the high initial $^{87}Sr/^{86}Sr$ ratio obtained from the alteration zone in pegmatite (sample ABS 3, see Fig. 9I). This alteration zone is associated with quartz veins that may reflect hydrothermal circulation that formed the Cu-Au mineralisation in Mount Ablah.

5.2. Magmatic evolution of the Mount Ablah area: Constraints from in-situ Rb–Sr dating

Mount Ablah pegmatite and A-type granitoids (including the syenogranite (ABS 10)) are intruded into the metadiorite that was suggested to be emplaced in the lower Neoproterozoic (Tonian) period between 855 Ma and 815 Ma (Johnson, 2006, 2005). Thus, the much younger *in-situ* Rb–Sr age of 651 ± 20 Ma for the metadiorite sample (ABS 13) could reflect the timing of later (Cryogenian) isotopic disturbance and/or recrystallisation due to the development of Umm Farwah Shear zone. The timing of the Umm Farwah Shear zone was presumed to be as young as 605 Ma (Johnson et al., 2011) based on the whole-rock Rb–Sr age of A-type granitoids intruded in the Shuwas pluton (Fig. 2). However, the Cryogenian age of the metadiorite (sample ABS 13) suggests that the Shuwas pluton was affected by brittle-ductile deformation associated with the development of the shear zone, which could have been initiated at ca. 651 ± 20 Ma. This would suggest that the shear zone is linked to the Pan-African tectonism in the south of the Arabian Shield (Genna et al., 1999).

The development of the Umm Farwah shear zone was associated with partial melting and crustal fusion that is believed to have produced the granitoids exposed in the Shuwas pluton as shown in Fig. 2 (Moufti, 2001). The *in-situ* Rb–Sr dating of the syenogranite constrained in this study at 633 ± 84 Ma (Fig. 9B), with a large uncertainty due to the low and not very radiogenic $^{87}Sr/^{86}Sr$ ratios in the analysed feldspars. Although this large uncertainty makes the *in-situ* Rb–Sr age of syenogranite rather poorly constrained, the mean of the age of 633 Ma is close to other published ages for granitoids in the Ablah area (i.e., 617 ± 17 Ma for syenite, and 605 ± 5 Ma for syenogranite (Moufti, 2001)). This in turn implies that the partial melting, associated with Umm Farwah shear zone, and the formation of syenogranite probably started at around 633 Ma or during the Cryogenian/Ediacaran transition, with the following 'cooling phase' allowing isotopic closure lasting up to 25 Ma until ca.605 Ma.

5.3. Paragenetic sequence of the Mount Ablah Cu-Au mineralisation

The Mount Ablah pegmatite contains two types of mineralisation which are the greisen and the Cu-Au mineralisation in the alteration zone in pegmatite. The greisen in Mount Ablah is considered a source for

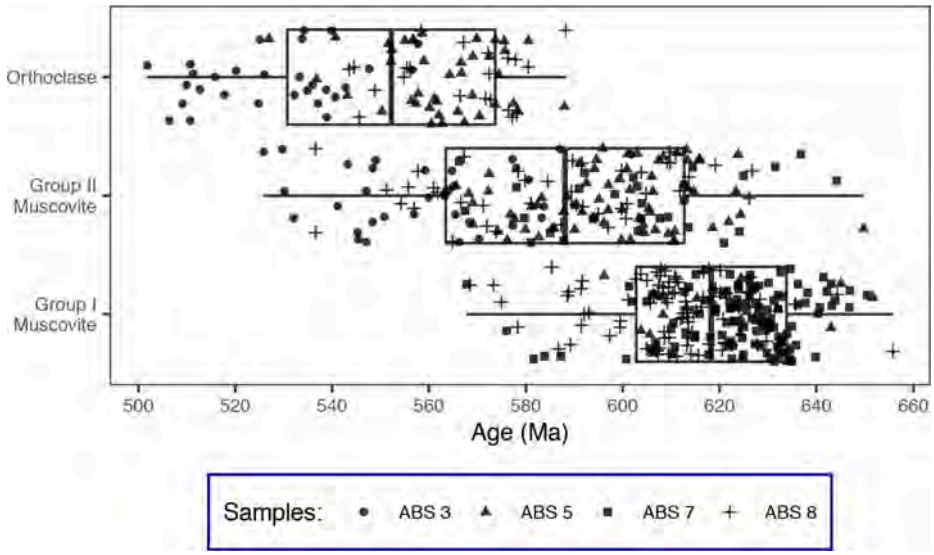

Fig. 10. Boxplot diagram shows the age distribution of orthoclase, Group I muscovite and Group II muscovite in the samples ABS 3, ABS 5, ABS 7 and ABS 8. The box illustrates the mean of the ages and standard deviation.

fluorite and Y (Jackson, 1986) whereas the Cu and Au are mostly concentrated in the quartz-associated alteration zones in the pegmatite (Salimo, 2015). Our *in-situ* Rb–Sr data indicated that pegmatite emplacement occurred between 626 and 611 Ma as indicated from Group I muscovite in the partially altered pegmatite (ABS 5 and ABS 8). This age is in agreement with the age of most of the post-tectonic intrusions in the Arabian Shield whose ages scatter around 620 Ma (Robinson et al., 2014), and it overlaps the crystallisation age inferred from the syenogranite (sample ABS 10) at 633 ± 84 Ma, which seems to indicate that the pegmatite was formed at around the same time as the syenogranite and probably from the same or related magma sources. Subsequently, the greisenisation process occurred at 601 ± 12 Ma as indicated by the Group II muscovite in the greisen (sample ABS 7). Noticeably, the age of the greisen is in agreement with the lower limit of the magmatic process that formed the A-type granitoids (605 ± 5 Ma) in the Shuwas pluton (Moufti, 2001) and Mount Ablah pegmatite (625 ± 19 Ma), which could indicate that the greisen was formed from residual magmatic fluids rich in volatiles, specifically fluorine. This can explain the presence of economic fluorite deposit in the Mount Ablah (Peterková and Dolejš, 2019; Smirnov, 2015). In addition, this is also supported by agreement in the initial $^{87}Sr/^{86}Sr$ ratio between Group II muscovite in the greisen (sample ABS 7) and from feldspars in the syenogranite (ABS 10) and Group I muscovite in the pegmatite (sample ABS 5). Later, the Mount Ablah pegmatite was affected by a later stage of alteration events that form the Cu-Au mineralisation. This is illustrated by data from Group II muscovite in altered pegmatite (ABS 3) and from orthoclase which seem to record the timing of these later stage events between 574 and 530 Ma (Fig. 10). The younger ages for orthoclase comparing with the primary Group I muscovite indicate that Rb-Sr of orthoclase was diffused during the alteration process whereas muscovite was more resistant to alteration. This indicates that the predominant temperature during the alteration event was between 475 and 500 °C as this range lies close or above the closure temperature of orthoclase (Giletti, 1990) but lower than the closure temperature of muscovite (Dodson, 1973)

6. Conclusions

The *in-situ* Rb–Sr dating of K-bearing minerals such as muscovite and K-feldspar, coupled with published geochronological data from the Mount Ablah area including the Shuwas pluton, allows us to constrain the ages of these mineral sequences with implications for the timing of multiple events affecting the study the area. Using the in-situ Rb-Sr dating technique, we were able to:

- Constrain, for the first time, the timing of the development of Umm Farwah Shear Zone at 651 ± 20 Ma which could open a new insight toward understanding the development of the southern part of the Arabian Shield as the shear zone is a major structure in the Asir terrane.
- Determine the timing of emplacement of Ablah pegmatite at 625 ± 19 Ma.
- Constrain the timing of the greisenisation process that formed the greisen deposit between 613 Ma and 589 Ma.
- Constrain the timing of alteration event that formed the Cu-Au mineralisation in Mount Ablah between 580 Ma and 530 Ma.

Author contribution

Ahmad Redaa: Data collection, data processing, interpretation, visualisation, writing original draft and editing. **Juraj Farkaš:** Supervision, interpretation, reviewing and editing. **Ahmed Hassan:** Supervision the field work and reviewing. **Alan S. Collins:** Supervision and reviewing. **Sarah Gilbert:** Set-up the LA-ICP-MS/MS for the in-situ Rb-Sr analysis and reviewing the draft. **Stefan C. Löhr:** Analysing the samples by the SEM and reviewing the draft.

Declaration of Competing Interest

The authors declare that they have no known competing financial interests or personal relationships that could have appeared to influence the work reported in this paper.

Acknowledgement

The authors thank the Saudi Arabian Mining Company (Ma'aden) and Mr. Zaid Al Moald for providing access to the core samples of Mount Ablah. We also thank King Abdulaziz University and Prof. Hesham Harbi for facilitating the field trip to the study area. Adelaide Microscopy and Mr. Ken Neubauer are thanked for assistance in the SEM analysis. Additional thanks go to the iolite team specifically to Bence Paul and Joe Petrus for providing a licence for iolite4 software. Finally, we would also like to thank the editor and two reviewers (Prof. Yehia H. Dawood and an anonymous reviewer) for their constructive comments and criticism, which improved the overall quality of this study.

Appendix A. Supplementary material

Supplementary data to this article can be found online at https://doi.org/10.1016/j.jseaes.2021.105037.

References

Agar, R.A., 1992. The tectono-metallogenic evolution of the Arabian Shield. Precambrian Res. 58 (1-4), 169–194.

Alessio, B.L., Blades, M.L., Murray, G., Thorpe, B., Collins, A.S., Kelsey, D.E., Foden, J., Payne, J., Al-Khirbash, S., Jourdan, F., 2018. Origin and tectonic evolution of the NE basement of Oman: a window into the Neoproterozoic accretionary growth of India? Geol. Mag. 155, 1150–1174.

Armistead, S.E., Collins, A.S., Redaa, A., Jepson, G., Gillespie, J., Gilbert, S., Blades, M.L., Foden, J.D., Razakamanana, T., 2020. Structural evolution and medium-temperature thermochronology of central Madagascar: implications for Gondwana amalgamation. J. Geol. Soc. London. 177 (4), 784–798.

Blades, M.L., Alessio, B.L., Collins, A.S., Foden, J., Payne, J.L., Glorie, S., Holden, P., Thorpe, B., Al-Khirbash, S., 2020. Unravelling the Neoproterozoic accretionary history of Oman, using an array of isotopic systems in zircon. J. Geol. Soc. London. 177 (2), 357–378. https://doi.org/10.1144/jgs2018-125.

Blades, M.L., Collins, A.S., Foden, J.D., Payne, J.L., Stüwe, K., Abu-Alam, T., Makroum, F., Hassan, M., 2021. Age and hafnium isotope evolution of Sudanese Butana and Chad illuminates the Stenian to Ediacaran evolution of the south and east Sahara. Precambrian Res.

Bokhari, F., Kramers, J., 1981. Island arc character and late Precambrian age of volcanics at Wadi Shwas, Hijaz, Saudi Arabia: geochemical and Sr and Nd isotopic evidence. Earth Planet. Sci. Lett. 54 (3), 409–422. https://doi.org/10.1016/0012-821X(81)90057-1.

Charbit, S., Guillou, H., Turpin, L., 1998. Cross calibration of K-Ar standard minerals using an unspiked Ar measurement technique. Chem. Geol. 150, 147–159. https://doi.org/10.1016/S0009-2541(98)00049-7.

Cherniak, D.J., Watson, E.B., 2001. Pb diffusion in zircon. Chem. Geol. 172 (1-2), 5–24. https://doi.org/10.1016/S0009-2541(00)00233-3.

Collins, A.S., Blades, M.L., Merdith, A.S., Foden, J.D., 2021a. Closure of the Proterozoic Mozambique Ocean was instigated by a late Tonian plate reorganization event. Commun. Earth Environ. 2, 75. https://doi.org/10.1038/s43247-021-00149-z.

Collins, A.S., Blades, M.L., Merdith, A.S., 2021b. Chapter 8: The Arabian Nubian Shield within the Neoproterozoic Plate Tectonic Circuit. In: Hamimi, Z., Fowler, A.-.-R., Liégeois, J.-.-P., Collins, A.S., Abdelsalam, M.G., Abd El-Wahed, M. (Eds.), The Geology of the Arabian-Nubian Shield. Springer.

Collins, A.S., Pisarevsky, S.A., 2005. Amalgamating eastern Gondwana: The evolution of the Circum-Indian Orogens. Earth-Sci. Rev. 71 (3-4), 229–270. https://doi.org/10.1016/j.earscirev.2005.02.004.

Derkowski, A., Środoń, J., Franus, W., Uhlík, P., Banaś, M., Zieliński, G., Čaplovičová, M., Franus, M., 2009. Partial dissolution of glauconitic samples: implications for the methodology of K-Ar and Rb-Sr dating. Clays Clay Min. 57, 531–554. https://doi.org/10.1346/CCMN.2009.0570503.

Dodson, M.H., 1973. Closure Temperature in Cooling Geochronological and Petrological Systems. Contrib. Mineral. Petrol. 40 (3), 259–274. https://doi.org/10.1007/BF00373790.

Garbe-Schönberg, D., Müller, S., 2014. Nano-particulate pressed powder tablets for LA-ICP-MS. J. Anal. At. Spectrom. 29 (6), 990–1000. https://doi.org/10.1039/C4JA00007B.

Genna, A., Guerrot, C., Deschamps, Y., Nehlig, P., Shanti, M., 1999. Les formations Ablah d'Arabie Saoudite (datation et implication géologique). Comptes Rendus l'Académie des Sci. IIA-Earth Planet. Sci. 329 (9), 661–667.

Giletti, B.J., 1990. Rb and Sr diffusion in alkali feldspars, with implications for cooling histories of rocks. Geochim. Cosmochim. Acta 55, 1331–1343.

Govindaraju, K., 1995. 1995 Working values with confidence limits for twenty-six CRPG, ANRT and IWG-GIT geostandards. Geostandards Newsletter 19, 1–32. https://doi.org/10.1111/j.1751-908X.1995.tb00164.x.

Greenwood, W.R., 1975. Geology of Al 'Aqiq quadrangle, sheet 20/41D, Kingdom of Saudi Arabia. Jeddah.

Hogmalm, K.J., Zack, T., Karlsson, A.K.O., Sjöqvist, A.S.L., Garbe-Schönberg, D., 2017. In situ Rb-Sr and K-Ca dating by LA-ICP-MS/MS: an evaluation of N2O and SF6 as reaction gases. J. Anal. At. Spectrom. 32, 305–313. https://doi.org/10.1039/C6JA00362A.

Jackson, N.J., 1986. Mineralization associated with felsic plutonic rocks in the Arabian Shield. J. African Earth Sci. 4, 213–227. https://doi.org/10.1016/S0899-5362(86)80083-5.

Johnson, P.R., 2006. Explanatory notes to the map of Proterozoic geology of western Saudi Arabia. Saudi Geological Survey, Jeddah.

Johnson, P.R., 2005. Proterozoic geology of western Saudi Arabia, West-central sheet, (Amended September 2005), notes on Proterozoic stratigraphy. Saudi Geological Survey, Jeddah.

Johnson, P.R., Andresen, A., Collins, A.S., Fowler, A.R., Fritz, H., Ghebreab, W., Kusky, T., Stern, R.J., 2011. Late Cryogenian-Ediacaran history of the Arabian-Nubian Shield: A review of depositional, plutonic, structural, and tectonic events in the closing stages of the northern East African Orogen. J. African Earth Sci. 61 (3), 167–232. https://doi.org/10.1016/j.jafrearsci.2011.07.003.

Johnson, P.R., Woldehaimanot, B., 2003. Development of the Arabian-Nubian Shield: Perspectives on accretion and deformation in the northern East African Orogen and the assembly of Gondwana.

Kirkland, C.L., Yakymchuk, C., Szilas, K., Evans, N., Hollis, J., McDonald, B., Gardiner, N. J., 2018. Apatite: a U-Pb thermochronometer or geochronometer? Lithos 318–319, 143–157. https://doi.org/10.1016/j.lithos.2018.08.007.

Marzouki, F.M.H., Jackson, N.J., Ramsay, C.R., Darbyshire, D.P.F., 1982. Composition, age and origin of two proterozoic diorite—tonalite complexes in the Arabian shield. Precambrian Res. 19 (1), 31–50. https://doi.org/10.1016/0301-9268(82)90018-3.

McFarlane, C., Mark Harrison, T., 2006. Pb-diffusion in monazite: Constraints from a high-T contact aureole setting. Earth Planet. Sci. Lett. 250 (1-2), 376–384. https://doi.org/10.1016/j.epsl.2006.06.050.

Merdith, A.S., Williams, S.E., Collins, A.S., Tetley, M.G., Mulder, J.A., Blades, M.L., Young, A., Armistead, S.E., Cannon, J., Zahirovic, S., Müller, R.D., 2021. Extending full-plate tectonic models into deep time: Linking the Neoproterozoic and the Phanerozoic. Earth-Sci. Rev. 214, 103477. https://doi.org/10.1016/j.earscirev.2020.103477.

Moufti, M., 2001. Age, geochemistry and origin of peraluminous A-type granitoids of the Ablah-Shuwas pluton, Ablah Graben Arabian Shield. Acta Mineral. 42, 5–20.

Nehlig, P., Salpeteur, I., Asfirane, F., Bouchot, V., Eberlé, J.M., Genna, A., 1999. The Mineral Potential of the Arabian Shield: A reassessment. In: Proceedings of the IUGS/UNESCO Meeting on the "Base and Precious Metal Deposits in the Arabian Shield", Jeddah, pp. 12–19.

Nettle, D., Halverson, G.P., Cox, G.M., Collins, A.S., Schmitz, M., Gehling, J., Johnson, P. R., Kadi, K., 2014. A middle–late Ediacaran volcano-sedimentary record from the eastern Arabian-Nubian shield. Terra Nov. 26 (2), 120–129. https://doi.org/10.1111/ter.12077.

Olierook, H.K.H., Rankenburg, K., Ulrich, S., Kirkland, C.L., Evans, N.J., Brown, S., McInnes, B.I.A., Prent, A., Gillespie, J., McDonald, B., 2020. Resolving multiple geological events using in situ Rb–Sr geochronology: implications for metallogenesis at Tropicana, Western Australia. Geochronology 2, 283–303.

Paton, C., Hellstrom, J., Paul, B., Woodhead, J., Hergt, J., 2011. Iolite: Freeware for the visualisation and processing of mass spectrometric data. J. Anal. At. Spectrom. 26 (12), 2508. https://doi.org/10.1039/c1ja10172b.

Peterková, T., Dolejš, D., 2019. Magmatic-hydrothermal transition of Mo-W-mineralized granite-pegmatite-greisen system recorded by trace elements in quartz: Krupka district, Eastern Krušné hory/Erzgebirge. Chem. Geol. 523, 179–202. https://doi.org/10.1016/j.chemgeo.2019.04.009.

Rafiei, M., Löhr, S., Baldermann, A., Webster, R., Kong, C., 2020. Quantitative petrographic differentiation of detrital vs diagenetic clay minerals in marine sedimentary sequences: Implications for the rise of biotic soils. Precambrian Res. 350, 105948. https://doi.org/10.1016/j.precamres.2020.105948.

Redaa, A., Farkaš, J., Gilbert, S., Collins, A.S., Wade, B., Löhr, S., Zack, T., Garbe-Schönberg, D., 2021. Assessment of elemental fractionation and matrix effects during in-situ Rb–Sr dating of phlogopite by LA-ICP-MS/MS: Implications for the accuracy and precision of mineral ages. J. Anal. At. Spectrom. 36 (2), 322–344. https://doi.org/10.1039/D0JA00299B.

Robinson, F.A., Foden, J.D., Collins, A.S., 2015. Geochemical and isotopic constraints on island arc, synorogenic, post-orogenic and anorogenic granitoids in the Arabian Shield, Saudi Arabia. Lithos 220–223, 97–115. https://doi.org/10.1016/j.lithos.2015.01.021.

Robinson, F.A., Foden, J.D., Collins, A.S., Payne, J.L., 2014. Arabian Shield magmatic cycles and their relationship with Gondwana assembly: Insights from zircon U-Pb and Hf isotopes. Earth Planet. Sci. Lett. 408, 207–225. https://doi.org/10.1016/j.epsl.2014.10.010.

Salimo, L., 2015. Al Hajar Project - Preliminary review of Ablah prospect. Jeddah.

Şengör, A.M.C.., Lom, N., Zabcı, C., Sunal, G., Öner, T., 2020. Reconstructing orogens without biostratigraphy: The Saharides and continental growth during the final assembly of Gondwana-Land. Proc. Natl. Acad. Sci. 117 (51), 32278–32284. https://doi.org/10.1073/pnas.2015117117.

Şengün, F., Bertrandsson Erlandsson, V., Hogmalm, J., Zack, T., 2019. In situ Rb-Sr dating of K-bearing minerals from the orogenic Akçaabat gold deposit in the Menderes Massif, Western Anatolia, Turkey. J. Asian Earth Sci. 185, 104048. https://doi.org/10.1016/j.jseaes.2019.104048.

Shanshan, L., Santosh, M., Farkas, J., Redaa, A., Ganguly, S., Kim, S.W., Zhang, C., Gilbert, S., Zack, T., 2020. Coupled U-Pb and Rb-Sr laser ablation geochronology trace Archean to Proterozoic crustal evolution in the Dharwar Craton, India. Precambrian Res. 343.

Smirnov, S.Z., 2015. The fluid regime of crystallization of water-saturated granitic and pegmatitic magmas: a physicochemical analysis. Russ. Geol. Geophys. 56, 1292–1307.

Stern, R.J., 2002. Crustal evolution in the East African Orogen: a neodymium isotopic perspective. J. African Earth Sci. 34 (3-4), 109–117. https://doi.org/10.1016/S0899-5362(02)00012-X.

Stern, R.J., Johnson, P., 2010. Continental lithosphere of the Arabian Plate: A geologic, petrologic, and geophysical synthesis. Earth-Sci. Rev. 101 (1-2), 29–67. https://doi.org/10.1016/j.earscirev.2010.01.002.

Stoeser, D.B., Frost, C.D., 2006. Nd, Pb, Sr, and O isotopic characterization of Saudi Arabian Shield terranes. Chem. Geol. 226 (3-4), 163–188.

Tillberg, M., Drake, H., Zack, T., Kooijman, E., Whitehouse, M.J., Åström, M.E., 2020. In situ Rb-Sr dating of slickenfibres in deep crystalline basement faults. Sci. Rep. 10, 1–13.

Vermeesch, P., 2018. IsoplotR: A free and open toolbox for geochronology. Geosci. Front. 9 (5), 1479–1493.

GEOLOGY | THE GEOLOGICAL SOCIETY OF AMERICA®

https://doi.org/10.1130/G49187.1

Manuscript received 29 October 2020
Revised manuscript received 30 July 2021
Manuscript accepted 3 August 2021

Published online 20 September 2021

Unraveling the histories of Proterozoic shales through *in situ* Rb-Sr dating and trace element laser ablation analysis

Darwinaji Subarkah[1], Morgan L. Blades[1], Alan S. Collins[1], Juraj Farkaš[1], Sarah Gilbert[2], Stefan C. Löhr[3], Ahmad Redaa[1], Eilidh Cassidy[1] and Thomas Zack[1,4]

[1]Tectonics and Earth Systems, and MinEx CRC, Department of Earth Sciences, University of Adelaide, Adelaide, SA 5005, Australia
[2]Adelaide Microscopy, University of Adelaide, Adelaide, SA 5005, Australia
[3]Department of Earth and Environmental Sciences, Macquarie University, Sydney, NSW 2109, Australia
[4]Department of Earth Sciences, University of Gothenburg, 405 30 Göteborg, Sweden

ABSTRACT

Authigenic components in marine sediments are important archives for past environment reconstructions. However, defining reliable age constraints and assessing the effects of post-depositional overprints in Precambrian sequences are challenging. We demonstrate a new laser-based analytical approach that has the potential to rapidly and accurately evaluate the depositional and alteration histories of Proterozoic shales. Our study employs a novel application of *in situ* Rb-Sr dating coupled with simultaneous trace-element analysis using reaction-cell laser ablation–inductively coupled plasma–tandem mass spectrometry (LA-ICP-MS/MS). We present results from shales sourced from two wells in the Proterozoic McArthur Basin, northern Australia. These rocks have been widely used by previous studies as a key section for ancient biogeochemical and paleo-redox reconstructions. Shales from well UR5 yielded initial $^{87}Sr/^{86}Sr$ ratios, Rb-Sr ages, and rare earth element plus yttrium (REEY) patterns similar to those of a dolerite sampled from the same core. We propose that the UR5 samples chronicle hydrothermal alteration instigated by the dolerite intrusion. In contrast, a correlative shale from well UR6 yielded an age consistent with the expected depositional age (1577 ± 56 Ma) with REEY and initial $^{87}Sr/^{86}Sr$ ratios similar to ca. 1.5 Ga seawater. We suggest that this sample records the minimum depositional age and early marine diagenetic history for this unit. This new technique can date Proterozoic shales quickly, cheaply, and with minimum sample preparation. Importantly, ages are triaged to differentiate between those recording primary marine versus secondary processes. This novel approach provides a potentially powerful tool for dating and fingerprinting the vast array of ancient marine shales for further studies of Earth systems through deep time.

INTRODUCTION

Analyses of the sedimentary record have been integral in constraining how Earth systems have evolved over geological time. For example, geochemical proxies of seawater paleo–redox conditions reveal key periods of fluctuating oxygen levels that are intrinsically linked to the development of life (e.g., Lyons et al., 2014; Planavsky et al., 2015). Furthermore, the radiogenic $^{87}Sr/^{86}Sr$ isotope record of seawater inferred from marine carbonates reflects the balance between Sr input from continental weathering versus that from submarine hydrothermal systems, reflecting global-scale tectonic changes (Kuznetsov et al., 2014). However, these archives are meaningful only if one is able to accurately date and assess the primary compositions of the rocks investigated. These prerequisites are further complicated by the lack of a diverse faunal record in the Proterozoic, restricting the use of biostratigraphy to constrain depositional ages. Consequently, an array of other chronological techniques has been developed to date Precambrian sedimentary rocks.

Shales are common throughout the Precambrian, but dating sedimentary packages dominated by shales has proven to be difficult. Re-Os dating of organic-rich shales is a powerful technique for attaining depositional ages (Ravizza and Turekian, 1989; Kendall et al., 2009). However, this method has limitations. There is a low abundance of Re in natural environments, such that many shales are too Re-poor to date (e.g., Rainbird et al., 2020). In addition, the method is costly and time consuming and yields hard-won but limited data. Sample intervals also commonly represent deposition over tens to hundreds of centimeters vertically and as much as several kilometers laterally (e.g., Kendall et al., 2009; Rainbird et al., 2020). Detrital zircons are useful for analyzing provenance and establishing maximum depositional ages (e.g., Yang et al., 2019) where sand units are available. Dating volcanic beds in sedimentary units is the most precise method to obtain depositional ages (e.g., Southgate et al., 2000), but many sequences are devoid of such lithologies. Similarly, direct dating of intrusions in sedimentary rocks or early diagenetic minerals such as xenotime (Rasmussen et al., 2004) can provide minimum depositional ages of sediments but rely on specific geological conditions to be met.

Alternatively, the Rb-Sr isotopic system can date deposition (Compston and Pidgeon, 1962; Nebel, 2014) and early diagenetic illite formation in shales (Gorokhov et al., 2001). However, the past limitation of beta-decay-system chronometers such as ^{87}Rb-^{87}Sr was that daughter and parent isotopes could not be differentiated by traditional mass spectrometry. Instead, an arduous process of whole-rock digestion and column chromatography, requiring large sample volumes, was needed. This restricted the number of analyses undertaken and also prohibited effective identification and isolation of detrital or diagenetic phases, causing the technique to lose popularity. The development of tandem inductively coupled plasma–mass spectrometry (ICP-MS/MS) instruments allows for many of these challenges to be overcome (Zack and Hogmalm, 2016; Redaa et al., 2021). Introduction of a reactive gas into a reaction cell between the two quadrupoles in an ICP-MS/MS system enables the online separation of ^{87}Sr from ^{87}Rb via

CITATION: Subarkah, D., et al., 2021, Unraveling the histories of Proterozoic shales through in situ Rb-Sr dating and trace element laser ablation analysis: Geology, v. XX, p. , https://doi.org/10.1130/G49187.1

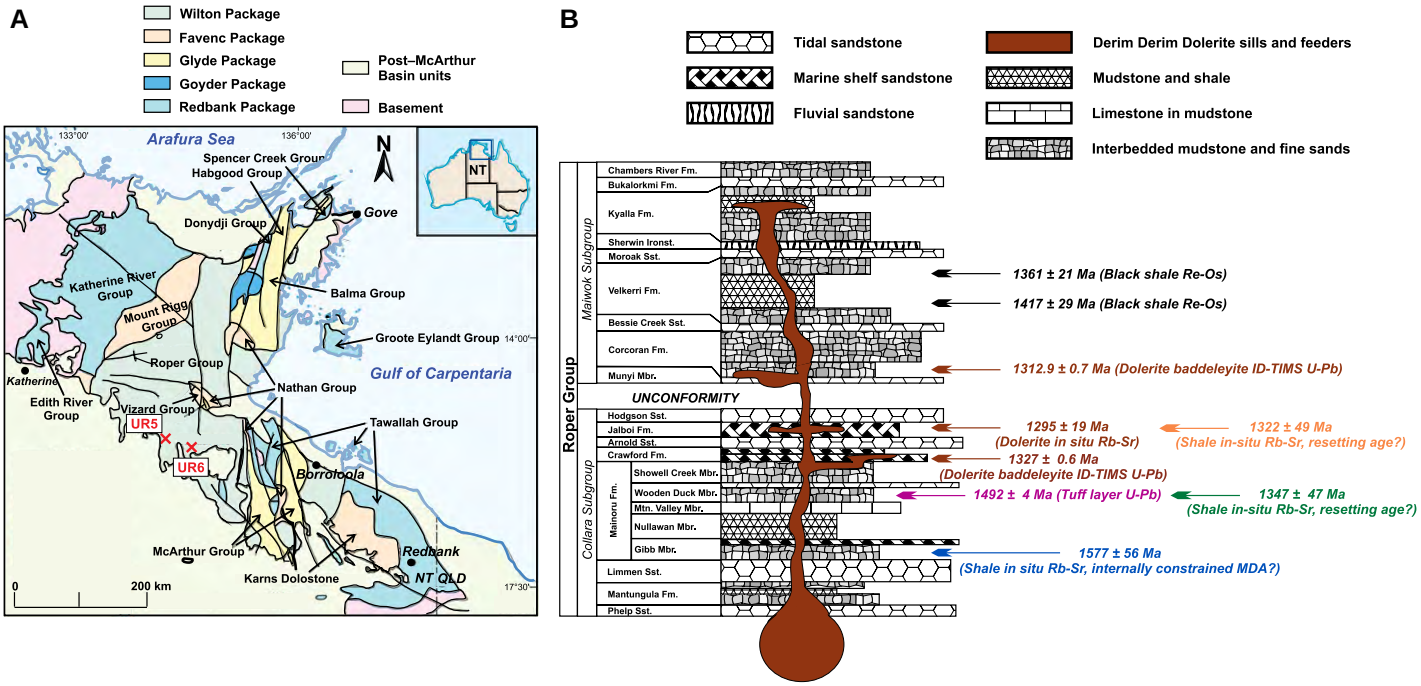

Figure 1. (A) Geological map of McArthur Basin (northern Australia) with localities of sampled wells. NT—Northern Territory; QLD—Queensland. (B) Stratigraphic log of Roper Group modified from Ahmad and Munson (2013) with summarized geochronological constraints. U-Pb tuff age (purple): Southgate et al. (2000); U-Pb ages of sill (brown) cross-cutting Crawford and Corcoran Formations: Bodorkos et al. (2020) and Yang et al. (2020), respectively; Re-Os shale ages (black): Kendall et al. (2009); *in situ* Rb-Sr ages (orange, green, blue): from this study. Fm.—Formation; Ironst.—Ironstone; Sst.—Sandstone; Mbr.—Member; Mtn.—Mountain; ID-TIMS—isotope dilution–thermal ionization mass spectrometry; MDA—minimum depositional age.

measurement of the mass-shifted reaction product (Zack and Hogmalm, 2016; Hogmalm et al., 2017). This setup allows for direct, *in situ* Rb-Sr dating of minerals and rocks when coupled to a laser ablation system. *In situ* Rb-Sr dating is capable of analyzing paragenetic phases while maintaining their microscale textural context (Armistead et al., 2020; Tamblyn et al., 2020). Precision in Rb-Sr age is primarily a function of a good spread in $^{87}Rb/^{86}Sr$ ratios, the number of data points used to define the regression line, and the errors on each individual analysis (Nebel, 2014).

We illustrate a novel application of *in situ* Rb-Sr dating coupled with trace elemental analysis from a set of Proterozoic shales from the McArthur Basin (northern Australia; Fig. 1). A dolerite intrusion intersecting some of the studied shales was also analyzed. Geochemical and geochronological data collected simultaneously are used to distinguish the different depositional and alteration histories of these rocks.

REGIONAL GEOLOGY

The northern Australian Proterozoic McArthur Basin is intra-cratonic and consists of four unconformity-bound sedimentary packages (Ahmad and Munson, 2013). The Roper Group (ca. 1.6–1.3 Ga) (Fig. 1B) is a sequence of marine shelf siliciclastic sediments (Yang et al., 2018) that forms the youngest part of the McArthur Basin. The Collara Subgroup is dated by U-Pb zircon from a 1492 ± 4 Ma tuff (Fig. 1B; Southgate et al., 2000). It forms the oldest part of the Roper Group and is the focus of our study.

We sampled the Derim Derim Dolerite (from well UR5, sample UR5_229; Fig. 1A) that intrudes most formations of the Roper Group (Ahmad and Munson, 2013). U-Pb thermal ionization mass spectrometry (TIMS) analyses of the same suite sampled at locations >200 km apart yielded ages of 1327.5 ± 0.6 Ma (Bodorkos et al., 2020) and 1312.9 ± 0.7 Ma (Yang et al., 2020), respectively.

We sampled the Collara Subgroup in two wells: UR5 and UR6 (Fig. 1A). Shale samples analyzed in this study are from the Gibb and Wooden Duck Members (Mainoru Formation; samples UR6_269 and UR5_578, respectively) and the Jalboi Formation (sample UR5_139). Shales from well UR5 were picked to constrain the alteration aureole of the Derim Derim intrusion.

ANALYTICAL METHODS

The mineralogy and petrography of the shales were characterized by energy-dispersive X-ray spectroscopy (EDS) mapping with Nanomin software (Rafiei et al., 2020) at Macquarie University (Sydney, Australia) following the approach of Rafiei et al. (2020) complemented with bulk powder X-ray diffraction (XRD). The dolerite was mapped for its petrographic textures and elemental composition using a scanning electron microscope at Adelaide Microscopy (Adelaide, Australia; see the Supplemental Material[1]). Laser analyses were performed at Adelaide Microscopy following Redaa et al. (2021). Phlogopite nano-powder Mica-Mg as well as its natural mineral crystal (MDC) sourced from Bekily, Madagascar (Govindaraju et al., 1994), were used as standards for data normalization. In addition, an illite pressed powder pellet from Fithian, Illinois, USA (Kralik, 1984), was analyzed as a complementary in-house comparison to assess possible matrix differences between the phlogopite standards and the illite-rich shales analyzed in this study. Finally, the morphology and structure of laser craters in standards and samples were imaged using an Olympus FV3000 confocal microscope (Fig. S5 in the Supplemental Material). Methodologies are extensively discussed in the Supplemental Material.

RESULTS

The pit-depth profiles show that samples analyzed in this study have similar ablation characteristics to the Mica-Mg nano-powder standard and the Fithian illite pellet as opposed to the MDC mineral flake (Fig. S5; see the

[1]Supplemental Material. Extended methods and dataset. Please visit https://doi.org/10.1130/GEOL.S.16569531 to access the supplemental material, and contact editing@geosociety.org with any questions.

Supplemental Material). Semiquantitative and microscale identification of the studied shales are reported in Figure 2. The Gibb Member shale (sample UR6_269) gave an age of 1577 ± 56 Ma with initial $^{87}Sr/^{86}Sr$ ratio of 0.7046 ± 0.0073. The Derim Derim Dolerite (sample UR5_229) yielded an age of 1295 ± 19 Ma (initial $^{87}Sr/^{86}Sr$ ratio: 0.7314 ± 0.010). The Jalboi Formation shale (sample UR5_139) gave an age of 1322 ± 49 Ma (initial $^{87}Sr/^{86}Sr$ ratio: 0.7260 ± 0.023). Finally, the Wooden Duck Member shale (sample UR5_578) had an age of 1347 ± 47 Ma (initial $^{87}Sr/^{86}Sr$ ratio: 0.7339 ± 0.015). REEY values from all shale samples were normalized to those of sample UR_269 because this is interpreted to be the best-preserved shale, with an initial $^{87}Sr/^{86}Sr$ ratio reflective of ca. 1.5 Ga seawater (Fig. 3) and the least-altered mineralogy (Fig. 2). All remaining samples show a normalized light REE (LREE) depletion (Fig. 3B). The Jalboi Formation shale is located closest to the dolerite intrusion and has REEY patterns most similar to those of the dolerite.

DISCUSSION

The majority of illite in Proterozoic shales of the McArthur Basin is believed to have formed during early marine diagenesis via reverse weathering processes in equilibrium with paleo-seawater, as opposed to being detrital products of continental weathering from soils like those commonly found in Phanerozoic shales (Rafiei and Kennedy, 2019). The widespread formation of authigenic marine clays has been proposed to be a major sink for Si during the Precambrian due to the absence of pelagic Si-mineralizing organisms (Isson and Planavsky, 2018). Therefore, these shales are prime candidates for *in situ* Rb-Sr dating to determine their depositional or early marine diagenetic histories. The dominance of cogenetic phases eases laser targeting and provides a good spread in $^{87}Rb/^{86}Sr$ ratios. However, high-resolution microscale mineral identification is important for confirming the authigenic mineral dominance and avoiding detrital-phase contamination (see the Supplemental Material).

The abundant clays in the Gibb Member shale UR6_269 are dominantly illite and do not show typical irregular, detrital morphologies, supporting our interpretation of their authigenic origin. Sample UR6_269 is also the only sample to preserve siderite micronodules (Fig. 2A), which are intergrown with an illite and chlorite matrix, suggesting an early-diagenetic origin. This is commonly found in marine shales precipitating under anoxic conditions with high levels of ferrous iron (Fe^{2+}) and limited sulfur (HS^-) availability (Mozley and Wersin, 1992). The Rb-Sr age of the Gibb Member shale is within its depositional age (Southgate et al., 2000), suggesting that the analyzed bulk-composition illite matrix of this sample formed authigenically during or soon after deposition. Furthermore, the initial $^{87}Sr/^{86}Sr$ ratio of this shale (Fig. 3) is within error of estimates for coeval paleo-seawater (Kuznetsov et al., 2014), further confirming the marine origin of the dated assemblage. Although within error, the centroid value is slightly more radiogenic than that of paleo-seawater, which may reflect its shallow-marine or semi-restricted depositional environment (El Meknassi et al., 2020). Nevertheless, we conclude that the geochronology, isotope geochemistry, and petrography of the Gibb Member shale reflect an early-diagenetic signature in equilibrium with contemporaneous ocean water, as opposed to a late-stage nonmarine alteration event.

Bulk XRD data and spectral reflectance analyses of the Derim Derim Dolerite sample UR5_229 (see the Supplemental Material, and Fig. S3; Smith, 2015) indicate its extensive alteration and chloritization. In addition, backscatter electron imaging and elemental mapping of

A

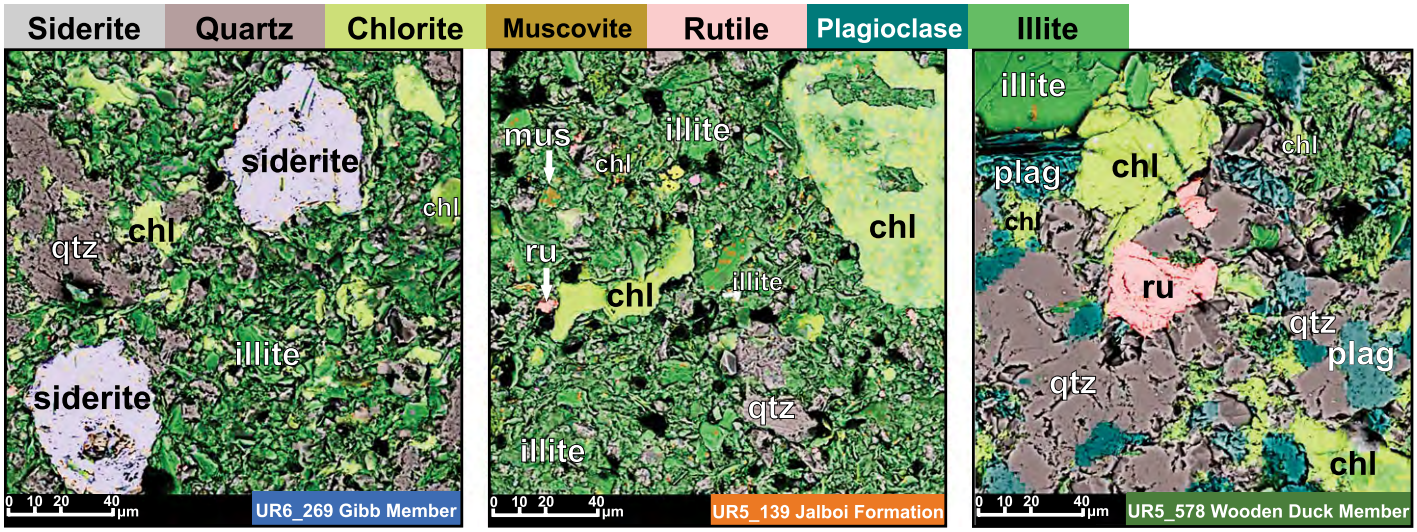

B

Mineralogy	UR6_269 Gibb Member	UR5_139 Jalboi Formation	UR5_578 Wooden Duck Member
	Nanomin (wt %)	*Nanomin (wt %)*	*Nanomin (wt %)*
Illite	62%	67%	28%
Quartz	16%	23%	36%
Alkali feldspar	1.5%	3.3%	9.2%
Plagioclase	0.36%	0.75%	8.6%
Chlorite	5.7%	2.3%	14%
Muscovite	4.0%	1.9%	1.2%
Siderite	6.6%	0.0%	0.0%
Other	3.6%	1.4%	2.4%

Figure 2. (A) Microscale energy dispersive X-ray spectroscopy (EDS) mineral maps of all shale samples. Qtz—quartz; Chl—chlorite; Ru—rutile; Plag—plagioclase. (B) Semiquantitative mineralogical data obtained by Nanomin software (Rafiei et al., 2020).

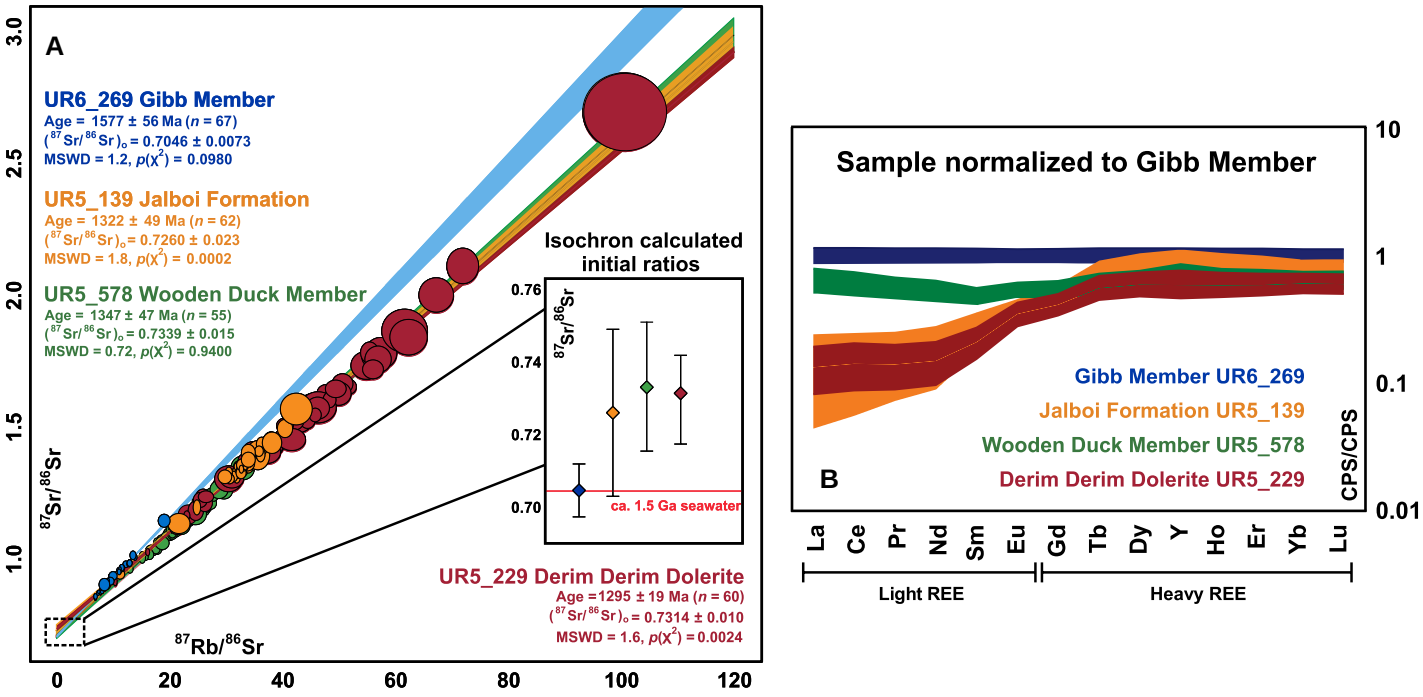

Figure 3. (A) Summary of Rb-Sr isotopic data and $^{87}Sr/^{86}Sr$ initial ratios of the samples (see inset). $^{87}Sr/^{86}Sr$ initial value of sample UR6_269 overlaps with that of seawater ca. 1.5 Ga (Kuznetsov et al., 2014). MSWD—mean squared weighted deviation; $(^{87}Sr/^{86}Sr)_0$—initial $^{87}Sr/^{86}Sr$ ratio. (B) Average rare earth element (REE) plus yttrium (REEY) patterns of shale samples, normalized to REEY values of Gibb Member shale. CPS—count per second.

sample UR5_229 (Fig. S2) reveals many K-rich (and, by inference, Rb-rich) phases. Rb-enriched secondary chlorite is a common product of hydrothermal alteration of mafic protoliths (Duane et al., 2004). The high initial $^{87}Sr/^{86}Sr$ ratio of this sample (Fig. 3) suggests fluid-rock interaction processes involving substantial influx of radiogenic crustal fluids during the purported potassic alteration of the dolerite. The Rb-Sr age obtained from sample UR5_229 dolerite overlaps, within error, the crystallization ages of Derim Derim intrusions obtained elsewhere in the McArthur Basin (Bodorkos et al., 2020; Yang et al., 2020), indicating that this fluid-infiltration event likely happened during or soon after dike intrusion.

Energy-dispersive X-ray spectroscopy screening of shales from both the Jalboi Formation and Wooden Duck Member shows evidence for substantial post-depositional alteration (Fig. 2), likely caused by the Derim Derim Dolerite intrusion. Specifically, large chlorite aggregates in the Jalboi Formation replace other earlier clay constituents. In the Wooden Duck Member, illite aggregates display morphologies inconsistent with an early-diagenetic origin, showing fissile and foliated matrices interlocking with quartz overgrowth. In addition, the presence of rutile in these rocks implies secondary redistribution of titanium. Ages and initial $^{87}Sr/^{86}Sr$ ratios from the Jalboi Formation and Wooden Duck Member shales overlap with those from the Derim Derim Dolerite, yielding highly radiogenic and nonmarine values (Fig. 3). Evidence for higher initial $^{87}Sr/^{86}Sr$ ratios in marine carbonates and shales is commonly related to secondary processes such as (1) influence from late-stage diagenetic processes (Phan et al., 2019), (2) the introduction of radiogenic Sr via later diagenetic fluid-rock interactions and metasomatism (Poitrasson et al., 1995), and (3) inputs of radiogenic Sr sourced from detrital grains.

Fluid-rock interaction processes also have significant impact on REEY solubility and transport during later alteration. Both shales from well UR5 are depleted in LREEs when normalized to the Gibb Member shale. The Jalboi Formation shows extreme depletion and has a similar REEY pattern to that of the dolerite intrusion (Fig. 3). Multiple factors and processes could have caused the relative LREE depletion observed in these shales. However, the increased LREE depletion with increased proximity of the shales to the intrusion suggests that intrusion-induced hydrothermal alteration is the most likely cause. Physical and chemical buffers have been shown to play a major role in fluid-rock interaction and alteration in marine sediments (Park et al., 2019).

Taken together, the resetting of the Rb-Sr chronometer with highly radiogenic initial $^{87}Sr/^{86}Sr$ ratios, the observed depletions of LREEs, as well as the petrography of the altered shales collected in vicinity of dolerite dike in well UR5 clearly demonstrate that these rocks were altered during or soon after the dolerite emplacement. Previous studies have used the total Fe species measured in shales from well UR5 to infer periods of anoxia during the Proterozoic (Shen et al., 2003). We argue these altered shales may not faithfully record primary paleo–redox conditions because their bulk chemistry has likely been affected by the dolerite intrusion. Consequently, any interpretations made from these rocks to reconstruct past paleoenvironments should be treated with caution.

CONCLUSIONS

We present the first *in situ* Rb-Sr dating and elemental analyses of Proterozoic illite-rich shales as well as an altered dolerite intrusion. The Gibb Member shale from an intrusion-absent borehole was abundant in authigenic illite and yielded a Rb-Sr age consistent with the depositional age for the unit. In addition, the sample's initial $^{87}Sr/^{86}Sr$ ratio overlaps with that of ca. 1.5 Ga seawater. In contrast, the Jalboi Formation and Wooden Duck Member shales were sourced from a well containing a dolerite intrusion. We demonstrate that their Rb-Sr isotopic systems were reset by the intrusion and their chemistry has affinities to the altered dolerite. As such, we show that the chronological and geochemical data obtained together by this novel approach can be used to constrain the histories of Precambrian shales effectively where authigenic phases make up the dominant Rb-Sr–bearing constituents.

ACKNOWLEDGMENTS

This work was supported by the Australian Research Council projects LP160101353 and DP210100462, forming MinEx CRC contribution

#2021/47. Initial development of the *in situ* Rb-Sr dating technique at the University of Adelaide (Australia) was supported by Agilent Technologies Australia Ltd. We thank Marissa Tremblay, Kai Rankenburg, Timothy Lyons, and an anonymous reviewer, who all positively contributed to this paper with their constructive inputs. We also acknowledge and thank William Clyde for his valuable assessment of this work as the Science Editor.

REFERENCES CITED

Ahmad, A., and Munson, T.J., compilers, 2013, Geology and Mineral Resources of the Northern Territory: Northern Territory Geological Survey Special Publication 5, https://geoscience.nt.gov.au/gemis/ntgsjspui/handle/1/81446.

Armistead, S.E., Collins, A.S., Redaa, A., Jepson, G., Gillespie, J., Gilbert, S., Blades, M.L., Foden, J.D., and Razakamanana, T., 2020, Structural evolution and medium-temperature thermochronology of central Madagascar: Implications for Gondwana amalgamation: Journal of the Geological Society, v. 177, p. 784–798, https://doi.org/10.1144/jgs2019-132.

Bodorkos, S., Crowley, J.L., Claoué-Long, J.C., Anderson, J.R., and Magee, C.W., Jr., 2020, Precise U-Pb baddeleyite dating of the Derim Derim Dolerite, McArthur Basin, Northern Territory: Old and new SHRIMP and ID-TIMS constraints: Australian Journal of Earth Sciences, v. 68, p. 36–50, https://doi.org/10.1080/08120099.2020.1749929.

Compston, W., and Pidgeon, R.T., 1962, Rubidium-strontium dating of shales by the total-rock method: Journal of Geophysical Research, v. 67, p. 3493–3502, https://doi.org/10.1029/JZ067i009p03493.

Duane, M.J., Kruger, F.J., Turner, A.M., Whitelaw, H.T., Coetzee, H., and Verhagen, B.T., 2004, The timing and isotopic character of regional hydrothermal alteration and associated epigenetic mineralization in the western sector of the Kaapvaal Craton (South Africa): Journal of African Earth Sciences, v. 38, p. 461–476, https://doi.org/10.1016/j.jafrearsci.2004.03.002.

El Meknassi, S., et al., 2020, Seawater $^{87}Sr/^{86}Sr$ ratios along continental margins: Patterns and processes in open and restricted shelf domains: Chemical Geology, v. 558, 119874, https://doi.org/10.1016/j.chemgeo.2020.119874.

Gorokhov, I.M., Siedlecka, A., Roberts, D., Melnikov, N.N., and Turchenko, T.L., 2001, Rb-Sr dating of diagenetic illite in Neoproterozoic shales, Varanger Peninsula, northern Norway: Geological Magazine, v. 138, p. 541–562, https://doi.org/10.1017/S001675680100574X.

Govindaraju, K., Rubeska, I., and Paukert, T., 1994, 1994 Report on zinnwaldite ZW-C analysed by ninety-two GIT-IWG member-laboratories: Geostandards Newsletter, v. 18, p. 1–42, https://doi.org/10.1111/j.1751-908X.1994.tb00502.x.

Hogmalm, K.J., Zack, T., Karlsson, A.K.-O., Sjöqvist, A.S.L., and Garbe-Schönberg, D., 2017, In situ Rb-Sr and K-Ca dating by LA-ICP-MS/MS: An evaluation of N_2O and SF_6 as reaction gases: Journal of Analytical Atomic Spectrometry, v. 32, p. 305–313, https://doi.org/10.1039/C6JA00362A.

Isson, T.T., and Planavsky, N.J., 2018, Reverse weathering as a long-term stabilizer of marine pH and planetary climate: Nature, v. 560, p. 471–475, https://doi.org/10.1038/s41586-018-0408-4.

Kendall, B., Creaser, R.A., Gordon, G.W., and Anbar, A.D., 2009, Re-Os and Mo isotope systematics of black shales from the Middle Proterozoic Velkerri and Wollogorang Formations, McArthur Basin, northern Australia: Geochimica et Cosmochimica Acta, v. 73, p. 2534–2558, https://doi.org/10.1016/j.gca.2009.02.013.

Kralik, M., 1984, Effects of cation-exchange treatment and acid leaching on the Rb-Sr system of illite from Fithian, Illinois: Geochimica et Cosmochimica Acta, v. 48, p. 527–533, https://doi.org/10.1016/0016-7037(84)90281-3.

Kuznetsov, A.B., Semikhatov, M.A., and Gorokhov, I.M., 2014, The Sr isotope chemostratigraphy as a tool for solving stratigraphic problems of the Upper Proterozoic (Riphean and Vendian): Stratigraphy and Geological Correlation, v. 22, p. 553–575, https://doi.org/10.1134/S0869593814060033.

Lyons, T.W., Reinhard, C.T., and Planavsky, N.J., 2014, The rise of oxygen in Earth's early ocean and atmosphere: Nature, v. 506, p. 307–315, https://doi.org/10.1038/nature13068.

Mozley, P.S., and Wersin, P., 1992, Isotopic composition of siderite as an indicator of depositional environment: Geology, v. 20, p. 817–820, https://doi.org/10.1130/0091-7613(1992)020<0817:ICOSAA>2.3.CO;2.

Nebel, O., 2014, Rb-Sr dating, *in* Rink, W.J., and Thompson, J., eds., Encyclopedia of Scientific Dating Methods: Dordrecht, Springer, https://doi.org/10.1007/978-94-007-6326-5_116-1.

Park, Y., et al., 2019, The lead-up to the Sturtian Snowball Earth: Neoproterozoic chemostratigraphy time-calibrated by the Tambien Group of Ethiopia: Geological Society of America Bulletin, v. 132, p. 1119–1149, https://doi.org/10.1130/B35178.1.

Phan, T.T., Hakala, J.A., Lopano, C.L., and Sharma, S., 2019, Rare earth elements and radiogenic strontium isotopes in carbonate minerals reveal diagenetic influence in shales and limestones in the Appalachian Basin: Chemical Geology, v. 509, p. 194–212, https://doi.org/10.1016/j.chemgeo.2019.01.018.

Planavsky, N.J., Tarhan, L.G., Bellefroid, E.J., Evans, D.A.D., Reinhard, C.T., Love, G.D., and Lyons, T.W., 2015, Late Proterozoic transitions in climate, oxygen, and tectonics, and the rise of complex life: The Paleontological Society Papers, v. 21, p. 47–82, https://doi.org/10.1017/S1089332600002965.

Poitrasson, F., Pin, C., and Duthou, J.-L., 1995, Hydrothermal remobilization of rare earth elements and its effect on Nd isotopes in rhyolite and granite: Earth and Planetary Science Letters, v. 130, p. 1–11, https://doi.org/10.1016/0012-821X(94)00257-Y.

Rafiei, M., and Kennedy, M., 2019, Weathering in a world without terrestrial life recorded in the Mesoproterozoic Velkerri Formation: Nature Communications, v. 10, 3448, https://doi.org/10.1038/s41467-019-11421-4.

Rafiei, M., Löhr, S., Baldermann, A., Webster, R., and Kong, C., 2020, Quantitative petrographic differentiation of detrital vs diagenetic clay minerals in marine sedimentary sequences: Implications for the rise of biotic soils: Precambrian Research, v. 350, 105948, https://doi.org/10.1016/j.precamres.2020.105948.

Rainbird, R.H., Rooney, A.D., Creaser, R.A., and Skulski, T., 2020, Shale and pyrite Re-Os ages from the Hornby Bay and Amundsen basins provide new chronological markers for Mesoproterozoic stratigraphic successions of northern Canada: Earth and Planetary Science Letters, v. 548, 116492, https://doi.org/10.1016/j.epsl.2020.116492.

Rasmussen, B., Fletcher, I.R., Bengtson, S., and McNaughton, N.J., 2004, SHRIMP U-Pb dating of diagenetic xenotime in the Stirling Range Formation, Western Australia: 1.8 billion year minimum age for the Stirling biota: Precambrian Research, v. 133, p. 329–337, https://doi.org/10.1016/j.precamres.2004.05.008.

Ravizza, G., and Turekian, K.K., 1989, Application of the ^{187}Re-^{187}Os system to black shale geochronometry: Geochimica et Cosmochimica Acta, v. 53, p. 3257–3262, https://doi.org/10.1016/0016-7037(89)90105-1.

Redaa, A., Farkaš, J., Gilbert, S., Collins, A.S., Wade, B., Löhr, S., Zack, T., and Garbe-Schönberg, D., 2021, Assessment of elemental fractionation and matrix effects during in situ Rb-Sr dating of phlogopite by LA-ICP-MS/MS: Implications for the accuracy and precision of mineral ages: Journal of Analytical Atomic Spectrometry, v. 36, p. 322–344, https://doi.org/10.1039/D0JA00299B.

Shen, Y., Knoll, A.H., and Walter, M.R., 2003, Evidence for low sulphate and anoxia in a mid-Proterozoic marine basin: Nature, v. 423, p. 632–635, https://doi.org/10.1038/nature01651.

Smith, B.R., 2015, HyLogger drillhole report for Urapunga 5, McArthur Basin, Northern Territory: Northern Territory Geological Survey HyLogger Data Package 0042.

Southgate, P.N., et al., 2000, Chronostratigraphic basin framework for Palaeoproterozoic rocks (1730–1575 Ma) in northern Australia and implications for base-metal mineralisation: Australian Journal of Earth Sciences, v. 47, p. 461–483, https://doi.org/10.1046/j.1440-0952.2000.00787.x.

Tamblyn, R., Hand, M., Morrissey, L., Zack, T., Phillips, G., and Och, D., 2020, Resubduction of lawsonite eclogite within a serpentinite-filled subduction channel: Contributions to Mineralogy and Petrology, v. 175, 74, https://doi.org/10.1007/s00410-020-01712-1.

Yang, B., Smith, T.M., Collins, A.S., Munson, T.J., Schoemaker, B., Nicholls, D., Cox, G., Farkas, J., and Glorie, S., 2018, Spatial and temporal variation in detrital zircon age provenance of the hydrocarbon-bearing upper Roper Group, Beetaloo Sub-basin, Northern Territory, Australia: Precambrian Research, v. 304, p. 140–155, https://doi.org/10.1016/j.precamres.2017.10.025.

Yang, B., Collins, A.S., Blades, M.L., Capogreco, N., Payne, J.L., Munson, T.J., Cox, G.M., and Glorie, S., 2019, Middle–late Mesoproterozoic tectonic geography of the North Australia Craton: U-Pb and Hf isotopes of detrital zircon grains in the Beetaloo Sub-basin, Northern Territory, Australia: Journal of the Geological Society, v. 176, p. 771–784, https://doi.org/10.1144/jgs2018-159.

Yang, B., Collins, A.S., Cox, G.M., Jarrett, A.J.M., Denyszyn, S., Blades, M.L., Farkaš, J., and Glorie, S., 2020, Using Mesoproterozoic sedimentary geochemistry to reconstruct basin tectonic geography and link organic carbon productivity to nutrient flux from a northern Australian large igneous province: Basin Research, v. 32, p. 1734–1750, https://doi.org/10.1111/bre.12450.

Zack, T., and Hogmalm, K.J., 2016, Laser ablation Rb/Sr dating by online chemical separation of Rb and Sr in an oxygen-filled reaction cell: Chemical Geology, v. 437, p. 120–133, https://doi.org/10.1016/j.chemgeo.2016.05.027.

Printed in USA

Precambrian Research 343 (2020) 105709

Contents lists available at ScienceDirect

Precambrian Research

journal homepage: www.elsevier.com/locate/precamres

Coupled U-Pb and Rb-Sr laser ablation geochronology trace Archean to Proterozoic crustal evolution in the Dharwar Craton, India

Shan-Shan Li[a,b], M. Santosh[a,c,*], Juraj Farkaš[c], Ahmad Redaa[c,d], Sohini Ganguly[e], Sung Won Kim[f], Cun Zhang[a], Sarah Gilbert[g], Thomas Zack[c,h]

[a] School of Earth Sciences and Resources, China University of Geosciences Beijing, 29 Xueyuan Road, Beijing 100083, China
[b] Department of Geology and Geological Engineering, Colorado School of Mines, Golden, CO 80401, USA
[c] Department of Earth Sciences, University of Adelaide, North Terrace, Adelaide, SA 5005, Australia
[d] Faculty of Earth Sciences, King Abdulaziz University, Jeddah, Saudi Arabia
[e] School of Earth, Ocean and Atmospheric Sciences, Goa University, Taleigao Plateau, Goa 403206, India
[f] Geological Research Division, Korea Institute of Geoscience and Mineral Resources, Daejeon 305-350, South Korea
[g] Adelaide Microscopy, University of Adelaide, North Terrance, Adelaide, SA 5005, Australia
[h] Department of Earth Sciences, University of Gothenburg, Sweden

ARTICLE INFO

Keywords:
In-situ Rb-Sr geochronology
Zircon U-Pb-Hf isotopes
Western Dharwar Craton
Karwar Block
Crustal growth
Metamorphism

ABSTRACT

The Western Dharwar Craton (WDC) and the Karwar Block (KB) in southern Peninsular India provide important windows to Earth's early crustal evolution and continental growth as these domains likely represent fragments of the first landmass or supercontinent on our planet. Here we employ, for the first time, a coupled laser ablation zircon U-Pb dating and in-situ Rb-Sr dating of micas (biotite, muscovite) and feldspars to evaluate the Meso- to Neoarchean crustal evolution and Proterozoic magmatism/metamorphism in the Karwar Block. This novel approach based on integrated geochronological results show that the WDC and KB experienced (i) a major Mesoarchean continental growth event (c. 3.2 to 2.9 Ga), (ii) younger Neoarchean and Paleoproterozoic magmatism/migmatization (syn- and post-tectonic granite formation events at c. 2.8–2.6 Ga and 2.2 Ga, respectively), and (iii) Mesoproterozoic metamorphism/thermal imprint (as young as 1.2 Ga). The zircon εHf(t) values exhibit a range from +0.4 to +9.8 in amphibolite, hornblende gneiss and trondhjemite (3.28–3.08 Ga), as well as the +6.1 to +9.7 range for 2.96 Ga old zircons in porphyritic granite, which suggests juvenile source for the magmatism that constructed this crustal block.

Overall, this study illustrates the benefits of using coupled zircon U-Pb and in-situ Rb-Sr mica and feldspar dating approaches, as the former (U/Pb) provides robust constraints or a 'baseline age' for initial crystallization of crustal sequences whereas the latter (Rb/Sr) is sensitive to younger magmatic and metamorphic events. Thus, the integration of these two laser ablation ICP-MS based geochronometers applied to crustal evolution studies, has the potential to provide more comprehensive insights into continental growth in the early Earth, and later magmatic and metamorphic history of the region.

1. Introduction

Zircon occurs as a common accessory mineral in a wide range of rocks that make up the continental crust, and provides a potential tool to trace the timing of major geological events (Watson and Harrison, 1983; Bea, 1996; Corfu et al., 2003). As a durable mineral, zircon is widely used to derive information on magmatic, hydrothermal and metamorphic events (Miller et al., 2007; Heaman and Parrish, 1991; Li et al., 2019), as well as to trace the crustal and mantle evolution history (Dhuime et al., 2011; Hawkesworth and Kemp, 2006; Pupin, 1980). In situ U-Th-Pb and Lu-Hf isotopic characterization of zircon allow for precise dating and have wide applications in geological and tectonic processes (Corfu, 2013; Vermeesch, 2018; Andersen et al., 2002). The Lu-Hf isotopes in zircon provide information on magma source characteristics (Amelin et al., 1999; Andersen et al., 2002; Bea et al., 2018). To complement the popular zircon-based studies of crustal evolution, here we use a novel in-situ Rb-Sr dating approach (Zack and Hogmalm, 2016; Hogmalm et al., 2017) applied to relatively low-temperature phyllosilicate minerals of the mica group (biotite, muscovite) that commonly occur in igneous and metamorphic rocks. In-situ Rb-Sr

* Corresponding author at: School of Earth Sciences and Resources, China University of Geosciences Beijing, 29 Xueyuan Road, Beijing 100083, China.
E-mail address: santosh@cugb.edu.cn (M. Santosh).

https://doi.org/10.1016/j.precamres.2020.105709
Received 7 October 2019; Received in revised form 8 March 2020; Accepted 17 March 2020
Available online 24 March 2020
0301-9268/

dating can avoid the disadvantage of zircon zonation produced age varieties and age mixing, by using a micro-scale analysis from the K-rich minerals (Tillberg et al., 2020). The method has been widely used for the interpretation of the timing of orogenic events, as well as uplift and exhumation histories (Hogmalm et al., 2017; Tillberg et al., 2020). Combining the isotopic data from zircon (U-Pb, Lu-Hf) and mica group minerals (Rb-Sr) provides a new approach with better insights into the history of crustal evolution and major crystallization and orogenic/metamorphic events (Armistead et al.,2020).

The Dharwar Craton incorporates Paleoarchean to Neoarchean crustal rocks (c.3.4–2.5 Ga) with multiple magmatic and metamorphic history, providing a window to the evolution of Early Earth (Lancaster et al., 2015; Jayananda et al., 2018). The craton comprises three major blocks, termed as Western Dharwar Craton (WDC), Central Dharwar Craton (CDC) and Eastern Dharwar Craton (EDC) (Li et al., 2018a; Jayananda et al., 2020). The Karwar Block (KB) is located in the western periphery of WDC and its tectonic relation to WDC is controversial (Ishwar-Kumar et al., 2016; Armistead et al., 2018). Since the KB preserves some of the oldest crust in Dharwar, with only limited precise geochronological so far carried out on the magmatic rock suites, we selected this region to apply the combined geochronological methods.

In this paper, we present the results from coupled zircon U-Pb and in-situ Rb-Sr geochronology to constrain the timings of magmatic and metamorphic episodes in the Karwar Block (KB) of southern India, and its relation with the Western Dharwar Craton (WDC), with a view to trace early crustal evolution and continental growth. We also present results from geochemistry and zircon Lu-Hf isotopes to trace the magma source and petrogenesis.

2. Geological setting

The Dharwar Craton is one of the largest cratonic nuclei in Peninsular India and has been subdivided into the western, eastern and central Dharwar domains. The Chitradurga greenstone belt separates the western Dharwar Craton (WDC) to the west and central Dharwar Craton (CDC) to the east; the CDC and eastern Dharwar Craton (EDC) amalgamated along the Kolar-Kadiri greenstone belt (Li et al., 2018a; Santosh and Li, 2018; Peucat et al., 2013; Jayananda et al., 2018; Wang and Santosh, 2019; Han et al., 2019) (Fig. 1A). A number of micro-blocks were amalgamated along the southern margin of the Dharwar Craton during the late Archean, including the Mesoarchean Coorg Block, and the Meso- to Neoarchean Nilgiri, Biligirirangan, Shevaroy and Madras Blocks from west to east (Li et al., 2018b; Ishwar-Kumar et al., 2016) (Fig. 1A). The Karwar Block (KB) along the western margin of the peninsula was defined as a discrete block separated by the Kumta Suture zone from the WDC. The tectonic history of KB remains controversial, with some studies correlating the Kumta Suture Zone with the Betsimisaraka Suture Zone in Madagascar (Ishwar-Kumar et al., 2016). Another classification considers the Karwar Block to be part of the WDC (Armistead et al., 2018; Rekha et al., 2013, 2014).

The Shimoga-Goa supracrustal belt extends contiguously until it is concealed beneath the Arabian Sea and the Deccan Traps in the north which dominate the Karwar Block (Fig. 1B). The belt possibly continues beneath the Traps up to the Narmada, where the Narmada-Son lineament terminates this supracrustal belt. The Shimoga-Goa belt extends NNW-SSE over a length of approximately 250 km and has a maximum width of about 120 km at Dharwar. The thickest accumulation of mafic volcanics of this schist belt is occurring at Bababudan and Kudremukh which forms the southern extensions of this belt. The Neoarchean supracrustal sequences of Goa are comparable with Dharwar greenstone belts and are unconformably overlying the 3.3–3.4 Ga Anmode Ghat TTG gneisses and 2.7–2.9 Ga Chandranath granite gneiss. These supracrustals have been classified as Barcem Group and Ponda Group (Dessai, 2011). The Barcem Group has been postulated to be equivalent to the Bababudan Group and it comprises peridotite, metagabbro, talc-chlorite schist, red phyllite, quartz-sericite schist, quartzite and massive, schistose, vesicular metabasalts. The younger supracrustal sequence is dominated by clastics and is assigned to a new stratigraphic group formally termed the Ponda Group which is equivalent to the Chitradurga Group of the Dharwar Supergroup (Dessai, 2011; Dhoundial et al., 1987; Devaraju et al., 2010). This group rests on a basement of the 2.7–2.9 Ga Chandranath granite gneiss with a distinct unconformity marked by a polymict, granite-clast metaconglomerate. The conglomerate displays many similarities with the Talya conglomerate that occurs at the base of the Chitradurga Group. It is overlain by a psamolitic sequence which is followed in ascending order by the chemogenic sediments that host the BIF and by the deep water turbidite sequence (argillite-greywacke association) with intercalations of mafic volcanics. The supracrustal sequence is intruded by the Bondla layered mafic–ultramafic complex along a major shear zone (NW-SE) that largely controls the course of the northwesterly flowing tributary of River Mandovi (Dessai, 2011, 2009). The later intrusion of Canacona potassic granite marks the craton stabilization events in this sector. In this study, we collected representative samples of different rocks types from KB represent preserved vestiges of ancient crustal components that provide an ideal test bed for understanding Archean tectono-thermal events concurrent with primitive crust-mantle interactions, crustal reworking and juvenile crustal growth.

The amphibolite (GOA-1–1), porphyritic granite (GOA-1–2), Hbl-gneiss (GOA-1–3) and granodiorite (GOA-1–5) were collected from the same location at the beach section cliff of Palolem-Canacona sector (15°00′16.66″, 74°01′37.04″). The hornblende gneiss (GOA-1–3) is medium to coarse grain and foliated and show compositional layering of mafic and feldspathic bands. The mafic bands correspond to the amphibolite or diorite, and the felsic bands are mostly granodiorite. The mafic rich part was collected for petrologic and geochronologic studies (Fig. 2). The large exposure of amphibolite (GOA-1–1) is a melanocratic rock with amphibole layers. The rock is medium to fine grain and is traversed by quartz veins. The porphyritic granite (GOA-1–2) contains coarse grain pink K-feldspar (up to 5 cm) surrounded by a medium grain granitic matrix. This disequilibrium texture indicates re-melting and recrystallization. The trondhjemite (GOA-11–1) sample was collected from a hill cutting along the highway about 5 km from Mollem (15°24′34.31″, 74°14′25.12″) where leucocratic, foliated and partly weathered medium grain trondhjemite is exposed. The rock is deformed and partly stretched, and composed dominantly of white plagioclase and quartz (Fig. 2). Tiny flakes of muscovite are scattered along the foliation.

3. Analytical methods

3.1. Geochemistry

Whole-rock samples were analyzed for major, trace, and rare earth element (REE) abundances using inductively coupled plasma atomic emission spectrometry (ICP-AES) (ENVIRO II; Thermo Jarrel-Ash) and ICP mass spectrometry (ICP-MS) (Optima 3000; Perkin-Elmer) at Activation Laboratories, Ltd. (Ancaster, ON, Canada).

3.2. Elemental mapping via SEM with x-ray detector

Selected samples (GOA-1–1, 1–2, 1–3 and 11–1) that were also dated via in-situ Rb-Sr method (see below), were also analyzed and mapped for elemental abundances using the FEI Quanta 450 high-resolution field emission Scanning Electron Microscope (SEM), located at Adelaide Microscopy (University of Adelaide), and the equipped with the x-ray (SDD EDS) detector for micro-scale level mapping of elemental composition.

3.3. In-situ Rb-Sr geochronology

The Rb-Sr ages of mica minerals (biotite and muscovite) were

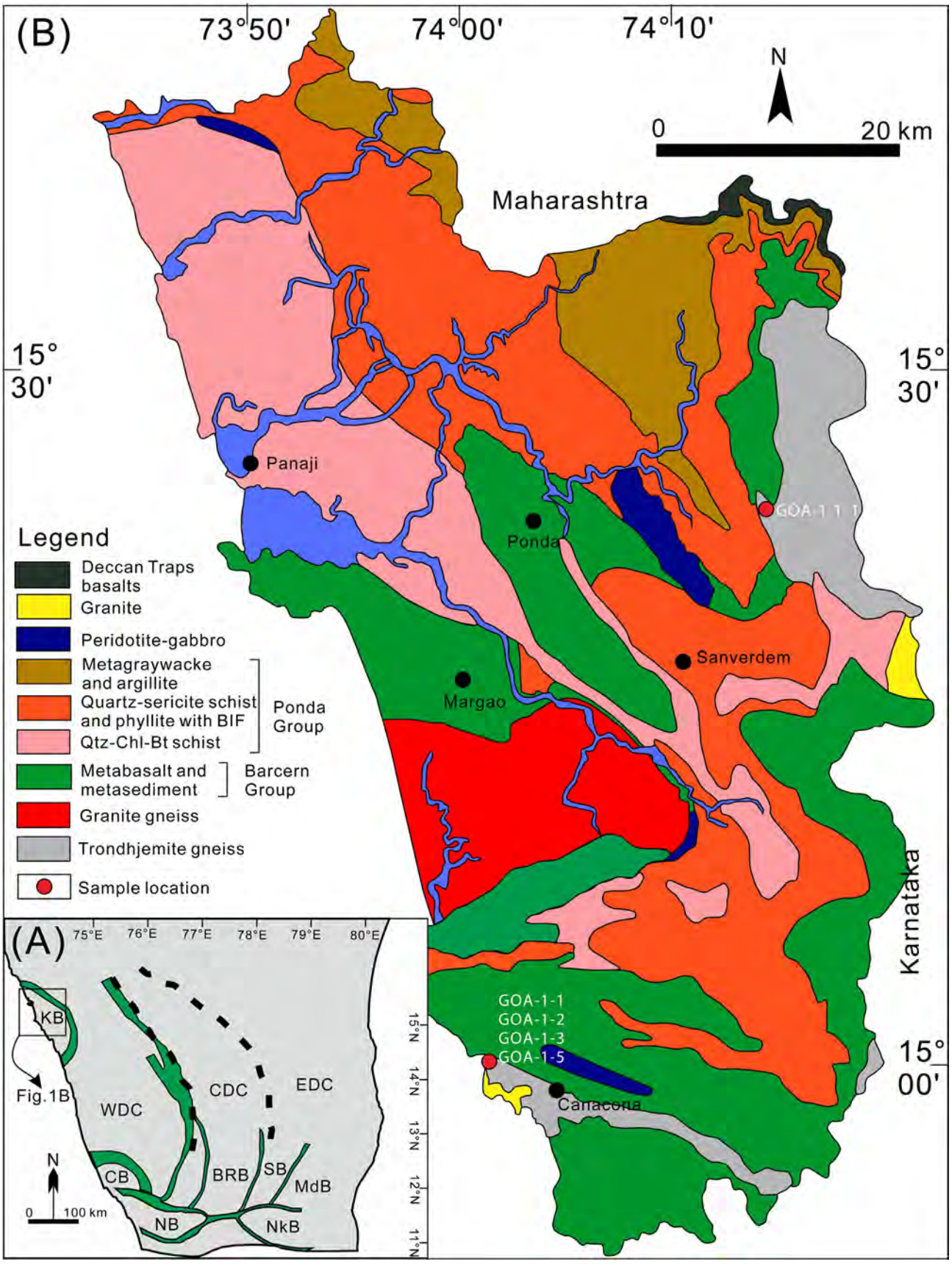

Fig. 1. (A) Geological and tectonic map of the Dharwar Craton, with the study area documented herein indicated by a black box. Bold, black lines represent the interpreted positions of terrane boundaries between the three main cratons: the Western Dharwar Craton (WDC), the Central Dharwar Craton (CDC), and the Eastern Dharwar Craton (EDC). Abbreviations for other fundamental geological features are as follows: KB—Karwar Block; CB—Coorg Block; BRB—Billigiri Rangan Block; SB—Shevaroy Block; MdB—Madras Block; NB—Nilgiri Block; NkB—Namakkal Block. Figure after Li et al. (2018a) and Peucat et al. (2013). (B) Geological map of the study area at the Karwar Block, western Dharwar Craton, showing sample locations (modified after Geological Survey of India, 1996; Dessai, 2011).

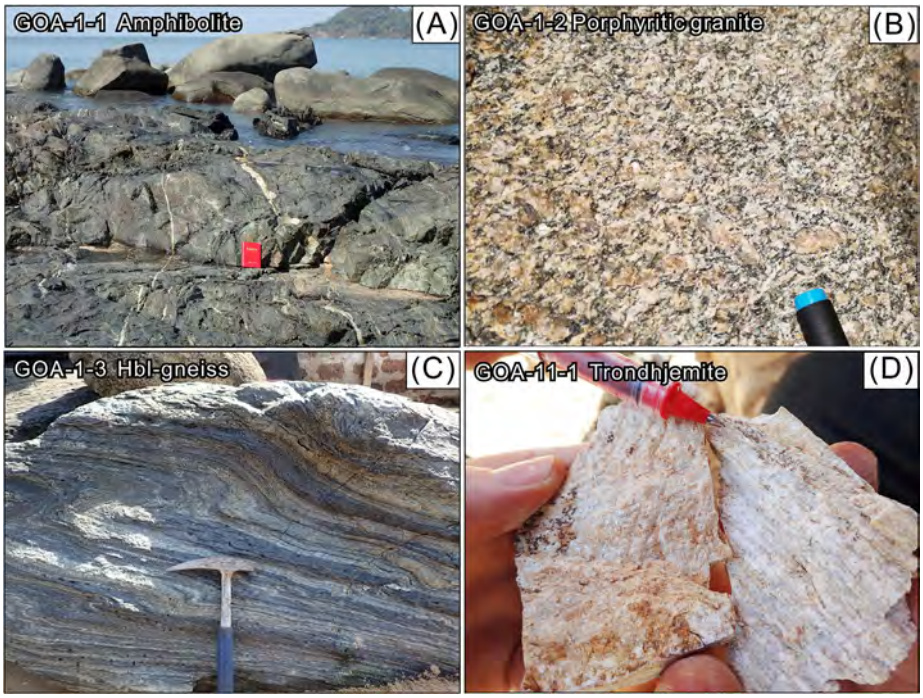

Fig. 2. Field photographs showing outcrops of samples investigated in this work. (A) Amphibolite (GOA-1–1) intercalate with quartz veins showing foliation, (B) Porphyritic granite (GOA-1–2) showing porphyritic texture with K-feldspar surrounded by plagioclase, (C) Hornblende gneiss (GOA-1–3) showing compositional banding (D) Trondhjemite (GOA-11–1) displaying elongated quartz and feldspar.

acquired following a modified approach of Zack and Hogmalm (2016) and Hogmalm et al. (2017), using N_2O reaction gas in a collision cell ICP-MS/MS (Agilent 8900) coupled with a laser ablation (LA) system (RESOlution-LR ArF 193 nm excimer laser) at Adelaide Microscopy (University of Adelaide). Briefly, analyses were done from mounted and polished rock chips containing mica minerals, using a 74 μm laser beam size, ablated in a He atmosphere (0.35 L/min) with Ar carrier gas (1.05 L/min) at a fluence of ~ 3.5 J/cm^2 and a repetition rate of 5 Hz. Using N_2O as the reaction gas in the ICP-MS/MS, ^{85}Rb was measured on mass (at 85 amu) with a dwell time of 0.01 s, and the Sr isotopes were measured as Sr-^{16}O reaction products: ^{86}Sr at 102 amu, ^{87}Sr at 103 amu and ^{88}Sr at 104 amu, with dwell times of 0.05, 0.05 and 0.02 s respectively. Each analysis included 20 s of gas background and 40 s of ablation signal. Details of the LA-ICP-MS/MS instrumental setup used this study are available in Table S1 in the Supplementary Material A.

The in-situ LA-ICP-MS/MS Rb-Sr ages were calculated using a phlogopite nano-powder Mica-Mg (CRPG, France) pressed powder pellet as the primary reference material (cf., Hogmalm et al. 2017), and processed using the Iolite software (Paton et al., 2011) with a customised data reduction algorithm. The latter involves the following steps: 1) calculating the average back ground subtracted sensitivity (cps) for ^{85}Rb, ^{86}Sr and ^{87}Sr over a specified region of interest in the analysis signal; 2) converting the measured ^{85}Rb cps to ^{87}Rb cps, based on the natural abundance of Rb isotopes: ^{87}Rb/^{85}Rb = 0.38562 (Rosman and Taylor, 1998); 3) calculating raw ratios of interest: ^{87}Sr/^{86}Sr and ^{87}Rb/^{86}Sr ; and finally 4) correcting the raw ratios for instrument mass bias against the Mica-Mg reference material (^{87}Sr/^{86}Sr = 1.8525 ± 0.0024 and ^{87}Rb/^{86}Sr = 154.6 ± 1.93; as reported by Hogmalm et al., 2017). Reported uncertainties are 2 sigma internal errors. A secondary mineral standard was also analyzed in each analytical session: MDC, which is a massive phlogopite from the Bekily deposits of South Madagascar from which Mica-Mg powder standard was originally sourced (Govindaraju, 1979), and has an expected age of 519.4 ± 6.5 Ma (recalculated by Hogmalm et al., 2017). Finally, the Rb-Sr age for unknown samples was calculated from the corrected ^{87}Rb/^{86}Sr and ^{87}Sr/^{86}Sr ratios using the Isoplot R software (Vermeesch, 2018).

3.4. Zircon U-Pb and Lu-Hf isotopes

Zircon separation from the crushed rocks was performed at the Yu'neng Geological and Mineral Separation Survey Centre, Langfang City, Hebei Province in China using a magnetic separator and density methods, followed by handpicking under a binocular microscope. The external morphology of each zircon grain was studied using a binocular microscope under reflected light. Grains were then mounted onto an epoxy resin disk, polished to expose their internal texture, and were examined under transmitted and reflected light. The internal zircon textures were studied using cathodoluminescence (CL) images and back-scattered electron (BSE) microscopy images acquired on a scanning electron microscope (SEM) (JSM510) equipped with a Gatan CL probe at the Beijing Geoanalysis Centre.

Zircon Th-U-Pb and Lu-Hf isotopic compositions were measured using a Nu Plasma II Multi Collector Inductively Coupled Plasma Mass Spectrometer equipped with a New Wave Research 193 nm ArF excimer Laser Ablation system (LA-MC-ICPMS) at the Korea Basic Science Institute (KBSI). The Nu Plasma II mass spectrometer contains fixed collectors including 16 Faraday detectors and five ion-counting electron multipliers. The collectors were set for simultaneous U-Pb age determination in the following array: ^{202}Hg (IC 4), ^{204}(Hg + Pb) (IC 3), ^{206}Pb (IC 2), ^{207}Pb (IC 1), ^{208}Pb (IC 0), ^{232}Th (high 7), and ^{238}U (high 9). ^{235}U was calculated from the signal at mass 238 using a natural ^{238}U/^{235}U ratio of 137.88 (Hiess et al., 2012). Mass number 204 was used as a monitor for common ^{204}Pb after discarding background ^{204}Hg. The laser beam size and frequency for U-Pb isotopic analysis were 15 μm and 5 Hz respectively, adjusted according to the grain size and the U content of the zircon. Energy density varies at 2 – 5 J/ cm2. Helium (970 mL/min) was used as a carrier gas. Background intensities, dwell time, and wash out time were 30 s, 30 s, and 20 s, respectively. A time-resolved analytical (TRA) procedure was employed to monitor the measured isotope ratio. Signal intensities were collected from each collector every 0.2 s (integration time). Raw data were corrected for background, laser-induced elemental fractionation, mass discrimination, and drift in ion counter gains. U-Pb isotope ratios were calibrated by concordant reference zircon 91,500 (Wiedenbeck et al., 1995), which was used at the beginning and end of each analytical session and at regular intervals during each session, according to protocols adapted

from Andersen et al., (2002). All ages were calculated with 1σ error, and data reduction was conducted using Iolite 2.5 (Paton et al., 2011) and Isoplot R (Vermeesch, 2018) software.

The Lu-Hf isotopes were measured either by ablating into the pre-existing crater from the U-Th-Pb analysis or as new ablations within the same cathodoluminescence domains. For analysis, ten Faraday collectors were set to simultaneously detect the required isotopes: ^{172}Yb (low 4), ^{173}Yb (low 3), ^{174}(Yb + Hf) (low 2), ^{175}Lu (low 1), ^{176}(Yb + Lu + Hf) (axial), ^{177}Hf (high 1), ^{178}Hf (high 2), ^{179}Hf (high 3), ^{180}Hf (high 4) and ^{182}W (high 6). Laser parameters used were: beam size of 50 μm, 10 Hz repetition rate, and fluence of 6–8 J/cm^2. He (650 mL/min) and N_2 (2 mL/min) were used as carrier gases to enhance Hf isotope intensity (Iizuka and Hirata, 2005). Each analysis was measured in time resolved mode and consisted of 35 s background, 60 s of ablation signal and 15 s washout between analyses. Signal intensities for each detector were collected every 0.2 s (integration time). The interference of ^{176}Lu and ^{176}Yb on the ^{176}Hf signal were corrected by using the procedures of Chu et al. (2002) and Vervoort et al. (2004), respectively. Mass bias of the measured Hf isotopic ratio was corrected to ^{179}Hf/^{177}Hf = 0.7325, using an exponential correction law (Russel et al., 1978; Patchett et al., 1981). The ^{176}Lu/^{177}Hf and ^{176}Yb/^{177}Hf ratios were calculated after Iizuka and Hirata (2005). Initial εHf values were calculated using a ^{176}Lu decay constant of 1.865 × 10^{-11} year^{-1} (Scherer et al., 2001) and the chondritic values suggested by Blichert-Toft and Albarède (1997). Single-(T_{DM}) and two-stage model ages (T_{2DM}) were calculated with reference to suggested parameters for depleted mantle (Griffin et al., 2000) and average continental crust (Rudnick and Gao, 2005). All ratios are reported with 2σ errors. During the sample analysis, to evaluate the precision and accuracy of ^{176}Hf/^{177}Hf ratios, two reference zircons 91,500 (0.282297; Griffin et al., 2000) and Qinghu (0.282482) were repeatedly analyzed at the beginning and end of each analytical session, and at regular intervals during the session. Data reduction was carried out using Iolite 2.5 processing software (Paton et al., 2011).

4. Results

4.1. Petrology and geochemistry

The major and trace element analytical data from five studied samples are given in Table S4, Supplementary Material B and plotted in Figs. 3–4.

Amphibolite GOA-1–1

The sample is composed of plagioclase (40%), amphibole (50%), quartz (7%), and relict clinopyroxene (2%) and traces of biotite (< 1%). Plagioclase and amphibole are medium grain, euhedral to anhedral. The major oxide composition is characterized by moderate SiO_2 (50.96 wt%), Al_2O_3 (14.55 wt%), $Fe_2O_3^T$ (9.79 wt%), MgO (8.37 wt%), TiO_2 (0.547 wt%), low MnO (0.158 wt%), P_2O_5 (0.03 wt %), and high CaO (10.34 wt%). Total alkali content is 3.44 wt%. Among the large ion lithophile elements (LILE), the samples contain moderate Sr (134 ppm) and Ba (22 ppm) with low Rb (14 ppm). Primitive mantle normalized trace element patterns reflect distinct negative anomalies of Nb and Ta and positive anomalies of Zr and Hf. Chondrite normalized REE patterns (Fig. 4) show flat REE patterns. For details on elemental and mineralogical composition of sample GOA-1–1 (amphibolite), analysed via SEM and x-ray detection, see also data in Table S7 Supplementary Material.

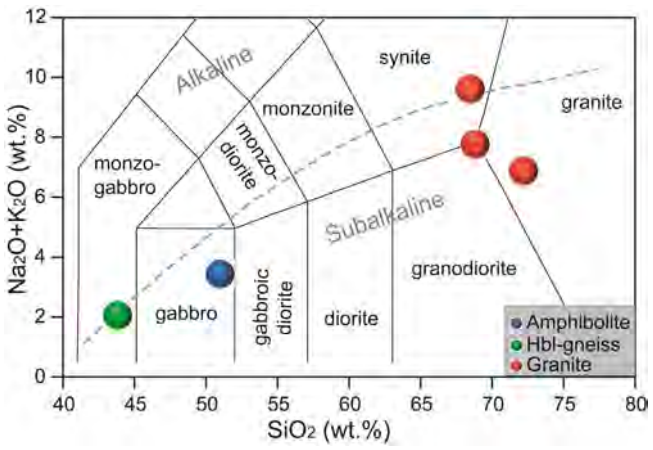

Fig. 3. Total alkali vs. silica diagram plot in the fields for granitoids, amphibolite, Hbl-gneiss (after Wilson, 1989).

Hbl-gneiss GOA-1–3

The rock is dominantly composed of amphibole (60%), epidote (18%), plagioclase and potassium feldspars (15%), quartz (4%) and minor biotite (< 3%). Foliation is mainly defined by elongated amphibole-rich layers. The rock shows relatively low SiO_2 content of 43.79 wt% with moderate concentrations of TiO_2 (0.558 wt%), Al_2O_3 (16.38 wt%) and $Fe_2O_3^T$ (11.71 wt%). When plotted on a total alkali vs. silica (Fig. 3) diagram, the rock corresponds to a mafic composition of monzo-gabbro. The rock is magnesian and has high MgO content (7.61 wt%). Detail elemental and mineralogical composition of sample GOA-1–3 (Hbl-gneiss), analysed via SEM and x-ray detection, is also available in Table S7 Supplementary Material.

The trace element chemistry is marked by depleted concentrations for transitional trace elements (Ni, Co). The primitive mantle normalized trace element abundance (Fig. 4) pattern is characterized by negative anomalies of Nb, Ta, and Ti and moderately positive anomalies of Zr and Hf. Chondrite normalized REE patterns (Fig. 4) for the studied samples show moderate LREE/MREE fractionation trends and flat MREE/HREE. Negative Eu anomalies suggest fractionation of plagioclase in the parent melt.

Granitoids

Three specimens of different compositional rocks were analyzed. The porphyritic granite (GOA-1–2) is composed of K-feldspar (40%), plagioclase (20%), quartz (30%), biotite (10%), with accessory titanite. Coarse grain K-feldspar is surrounded by quartz. The granodiorite sample GOA-1–5 shows similar composition. The trondhjemite sample (GOA-11–1) is composed of plagioclase and K-feldspars (80%), quartz (10%), muscovite (8%) and biotite (< 2%). Plagioclase appears as medium to fine grain, with marginal alternation to muscovite. For details on elemental and mineralogical composition of samples GOA-1–2 (granite) and GOA-11–1 (trondhjemite), analysed via SEM and x-ray detection, please also see data in Table S7 Supplementary Material.

Overall, the granitoids show SiO_2 concentrations ranging from 68.44 wt% to 72.18 wt% with low TiO_2 (0.093–0.395 wt%) and $Fe_2O_3^T$ (1.04–3.42 wt%), and moderate Al_2O_3 (14.64–17.29 wt%) contents. In terms of total alkali vs. silica (Fig. 3) variations, the rock corresponds to syeno-granite to granite. The trace element chemistry for these rocks is marked by depleted concentrations for transitional trace elements (Ni, Co and Cr) and HFSE with respect to LILE and LREE. Primitive mantle normalized trace element patterns reflect distinct negative anomalies of Nb and Ta (Fig. 4). Chondrite normalized REE patterns (Fig. 4) show pronounced LREE enrichment with flat HREE patterns. Most of the samples show negative Eu anomalies.

4.2. Zircon U-Pb geochronology

Four samples were selected for zircon U-Pb analysis and the data are given in Table S5, Supplementary Material B and plotted in Figs. 5–6. Detailed description of zircon morphology is provided in Supplementary Material C.

GOA-1–1 Amphibolite

Twenty-six spots were analyzed and excluding five discordant spots, the remaining twenty one spots show ^{207}Pb/^{206}Pb ages in the range of 3061–3395 Ma, among which nine concordant analyses yield weighted

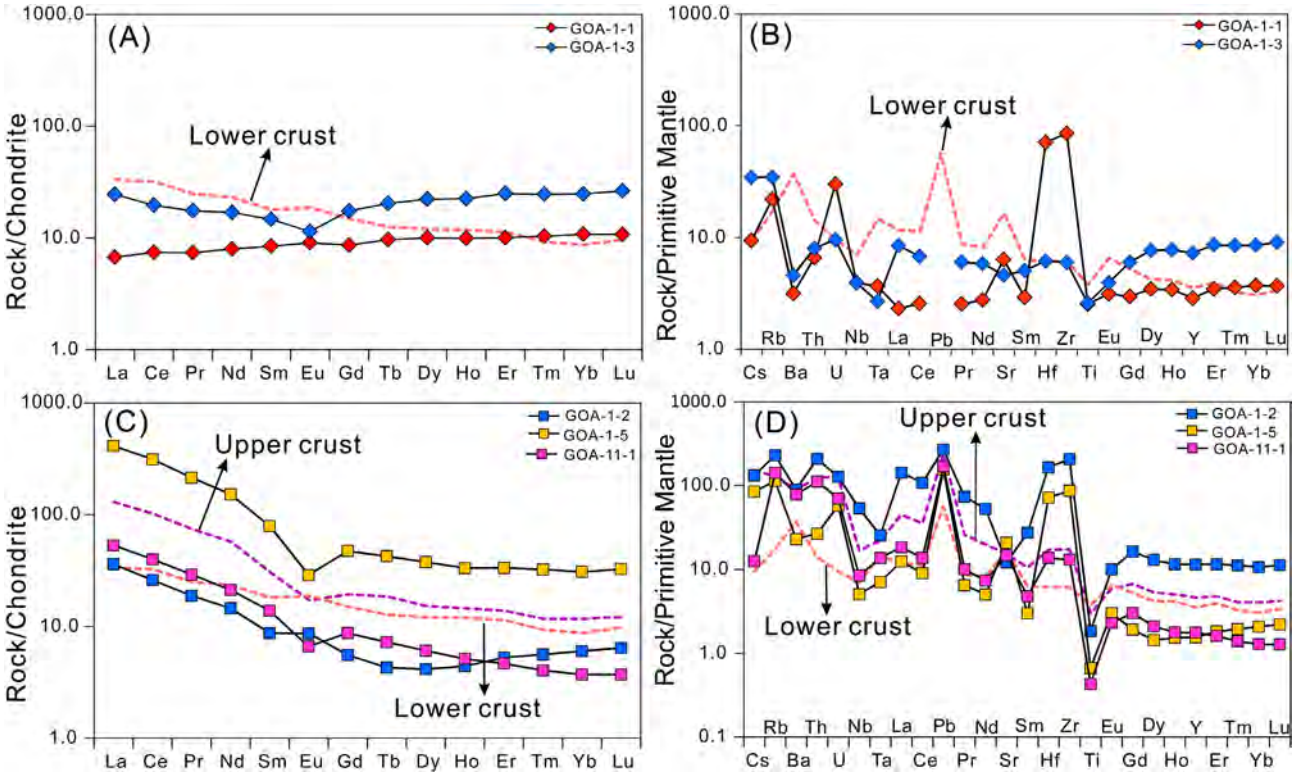

Fig. 4. Primitive mantle normalized trace element abundance patterns (B) and (D) and chondrite-normalized REE patterns (A) and (C) (normalization values are from Sun and McDonough, 1989) for amphibolite, Hbl-gneiss and granitoids from Karwar Blobk.

mean $^{207}Pb/^{206}Pb$ age of 3147 ± 4.3 Ma (MSWD = 3.2, n = 9) (Fig. 5). The grains have Th contents up to 281 ppm, and U in the range of 6.7–453 ppm, with Th/U ratios up to 0.62.

GOA-1–2 Porphyritic granite

Thirty spots were analyzed and excluding two discordant spots, the remaining twenty-eight spots show $^{207}Pb/^{206}Pb$ ages in the range of 3015–2951 Ma, with some data showing reverse concordance. Their Th and U contents are in the range of 113.7–642 ppm and 81.6–658 ppm, with Th/U ratios in the range of 0.27–1.66. Fifteen concordant spots yield weighted mean age of 2966 ± 3.6 Ma (MSWD = 2.7, n = 15) (Fig. 5).

GOA-1–3 Hornblende gneiss

Forty five grains from this sample show $^{207}Pb/^{206}Pb$ age of 3437–2986 Ma and define two age populations. One group includes twenty one spots with weighted mean age of 3156 ± 3.8 Ma (MSWD = 2.2, n = 21) which is interpreted as the magmatic emplacement age (Fig. 6). Their Th and U contents are in the range of 0.26–7.4 ppm and 17.63–198.9 ppm, with Th/U ratios up to 0.07. The remaining fifteen spots display weighted mean $^{207}Pb/^{206}Pb$ age of 3084 ± 3.8 Ma (MSWD = 2.5, n = 15) representing zircon recrystallization or overgrowth. Their Th and U contents show ranges of 0.12–6.06 ppm and 20.77–127.7 ppm, with Th/U ratios up to 0.05.

GOA-11–1 Trondhjemite

A total of thirty grains were analyzed from GOA-11–1, and excluding those discordant spots, eighteen spots show $^{207}Pb/^{206}Pb$ age range from 3390 Ma to 3045 Ma with peak age at 3280 Ma (Fig. 6). Their Th, U contents show a range of 29.7–671.2 ppm and 137.7–718 ppm, with Th/U ratios in the range of 0.08–1.34.

4.3. Rb-Sr geochronology of micas and feldspars

Four samples (GOA-1–1, GOA-1–2, GOA-1–3 and GOA-11–1) of the different lithologies and mineralogical compositions (see Fig. 7, and data in Table S7 Supplementary Material) were selected for in-situ Rb-Sr analyses via LA-ICP-MS/MS, and the results are given in Table S2 in Supplementary Material A (see also, Fig. S2). The calculated in-situ Rb-Sr ages are presented in Fig. 8. Briefly, the in-situ Rb-Sr isochrons of total 7 plagioclase from amphibolite (GOA-1–1), and 2 plagioclase, 2 biotite and 17 K-feldspar from Hbl-gneiss (GOA-1–3), samples collected at the Palolem-Canacona site both yielded Mesoarchean ages (3450 ± 130 Ma and 2973 ± 38 Ma, respectively, MSWD < 1, see Fig. 8A and 8C) which thus overlap within the error with zircon U-Pb ages acquired from these two samples (GOA-1–1 = 3147 ± 4 Ma, and GOA-1–3 = 3084 ± 1 Ma). For details see also a comparison of Rb-Sr and U-Pb ages reported in Table S3 in Supplementary Material A. Note that the in-situ Rb-Sr dating of sample GOA-1–3 (Hbl-gneiss) is based on the analysis of feldspars (K-feldspar and plagioclase) and some trace biotite, where the latter yielded highly radiogenic values and all data together define a well constrained isochron with an initial $^{87}Sr/^{86}Sr$ ratio (I_{Sr}) of 0.713 ± 0.002 (see Fig. 8C). This value is also in agreement with other published initial $^{87}Sr/^{86}Sr$ ratios (I_{Sr}) reported for Mesoarchean gneisses and TTGs from the WDC (i.e., I_{Sr} ranging from ~ 0.704 to 0.720; see Dhoundial et al., 1987 and references therein). It is reasonable to assume that the more "mafic" sample GOA-1–1 (amphibolite/metadiorite) had less radiogenic initial ratio than the above I_{Sr} of 0.713, and likely closer to least radiogenic I_{Sr} reported in the literature (i.e., 0.704). Taking into account the latter I_{Sr} value, the calculated Rb-Sr age of GOA-1–1 would be 3280 ± 140 Ma (rather than 3450 ± 130 Ma for I_{Sr} of 0.713), and thus still within Mesoarchean age, and actually closer to zircon U-Pb age for this sample which yielded 3147 ± 4 Ma (see Table S3 in Supp. Material). However, the sample GOA-1–1 lacked well-defined large mica grains that could be targeted via LA, and the acquired in-situ Rb-Sr isochron thus represents predominantly plagioclase (plg) feldspar ages (see also Fig. 7 with SEM and elemental maps). Such predominant contribution of plagioclase signal is also obvious from fairly non-radiogenic $^{87}Sr/^{86}Sr$ values acquired from GOA-1–1 and a limited spread in $^{87}Rb/^{86}Sr$ ratios (Fig. 8A), which translates into poor constraints on the initial $^{87}Sr/^{86}Sr$

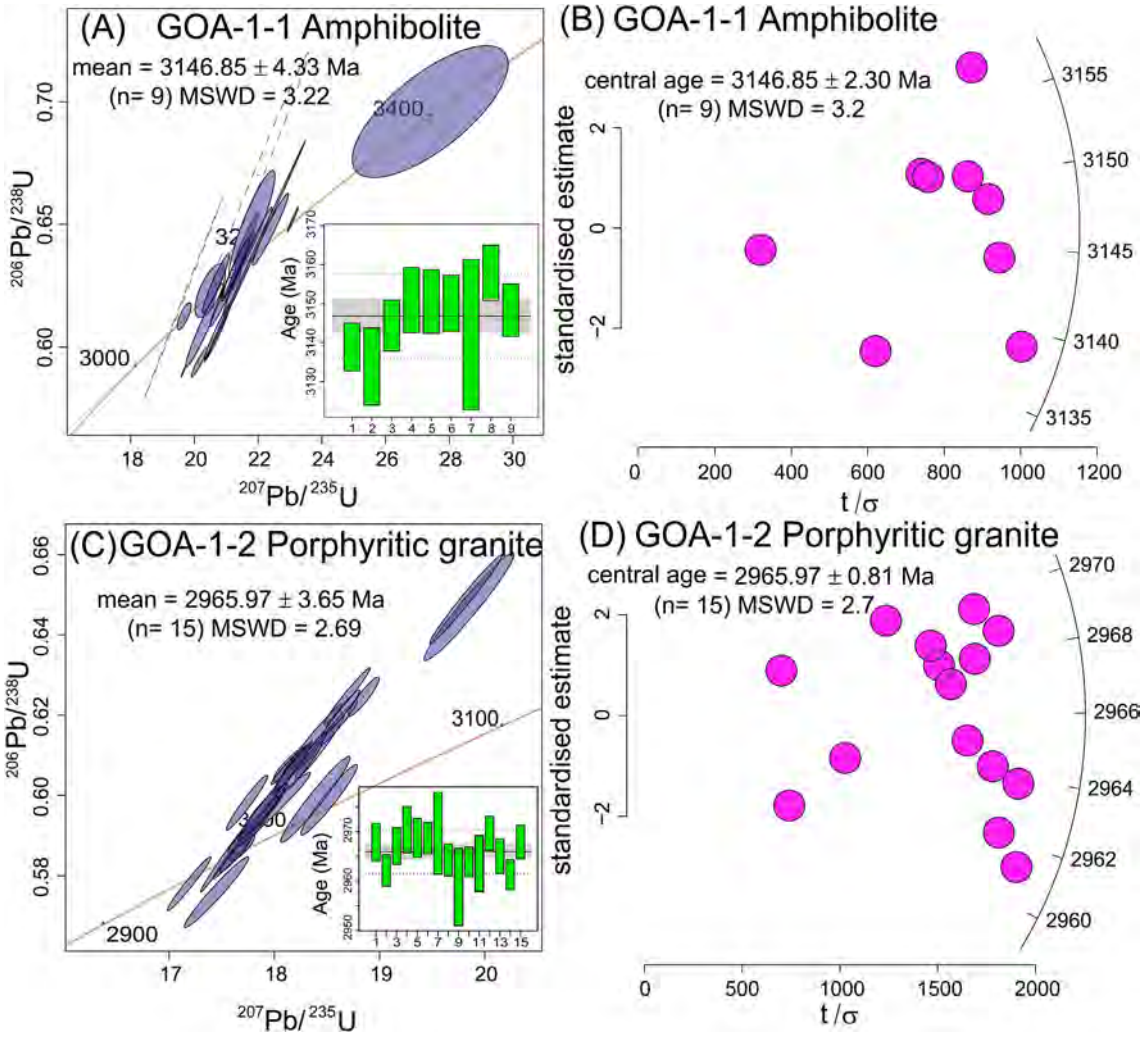

Fig. 5. Wetherill U-Pb concordia diagram, weighted average and radial plots: (A) and (B) amphibolite for GOA-1–1; (C) and (D) Porphyritic granite for GOA-1–2. All uncertainties are 1σ, including the width of the weighted mean ages error bar.

ratio for this sample. Therefore, the age of this sample was modeled by setting the initial $^{87}Sr/^{86}Sr$ ratio at 0.713 similar as the initial $^{87}Sr/^{86}Sr$ ratio of GOA-1–3.

The third sample from this location is porphyritic granite (GOA-1–2) from which we carried out in-situ Rb-Sr analyses of 1 plagioclase, 3 K-feldspar and 2 biotite and the biotite-based in-situ Rb-Sr age yielded an age of 2244 ± 35 Ma (MSWD = 0.32, I_{Sr} = 0.728 ± 0.002, see Fig. 8B), (and also Fig. 7with SEM and elemental maps), which is thus significantly younger (by about 720 Ma) than the Mesoarchean age for this granite defined by zircon U-Pb dating which gave an age of 2966 ± 4 Ma.

Finally, the in-situ Rb-Sr analyses of 3 plagioclase, 21 K-feldspar and 3 muscovite from sample of trondhjemite (GOA-11–1) collected from another locality (near Mollem) yielded discordant Rb-Sr data (see Fig. 8), suggesting an incomplete resetting of the Rb-Sr isotope system in this particular rock. Specifically, the muscovite and feldspar based Rb-Sr data (see Fig. 7 with SEM and elemental maps) define together two main trends (i.e., modeled isochrones) with calculated Proterozoic ages of 2706 ± 28 Ma and 1185 ± 29 Ma (see Fig. 8D), which are thus significantly younger than the expect Mesoarchean age, the latter confirmed by the zircon U-Pb dating of this sample which gave ages from 3390 to 3045 Ma (for details see Table S5 in Supplementary Material B). Muscovite yielding the younger age (1185 ± 29 Ma) trend is distinguished from textural evidence of its formation below closure temperature (500 °C), so the age is unable to represent metamorphic/hydrothermal event (Jenkin, 2009). In the absence of clear indicators for formation temperatures of studied micas, we treat 1185 ± 29 Ma as cooling ages.

Finally, our secondary mineral mica standard MDC-phlogopite, which should have an equivalent age as the Mica-Mg nano-powder standard, yielded a mean Rb-Sr age of 543 ± 7 Ma (for details see Fig. S1 in the Supplementary Material A). Although precise, this age is systematically older (about 4.5%) than the expected mean age of mica-Mg, or mineralization in Bekily area, which based on published data and different dating techniques ranges from: 524 ± 34 Ma (U-Pb zircon lower intercept), 522 ± 12 Ma (K-Ar dating of Mica-Mg powder), and 518 ± 8 (Rb-Sr of phlologopite crystal), see Hogmalm et al. (2017) and references therein. The reason for this systematically older age of our MDC sample is not clear, but we speculate that it is either related to (i) un-corrected analytical bias from the difference in ablation characteristics between a pressed powder pellet (Mica-Mg) and the crystalline phlogopite mineral (MDC); or (ii) natural variability in ages of local mineralisation in Bekily area (i.e., MDC sample is from personal collection, and thus not identical to Mica-Mg which was prepared and distributed by the Centre de Recherches Petrographiques et Geochimiques (CRPG), (Govindaraju, 1979), or (iii) it could be also due to natural inhomogeneity and internal variability of the Rb-Sr isotope system in our MDC sample. The latter is supported by our data and internal variability in Rb-Sr ages collected from MDC over the course of this study (for details see Fig. S1 in the Supplementary Material A).

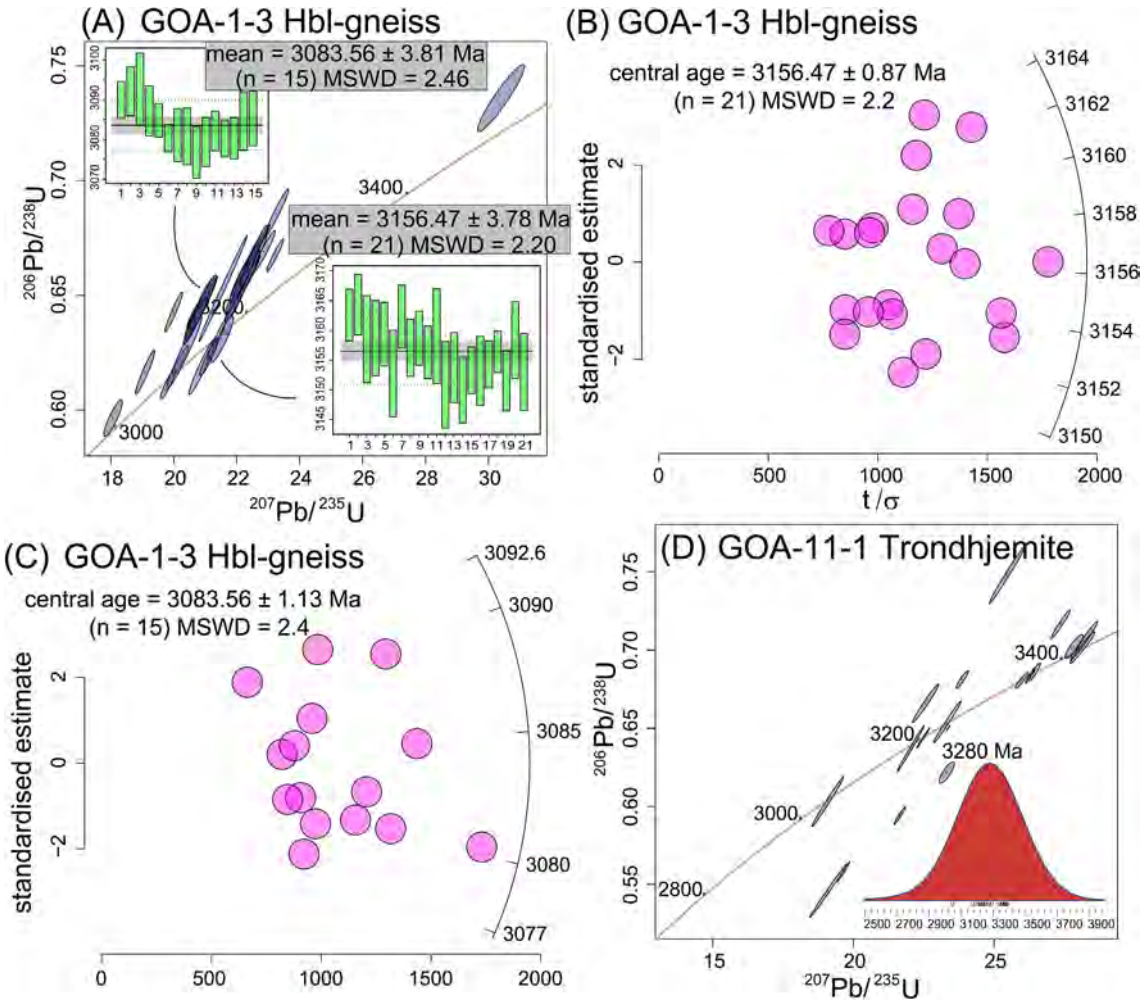

Fig. 6. Wetherill U-Pb Concordia diagram, weighted average and radial plots: (A) and (B) and (C) Hbl-gneiss for GOA-1–3; (D) Trondhjemite for GOA-11–1 with density plot. All data point uncertainties are 1σ, including the width of the weighted mean ages error bar.

Alternatively, and probably most likely, this systematic difference between in-situ Rb-Sr ages of Mica-Mg (nano-powder) and MDC (crystal) samples could be related to (iv) different ablation properties of these two forms of phlogopite during LA-ICP-MS/MS analyses. The elemental fractionation between Rb and Sr during laser ablation can cause systematic shifts in $^{87}Rb/^{86}Sr$ ratios, thus affecting the Rb-Sr ages of nano-powder versus crystal forms of the same material. These effects, which are likely laser-specific, need further systematic investigations to be precisely characterized. Considering the above uncertainties (i.e., different ablation properties and also natural variation in phlogopite ages), we present in this study two errors on the acquired in-situ Rb-Sr ages from our samples (see data in Fig. 8). One is the standard error of the isochron (typically about 2% on age estimates) calculated via Isoplot R, and the other is a conservative error (about 4.5%) which takes into account the additional uncertainty in the accuracy derived from the above mentioned inconsistency between the published and measured Rb-Sr ages for the MDC secondary standard. Both errors are reported in Fig. 8, and Table S3 in Supplementary Material A. Importantly, regardless of the errors used these do not change the main conclusions of this study.

4.4. Lu-Hf isotopes

Zircon grains from four U-Pb dated samples were analyzed for Lu-Hf and the results are plotted in Fig. 9. The data are given in Table S6, Supplementary Material B.

4.4.1. GOA-1–1 amphibolite

Six spots on zircon grains from this sample yield $^{176}Hf/^{177}Hf_i$ ratios from 0.280841 to 0.280962 and $^{176}Lu/^{177}Hf$ of 0.00045–0.00055. The data yield positive εHf(t) values of + 2.9 to + 7.5 when plotted with the $^{207}Pb/^{206}Pb$ ages of 3110–3169 Ma, and T^C_{DM}age (crustal residence age) of 3061–3333 Ma (Fig. 9). This suggests a depleted mantle (juvenile) source of this sample.

4.4.2. GOA-1–2 porphyritic granite

Eleven spots have $^{176}Hf/^{177}Hf_i$ ratios of 0.281048–0.281159 and $^{176}Lu/^{177}Hf$ of 0.00085–0.00187. The data yield positive εHf(t) values of + 6.1 to + 9.7 when plotted with $^{207}Pb/^{206}Pb$ ages of 2951–3015 Ma, and $T^C_{DM}$of 2766–2998 Ma.

4.4.3. GOA-1–3 hornblende gneiss

Twelve spots have $^{176}Hf/^{177}Hf_i$ ratios of 0.280814–0.281106 and $^{176}Lu/^{177}Hf$ of 0.00003–0.00036. The data yield positive εHf(t) values of + 1.9 to + 9.8 when plotted with $^{207}Pb/^{206}Pb$ ages of 2986–3169 Ma, together with T^C_{DM}age of 2856–3390 Ma, suggesting the magma dominantly derived from juvenile source with slightly reworked components.

4.4.4. GOA-11–1 trondhjemite

Five spots have $^{176}Hf/^{177}Hf_i$ ratios in the range of 0.280716–0.280910 and $^{176}Lu/^{177}Hf$ of 0.00038–0.00214. The data yield positive εHf(t) values of + 0.4 to + 6.9 when plotted by

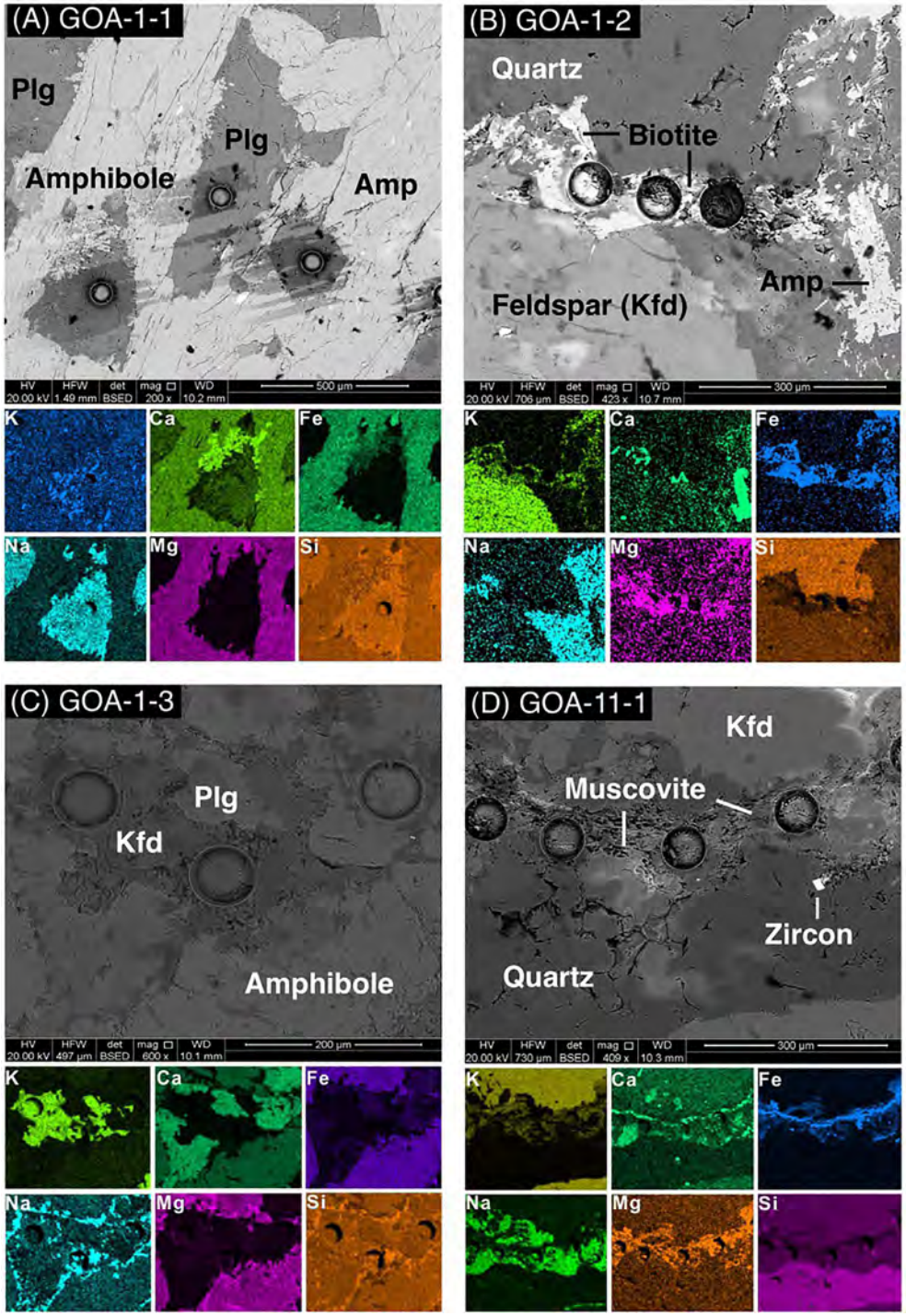

Fig. 7. SEM images and maps of selected elements for samples GOA-1–1 (A), GOA-1–2 (B), GOA-1–3 (C) and GOA-11–1 (D), analysed with the FEI Quanta 450 field emission Scanning Electron Microscope (SEM), equipped with the x-ray (SDD EDS) detector of a high-resolution elemental mapping (see also data in Table S7, in Supplementary Material). Note that the circles (with a diameter of 74 μm) are craters after in-situ Rb-Sr dating using a spot size of 74 μm. Abbreviations used: Plg = Plagioclase, Amp = Amphibole, Kfd = K-Feldspar.

$^{207}Pb/^{206}Pb$ ages of 3045–3378 Ma suggesting juvenile magma source, with T^{C}_{DM} of 3139–3547 Ma.

5. Discussion

5.1. Crustal evolution and metamorphism

The western Dharwar Craton (WDC) preserves the records of crustal growth and craton building in the early earth (Jayananda et al., 2015, 2018; 2020; Lancaster et al., 2015; Taylor et al., 1984). However, the crustal evolution history of the craton remains controversial, particularly with regard to the position of the Karwar Block (KB) and timing of later post-Mesoarchean igneous and metamorphic events. In this study, we combine traditional zircon-based U-Pb dating with a novel mica-based in-situ Rb-Sr dating to constrain magmatic and metamorphic history of the KB with respect to WDC, and to evaluate the tectonic evolution of the WDC.

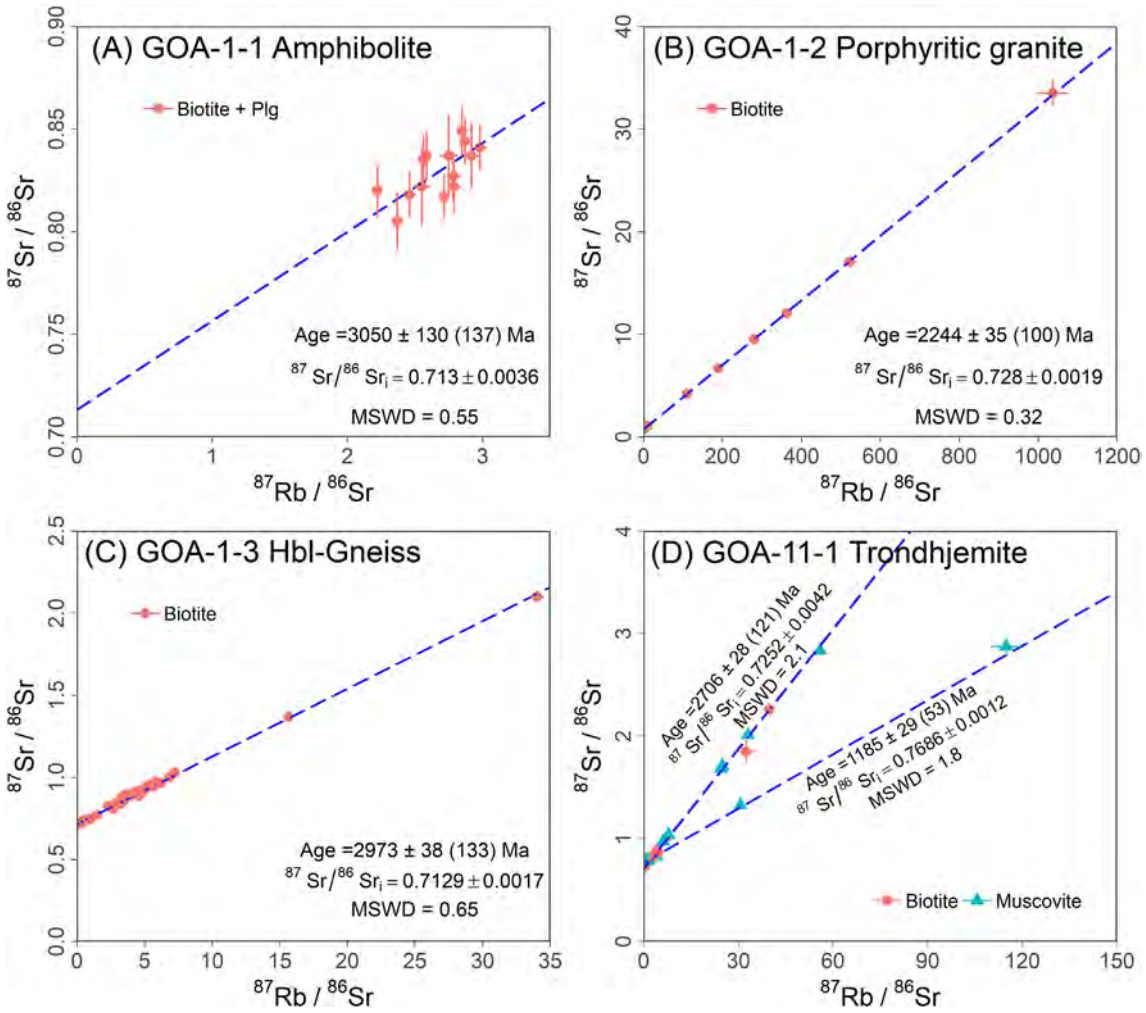

Fig. 8. In-situ Rb-Sr dating and constructed isochrons for samples: (A) amphibolite GOA-1–1; (B) Porphyritic granite GOA-1–2; (C) Hbl-gneiss GOA-1–3; and (D) Trondhjemite GOA-11–1. Uncertainties on individual data points are 2σ standard error. The reported errors (2σ) for Rb-Sr ages (in Ma), typically around 2%, are calculated via Isoplot R, where the second error (reported in brackets) represents a 'conservative' or maximum error (~4.5%) constrained by the accuracy of the MDC secondary mica standard (for details see also information in the Method Section, and Fig. S1 in Supplementary Material A).

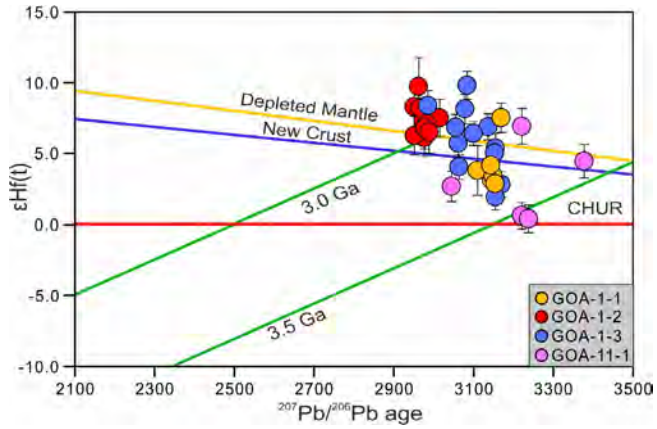

Fig. 9. εHf(t) versus $^{206}Pb/^{207}Pb$ age plots; error bars represent 2σ uncertainties. The 'new crust' line is after Dhuime et al., (2011). Crustal model ages T^{C}_{DM} were calculated using representative bulk crustal value $^{176}Lu/^{177}Hf$ = 0.015 (Griffin et al., 2002).

5.1.1. Juvenile crustal growth and greenstone belts

In WDC, the published detrital zircon ages from Sargur supracrustal rocks and Chitradurga greenstone belt show magmatism and juvenile crustal growth at 3.4 to 2.7 Ga (Lancaster et al., 2015; Maibam et al. 2016; Pahari et al., 2019; Jayananda et al., 2015; Raju et al., 2014), with later intrusions (*syn*-tectonic granites) dated at 2.68–2.63 Ga (Hokada et al., 2013). Similarly, Santosh and Li (2018) reported 3.32 Ga from basement TTG gneisses and 2.59–2.62 Ga for the gabbro-anorthosite suite between the western and central Dharwar Craton. The high grade rocks including garnet-amphibolite and garnet granulite give detrital zircon ages of 3.10–3.03 Ga, 2.97–2.86 Ga and 2.61–2.51 Ga for the protolith magma in WDC (Li et al., 2018a). Zircon and titanite SHRIMP dating from the Gadag greenstone belt, in the eastern margin of WDC, suggest a short-lived magmatic event at around 2.56 Ga (Mohan et al., 2014), correlated with the amalgamation of Western and Eastern Dharwar blocks. The Neoarchean magmatism from granitoids of the KB also show similar ages (Devaraju et al., 2007).

5.1.2. Suture Zones, magmatic and metamorphic events

The 3.06 Ga and 3.16 Ga *para*-schist and phyllites from the Shimoga schist belt of KB were intruded by the 2.92 Ga granitic plutons, with Neoarchean ages of 2.44–2.62 Ga recorded from the overlying phyllites/schists and polymict conglomerates. These have been correlated to the metamorphic event occurring during the amalgamation and collision between the western and central Dharwar Craton domains (Rekha et al., 2013). Thus, it is considered that the 3.1–3.0 Ga Mesoarchean Shimoga schist belt and the 3.2–3.0 Ga Sargur Group share the same

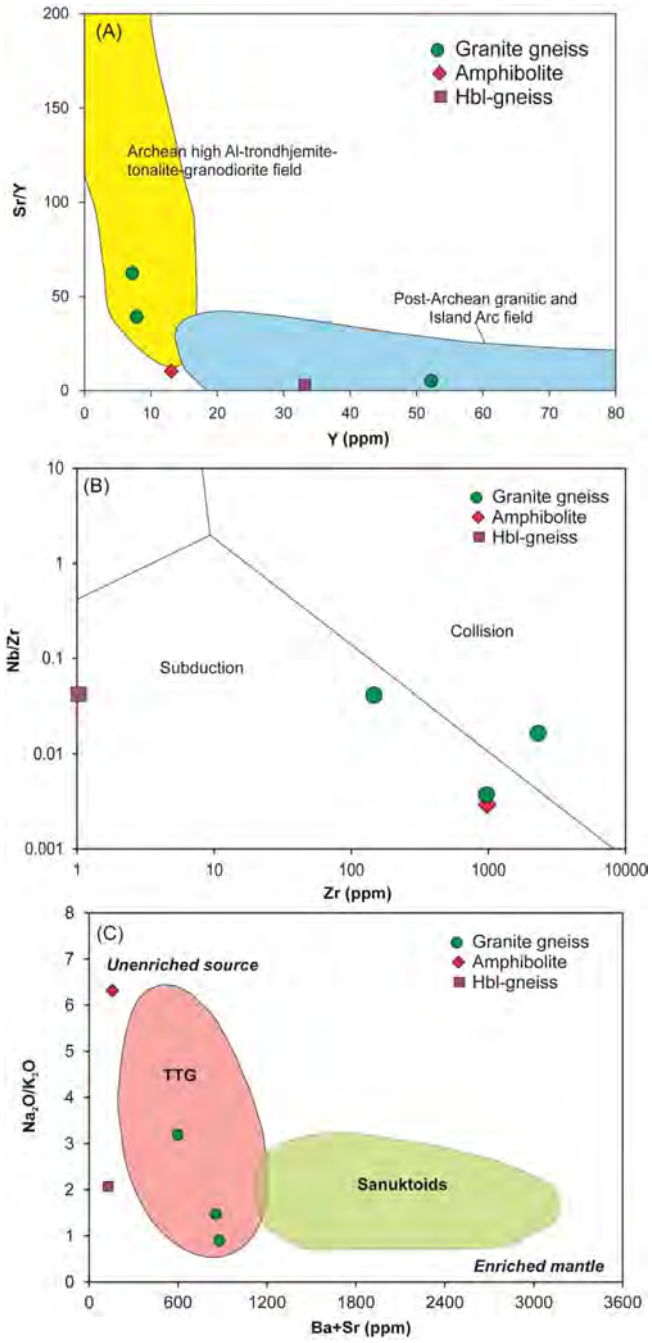

Fig. 10. (A) Plots of Y vs. Sr/Y compositions for the studied rocks from Plaolem-Canacona and Anmod Ghat suggesting their affinity to high-Al Archean TTG and a magmatic parentage with subduction input. The fields are from Drummond and Defant (1990), (B) Nb/Zr vs. Zr plot with fields from Thieblemont and Tegyey (1994) showing subduction-collision tectonic regime for the emplacement of the studied rocks, (C) Na_2O/K_2O vs. Ba + Sr plot (after Halla et al., 2009) showing an unenriched primitive basaltic source (low Ba + Sr, high Na_2O/K_2O) for the studied rocks.

magmatic and metamorphic history (Rekha et al., 2013; Li et al., 2018a, Hokada et al., 2013). The detrital zircon U-Pb ages derived from sandstone of Karwar, show two age peaks at ~ 3.10 Ga and ~ 2.5 Ga, which are interpreted to indicate Mesoarchean juvenile crustal growth and crust recycling during the Neoarchean (Armistead et al., 2018). The ~ 3.4 Ga Sm-Nd isotopic and ~ 3.33 Ga zircon U-Pb ages from the Anmod Ghat trondhjemite to the east of Gadag along the Goa coast constitute the oldest Penisular gneiss, which was intruded by the 2.56–2.65 Ga granitic plutons including the Chandranath granite, Dudhsagar granite and the Ramnagar migmatite-granite gneiss-porphyritic granite (Devaraju et al., 2007). Whole-rock Rb-Sr ages show similar results for the Goa Group: ~3.4 Ga for the Anmod Ghat trondhjemite gneiss, 2.65 Ga for the Chandranath granodiorite-granite and Londa migmatites, and 2.56 Ga for the Dudhsagar granite; whereas the Canacona granite yield late Archean age of 2.40 Ga with large uncertainty (Dhoundial et al., 1987).

Detrital zircon SHRIMP U-Pb ages coupled with electron microprobe-CHIME zircon dating from quartz-phengite schist along the Kumta Suture zone show age populations with peaks at 3.28–2.99 Ga, ~3.75 Ga and ~1.70 Ga (Ishwar-Kumar et al., 2016). Based on K-Ar dating of metamorphic garnet-biotite schist, TTG gneiss and amphibolite, the likely peak of the metamorphic event in WDC was at 1.32 to 1.38 Ga in the Kumta suture zone associated with KB (Ishwar-Kumar et al., 2016). In the high-grade terrains of WDC, such as the Mercara Suture Zone, the K-Ar ages of gneisses are as young as 0.93 Ga (Ishwar-Kumar et al., 2016). Furthermore, constraints from the U-Pb dating of zircons from these aforementioned suture zones yielded lower intercept ages ranging from 1.46 to 1.10 Ga (Ishwar-Kumar et al., 2016), thus pointing to common Mesoproterozoic metamorphic event(s) in WDC. Importantly, the above Mesoproterozoic suture zones in western Peninsular India might represent eastern extensions of the Betsimisaraka Suture Zone in Madagascar. Alternative models correlate the WDC with the Antongil-Msaora Block in Madagascar (Armistead et al., 2018; Rekha et al., 2013, 2014).

5.2. Crustal evolution and metamorphism: Insights from coupled in-situ Rb-Sr and U-Pb geochronometers

In this study, representative samples including gneissic and intermediate rocks, were collected from the Karwar Block to trace the Mesoarchean crustal history and its correlations with those in the western Dharwar Craton. Trondhjemite (GOA-11–1) sample was collected from Anmod Ghat sector of Goa, while the rest from Palolem-Canacona sector. These two sectors preserve the ancient continental crust that is comparable with the Gorur Gneiss and Peninsular Gneissic Complex (PGC) of Dharwar Craton. From coupled laser ablation dating of zircons (U-Pb) and micas (in-situ Rb-Sr) from these rocks, the amphibolite (GOA-1–1) has a $^{207}Pb/^{206}Pb$ age range of 3.06 to 3.39 Ga (with weighted mean age of 3.14 Ga), which overlaps within error with the in-situ Rb-Sr biotite age of 3.05 ± 0.13 Ga (Fig. 8A). Hornblende gneiss (GOA-1–3) has a $^{207}Pb/^{206}Pb$ age of 2.98 to 3.43 Ga (with two dominant groups at 3.15 Ga and 3.08 Ga), and similarly the biotite-based Rb-Sr dating from this sample gives a Mesoarchean age of 2.97 ± 0.13 Ga (Fig. 8C), which overlaps with the zircon ages. The porphyritic granite (GOA-1–2) also shows Mesoarchean zircon ages of 2.95 to 3.01 Ga (with weighted mean age of 2.96 Ga), which are however significantly older than the in-situ Rb-Sr biotite age of this sample 2.24 ± 0.10 Ga (Fig. 8B), suggesting Paleoproterozoic crystallization or resetting event for these biotites.

Finally, trondhjemite (GOA-11–1) has $^{207}Pb/^{206}Pb$ zircon ages with a large range from 3.39 Ga to 3.04 Ga (with a peak at 3.28 Ga), and also discordant Rb-Sr data acquired from biotite and muscovite, suggesting a partial resetting of the Rb-Sr isotope system in this sample (Fig. 8D). Nevertheless, the in-situ Rb-Sr data define two main trends, one with a Meso/Neoarchean model age of about 2.71 ± 0.12 Ga (biotite and muscovite data), and the other defined only by muscovite, gives a Proterozoic age of 1.19 ± 0.05 Ga (Fig. 8D).

5.2.1. Interpretations based on the coupled in-situ Rb-Sr and U-Pb data

The combined in-situ Rb-Sr ages of micas (biotite, muscovite) and U-Pb zircon ages from the Karwar Block (KB) of the western Dharwar Craton (WDC), revealed (i) a common Mesoarchean (3.3 to 3.0 Ga) supracrustal formation event, (ii) younger Neoarchean and Paleoproterozoic granite formation or migmatisation (syn- and post-tectonic events, c. 2.8–2.6 Ga and 2.2 Ga, respectively), and also (iii) a

Mesoproterozoic cooling (as young as 1.2 Ga).

Overall, results of this study and other published work from the KB and WDC indicate that the c.3.15–3.08 Ga TTG gneiss and c.3.4–3.3 Ga Anmod Ghat trondhjemite gneiss are equivalent to the 3.3–3.2 Ga Sargur Group. Thus, the age distributions in Karwar and Western Dharwar Craton show the same magmatic history: the oldest basement rocks formed at 3.5–3.1 Ga, followed by multiple magmatic and granite formation events, followed by Mesoproterozoic (c. 1.5 to 1.1 Ga) suturing of the region (Ishwar-Kumar et al., 2016, and in-situ Rb-Sr muscovite data from this study).

5.3. Magma provenance and links to Proterozoic metamorphic events

The Lu-Hf isotopic ratios of zircons from the amphibolite (GOA-1–1) yield positive εHf(t) values of +2.9 to +7.5 suggesting a juvenile magma source. The T_{DM}^{C}ages are in the range 3061–3333 Ma, and thus comparable with ages constrained by U-Pb (3110–3169 Ma) and/or in-situ Rb-Sr dating (3.05 ± 0.12 Ga). The porphyritic granite (GOA-1–2) shows positive εHf(t) values of +6.1 to +9.7 coupled with a T_{DM}^{C}age of 2.76–2.99 Ga, which agrees with the zircon $^{207}Pb/^{206}Pb$ ages of 2.95–3.02 Ga but is much older than in-situ biotite Rb-Sr ages (2.24 ± 0.12 Ga). This implies that the zircons were sourced from juvenile components but the main granite emplacement or formation event (recorded by biotite Rb-Sr ages) was likely related to later (Paleoproterozoic) post-tectonic processes documented in this region (Dhoundial et al., 1987). Zircons in the hornblende gneiss (GOA-1–3) yield positive εHf(t) values of + 1.9 to + 9.8 together with T_{DM}^{C}age of 2.86–3.39 Ga indicating a Mesoarchean juvenile source. This age is also confirmed by zircon U-Pb (c. 3084 Ma) and in-situ biotite Rb-Sr dating (~2.97 Ga). The trondhjemite (GOA-11–1) show positive εHf(t) values of + 0.4 to + 6.9 and $T_{DM}^{C}$of 3.14–3.55 Ga, with a Mesoarchean U-Pb zircon age (with a peak at 3.28 Ga). This contrasts with the much younger and partially rest Rb-Sr micas with ages spanning from Neoarchean to Mesoproterozoic (from ~ 2.71 to 1.19 Ga). Overall, the Lu-Hf isotopic ratios and the trace element concentrations of this sample indicate a magma provenance from the juvenile lower crust. The Rb-Sr dating of biotite and muscovite confirms later isotopic resetting, likely due to younger metamorphism (i.e., neoformation of muscovite) related to the Mesoproterozoic suturing event(s) linked to the formation of the Kumta Shear Zone (Ishwar-Kumar et al., 2016). Such common Mesoproterozoic metamorphic/suturing events (1.47 to 1.10 Ga) affecting the Karwar Block and the Western Dharwar Craton are also confirmed by K-Ar dating of phengite schists and U-Pb dating of metasedimentary rocks from this region (Ishwar-Kumar et al., 2016 and references therein).

As to the magma source, previous Lu-Hf ratios from garnet-biotite schist (2.20–2.73 Ga, 2.98–3.42 Ga) along the Kumta Suture zone shows both positive and negative εHf(t) values of −9.2 to + 5.6 and −5.1 to 1.6 Ga, T_{DM}^{C}ages of 3747–2792 Ma and 3747–3373 Ma, suggesting magma derivation from a mixed juvenile and reworked crustal source (Ishwar-Kumar et al., 2016) (Fig. 12). Detrital zircons from sandstone in the KB (3.5–3.1 Ga) show positive εHf(t) with minor negative values −3.32 to + 3.39, indicating that the magmatic rocks at the source were dominantly derived from juvenile sources together with recycled crust (Armistead et al., 2018). However, zircons from the sandstone with 2.56–2.54 Ga ages show dominantly negative εHf(t) values of −11.67 to + 3.92, again suggesting a mixed magma source (Armistead et al., 2018).

In comparison, the 3.2–3.4 Ga Kaladurga gneissic clast of the Dharwar Supergroup shows positive εHf(t) of + 2.2 to + 4.2, and the 3.14–3.27 Ga Kartikere conglomerate from Bababudan Group yield positive εHf(t) values of + 1.3 to + 4.3, indicating juvenile components in the magma source of the provenance rocks (Maibam et al., 2016). However, the 3.22–3.42 Ga Kabini Dam paragneiss of Sargur Group shows positive εHf(t) values of + 0.8 to + 3.8 and the 2.7–3.1 Ga group yield negative εHf(t) values of −1.5 to −7.5,

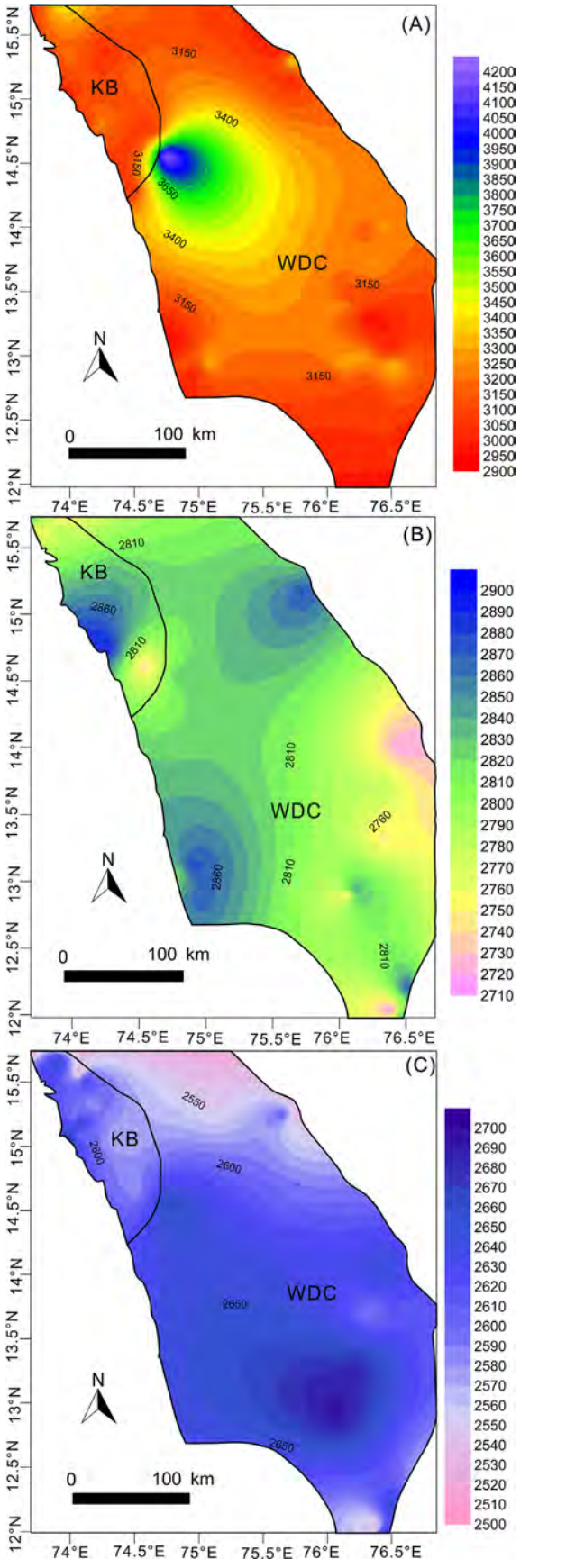

Fig. 11. Zircon, monazite, and titanite age contour maps for Meso to Neoarchean magmatic rocks in the Karwar and Western Dharwar Blocks. (A) Mesoarchean magmatic ages, (B) and (C) Neoarchean magmatic ages. Scale in Ma.

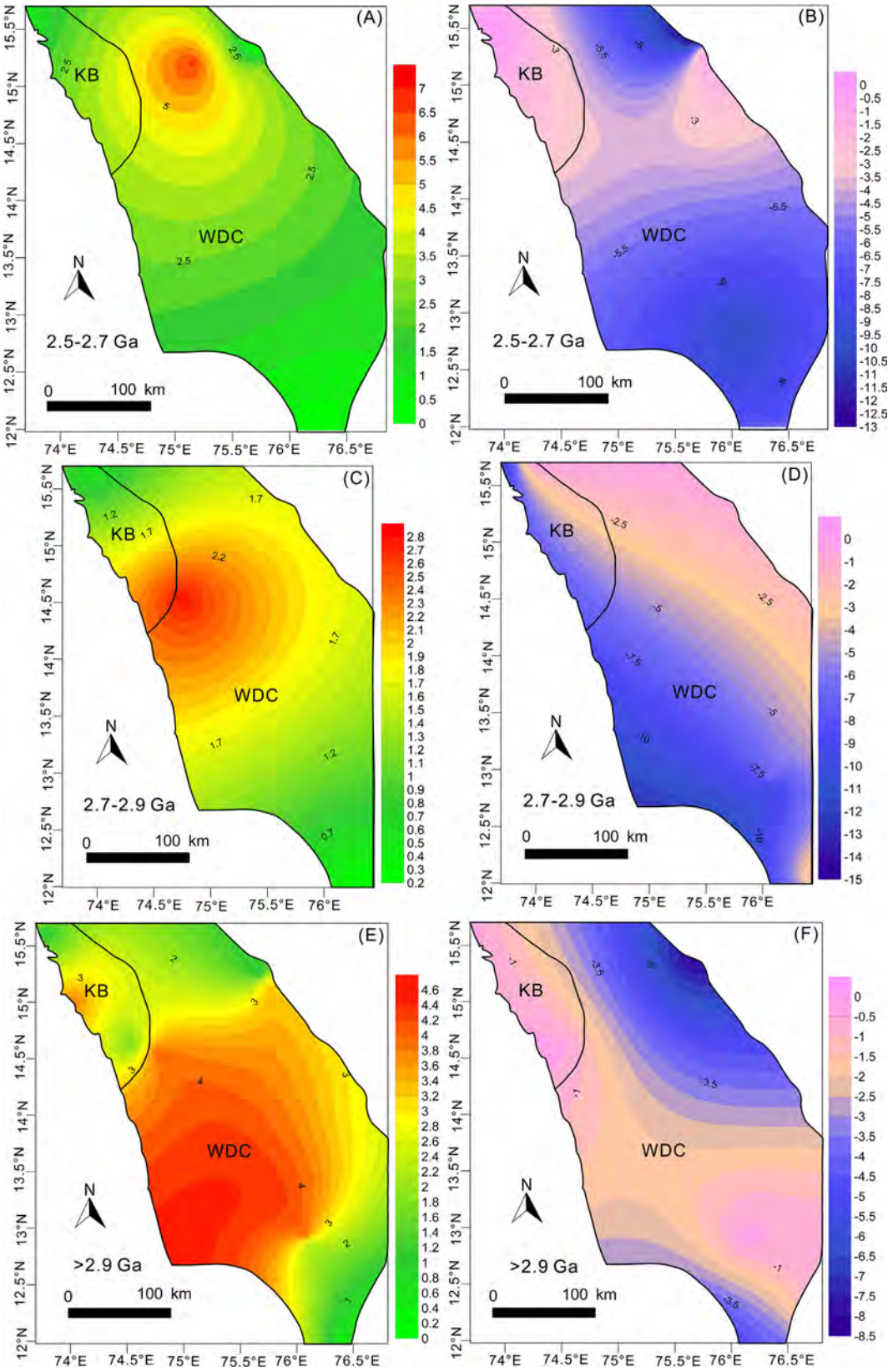

Fig. 12. Zircon Hf isotopic ratio contour maps for Meso to Neoarchean magmatic rocks in the Karwar Block and Western Dharwar Block. (A), (C) and (E) εHf(t) value above zero, (B), (D) and (F) εHf(t) value below zero.

suggesting that the magmas were sourced both from juvenile and reworked crustal rocks (Maibam et al., 2016). The ~2.6 Ga anorthosite-gabbro suite between the western and central Dharwar Craton yield dominantly negative εHf(t) values of −5.3 to +0.9, indicating that the magma was contaminated with reworked crustal rocks (Santosh and Li, 2018). The TTG gneiss from this zone with a c.3.3 Ga emplacement age, mainly shows positive εHf(t) with minor negative values of −0.2 to +1.3, indicating a juvenile provenance (Santosh and Li, 2018). Positive εNd(t) values from the TTG gneiss of Holenarsipur greenstone belt and Bababudan greenstone belt in the western Dharwar Craton, also indicate that the protolith magma was sourced from the juvenile mafic lower crust (Jayananda et al., 2015). Overall, the acquired Hf isotope data from the Mesoarchean (3.28–3.08 Ga) amphibolite, hornblende gneiss and trondhjemite indicate juvenile sources for the magma. Combining all data, the Karwar Block and the western Dharwar Craton experienced continental growth during Mesoarchean (3.3–3.1 Ga) followed by syn- to post-tectonic (2.9–2.6 Ga and 2.2 Ga, respectively) granitic magma formation and intrusion (Figs. 11–12, and Fig. 8B), and subsequent Mesoproterozoic (1.2 Ga) metamorphism linked to suturing of this region. The Neoarchean syn-tectonic (2.7–2.5 Ga) magmatic event coincides with the amalgamation between the KB and WDC (Fig. 12), and post-tectonic Paleoproterozoic intrusion event (~2.2 Ga) in WDC is likely to be lineament controlled (Dhoundial et al., 1987).

5.4. Tectonic implications

The amphibolite characterized by low REE, Sr (134 ppm) and Ba (22 ppm) and relatively low Rb (14 ppm) concentrations together with negative anomalies of Nb and Ta, and flat REE patterns, suggesting magma is provenanced from the lower crust (Fig. 4). The Hbl-gneiss are magnesian with high MgO content (7.61 wt%), depleted in Ni and Co, have negative anomalies of Nb, Ta, and Ti and positive anomalies of Zr and Hf. The negative Eu anomalies for Hbl-gneiss suggest fractionation of plagioclase in the parent melt. Granitoids are marked by depleted concentrations for transitional trace elements (Ni, Co and Cr) and HFSE with respect to LILE and LREE. Negative anomalies of Nb and Ta along with distinct LREE enrichment, indicate a magma sourced from the lower crust (Fig. 4).

The LREE/MREE, LREE/HREE and MREE/HREE compositions (Supplementary Material B) for the studied rocks suggest variable degrees of mantle melting in multiple phases and at different crustal levels. $(Nb/La)_{PM}$ and $(Th/Nb)_{PM}$ ratios (Supplementary Material B) are attributed to (i) reworking of older crustal components and (ii) generation of parent magma from a source of mantle metasomatized by subduction components. On Sr/Y vs. Y plot (Fig. 10A), the TTG and granite gneiss corresponds to the high Al Archean TTG domain involving a subduction input in their genesis. The Sr/Y vs. Y variations for the amphibolite and hornblende gneiss samples also reflects a subduction imprint. The HFSE chemistry (Fig. 10B) for the studied rocks corroborates a subduction-collision regime for their origin and evolution. $Na_2O + K_2O$ vs. Ba + Sr plots (Fig. 10C) conform to an unenriched, juvenile mantle heritage for the studied rocks. Tonalite-trondhjemite-granodiorite (TTG) gneisses and potassic granitoids comprise integral manifestations of Precambrian crust building episodes and yield robust evidence for primitive mantle differentiation and crustal evolution in early earth. TTGs, in particular, represents primary felsic continental crust fractionated from the mantle. In this study, the geochemistry and coupled Rb-Sr and U-Pb geochronometers for the studied rocks from Goa document a record of crustal evolution involving a 3.2–2.9 Ga Mesoarchean continental growth event preserved in TTG and amphibolites from Palolem-Canacona and Anmod Ghat sector, whereas a syn- and post-tectonic granite intrusion at c. 2.8–2.6 Ga and 2.2 Ga is marked by the potassic Canacona granites. The structure and composition of these rocks were overprinted by Mesoproterozoic (1.2 Ga) metamorphism. The geochemical and zircon Lu-Hf isotope systematics for the trondhjemite, hornblende gneiss, amphibolite and granite gneiss from Palolem-Canacona and Anmod Ghat sectors of Goa invoke episodic/multi-stage magma generation through partial melting and crustal reworking in the lower part of thick basaltic oceanic protocrust underlain by an embryonic hot subduction zone during Meso-Neoarchean timeframe.

6. Conclusions

1. This is the first study that employs in-situ laser ablation Rb-Sr dating of micas (biotite, muscovite) and feldspars (plagioclase, K-feldspar), coupled with the laser ablation U-Pb zircon dating, performed on identical rocks from the Karwar Block (KB) of the western Dharwar Craton (WDC) in India, which represent crustal fragments of the first landmass on one of the first supercontinents on our planet. These integrated geochronological Rb-Sr and U-Pb results show evidence for (i) a common Mesoarchean (3.3 to 3.0 Ga) supracrustal formation event, (ii) younger Neoarchean and Paleoproterozoic granite formation or migmatisation (syn- and post-tectonic events, 2.8–2.6 Ga and 2.2 Ga, respectively), and (iii) Mesoproterozoic cooling (as young as 1.2 Ga).
2. The positive εHf(t) values of + 0.4 to + 9.8 from the 3.28–3.08 Ga amphibolite, hornblende gneiss and trondhjemite, together with the positive values of + 6.1 to + 9.7 from the 2.96 Ga porphyritic granite, indicate multiple magma generations from predominantly juvenile sources.
3. The εHf(t) and U-Pb age data from the WDC and KB indicate a major magmatic event derived from depleted mantle sources and continental growth during 3.3–2.9 Ga, 2.9–2.7 Ga and 2.7–2.55 Ga.
4. The negative Nb-Ta anomalies and low concentrations of REE from the amphibolite, Hbl gneiss and granitoids indicate input from the lower crust.
5. This study showed that the integration of in-situ Rb-Sr dating of micas and feldspars, coupled with U-Pb dating of zircons, has the potential to provide a more comprehensive reconstruction of the early Earth's crustal evolution, and the history of magmatic and metamorphic events.

Declaration of Competing Interest

The authors declare that they have no known competing financial interests or personal relationships that could have appeared to influence the work reported in this paper.

Acknowledgements

We thank Prof. G.C. Zhao, Editor for his encouragement and two anonymous referees for providing us with constructive comments which helped in improving our paper. This study forms part of the PhD research of Shan-Shan Li. M. Santosh acknowledges support from Foreign Expert position at the China University of Geosciences Beijing, China and Professorial position at the University of Adelaide, Australia. The research was jointly supported though the Excellent Supervisor Funding [M. Santosh] from China University of Geosciences, Beijing (Grant No 2-9-2018-155) to Shan-Shan Li, and the Chinese Scholarship Council (File No. 201806400023) Scholarship to Shan-Shan Li for joint PhD research between CUGB and Colorado School of Mines. SG acknowledges DST-INSPIRE Faculty project [IFA14-EAS-25] for research funding.

Appendix A. Supplementary data

Supplementary data to this article can be found online at https://doi.org/10.1016/j.precamres.2020.105709.

References

Amelin, Y., Lee, D.C., Halliday, A.N., Pidgeon, R.T., 1999. Nature of the Earth's earliest crust from hafnium isotopes in single detrital zircons. Nature 399, 252–255.

Andersen, T., Griffin, W.L., Pearson, N.J., 2002. Crustal evolution in the SW part of the Baltic Shield: the Hf isotope evidence. J. Petrol. 43 (9), 1725–1747.

Armistead, S.E., Collins, A.S., Payne, J.L., Foden, J.D., De Waele, B., Shaji, E., Santosh, M., 2018. A re-evaluation of the Kumta Suture in western peninsular India and its extension into Madagascar. J. Asian Earth Sci. 157, 317–328.

Armistead, S.E., Collins, A.S., Redaa, A., Jepson, G., Gillespie, J., Gilbert, S., Blades, M.L., Foden, J.D., Razakamanana, T., 2020. Structural evolution and medium-temperature thermochronology of central Madagascar: implications for Gondwana amalgamation. J. Geol Soc. https://doi.org/10.1144/jgs2019-132.

Bea, F., 1996. Residence of REE, Y, Th and U in Granites and Crustal Protoliths; Implications for the Chemistry of Crustal Melts. J. Petrol. 37, 521–552.

Bea, F., Montero, P., Molina, J.F., Scarrow, J.H., Cambeses, A., Moreno, J.A., 2018. Lu-Hf ratios of crustal rocks and their bearing on zircon Hf isotope model ages: The effects of accessories. Chem. Geol. 484 (5), 179–190.

Blichert-Toft, J., Albarède, F., 1997. The Lu-Hf isotope geochemistry of chondrites and the evolution of the mantle-crust system. Earth Planet. Sci. Lett. 148, 243–258.

Chu, N.C., Taylor, R.N., Chavagnac, V., Nesbitt, R.W., Boella, M., Milton, J.A., 2002. Hf isotope ratio analysis using multi-collector inductively coupled plasma mass spectrometry: an evaluation of isobaric interference corrections. J. Anal. At. Spectrom 17, 1567–1574.

Corfu, F., Hanchar, J. M., Hoskin, P. W. Kinny, P., 2003. Atlas of zircon textures. In: Hanchar, J. M. Hoskin, P. W. O. (eds) Zircon. Mineralogical Society of America and Geochemical Society, Reviews in Mineralogy and Geochemistry 53, 469–500.

Corfu, F., 2013. A century of U-Pb geochronology: the long quest towards concordance. Bull. Geol. Soc. Am. 125 (1–2), 33–47.

Dessai, A.G., Arolkar, D.B., French, D., Viegas, A., Viswanath, T.A., 2009. Petrogenesis of the Bondla layered mafic-ultramafic complex, Usgaon. Goa. J. Geol. Soc. India 73 (5), 697–714.

Dessai, A.G., 2011. The geology of Goa Group: Revisited. J. Geol. Soc. India 78, 233–242.

Devaraju, T.C., Sudhakara, T.L., Kaukonen, R.J., Viljoen, R.P., Alapieti, T.T., Ahmed, S.A., Sivakumar, S., 2010. Petrology and geochemistry of greywackes from Goa-Dharwar sector, western Dharwar craton: implications for volcanoclastic origin. J. Geol. Soc. India 75 (3), 465–487.

Devaraju, T.C., Huhma, H., Sudhakara, T.L., Kaukonen, R.J., Alapieti, T.T., 2007. Petrology, geochemistry, model SmNd ages and petrogenesis of the granitoids of the northern block of Western Dharwar Craton. J. Geol. Soc. India 70, 889–911.

Dhoundial, D.P., Paul, D.K., Sarkar, A., Trivedi, J.R., Gopalan, K., Potts, P.J., 1987. Geochronology and geochemistry of Precambrian granitic rocks of Goa. SW India. Precambrian Res. 36 (3), 287–302.

Dhuime, B., Hawkesworth, C., Cawood, P., 2011. When continents formed. Science 331, 154–155.

Drummond, M.S., Defant, M.J., 1990. A model for trondhjemite-tonalitedacite genesis and crustal growth via slab melting: Archaean to modern comparisons. J. Geophys. Res. 95, 21503–21521.

Geological Survey of India, 1996. Geological and Mineral Map of Goa. Government of India.

Govindaraju, K., 1979. Report (1968–1978) on Two Mica Reference Samples: Biotite Mica-Fe and Phlogopite Mica-Mg. Geostand. Geoanal. Res. 3, 3–24.

Griffin, W.L., Pearson, N.J., Belousova, E., Jackson, S.E., van Achtersergh, E., O'Reilly, S.Y., Shee, S.R., 2000. The Hf isotope composition of cratonic mantle: LAM-MC-ICPMS analysis of zircon megacrysts in Kimberlites. Geochim. Cosmochim. Aata 64, 133–147.

Griffin, W.L., Wang, X., Jackson, S.E., Pearson, N.J., O'Reilly, S.Y., Xu, X., Zhou, X., 2002. Zircon chemistry and magma mixing, SE China: in-situ analysis of Hf isotopes, Tonglu and Pingtan igneous complexes. Lithos 61, 237–269.

Halla, J., van Hunen, J., Heilimo, E., Holtta, P., 2009. Geochemical and numerical constraints on Neoarchean plate tectonics. Precambr. Res. 17, 155–162.

Han, Y.S., Santosh, M., Ganguly, S., Li, S.S., 2019. Evolution of a Mesoarchean supra-subduction zone mantle wedge in the Dharwar Craton, southern India: Evidence from petrology, geochemistry, zircon U-Pb geochronology, and Lu–Hf isotopes. J. Geol. 54, 2935–2956.

Hawkesworth, C.J., Kemp, A.I.S., 2006. Using hafnium and oxygen isotopes in zircons to unravel the record of crustal evolution. Chem. Geol. 226, 144–162.

Heaman L, Parrish R., 1991. U-Pb geochronology of accessory minerals. In: Heaman LM, Ludden JN (eds) Mineral Assoc Can Short Course Ser. 19, 59-102.

Hiess, J., Condon, D.J., McLean, N., Noble, S.R., 2012. $^{238}U/^{235}U$ systematics in terrestrial uranium-bearing minerals. Science 355, 16101–16614.

Hogmalm, K.J., Zack, T., Karlsson, A.K., Sjoqvist, A.S.L., Grabe-Schonberg, D., 2017. In situ Rb-Sr and K-Ca dating by LA-ICP-MS/MS: An evaluation of N_2O and SF_6 as reaction gases. J. Anal. At. Spectrom. 32, 305–313.

Hokada, T., Horie, K., Satish-Kumar, M., Ueno, Y., Nasheeth, A., Mishima, K., Shiraishi, K., 2013. An appraisal of Archaean supracrustal sequences in Chitradurga schist belt, Western Dharwar Craton, southern India. Precambr. Res. 227, 99–119.

Iizuka, T., Hirata, T., 2005. Improvements of precision and accuracy in in-situ Hf isotope microanalysis of zircon using the laser ablation-MC-ICPMS technique. Chem. Geol. 220, 121–137.

Ishwar-Kumar, C., Santosh, M., Wilde, S., Tsunogae, T., Itaya, T., Windley, B., Sajeev, K., 2016. Mesoproterozoic suturing of Archean crustal blocks in western peninsular India: implications for India-Madagascar correlations. Lithos 263, 143–160.

Jayananda, M., Chardon, D., Peucat, J.J., Tushipokla, Fanning, C.M., 2015. Paleo- to Mesoarchean TTG accretion and continental growth in the western Dharwar Craton, Southern India: Constraints from SHRIMP U-Pb zircon geochronology, whole-rock geochemistry and Nd–Sr isotopes. Precambr. Res. 268, 295–322.

Jayananda, M., Santosh, M., Aadhiseshan, K.R., 2018. Formation of Archean (3600–2500 ma) continental crust in the Dharwar Craton, southern India. Earth-Sci. Rev. 181, 12–42.

Jayananda, M., Aadhiseshan, K.R., Kusiak, M.A., Wilde, S.A., Kowete-u Sekhamo, M., Santosh, M., Gireesh, R.V., 2020. Multi-stage crustal growth and Neoarchean geodynamics in the Eastern Dharwar Craton, southern India. Gondwana Res. 78, 228–260.

Jenkin, G.R.T., 2009. Do cooling paths derived from mica Rb-Sr data reflect true cooling paths? Geology 25, 907–910.

Lancaster, P.J., Dey, S., Storey, C.D., Mitra, A., Bhunia, R.K., 2015. Contrasting crustal evolution processes in the Dharwar craton: Insights from detrital zircon U-Pb and Hf isotopes. Gondwana Res. 28, 1361–1372.

Li, S.S., Palin, R.M., Santosh, M., Shaji, E., Tsunogae, T., 2019. Extreme thermal metamorphism associated with Gondwana assembly: Evidence from sapphirine-bearing granulites of Rajapalayam, southern India. Geol. Soc. Am. Bull., https://doi.org/10.1130/B35378.1.

Li, S.S., Santosh, M., Ganguly, S., Thanooja, P.V., Sajeev, K., Pahari, A., 2018a. Neoarchean microblock amalgamation in southern India: evidence from the Nallamalai Suture Zone. Precambrian Res. 314, 1–27.

Li, S.S., Santosh, M., Palin, R.M., 2018b. Metamorphism during the Archean-Paleoproterozoic transition associated with microblock amalgamation in the Dharwar Craton. India. J. Petrol. 59 (12), 2435–2462.

Maibam, B., Gerdes, A., Goswami, J.N., 2016. U-Pb and Hf isotope records in detrital and magmatic zircon from eastern and western Dharwar craton, southern India: Evidence for coeval Archaean crustal evolution. Precambrian Res. 275, 496–512.

Miller, J.S., Matzel, J.E.P., Miller, C.F., Burgess, S.D., Miller, R.B., 2007. Zircon growth and recycling during the assembly of large, composite arc plutons. J. Volcanol. Geotherm. Res. 167 (1–4), 282–299.

Mohan, M.R., Sarma, D.S., Mc Naughton, N.J., Fletcher, I.R., Wilde, S.A., Siddiqui, M.H., Rasmussen, B., Krapez, B., Gregory, C.J., Kamo, S.L., 2014. SHRIMP zircon and titanite U-Pb ages, Lu-Hf isotope signatures and geochemical constraints for 2.56 Ga granite magmatism in western Dharwar craton, southern India: evidence for short-lived Neoarchean episodic crustal growth. Precambrian Res. 243, 197–220.

Pahari, A., Tang, L., Manikyamba, C., Santosh, M., Subramanyam, K.S.V., Ganguly, S., 2019. Meso-Neoarchean magmatism and episodic crustal growth in the Kudremukh-Agumbe granite-greenstone belt, western Dharwar Craton. India. Precambrian Res. 323, 16–54.

Patchett, P.J., Kuovo, O., Hedge, C.E., Tatsumoto, M., 1981. Evolution of continental crust and mantle heterogeneity: evidence from Hf isotopes. Contrib. Mineral. Petrol. 78, 279–297.

Paton, C., Hellstrom, J., Paul, B., Woodhead, J., Hergt, J., 2011. Iolite: freeware for the visualization and processing of mass spectrometric data. J. Anal. At. Spectrom. 26, 2508–2518.

Peucat, J.J., Jayananda, M., Chardon, D., Capdevila, R., Fanning, C.M., Paquette, J.L., 2013. The lower crust of the Dharwar Craton, Southern India: Patchwork of Archean granulitic domains. Precambrian Res. 227, 4–28.

Pupin, J.P., 1980. Zircon and granite petrology. Contrib. Mineral. Petrol. 73 (3), 207–220.

Raju, P.V.S., Eriksson, P.G., Catuneanu, O., Sarkar, S., Banerjee, S., 2014. A review of the inferred geodynamic evolution of the Dharwar craton over the ca. 3.5–2.5 Ga period, and possible implications for global tectonics. Can. J. Earth Sci. 51, 312–325.

Rekha, S., Bhattacharya, A., Chatterjee, N., 2014. Tectonic restoration of the Precambrian crystalline rocks along the west coast of India: Correlation with eastern Madagascar in East Gondwana. Precambr. Res. 252, 191–208.

Rekha, S., Viswanath, T., Bhattacharya, A., Prabhakar, N., 2013. Meso/Neoarchean crustal domains along the north Konkan coast, western India: the Western Dharwar Craton and the Antongil-Masora Block (NE Madagascar) connection. Precambr. Res. 233, 316–336.

Rosman, K.J.R., Taylor, P.D., 1998. Isotopic composition of the elements. Pure Appl. Chem. 70, 217–235.

Rudnick, R.L., Gao, S., 2005. Composition of the continental crust. In: Rudnick, R.L. (Ed.), The Crust: Treaties on Geochemistry, pp. 1–64.

Russel, W.A., Papanastassiou, D.A., Tombrello, T.A., 1978. Ca isotope fractionation on the earth and other solar system materials. Geochim. Cosmochim. Acta 42, 1075–1090.

Santosh, M., Li, S.S., 2018. Anorthosites from an Archean continental arc in the Dharwar Craton, southern India: implications for terrane assembly and cratonization. Precambr. Res. 308, 126–147.

Scherer, E., Münker, C., Mezger, K., 2001. Calibration of the Lutetium-Hafnium Clock. Science 293, 683–687.

Sun, S.S., McDonough, W.F., 1989. Chemical and isotopic systematics of oceanic basalts: implications for mantle composition and processes. In: Saunders, A.D., Norry, M.J. (Eds.), Magmatism in Ocean Basins. Special Publication. Geol. Soc. London, vol.42 pp. 313-345.

Taylor, P.N., Chadwick, B., Moorbath, S., Ramakrishnan, M., Viswanatha, M.N., 1984. Petrography, chemistry and isotopic ages of Peninsular Gneiss, Dharwar acid volcanic rocks and the Chitradurga Granite with special reference to the late Archaean evolution of the Karnataka craton, southern India. Precambr. Res. 23, 349–375.

Thieblemont, D., Tegyey, M., 1994. Geochemical discrimination of differentiated magmatic rocks attesting for the variable origin and tectonic setting of calc-alkaline magmas. Comptes Rendus De Academie Des Sciences Series II 319, 87–94.

Tillberg, M., Drake, H., Zack, T., Kooijman, E., Whitehouse, M.J., Åström, M.E., 2020. In situ Rb-Sr dating of slickenfibres in deep crystalline basement faults. Sci. Rep. 10, 562.

Vermeesch, P., 2018. Isoplot R: A free and open toolbox for geochronology. Geosci. Front. 9 (5), 1479–1493.

Vervoort, J.D., Patchett, P.J., Söderlund, U., Baker, M., 2004. Isotopic composition of Yb and the determination of Lu concentrations and Lu/Hf ratios by isotope dilution using MC-ICPMS. Geochem. Geophys. Geosyst. 5, Q11002.

Wang, J.Y., Santosh, M., 2019. Eoarchean to Mesoarchean crustal evolution in the Dharwar craton, India: Evidence from detrital zircon U-Pb and Hf isotopes. Gondwana Res. 72, 1–14. https://doi.org/10.1016/j.gr.2019.02.006.

Watson, E.B., Harrison, T.M., 1983. Zircon saturation revisited: temperature and composition effects in a variety of crustal magma types. Earth Planet Sci Lett. 64, 295–304.

Wiedenbeck, M., Allé, P., Corfu, F., Griffin, W.L., Meier, M., Oberli, F., von Quadt, A., Roddick, J.C., Spiegel, W., 1995. Three natural zircon standards for U-Th-Pb, Lu-Hf, trace element and REE analyses. Geostandard. Newslett. 19, 1–23.

Wilson, M., 1989. Igneous Petrogenesis. Unwin Hyman, London, pp. 466.

Zack, T., Hogmalm, K.J., 2016. Laser ablation Rb/Sr dating by online chemical separation of Rb and Sr in an oxygen-filled reaction cell. Chem. Geol. 437, 120–133.

Research article

JGS
Journal of the Geological Society

Published online March 3, 2020

https://doi.org/10.1144/jgs2019-132 | Vol. 177 | 2020 | pp. 784–798

Structural evolution and medium-temperature thermochronology of central Madagascar: implications for Gondwana amalgamation

Sheree E. Armistead[1,2,3]*, Alan S. Collins[1], Ahmad Redaa[1,4], Gilby Jepson[1,5], Jack Gillespie[1,6], Sarah Gilbert[7], Morgan L. Blades[1], John D. Foden[1] and Théodore Razakamanana[8]

[1] Tectonics & Earth Systems Research Group, Mawson Centre for Geoscience, Department of Earth Sciences, University of Adelaide, Adelaide, SA, 5005 Australia
[2] Geological Survey of Canada, 601 Booth Street, Ottawa, ON, K1A 0E9 Canada
[3] Mineral Exploration Research Centre, Harquail School of Earth Sciences, Laurentian University, Sudbury, ON, P3E 2C6 Canada
[4] Faculty of Earth Sciences, King Abdulaziz University, Jeddah, 21598 Saudi Arabia
[5] Department of Geosciences, University of Arizona, 1040 E. 4th Street, Tucson, AZ, 85721 USA
[6] The Institute for Geoscience Research (TIGeR), School of Earth and Planetary Sciences, Curtin University, Perth, WA, 6102 Australia
[7] Adelaide Microscopy, University of Adelaide, Adelaide, SA, 5005 Australia
[8] Département des Sciences de la Terre, Université de Toliara, Toliara, 601 Madagascar

SEA, 0000-0002-9614-3553; AR, 0000-0003-1208-8567; GJ, 0000-0003-0151-3062; JG, 0000-0002-3061-6223; SG, 0000-0003-3259-7983; JDF, 0000-0003-3564-7253

* Correspondence: sheree.armistead@adelaide.edu.au

Abstract: Madagascar occupied an important place in the amalgamation of Gondwana and preserves a record of several Neoproterozoic events that are linked to orogenesis of the East African Orogen. In this study, we integrate remote sensing, field data and thermochronology to unravel complex deformation in the Ikalamavony and Itremo domains of central Madagascar. The deformation sequence comprises a gneissic foliation (S_1), followed by south- to SW-directed, tight to isoclinal, recumbent folding (D_2). These are overprinted by north-trending upright folds that formed during an approximately east–west shortening event (D_3). Together these produced type 1 and type 2 fold interference patterns throughout the Itremo and Ikalamavony domains. We show that the Itremo and Ikalamavony domains were deformed together in the same orogenic system, which we interpret as the *c*. 630 Ma collision of Azania with Africa along the Vohibory Suture in southwestern Madagascar. In eastern Madagascar, deformation is syn- to post-550 Ma, and probably formed in response to final closure of the Mozambique Ocean along the Betsimisaraka Suture that amalgamated Madagascar with the Dharwar Craton of India. Apatite U–Pb and novel laser ablation triple quadrupole inductively coupled plasma mass spectrometry (LA-QQQ-ICP-MS) muscovite and biotite Rb–Sr thermochronology indicates that much of central Madagascar cooled through *c*. 500°C at *c*. 500 Ma.

Supplementary material: A detailed geological map of central Madagascar (Supplementary A), detailed methods and geo- and thermochronology results (Supplementary B), isotopic data for geo- and thermochronology (Supplementary C) and Landsat images and structural interpretation examples (Supplementary D) are available at https://doi.org/10.6084/m9.figshare.c.4840575

Received 19 August 2019; **revised** 28 January 2020; **accepted** 1 February 2020

The amalgamation of central Gondwana occurred through convergence at several discrete subduction and collisional zones, collectively forming the East African Orogen. Madagascar was located in the centre of Gondwana and provides an ideal natural laboratory to study how this supercontinent coalesced (Fig. 1a) (Tucker *et al.* 1999; Collins and Windley 2002; Collins 2006). Of particular interest and contention is how and when the Archean nucleus of Madagascar amalgamated with the Dharwar Craton of India to the east and East Africa to the west, as well as with smaller continental blocks of equivocal origin. Reconciling this tectonic history has major implications for global plate-tectonic models of the Neoproterozoic (e.g. Merdith *et al.* 2017).

Central Madagascar comprises the Archean Antananarivo Domain, the Proterozoic Itremo sub-domain and the Neoproterozoic Ikalamavony Domain. These terranes are bounded by two postulated major sutures: the eastern Betsimisaraka Suture and the western Vohibory Suture (mapped as the Ampanihy shear zone in Fig. 1b). These sutures resulted from at least two distinct orogenic events that amalgamated central Madagascar, the Dharwar Craton and Africa within Gondwana (Fig. 1a). However, the timing, location and direction of subduction leading to these orogenic events remain contentious. Two end-member models are generally evaluated for the amalgamation of Madagascar: (1) the Dharwar–central Madagascar collision (eastern suture) occurred in the late Archean, and that central Madagascar and the Dharwar Craton existed as the 'Greater Dharwar Craton' through the entire Proterozoic eon (Tucker *et al.* 2011), and widespread Neoproterozoic–Cambrian magmatism and metamorphism in Madagascar resulted from Madagascar–Africa collision (western suture); or (2) the Dharwar Craton and central Madagascar were separate terranes that were sutured during a major Ediacaran–Cambrian East African orogenic event (the Malagasy Orogeny of Collins and Pisarevsky 2005), marked by the Betsimisaraka Suture in eastern Madagascar (Fig. 1b). An age of *c*. 750–650 Ma for this suture has alternatively been proposed (Fitzsimons and Hulscher 2005). Several researchers have proposed that the central

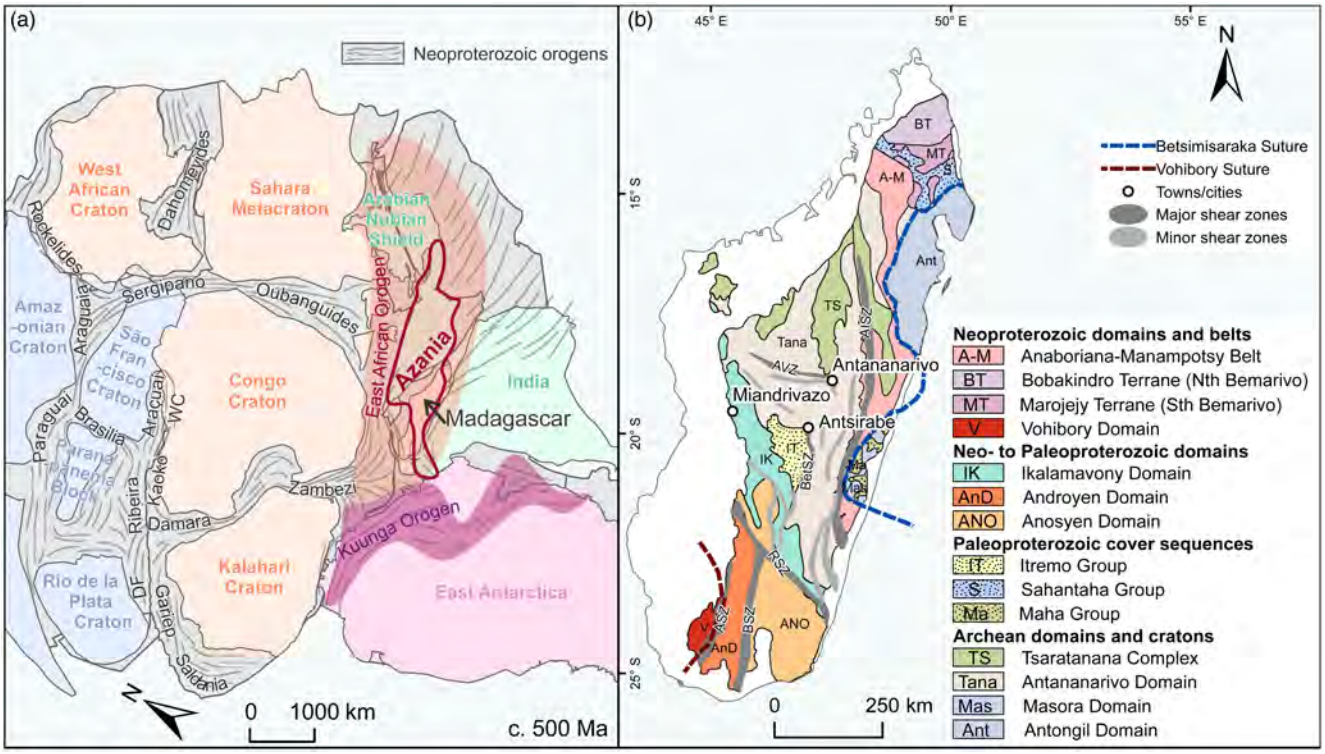

Fig. 1. (**a**) Tectonic map of Gondwana made using GPlates exported geometries from Merdith *et al.* (2017) in ArcGIS; projected in Hotine Oblique Mercator with Madagascar in the centre (reconstructed position; latitude +40°, longitude –75°). DF, Dom Feliciano Belt; WC, West Congo. (**b**) Present-day map of the geological domains of Madagascar after De Waele *et al.* (2011). AISZ, Angavo–Ifanadiana shear zone; AVZ, Antananarivo virgation zone; BetSZ, Betsileo shear zone; RSZ, Ranotsara shear zone; BSZ, Beraketa shear zone; ASZ, Ampanihy shear zone.

Madagascar–Africa collision occurred at *c*. 650–630 Ma (Collins and Windley 2002; Collins and Pisarevsky 2005; Emmel *et al.* 2008; Jöns and Schenk 2011; Horton *et al.* 2016). Others have suggested a *c*. 850–750 Ma age for a suture in western Madagascar (Moine *et al.* 2014). The proximity of these two suture zones makes it difficult to unravel the timing of events, as more recent events have obscured the record of earlier events through high-temperature resetting of key minerals used for thermochronology and metamorphism.

Regional geology

Madagascar is made up of several domains ranging in age from Archean to Neoproterozoic (Fig. 1b). The centre of Madagascar is made up of the Antananarivo Domain, which has a basement of *c*. 2500 Ma magmatic gneisses (Tucker *et al.* 1999; Kröner *et al.* 2000; Collins and Windley 2002), known as the Betsiboka Suite (Roig *et al.* 2012), interleaved with the Ambatolampy Group granulite- and amphibolite-facies metasedimentary rocks (Archibald *et al.* 2015). To the east of the Antananarivo Domain is the Antongil–Masora Domain, which contains gneisses that have ages of *c*. 3100 and *c*. 2500 Ma and are interpreted as a continuation of the Dharwar Craton of India (Tucker *et al.* 1999; Schofield *et al.* 2010; Armistead *et al.* 2017).

Overlying the Antananarivo Domain is the Itremo Group (Figs. 1b and 2). Classified as a sub-domain of the Antananarivo Domain by Roig *et al.* (2012), the Itremo Group consists of quartzites, schists and marbles with a maximum depositional age of *c*. 1600 Ma (Cox *et al.* 1998; Fernandez *et al.* 2003). The Itremo Group is interpreted as a continental margin sequence that was deposited on the Antananarivo Domain basement (Cox *et al.* 1998, 2004). The Itremo nappes in the Itremo Domain have been investigated extensively owing to their prominence in remotely sensed data and availability of outcrops (Collins *et al.* 2003*b*; Tucker *et al.* 2007).

To the SW, thrust over the Itremo Group, is the Ikalamavony Group within the Ikalamavony Domain, similarly made up of quartzites, schists and marbles but with a maximum depositional age of *c*. 1000 Ma (Tucker *et al.* 2014; Archibald *et al.* 2017*a*). In places the Ikalamavony Domain is in tectonic contact directly with the Antananarivo Domain basement, with no Itremo Group rocks separating them (Figs 1b and 2). Unique to the Ikalamavony Domain is the *c*. 1000 Ma Dabolava Suite, which is composed of granitic to gabbroic orthogneiss (Archibald *et al.* 2017*a*). The Dabolava Suite and the age-equivalent Ikalamavony Group have been interpreted as an oceanic arc terrane (Archibald *et al.* 2017*a*). This terrane must have accreted prior to the intrusion of the *c*. 850–750 Ma Imorona–Itsindro Suite, which intrudes the Ikalamavony, Itremo and Antananarivo domains, placing a minimum age on the juxtaposition of the three central Madagascan domains. The relationship between the Ikalamavony Domain and the Itremo Group remains poorly understood, and is the focus of this study.

To the south of these metasedimentary terranes are the Proterozoic Anosyen, Androyen and Vohibory domains (de Wit *et al.* 2001; Emmel *et al.* 2008; Jöns and Schenk 2008; Boger *et al.* 2014; Horton *et al.* 2016). In northern Madagascar is the *c*. 800–700 Ma Bemarivo Domain, which formed as an exotic juvenile arc terrane that amalgamated with Madagascar at *c*. 520 Ma, possibly in relation to the Betsimisaraka Suture (Jöns *et al.* 2009; Thomas *et al.* 2009; Armistead *et al.* 2019).

Regional structural and geochronological framework for central Madagascar

This study focuses on central Madagascar including parts of the Ikalamavony and Antananarivo domains and the Itremo sub-domain (Figs 1b and 2). The structural relationships between these domains has not yet been studied in detail. We use structural geology and various geochronological methods to define and

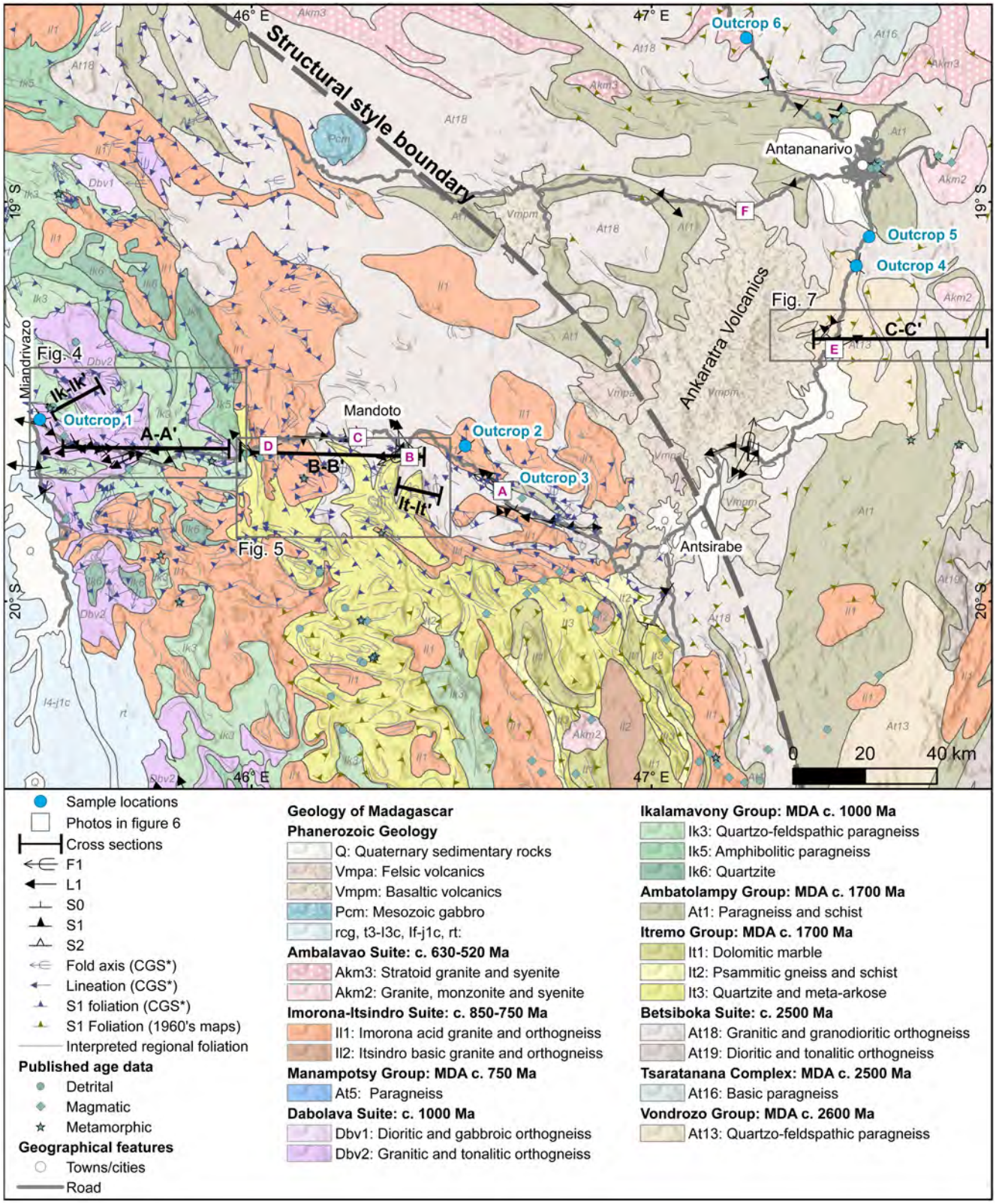

Fig. 2. Geological map of central Madagascar (Roig *et al.* 2012) with sample locations, photograph locations for Figure 6 (labelled A–F) our remote sensing interpretation, new structural measurements and structural measurements from Service Géologique de Madagascar (1962, 1963*a*,*b*), Moine (1968) and Council for Geoscience (CGS; Macey *et al.* (2009)), and published geochronology. Approximate ages for sedimentary groups are given as maximum depositional ages (MDA). A more detailed PDF copy of this map where layers can be turned on and off, and further information can be obtained from the model tree in a pdf viewer is provided in Supplementary A.

distinguish deformation events in central Madagascar. Collins *et al.* (2003*b*) and Tucker *et al.* (2007) undertook comprehensive studies of the structure of the Itremo Group in central Madagascar. This area contains spectacularly folded sequences visible from satellite imagery. Collins *et al.* (2003*b*) interpreted a D_1 event that produced 10 km scale recumbent, isoclinal folding predating *c.* 800–780 Ma intrusive rocks of the Imorona–Itsindro Suite. D_2 was interpreted as a local deformation event that occurred synchronously with *c.* 800–

780 Ma intrusions. D_3 was interpreted as an east–west shortening event with thrusting and at least two phases of upright folding. D_4 is expressed as post-550 Ma normal shearing and locally marks the boundary between the least metamorphosed parts of the Itremo Group and the granulite-facies Betsiboka Suite and Ambatolampy Group of the Antananarivo Domain (Betsileo Shear Zone; Fig. 1b; Collins *et al.* 2000). Tucker *et al.* (2007) interpreted a similar history for the Itremo Group with kilometre-scale fold and thrust nappes, and east-directed vergence. This resulted in inversion and repetition of the Archean Antananarivo Domain gneisses and the Proterozoic Itremo Group, with high-grade (old) rocks being thrust over low-grade (young) rocks. The inversion was followed by east–west shortening that resulted in upright folding of nappes to produce kilometre-scale fold interference patterns. This shortening event occurred within a sinistral transpressive regime and was interpreted as being associated with the Ranotsara Shear Zone (Fig. 1b) in southern Madagascar (Tucker *et al.* 2007). Although these models are similar in their sequence and style of deformation, they differ in that Tucker *et al.* (2007) interpreted the timing of deformation as occurring after *c.* 720 Ma, whereas Collins *et al.* (2003*b*) interpreted the early nappes as forming before *c.* 800–780 Ma, and the upright folding as having occurred after the *c.* 780 Ma intrusive rocks.

The region between the easternmost part of our study area and the east coast of Madagascar (approximately the location of the Betsimisaraka Suture in Fig. 1b) was studied from a structural perspective by Martelat *et al.* (2000), Nédélec *et al.* (2000), Collins *et al.* (2003*a*), Raharimahefa and Kusky (2006, 2009) and Raharimahefa *et al.* (2013). Interpretations of this region generally include a D_1 event characterized by north–south-striking foliations that dip to the west, with a top-to-the-east sense of movement (Nédélec *et al.* 2000; Collins *et al.* 2003*a*). These rocks are reworked by D_2 shear zones such as the Angavo Shear Zone and the Antananarivo virgation zone (Fig. 1b) that underwent low-pressure, granulite conditions (Paquette and Nédélec 1998; Nédélec *et al.* 2000). D_3 is characterized by >20 km wide mylonitic high-strain zones and smaller discrete shear zones (Collins *et al.* 2003*a*). These dip gently to the west, with a top-to-the-east sense of movement. D_4 is characterized by poorly preserved late-stage folding (Collins *et al.* 2003*a*). A synkinematic granite within the Angavo Shear Zone constrains deformation here to *c.* 550 Ma (Raharimahefa and Kusky 2010).

Precise dating of deformation in Madagascar is difficult owing to resetting from successive overlapping thermo-tectonic events. Latest metamorphism in the Anosyen and Androyen domains to the south of our study area is constrained to *c.* 580–520 Ma (Fig. 3) (Paquette *et al.* 1994; Martelat *et al.* 2000; de Wit *et al.* 2001; Collins *et al.* 2012) and attributed to high-strain shearing along the Ampanihy and Beraketa shear zones (Fig. 1b) (Boger *et al.* 2014, 2015). Jöns and Schenk (2011) and Horton *et al.* (2016) demonstrated that in southern Madagascar, high-grade metamorphism yielded ages of *c.* 650–600 Ma west of the Vohibory Suture (Fig. 3), but recorded ages of *c.* 560–530 Ma to the east of this suture. In central Madagascar, U–Pb dating of zircon rims and titanite has been used to constrain latest metamorphism in the Itremo Group to *c.* 550–500 Ma (Tucker *et al.* 2007). Further east, between the easternmost part of the study area and the east coast of Madagascar, metamorphism has been dated to *c.* 560–520 Ma (Kröner *et al.* 2000; Collins *et al.* 2003*c*; BGS–USGS–GLW 2008). From this, it is clear that whatever event was taking place at *c.* 580–520 Ma, its effects were widespread and resulted in metamorphism throughout most of Madagascar, sparing, perhaps, the far southwest.

The cross-cutting relationships and deformation history of the rocks within the terranes that make up Madagascar can provide clues to the timing of major orogenic events. Here we use structural geology to understand the deformation history of a poorly understood part of central Madagascar, which lies between the two hypothesized suture zones. We attempt to link up previous structural studies and further extend these interpretations to cover the entire central Madagascar region. We have used remotely sensed data such as satellite imagery and Landsat images to interpret the structural framework of central Madagascar, and have integrated

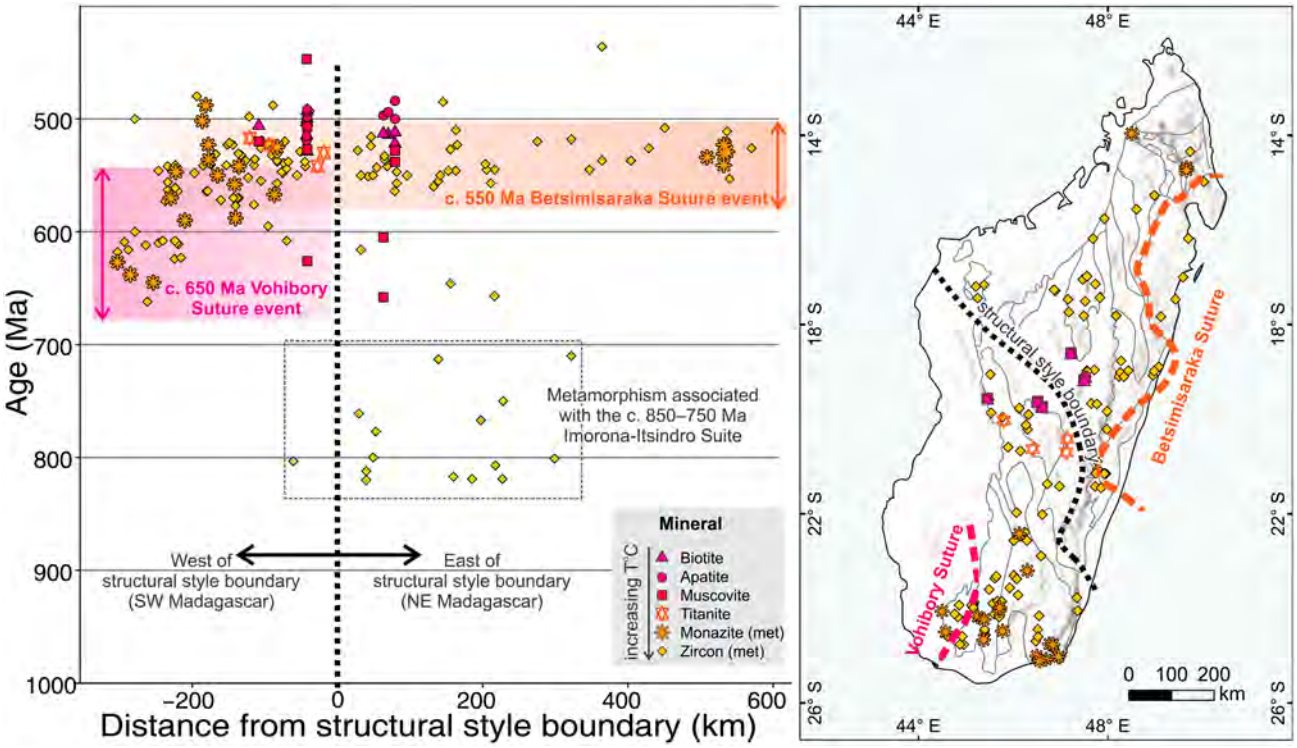

Fig. 3. Summary of published metamorphic data for Madagascar and new data collected in this study. Biotite, apatite and muscovite are from this study. Metamorphic minerals zircon, monazite and titanite are from the compilation of Tucker *et al.* (2014). Locations of data points are shown in the map to the right; terranes are the same as those in Figure 1b.

existing geochronological and structural data (Supplementary A). We have ground-truthed this interpretation by collecting structural data and key rock samples for U–Pb zircon, U–Pb apatite, Rb–Sr muscovite and Rb–Sr biotite analysis (Supplementary B and Supplementary C). Rb–Sr mica laser ablation triple quadrupole inductively coupled plasma mass spectrometry (LA-QQQ-ICP-MS) dating in particular is a novel technique and this research represents some of the first published ages using this technique. These isotopic systems span a wide range of closure temperatures from which we can reconstruct the temporal and thermal evolution of this region.

Structure of central Madagascar

Large-scale structures, fold interference patterns, faults and shear zones are recognizable in remotely sensed data in the region west of Antsirabe (Fig. 2). Examples of Landsat images used for interpretation are presented in Supplementary D. East of Antsirabe, poly-deformed folds are not observed and the structural style changes significantly. We have delineated this as a 'structural style boundary' in Figure 2. Here we further extend previous interpretations of the Itremo sub-domain (Collins *et al.* 2003*b*; Tucker *et al.* 2007) to the Ikalamavony Domain, where identification of lithostratigraphy from remotely sensed data is more difficult, and interpretation is less straightforward.

Ikalamavony Domain

The Ikalamavony Domain contains metasedimentary rocks of the Ikalamavony Group, which are dominated by paragneiss, schist, quartzite and amphibolite (Fig. 4). We observe many of the gneisses with bands of mylonite, indicating a high-strain environment. Based on remote sensing data, we interpret a thrust fault separating the Ikalamavony Domain and Itremo sub-domain (Fig. 5). This fault is interpreted based on the sharp contrast in lithologies and the linear nature of the fault observed in remote sensing data. Owing to the scarcity of fresh outcrop, we were unable to observe this fault in the field; however, rocks were more strongly deformed in this area.

D_1 deformation

The first recognizable deformation event at the outcrop scale is defined by a pervasive foliation observed in orthogneisses, paragneisses and metasedimentary rocks. In orthogneisses and paragneisses, the foliation is typically defined by the elongation and alignment of biotite, feldspar and quartz. In metasedimentary rocks such as schist and paragneiss, the foliation is commonly defined by the orientation of biotite crystals and biotite-rich layers. Primary sedimentary features such as bedding were difficult to recognize owing to significant metamorphism and recrystallization.

In remotely sensed data, linear or curvilinear trends such as ridges are interpreted as being representative of the S_1 foliation. Quartzite units in particular, which are less common than in the Itremo sub-domain, are easy to recognize in remotely sensed data owing to the large contrast in different Landsat bands (e.g. Supplementary D). In the Ikalamavony Domain the orientation of measured S_1 foliations is dominantly NW-trending, and lineations and fold axes plunge moderately toward the west.

D_2 deformation

D_2 deformation is most easily identifiable from remotely sensed data owing to the large-wavelength (>1 km) folds. F_2 antiforms and synforms are identifiable by the repetition of mapped geological units and constrained by structural measurements (Fig. 4). D_2 is defined by tight to isoclinal folds with axial traces approximately parallel to S_1 in fold limbs. At the outcrop scale we observe these as decimetre- to metre-scale asymmetric, tight to isoclinal folds. F_2 folds are similar-type folds, with thickened hinge zones and thinned limbs. An axial planar foliation is difficult to recognize in outcrops, but sometimes occurs as the alignment of biotite in hinge zones. Owing to the isoclinal nature of folding, F_2 axial traces are approximately parallel to S_1 at the regional scale. F_2 folds would have formed with axial traces striking roughly east–west; however, owing to subsequent deformation during D_3 and D_4, they are now preserved with variable orientations.

D_3 deformation and associated fold interference patterns

We do not observe evidence for a third-generation deformation event at the outcrop scale; however, D_3 folds are recognizable in remotely sensed data. The folding of F_2 folds during D_3 has produced a series of fold interference patterns. Type 1 and type 2 fold interference patterns are observed in remotely sensed data (Figs 4 and 5). Type 1 fold interference patterns occur when an upright folding event is overprinted by an orthogonal upright folding event (Grasemann *et al.* 2004) and are shown in Supplementary D(b). Type 2 fold interference patterns occur when a recumbent fold is orthogonally overprinted by an upright fold (Grasemann *et al.* 2004) and are shown in Figure 5. We interpret D_3 as the result of roughly NE–SW shortening (present-day orientation). Cross-section Ik–Ik' (Fig. 4) has F_2 folds that are very tight to isoclinal, with axial traces approximately parallel to F_3 in F_3 fold limbs. This formed by roughly SE-directed recumbent folding that was overprinted by a north- to NW-trending F_3 fold.

D_4 deformation

The axial traces of F_3 folds vary across the Ikalamavony Domain, indicating a fourth generation of deformation. For example, the F_3 fold axes vary from NW-trending in the west near Miandrivazo (e.g. Ik–Ik' cross-section in Fig. 4), and curve to become north- to NE-trending in the centre of the map in Figure 4. We suggest this is caused by large-wavelength (*c.* 30–50 km) F_4 open folding with approximately east–west shortening.

Itremo–Antananarivo Domain

The Itremo Group is a continental marginal sequence deposited on basement rocks of the Antananarivo Domain (e.g. Cox *et al.* 1998, 2004). Therefore, we consider these 'domains' together. Transect B–B' (Fig. 5) contains metasedimentary rocks of the Itremo Group, which are dominantly quartzites, marbles and schists, with minor conglomerates. The majority of quartzites that we observe are strongly recrystallized and it is often difficult to recognize primary sedimentary features. The Itremo–Antananarivo Domain was intruded by the *c.* 850–750 Ma Imorona–Itsindro Suite, after early deformation (Collins *et al.* 2003*b*). Together, these suites of rocks underwent a complex deformation history that must post-date the intrusion of the Imorona–Itsindro Suite.

Deformation intensity appears to weaken towards the east of the Itremo sub-domain, with an absence of complex fold interference patterns between Antsirabe and Antananarivo. The Imorona–Itsindro Suite in particular becomes progressively less deformed to the east. In the west, the Imorona–Itsindro Suite is folded into fold interference patterns, whereas in the east it appears to be folded into only weakly defined F_3 folds. This is consistent with our sampling of *c.* 850–750 Ma rocks along this weakly deformed margin (along the main road in Fig. 2), where rock samples appear undeformed or very weakly deformed (documented in Table 1).

D_1 deformation

The orientation of S_1 is variable in the Itremo sub-domain owing to the abundance of poly-deformed folds. Similar to the Ikalamavony

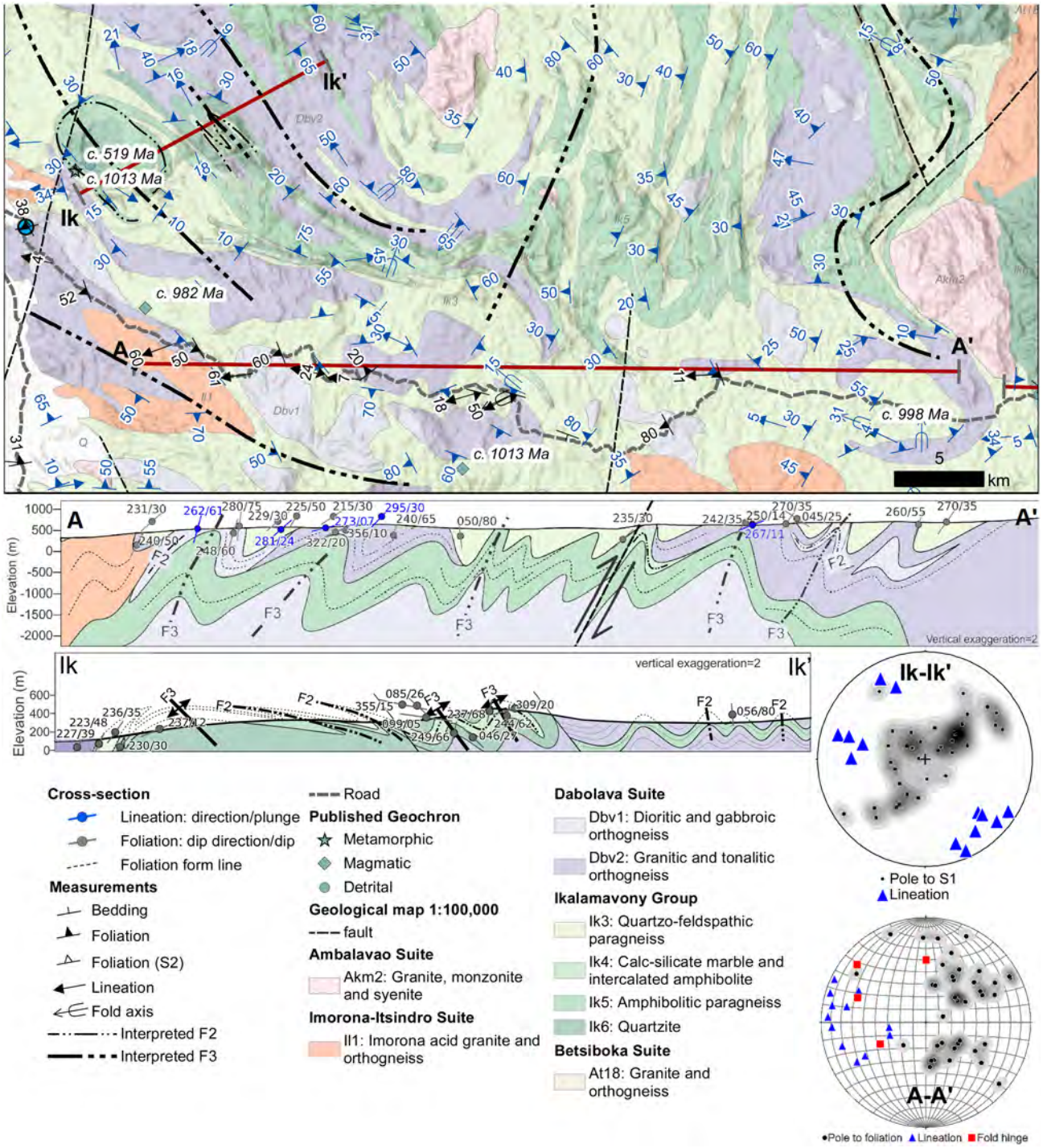

Fig. 4. Geological map, structural data and cross-sections through the Ikalamavony Domain using both our new data (black) and previously published data (blue) (Macey *et al.* 2009). Fold axis measurements are generally interpreted to be F_2 folds as we do not observe any overprinting fold generations in the field. A–A' shows the overall trend of structures in the Ikalamavony Domain. Ik–Ik' is an example of type 2 fold interference patterns with NW-trending third-generation upright folds. Sections were generated using QProf plugin in QGIS. Structural measurements (dip direction/dip) within *c*. 2 km of the section are projected along the profile. Topographic profile was derived from 30 arc-second digital elevation model (DEM) of Africa (US Geological Survey; USGS). Geological polygons are from Council for Geosciences 1:100 000 mapsheets (Macey *et al.* 2010).

Domain, foliations strike dominantly NNW, with lineations and fold axes plunging moderately toward WNW. Like the Ikalamavony Domain, the first-generation foliation at the outcrop scale is typically defined by the elongation and alignment of biotite, feldspar and quartz in orthogneisses and paragneisses (Fig. 6a). In metasedimentary rocks such as quartzites and marbles, the foliation is sometimes defined by the orientation of biotite crystals and biotite-rich layers, but is often difficult to recognize owing to significant recrystallization of quartz and a lack of other minerals. Primary sedimentary features such as bedding were difficult to recognize in quartzites owing to significant recrystallization. Within the quartzite packages, there are several conglomerate units with large (up to *c*. 5 cm) pebbles (Fig. 6b). Here we observe S_0 as the interbedded pebble layers, and S_1 as the flattening of pebbles.

D_2 deformation

Identical to the Ikalamavony Domain, D_2 is defined by tight to isoclinal folds with axial traces approximately parallel to S_1 in fold limbs. At the outcrop scale we observe these as decimetre- to

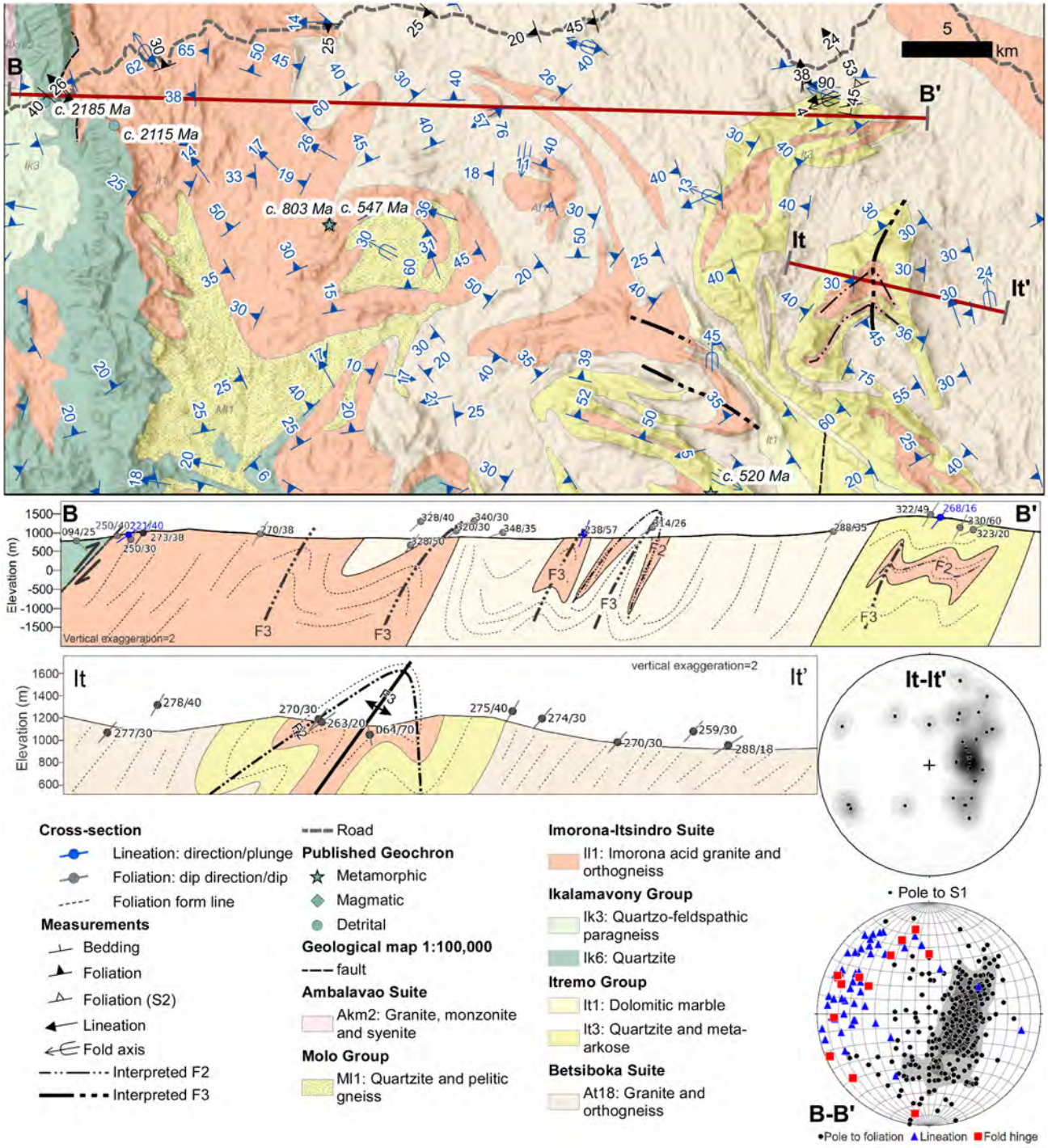

Fig. 5. Geological map, structural data and cross-sections through the Itremo–Antananarivo Domain using both our new data and previously published data (Macey *et al.* 2009). Measured fold axes are generally interpreted to be F_2 folds as we do not observe any overprinting fold generations in the field. Similar to the Ikalamavony transect, the Itremo transect contains moderately to steeply west-dipping foliations, west-plunging lineations and west- to NW-plunging folds. It–It' is an example of a type 2 fold interference pattern with D_2 south-directed recumbent folding overprinted by an F_3 north- to NE-trending upright fold. Geological polygons are from Council for Geosciences 1:100 000 mapsheets (Macey *et al.* 2010). Sections were generated using QProf plugin in QGIS. Structural measurements (dip direction/dip) within *c.* 2 km of the section are projected along the profile. Topographic profile was derived from 30 arc-second DEM of Africa (USGS).

metre-scale asymmetric, tight to isoclinal folds (Fig. 6c and d). F_2 folds are similar-type folds, with thickened hinge zones and thinned limbs. F_2 axial traces are approximately parallel to S_1 at the regional scale. F_2 folds are recognizable in remotely sensed data as *c.* 500–1000 m wavelength, tight to isoclinal folds (Fig. 5). The original orientation of F_2 folds would have had roughly east–west-striking axial traces, but have been subsequently deformed during D_3 and D_4. Further south where structures are more north–south trending, Tucker *et al.* (2007) interpreted east- or SE-directed vergence from these fold trends.

D_3 deformation and associated fold interference patterns

Similar to the Ikalamavony Domain, we do not observe evidence for a third-generation deformation event at the outcrop scale; however, D_3 folds are recognizable in remotely sensed data. The majority of

Table 1. *Summary of sample descriptions, outcrop and cross-cutting relationships, and age data*

Sample number	Transect	Outcrop	Sample description	Magmatic suite	Latitude	Longitude	Elevation (m)	Zircon U–Pb age (Ma)	Apatite U–Pb age (Ma)	Muscovite Rb–Sr age (Ma)	Biotite Rb–Sr age (Ma)
M16-24	West	1	Undeformed K-feldspar-rich granite. Intrudes deformed gabbro interpreted as the Dabolava Suite	Ambalavao	−19.5443	45.47028	182	576 ± 24	–	519 ± 69	505 ± 59
M16-32	West	2/A	Coarse-grained gneiss with 1–2 cm biotite phenocrysts	Betsiboka	−19.6107	46.53399	989	2553 ± 24	519 ± 11	446 ± 161	502 ± 20
M16-33	West	2/D	Undeformed fine-grained granodioritic dyke; intrudes M16-32	Imorona–Itsindro	−19.6107	46.53399	989	798 ± 24	–	–	–
M16-34	West	2/C	Thin dyke intruding M16-32	Betsiboka	−19.6107	46.53399	989	2511 ± 14	515 ± 7	–	–
M16-35	West	2/B	K-feldspar-rich deformed dyke	Betsiboka	−19.6107	46.53399	989	2583 ± 26, 2494 ± 14*	502 ± 6	–	513 ± 18
M16-15	West	3/A	K-feldspar- and biotite-rich, foliated orthogneiss	Betsiboka	−19.7239	46.62736	1067	2456 ± 17	492 ± 5	624 ± 152	528 ± 18
M16-16	West	3/B	Undeformed granite, occasionally very weakly foliated	Imorona–Itsindro	−19.7239	46.62736	1067	795 ± 24	498 ± 7	506 ± 82	499 ± 68
M16-17	West	3/C	Pegmatite veins, K-feldspar rich	Imorona–Itsindro	−19.7239	46.62736	1067	*c.* 795	494 ± 7	526 ± 39	492 ± 51
M16-46	East	4/A	Foliated orthogneiss, medium-grained, K-feldspar and biotite rich	Betsiboka	−19.1599	47.51211	1351	2522 ± 8, 543 ± 27†	497 ± 15	604 ± 211	512 ± 24
M16-47	East	4/B	Undeformed cross-cutting granite	Imorona–Itsindro	−19.1599	47.51211	1351	798 ± 48, 532 ± 44†	–	657 ± 98	–
M16-45	East	5	Medium-grained granite, undeformed	Ambalavao	−19.0869	47.54429	1312	543 ± 18	507 ± 35	–	512 ± 16
M16-52	East	6/A	Granite, very weakly foliated	Ambalavao	−18.589	47.23721	1359	568 ± 16	484 ± 14	527 ± 51	511 ± 16
M16-53	East	6/B	Cross-cutting K-feldspar-rich granite	Ambalavao	−18.589	47.23721	1359	*c.* 568	500 ± 10	537 ± 35	521 ± 18

Letters given for each outcrop are the interpreted order of formation or intrusion, based on cross-cutting relationships. All zircon ages are interpreted as magmatic crystallization ages except for *metamorphic ages and †lower intercept ages.

F_3 fold axial traces are roughly north–south striking, and orthogonally overprint F_2 folds. We therefore interpret D_3 as an approximately east–west shortening event. The folding of F_2 folds during D_3 has produced a series of fold interference patterns. Type 2 fold interference patterns are observed in remotely sensed data in the Itremo sub-domain (Fig. 5).

Adding to the complexity of the structure in It–It' is the juxtaposition of older units (the Archean Betsiboka Suite) structurally above younger units (Paleoproterozoic Itremo Group). Tucker *et al.* (2007) observed that the kilometre-scale fold and thrust nappes (our interpreted D_2), resulted in the inversion and repetition of Archean and Proterozoic rocks. This interpretation accounts for why the It–It' section contains older units that appear structurally above younger units.

D_4 deformation

The trend of structures varies from the NW of central Madagascar near Miandrivazo, to the SE of the study area along the eastern margin of the Itremo Group (Fig. 2). Near Miandrivazo (e.g. Fig. 4), F_3 axial traces generally trend NW–SE. In the Itremo Group and further to the south, these structures are generally north–south trending. This trend broadly follows the curve of our structural style boundary between the western and eastern transects delineated in Figure 3. This regional variation may relate to D_4 deformation or may relate to orogenic bending as orogenesis progressed.

Antananarivo Domain

Precambrian outcrops between Antsirabe and Antananarivo are scarce due to the widespread coverage of the Ankaratra Volcanics (Fig. 2). Generally, deformation in this area is much less intense than in the Ikalamavony Domain and Itremo sub-domain, and we observe fewer deformation events (Fig. 7). To the east of the Antananarivo–Antsirabe road (Figs 2 and 7), there is a distinct change in structural trend. In the Ikalamavony and Itremo domains, structures dominantly trend NW. North of Antananarivo, structures trend roughly east–west (approximately the location of Antananarivo virgation zone in Fig. 2), and between Antananarivo and Antsirabe (Fig. 7) structures trend roughly north–south. This region was studied in detail by Nédélec *et al.* (2000), Collins *et al.* (2003*a*), Raharimahefa and Kusky (2006, 2009) and Raharimahefa *et al.* (2013). The intensity of these structures increases toward the east, with at least four phases of deformation recognized, resulting from the Betsimisaraka Suture in eastern Madagascar.

D_1 deformation

Much like the western transect, at the outcrop scale we observe a pervasive foliation within the Betsiboka Suite, which we interpret as an S_1 foliation (Fig. 6e and f). The foliation is commonly preserved by the alignment of biotite, feldspar and quartz in orthogneisses. Structural measurements indicate that S_1 foliations between Antsirabe and Antananarivo dominantly strike roughly NNE, and dip moderately to the west (Fig. 7). North of Antananarivo, S_1 is more variable, and folded following the Antananarivo virgation zone (e.g. Nédélec *et al.* 2000). We observe a well-defined gneissic foliation within the Archean Betsiboka Suite, which may have originally formed prior to Neoproterozoic deformation. If this is the case, then subsequent Neoproterozoic deformation had approximately the same orientation, as we do not observe cross-cutting fabrics.

D_2 deformation

We do not observe D_2 structures at the outcrop scale in this section. However, the repetition of mapped Ambatolampy Group within the

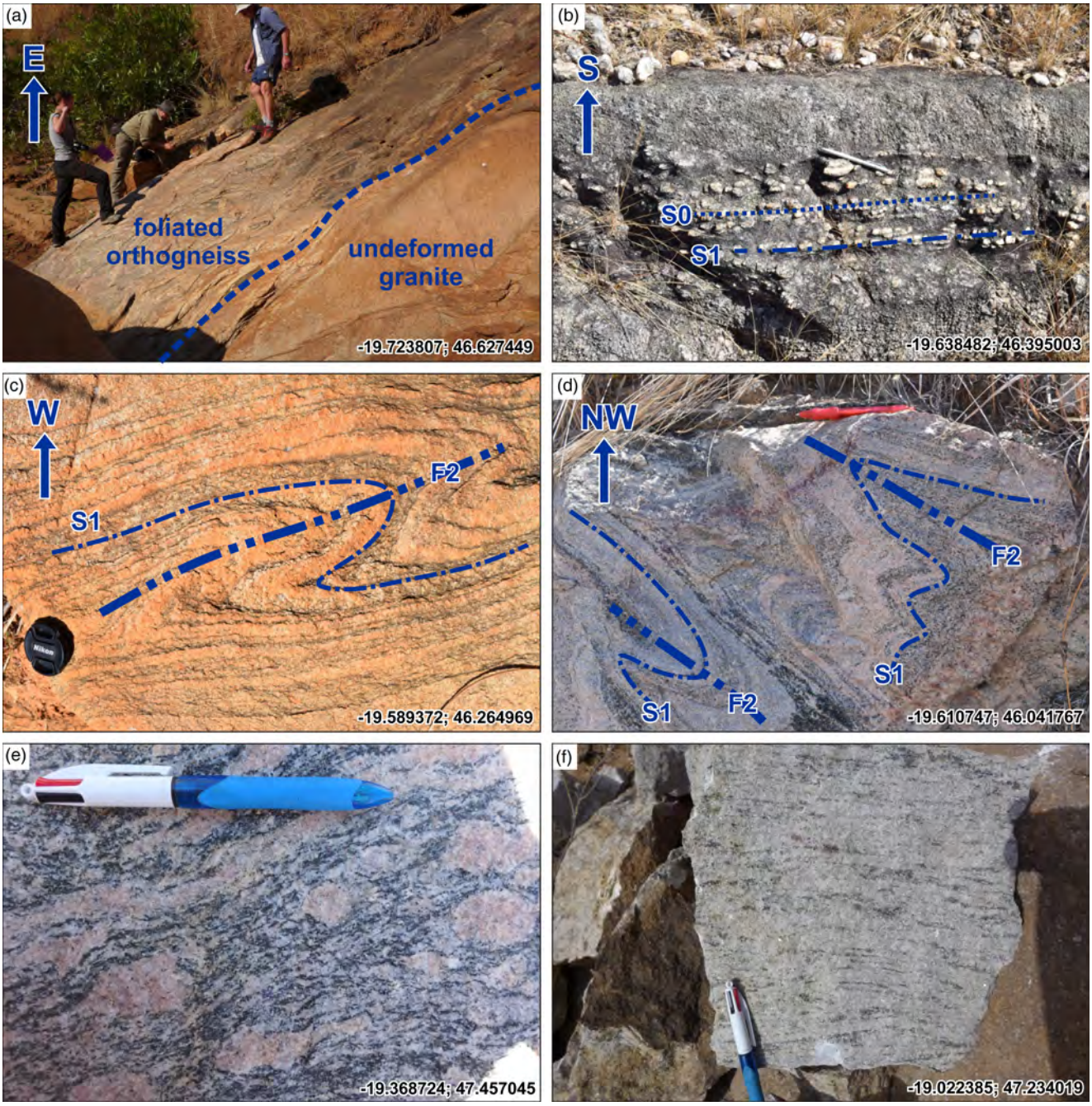

Fig. 6. Examples of samples and field outcrops; latitude and longitude are given in lower right corner and locations are shown in Figure 2. (**a**) Outcrop of foliated gneiss (left) intruded by undeformed granite (right); (**b**) flattened conglomerate where S_1 is parallel to S_0 in the Itremo Group of the Itremo sub-domain; (**c**) S_1 foliation folded around an F_2 fold in the Itremo sub-domain; (**d**) S_1 foliation folding around F_2 folds in the Itremo sub-domain; (**e**) S_1 foliation in a sample of augen gneiss of the Betsiboka Suite in the Antananarivo Domain; (**f**) S_1 foliation in a sample of gneiss from the Antananarivo Domain, west of Antananarivo.

Betsiboka Suite (Fig. 7) indicates that the two elongated Ambatolampy Group bodies in Figure 7 represent tight to isoclinal F_2 folds.

Thermochronology

A range of magmatic and orthogneiss samples were collected with the aim of having a representative sample set of the major magmatic suites of central Madagascar. This is important for determining overprinting relationships of key structural events, and determining relative and absolute timing constraints on these events. We used four geochronology or thermochronology techniques: zircon U–Pb (closure temperature *c*. 900–1000°C), apatite U–Pb (closure temperature *c*. 350–550°C), muscovite Rb–Sr (closure temperature *c*. 500–600°C) and biotite Rb–Sr (closure temperature *c*. 300–400°C). The results are summarized in Figure 8 and are documented more extensively in Supplementary B. Detailed methods for these techniques are also provided in Supplementary B. Rb–Sr mica dating using LA-QQQ-ICP-MS is a novel technique, and our data are some of the first published data of this kind. The good agreement of Rb–Sr mica ages with U–Pb apatite ages, which have similar closure temperatures, demonstrates that Rb–Sr mica dating is a useful tool for dating medium-temperature events. Because of the abundance of samples (41 in total), detailed results for each sample and outcrop, including plots of isotopic data, are provided in Supplementary B. Sample descriptions, location and age data are summarized in Table 1. Isotopic data are given in Supplementary C.

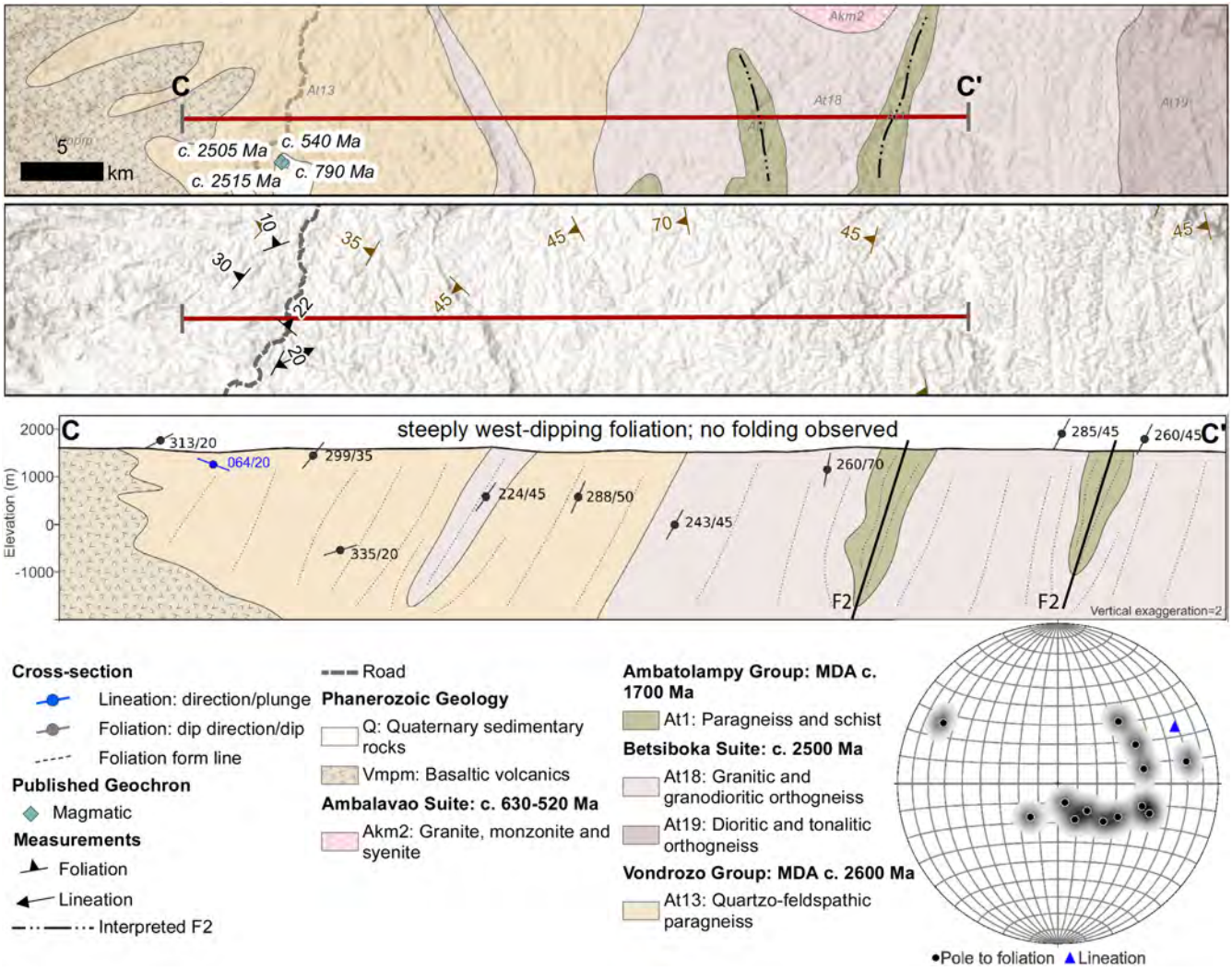

Fig. 7. Geological map, structural data and cross-section through the Antananarivo Domain. This transect does not contain the complex folding that we observe in the Ikalamavony and Itremo domains. Here, foliations are steeply west-dipping. Geological polygons are from Roig *et al.* (2012). Sections were generated using QProf plugin in QGIS. Structural measurements (dip direction/dip) within *c.* 2 km of the section are projected along the profile. Topographic profile was derived from 30 arc-second DEM of Africa (USGS).

Discussion

Structural evolution of central Madagascar

The structural styles of the Ikalamavony and Itremo domains are indistinguishable and we suggest that D_1–D_3 (and possibly D_4) in both domains were the result of the same orogenic system. Type 1 and type 2 fold interference patterns are common in fold-and-thrust belts, and more commonly form during progressive deformation rather than discrete deformation events. A myriad of complex processes ranging from rheological contrasts to progressive rotation during deformation commonly cause fold structures with trends that are oblique to the transport direction of the overall fold-and-thrust belt (e.g. Poblet and Lisle 2011). Therefore, we suggest that D_1–D_3 in the Ikalamavony Domain and Itremo sub-domain formed during the same orogenic event, through progressive deformation, consistent with the interpretation based on metamorphism in this region by Moine *et al.* (2014).

A structure with very similar geometry and orientation to the type 2 interference pattern highlighted in Figure 5 was modelled by Armistead *et al.* (2018). They showed that this type of feature formed from south-directed, tight, recumbent folding that was orthogonally overprinted by third-generation upright folding. In our example from the Itremo Group, the F_2 recumbent folding formed during south to slightly SW-directed folding that locally formed by roughly north–south shortening. The overprinting F_3 upright fold formed during roughly east–west shortening that resulted in a north- to NE-trending axial trace. These interpreted kinematics are consistent with previous interpretations for deformation in the Itremo Group (Collins *et al.* 2003*b*; Tucker *et al.* 2007).

As pointed out by Tucker *et al.* (2007), nappes in the southern Itremo Domain are east-verging and were probably produced within a zone of west-dipping subduction (present-day direction). We interpret structures in our study areas of the Ikalamavony and Itremo domains to be dominantly NW-trending, with NE-directed vergence, developed as a result of roughly NE–SW shortening (present-day orientation). We propose that continental collision southwest of the Ikalamavony Domain and Itremo sub-domain was responsible for deformation in central Madagascar. Subduction prior to continental collision was roughly SW dipping.

Tucker *et al.* (2007) proposed that complex folds in the Itremo sub-domain can be broadly considered in two groups: 'high-grade, internal nappes' and 'low-grade, external nappes'. These were considered to be separated by a west-dipping thrust fault, although the exact location of this boundary is ambiguous from the highly schematic diagrams presented in that study. We broadly agree that metamorphic grade and deformation intensity appear to increase toward the west; however, a sharp tectonic boundary has not been observed in this study within the Itremo Group. We do, however, see

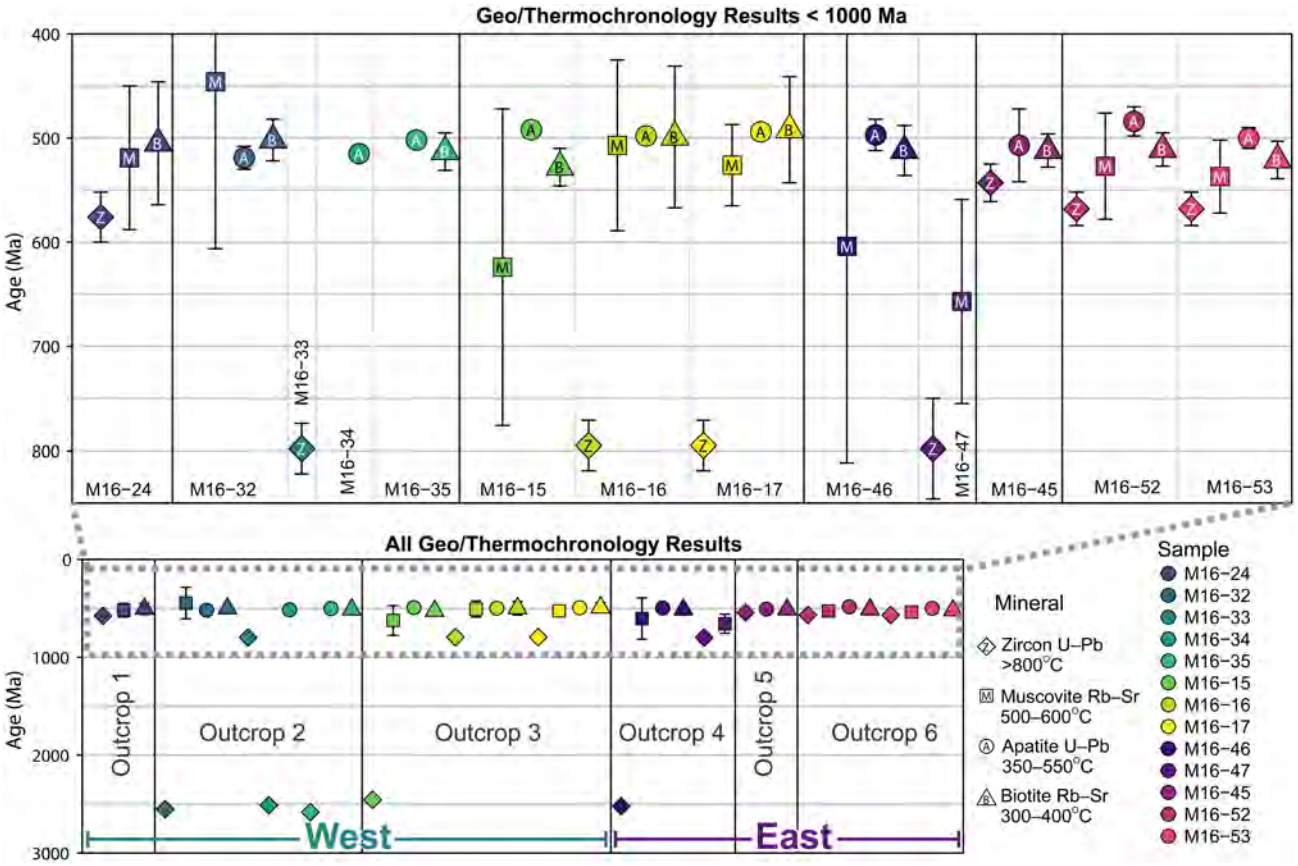

Fig. 8. Summary of geo- and thermochronology data for each sample and outcrop collected in this study. Error bars are 2σ. Sample locations are shown in Figure 2. The lower figure shows all of the sample data collected, and the upper figure focuses on all data that are younger than 1000 Ma. Plots of isotopic data associated with these calculated ages are presented in Supplementary B.

a major tectonic boundary between the Ikalamavony Domain and the Itremo–Antananarivo Domain. This boundary may more accurately reflect the boundary between the internal and external nappes proposed by Tucker *et al.* (2007).

The weakly defined, open folding associated with D_4 may have occurred in the late stages of folding and thrusting of the Itremo sub-domain and Ikalamavony Domain, or may be related to far-field deformation associated with orogenesis in eastern Madagascar (Collins *et al.* 2003*a*).

In the eastern part of the study area, east of the 'structural style boundary' in Figures 2 and 3, the deformation style changes in orientation and intensity. Transect C–C' is less deformed than the Ikalamavony and Itremo transects (Fig. 9), and we do not observe any complex fold interference patterns here. The orientation of structures also changes, and becomes more north- to NE-trending. Further east of our C–C' transect is the dextral Angavo Shear Zone, which was active at 550 ± 4 Ma (Raharimahefa and Kusky 2010). Collins *et al.* (2003*a*) constructed a cross-section from Antananarivo eastwards to Brickaville along the east coast of Madagascar (Fig. 9). This transect region contains a deformation sequence distinct from the Ikalamavony and Itremo domains and was therefore caused by a different tectonic event. Although controversial, there is significant metamorphic and structural evidence that the sequence of deformation described by Collins *et al.* (2003*a*) can be attributed to the *c.* 550 Ma Betsimisaraka Suture that amalgamated Madagascar with the Dharwar Craton of India.

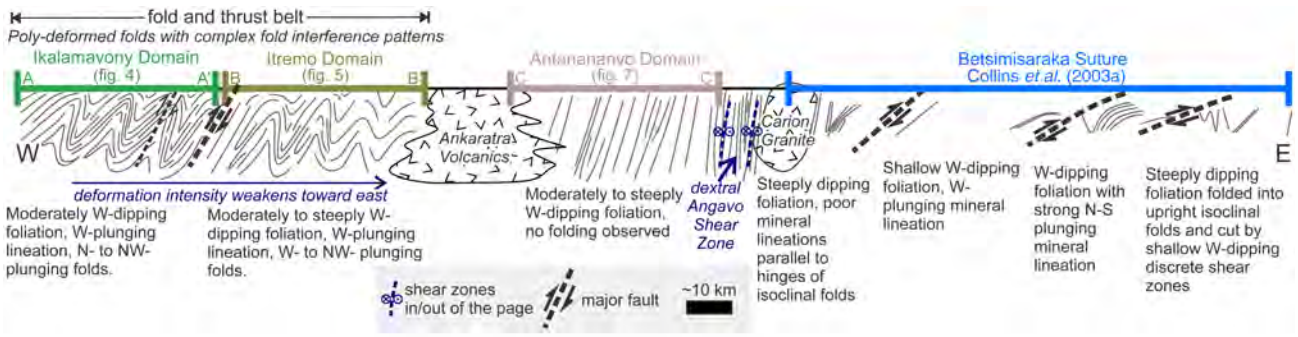

Fig. 9. Schematic cross-section through central Madagascar from Miandrivazo to Brickaville, combining the cross-sections of Figures 4, 5 and 7 and that of Collins *et al.* (2003*a*). The Ikalamavony and Itremo domains preserve the same structural styles and kinematics. A change in structural style occurs east of these sections, with the Antananarivo Domain section containing no complex fold interference patterns. Further east, Collins *et al.* (2003*a*) interpreted intense deformation associated with the Neoproterozoic–Cambrian Betsimisaraka Suture.

Temporal constraints on deformation

Relative timing of deformation

Understanding the ages of geological units that are deformed and undeformed can help constrain the timing of deformation. At the regional scale in the western transect, the *c*. 850–750 Ma Imorona–Itsindro Suite is poly-deformed, and therefore was intruded prior to the onset of at least D_2 and D_3. In the eastern transect and in the region studied by Nédélec *et al.* (2000), Collins *et al.* (2003*a*) and Raharimahefa and Kusky (2006, 2009), the Imorona–Itsindro Suite is not poly-deformed into complex fold interference patterns but instead is elongated along the length of the *c*. 550 Ma Angavo shear zone (Figs 1b and 9). This indicates that different structural regimes are responsible for deformation in the west and east of Madagascar.

In the Ikalamavony Domain and Itremo sub-domain, the *c*. 550 Ma Ambalavao Suite is undeformed and therefore provides a minimum age constraint on deformation here. In the east, the Ambalavao Suite is represented by both deformed and undeformed rocks. We therefore suggest that deformation in the Ikalamavony Domain and Itremo sub-domain occurred between *c*. 750 and *c*. 550 Ma, which is consistent with interpretations by Tucker *et al.* (2007). Deformation in eastern Madagascar probably occurred later at *c*. 550 Ma, which is consistent with age determinations for the Angavo Shear Zone and Antananarivo virgation zone (Paquette and Nédélec 1998; Nédélec *et al.* 2000; Meert *et al.* 2003; Raharimahefa and Kusky 2010).

Thermochronology

We have used minerals that record a range of temperatures in an attempt to capture different stages of the tectonic evolution of Madagascar. Our sampling included the major magmatic suites of Madagascar, including the *c*. 2500 Ma Betsiboka Suite, the *c*. 850–750 Ma Imorona–Itsindro Suite and the *c*. 550 Ma Ambalavao Suite (Fig. 8). Interestingly, apatite U–Pb ages, which record when the minerals were cooled through *c*. 350–550°C (Chamberlain and Bowring 2001; Schoene and Bowring 2007), are all within a narrow age range from 519 ± 11 to 484 ± 14 Ma, regardless of their magmatic crystallization age. Muscovite and biotite, which have Rb–Sr closure temperatures of *c*. 500–600°C (Armstrong *et al.* 1966) and *c*. 300–400°C (Verschure *et al.* 1980; Del Moro *et al.* 1982; Jenkin *et al.* 2001), respectively, also record ages within a narrow range between 657 ± 98 and 446 ± 161 Ma for muscovite (albeit with large uncertainties) and between 528 ± 18 and 492 ± 51 Ma for biotite. This implies that the final stages of orogenesis in Madagascar, regardless of whether this was in the west or east, affected the entire central region of the island, where rocks were either reset to at least *c*. 500°C or cooled through *c*. 500°C at *c*. 500 Ma.

Multiple thermochronometers have provided insights into the medium-temperature thermo-tectonic evolution across the western and eastern part of Madagascar. As we have shown here, the more recent *c*. 520–480 Ma thermo-tectonic event affected the entire island such that it cooled synchronously through *c*. 500–300°C at *c*. 500 Ma. The *c*. 520–480 Ma regional thermal perturbation would have overprinted prior events, obscuring any evidence of a pre-existing thermo-tectonic evolution. Using thermochronometers that record temperatures higher than *c*. 600°C (e.g. monazite U–Pb) in future research may provide further constraints on the timing of orogenesis, particularly in regions distal from the collision zone and in rocks that are not in contact with the Ambalavao Suite, where temperatures during the *c*. 550 Ma event may not have been hot enough to cause complete reset. Without direct dating of the structures observed, we need to look further afield for evidence of subduction and collision that resulted in deformation of central Madagascar.

Tectonic model for the evolution of central Madagascar

The boundaries between the major domains in southern Madagascar represent possible suture zones responsible for deformation in the Ikalamavony Domain and Itremo sub-domain. Prior to the juxtaposition of the Itremo sub-domain and Ikalamavony Domain, we agree with previous interpretations that the Itremo Group was deposited on the Antananarivo Domain basement (Fig. 10a) (Cox *et al.* 1998, 2004) and that the Ikalamavony Domain evolved as an exotic island arc terrane (Fig. 10b) (Archibald *et al.* 2017*a*). The presence of the Imorona–Itsindro Suite in the Ikalamavony Domain indicates that it must have accreted to central Madagascar before *c*. 850 Ma (Fig. 10c). A large west-dipping thrust fault separating the Ikalamavony Domain from the Itremo sub-domain (Figs 5 and 9) possibly represents this suture zone (schematic thrust in Fig. 10c). This implies west-dipping subduction, which is consistent with previous models for the accretion of the Ikalamavony Domain to central Madagascar (e.g. Boger *et al.* 2019).

Based on the interpreted kinematics and overprinting relationships, deformation of the Ikalamavony Domain and Itremo sub-domain was the result of continental collision. Increasing deformation intensity in the Ikalamavony Domain and the orientation of structures imply that the collision zone must have lain SW of these domains.

Boger *et al.* (2014, 2019) suggested that the Beraketa high-strain zone that separates the Anosyen and Androyen domains represents a *c*. 580–520 Ma suture. This interpretation was based on *c*. 630–600 Ma metamorphism restricted to the west of this high-strain zone, and widespread *c*. 580–520 Ma magmatism and metamorphism on both sides of the high-strain zone. In this model, the subduction zone was east-dipping (present-day direction), and resulted in the syn- to post-tectonic Ambalavao granites throughout Madagascar (Fig. 10). However, the structures we have described and those described by Tucker *et al.* (2007) require a roughly west-dipping (top to the east; present-day direction) sense of movement, making an east-dipping subduction zone beneath the Antananarivo Craton at this time unlikely.

Boger *et al.* (2014, 2019) interpreted that another west-dipping subduction zone was active beneath the Vohibory Domain until *c*. 650 Ma (Fig. 10e), and that collision between the Vohibory Domain and Androyen Domain occurred at *c*. 630–610 Ma (Fig. 10f), outboard from the Antananarivo Craton (marked by the Ampanihy high-strain zone–Vohibory Suture in Fig. 1b). In this model, subduction was west dipping (Fig. 10e and f). Horton *et al.* (2016) also interpreted that the Androyen and Anosyen domains collided with the Vohibory Domain at *c*. 630 Ma, based on monazite and zircon geochronology. In our view, this collision zone is most consistent with evidence we see from a structural perspective. We therefore propose that the Vohibory Suture was responsible for high-intensity deformation and poly-deformed folds in the Ikalamavony and Itremo domains. It is likely that deformation associated with this event is present in the Androyen and Anosyen domains; however, structures are much more steeply dipping and more highly strained here, meaning that recognition of distinct folding events is difficult (Fig. 10e). As interpreted by Boger *et al.* (2014, 2019), the Vohibory Suture would have been west dipping (present-day direction), resulting in the emplacement of the *c*. 630 Ma Marasavoa Suite in the Vohibory Domain. Metamorphism of this age is also recorded in the Androyen Domain.

A change in deformation style and kinematics toward the east of Madagascar and younger geochronological constraints indicate that complex folding in eastern Madagascar formed in response to a different event from that in the west (Fig. 10g). Although we did not look at this region in great detail, the changes across central Madagascar from west to east, combined with extensive structural

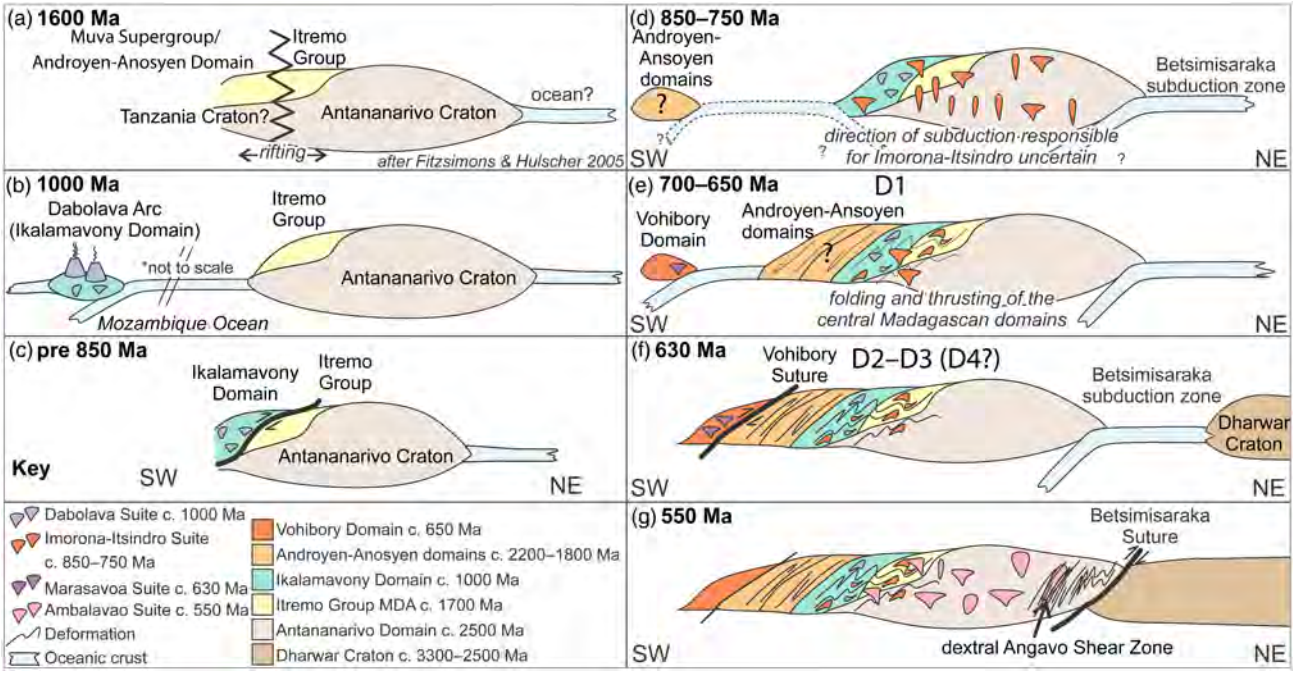

Fig. 10. Schematic diagram showing our interpretation of the evolution of central Madagascar. (**a**) Some time after the deposition of the Itremo Group–Muva Supergroup onto the Antananarivo Craton–Tanzania Craton, these regions begin to rift (Cox *et al.* 2004; Fitzsimons and Hulscher 2005); (**b**) at *c.* 1000 Ma the Dabolava Arc forms as an oceanic island arc outboard from the Antananarivo Domain (Archibald *et al.* 2017*a*); (**c**) prior to the intrusion of the *c.* 850–750 Ma Imorona–Itsindro Suite, the Ikalamavony Domain is thrust over the Antananarivo–Itremo Domain; (**d**) the intrusion of the Imorona–Itsindro Suite results from Andean-type subduction, with polarity uncertain (Archibald *et al.* 2017*b*); (**e**) west-dipping subduction occurs beneath the Vohibory Domain, with the beginning of deformation (D_1); (**f**) closure of the Mozambique Ocean along the Vohibory Suture results in complex deformation that we have interpreted in central Madagascar (D_2–D_3, and possibly D_4); (**g**) final amalgamation of central Gondwana occurs along the *c.* 550 Ma Betsimisaraka Suture.

studies published on eastern Madagascar (Martelat *et al.* 2000; Nédélec *et al.* 2000; Collins *et al.* 2003*a*; Raharimahefa and Kusky 2006, 2009; Raharimahefa *et al.* 2013), indicate that a west-dipping subduction zone was active at *c.* 550 Ma, somewhere in the region of the Betsimisaraka Suture.

Conclusions

We have integrated remote sensing, field data and thermochronology to unravel complex deformation in the Ikalamavony and Itremo domains of central Madagascar. We have recognized four generations (D_1–D_4) of deformation that resulted in complex fold interference patterns in the Ikalamavony and Itremo domains of central Madagascar. We interpret deformation here as the result of *c.* 630 Ma collision of Azania with Africa along the Vohibory Suture in southwestern Madagascar. In eastern Madagascar, deformation is syn- to post-550 Ma, and probably formed in response to the final closure of the Mozambique Ocean along the Betsimisaraka Suture that amalgamated Madagascar with the Dharwar Craton of India. Apatite U–Pb and novel LA-QQQ-ICP-MS muscovite and biotite Rb–Sr thermochronology indicates that much of central Madagascar cooled through *c.* 500°C at *c.* 500 Ma. We have shown the importance of using medium-temperature thermochronometers to date the cooling stages after orogenesis, and the potential for Rb–Sr mica dating to provide useful thermochronological constraints.

Acknowledgements EarthArXiv is thanked for hosting a preprint version of this paper; earlier versions of this paper can be found there at doi.org/10.31223/osf.io/x46vc. We would like to thank P. Macey, from the Council for Geoscience, South Africa, for providing additional structural data. R. Tamblyn is thanked for helpful discussions about Rb–Sr data. We thank B. Emmel, the editor D. Gasser and two anonymous reviewers for their helpful feedback. This paper was also reviewed as part of S.A.'s PhD thesis by K. Goodenough and P. Johnson; their valuable feedback greatly improved this paper. This is a contribution to IGCP projects 628 (Gondwana Map) and 648 (Supercontinent Cycles and Global Geodynamics).

Funding S.A. was funded by an Australian government PhD Scholarship and A.C. is funded by Australian Research Council Future Fellowship FT120100340.

Author contributions **SEA:** conceptualization (lead), data curation (lead), formal analysis (lead), investigation (lead), methodology (lead), writing – original draft (lead), writing – review & editing (lead); **ASC:** conceptualization (equal), funding acquisition (lead), writing – original draft (supporting), writing – review & editing (supporting); **AR:** methodology (equal), validation (equal); **GJ:** methodology (equal), validation (equal), visualization (equal); **JG:** methodology (equal), validation (equal), visualization (equal); **SG:** data curation (equal), methodology (supporting), validation (supporting); **MLB:** data curation (supporting), investigation (supporting); **JDF:** supervision (supporting); **TR:** investigation (supporting), project administration (supporting)

Scientific editing by Deta Gasser

References

Archibald, D.B., Collins, A.S. *et al.* 2015. Towards unravelling the Mozambique Ocean conundrum using a triumvirate of zircon isotopic proxies on the Ambatolampy Group, central Madagascar. *Tectonophysics*, **662**, 167–182, https://doi.org/10.1016/j.tecto.2015.02.018

Archibald, D.B., Collins, A.S., Foden, J.D., Payne, J.L., Macey, P.H., Holden, P. and Razakamanana, T. 2017*a*. Stenian–Tonian arc magmatism in west–central Madagascar: the genesis of the Dabolava Suite. *Journal of the Geological Society, London*, **175**, 111–119, https://doi.org/10.1144/jgs2017-028

Archibald, D.B., Collins, A.S., Foden, J.D. and Razakamanana, T. 2017*b*. Tonian arc magmatism in central Madagascar: the petrogenesis of the Imorona–Itsindro Suite. *Journal of Geology*, **125**, 271–297, https://doi.org/10.1086/691185

Armistead, S.E., Collins, A.S., Payne, J.L., Foden, J.D., De Waele, B., Shaji, E. and Santosh, M. 2017. A re-evaluation of the Kumta Suture in western peninsular India and its extension into Madagascar. *Journal of Asian Earth Sciences*, **157**, 317–328, https://doi.org/10.1016/j.jseaes.2017.08.020

Armistead, S.E., Betts, P.G., Ailleres, L., Armit, R.J. and Williams, H.A. 2018. Cu–Au mineralisation in the Curnamona Province, South Australia: A hybrid stratiform genetic model for Mesoproterozoic IOCG systems in Australia. *Ore Geology Reviews*, **94**, 104–117, https://doi.org/10.1016/j.oregeorev.2018.01.024

Armistead, S.E., Collins, A. *et al.* 2019. Evolving marginal terranes during Neoproterozoic supercontinent reorganisation: constraints from the Bemarivo Domain in northern Madagascar. *Tectonics*, **38**, 2019–2035, https://doi.org/10.1029/2018TC005384

Armstrong, R.L., Jäger, E. and Eberhardt, P. 1966. A comparison of K–Ar and Rb–Sr ages on Alpine biotites. *Earth and Planetary Science Letters*, **1**, 13–19, https://doi.org/10.1016/0012-821X(66)90097-5

BGS–USGS–GLW. 2008. Revision de la cartographie géologique et minière des zones Nord et Centre de Madagascar – British Geological Survey Research Report CR/08/078. Republique de Madagascar Ministère de L'engergie et des Mines, 1-1049.

Boger, S.D., Hirdes, W., Ferreira, C.A.M., Schulte, B., Jenett, T. and Fanning, C.M. 2014. From passive margin to volcano-sedimentary forearc: The Tonian to Cryogenian evolution of the Anosyen Domain of southeastern Madagascar. *Precambrian Research*, **247**, 159–186, https://doi.org/10.1016/j.precamres.2014.04.004

Boger, S.D., Hirdes, W., Ferreira, C.A.M., Jenett, T., Dallwig, R. and Fanning, C.M. 2015. The 580–520 Ma Gondwana suture of Madagascar and its continuation into Antarctica and Africa. *Gondwana Research*, **28**, 1048–1060, https://doi.org/10.1016/j.gr.2014.08.017

Boger, S.D., Maas, R. *et al.* 2019. The tectonic domains of southern and western Madagascar. *Precambrian Research*, **327**, 144–175, https://doi.org/10.1016/j.precamres.2019.03.005

Chamberlain, K.R. and Bowring, S.A. 2001. Apatite–feldspar U–Pb thermochronometer: a reliable, mid-range (~450°C), diffusion-controlled system. *Chemical Geology*, **172**, 173–200, https://doi.org/10.1016/S0009-2541(00)00242-4

Collins, A.S. 2006. Madagascar and the amalgamation of Central Gondwana. *Gondwana Research*, **9**, 3–16, https://doi.org/10.1016/j.gr.2005.10.001

Collins, A.S. and Pisarevsky, S.A. 2005. Amalgamating eastern Gondwana: The evolution of the Circum-Indian Orogens. *Earth-Science Reviews*, **71**, 229–270, https://doi.org/10.1016/j.earscirev.2005.02.004

Collins, A.S. and Windley, B.F. 2002. The tectonic evolution of central and northern Madagascar and its place in the final assembly of Gondwana. *Journal of Geology*, **110**, 325–339, https://doi.org/10.1086/339535

Collins, A.S., Razakamanana, T. and Windley, B.F. 2000. Neoproterozoic extensional detachment in central Madagascar: implications for the collapse of the East African Orogen. *Geological Magazine*, **137**, 39–51, https://doi.org/10.1017/S001675680000354X

Collins, A.S., Fitzsimons, I.C.W., Hulscher, B. and Razakamanana, T. 2003*a*. Structure of the eastern margin of the East African Orogen in central Madagascar. *Precambrian Research*, **123**, 111–133, https://doi.org/10.1016/S0301-9268(03)00064-0

Collins, A.S., Johnson, S., Fitzsimons, I.C., Powell, C.M., Hulscher, B., Abello, J. and Razakamanana, T. 2003*b*. Neoproterozoic deformation in central Madagascar: a structural section through part of the East African Orogen. Geological Society, London, Special Publications, **206**, 363–379, https://doi.org/10.1144/GSL.SP.2003.206.01.17

Collins, A.S., Kröner, A., Fitzsimons, I.C.W. and Razakamanana, T. 2003*c*. Detrital footprint of the Mozambique ocean: U–Pb SHRIMP and Pb evaporation zircon geochronology of metasedimentary gneisses in eastern Madagascar. *Tectonophysics*, **375**, 77–99, https://doi.org/10.1016/S0040-1951(03)00334-2

Collins, A.S., Kinny, P.D. and Razakamanana, T. 2012. Depositional age, provenance and metamorphic age of metasedimentary rocks from southern Madagascar. *Gondwana Research*, **21**, 353–361, https://doi.org/10.1016/j.gr.2010.12.006

Cox, R., Armstrong, R.A. and Ashwal, L.D. 1998. Sedimentology, geochronology and provenance of the Proterozoic Itremo Group, central Madagascar, and implications for pre-Gondwana palaeogeography. *Journal of the Geological Society, London*, **155**, 1009–1024, https://doi.org/10.1144/gsjgs.155.6.1009

Cox, R., Coleman, D.S. *et al.* 2004. Proterozoic tectonostratigraphy and paleogeography of central Madagascar derived from detrital zircon U–Pb age populations. *Journal of Geology*, **112**, 379–399, https://doi.org/10.1086/421070

Del Moro, A., Puxeddu, M., di Brozolo, F.R. and Villa, I.M. 1982. Rb–Sr and K–Ar ages on minerals at temperatures of 300°–400°C from deep wells in the Larderello geothermal field (Italy). *Contributions to Mineralogy and Petrology*, **81**, 340–349, https://doi.org/10.1007/BF00371688

De Waele, B., Thomas, R.J. *et al.* 2011. Provenance and tectonic significance of the Palaeoproterozoic metasedimentary successions of central and northern Madagascar. *Precambrian Research*, **189**, 18–42, https://doi.org/10.1016/j.precamres.2011.04.004

de Wit, M.J., Bowring, S.A., Ashwal, L.D., Randrianasolo, L.G., Morel, V.P.I. and Rambeloson, R.A. 2001. Age and tectonic evolution of Neoproterozoic ductile shear zones in southwestern Madagascar, with implications for Gondwana studies. *Tectonics*, **20**, 1–45, https://doi.org/10.1029/2000TC900026

Emmel, B., Jons, N. *et al.* 2008. From closure of the Mozambique Ocean to Gondwana breakup: new evidence from geochronological data of the Vohibory Terrane, southwest Madagascar. *Journal of Geology*, **116**, 21–38, https://doi.org/10.1086/524121

Fernandez, A., Schreurs, G., Villa, I.M., Huber, S. and Rakotondrazafy, M. 2003. Age constraints on the tectonic evolution of the Itremo region in Central Madagascar. *Precambrian Research*, **123**, 87–110, https://doi.org/10.1016/S0301-9268(03)00063-9

Fitzsimons, I.C.W. and Hulscher, B. 2005. Out of Africa: detrital zircon provenance of central Madagascar and Neoproterozoic terrane transfer across the Mozambique Ocean. *Terra Nova*, **17**, 224–235, https://doi.org/10.1111/j.1365-3121.2005.00595.x

Grasemann, B., Wiesmayr, G., Draganits, E. and Fusseis, F. 2004. Classification of refold structures. *Journal of Geology*, **112**, 119–125, https://doi.org/10.1086/379696

Horton, F., Hacker, B., Kylander-Clark, A., Holder, R. and Jöns, N. 2016. Focused radiogenic heating of middle crust caused ultrahigh temperatures in southern Madagascar. *Tectonics*, **35**, 293–314, https://doi.org/10.1002/2015TC004040

Jenkin, G.R.T., Ellam, R.M., Rogers, G. and Stuart, F.M. 2001. An investigation of closure temperature of the biotite Rb–Sr system: The importance of cation exchange. *Geochimica et Cosmochimica Acta*, **65**, 1141–1160, https://doi.org/10.1016/S0016-7037(00)00560-3

Jöns, N. and Schenk, V. 2008. Relics of the Mozambique Ocean in the central East African Orogen: evidence from the Vohibory Block of southern Madagascar. *Journal of Metamorphic Geology*, **26**, 17–28, https://doi.org/10.1111/j.1525-1314.2007.00745.x

Jöns, N. and Schenk, V. 2011. The ultrahigh temperature granulites of southern Madagascar in a polymetamorphic context: implications for the amalgamation of the Gondwana supercontinent. *European Journal of Mineralogy*, **23**, 127–156, https://doi.org/10.1127/0935-1221/2011/0023-2087

Jöns, N., Emmel, B., Schenk, V. and Razakamanana, T. 2009. From orogenesis to passive margin—the cooling history of the Bemarivo Belt (N Madagascar), a multi-thermochronometer approach. *Gondwana Research*, **16**, 72–81, https://doi.org/10.1016/j.gr.2009.02.006

Kröner, A., Hegner, E., Collins, A.S., Windley, B.F., Brewer, T.S., Razakamanana, T. and Pidgeon, R.T. 2000. Age and magmatic history of the Antananarivo Block, central Madagascar, as derived from zircon geochronology and Nd isotopic systematics. *American Journal of Science*, **300**, 251–288, https://doi.org/10.2475/ajs.300.4.251

Macey, P.H., Bisnath, A., Yibas, B., Robson, L. and Andriamanantsoa, E. 2009. *Carte Géologique de Madagascar*. Council for Geoscience, Pretoria.

Macey, P.H., Thomas, R.J. *et al.* 2010. Mesoproterozoic geology of the Nampula Block, northern Mozambique: Tracing fragments of Mesoproterozoic crust in the heart of Gondwana. *Precambrian Research*, **182**, 124–148, https://doi.org/10.1016/j.precamres.2010.07.005

Martelat, J.-E., Lardeaux, J.-M., Nicollet, C. and Rakotondrazafy, R. 2000. Strain pattern and late Precambrian deformation history in southern Madagascar. *Precambrian Research*, **102**, 1–20, https://doi.org/10.1016/S0301-9268(99)00083-2

Meert, J.G., Nédélec, A. and Hall, C. 2003. The stratoid granites of central Madagascar: paleomagnetism and further age constraints on Neoproterozoic deformation. *Precambrian Research*, **120**, 101–129, https://doi.org/10.1016/S0301-9268(02)00161-4

Merdith, A.S., Collins, A.S. *et al.* 2017. A full-plate global reconstruction of the Neoproterozoic. *Gondwana Research*, **50**, 84–134, https://doi.org/10.1016/j.gr.2017.04.001

Moine, B. 1968. *Massif Schisto-Quartzo-Dolomitique: Region d'Ambatofinandrahana centre-ouest du socle cristallin precambrien de Madagascar*. Centre de l'Institut Géographique National, Tananarive.

Moine, B., Bosse, V., Paquette, J.-L. and Ortega, E. 2014. The occurrence of a Tonian–Cryogenian (~850 Ma) regional metamorphic event in Central Madagascar and the geodynamic setting of the Imorona–Itsindro (~800 Ma) magmatic suite. *Journal of African Earth Sciences*, **94**, 58–73, https://doi.org/10.1016/j.jafrearsci.2013.11.016

Nédélec, A., Ralison, B., Bouchez, J.L. and Grégoire, V. 2000. Structure and metamorphism of the granitic basement around Antananarivo: A key to the Pan-African history of central Madagascar and its Gondwana connections. *Tectonics*, **19**, 997–1020, https://doi.org/10.1029/2000TC900001

Paquette, J.-L. and Nédélec, A. 1998. A new insight into Pan-African tectonics in the East–West Gondwana collision zone by U–Pb zircon dating of granites from central Madagascar. *Earth and Planetary Science Letters*, **155**, 45–56, https://doi.org/10.1016/S0012-821X(97)00205-7

Paquette, J.-L., Nédélec, A., Moine, B. and Rakotondrazafy, M. 1994. U–Pb, single zircon Pb-evaporation, and Sm–Nd isotopic study of a granulite domain in SE Madagascar. *Journal of Geology*, **102**, 523–538, https://doi.org/10.1086/629696

Poblet, J. and Lisle, R.J. 2011. Kinematic evolution and structural styles of fold-and-thrust belts. Geological Society, London, Special Publications, **349**, 1–24, https://doi.org/10.1144/SP349.1

Raharimahefa, T. and Kusky, T.M. 2006. Structural and remote sensing studies of the southern Betsimisaraka Suture, Madagascar. *Gondwana Research*, **10**, 186–197, https://doi.org/10.1016/j.gr.2005.11.022

Raharimahefa, T. and Kusky, T.M. 2009. Structural and remote sensing analysis of the Betsimisaraka Suture in northeastern Madagascar. *Gondwana Research*, **15**, 14–27, https://doi.org/10.1016/j.gr.2008.07.004

Raharimahefa, T. and Kusky, T.M. 2010. Temporal evolution of the Angavo and related shear zones in Gondwana: Constraints from LA-MC-ICP-MS U–Pb zircon ages of granitoids and gneiss from central Madagascar. *Precambrian Research*, **182**, 30–42, https://doi.org/10.1016/j.precamres.2010.06.013

Raharimahefa, T., Kusky, T.M., Toraman, E., Rasoazanamparany, C. and Rasaonina, I. 2013. Geometry and kinematics of the late Proterozoic Angavo

Shear Zone, Central Madagascar: Implications for Gondwana assembly. *Tectonophysics*, **592**, 113–129, https://doi.org/10.1016/j.tecto.2013.02.014

Roig, J., Tucker, R., Delor, C., Peters, S. and Théveniaut, H. 2012. *Carte géologique de la République de Madagascar à 1/1 000 000*. Ministère des Mines, PGRM, Antananarivo.

Schoene, B. and Bowring, S.A. 2007. Determining accurate temperature–time paths from U–Pb thermochronology: An example from the Kaapvaal craton, southern Africa. *Geochimica et Cosmochimica Acta*, **71**, 165–185, https://doi.org/10.1016/j.gca.2006.08.029

Schofield, D.I., Thomas, R.J. *et al.* 2010. Geological evolution of the Antongil Craton, NE Madagascar. *Precambrian Research*, **182**, 187–203, https://doi.org/10.1016/j.precamres.2010.07.006

Service Géologique de Madagascar. 1962. *Moramanga–Brickaville*. Service Géologique de Madagascar.

Service Géologique de Madagascar. 1963*a*. *Antsirabe–Ampatolampy*. Service Géologique de Madagascar.

Service Géologique de Madagascar. 1963*b*. *Miarinarivo–Tanarive*. Service Géologique de Madagascar.

Thomas, R.J., De Waele, B. *et al.* 2009. Geological evolution of the Neoproterozoic Bemarivo Belt, northern Madagascar. *Precambrian Research*, **172**, 279–300, https://doi.org/10.1016/j.precamres.2009.04.008

Tucker, R., Ashwal, L., Handke, M., Hamilton, M., Le Grange, M. and Rambeloson, R. 1999. U–Pb geochronology and isotope geochemistry of the Archean and Proterozoic rocks of north–central Madagascar. *Journal of Geology*, **107**, 135–153, https://doi.org/10.1086/314337

Tucker, R.D., Kusky, T.M., Buchwaldt, R. and Handke, M.J. 2007. Neoproterozoic nappes and superposed folding of the Itremo Group, west–central Madagascar. *Gondwana Research*, **12**, 356–379, https://doi.org/10.1016/j.gr.2006.12.001

Tucker, R., Roig, J.-Y. *et al.* 2011. Neoproterozoic extension in the Greater Dharwar Craton: a reevaluation of the "Betsimisaraka suture" in Madagascar. *Canadian Journal of Earth Sciences*, **48**, 389–417, https://doi.org/10.1139/E10-034

Tucker, R.D., Roig, J.Y., Moine, B., Delor, C. and Peters, S.G. 2014. A geological synthesis of the Precambrian shield in Madagascar. *Journal of African Earth Sciences*, **94**, 9–30, https://doi.org/10.1016/j.jafrearsci.2014.02.001

Verschure, R.H., Andriessen, P.A.M., Boelrijk, N.A.I.M., Hebeda, E.H., Maijer, C., Priem, H.N.A. and Verdurmen, E.A.T. 1980. On the thermal stability of Rb–Sr and K–Ar biotite systems: Evidence from coexisting Sveconorwegian (*ca*. 870 Ma) and Caledonian (*ca*. 400 Ma) biotites in SW Norway. *Contributions to Mineralogy and Petrology*, **74**, 245–252, https://doi.org/10.1007/BF00371694

Australian Geoscience Council Convention, Adelaide, Australia, Form: poster.

A new Technique in Dating Proterozoic Shear Zones: In-situ Rb-Sr dating of Umm Farwah Shear zone, Arabian Shield using LA-QQQ

Ahmad Redaa[1,2], Ahmed Hassan[2], Juraj Farkas[1], Sarah Gilbert[1], Thomas Zack[3], Alan Collins[1]

[1]The University of Adelaide, Adelaide, Australia

[2]King Abdulaziz University, Jeddah, Saudi Arabia

[3] University of Gothenburg, Gothenburg, Sweden

Rb-Sr dating system is a powerful geochronological tool to constrain the time of magma crystallisations. The $^{87}Rb/^{86}Sr$ and $^{87}Sr/^{86}Sr$ ratios is required to determine the ages, but the similarity of parent and daughter masses was preventing the in-situ Rb-Sr dating, and the column chemistry is needed to solve the isobaric interference between ^{87}Rb and ^{87}Sr, which can be time consuming. Attaching a laser ablation (LA) with triple quadrupole inductively coupled plasma mass spectrometry (QQQ-ICP) allows the in-situ Rb-Sr dating of igneous minerals in solid form with no need for dissolving whole samples. The QQQ-ICP system composed of a reaction cell sandwiched between two quadrupoles, and filling the cell with gases such as O_2 or N_2O shifts the Sr to SrO^+, as a result of the online reaction, whereas Rb does not react. Consequently, the Sr isotopes mass will be shifted to higher values by adding 16 amu of the oxygen, and the QQQ-ICP detector will count the Sr signal based on the new masses whereas the Rb signals will be counted at the original Rb mass. The technique was applied to constrain the age of phlogopite sample from Bekily region, Madagascar, and the results were corrected against the Mica-Mg nano-powder pellet.

Geoanalysis 2018, Sydney, Australia, Form: oral presentation.

Testing the limits of in-situ Rb-Sr dating of igneous minerals by LA-ICP-QQQ

Ahmad Redaa[1], Juraj Farkas[2], Sarah Gilbert[3], Thomas Zack[4], Fred Fryer[5], Benjamin Wade[6], Alan Collins[7]

[1]The University of Adelaide (ahmad.redaa@adelaide.edu.au)
[2]The University of Adelaide (juraj.farkas@adelaide.edu.au)
[3]The University of Adelaide (sarah.gilbert@adelaide.edu.au)
[4]University of Gothenburg (thomas.zack@gu.se)
[5]Agilent Technologies (fred_fryer@agilent.com)
[6]The University of Adelaide (benjamin.wade@adelaide.edu.au)
[7]The University of Adelaide (alan.collins@adelaide.edu.au)

Rb-Sr dating system is a powerful tool to constrain the timing of igneous rocks crystallisation. Coupling a laser ablation (LA) system with a "triple quad" inductivly coupled plasma mass spectrometer (ICP-QQQ) makes the in-situ Rb-Sr dating of individual igneous minerals possible [1]. The precision and accuracy of this technique is sensitive to several analytical parameters, including the spot size of the laser beam, and related matrix and down hole fractionation effects. This study aims to investigate the impact of these issues on the Rb-Sr age of an igneous mica analysed by an Agilent 8900 ICP-QQQ filled with N_2O as a reaction gas. The mica (MDC), which has an expected age of 519.4 ± 6.5 Ma [1], was collected from the Ampandrandava phlogopite quarry, Madagascar, mounted vertically and ablated by two different models of laser. One an ASI RESOlution ArF 193µm excimer system, the other an ESI NWR213 Nd-YAG system. All results were corrected to the primary Mica Mg nano-powder pellet standard [1]. The obtained age of MDC mica from the NWR213 laser is 521.2 ± 6.6 Ma, whereas the obtained age from the excimer laser is 528 ± 4 Ma. The ages are within the expected range but the raw signals from both lasers were vary and influenced by ablation characteristics of each laser including the ablation rate and aerosol formation processes. In addition, the differences between the Mica-Mg and MDC in physical properties have significant impact on the accuracy by adding 5 – 10% of uncertainty onto any unknown sample. The precision and the accuracy can be assessed by using the MDC mica as a secondary standard because it has well-known age and its RSD of $^{87}Rb/^{86}Sr$ did not exceed 1.75% with the excimer laser.

[1] Hogmalm, et al. (2017), *Journal of Analytical Atomic Spectrometry* **32**, 305-313.

The first in-situ Rb/Sr dating of biotite in the Arabian Shield

Ahmad A. Reda [1,2*], Lise M. Jensen [1], Juraj Farkas[1], Thomas Zack[3], Alan Collins[1], John Foden[1]

1 The University of Adelaide, Adelaide (Australia) *(ahmad.redaa@adelaide.edu.au)

2 King Abdulaziz University, Jeddah (Saudi Arabia)

3 University of Gothenburg, Gothenburg (Sweden)

Rubidium and strontium Rb-Sr radiogenic system is useful as a geochronological tool to constrain the formation and/or cooling age for important major igneous minerals such as Rb-rich micas and/or feldspars. The analytical challenges related to precise Rb-Sr age determinations are related to isobaric interferences between the ^{87}Rb and ^{87}Sr. The use of column chemistry method can solve the isobaric issues. However, the disadvantage is that this method is time-consuming, might cause isotopic fractionation (although this is commonly corrected via normalisation), and the introduction of blank. A reaction cell placed between two quadrupoles is allowing online separation of Rb and Sr by reacting them with different gases such as O_2, N_2O and SF_6 within the cell. Consequently, Sr will react to produce new components whereas Rb will not react. The second quadrupole (Q2) will filter ions based on mass-to-charge (*m/z*), whereby Sr is separated from Rb by difference of mass. Laser ablation coupled with such a triple quadrupole inductively coupled plasma mass spectrometer (ICP-QQQ) makes in-situ analysis of Rb-Sr possible to date individual minerals(Zack & Hogmalm 2016), similar to U-Pb zircon dating. This study aims to apply this method to date the post-tectonic Kawr Suite (KW) located in the southeast of Asir terrain, Arabian Shield. Seven grains of biotite were picked from KW granodiorite by hand under binocular microscope, mounted and polished. An Agilent 8900 ICP-QQQ was used to analyse the Rb and Sr in MS/MS mode, and the instrument settings were adjusted during NIST SRM 610 ablation. The N_2O gas (5% total flow) was used for online chemical separation, and about 99% of the Sr shifted to SrO^+. The size of laser spots was 74 µm, and the ablation period was 84 seconds. The results were corrected to Mica-Mg (nano-particulate pressed powder of natural micas) which was developed to calibrate minerals with high Rb and low Sr (Hogmalm et al. 2017). The acquired LA-QQQ Rb-Sr isochron age of the Kawr Suite is 675±40 Ma. This age is within the error and overall range of the published U-Pb ages of Kawr Suite (650-620 Ma (Johnson 2006)). Error on ages are expected to decline with further analysis to values around 1.5% or better (Hogmalm et al. 2017). The further applications for this LA-QQQ technique in the Arabian Shield are provenance identification of micas and dating of detrital micas.

Hogmalm, KJ, Zack, T, Karlsson, AKO, Sjoqvist, ASL & Garbe-Schonberg, D 2017, 'In situ Rb-Sr and K-Ca dating by LA-ICP-MS/MS: an evaluation of N2O and SF6 as reaction gases', *Journal of Analytical Atomic Spectrometry*, vol. 32, no. 2, pp. 305-313.

Johnson, PR 2006, *Explanatory notes to the map of Proterozoic geology of western Saudi Arabia*, Technical Report SGS-TR-2006-4, Saudi Geological Survey, Jeddah.

Zack, T & Hogmalm, KJ 2016, 'Laser ablation Rb/Sr dating by online chemical separation of Rb and Sr in an oxygen-filled reaction cell', *Chemical Geology*, vol. 437, pp. 120-133.